

Research and Technology 1988

GODDARD SPACE FLIGHT CENTER

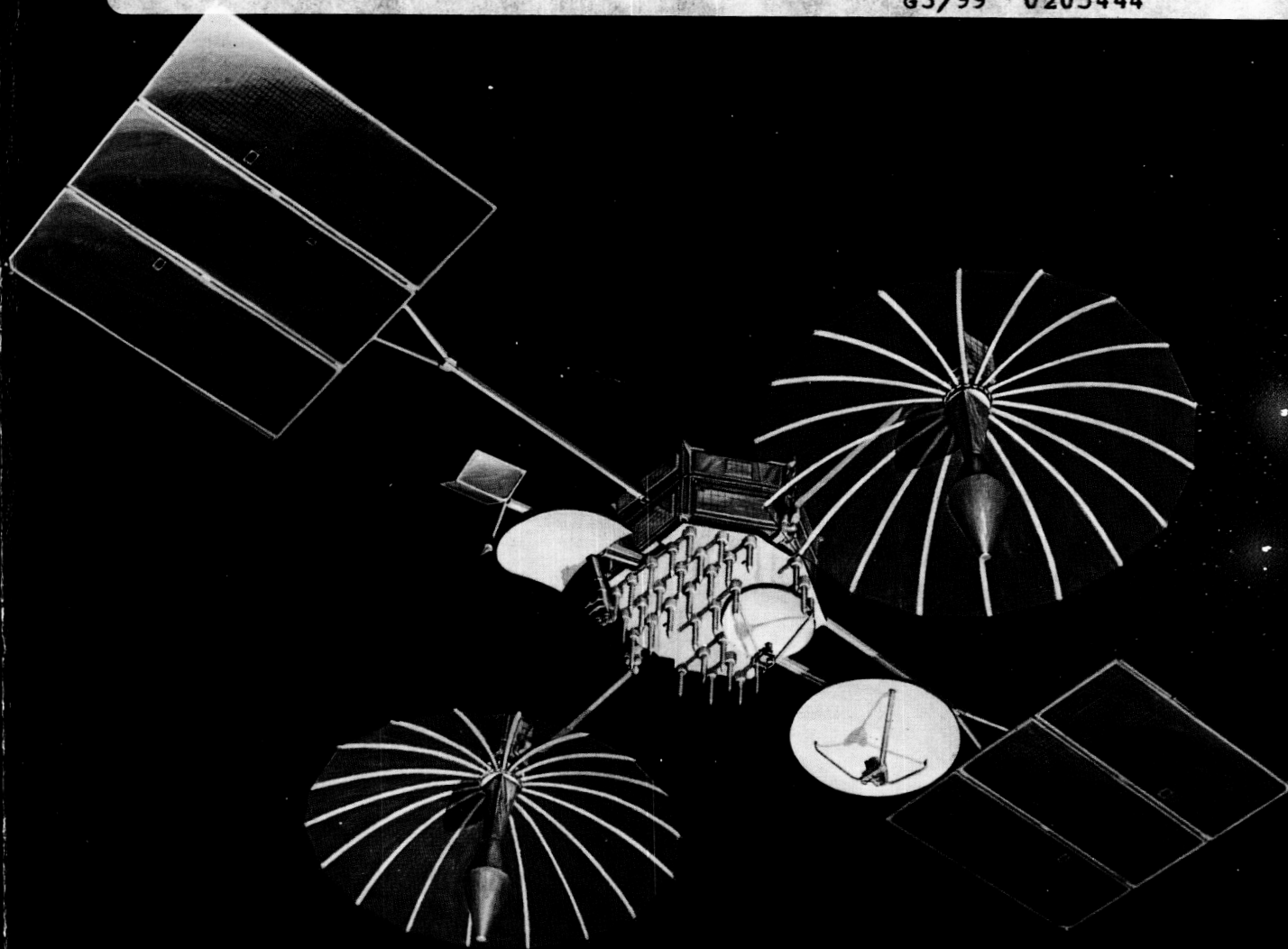
(NASA-TM-101246) RESEARCH AND TECHNOLOGY,
1988 Annual Report (NASA / Goddard Space
Flight Center) 300 p

N89-25109

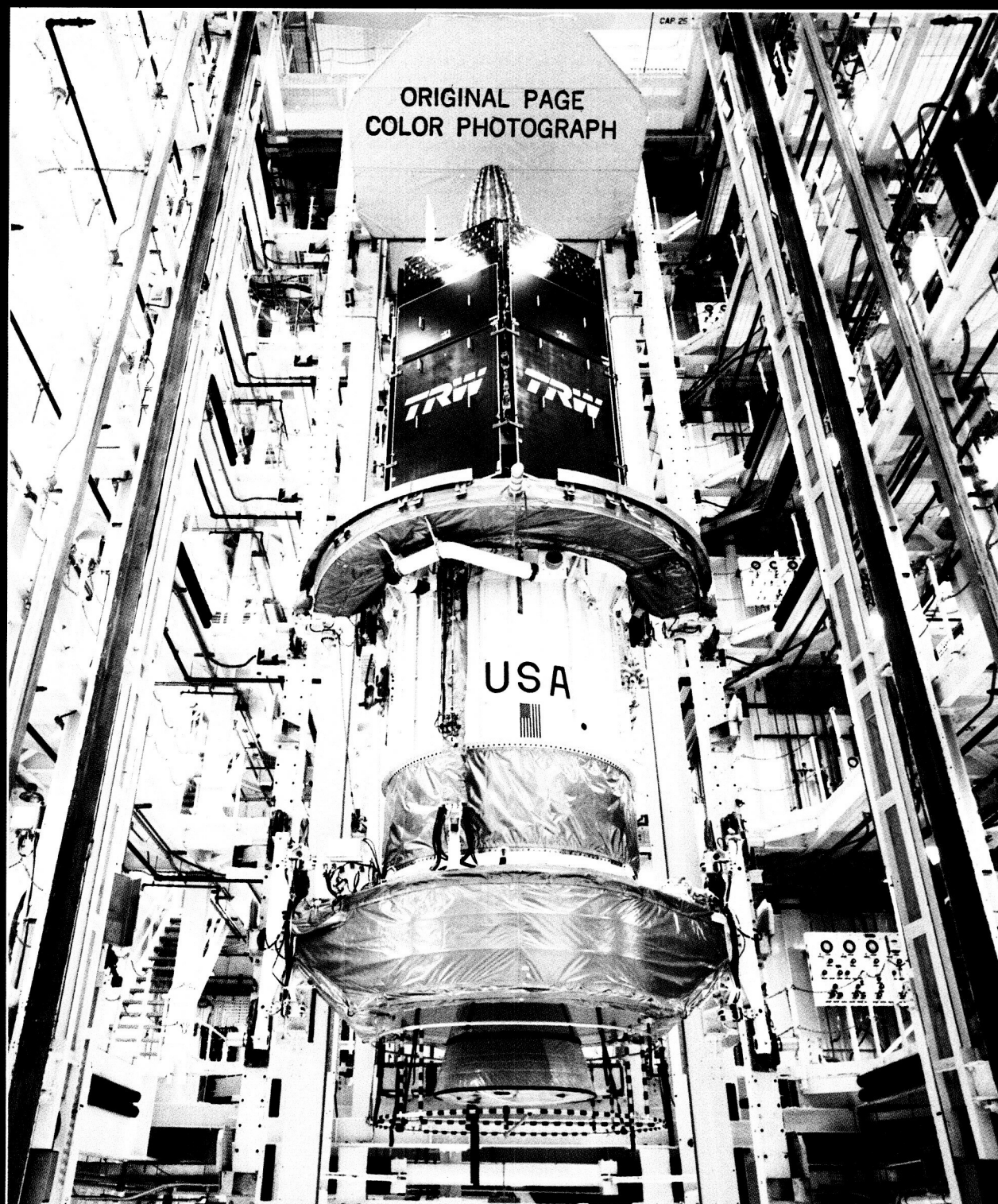
CSCL 05D

Unclas

G3/99 0205444



NASA



Preparations underway, in Kennedy Space Center's Vertical Processing Facility, to integrate the Tracking and Data Relay Satellite (TDRS-C) and the Inertial Upper Stage (IUS) into the Payload Transporter Canister.

ORIGINAL COPIES
COLOR ILLUSTRATIONS

Research and Technology 1988

ANNUAL REPORT OF THE
GODDARD SPACE FLIGHT CENTER

Foreword

On September 29, 1988, NASA resumed shuttle flights following the *Challenger* accident of nearly 3 years earlier. Another event of great importance also occurred that same day. The second of a three-satellite constellation of Tracking and Data Relay Satellites was launched from the shuttle and successfully placed in geosynchronous orbit.

In the near future, a third satellite will be launched to complete an operational system which will form the backbone of NASA's near-Earth tracking and data acquisition capability into the next century. These relay satellites represent the culmination of many years of study and technology assessment not unlike the work being represented in Goddard's *1988 Annual Research and Technology Report*. The approach then, as now, was to carefully evaluate many concepts and eventually prove feasibility. In the early 1960s, it was recognized that only limited contact with low-altitude orbiting satellites could be provided by a practical number of ground stations. Future spaceflight missions would require increasingly higher data rates, and real-time operations would be important for some experiments. We are now on the verge of having near-continuous contact and a broad range of data services for spaceflight missions. Most new programs have designed their operations around the Tracking and Data Relay Satellite System (TDRSS) services. The shuttle, with its 50-megabit-per-second data link, and the Landsat satellite, operating at 85 megabits per second, are two current examples of spacecraft designs tailored to use the TDRSS. The Hubble Space Telescope requires near-continuous contact for health and safety purposes, a requirement met by the TDRSS multiple-access service.

The research and technology initiatives of the 1960s led to realization of a TDRSS and many of the spaceflight scientific experiments in orbit or near launch today. I suggest you review the contents of this *Annual Report* as it contains a vision of future NASA programs and advances in technology which will enable our continuing exploration of the Earth and the universe.



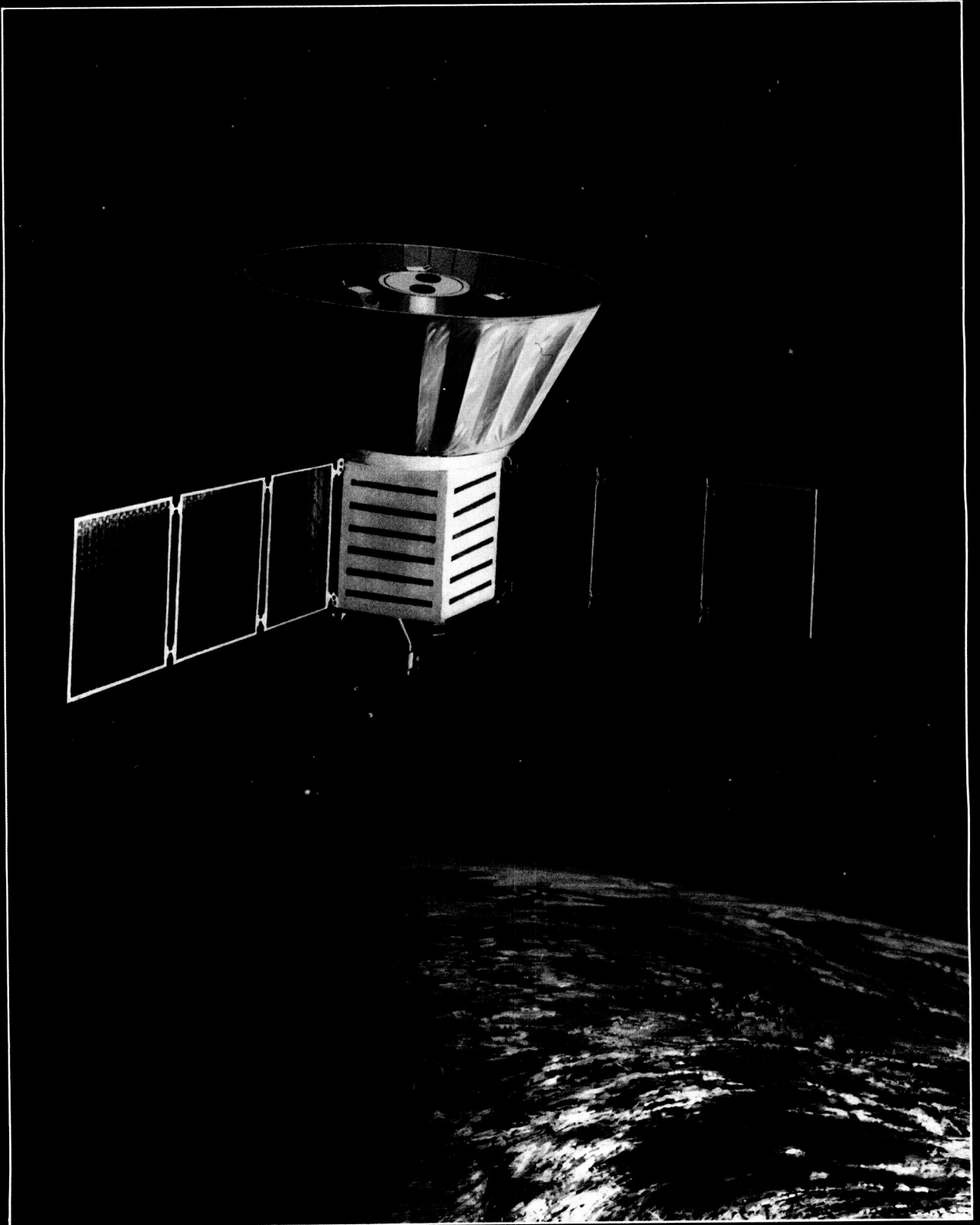
John W. Townsend, Jr.
Director

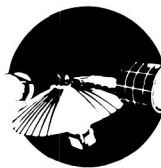
Contents



	<i>Page</i>
FLIGHT PROJECTS AND MISSION DEFINITION STUDIES	1
Flight Projects	1
Space Station Freedom	11
TECHNOLOGY	21
Sensors and Space Technology	21
Space Communication Systems	52
System and Software Engineering	76
User Space Data Systems	100
Techniques	120
SPACE AND EARTH SCIENCES	135
Terrestrial, Land, Climate	135
Atmospheres	164
Ocean	192
SN 1987A	214
Astronomy	222
High Energy Astrophysics	235
Solar System	248
INSTITUTIONAL TECHNOLOGY	287
Institutional Technology	287
INDEX	293

Flight Projects and Mission Definition Studies





The Flight Projects Directorate has enjoyed an exciting year, including preparations for the successful 1988 launch of TDRS-3 aboard Discovery and for the 1989 launch of COBE, NASA's first cosmology mission, now being built at Goddard.

FLIGHT PROJECTS

TRACKING AND DATA RELAY SATELLITE SYSTEM

The Tracking and Data Relay Satellite System (TDRSS) has been developed as the National Aeronautics and Space Administration's (NASA) tracking and data network from the 1980s well into the twenty-first century. Once fully operational, the system will replace the present Space Tracking and Data Network (STDN).

The system is comprised of three satellites in geosynchronous orbit and a central ground station located at White Sands, New Mexico. The two operational satellites will be located over the Equator 130° apart at 41° W longitude and 171° W longitude. The third satellite will serve as a spare and will be located at 79° W longitude.

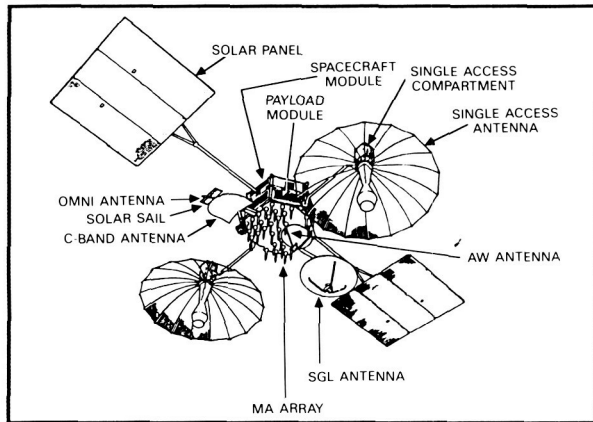
Originally designed as a shared system with two satellites dedicated to NASA's missions, one dedicated to commercial service (C- and Ku-band), and a shared spare. The shared status was changed, prior to the TDRS-1 launch, to a fully dedicated NASA system. Although the commercial equipment

remains on board each spacecraft, there are no plans to utilize the commercial Ku-band; however, NASA is looking at possible use of the C-band transponders.

Each satellite is mounted on top of a two-stage solid rocket, the Boeing-built Inertial Upper Stage (IUS), and is launched via a space shuttle. After deployment from the shuttle, the first stage of the IUS takes the payload to geosynchronous altitude, at which time the second stage circularizes the orbit. While still attached to the IUS, the satellite's solar arrays, space-to-ground link antenna, and C-band antenna are deployed. Following separation from the IUS, the satellite's 16-ft (4.9-m) antennas are deployed and the satellite is oriented towards the Earth. See the accompanying figure.

The first Tracking and Data Relay Satellite (TDRS) was launched on April 4, 1983, but due to a failure of the IUS the spacecraft did not achieve geosynchronous orbit. Over the following 3 months, the orbit was boosted 8000 miles using the spacecraft's onboard one-lb thrusters. TDRS-1 achieved orbit on June 28, 1983. Following checkout it has since been providing service to the shuttle and other users, such as Landsat.

◀ *The Cosmic Background Explorer is scheduled for launch in mid-1989 to measure diffuse infrared and microwave radiation from the Big Bang, the cosmic explosion that started the expanding universe 15 billion years ago. The spacecraft and all three instruments were designed, built, and tested at Goddard Space Flight Center.*



The Tracking and Data Relay Satellite System consists of three satellites (represented in the figure) and a central ground station. TDRS-3 achieved orbit via the September 1988 launch of Discovery.

After TDRS-B was lost on *Challenger*, TDRS-C and -D (TDRS-3 and -4) were scheduled for launch in late 1988 and early 1989. The system is planned to be operational in mid-1989.

The TDRSS satellite telecommunications payload operates as a repeater, relaying signals to and from the Earth station and user satellites. It provides forward and return service to user satellites in two categories. The S-band Multiple Access Service can support up to 20 users simultaneously at data rates up to 50 Kbps. The Single Access Service can support one user at a time at S-band up to 6 mbps or at Ku-band up to 300 mbps. No signal processing is done on board. As many functions as possible have been removed from the satellite and implemented in the Earth station. This removal increases system reliability and availability since Earth station hardware is available for repair and calibration throughout the life of the system.

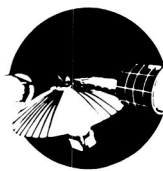
The telecommunications design incorporates many features to ensure performance; provide operational flexibility to accommodate abnormal mission conditions; and achieve reliable, long-life operation. Key features are:

- Shaped high-efficiency 16-ft (4.9-m) diameter antennas ensure link performance margins for single access forward and return services at S- and Ku-band.

- Multiple-access design provides ≥ 1 dB link margins with 6 of 30 elements failed in the return channel and 4 of 12 elements failed in the forward channel.
- Two-for-one (or greater) redundancy in all active circuits (except for limited parts of the multiple-access system) virtually eliminates single-point failures.
- Independent ground-controlled gain adjustments in all single-access forward channels ensure meeting International Radio Consultative Committee (CCIR) flux density restrictions.
- Independent gain adjustments in all return channels ensure optimum downlink power utilization to minimize interference and rain outage.
- Ground-implemented antenna pointing and frequency control reduce complexity of the satellite.

Satellite and payload characteristics are presented in the following tables.

Individual Satellite Characteristics	
Size	57.2 ft x 42.6 ft
Weight	4637 lb
Electrical Power	1700 W end of life
Attitude Control	3-axis stabilization
Telecommunications Channels	2 S-band duplex 1 K-band duplex 20-user S-band multiple access return One S-band multiple access forward
Data Rates	100 bps to 300 Mbps
Operational Orbit	Geosynchronous 22,300 statute miles circular
Launch Vehicles	Space shuttle Inertial Upper Stage
Lifetime	10 yr
Operational Use	1983-1998



Telecommunications Payload Characteristics

Repeater Type	K- and S-band communication with users K-band downlink to Earth station
Effective Radiated Power	Multiple Access Service—34 dBW S-band Single Access Service—46.1 dBW K-band Single Access Service—48.5 dBW Space-to-Ground Link—53.36 dBW Control Range—20 dB
Total SGL Bandwidth	Downlink—650 MHz Uplink—625 MHz
Multiple Access Antenna	30-element phased array Element type—Helix FOV $\pm 13.0^\circ$
Single Access Antenna	Two 4.9-meter deployable parabolic antennas operating at both S- and K-band Transmit/receive beamwidth K-band $0.31/0.28^\circ$ S-band $2.0/1.9^\circ$ Pointing Accuracy: 0.21°
Space-to-Ground Link Antenna	Antenna type—2-meter paraboloid Transmit/receive beamwidth $0.75^\circ/0.70^\circ$

The TDRS will relay data to and from the user satellites and the White Sands Ground Terminal (WSGT) at data rates from 100 bps up to 300 Mbps. TDRSS provides simultaneous data relay services for up to 26 user spacecraft through 85 to 100 percent of each spacecraft's orbit, whereas current Earth stations only provide up to 15 to 20 percent orbital tracking of a user.

The spacecraft's three-axis stabilization maintains attitude control. Body-fixed momentum wheels in a vee configuration and monopropellant hydrazine thrusters interact with Earth and Sun sensors to stabilize and point the satellite-fixed antennas at

Earth targets. Steerable antennas are pointed by command through precision gimbal drives. Hydrazine thrusters are used for satellite positioning and north-south and east-west stationkeeping.

While a ground station presently exists at White Sands, a second ground station is under construction about 3 miles away. This second station, when operational in early 1993, will provide backup to the existing station and increase service capability to support mission loading for the 1990s.

Contact: Dale W. Harris
Code 405

Sponsor: Office for Space Operations

Dr. Dale W. Harris is the Tracking and Data Relay Satellite Project Manager and received his PhD degree from the University of Maryland.

COSMIC BACKGROUND EXPLORER MISSION

The Cosmic Background Explorer (COBE) has been specifically designed for studying the "Big Bang," the primeval explosion that is believed to have started the expansion of the universe. It will also measure the diffuse infrared and microwave background radiation that includes the primary remnant of the explosion. In addition, COBE instruments will determine the spectrum of the radiation and the variances between different points of the sky, with far better sensitivities than can be achieved with other techniques. COBE is being designed, integrated, and tested by engineers, scientists, and technicians at the Goddard Space Flight Center; certain major subsystems, such as the liquid helium cooled Dewar, have been procured from selected contractors. The planned mission lifetime for COBE is 1 year.

The COBE Observatory will carry three instruments: the Differential Microwave Radiometer (DMR), the Far Infrared Absolute Spectrophotometer (FIRAS), and the Diffuse Infrared Background Experiment (DIRBE). Using standard microwave receivers, the DMR will measure the anisotropy of the cosmic background radiation at wavelengths of 3.3, 5.7, and 9.6 mm, with an angular

resolution of 7° . The FIRAS will measure the spectrum (the intensity as a function of wavelength) over a wavelength range of $100\ \mu\text{m}$ to $1\ \text{cm}$, with a 5 percent spectral resolution and a 7° angular resolution; it is a cryogenically cooled polarizing Michelson interferometer. The DIRBE will measure the brightness of the sky at wavelengths from 1 to $300\ \mu\text{m}$, with a 1° angular resolution in 10 bands; it is a cryogenically cooled, off-axis, Gregorian telescope.

The three COBE instruments will be pointed away from the Earth to survey the cosmos—FIRAS along the spin axis, and the DMR and DIRBE 30° off the spin axis. These instruments are located inside a large, deployable RF/thermal shield designed to protect against thermal and electromagnetic radiation from the Sun, the Earth, and the Observatory. Within the RF/thermal shield is a liquid helium Dewar, similar to that flown on board the Infrared Astronomical Satellite. To satisfy the requirements of two of the COBE experiments, the Observatory will rotate at approximately 1 rpm.

Scientific and ancillary data will be stored continuously on one of the two Observatory tape recorders; the recorder will be played back once each day to the ground system, located at the Wallops Flight Facility. The Tracking and Data Relay Satellite System will be used to provide orbit tracking and to relay telemetry and commands to and from the Observatory in its mission orbit.

The COBE Observatory was originally designed to be launched by the Space Shuttle from the Western Space and Missile Center (WSMC). As a result of the Challenger Shuttle accident, COBE has been redesigned as shown in the figure for launch by a Delta 5920 Expendable Launch Vehicle from the WSMC. During the past year, the spacecraft structure for a Delta launch has been fabricated and successfully tested. Assembly of the Observatory has begun, in preparation for system-level testing. The two cryogenically cooled instruments (FIRAS and DIRBE) have been installed in the flight Dewar, which in turn has been mechanically installed on the spacecraft structure. The three DMR receivers have been rebuilt to satisfy the space constraints of the Delta payload fairing, and calibration testing of all the instruments has been completed at the instrument level, in preparation for testing at the Observatory level. The designs for the Solar Array, RF/thermal

shield, and antennae boom deployable systems have been completed; testing of the hardware will commence shortly. Once the Observatory is totally assembled, it will be subjected to environmental testing, to demonstrate that it can survive launch and mission environments. Current plans are to launch COBE during the second quarter of calendar year 1989.

Contact: Roger Mattson
Code 401

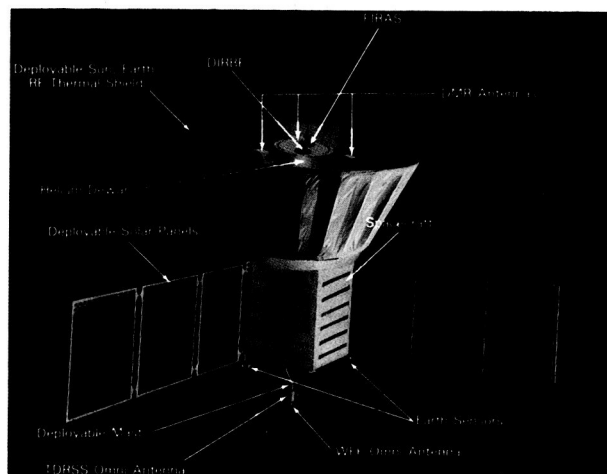
Sponsor: Office of Space Science and
Applications

Mr. Roger Mattson, COBE Project Manager, has been at Goddard for 25 years. Mr. Mattson, who holds a BS degree in chemical engineering, was Project Manager for the first successfully launched, commercially developed upper stage, and he was the first NASA employee to attend the National War College.

COSMIC BACKGROUND EXPLORER TO OBSERVE PRIMEVAL EXPLOSION

The National Aeronautics and Space Administration's first cosmology mission, the Cosmic Background Explorer (COBE) satellite, is being built at Goddard Space Flight Center (GSFC) for launch in 1989. It will observe the Big Bang, the primeval explosion that started the expansion of the universe 15 billion years ago. The COBE instruments will measure the radiative remnant of the Big Bang (the 2.7°K cosmic background radiation), and will search for the radiation of the first objects (galaxies, galaxy clusters, or unknown objects) to form following the explosion. The COBE builds on a heritage of hundreds of experiments at lower altitude, where the atmosphere limits researchers' capabilities, and on the work of a previous satellite, the Infrared Astronomy Satellite (IRAS).

The COBE's three instruments will enable scientists to search for the causes of galaxy formation and clustering, the nature of the large-scale structure of the universe, and the basic structure of the primeval explosion. They will also reveal subsequent emissions from more local sources, such as interplanetary, interstellar, and intergalactic dust, and electrons,



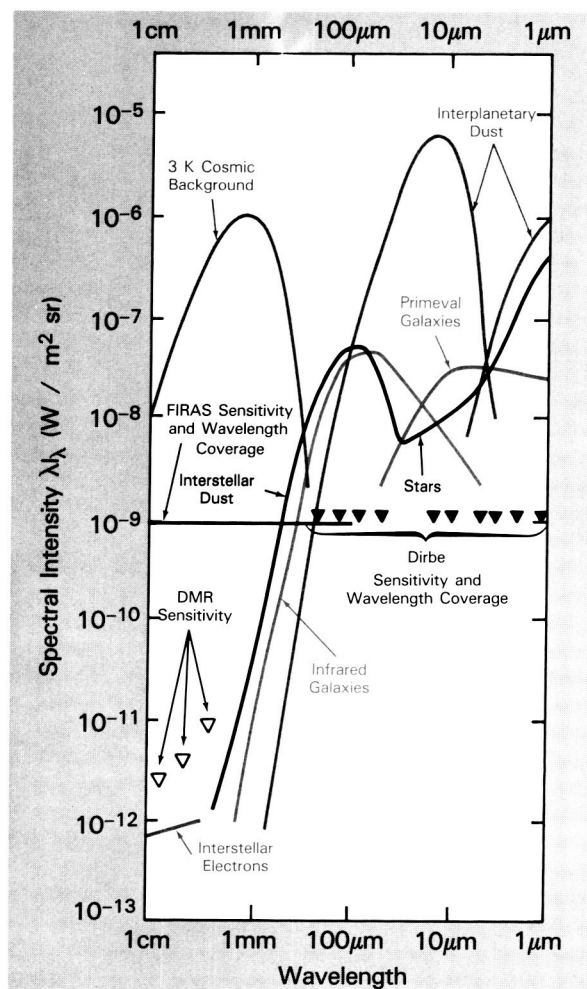
COBE Explorer Satellite planned for launch in 1989.

atoms, and molecules, as well as more visible objects, such as stars. The second figure shows the brightness of the sky seen by COBE, with instrument sensitivity and wavelength coverage.

The Differential Microwave Radiometers (DMR) will map the sky at wavelengths of 3.3, 5.7, and 9.6 mm, using Dicke-switched diode-mixer receivers. The corrugated horn antennas have 7° beamwidths, and are operated in pairs to determine differences in brightness between different parts of the sky. Such differences would arise from structure in the primeval explosion. The sensitivities are 0.1 milliKelvin for each 7° pixel at 3.3 and 5.7 mm, and 0.3 mK at 9.6 mm, small enough for researchers to detect differences of a few parts per million between one half of the sky and the other half.

The Far Infrared Absolute Spectrophotometer (FIRAS) will measure the spectrum of the 2.7°K radiation, and compare it to a blackbody with an emissivity of 0.9999. It also has a 7° beamwidth, but covers the spectral range from $100\ \mu\text{m}$ to 1 cm, with a spectral resolution of 3 percent, or $0.2\ \text{cm}^{-1}$, whichever is larger. Its sensitivity and accuracy are better than $10^{-9}\ \text{W}/\text{cm}^2\text{sr}$, 1 part in 1000 of the peak spectral intensity of the cosmic background radiation, for each pixel and spectral element. This sensitivity is quite sufficient to detect extremely small but important traces of energy released soon after the Big Bang.

The Diffuse Infrared Background Experiment (DIRBE) will map the sky from 1 to $300\ \mu\text{m}$



Brightness of sky seen by COBE, with instrument sensitivity and wavelength coverage.

wavelength, with a beamwidth of 0.7° , in 10 spectral bands. Its sensitivity will be the same as that of the FIRAS, quite sufficient to detect the emission from primeval galaxies if they were bright during their formation. DIRBE is also designed to measure the emission from local interplanetary dust accurately enough to distinguish it from the cosmic infrared background radiation.

During 1988, GSFC engineers completed the three instruments and the spacecraft, and began assembly and testing for launch. GSFC was responsible for developing all three instruments as well as the spacecraft, functioning as its own prime contractor. The spacecraft was completely redesigned for launch on a Delta expendable rocket following the

Challenger shuttle explosion in 1986. This formidable challenge involved reducing the weight by more than half, and designing deployment mechanisms for the instrument shield, the solar arrays, and the telemetry antenna. Fortunately, no scientific requirements were sacrificed in the redesign, although one instrument (the microwave radiometer) had to be repackaged.

The spacecraft will be launched from California into a near polar Sun-synchronous 900 km altitude orbit, with a 6 a.m./p.m. node crossing time. This orbit permits the instruments to survey the entire sky in 6 months, while protecting them from direct radiation from both the Earth and the Sun. The spacecraft spins about its symmetry axis to scan two of the instruments more rapidly across the sky, and to enable them to eliminate systematic errors by comparing data taken in different directions.

The COBE Science Team is composed of United States scientists from five universities, GSFC, and the Jet Propulsion Laboratory, who will use the data to help answer such questions as: How did the universe begin? How did galaxies form? What is the electromagnetic energy content of the universe? What were the first objects to form from the primeval soup? The data will be reduced and analyzed at GSFC by scientists and software specialists, and will be delivered to the National Space Science Data Center for use by the public within 3 years of launch.

Contact: John C. Mather
Code 685

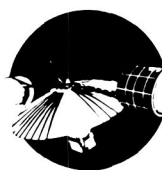
Sponsor: Office of Space Science and Applications

Dr. John C. Mather, Head of the Infrared Astrophysics Branch, is also Project Scientist for the Cosmic Background Explorer, Principal Investigator for the Far Infrared Absolute Spectrophotometer, and Co-Investigator for the Infrared Array Camera for the Space Infrared Telescope Facility. His interests include cosmology, and infrared astronomy and technology. Dr. Mather holds a PhD in physics.

THE UPPER ATMOSPHERE RESEARCH SATELLITE MISSION

The objectives of the Upper Atmosphere Research Satellite (UARS) Mission are: to understand the mechanisms that control upper atmosphere structure and variability; to assess man's impact on the Earth's ozone layer; to assess the potential effect of stratospheric change on weather and climate; and to develop an effective strategy for stratospheric monitoring. Meeting these objectives requires coordinated measurements of atmospheric chemistry, winds, and energy input on a global scale. These data will be acquired by a single observatory containing the 10 scientific instruments listed below:

UARS Energy Input Measurements		
Instrument	Description and Measurements	Investigator, Institution
SOLSTICE—Solar-Stellar Irradiance Comparison Experiment	<ul style="list-style-type: none"> • Full disk solar irradiance spectrometer incorporating stellar comparison • Solar spectral irradiance: 115–440 nm 	G. J. Rottman, University of Colorado
SUSIM—Solar Ultraviolet Spectral Irradiance Monitor	<ul style="list-style-type: none"> • Full disk solar irradiance spectrometer incorporating onboard calibration • Solar spectral irradiance: 120–400 nm 	G. E. Brueckner, Naval Research Laboratory (NRL)
PEM—Particle Environment Monitor	<ul style="list-style-type: none"> • X-ray, proton, and electron spectrometers • In situ energetic electrons and protons; remote sensing of electron energy deposition 	J. D. Winningham, Southwest Research Institute



UARS Species and Temperature Measurements		
Instrument	Description and Measurements	Investigator, Institution
CLAES—Cryogenic Limb Array Etalon Spectrometer	<ul style="list-style-type: none"> • Solid-cryogen cooled interferometer sensing atmospheric infrared emissions • T, CF₂Cl₂, CFC1₃, ClONO₂, CH₄, O₃, NO₂, N₂O, HNO₃, and H₂O 	A. E. Roche, Lockheed Palo Alto Research Laboratory
ISAMS—Improved Stratospheric and Mesospheric Sounder	<ul style="list-style-type: none"> • Mechanically cooled radiometer sensing atmospheric infrared emissions • T, O₃, NO, NO₂, N₂O, HNO₃, H₂O, CH₄, and CO 	F. W. Taylor, Oxford University
MLS—Microwave Limb Sounder	<ul style="list-style-type: none"> • Microwave radiometer sensing atmospheric emissions • ClO, O₃, H₂O, and H₂O₂ 	J. W. Waters, Jet Propulsion Laboratory (JPL)
HALOE—Halogen Occultation Experiment	<ul style="list-style-type: none"> • Gas filter/radiometer sensing sunlight occulted by the atmosphere • HF, HCL, CH₄, NO, CO₂, H₂O, O₃, and NO₂ 	J. M. Russell, National Aeronautics and Space Administration (NASA)/Langley Research Center (LaRC)

UARS Wind Measurements		
Instrument	Description and Measurements	Investigator, Institution
HRDI—High Resolution Doppler Imager	<ul style="list-style-type: none"> • Fabry-Perot spectrometer sensing atmospheric emission and scattering • Two-component wind: 10–110 km 	P. B. Hays, University of Michigan
WINDII—Wind-Imaging Interferometer	<ul style="list-style-type: none"> • Michelson interferometer sensing atmospheric emission and scattering • Two-component wind: 80–110 km 	G. G. Shepherd, York University, Canada

The UARS observatory will be a 3-axis stabilized, Earth-oriented satellite, and will use the Multimission Modular Spacecraft for attitude control, communica-

tions, and power storage. The observatory will orbit the Earth at an altitude of 600 km, and an inclination of 57°.

Instrument of Opportunity		
Instrument	Description and Measurements	Scientist, Institution
ACRIMII—Active Cavity Radiometer Irradiance Monitor	<ul style="list-style-type: none"> • Full disk solar irradiance radiometer • Continuation of solar constant measurements 	R. C. Willson, Jet Propulsion Laboratory (JPL)

Since analysis of coordinated measurements is essential to the mission, a Central Data Handling Facility (CDHF) will be implemented at Goddard Space Flight Center for data processing and storage. Computer-based remote terminals will be located at each of the Principal Investigator facilities for communication with the CDHF and for performing data analysis.

Instrument designs have been completed; fabrication and testing of instrument flight hardware are now well underway. Fabrication and testing of the observatory subsystem are also underway following completion of the critical design review that was conducted in early 1988.

Current project planning is based on launch of the observatory in the fall of 1991, 18 months of flight operations, and 12 additional months of data processing and analysis.

Contact: Luis Gonzales
Code 430

Sponsor: Office of Space Science and Applications

Mr. Luis Gonzales holds a BS degree in electrical engineering. Currently, he serves as Project Manager for the UARS Project. Mr. Gonzales, who has been with Goddard for 24 years, received the NASA Exceptional Service Medal in 1977 and 1983.

SEARCH AND RESCUE SATELLITE-AIDED TRACKING MISSION

During fiscal year 1988, the Search and Rescue (SAR) Satellite-Aided Tracking (SARSAT) mission of the Meteorological Satellite (Metsat) Project continued

to improve the ground system and its operational state. Two new areas of research were initiated during the year. One is the development of a spacecraft-borne 406 MHz interferometer to resolve the first-pass position ambiguity associated with Doppler location processing. Progress in this area led researchers to propose flying an experiment on an early TIROS spacecraft. The other research area is the development of new search methods from space to locate airplanes (and, in the future, ships) without a functioning beacon. Multispectral scanning, synthetic aperture radar, and high-altitude photography are the initial methods of choice. This research is just beginning; initial results, enabling researchers to evaluate these methods' feasibility, are expected during fiscal year 1989.

A technical experiment to receive and process 406 MHz early alert distress data via the Geostationary Operational Environmental Satellite-H (GOES-H) was also completed. The experiment demonstrated the feasibility of receiving and decoding error-free messages. A processing threshold of 27.5 dB-Hz in received signal C/No was achieved for a 95 percent rate of successful alert message detection. At a received signal C/No of 28 dB-Hz, this figure was 99 percent; 90 percent of all first alerts were generated by the processor within 9 minutes of beacon activation. At the nominal received signal C/No of 32 dB-Hz, the processor achieved a 100 percent rate of successful message detection; all first alerts were generated with 4 minutes of beacon activation. Researchers from France and Canada participated in this experiment.

The SAR mission of the Metsat Project at Goddard Space Flight Center is responsible for the research and development activities of the SARSAT Project, an international cooperative project whose principal



partners are the United States, Canada, France, and the Soviet Union. Many other nations also participate, providing ground stations and utilizing SARSAT data. The National Oceanic and Atmospheric Administration (NOAA) manages the United States participants, which include the National Aeronautics and Space Administration (NASA), the Department of Transportation, and the Department of Defense. Canada provides the spaceborne repeater for relay of the 121.5 and 243 MHz signals from Emergency Locator Transmitters (ELT), carried by over 200,000 United States aircraft, and Emergency Position Indication Radio Beacons (EPIRB), carried by more than 2000 ships. Canada also provides a repeater for beacons operating at 406 MHz. France provides a spaceborne processor for the 406 MHz beacons. The United States integrates these two instruments on board the Tiros Series of NOAA environmental satellites. Each country provides its own ground system. The location of the ELTs and EPIRBs is accomplished with the same Doppler location principle demonstrated by satellite data collection systems such as the Nimbus random access memory system (RAMS) and the ARGOS system. The Soviet Union cooperates with the SARSAT partners by making its own SAR satellite system, COSPAS, interoperable with the SARSAT system. The SARSAT equipment will also be carried by NOAA-I, -J, -K, -L, and -M meteorological satellites to be launched during the next few years. GOES-H will perform 406 MHz SARSAT experiments from geosynchronous altitude.

The first spacecraft with satellite-aided tracking capability, the Soviet COSPAS-1 satellite, was launched in June 1982, and made available to the SARSAT Project in September 1982. The first rescues with the help of this system also occurred during that month. The second Soviet satellite, COSPAS-2, and the United States, Canadian, and French SARSAT systems were launched on board NOAA's NOAA-8 operational environmental satellite in 1983. COSPAS-3 was launched in June 1984. NOAA-8 failed in December 1985. NOAA-9 was launched in December 1984, NOAA-10 in September 1986, and NOAA-11 in September 1988. The satellites were being used by the United States Air Force and United States Coast Guard to assist in real world rescue operations using ELTs employed by the aeronautical community and EPIRBs employed by the maritime community.

The 121.5 and 243 MHz beacons have no requirement for a stable frequency component, and no unique identification. Therefore, satellite detection and location of these beacons presents many problems, including: occasional poor location and image rejection; lack of unique identification, meaning that rescue personnel are unable to relate detections to specific beacons; and restricted coverage, limiting the regions in which the satellite can view a ground station and beacon simultaneously. These problems are eliminated with the 406 MHz system. The 406 MHz system became operational in 1985.

The SARSAT System, which began as a NASA research project, is now being used operationally. SARSAT and COSPAS are credited with helping search and rescue forces save over 1150 distress victims. Based on this past success, NASA is pursuing the new areas of technology described here, which have the exciting potential of helping to save even more distress victims.

Contact: Fred Flatow
Code 480

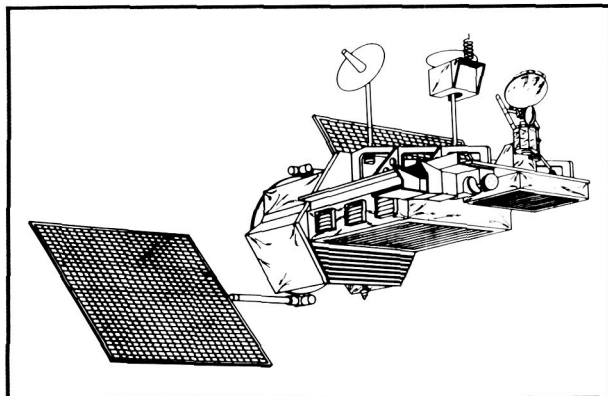
Sponsor: Office of Space Science and Applications

Mr. Fred Flatow is the SAR Mission Manager of the METSAT Project. Mr. Flatow, who holds an MS degree in engineering from George Washington University, specializes in communications. He has been with Goddard for 22 years, and he recently received the Yuri Gagarin Award, Federation of Cosmonautics of the U.S.S.R.

THE TROPICAL RAINFALL MEASURING MISSION

The National Aeronautics and Space Administration (NASA) and the Communications Research Laboratory (CRL) of Japan are studying the technological and programmatic features of the Tropical Rainfall Measuring Mission (TRMM).

The scientific objective of TRMM is to obtain a 3-year data set of monthly averaged rainfalls in grid boxes of 360,000 square kilometers, with an accuracy of better than 20 percent for the portion of the globe between the latitudes of 35°N to 35°S.



The TRMM spacecraft.

Present plans are for the TRMM satellite, shown in the figure, to be a free-flyer spacecraft in a nominal 350 km circular orbit at an inclination of 35°. With a launch scheduled for 1994, and a planned mission lifetime of 3 years, the TRMM will operationally overlap the Tropical Oceans and Global Atmosphere (TOGA) program. This anticipated joint venture between the United States and Japan includes a division of responsibility for the instruments, the spacecraft, the launch vehicle, and the scientific analysis. According to current plans, Japan will supply the Precipitation Radar, a Data Relay and Tracking Satellite Terminal (DRTST), the launch vehicle (H II), and launch services. The United States will supply the spacecraft, the microwave radiometers, the visual and infrared sensor instrument, and tracking and data communications services, utilizing NASA's Tracking Data Relay Satellite System (TDRSS).

Contact: Thomas Keating
Code 402

Sponsor: Office of Space Science and Applications

Mr. Thomas Keating is Study Manager of the Tropical Rainfall Measuring Mission. He earned an MS degree in electrical engineering from The Catholic University of America. Mr. Keating has 25 years of experience at Goddard, where he has received two Special Achievement Awards and a Performance Award.

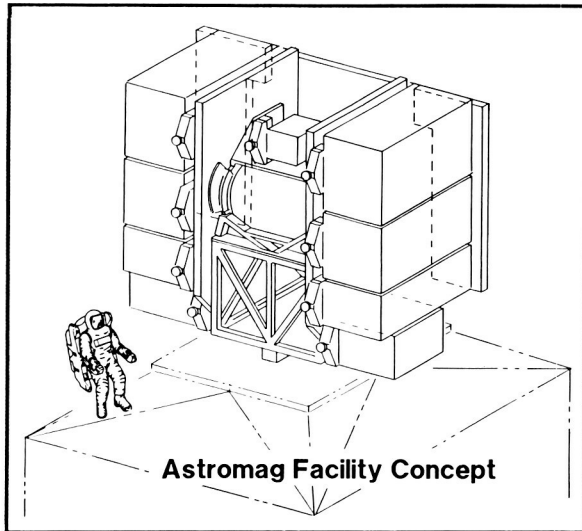
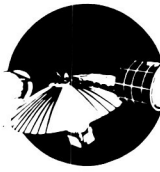
ASTROMAG, A PARTICLE ASTROPHYSICS MAGNET FACILITY

Astromag is an attached payload for Space Station Freedom. Comprising a superconducting magnet core facility and a series of replaceable instruments, it will service a wide variety of science experiments, primarily in the field of particle astrophysics.

Particle astrophysics stands today at a critical juncture in its development. Observations over the past several years have given unexpected results for the elemental and isotopic composition of cosmic-ray nuclei, and for the cosmic-ray abundances of anti-protons and positrons. Concurrently, theoretical developments have presented scientists with a new framework in which to understand the acceleration of these particles. These results have raised new questions about the origins of energetic particles in astrophysical settings, which are related to fundamental questions of astrophysics, cosmology, and elementary particle physics. Examples of some of these questions include the following: What is the source of the large abundances of antiprotons observed in the cosmic radiation? Is there evidence for known or unknown particles that could account for missing mass in the universe? What is the nucleosynthetic history of this sample of nonsolar system material? To answer these questions, scientists must employ large instruments with long space exposures; the development of a permanently manned Space Station offers researchers the opportunity to perform needed experiments.

Early in 1988, the Astromag magnet and supporting system were designated a "Core Facility," to be installed on Space Station Freedom as a permanent facility. Experiments for Astromag were solicited in a general Announcement of Opportunity for all space science attached payloads. The role of the Astromag Definition Team was restricted to Core Facility definition. Astromag was formally designated a Goddard Space Flight Center Phase A study, and preliminary system design began. Overall system design continued through the year, while subsystem studies were started for the cryogenic magnet assembly, and for the servicing design that is essential to Astromag operation and maintenance.

The accompanying figure illustrates the conceptual arrangement of the core facility and a nominal set



Conceptual design of the Astromag facility. Opposing magnets cancel the torque that a single magnet would apply to the Space Station, and permit two concurrent experiments with different instrumentation. Instruments may be replaced in orbit, so that researchers can conduct new experiments.

of instruments. Servicing and safety concerns, and the desire to reduce the facility's ambient magnetic

flux were the primary considerations that dictated mounting Astromag on an outrigger, away from the Space Station's main truss. This arrangement permits all servicing to take place on a single face of the payload. Developers of the FTS (Flight Telerobotic Servicer) have selected Astromag as a model for their development activities, thereby enhancing the efficiency and compatibility of the two designs.

Because the Core Facility has been delineated as a separate development entity, preliminary Astromag system design is now scheduled for completion in 1988; Phase A is scheduled for completion in early 1989.

Contact: William D. Hibbard
Code 402

Sponsor: Office of Space Science and
Applications

Mr. William Hibbard is Study Manager of Astromag with the Advanced Missions Analysis Office. Mr. Hibbard, who earned a BSEE degree from Ohio University, has been with Goddard for 27 years.

SPACE STATION FREEDOM

SPACE STATION FREEDOM PROJECT

The advent of an operational space station in the 1990s timeframe will usher the National Aeronautics and Space Administration (NASA) into a new and exciting era of space exploration. The new era will feature increased deployment of self-managing, semi-autonomous space systems, increased reliance on telerobotic techniques and principles to conduct routine on-orbit operations and maintenance activities, and manned participation in scientific research performed in microgravity environments. Responsibilities for conducting the research and technology development efforts needed to implement Space Station Freedom's elements are distributed among the

various NASA centers. Goddard Space Flight Center (GSFC), for example, is responsible for providing four major flight elements for Freedom: Customer Servicing and Assembly Facility; Attached Payload Accommodation Equipment; Platforms; and the Flight Telerobotic Servicer.

Contact: George Alcorn*
Code 700

Sponsor: Space Station Freedom Project

*The following articles represent the efforts of many engineers working on Space Station Freedom.

PLATFORM MANAGEMENT SYSTEM TEST BED AND EVOLUTION STUDY

The Platform Management System (PMS) will manage operations of payloads and systems on board an unmanned Space Station Freedom platform. The PMS performs real-time or near real-time management functions that include managing short-term plans; managing platform operations; monitoring platform onboard operations; supporting onboard testing; conflict identification and resolution; global fault management; and transaction checking. The first figure shows that the PMS consists of both a flight and ground portion: the Platform Management Application (PMA) and the Platform Management Ground Application (PMGA), respectively.

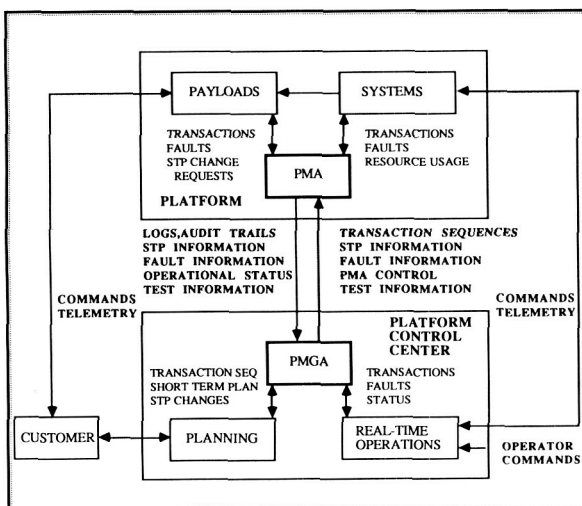
Two significant research and technology efforts related to the PMS development were led by J. Hartley of Code 512, and performed by organizations throughout GSFC: the PMS Test Bed and the PMS Evolution Study.

The approach used by the PMS to manage platform operations is based on a resource allocation and usage control-and-monitoring scheme, rather than on execution of an integrated and constraint-checked command time line, as has been done traditionally. This

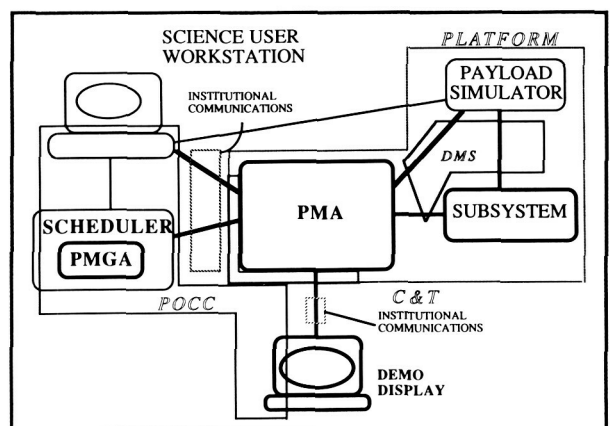
new approach requires early efforts to demonstrate the feasibility of these concepts.

The PMS Test Bed Pilot is an enhancement of the Space Station End-to-End Test Capability (ETC) test bed effort. The test bed is a prototype of the PMS software implemented in the Ada programming language. This prototype will be integrated with existing test bed elements, including a science user workstation, a scheduler, and a payload simulator. The second figure shows the PMS Test Bed elements and their mapping to elements of the Space Station Information System (SSIS). The purpose of the test bed is to validate the current PMS architecture, to explore the implications of telepresence and transactions/management for platform operations, to identify potential commonality between the PMS and the Operations Management System (OMS), and to gain experience in the management and development of Ada software.

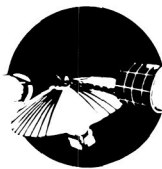
The top-level design of the PMS has been completed using the General Object-Oriented Design (GOOD) method; it was reviewed at the PMS Prototype Design Review in May 1988. The design decomposition includes an operations manager, a configuration manager, and platform state manager objects, providing support for time-keeping, logging, and network communications. The test bed is well into the implementation phase. As the test bed process continues, many PMS issues are being raised and



Distribution of the Platform Management System (PMS). The PMS has both a flight component, the Platform Management Application (PMA), and a ground component, the Platform Management Ground Application (PMGA).



PMS Test Bed Phase 1. Phase 1 of the PMS Test Bed is an implementation using computers and networks local to GSFC. A mapping of test bed elements to parts of the Space Station Freedom Information System is shown.



tracked, so that they can be resolved prior to implementation of the PMS components by the Work Package 3 (WP-3) and Customer Data and Operations System (CDOS) contractors.

Once the first phase of the test bed is completed, expansion of the test bed is planned. Future activities include porting the PMA software to run on a Data Management System (DMS) test bed that provides a more realistic environment, enhancing the PMA functionality to include the remaining transaction management functions and more sophisticated platform fault management, enhancing the subsystem models to further explore the PMA-core system interface, and integration with the CDOS test bed to clarify ground system interfaces.

Researchers have also begun to define the PMS functions required for the mature platform operations era. The objectives of the recent study include: defining how to increase the operational productivity of the platform by providing enhanced capability to respond to changing events; influencing the initial PMS design by identifying required hooks and scars; and evaluating potential automation techniques that are appropriate given predicted onboard computing resources.

Some initial platform operations scenarios have been defined. The focus is on PMS-related functions where operations enhancements are likely to occur. Operations productivity has been defined in terms of scientific productivity of the platform, as well as the level of automation of the ground system. An outline of the Platform Operations Productivity Enhancement Report (POPER) has been completed and work is underway on the first draft of the document.

Future plans include: completing the operations productivity analysis, mapping out an evolution plan for the PMS, documenting the impacts of this plan on the initial PMS, and prototyping some of the PMS functional enhancements. Although no preconceived notions of how the PMS should evolve currently exist, it is likely that greater operations productivity can be achieved through application of artificial intelligence techniques to the PMS. Prototyping these applications will help researchers understand how artificial intelligence can be implemented effectively as part of the flight software system.

FLAT PLATE INTERFACE PROTOTYPE

The Flat Plate Interface Prototype (FPIP) is an engineering model used to demonstrate the concept of a "connectorless interface" for on-orbit integration of payloads. This effort is led by Robyn King of Code 735.2. The FPIP consists of two halves: a Space Station Freedom side and a payload side. When both halves are physically mated, the interface is complete, and the four principal interface functions (data, power, thermal, and structural) are realized.

The FPIP data system employs free space optical links of six simplex data channels. Each channel supports a maximum data rate transfer of 100 megabits per second. The FPIP power interface is capable of transferring a maximum of 500 watts, at 98 percent efficiency, to attached payloads. Electrical power is supplied to the payload via a pair of split core transformers; the primary transformer is located on the space station side, the secondary on the payload side. The FPIP employs a thermal-contact heat exchanger in order to remove heat from the payload back to the Space Station. This thermal interface subsystem can transfer 520 watts of thermal energy with a temperature difference of 9°F across the interface boundary. In order to align both the optical data system and electric power flux system, as well as maintain the requisite contact pressure of the heat exchanger, a structural latch engagement system is employed. It is a self-coupling rollerscrew, capable of robotic or manual engagement.

The FPIP was designed and fabricated so that the interactions of an integrated "connectorless interface" could be tested. During 1988, the FPIP was subjected to exhaustive testing such as thermal vacuum, EMI mapping, bit error rate, and mate and de-mate cycles. It has been tested to its specifications, and has met or exceeded initial specification requirements.

Contact: George Alcorn
Code 700

Sponsor: Space Station Freedom Project

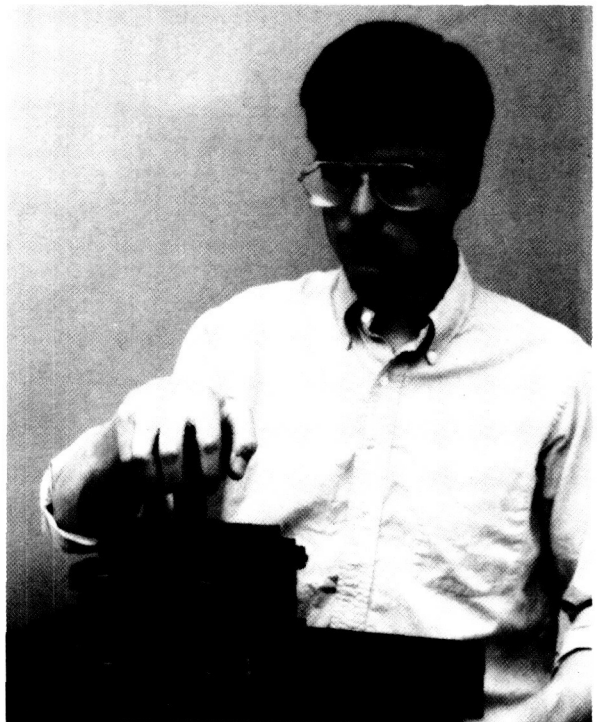
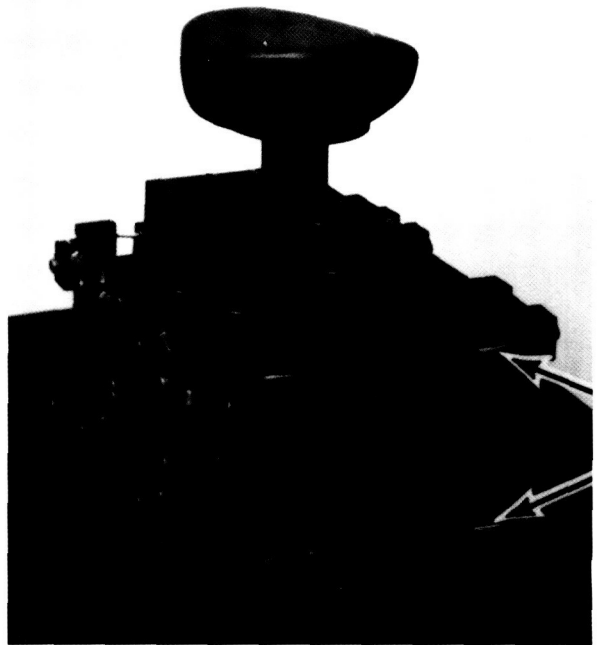
END EFFECTOR MECHANISMS AND ROBOT-FRIENDLY PAYLOAD LATCHING SYSTEMS

The Goddard Space Flight Center (GSFC) Electromechanical Branch, under the direction of John Vranish of Code 716.1, is conducting a research and technology effort whose primary focus is in two areas: End Effector Mechanisms, and Robot-Friendly Payload Latching Systems. Included as components of each system are the mechanical structures, the sensors that monitor system status, the controllers, and the mechanical and electronic interfaces. In both areas, several significant events have recently occurred.

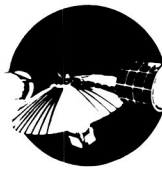
In the first area—End-Effector-related Mechanisms—a gripper/nut runner proof-of-principle prototype was developed and demonstrated. This prototype successfully performed a complete payload changeout in the robot laboratory. Driven by a robot wrist motor (for the nut runner), and equipped with a dedicated motor for the gripper, this system represents a potentially significant step forward in the technology of End Effectors for space applications. By using the robot wrist motor, the system is made significantly more simple and compact, thus increasing its reliability, and enhancing robot dexterity.

This gripper is referred to as “The Split-Rail Parallel Gripper.” It has many advantageous features, and was selected to be the basis for a National Aeronautics and Space Administration (NASA) technology utilization project in which industry and NASA will jointly develop an intelligent sensory-interactive gripper for industrial use.

The 6 Degree-of-Freedom (DoF) Compliant Joy Stick proof-of-principle prototype illustrated in the figure was also demonstrated. This device was used to teleoperate a robot in the lab. It represents a significant simplification in the state-of-the-art in non-force-reflecting, user-friendly compliant joy sticks. Thus, it promises to be more reliable and less expensive than existing devices.



During fiscal year 1988 the 6 Degree-of-Freedom (DoF) Compliant Joy Stick shown above was successfully used to teleoperate a robot in the Tele-robotics Laboratory.



In the second research and technology area—Robot-Friendly Payload Latching Systems—a proof-of-principle prototype of an Orbital Replacement Unit (ORU) was demonstrated in the robot lab. This unique system promises to have an important impact on payloads throughout Space Station Freedom and is already receiving recognition. It has several robot-friendly features. It permits the robot to attach (or detach) the payload by means of a single grasp point, permitting the robot to maintain excellent control of the payload at all times. It has a torque-multiplying feature that allows the robot to attach the payload more securely, or detach it with a greater margin of safety. It attaches each payload with multiple latches; thus, the system is redundant, and inherently very safe. It also has an inherently high strength-to-weight ratio. This system is under consideration for early deployment in space as part of the Flight Telerobotic Servicer (FTS) Demonstration Test Flight.

Improvements to both systems are envisioned during the upcoming months. The gripper/nut runner will receive a safety-enhancing mechanism that will provide for better control over the payload during attachment and/or detachment operations. The gripper itself will receive fingers that use a new principle in the gripping process. The 6 DoF Compliant Joy Stick will be redesigned so as to provide a much improved operator feel. The ORU attachment system will receive improvements that will improve both performance and reliability through simplifications.

In addition, new mechanical systems will be added. An autochanger will be introduced that will enable the robot to change and store its end effectors in zero gravity conditions. A robot-friendly fluid coupler will also be introduced. Work will begin on a robot "foot" that will enable the robot to attach itself more properly to the work site.

A sensor will be incorporated into the mechanical systems. It will include force and position information for the gripper and torque for the nut runner. The ORU attachment system will receive a suite of sensors that will monitor its status (e.g., latched/unlatched; electrical connectors properly engaged; and temperature).

A controller will be developed for the end effector. This controller will permit the gripper to operate in an autonomous mode, a teleoperator mode, or a

shared-control mode. The particular concerns inherent in the safe handling of objects in space will receive close attention.

Contact: George Alcorn
Code 700

Sponsor: Space Station Freedom Project

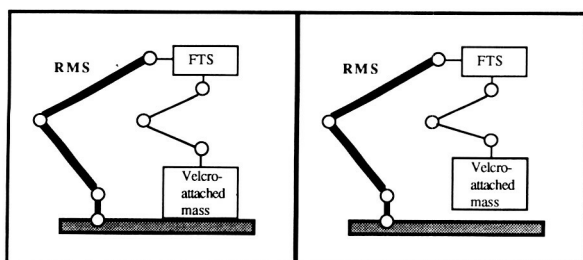
CONTROL ANALYSIS CAPABILITY FOR FLEXIBLE ROBOTIC SYSTEMS

Multibody dynamics software programs are currently used for a broad range of simulation applications. The more popular applications include robotics, tanks, Strategic Defense Initiative applications, automobiles, farm machinery, spacecraft, and biomechanics. Unfortunately, as the number of moving bodies included in these software programs increases, and as complexities associated with defining body flexibility are introduced, computational speeds degrade. In support of the Space Station Freedom Flight Telerobotic Servicer (FTS) Project, Harold P. Frisch of Goddard Space Flight Center (GSFC) Code 712.1 directed a Controls Analysis Capability Study for Flexible Robotic Systems. The objective of this study was twofold: to demonstrate that low cost, flexible robot simulation models that are compatible with control system design and analysis needs can be developed; and to demonstrate that implementation of newly discovered methods for defining multiflexible body equations of motion can enhance computational speed by one or two orders of magnitude.

Investigators at the National Science Foundation/Army/Goddard Industry/University Cooperative Research Center at the University of Iowa were given three coupled Remote Manipulator System (RMS)/FTS problems. RMS flexibility data provided by the Johnson Space Center were to be used in the simulation, and FTS control algorithms were to be developed to support each robot task defined. Each of the tasks simulated use of the FTS to do work while attached to the flexible RMS. Two of the tasks involved removing a velcro-attached payload from a worksite, while the third addressed an Orbital Replacement Unit (ORU) handoff problem that involved the flexible RMS and the FTS. An example of the type of problem researched is shown in the

figure. To demonstrate the computational speed improvement potential of the new algorithm, one of the payload pickup problems was repeated, enabling scientists to compare the results to a baseline capability.

All simulations were created and exercised to provide investigators with the engineering insight needed to appreciate the complexities associated with defining safe operational scenarios for highly flexible robotic systems. The pilot code used to evaluate the new algorithm demonstrated an improvement in computational speed by a factor of 26. Improvement by at least another order of magnitude is expected when methodologies are implemented on a parallel processing computing system.



Tasks simulated in conjunction with this effort were representative of using the FTS to do useful work while attached to the RMS.

New multibody algorithms have made it possible to create low cost, high speed, and even real-time simulations of complex mechanical equipment such as flexible robots. Ongoing work is directed toward this goal.

Contact: George Alcorn
Code 700

Sponsor: Space Station Freedom Project

THERMAL SYSTEMS

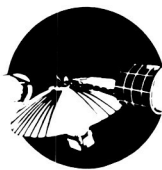
Large space-based facilities such as the Space Station Freedom will require a two-phase central thermal bus for effective temperature control. The number of dispersed loads, the long distances between them, their need for independent operations, and the sheer magnitude of the total power involved make the more traditional approaches unsuitable.

Two-phase fluid loops have the potential to meet these large heat transfer requirements because of the large latent heat of fusion of the working fluid. In addition, two-phase fluid loops can operate at near-isothermal temperatures. One two-phase fluid loop that has been under investigation at Goddard Space Flight Center (GSFC) for several years is the Capillary Pump Loop (CPL). In this system, capillary wicks are used to position fluid at the evaporating interface (the cold plate surface) and are used to pump fluid around the loop. In addition to having the general advantages of two-phase loops, the CPL has no moving parts. This increases the reliability of the system, and results in a low-vibration cold plate.

Another type of system being investigated is the mechanically pumped loop. This is also a two-phase loop, but a mechanical pump is used to pump the working fluid. Several different types of mechanically pumped loops are under development. Some use capillary structures to provide fluid management. Others use various means to assure separation of the liquid and gas phases of the working fluid.

Two-phase fluid behavior is difficult to predict on the ground, while even less is known about its behavior in a microgravity environment. As a result, flight experiments are required to verify system behavior. Several small CPL flight experiments have already been flown on the shuttle, but these were just proof-of-concept experiments. In an effort to meet Space Station Freedom requirements in a logical manner, a program of flight experiments was developed under the name of Thermal Energy Management Process (TEMP).

One of the experiments in the TEMP program is called TEMP 2C. The Preliminary Design Review (PDR) and the Critical Design Review (CDR) for TEMP 2C were held during fiscal year 1988. This experiment is a hybrid (capillary and mechanically pumped) two-phase heat transfer experiment. It is essentially a CPL loop with a mechanical pump added to assist in ground testing, repriming, and transient operation of the loop. A hybrid CPL is one system being considered for use as the Space Station Freedom instrument thermal bus control system. The TEMP 2C experiment will be integrated with a similar experiment from Johnson Space Center (JSC). This coexperiment, referred to as TEMP 3C,



is a mechanically pumped two-phase loop that simulates the Space Station Freedom central thermal bus. The combined TEMP 2C/TEMP 3C experiment is known as the Two-Phase Integrated Thermal System (TPITS). TEMP 2C and TEMP 3C are linked through a heat exchanger that is part of the TEMP 2C package. It acts as the condenser for the TEMP 2C working fluid.

The schematic for the TEMP 2C experiment is shown in the figure. It has two 3-by-5-foot evaporator plates (cold plates). The first of these is a capillary cold plate, with 12 capillary pumps in parallel. The second cold plate has four capillary pumps and eight heat pipes that are used to collect the energy input to the plate and transport it to the capillary pumps. The experiment has about 25 feet each of vapor and liquid transport line, which approximates the transport lengths expected on Freedom Station.

TEMP 2C dumps its thermal energy to the TEMP 3C experiment through an Interface Heat Exchanger (IHX). This is a two-phase to two-phase heat exchanger that acts as a condenser to TEMP 2C and an evaporator to TEMP 3C. After traveling through

the IHX, the condensed TEMP 2C fluid (ammonia) passes through a subcooler before returning to the evaporator. Cooling to the subcooler is provided by the Payload Bay Active Thermal Control Subsystem, which also cools the condensers on the TEMP 3C experiment.

In addition to the components already described, the TEMP 2C includes a mechanical pump, and the accompanying valves to allow hybrid or pure CPL operation. A starter pump is also included, which will facilitate start-up, and improve fluid management of the system. There is a noncondensable gas (NCG) trap in the system to trap any NCGs that could adversely affect system operation. The entire system will be instrumented with numerous thermocouples, pressure transducers, and a flow meter.

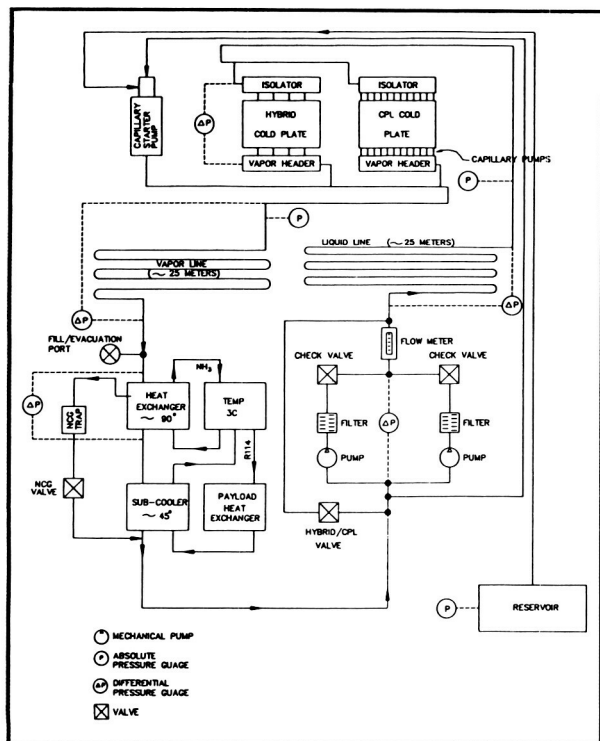
The TPITS experiment will fly on a shuttle mission. The TEMP 2C portion of the experiment will be run for at least 12 hours. During this time, heat transport limit tests will be run in both the capillary and mechanically pumped modes. In addition, dryout and repriming tests will be done, and the possibility of warming the system using TEMP 3C (heat load sharing) will be investigated.

Contact: George Alcorn
Code 700

Sponsor: Space Station Freedom Project

ROTARY FLUID COUPLER

Applications involving moving loads, such as those associated with the Payload Pointing System (PPS), present the serious problem of transferring the refrigerant across a flexible, or rotating, joint. Traditional approaches such as flexible hoses limit movement, require unwinding, and are also unreliable. A fluid coupler that could continuously rotate along at least one axis would thus offer a significant advantage. However, devices capable of transferring ammonia with the low torque and negligible leakage rate needed for PPS type applications do not presently exist. The rotary fluid coupler (RFC) is being developed to meet this need. Its primary design specifications include a very low torque limit of 20 in-lb or less, a maximum leakage rate of 0.02 lb/year,



TEMP 2C Mechanical Schematic.

a maximum pressure drop of 0.1 psi, negligible thermal crosstalk, ammonia compatibility, and a lifetime of 10 years, or 120,000 revolutions. Individually, these requirements are difficult to meet; as a group, they represent a serious design challenge.

The basic RFC design involves a rotating shaft within a cylindrical housing port. Vapor from the payload enters the RFC at the shaft end, and follows an annular path about the double-vacuum-jacketed liquid line. The vapor is then diverted 90° through a ported shaft wall, into a circumferential housing flow channel, and then out the housing port. Liquid flows down the center axis inside of a vacuum jacket that provides thermal isolation. Mechanically actuated face seals are used to provide the critical sealing function, while still maintaining low torque and low leakage. Preliminary design studies and component testing indicate that this design should meet the specifications.

Contact: George Alcorn
Code 700

Sponsor: Space Station Freedom Project

SPACE STATION FREEDOM RESEARCH AND DEVELOPMENT FACILITIES

There are presently three Space Station Freedom facilities that support research and development. Two are high-technology test beds, the Platform Data Management System (DMS) Test Bed and the Instrument Thermal Test Bed (ITTB), and the third is the Telerobotics Laboratory.

The Platform DMS Test Bed is a fiber-optics based advanced data system for platform applications. The system uses a passive Star topology, and has a broadcast bandwidth of 100 Mb/s. It provides for packetized data distribution, autonomous data transmissions, and hierarchically structured network communications protocols. The absence of a central data poller improves the reliability of the system over past data system designs, and reduces the complexity of testing and integration of payloads with other users connected to the data bus.

Significant progress was made in upgrading network performance by replacing Emitter Coupled Logic

(ECL) circuitry (silicon bipolar) with modern gallium arsenide (GaAs) technology. GaAs offers improved speed, but the significant factor for its application in this system was the 85 percent reduction in power dissipated.

Work is proceeding to replace the Transistor-Transistor Logic (TTL) with Complementary Metal Oxide Semiconductor (CMOS) chips. The design of the CMOS chip has been completed, and fabricated integrated circuits are expected shortly. Even greater power saving than in the GaAs replacement of ECL is expected for the CMOS replacement of the TTL circuitry. The figure shows how many components are eliminated by replacing the ECL circuitry with a GaAs chip.

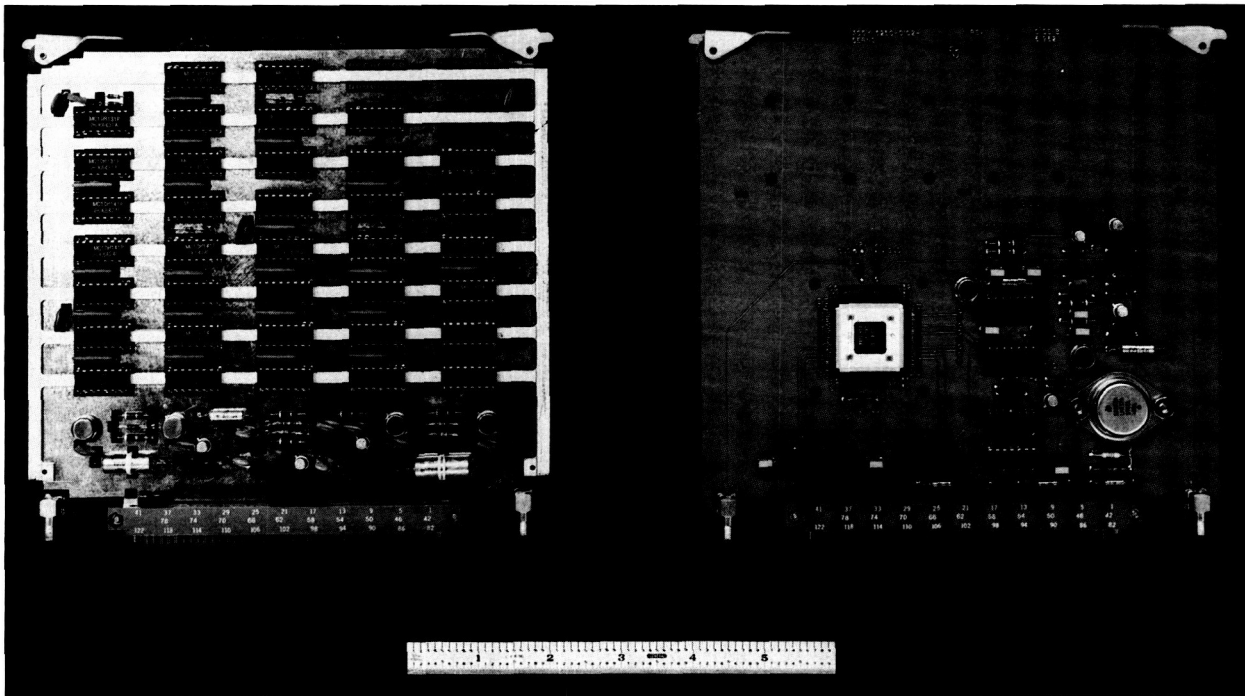
The Telerobotics Laboratory effort is led by Stanley Ollendorf of Code 706. The Space Station Freedom Project is responsible for the development of a Ground Telerobotics Laboratory, which provides for the test, evaluation, and development of ground and flight systems to support National Aeronautics and Space Administration robotics efforts. This high-bay facility will house robotics development and test equipment, and personnel. The facility will provide a high degree of repeatability, accuracy, and versatility for evaluating robot components, subsystems, and systems. The functional capabilities that the ground laboratory provides to the Space Station Freedom robotics program are: a system architecture containing robot control software; a computing facility to support development and evaluation of software for robot control systems; a convenient means of robot control and observation; and assessment of vision systems.

To augment and support the development of the Space Station Freedom elements, GSFC has evolved the concept of the ITTB. This facility will permit new items of thermal technology to be tested, qualified, and certified for application to the Space Station Freedom Program. The ITTB is flexible, and capable of being easily configured and reconfigured to test a wide variety of thermal components, subsystems, and systems. It is being designed to operate with capillary and mechanically pumped two-phase systems and components.

During fiscal year 1988, construction of many of the ITTB elements and a number of key test programs



ORIGINAL PAGE
BLACK AND WHITE PHOTOGRAPH



Significant performance gains will be realized by replacing existing Emitter Coupled Logic (ECL) circuitry with GaAs technology. Shown above are the components that will be replaced by the GaAs chip.

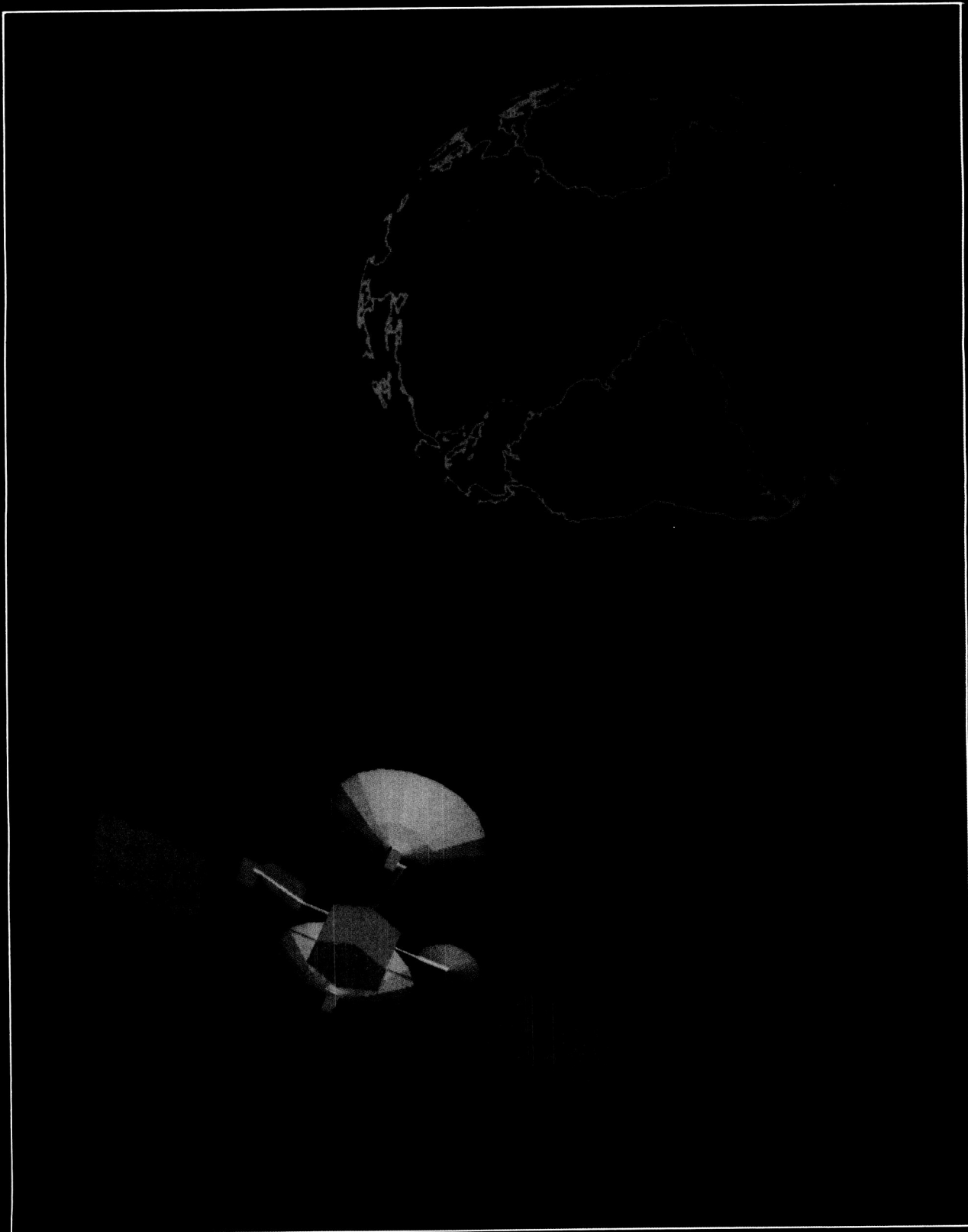
were initiated. Efforts to fabricate the Main Evaporator and Ultimate Condenser Sections of the ITTB were essentially completed. Fabrication of the Transport Section and delivery of the prototype capillary cold plates is anticipated shortly. Finally, another round of testing on the Hybrid Mechanical/Capillary pumped concept is planned in order to further define its performance and suitability for Freedom Station applications.

Contact: George Alcorn
Code 700

Sponsor: Space Station Freedom Project

Dr. George Alcorn, who holds a PhD degree in physics from Howard University, joined NASA in 1978. Before joining NASA, he served as an advisory engineer/scientist to IBM at its Manassas, Virginia facility. Dr. Alcorn is a noted plasma semiconductor device fabrication pioneer who was twice recognized by IBM's Chairman of the Board for his creative contributions and was the 1984 NASA/GSFC Inventor of the Year. He currently serves as Deputy Project Manager for Space Station Freedom Advanced Development activities.

Technology





High-performance graphic workstations augment numerical data displays with three-dimensional images for monitoring spacecraft flight parameters.

SENSORS AND SPACE TECHNOLOGY

ANTISTATIC TRANSPARENT FILM FOR SHIELDING PURPOSES

Antistatic polymeric films are used as shielding tents and bags for electronic components. In addition to having the capability to dissipate static electricity, these materials should also be stable and transparent. The static materials presently used are made by metal deposition on the surface of a polymer, or by addition of carbon particles to a polymer. There are some problems associated with these materials, such as their contaminating potential through shedding of particles, loss of conductivity with time, and low transmittance of light.

In the past few years research in the field of conductive polymers has been oriented towards the development of intrinsic conductive polymers. In these polymers, the ions that make it possible for the polymer to conduct electricity are integrated, forming part of the molecular structure of the polymer for better conductivity and stability. New intrinsic conductive polymers 1.0 to 10^4 siemens/cm with diverse potential applications have been developed, but there are still processability problems that need to be overcome.

The objective of the DDF-1986 research project was to develop a transparent, stable, conductive film for

antistatic purposes. High conductivity was not pursued, since for antistatic films to serve their purpose, they can have electrical conductivities as low as 10^{-11} siemens/cm. Researchers recently developed highly transmissive (~ 90 percent) and conductive 10^{-8} siemens/cm) polymeric film. The film has bulk conductivity in addition to surface conductivity, involving the bulk of the material in the conducting mechanism, as desired by its developers. The method used for developing the material consists of partial dehydrogenation of polyacrylonitrile (PAN)—without breaking the polymer chain by heating—in the presence of a metallic salt. The metal ions in the salt form a complex with certain sites on the polymeric chain. The developed material shows very low outgassing parameters. The conductivity of this film has remained constant for about 3 months at room temperature. Researchers are currently attempting to determine the material's long-term stability. This new material shows promising properties; researchers are currently studying the applicability of this film for specific antistatic shielding purposes.

Contact: Jeannette B. Stack
Code 313

Sponsor: Director's Discretionary Fund

◀ *The Tracking and Data Relay Satellite at geosynchronous orbit as displayed in near real time by the Flight Dynamics/Space Transportation System Three-dimensional Monitoring System.*

Ms. Jeannette B. Stack provides flight project support by doing X-ray diffraction and auger surface chemical analysis, and works on the DDF Project. She holds an MS degree in chemistry and has received a DDF study fellowship to obtain her PhD degree in physical chemistry.

A POLYMER FILM WITH IMPROVED STRENGTH FOR PYROELECTRIC APPLICATIONS

Pyroelectric polymers may be used in the direct conversion of heat into electrical energy in space systems. These materials will be manufactured at low cost. They provide an ultra-lightweight means of generating electrical power.

The Phase I goal of this Small Business Innovative Research project conducted by California's Chronos Research Laboratories, Incorporated, was to provide a means for forming pyroelectric polymer films with mechanical properties superior to those of the film that is presently available. The enhanced mechanical properties of these films will greatly improve the performance for pyroelectric applications such as pyroelectric generators, heat pumps, and refrigerators.

The Phase I objective was successfully accomplished. Previously, the pyroelectric film of copolymer vinylidene fluoride/trifluoroethylene was produced by compression molding with size limitation. Extrusion and blowing processes gave the film the desired size, but the film was brittle. After researchers tried various approaches, including biaxial extrusion and blowing, a new fabrication method was developed. The new method results in a film with greatly enhanced strength.

The improved film has a slightly higher heat capacity, and a lower heat conductivity, but this has an insignificant effect on energy generation. More importantly, the new film provides unusual gains in the lifetime of the material performance. To compare the durability of the enhanced film samples with the unmodified ones, a specific power cycle test was applied to both types of film. The power cycling consisted of thermal cycling between room temperature and 100°C, while electrical cycling between 20 and 40 MV/m was simultaneously applied. The power cycle is schematically illustrated in the accompanying

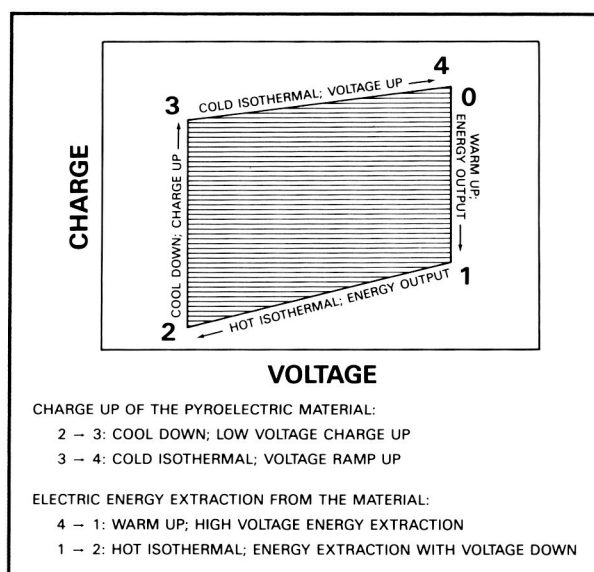
figure. The shaded area in the figure represents the net energy output.

In the case of the unmodified film, no specimen survived more than 10 power cycles before failing dielectrically.

The lifetime of the modified film performance was dramatically different. After more than 24 hours of continuous power cycling, the improved film was still producing electrical power as if it were new. With over 13,000 cycles, researchers halted the cycling experiment, without a noticeable decrease in the film's performance. The lifetime enhancement of the new film was at least a factor of 1300 over the unmodified specimens.

The film sample was then subjected to 60 Hz voltage cycling (10 to 40 MV/m) at a fixed high temperature of 100°C. After 15 hours of the voltage cycling (3,240,000 cycles), the sample was subjected again to power cycling, and showed essentially unchanged pyroelectric performance.

A similar series of experiments was conducted with another sample. The sample was electrically and visually monitored for 13 days. After a total of more than 67 million electrical cycles at 100°C, the film's electrical properties remained stable. The test was terminated without appreciable sample degradation. It



Pyroelectric power cycle.



should be noted that the 67 million voltage cycles applied in the test are comparable to 2 years of operation at 1 Hz, although caution should be used in extrapolating the performance.

With the success of the Phase I research, a durable pyroelectric film has been made available for further development, without film size limitation. In scheduled Phase II study, demonstration of extended lifetimes will be carried out, with moderately large-sized devices generating power in the range of 100 watts (currently the experiment is on the level of 1 watt).

Contact: S. Yen Lee
Code 313

Sponsor: Small Business Innovative Research
Program

Dr. S. Yen Lee, a polymer chemist, has been with Goddard since 1969. He is responsible for the development of improved or new materials to meet aerospace requirements. His publication topics include epoxy synthesis and formulations. Dr. Lee received his PhD degree from the University of Colorado.

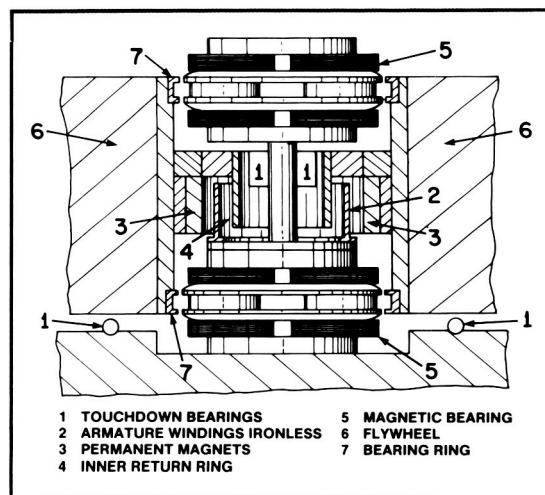
ADVANCED FLYWHEEL TECHNOLOGY FOR SPACECRAFT APPLICATIONS

High-speed composite rotor technology, when successfully integrated with magnetic suspension technology and high efficiency motor/generator technology, can lead to improvement in energy storage performance, particularly when it is applied in a low Earth orbit spacecraft for combined power and attitude control. Improvements by a factor of three in lifetime and energy density have been projected over current Ni/Cd battery technology. The moment of inertia of the energy storage wheel is much larger than that required by the reaction wheels for attitude control of a three-axis stabilized spacecraft; thus the combined functions of energy storage and attitude control can be accomplished using a minimum of four wheels in a tetrahedron configuration. The design of a 500 watt-hour wheel system is nearing completion under a Phase II Small Business Innovative Research contract. (The accompanying figure is a schematic representation of this system.) The 500 watt-hour wheel size is based on

a spacecraft with a payload requirement of approximately 4 KW. The design tools and methodology that have been developed to date can be applied to a wheel size scaling of about 10 to 1. Full-scale testing of the energy storage wheel system is planned once the fabrication of the first wheel is completed. Design goals for the system are: a system energy density of 20 Wh/kg, round trip efficiency of 80 percent, a bus voltage of 150 Vdc, and demonstrated cycle testing to 1000 cycles.

The composite rotor has been designed utilizing the latest improvements in composite materials, which should yield a usable system energy density that represents approximately 21 percent of the maximum energy density of the rotor. The rotor is designed to operate over a speed range from 75 percent of its maximum speed to 37.5 percent of its maximum speed, or from 60,000 rpm to 30,000 rpm. The composite rotor will be composed of five individual rings that are interference-assembled to form a multiring pierced disk. The resulting disk has an inside-to-outside diameter ratio of .45, an outside diameter of 28.0 cm, a thickness of 10.2 cm, and weighs approximately 6.8 kg.

The magnetic suspension and control system utilizes active positioning control in the radial direction, and passive control in the axial direction. Two identical magnetic bearings will be used for the complete suspension, one at the top of the rotor at its inner diameter, and one at the bottom. This two-bearing stack has been designed, built, and tested. Each



The 500 watt-hour wheel system.

magnetic bearing contains four permanent magnets and eight electromagnets to provide the necessary bias and control flux. The bearing stack contains backup ball bearings in the event of system failure.

An integral, permanent magnet, ironless armature, brushless direct current motor will be contained inside the inner diameter opening of the composite rotor, between the two magnetic bearing stacks. Power electronics for the motor/generator will be contained outside of the wheel assembly. The motor/generator utilizes a three-phase delta-connection armature with appropriate motor commutation-sensing electronics. Since the rotor speed varies over a speed range of 2 to 1, additional power electronics will be required to interface between the motor/generator and the spacecraft bus of 150 V.

Contact: G. Ernest Rodriguez
Code 711

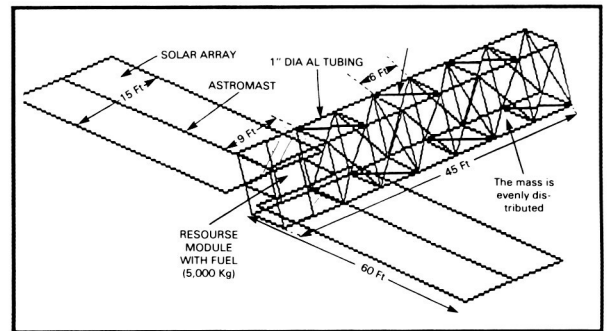
Sponsor: Small Business Innovative Research
Program

Mr. G. Ernest Rodriguez is an aerospace engineer with 26 years of experience in the research and development of spacecraft power systems at Goddard, and is currently a staff engineer in the Space Power Applications Branch.

ACTIVE VIBRATION CONTROL OF A FLEXIBLE SPACE STRUCTURE WITH PIEZOELECTRIC SENSORS/ACTUATORS

A typical space platform that might use piezoelectric sensors/actuators to control vibration consists of a rigid resource module, an instrument section, and deployable solar arrays. The accompanying figure shows such a generic space platform.

On the platform, the instrument section and solar arrays are quite long and limber, having lengths from 45 to 60 feet. These structural appendages can be very flexible. They are subject to thermal disturbances going in and out of the Earth's shadow, slewing attitude control maneuvers, and internal disturbances from moving parts in the instrument section. These disturbance-induced structural vibrations can persist for a long time, because of small inherent structural damping of the spacecraft. The persistent vibrations



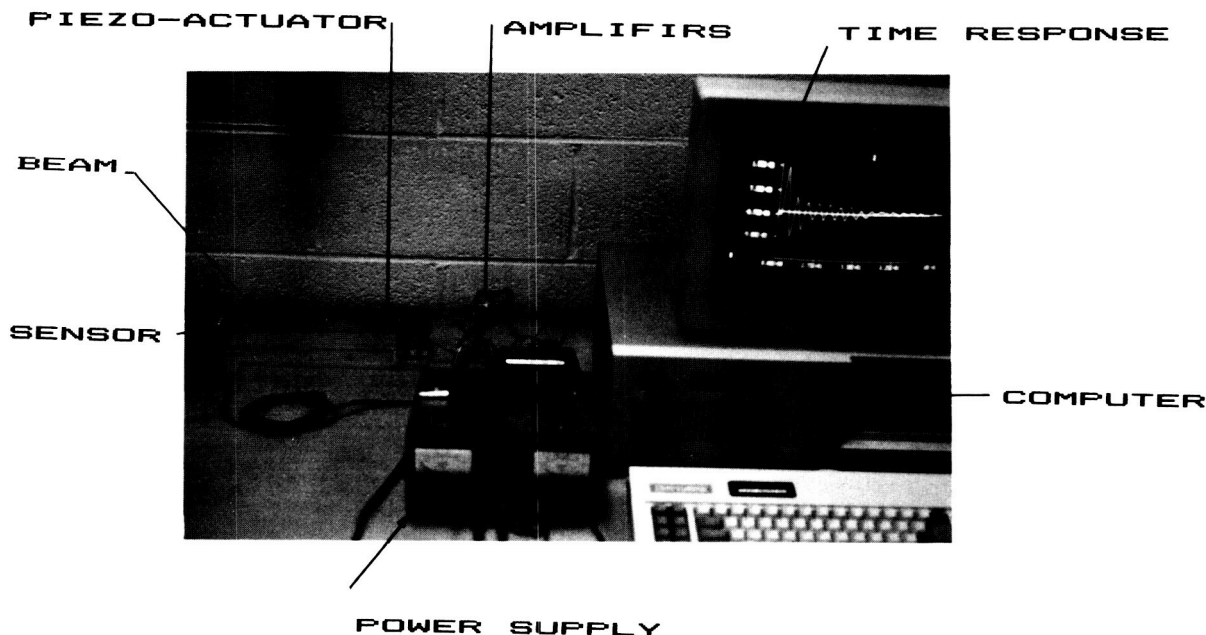
Generic space platform.

can degrade the scientific and engineering mission of the space platform.

Piezoelectric elements can simplify the implementation of active structural vibration damping systems, because they can serve both as sensor and as actuator. An attached piezoelectric element (sensor) can sense structural displacements by generating a voltage proportional to the displacements. Conversely, a voltage applied to a piezoelectric element (actuator) can apply a force to the parent structure to produce displacements. These sensors/actuators can easily be incorporated into trusslike structures/appendages, either integral with the truss, or placed at the ends of the appendages. The appendage tip is an ideal place to sense and control structural vibrations of a typical space platform, because it is never a vibration node.

Another desirable feature of structural vibration damping systems is to have global, inherently stable algorithms that use a few sensor/actuator pairs to significantly reduce the complexity and computing power required to make active structural damping systems practical.

Theoretical analyses and computer simulations have demonstrated that the Modified Independent Modal Space Control method, as well as the Positive Position Feedback method, can damp several vibration modes using a few sensor/actuator pairs. An active control system was successfully implemented to damp multivibration modes of a flexible beam, using one piezoelectric sensor/actuator pair that was time-shared among the various modes. Other algorithms were tested that did not perform as well in damping vibrations. The photo shows the laboratory test arrangements.



Active control of flexible beam by Piezo-actuators.

Work is also progressing on laboratory testing of the above algorithms and sensor/actuator pairs on a scaled generic space platform model.

Contact: Joseph V. Fedor
Code 712

Sponsor: Office of Aeronautics and Space
Technology

Dr. Joseph V. Fedor is a staff engineer at the Guidance and Control Branch of the Space Technology Division. He has over 25 years of aerospace experience in structural dynamics, mechanisms, thruster research, and orientation control of flexible gravity gradient, spinning, and momentum bias spacecraft. Dr. Fedor has participated in numerous flexible spacecraft flight programs.

LONG-LIFETIME STIRLING CYCLE CRYOGENIC COOLER

Many space instruments require ultralow temperature cooling to perform their measurements. Several Goddard Space Flight Center technology programs are under way to fulfill this need. One such program

is to develop an ultralow temperature (cryogenic) refrigerator that will operate in space for 3 to 5 years without maintenance.

The proof-of-principle model cooler successfully completed 37,057 hours (over 4 years) of operation in July, 1, 1988. The magnetic bearings operated for 54,048 hours over that time period.

Running silently, at an average speed of 25 cycles/s, the model generates 5 W of cooling power at a temperature of 65 °K when its compression heat is rejected at 300 °K. Its reciprocating components work without conventional bearings, seals, or lubricants because they are levitated and centered by magnetic bearings. A closed-loop servo system controls the position of the free-floating pistons. Moving magnet linear motors of a new design provide linear motion. The operating performance of the cooler has not changed during over 4 years of operations.

The second-generation cooler, the Technology Demonstration Model, is being fabricated; it is designed to survive Shuttle launch and operation in space. The launch specifications necessitated improvements in electromagnetic bearings, axial and radial position sensors, structural design of the

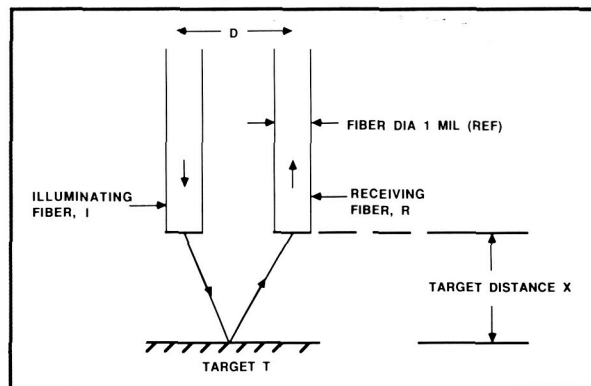
moving elements, and the axial counterbalance. As in the first-generation refrigerator, organic contamination has been eliminated by the use of all-metal and ceramic construction. Reductions in system input power result from an integral permanent magnetic displacer spring motor, and more efficient linear motors and drive electronics.

Improved Linear Variable Differential Transformers provide high-frequency capabilities to the axial control system. All clearance seal surfaces are specially treated with ion-plated titanium nitride to eliminate potential damage due to contact during launch and shipping. Transmitted vibrations are minimized by 6-degree-of-freedom spring mounts between the refrigerator and spacecraft. The counterbalance, a tuned spring mass system driven by a linear motor, and supported radially by magnetic bearings, cancels the unbalanced axial force generated during operation.

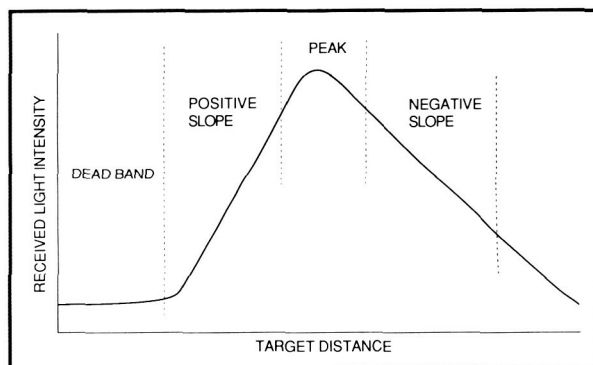
Construction of the prototype model continued over the past year. This model will have fiber optic sensors to interface with the magnetic bearing driver electronics. Researchers expect to conduct closed-loop testing of the magnetic bearing test fixture in the near future.

A reflection-based fiber optic position sensor has been built for use with the magnetic bearings. The principles of operation, construction, and performance of the sensor are outlined below. Reflection-based fiber optic sensors are commercially available for the purpose of on/off detection, e.g., for reading bar codes or checking for presence of objects. The sensor described below is for purposes of long-life analog distance measurement within a hermetic, organic-free environment for magnetic bearing control.

Optical fibers transmit light by means of total internal reflection. Consider a single optical fiber I that illuminates a reflective target T shown in the first figure. Part of the reflected light is received by a receiving fiber R. The amount of received light (other factors such as transmittance of the intervening medium and reflectivity of the target being constant) varies with the target distance as shown in the second figure. The location of the dead band, positive slope region, peak, and the negative slope depends on the diameter of the fibers I and R, and the distance D



Fiber pair with target.

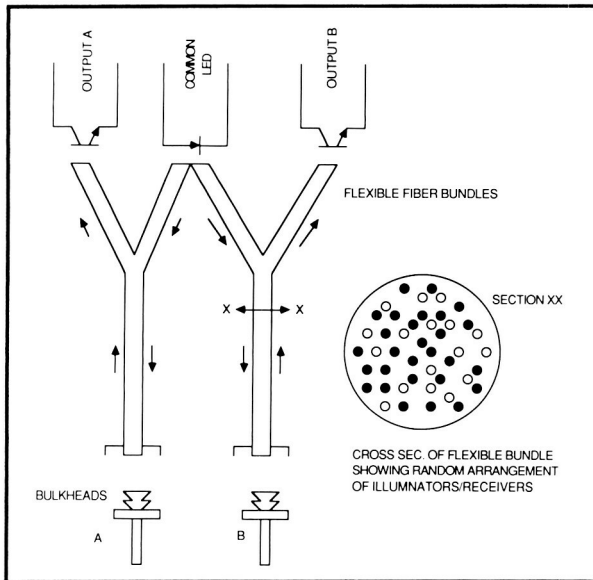


Response of fiber pair shown in first figure.

between them. In order to achieve acceptable signal/noise level, a single bundle consisting of N illuminator and N receiver fibers is used. The transfer characteristic of the bundle is a weighted sum of the responses of the N pairs, and depends on the geometric distribution of illuminators and receivers within the bundle. The random distribution of 1 mil diameter fibers used in this sensor yields a small dead zone, and a peak at approximately 10 mils.

A prototype sensor schematic is shown in the third figure. The bulkheads consist of a bundle of fused optic fibers (approximately 509,000 fibers joined to each other under pressure, so that they form a solid cylinder of leak-tight glass) metallurgically joined to a Cupra-Nickel sleeve. Bulkheads are soldered into the refrigerator housing with the ends of the fibers facing the shaft.

The light source is an infrared light emitting diode (LED). Light from the LED travels down a flexible

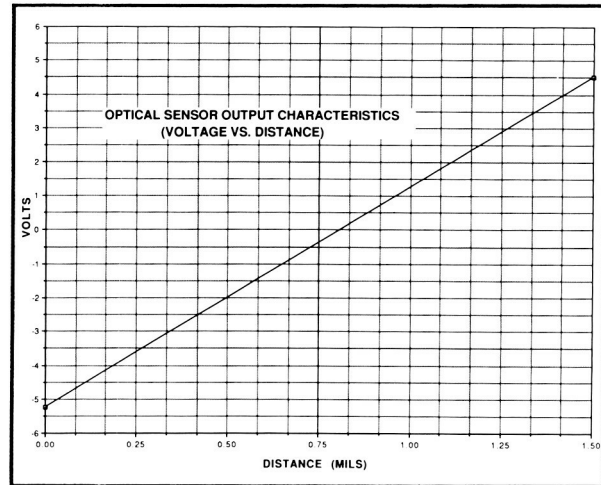


Prototype sensor.

bundle, through the bulkhead (fibers in the bulkhead are smaller, so that fiber-to-fiber alignment is not necessary at the flexible bundle-bulkhead connector). Light reflected by the shaft travels back up the bulkhead and through the receiving fibers (the receiving fibers are randomly mixed with the illuminating fibers within the flexible bundle). The receiving bundle terminates at a phototransistor that converts the received light into electrical current.

One LED serves as a light source for bulkheads that face the shaft from diametrically opposite locations. This arrangement compensates for long-term variation in the output of the LED. The two detectors are also mounted in the same metal casing, which should compensate for the already small temperature coefficient. The bulkhead provides for a hermetic and nonorganic means of conveying light into the housings. It also provides for decoupling of the comparatively sensitive optical electronics from the refrigerator housing, and associated housing fabrication operations.

A titanium block was used to obtain a response curve for the sensor, with bulkheads A and B looking at opposite parallel faces of the block. The response curve is shown in the fourth figure. The curve indicates that the sensor is sensitive (70 percent/mil or 3 percent/ μ for each phototransistor). A commercially available sensor of different design (and of



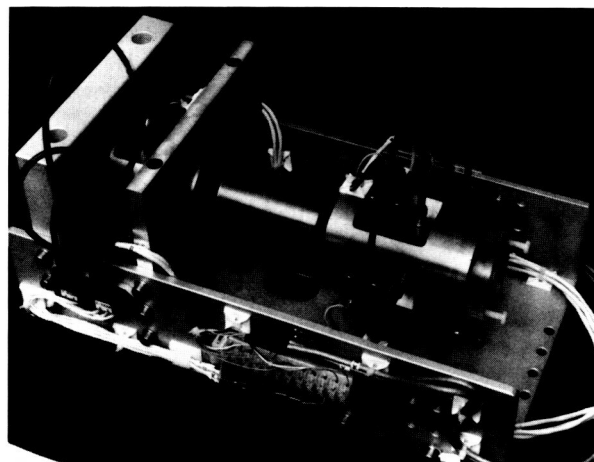
Output (volts versus position) of sensor.

much poorer sensitivity), but using the same optical electronic components and fibers, was found to have a temperature coefficient of $0.004 \text{ mil}/^\circ\text{C}$ in a single-ended mode. The frequency response of the optical sensor, including associated signal conditioning electronics, is also excellent: a bandwidth (-3 dB) of 16 kHz was measured.

The photo shows the magnetic bearing test fixture with fiber optics sensors.

This cooler development has won two IR-100 "Invention-of-the-Year" awards.

Contact: Max G. Gasser
Code 713



Magnetic bearing test fixture with fiber optic sensors.

**ORIGINAL PAGE
BLACK AND WHITE PHOTOGRAPH**

Sponsors: Office of Aeronautics and Space Technology, and United States Air Force Space Technology Center

Mr. Max G. Gasser is an aerospace engineer with 23 years of experience at Goddard. Mr. Gasser, who received his BS degree in chemical engineering from Virginia Polytechnic Institute, is involved with cryogenic cooler technology research and development for space applications. He received the IR-100 Award in 1983 and holds a patent on the Stirling cycle cryogenic cooler.

ALL-METAL COMPACT HEAT EXCHANGER FOR SPACEBORNE CRYOCOOLERS

The overall cycle efficiency (hence, input power requirements) of reverse-Brayton cryocoolers for space applications is highly sensitive to the thermal effectiveness of the heat exchangers. Applications for these cryocoolers in space dictate that these heat exchangers be as small and light as possible. To date, only heat exchangers employing organic materials have been able to achieve the high thermal effectiveness values required for these systems within the allowed size and weight limitations. However, heat exchangers with organic materials degrade cycle performance by leakage, and by system contamination. Therefore, a compact all-metal heat exchanger with high thermal effectiveness is required.

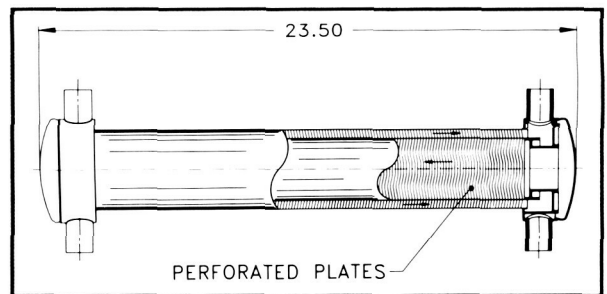
Goddard Space Flight Center (GSFC) has started to develop high-performance, all-metal heat exchanger. Two novel heat exchanger concepts were evaluated with respect to size, weight, and manufacturability, with the aim of achieving a thermal effectiveness in excess of 0.98. Detailed thermal models of the heat exchangers were developed, and fabrication and assembly techniques of key exchanger elements were demonstrated.

The specific objectives of this research are: to significantly reduce the weight of the heat exchanger; to combine high thermal effectiveness and low pressure drop; to develop innovative fabrication methods so a range of applications can be met; and to eliminate materials that can outgas and contaminate a closed-loop cryocooler. Because the thermal effectiveness goal is equal to or greater than 0.985, the exchanger will require 300 copper plates, with a total

of 1 million very narrow slots. To fabricate these plates, a new electric discharge machine (EDM) is being designed and developed. Researchers believe that this technology will advance the state of the art over the present perforated plate produced by the electron beam method.

The copper plate thickness is 0.016 inches, the slot width is 0.005 inches, and the slot length is 0.140 inches. The shell is number 321 stainless steel. Accompanying are the assembly drawing and a scanning electron microscope photograph of a test piece. The photo illustrates the smoothness and uniformity of the slot relative to holes produced by the electron beam method.

The only drawback to the new technology has been the slow cutting rate, but this has been increased by



All-metal compact slotted plate heat exchanger for spaceborne cryocoolers.



A scanning electron microscope photo of the all-metal heat exchanger (electric discharge machine slots through the copper plate).



a combination of greater circuit voltage, greater circuit capacitance, and greater cutting-head flushing. The cutting rate of the EDM slot-cutting test rig has advanced from $0.02 \text{ mm}^3/\text{min}$ to $1.03 \text{ mm}^3/\text{min}$ with acceptable quality.

The heat exchangers were sized to meet the specifications of a 5 W reverse-Brayton cycle cryocooler currently under development for GSFC. The specifications are: a 0.9 g/s balanced flow of neon; with 2.2 atm, 260°K inlet conditions at the warm end; and 1.2 atm, 70°K at the cold end. Thermal analyses of the heat exchangers show that an overall effectiveness (effectiveness including pressure-drop penalty) as high as 0.985 to 0.995 can be achieved with modest heat exchanger weights (less than 3 kg).

In addition to meeting the specialized needs of spaceborne cryocoolers, this heat exchanger technology may have widespread applications in commercial helium liquefiers and refrigerators.

Contact: Max G. Gasser
Code 713.1

Sponsor: Small Business Innovative Research
Program

A LONG-LIFETIME, LOW-VIBRATION, CLOSED-CYCLE CRYOCOOLER FOR SPACE

Turbomachinery is used in large-scale gas liquefaction plants, but the components are much too large for the National Aeronautics and Space Administration's needs. Recent advances in miniaturization have made turboexpanders as small as $\frac{1}{8}$ inch in diameter. These operate at very high speed when supported on self-acting (tilting pad) gas journal bearings with pressurized gas thrust bearings, or magnetic thrust bearings. The impeller for the centrifugal compressor is shown in the accompanying picture, compared to the size of a 1-cent coin.

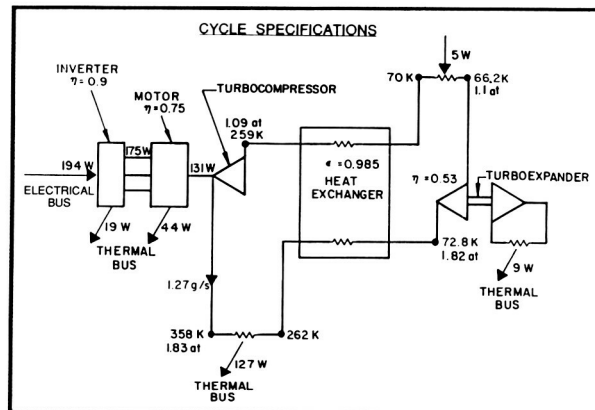
Unlike the Stirling cycle coolers, the gas-bearing turbomachinery produces no noise or vibration. However, at the present time, the magnetic bearing approach is much further ahead in its development.

When fully developed, the reverse-Brayton cycle approach should be much less expensive to build than

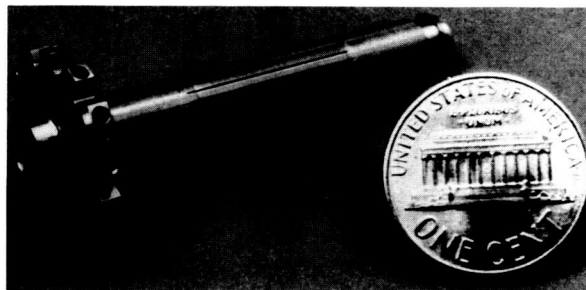
the magnetic Stirling, and should have similar efficiency for operating temperatures above approximately 40°K. The reliability would also be greater, due to the decreased electronics part count.

A program is under way to design and build a reverse-Brayton cycle system to produce 5 watts of cooling of 70°K. This cryocooler uses neon as the working fluid. The cycle specifications are given in the accompanying flow diagram. While operating, the moving parts are not in physical contact, so the system should have a very long lifetime. This system will use an all-metal heat exchanger, and should be free of contamination. Because it is self-acting, the system is simpler than the magnetic bearing approach, and requires only a compressor motor controller, instead of complex electronics.

Testing has started on an engineering model cryocooler. When completed, the all-metal compact heat exchanger will be tested in this closed-cycle cooler,



A reliable, long-lifetime, closed-cycle cryocooler for space (reverse-Brayton).



Centrifugal impeller and shaft for a 500,000-rpm compressor with gas bearings.

along with the three-phase inverter currently being developed for ultrahigh-speed motor drivers.

Contact: Max G. Gasser
Code 713

Sponsor: Small Business Innovative Research
Program

THREE-PHASE INVERTER FOR ULTRAHIGH-SPEED MOTOR DRIVE

Some of the long-lifetime cryocoolers being developed for space sensor applications are based on the reverse-Brayton cycle. An attractive implementation of the cycle would use high-speed miniature centrifugal compressors and turboexpanders running on gas bearings to provide reliable and vibration-free operation. Hardware development and demonstration programs are presently underway for three of the four key cryocooler components: the turboexpander, the turbocompressor, and the heat exchanger. Researchers are also developing the fourth key component: the variable frequency, three-phase inverter for driving the high-speed compressor motor.

The motor drive requirements for this application are very different from those of existing high-speed motors. The design speed is about five times higher (500,000 RPM), and the stator impedance is several times lower, thus drawing very high currents (up to 40 amps during start-up). A novel three-phase inverter concept that has the potential to generate extremely low harmonic content waveforms at frequencies of up to 10 KHz (or more) using very simple and reliable electronics is currently being evaluated. In addition, the inverter is compact and lightweight for space flight.

In order to obtain good performance from the motor, the supply waveforms must also satisfy the following requirements: 1) the waveform must have no subharmonic component; 2) each harmonic component must be balanced; and 3) the waveform must be free of even harmonics and direct current components. Also, the closer the waveform is to a true sinusoid, the better the performance of the motor.

Reduced harmonic content is particularly important in this application because engineers hope to

minimize the internal heat generation in the motor. Gas-bearing components operate at extremely tight clearances, and cannot tolerate excessive differential thermal expansion. Moreover, to avoid contamination, the motor is completely sealed; heat generated in the stator must be conducted out through the low thermal conductivity stator laminations.

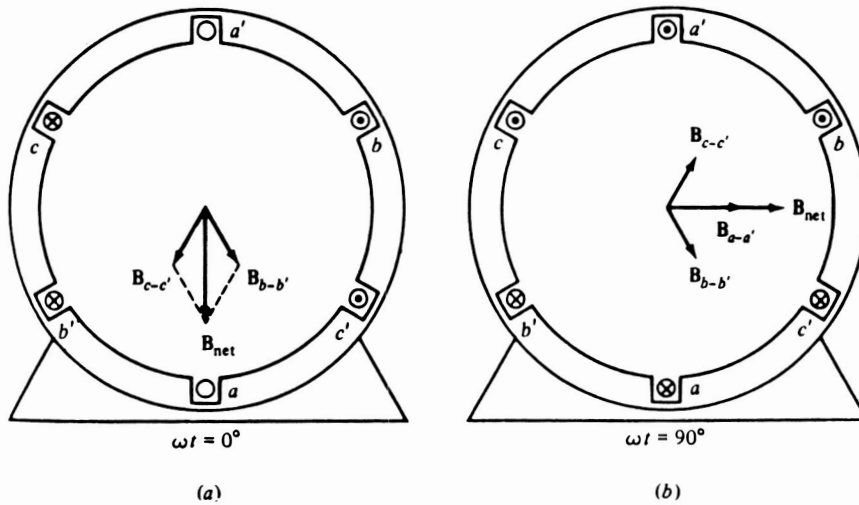
The reduced motor efficiency that would result from high harmonic content in the motor drive would also represent a direct loss in overall cryocooler efficiency. In typical space sensor systems, about 75 percent of the subsystem weight is nearly proportional to the power consumption. Therefore, any loss in motor efficiency translates directly into increased subsystem weight.

Variable-speed drives are commercially available from several suppliers, both in the United States and abroad. However, these drives are not well suited for this application. Most commercial drives use rectangular wave modulation, and their output has high harmonic content. Moreover, the drives are generally designed for lower frequencies, to power motors running at 100,000 rpm or less.

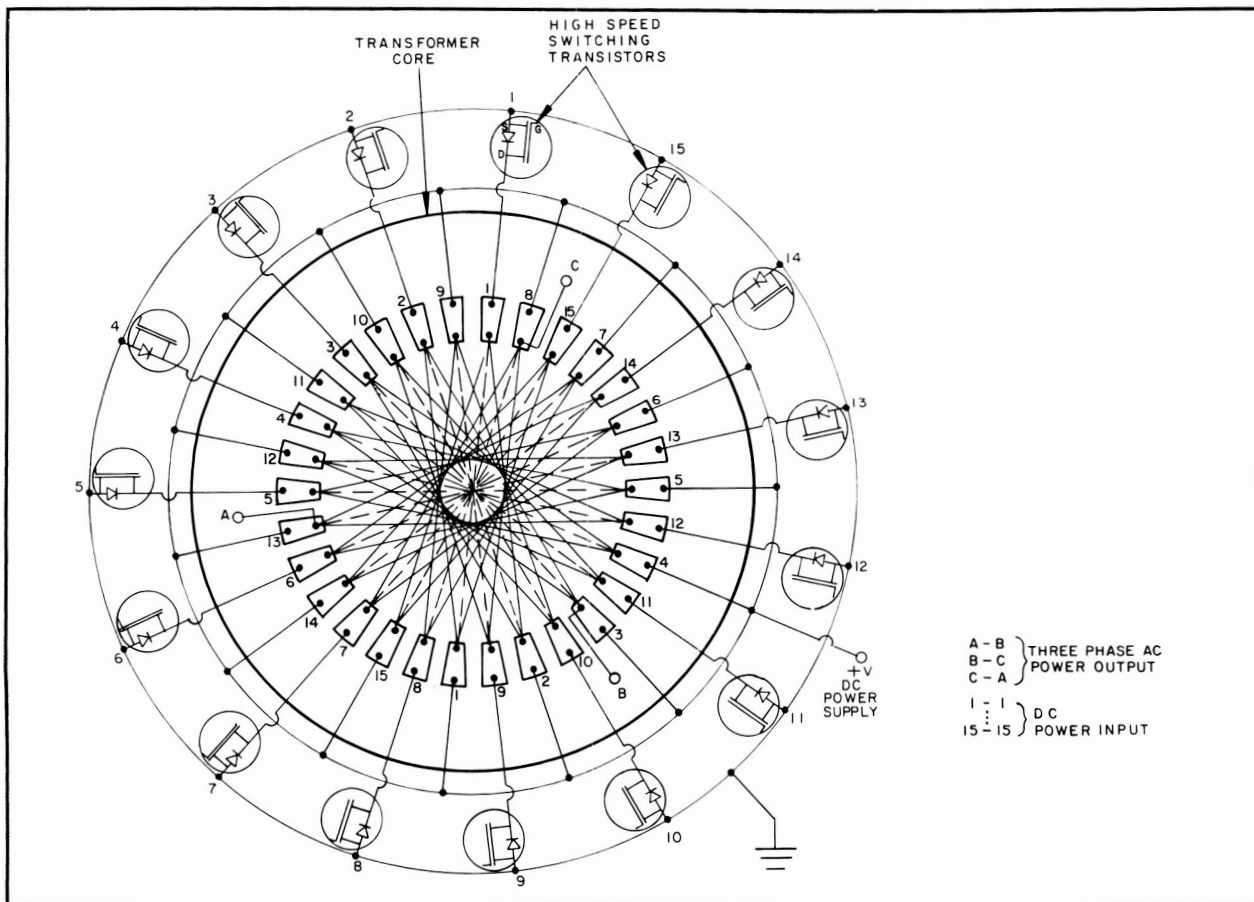
Advanced three-phase variable-speed motor drives presently under development use microprocessors to implement Pulse Width Modulation (PWM), thus reducing the harmonic content of the waveforms. Much progress has been made in this area, but, because of present computation speed limitations, this approach is not practical for the high speed needed in a miniature compressor or turboexpander. Most of the applications described in the literature have top frequencies of less than 200 Hz. The design speed of the National Aeronautics and Space Administration cryocooler compressor is 40 times higher.

The inverter specifications are shown in the table. The rotating-field inverter concept is shown in the two figures. A breadboard model is currently being fabricated and tested.

In addition to the turbocompressor application described above, there are widespread commercial applications for high-performance, variable-frequency, three-phase inverters. The use of variable-frequency, variable-speed motor drive systems has accelerated in recent years, driven by the need for



Rotating field inverter concept: rotating magnetic field in a 3 ϕ stator.



Rotating field inverter concept: rotating magnetic field by dc commutation.

ORIGINAL PAGE
BLACK AND WHITE PHOTOGRAPH

energy conservation, especially in process control and pumping applications.

Contact: Max G. Gasser
Code 713

Sponsor: Small Business Innovative Research
Program

GAS GAP HEAT SWITCH

A heat switch does for heat what an electrical switch does for electricity: it allows the heat to flow only when and where the operator wants it to flow. The Cryogenics Technology Section at the Goddard Space Flight Center (GSFC) has developed a gas gap heat switch for use in space.

To judge heat switch performance, researchers measure the thermal conductance of the switch when it is turned on and when it is turned off. Such measurements were recently carried out on the Goddard heat switch. With one end at 1.6°K, and the other end at 2.1°K, the switch has a conductance of more than 80 mW/°K when turned on, and a conductance of approximately 0.1 mW/°K when turned off.

The heat switch consists of two copper end pieces held in a Vespel cylinder, as shown in the accompanying photograph. (Vespel is a polyimide plastic made by E. I. DuPont de Nemours and Company.) A 0.01-inch gap separates the copper end pieces. Flooding the gap with helium gas allows heat to flow from one end piece to the other. Evacuating the gap stops heat flow.

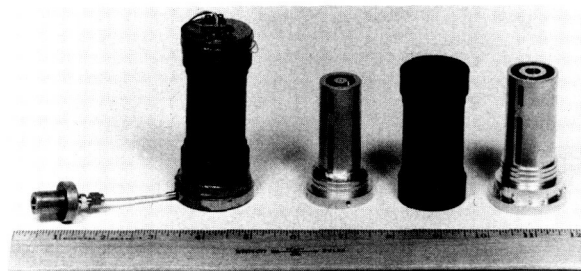
The copper end pieces are designed to allow the greatest possible heat flow when the switch is turned on. In practice, this means giving the pieces—and the gap—the greatest possible surface area. Each end piece consists of two concentric cylinders mounted on a plate. When the end pieces are mounted in the Vespel shell, these cylinders mesh without touching. The area of the gap is thus the surface area of the cylinders that form the gap's boundary. Although the Vespel shell is only $\frac{3}{4}$ inches in radius, and $3\frac{1}{16}$ inches long, the gas gap area when enclosed is over 11 square inches.

The helium for the switch is stored in a getter made of zeolite 5A. Zeolites, also called molecular sieves, are a class of crystals widely used to adsorb gases and liquids. Zeolites adsorb well because their structures are highly porous: a gram of zeolite can contain several hundred square meters of pore surface area. In the heat switch, the zeolite is glued to a copper base using silver-filled epoxy, which ensures good thermal contact between the base and the zeolites. Heating the base heats the zeolite and drives the helium out of the zeolite pores into the gas gap, turning the switch on. Cooling the base cools the zeolite, drawing the helium out of the gas gap into the zeolite pores, and turning the switch off.

This heat switch design is ideal for use in space because it has no complex plumbing, and no moving parts to wear out. Other types of heat switches have both. Some gap-type heat switches open valves to allow helium to flow into and out of the gap. In other heat switches, the heat flows between solid contacts that touch to allow heat to flow, and separate to block heat flow.

The Goddard heat switch is an important part of the Adiabatic Demagnetization Refrigerator (ADR). When turned on, the heat switch in the ADR allows the heat to flow from a paramagnetic salt pill at a temperature of about 2°K, to a helium bath at 1.5°K. When the heat switch is turned off, the temperature of the salt pill can be lowered to 0.1°K.

The heat switch presently being tested incorporates a 0.6 mil stainless steel foil liner inside the Vespel cylinder to overcome the room temperature porosity of the Vespel. Unfortunately, the stainless steel liner was applied with a thick epoxy bond line that



Gas gap heat switch (left, assembled; right, disassembled) showing the Vespel shell flanked by the copper end pieces.



dominates the off conductance of the switch. Based on existing thermal conductivity data, researchers believe that eliminating the epoxy will reduce the conductance of the heat switch between a 1.5°K helium bath and a 0.1°K salt pill to less than 0.01 mW/°K. This low thermal conductance will prevent heat from flowing into the salt pill, allowing the ADR to operate for more than 400 minutes between cycles.

Contacts: Brent A. Warner,
Aristides T. Serlemitos,
Susan R. Breon, and Stephen H. Castles
Code 713

Sponsor: Office of Space Science and Applications

Mr. Brent Warner has an MS degree in physics from the Ohio State University. Mr. Warner's responsibilities include adapting an Adiabatic Demagnetization Refrigerator for use in satellites where temperatures lower than liquid helium temperatures are needed.

Dr. Aristides T. Serlemitos is an aerospace engineer with 17 years of experience at Goddard. Dr. Serlemitos, who received his PhD degree in physics from the University of Maryland, developed and built composite bolometers that are considered among the best in the world.

Dr. Susan R. Breon is working on AXAF, Astromag, and liquid helium servicing. She earned a PhD degree in superfluid helium physics from the University of Wisconsin.

Dr. Stephen H. Castles, Head of the Cryogenics, Propulsion, and Fluid Systems Branch, has 10 years of experience at Goddard. He earned a PhD degree in physics from the University of Florida.

LOW-CURRENT SHIELDED MAGNET

The Cryogenics Technology Section of the Goddard Space Flight Center has procured a low-current shielded superconducting magnet. The magnet will be part of an Adiabatic Demagnetization Refrigerator (ADR). The magnet uses a low current to reduce the heat load on the long-life liquid helium Dewar that cools the magnet. The magnet must be

shielded to avoid interfering with other systems on the satellite. Cryomagnetics, Incorporated, designed and built the magnet.

A bath of liquid helium cools the magnet. The magnet itself contributes little heat to the bath because it is made of superconducting wire. The magnet's current leads contribute much more heat to the helium bath because they must be made of resistive (nonsuperconducting) wire. The leads are too warm to be superconducting because they connect the magnet to the power supply, which is at room temperature.

Resistive leads transmit heat to the cooling bath in two ways: through heat conduction, and through joule heating. It is difficult to design leads for a conventional, high-current magnet that reduce both heat loads to low levels. Changing the lead design to decrease heat conduction increases joule heating, and vice versa. Fortunately, by decreasing the electrical current carried by the leads, the joule heating is low, even with leads designed for low heat conduction.

The low-current magnet produces a field of 1 tesla per ampere, and will create fields as high as 1.7 tesla. (The Earth's magnetic field is about 5×10^{-5} tesla.) Conventional superconducting magnets require much higher currents—tens of amperes—for similar fields. The low-current magnet achieves such high current-to-field ratios by using many turns of much thinner wire than conventional magnets. An interesting consequence of this design is that the magnet has a net inductance of nearly 950 henries. It is believed to be the highest inductance magnet ever produced.

The shielding for this magnet must confine the magnetic field to the center of the magnet, preventing the field from reaching areas outside the magnet. There are three types of commonly used magnetic shielding: passive-ferromagnetic, passive-superconducting, and active. This magnet combines passive-superconducting with active-superconducting shielding to achieve the greatest possible shielding with the least weight.

In ferromagnetic shielding, ferromagnetic materials such as iron surround the magnet, confining most of the field within the shield. Ferromagnetic shielding's main drawbacks are that it is heavy, and

that it leaves an appreciable, though small, external field.

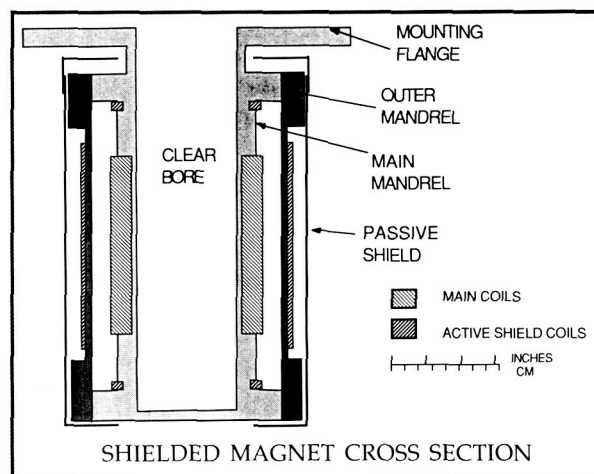
In passive-superconducting shielding, a shell of superconducting material surrounds the magnet. Since a superconductor completely blocks magnetic fields as long as the fields are not too strong, passive-superconducting shielding can completely block small, unwanted fields. Passive-superconducting shielding's main drawback is that it fails if the field is stronger than the critical field strength of the superconducting material.

In active shielding, magnetic coils set up a field that cancels out the main field in areas where low field is needed. Since active shields are part of the magnet, they can shield against fields as strong as the magnet itself can produce. Active shielding's main drawback is that a system of shield coils cannot reduce the fringing fields to zero everywhere without being unduly complicated.

An active shield surrounded by a passive-superconducting shield combines the strong points of both. A relatively simple active shield reduces the field at a cylindrical surface outside the magnet to a low level. An outer, passive-superconducting shield placed at this cylindrical surface blocks the remainder of the fringing field. Thus, this shield combines the high field performance of active shields with the complete blocking of passive-superconducting shields. The weight of the total shield, moreover, is less than that of a high-quality ferromagnetic shield.

The accompanying diagram shows a simplified cross section of the magnet. The magnet as a whole is cylindrical, as are the individual sections. The outermost section is the passive shield, a lead-coated aluminum cylinder with partly closed ends. Just inside the passive shield is the outer mandrel, an aluminum cylinder machined to support the outer active shield coils. Innermost is the main mandrel, an aluminum billet with a cylindrical cavity in the center, cylindrical spaces for mounting main and shield coils, and, at one end, a circular mounting flange.

Preliminary testing of the magnet was recently completed. These tests confirmed the performance of the magnet. Of particular interest to researchers is the fact that, with the central field set at 1.6 tesla, the stray field outside the passive shield was too small



Shielded magnet cross section.

to be detected with Hall probes usually sensitive enough to detect any field larger than 10^{-4} tesla.

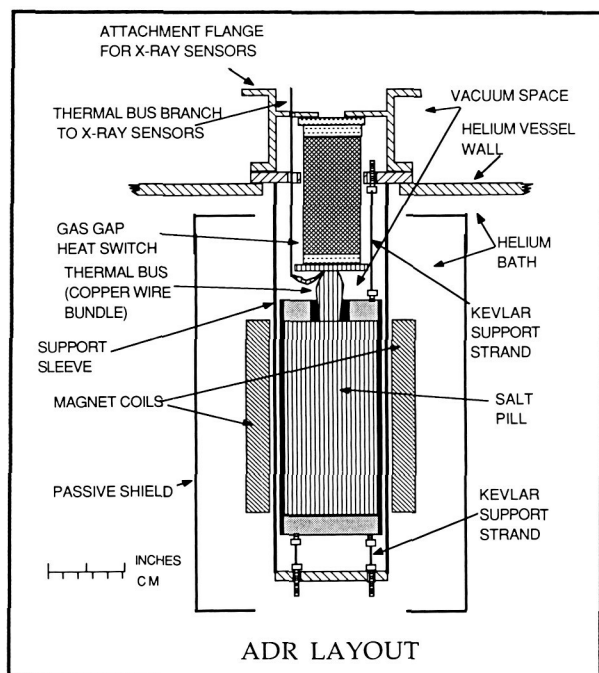
Contact: Brent A. Warner
Code 713

Sponsor: Office of Space Science and Applications

ADIABATIC DEMAGNETIZATION REFRIGERATOR

The Adiabatic Demagnetization Refrigerator (ADR) is a cryogenic cooling system that has been used for many years on the ground. Goddard Space Flight Center's Cryogenics Technology Section is now developing an ADR to cool X-ray sensors in the X-Ray Spectrometer (XRS), an instrument proposed for the Advanced X-ray Astrophysics Facility (AXAF). Cryogenic cooling of sensors in satellites is not new: the Infrared Astronomy Satellite (IRAS) used liquid helium to cool infrared sensors to 1.5°K. AXAF will use liquid helium to cool the ADR to 1.5°K, and the ADR will then cool the X-ray sensors from 1.5 to 0.1°K, greatly increasing detector sensitivity.

The Cryogenics Technology Section is now assembling a full-scale breadboard model ADR to test the basic design for the flight model. A schematic of the ADR is shown in the figure. Testing began in October 1988. Even though the helium bath temperature was



Layout of the Adiabatic Demagnetization Refrigerator.

1.7°K (0.2°K hotter than planned) the ADR cooled to 0.13°K.

At the center of the ADR is a cylinder ("pill") of paramagnetic salt, suspended in the field of an electromagnet. As the magnetic field increases or decreases, the salt responds by warming or cooling, respectively. To operate the ADR, the salt pill is thermally isolated, and the magnetic field is decreased, causing the salt pill to cool to 0.1°K. The X-ray sensors, which are connected to the salt pill by a bundle of copper wires, also cool to 0.1°K. Parasitic heat enters the salt pill, and sensors, from the warmer surrounding apparatus, but the ADR control electronics monitor the temperature, and slowly lower the magnetic field as needed to absorb the heat, and maintain the salt pill at 0.1°K.

Current plans call for the ADR to keep the sensors at 0.1°K for 400 minutes. After 400 minutes, however, the salt pill will have absorbed all the heat it can. The ADR will then be cycled back to 1.5°K, to exhaust its absorbed heat to the helium bath. The magnetic field is increased, heating the pill. Then the heat switch is turned on, providing a path for the heat to flow from the pill to the helium bath. When the

pill has exhausted the stored heat, the switch is turned off, preventing heat from flowing back into the salt pill when it is cooled by reducing the magnetic field.

In general, ADRs are well suited to use in space. The ADR's main rival on the ground is the liquid helium dilution refrigerator. The dilution refrigerator's main advantage is that it cools continuously; unlike the ADR, it does not have to warm up to exhaust the heat it absorbs. The dilution refrigerator's main disadvantages are that it operates inefficiently, it requires complex plumbing, and current versions depend on gravity to separate fluid mixtures. The ADR operates more efficiently, requires no plumbing, and is independent of gravity.

The Goddard ADR breadboard design is similar to that envisioned for the flight ADR. It has no moving parts, including none in the heat switch; the magnet and salt pill have been optimized for maximum cooling power with minimum weight; and a flightlike Kevlar fiber support system is used. Kevlar combines high strength with low thermal conductivity, and thus supports the salt pill with a large margin of safety while allowing a heat leak of less than 20 μ W into the pill.

Contacts: Aristides T. Serlemitsos,
Brent A. Warner, Susan R. Breon,
Stephen H. Castles, Stephen M. Volz,
and Frank N. Paczkowski
Code 713

Sponsor: Office of Space Science and Applications

Dr. Stephen M. Volz joined Goddard in 1986 and has worked on AXAF and COBE. He earned a PhD degree in superfluid helium physics from the University of Illinois.

Mr. Frank N. Paczkowski, a senior engineering technician, was educated at Syracuse University and the University of Maryland. Mr. Paczkowski has worked in several disciplines at Goddard.

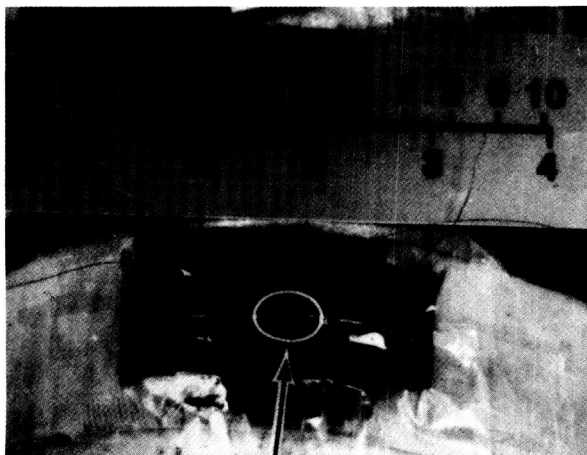
COLLISION AVOIDANCE/MANAGEMENT SKIN FOR ROBOT ARMS

Safety is a primary concern when robots are operated in space. Researchers at Goddard Space Flight Center

ORIGINAL PAGE
BLACK AND WHITE PHOTOGRAPH

(GSFC) are directly addressing that concern by employing a collision/management skin around the robot arms. Such a skin would allow the robot to sense the presence of an object to within the range of approximately 1 foot (plus permitting the robot to prevent a collision); to detect the edges of the object to ± 1 inch at a 2-inch range (permitting the robot to go around the obstacle); and when contact is made, to use tactile sensing to determine where on the robot arm, to ± 0.25 inches, and how hard, at a threshold of <8 ounces, such contact was made (permitting the robot to manage the contact). These requirements were addressed by employing a dual-mode radio frequency array of sensors. These proof-of-principle sensor prototypes used amorphous metallic glass materials to enhance their performance. Researchers are continuing to experiment with integrated circuit techniques, hoping to lower costs and improve reliability. The work is being done in-house at GSFC.

The proof-of-principle prototypes, one of which is shown in the photo, were successful. They were operated at frequencies of 100 kHz; thus, they will not create electromagnetic interference (EMI) problems. They were able to detect the proximity of a human hand at ranges of >1 foot, with a 1-mV signal; they were able to detect the edges of the hand to ± 1 inch at a 2-inch range; and they were able to detect tactile contact at a threshold of <8 ounces, with a signal $\gg 1$ mV. Since the tactile signal was 180° out of phase with the proximity signal, the two conditions were easily discriminated. Magnetic objects were identified by a shift in the signal dc bias. The

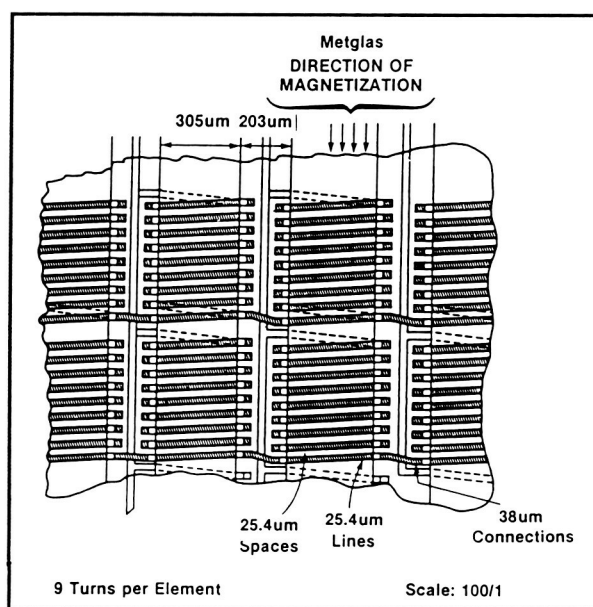


Sensor prototype.

sensor would have difficulty detecting objects that are totally nonconducting and nonionic; but it is extremely unlikely that such materials would exist in isolation on the Space Station or a space vehicle. In addition, the sensors were able to "see through" a 21-layer thermal blanket; thus they need not be exposed to the space environment. Also, since the signals produce essentially a continuous radio frequency sensing field around the robot arms, the robot cannot be blinded by problems that normally handicap optical sensors, such as sun glint, reflections, and heat. And, since the radio frequency field is sinusoidal, unfriendly EMI noise can be filtered out. The physical layout of sensor elements is shown in the figure.

Researchers are continuing to develop integrated circuit techniques to simplify the sensor arrays, lower their costs, and improve their reliability. These integrated circuit techniques revolve around the concept of etching microminiature transformer cores in metallic glass ribbons, and etching a planar, single-layer copper coil around the cores. To date the cores have been successfully etched and their small size suggests that sensors may be constructed as small as 0.020 by 0.020 inches if needed.

Researchers anticipate that a capability will be added to the skin permitting the robot arms to detect the



Physical layout of sensor elements.



proximity of a hot object. This will be accomplished by adding a layer of PVDF heat-detecting material to the thermal blanket. The RF sensor will "see through" this layer, as well as the rest of the thermal blanket.

Contact: John M. Vranish
Code 716

Sponsor: Director's Discretionary Fund

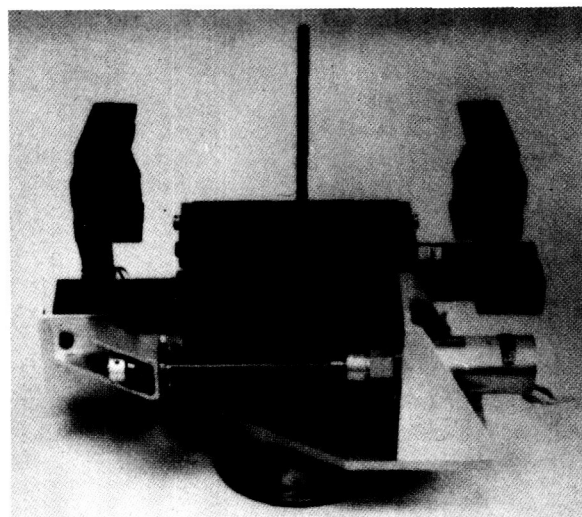
Mr. John Vranish, an aerospace engineer in the Electromechanical Branch, has written numerous papers and holds several patents in robotic electromechanical systems, mechanisms, and tactile/proximity/force sensors. His invention, the Robotic Derivator, was the top-rated Department of Defense Robot innovation in FY 1979. He received his MS degree in electrical engineering from the George Washington University.

ADVANCED MECHANISMS FOR ROBOTICS

Recent work at Goddard Space Flight Center's Electromechanical Branch has focused on end effector-related mechanisms, and robot-friendly payload latching systems. Included as components of each system are the mechanicals; the sensors to monitor the status of the system; the controllers; and the interfaces. The interfaces include mechanical and electronic (hardware and software).

Several significant in-house developments occurred during 1988.

- End effector-related mechanisms. The gripper/nut runner proof-of-principle prototype shown in the first photo was demonstrated. This prototype performed a complete payload changeout in the robot laboratory. Driven by the robot wrist motor (for the nut runner), and a dedicated motor for the gripper, this system represents a potentially significant step forward in the technology of end effectors for space applications. By using the robot wrist motor, the system is made significantly more simple and compact; thus, its reliability is improved, and robot dexterity is enhanced (due to shortening the axial length of the system).



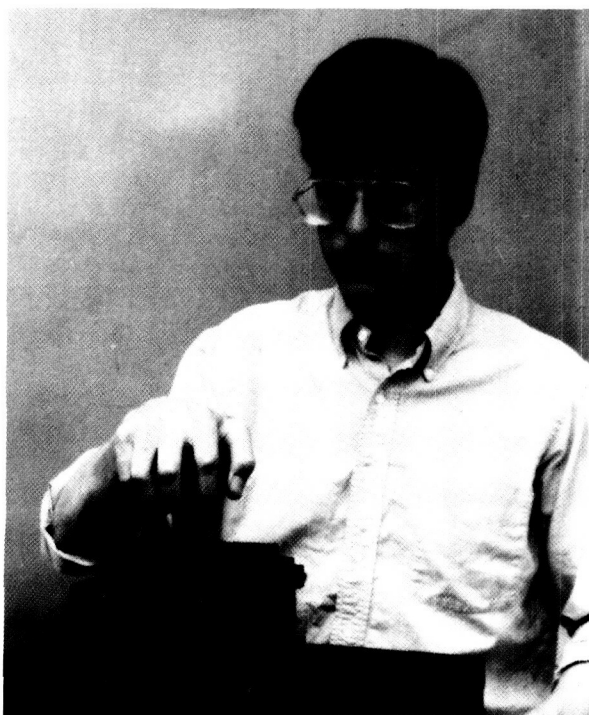
Sensory-interactive end effector.

This Split-Rail Parallel Gripper has many advantageous features in its own right. It has been selected as the basis for a National Aeronautics and Space Administration (NASA) technology utilization project, in which industry and NASA will cooperate to develop an intelligent sensory-interactive gripper for industrial use. This project has already received funding, and is commencing. The two main competitors for the Flight Telerobotic Servicer (FTS) have each requested, and have received, shop drawings of this gripper.

A 6 degree-of-freedom (DoF) compliant joy stick proof-of-principle prototype was also demonstrated in the robot lab. (The joy stick is shown in the second photo.) This device was used to teleoperate a robot. It represents a significant simplification in the state-of-the art in nonforce-reflecting, user-friendly, compliant joy sticks. Thus, it promises to be more reliable, and less expensive, than existing devices.

- Robot- (and Astronaut-) Friendly Payload Attachment Systems. A proof-of-principle prototype of an Orbital Replacement Unit (ORU) was demonstrated in the robot lab. (This device appears in the third photo.) This unique system promises to have an important impact on payloads throughout the Space Station, and is

ORIGINAL PAGE
BLACK AND WHITE PHOTOGRAPH



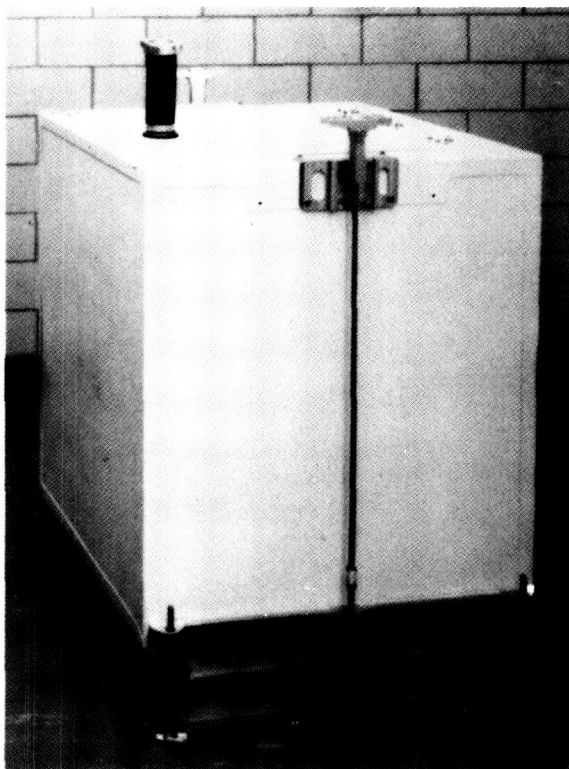
Six DoF user-friendly compliant joy stick.

already receiving recognition as such. It has several robot-friendly features. It permits the robot to attach (or detach) the payload by means of a single grasp point; thus, the robot maintains excellent control of the payload at all times. It has a torque-multiplying feature; thus, the robot can attach the payload more securely (or detach it with a greater margin of safety). It attaches each payload with multiple latches; thus, the system is redundant, and inherently very safe. It also has an inherently high strength-to-weight ratio. Invented by a member of the Electromechanical Branch, this system currently is being processed towards a patent. It is under consideration for early deployment in space, as part of the FTS Demonstration Test Flight (DTF).

In the future, those mechanical devices that have already been demonstrated will undergo improvements in their mechanicals. The gripper/nut runner will receive a safety-enhancing mechanism that will enable it to better control the payload while it is in the process of attaching or detaching that payload.



Payload latching system.





The gripper itself will receive fingers that use a new principle in the gripping process. The 6 degree-of-freedom compliant joy stick will be redesigned, so as to provide a much improved operator feel. The ORU attachment system will receive improvements that will improve both performance and reliability through simplification.

In addition, new mechanical systems will be added. An autochanger will be introduced that will enable the robot to change and store its end effectors in zero gravity. A robot-friendly fluid coupler will also be introduced. Work will begin on a robot "foot" that will enable the robot to more properly attach itself to the work site.

Sensor systems will be incorporated into the mechanical systems. These will provide force and position information for the gripper, and torque for the nut runner. The ORU attachment system will receive a suite of sensors that will monitor its status (latched/unlatched; electrical connectors properly engaged; temperature).

A controller will be developed for the end effector. This controller will permit the gripper to operate in an autonomous mode, a teleoperator mode, or a shared-control mode (elements of both autonomous and teleoperator control). The particulars necessary for the safe handling of objects in space will receive close attention.

Contact: John M. Vranish
Code 716

Sponsors: Space Station Project and Code S

CHARGE COUPLED DEVICES AND ASSOCIATED DRIVE ELECTRONICS FOR MODIS-T

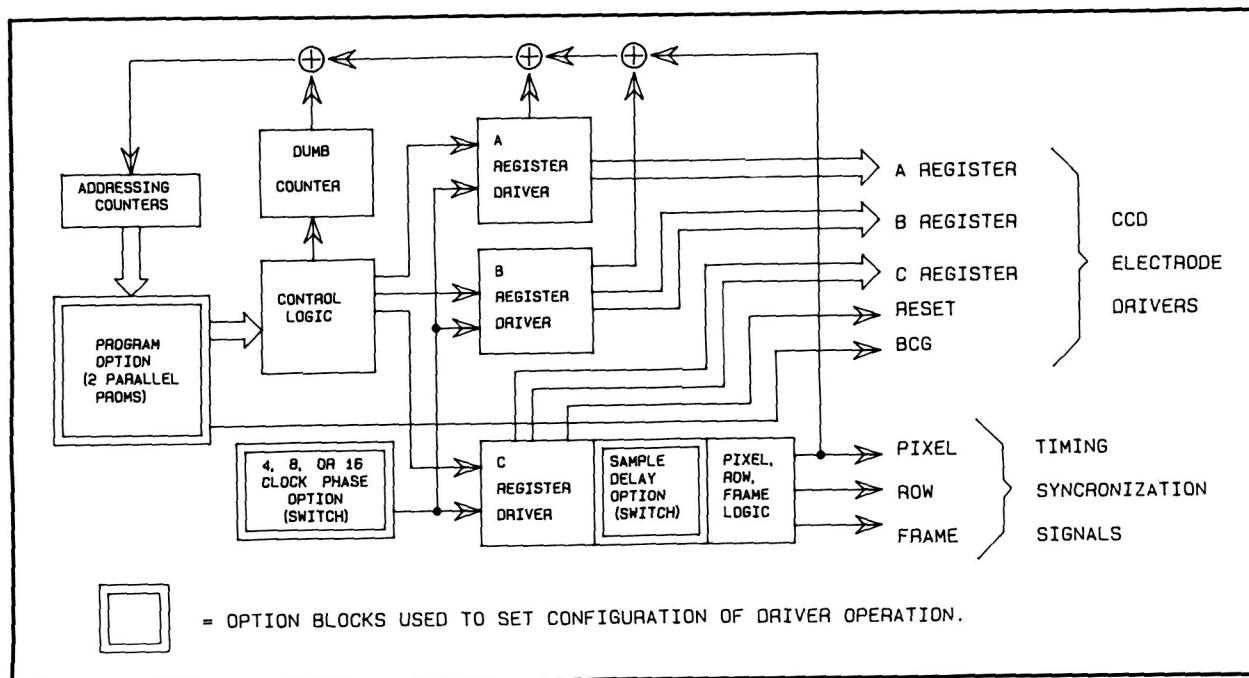
The Moderate Resolution Imaging Spectrometer-Tilttable (MODIS-T) instrument presents some unique requirements for the imaging focal plane. Most notable is the size of the Charge Coupled Device (CCD) imager elements (pixels). The instrument requires a pixel size of $200\text{ }\mu\text{m}$ by $200\text{ }\mu\text{m}$, in a 64 by 64 array. Relatively speaking, $200\text{ }\mu\text{m}$ square pixels are between 10-100 times larger than conventional CCD technology. In terms of microelectronic fabrication techniques, new problems arise in manufactur-

ing high-quality, high-performance CCD detectors at this larger scale. An in-house effort was initiated at Goddard Space Flight Center to design, fabricate, test, and evaluate CCD detector arrays that could be successfully fabricated despite the large pixel size. Included in this program was the design of five arrays with different charge transfer electrode characteristics. The five arrays were of differing densities, ranging from large-pixel 16-element arrays to smaller-pixel 128-element arrays.

The CCDs were designed at Goddard using Valid Logic System's Layout Editor. The wafers were then fabricated under contract. Initial results established the performance of a 4 by 16 array of $200\text{-}\mu\text{m}$ -square pixels, using a 16-phase clock. The wafer yield of this device at a functional level was in excess of 70 percent. Concurrent with the design of the CCD and associated drive electronics was the establishment of a detector test facility that could perform accurate radiometric measurements. A simple system to perform radiometric screening at the wafer level, using a fine fiber optic light injector, was designed to yield rough-order-of-magnitude charge transfer efficiency, and signal information. Candidate high-performance chips are then packaged and mounted in a laser-based optical test bench, where more accurate measurements are made.

The variations in the five CCD array designs forced flexibility in the driving ability of the associated electronics. Valid's Graphics Editor was used to design the driver, shown in the accompanying figure. Any of the five arrays can be driven with the design. The driver is used in conjunction with the detector test facility to test the CCDs. The electronics operator uses a single transistor-transistor logic (TTL) level input signal to start driving an array. In turn, the driver outputs timing signals to the detector test facility for synchronization of collected images. The other output signals of the drive electronics control the CCD device under test.

The analog output signal of the CCD is collected through a 12-bit, a/d converter into a first-in, first-out (FIFO) storage element. This occurs at rates up to 1 Mpix/sec. The digital representation of the image is displayed on a high-resolution graphics monitor. The Real Time Imaging mode collects frames continuously, and produces an updated frame every 2 seconds.



Block diagram of programmable driver for multiphase Charge Coupled Device.

Five objectives for the driver were kept in mind during its design. The circuit must: 1) drive voltages that produce reasonable potential wells under the CCD electrodes; 2) drive the CCDs in 4-, 8-, or 16-phase modes; 3) start the driving sequence on the toggle of a single TTL-level input signal; 4) allow programming of frame sequences required by arrays with more than 1800 pixel elements; 5) produce CCD and test facility control signals necessary for interfacing.

Designing the driver with a graphics editor (GED) allowed functional simulation, timing verification, and certain packaging analyses to be performed on the design before fabrication. Simulation of the driver verified its function with the master clock running up to 10 MHz. This suggests a maximum pixel rate of 500,000 pixels/sec. The design uses 54 TTL component chips.

Two versions of the hardware were fabricated: wire wrap and printed circuit board. Both were verified functionally with a digital analysis system. The master clock's highest operating frequencies were found to be 1 MHz and 10 MHz, for the wire wrap and printed circuit board versions, respectively. Both versions of hardware have driven the prototype detec-

tor arrays successfully. Data obtained from the driven arrays are being used to produce specifications for a flight version MODIS-T CCD array.

Contacts: Murzy Jhabvala, Audrey J. Ewin, Kenneth Reed, and Brent Mott
Code 724

Sponsor: Office of Space Science and Applications

Dr. Murzy Jhabvala works in the Instrument Microelectronics and Detectors Branch. In 14 years at Goddard he has designed integrated circuits and established fabrication techniques for CMOS, PMOS, VMOS, DMOS, CCDs, JFETs, Schottky barrier devices, and near and far infrared detectors. Dr. Jhabvala has received awards for special achievement and for patents. He has worked with a variety of materials including silicon, extrinsic silicon, intrinsic and extrinsic germanium, gallium arsenide, mercury cadmium telluride, and lead sulfide.

Ms. Audrey J. Ewin, who also works in the Instrument Microelectronics and Detectors Branch, is an electronics engineer with five years of experience at Goddard. She received her BS degree in engineering,



concentrating in electronics, from Widener University. Ms. Ewin works mostly on detector design, fabrication, test, and evaluation. Her work also includes the design and development of detector-related electronics.

Mr. Kenneth Reed, who works in the Instrument Microelectronics Branch, received his BS degree in electrical engineering from The Catholic University of America. He has worked at Goddard for eight years. He has carried out a wide variety of work in electronics. His present effort involves fabrication from board to chip design for generating timing pulses for Charge Coupled Device/Drivers.

Mr. Brent Mott, an electrical engineer in the Semiconductor Development Section, is involved in the detector development for AXAF and MODIS-T. He has a BS degree in physics and an MS degree in electrical engineering, both from the University of Maryland. Mr. Mott has three years of experience at Goddard.

MICROCALORIMETERS FOR XRS

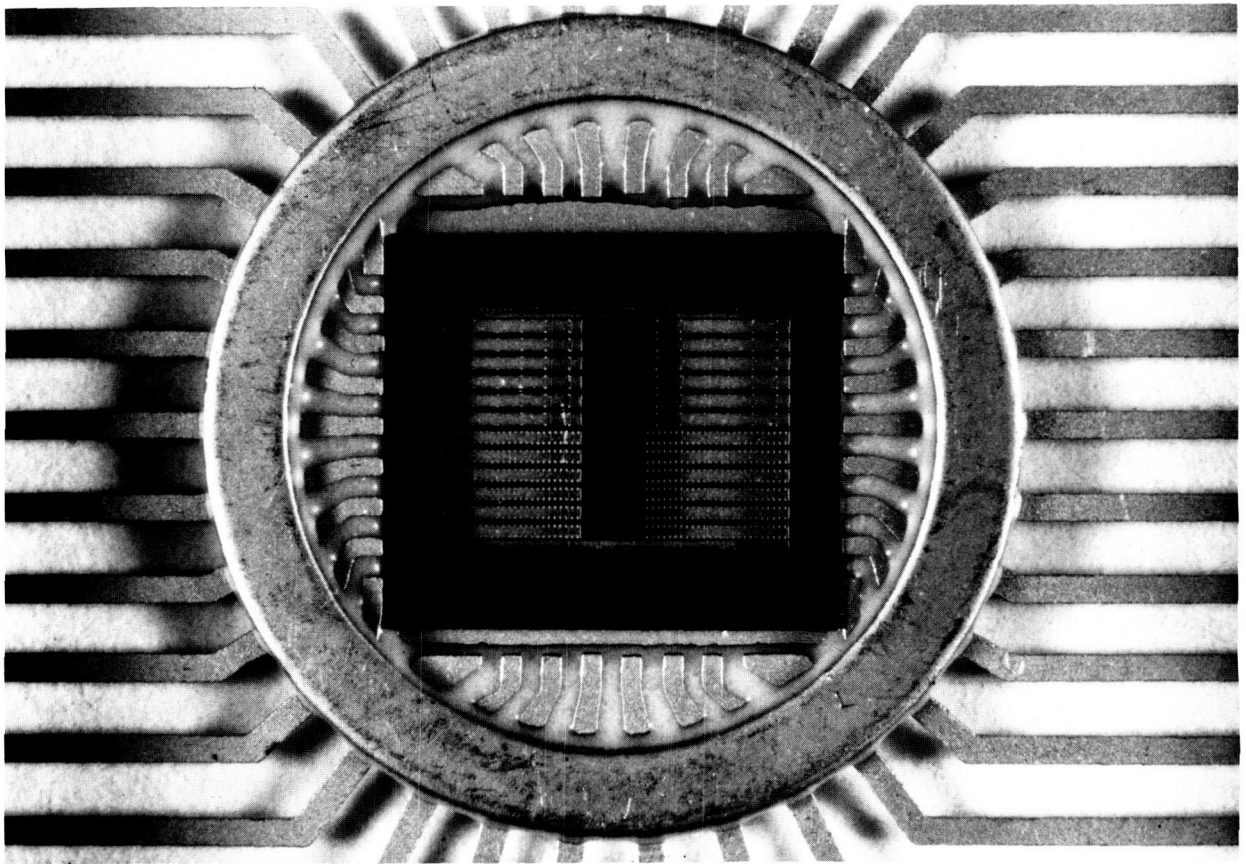
Linear arrays of X-ray calorimeters are being fabricated for Goddard's X-Ray Spectrometer (XRS), an instrument being developed as one of the Advanced X-Ray Astrophysics Facility (AXAF) focal plane instruments. The microcalorimeters will respond to individual X-ray photons with a signal proportional to the energy of the X ray, making the detectors sensitive energy spectrometers. Three of the linear arrays will be placed together to form a two-dimensional array for XRS. The arrays are monolithically fabricated from silicon by anisotropic etching with the energy sensing areas being formed by ion implantation. Initial proof-of-principle fabrication is currently underway in the Semiconductor Development Section at Goddard Space Flight Center (GSFC).

Drawing on the experience with bolometer-type detectors used in infrared (IR) observations, researchers at GSFC (X-Ray Astrophysics Branch) and the University of Wisconsin have pioneered the use of X-ray spectrometry with calorimeters. There are four characteristics of silicon calorimeters that give them a strong advantage over spectrometers involv-

ing diffraction or charge collection. First, the calorimeter energy resolution is ultimately limited only by thermodynamic power fluctuations which can be made as small as a few electron volts. Second, a calorimeter has a high intrinsic quantum efficiency over the X-ray band of interest to AXAF. Third, a calorimeter is sensitive to both ionizing and non-ionizing forms of energy. Fourth, since a calorimeter spectrometer is nondispersive, observations of extended sources with calorimeter arrays can be made without confusing energy with the angle of entrance of radiation into the instrument.

In its simplest form a calorimeter is a device with only three essential components: an absorbing material, a thermometer, and a thermal link to a cold reservoir. In the preliminary tests, the absorbing material was the silicon structure itself. Future designs will utilize a coating of an efficient X-ray absorber. The energy of the X ray is transformed into heat in the absorber which results in a rise in temperature which is sensed by the thermometer. The heat deposited by the X ray is then conducted away by the thermal link to the cold reservoir, returning the detector to its initial condition. The change in the resistance of the thermometer is proportional to the heat deposited in the detector and thus the energy of the X ray. To ensure a measurable change in temperature with the absorption of a single X ray, the heat capacity of the calorimeter must be kept small. To accomplish this, the detector volume is made small (at present about $3.0 \times 10^{-3} \text{ mm}^3$) and cooled to a low temperature (about 0.1 °K). The use of silicon is ideal due to its low specific heat at low temperatures.

The accompanying photo presents an engineering test array, including the main features of the arrays. The array is a linear ensemble of 12 rectangular calorimeters, each 1000 x 250 micrometers in area and 12 micrometers thick. The thermal link, mechanical support, and electrical connection to the detector thermometer are provided by four support beams 2500 micrometers long and only 12 x 20 micrometers in cross section. The support beams must be kept long and thin to control the time constant of the detectors, which is set by the ratio of detector heat capacity to thermal link conductance. The support beams have posts along their length to scatter phonons traveling down the beams, providing increased control over the thermal conductance to the cold reservoir.



Present engineering design for the XRS microcalorimeter array. The dark frame is the thick silicon mechanical support for the array while the 12 small rectangles are the detectors. The four thin dark lines running from each detector to the frame are the detector support beams which also provide thermal and electrical connections to the detectors.

The precise dimensional control is achieved by the use of an anisotropic etch which etches silicon preferentially along certain crystal planes giving great control over the shape of the volume removed. The first step in the fabrication of the calorimeter arrays is the thinning of the wafers over the areas where the arrays are to be located. The thinning is necessary to achieve the final device thickness of 12 micrometers. To accomplish this the silicon wafer is anisotropically etched from the back side through rectangular holes cut into a silicon dioxide coating. After the wafers are thinned, the thermometer, electrical leads, and contacts are formed by traditional photolithography and ion implantation. The thermometers are formed by implanting phosphorus compensated with boron at a concentration near the

metal-insulator transition to give a large change in resistance with a small change in temperature. The electrical leads and contact areas are degenerate-implanted arsenic. The final step is an anisotropic etch from the front side that defines the body and support beams leaving the detectors free standing.

As of this writing, microcalorimeter X-ray spectrometer arrays have been fabricated and used to detect X rays. Despite the low spectral resolution of these first monolithic devices, due to the difficulty of achieving the precise control required to produce thermometers with optimum resistance, the results demonstrate that the basic concept of monolithic calorimeters is sound.

ORIGINAL PAGE
BLACK AND WHITE PHOTOGRAPH



Contact: Brent Mott
Code 724

Sponsors: AXAF Project Office and Office of
Space Science and Applications

A MEASUREMENT OF THE MAGNETIC EARTH-IONOSPHERE CAVITY RESONANCES IN THE 3-30 Hz RANGE

Since the 1890s, scientists have been measuring the Earth-ionosphere cavity resonances. These electromagnetic signals are the result of the excitation by worldwide thunderstorm activity of the normal modes of the cavity formed by the surface of the Earth and the conducting layers of the upper ionosphere. A second source of excitation is the solar wind. The cavity thickness is estimated to be about 75 km, and the resonance frequencies were calculated by Schumann, using microwave cavity modeling, in the 1950s. These Earth-ionosphere cavity resonances are of interest because of their usefulness in atmosphere-ionospheric studies, and because of their potential for applications in wireless power transmission.

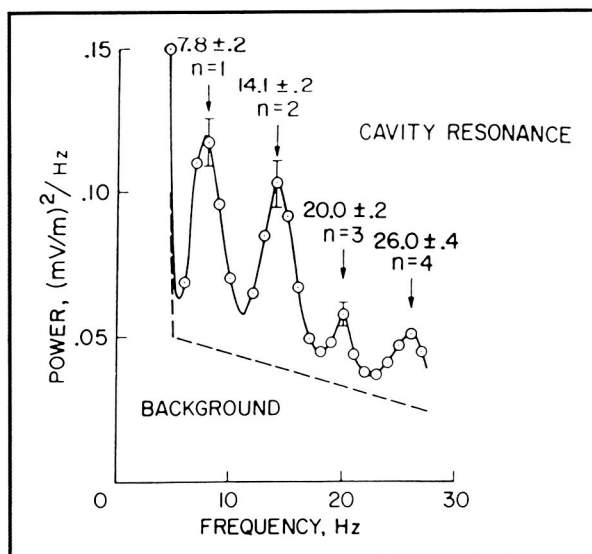
As a joint effort during the Summer Faculty Fellowship program in June and July 1988, Goddard Space Flight Center researchers made measurements of the magnetic field component of the Earth-ionosphere cavity resonances. The apparatus consisted of a search coil, low-noise amplifiers adapted from designs developed for the FIRAS experiment on the Cosmic Background Explorer (COBE) satellite, and a fast Fourier transform spectrum analyzer. The search coil and preamplifier combination are capable of detecting sinusoidal magnetic signals as small as 1 picoTesla rms.

The month of June is a time of only moderate cavity resonance activity, so considerable time was spent observing and waiting for activity of sufficient intensity and duration such that meaningful measurements could be made. Often a peak or peaks would appear and disappear before an analysis could be made. It was found that the maximum activity occurred during the early morning hours, corresponding to peak thunderstorm activity twelve hours away on the side of the Earth opposite the measurement site in Maryland. The site chosen was a location at

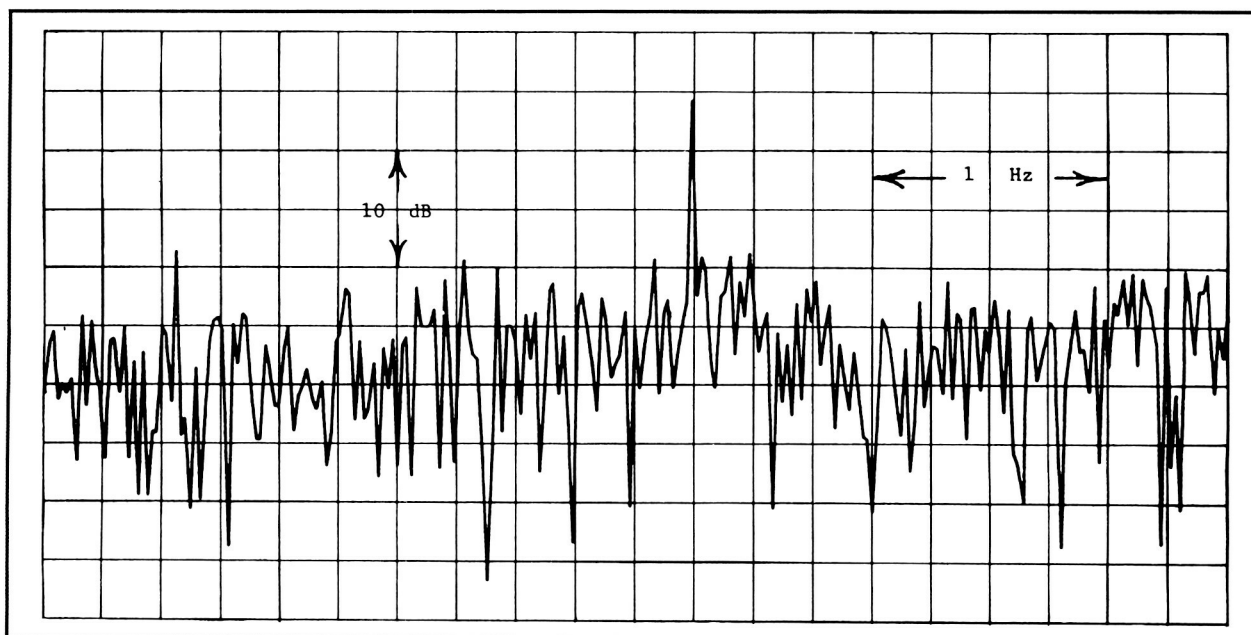
the bottom of a 12-foot deep gully approximately 100 yards from the nearest electric power wiring. This site location provided a relatively quiet electric and magnetic environment for the measurements. After several attempts at data collection, spectra of the 8-, 19-, 25-, 36-, and 42-Hz resonances were obtained.

The resulting measurements indicate that the sharpness of resonance, or "Q," values are at least on the order of 100-2000, the actual magnitudes being beyond the resolution capabilities of the analyzer. These magnitudes are at variance with the measured values, typically on the order of 8, commonly reported. To explain this apparent discrepancy, the researchers note that the resolution of the older analyzing equipment is on the order of 1 Hz, so it is not surprising that the calculated Qs would be limited to these low values. Also, the resonance frequencies were found to drift significantly over time periods on the order of 10 minutes, so averaging over such long time periods, as was done in the past, would be expected to distort the results. The first figure is an example of the apparent low-Q resonance data obtained previously. The second figure is a plot of our measurement of one of the resonances, at 42.27 Hz, with a Q value of at least 2000.

Scientists often complain that low-cavity Qs imply that wireless transmission of power on a global scale,



Extremely Low Frequency (ELF) spectrum, typical of data from the 1960s.



Cavity resonance response at 42.24 Hz and 1-minute averaging time.

which may be thought of simply as transformer coupling, would be impractical. Our current measurements indicate that the cavity Q s are one to two orders of magnitude higher than previously estimated and therefore would not be a limitation. The impact of high-cavity Q s on atmosphere-ionospheric research will stem from the fact that cavity resonance frequencies can now be measured with greater precision than previously was possible and hence become a more sensitive measure of the fluctuations in the condition of the ionosphere.

Contacts: John F. Sutton and Craig Spaniol
Code 728

Sponsor: NASA-ASEE Summer Faculty Fellowship Program

Dr. John F. Sutton designs low-noise, ultrastable amplifiers and thermal control systems for FIRAS and AXAF. He is also interested in the development of therapy equipment for the treatment of leukemia and AIDS. Dr. Sutton, who has a PhD in physics, has 28 years of experience at Goddard.

Dr. Craig Spaniol, a graduate of West Virginia State College and Rensselaer Polytechnic Institute, is a Professional Engineer working with the Instrument

Electronic System Branch and also Chairman of the Department of Industrial Technology at West Virginia State College.

REAL-TIME PROCESSOR FOR ARRAY SPECKLE INTERFEROMETRY

With the construction of several new large-aperture telescopes and the development of large-format array detectors in the IR ($\lambda = 2 - 5 \mu\text{m}$), the ability to obtain diffraction-limited seeing via infrared (IR) array speckle interferometry offers a potentially powerful new tool for the exploration of protoplanetary systems. Goddard Space Flight Center researchers are in the process of constructing a real-time processor to acquire image frames, perform array flat-fielding, execute a 64×64 element two-dimensional (2D) complex fast fourier transform (FFT), and accumulate the complex pixel phase differences for later image reconstruction, all within the 20–25 msec coherence time for speckles at $2 \mu\text{m}$ wavelength. The processor will be a compact unit controlled by a personal computer (PC) with real-time display and data storage capability. In this manner, the hardware will provide the ability to optimize observational parameters and obtain preliminary results on the telescope rather than waiting several



weeks before the data can be analyzed and viewed with off-line methods.

Currently all speckle techniques suffer from a major computational bottleneck; 40–100 images per second must be stored per observed object. The amount of stored data corresponds to several hundred MBytes of information for a single object for a one-hour integration. A typical observational run will consist of several objects as well as several reference sources. This information must subsequently be processed off line, that is 40–100 2D complex FFTs must be performed and averaged for every second of real-time observing. In addition, the complex pixel phase differences must also be accumulated in order to perform an image restoration. Usually a delay of several weeks occurs before the data can first be seen and longer before the information can be fully processed on a mainframe computer.

The figure shows a block diagram of the major features of the processor. A PC with high-resolution graphics display will provide the control, data display, and data archive for the real-time processor. In addition, the PC will be used to compile the microcode instructions for each of the separate pro-

cessor units and to download the code to provide the unit functions.

The most stringent requirement is the need to perform a complex 2D FFT in real time. Required are 32-bit floating point rather than fixed point calculations due to the large dynamic range which is necessary for the observations. Researchers are looking for low surface brightness features which may be masked by brighter objects. Brightness differences of 40–50 dB are possible with the dynamic ranges of current detector arrays, which have readout noise of less than 100 e⁻ with a full well depth of 10⁶e⁻. Performing a complex 2D FFT within 20–25 msec corresponds to performing about 20 million floating point operations per second (MFlops). In total, including all the operations necessary for the flat-fielding, 2D complex FFT, and phase and power spectrum accumulation, the processor must perform about 30 MFlops.

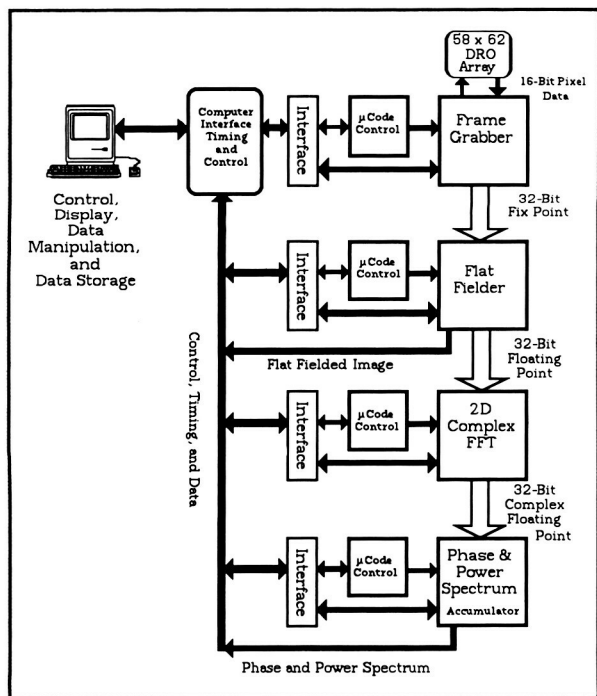
Contact: José M. Florez
Code 728

Sponsor: Director's Discretionary Fund

Mr. José M. Florez, head of the Instrument Electronic System Branch, is responsible for the design of several digital processors, including the Digital Electronics Box for the DIRBE instrument of the COBE spacecraft. He has a BS degree in electrical engineering from the University of Puerto Rico and has been with Goddard for 13 years.

MODELING A HIGH-POWER HYBRID CAPILLARY SYSTEM USING SINFAC

Two-phase heat transfer systems have begun to increase their share of the heat transfer duties associated with temperature control of spacecraft and instruments. They can provide an isothermal sink for multiple distributed loads and are able to handle much higher power levels than traditional thermal control technology. A variety of two-phase technologies have been developed recently. One of the most promising of those is the hybrid capillary loop. This system uses capillary-pumped evaporators, assisted by a mechanical pump, to supply the pressure head for the circulation of the heat transfer fluid (usually ammonia) in a thermal transport loop. This

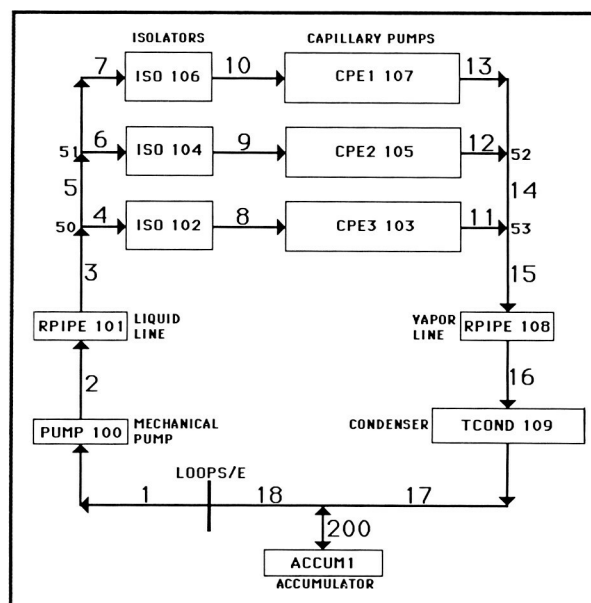


System block diagram of the speckle processor.

approach allows greater flexibility and load capacity while keeping the basic advantages of a capillary-pumped, two-phase system. But, two-phase flow systems are complex and hard to model. Until recently, reliable computer models were not available for simulating this type of system. One model developed over the last few years through an in-house effort is the System Improved Numerical Fluids Analysis Code (SINFAC). SINFAC was used to model a new high-power, hybrid capillary-pumped loop that is currently being tested. Simulation results were then compared to those from the actual experiment.

SINFAC is built into the input file for the Systems Improved Numerical Differencing Analyzer (SINDA), and it uses SINDA for calculation of the nodal heat transfer. SINFAC has a series of subroutines that represent the various parts of a fluid loop, such as evaporators, pumps, lines, merges, and splits. These subroutines are used to model the desired loop, with the user setting the specifications of each subroutine to reflect those of the actual system. In this project, the experimental hardware and the SINFAC model both consisted of three evaporator plates in parallel, isolators to each plate (isolators being used to prevent the back flow of vapor), a mechanical pump, liquid and vapor transport lines, an accumulator, and a condenser. The flow diagram for the SINFAC model is shown in the figure. The model was simplified slightly to reduce its complexity but without significantly affecting its validity for the actual system. A variety of parametric studies were conducted to evaluate the flexibility of the program and to determine the optimum values for the study.

The SINFAC model was used to simulate two test series, with each series consisting of three runs. The first series was a test of the heat load capacity of the system at different flow rates; and the second was a test of the system's response to nonuniform heat loads. The main bases of comparison were the system flow rate and the pressure differences across the evaporators and the mechanical pump. The program was run on a VAX 11/750 computer and took from 3 to 8 minutes to reach a converged solution. The validity of the model was supported by the simulation results, which closely reproduced those of the experiment, in some cases obtaining an almost exact correspondence. For example, at a heat load of 650 W/evaporator, the experimental and simulation



The SINFAC flow diagram for the high-power capillary system.

pressure rises across the evaporators were 4380 and 4450 N/m², respectively. In addition, for this particular run, the model showed a system overload (evaporator deprime) at 700 W/evaporator, which was also true of the experimental system. The model helped provide insight into some of the thermodynamic and flow characteristics of the system; such as localized flow rates, qualities, and pressures; that could not be determined during the experiment.

Since SINFAC uses a pseudo steady-state solution for transient behavior, it is not as effective for modeling systems that undergo rapid fluctuations. But, for steady-state or slightly transient conditions, the SINFAC program can be used effectively both as a design tool and as a modeling tool for single- and two-phase heat transport systems. As mentioned, the model results can be useful in obtaining characteristics of the system that cannot be obtained through the use of sensors. The model also can be used to predict the system response to conditions which may be difficult or dangerous to try experimentally.

Contact: Steve M. Benner
Code 732.2

Sponsor: Office of Aeronautics and Space
Technology



Dr. Steve M. Benner is responsible for the design, development, and testing of heat transfer systems, including capillary-pumped loops and heat pumps on the Space Station Project. Dr. Benner, with one year of experience at Goddard, is also interested in computer modeling of various thermal systems. He received his PhD degree in chemical engineering from Ohio State University.

DEVELOPMENT OF A SPACECRAFT ABSORPTION COOLING SYSTEM

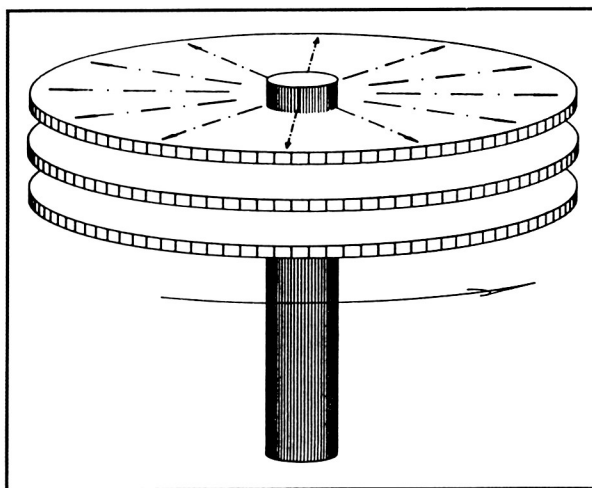
Over the past decade, spacecraft thermal control technology has developed so that heat acquisition, transport, and rejection can be performed with reasonable efficiency for most low-temperature applications. Conventional passive technology is generally suitable for typical conventional applications involving moderate temperature (minus 20° C to plus 50° C), low power (1 kW or less), and short transport distances (a few meters or less). Closed-loop, single-phase technology such as that used on the shuttle orbiter is capable of handling applications of somewhat higher power and longer transport distances. The two-phase thermal-control technology being developed for the Space Station is suitable for situations involving high power (75 kW and above) and long transport distances (hundreds of meters). Hence, while significant engineering development work remains, for most current thermal-control applications a technology base exists.

Current state of the art focuses on efficient one-way thermal management—acquiring and transporting heat at a higher temperature and rejecting it to a lower temperature sink. However, cooling a load to a temperature at or below its effective thermal sink is a much more difficult problem. This cooling is currently accomplished by boiling off stored cryogen. Unfortunately, this can be complicated and has a lifetime limited to the quantity of stored cryogen.

Another approach to cooling a load which is near or below its sink temperature is to employ a device that can provide two-way heat transfer by “pumping heat uphill.” Devices which perform this function are called heat pumps. A variety of heat pump designs and operating cycles exist. Absorption heat pumps offer some particular advantages for space applications where high-temperature waste heat is

available. These machines employ an absorbent/refrigerant pair in a heat-driven thermodynamic cycle to achieve a cooling effect. In the absorption cycle, a pressure differential is achieved via a physiochemical process (the affinity of the refrigerant and absorbent). The evaporation of the refrigerant generates the cooling effect. The resulting vapor is then absorbed into a concentrated absorbent. This solution is then mechanically pumped to a higher pressure. A high-temperature energy source is then used to regenerate (i.e., separate) the solution. While this technology has been applied to ground applications for some time, its suitability for space applications is unknown. This is due to the fact that the process, as currently employed, is gravity dependent. However, with different machine designs this need not be the case.

The objective is to develop the conceptual design and supporting analysis for an absorption chiller that will function in the microgravity of space. A small working model will also be fabricated and tested. Ground-based designs employ a falling film to generate the large surface area needed for effective absorption. In the absence of gravity, this approach will clearly not work. The concept developed here involves generation of a thin film by use of a rotating disk. (See figure.) The liquid absorbent is supplied through the hollow cylinder to the central region of the disk, where it is sprayed onto each disk face through holes drilled into the tube wall. The liquid is thrown outward by centrifugal force and forms a thin liquid layer on the disk. In an actual system, numerous stacked



Design of the rotating absorber unit.

disks could be used. The absorber unit is contained within an enclosure into which vapor refrigerant is introduced. It is absorbed into the concentrated absorbent. The now diluted solution is pumped to the regenerator, where waste heat (perhaps from a solar-dynamic or nuclear power generator) is used to regenerate the solution. The separated refrigerant is then evaporated to obtain the cooling effect. The vapor and concentrated absorbent are then combined in the absorber, completing the cycle. Hence, a cooling effect is achieved. The prime energy source used to drive the cycle is high-temperature heat.

Contact: Theodore D. Swanson
Code 732

Sponsor: Office of Aeronautics and Space
Technology

Mr. Theodore D. Swanson is a senior aerospace engineer with four years of experience at Goddard. Mr. Swanson, who holds an MS degree from the University of Maryland, designed the first ammonia-based, operational two-phase heat transfer test bed along with two ground-based photovoltaic power stations. He was also chairman of the "Workshop on Two-Phase Fluid Behavior in a Space Environment," sponsored by the Office of Aeronautics and Space Technology.

A HIGH POWER SPACECRAFT THERMAL MANAGEMENT SYSTEM

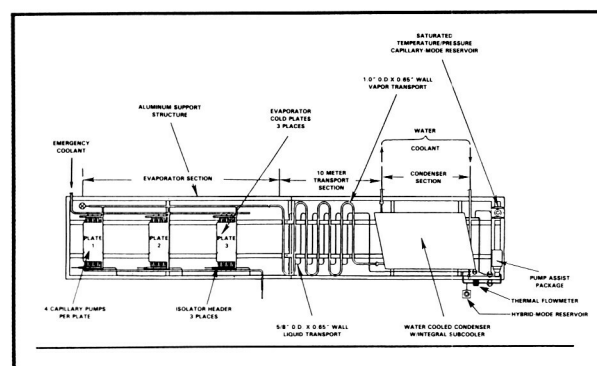
Evolving concepts of future large space platforms and spacecraft, such as the U.S. Space Station Freedom, have been an impetus to the development of thermal control systems which can acquire and reject tens of kilowatts of heat carried over tens of meters. Current thermal control techniques on spacecraft, some of which use passive means such as coatings or louvers, and others that require the circulation of a single-phase refrigerant, would be inappropriate for the high powers and long distances that are foreseen. Thermal systems which employ evaporation-condensation (two-phase) fluid cycles have demonstrated the potential for meeting these new thermal needs.

The development of both capillary and mechanically pumped two-phase fluid systems has been ongoing

for the past several years. In a capillary system, refrigerant is circulated without a mechanical pump. The required pressure head is derived from capillary action in a fine pore wick. This type of unit is inherently reliable because it contains no moving parts which could require servicing. However, a limitation of these types of systems is that the capillary pumping capability is small. A second type of fluid system employs a conventional mechanical pump to circulate the fluid. While the mechanical pump has a much larger pumping potential than the capillary pump, complex flow regulators and periodic maintenance of the pump may be required which could be difficult and costly, especially on unmanned free-flying platforms.

A third type of system being developed incorporates some of the operating features of both capillary and mechanically pumped heat transfer loops, and is known as a hybrid system. To demonstrate the feasibility of the hybrid concept, the High Power Spacecraft Thermal Management (HPSTM) system was designed, built and tested. This system operates as a capillary-pumped two-phase device at heat loads below 24 kW. When the flow rate required for evaporating higher heat loads exceeds the 24 kW potential of the capillary pumps, a mechanical pump in the liquid line is used to provide the extra flow needed for complete evaporation of the liquid.

As shown in the figure, the HPSTM system includes three modular "cold" plates, on which heat-dissipating instruments and equipment may be mounted. Four parallel capillary pumps are bonded to the surface of each cold plate. Each capillary pump



Schematic of the High Power Spacecraft Thermal Management System.



contains a wicking material which does the capillary pumping, and an evaporating surface where the heat applied evaporates the wicked liquid. Vapor then exits the pumps and flows 10 meters to a heat exchanger, which condenses the fluid. Liquid ammonia flows to a 10-meter-long liquid return line, or, if required, is bypassed to the mechanical pump before returning to the liquid line. A two-phase reservoir is used to control the saturation temperature and to compensate for volumetric changes in the loop.

Testing has shown that the HPSTM can transport up to 24 kW of heat over 10 meters in the capillary operating mode, and over 52 kW with the mechanical pump's assistance. These heat loads correspond to heat flux densities on the evaporator plates of 4.3 and 9.3 W/cm², respectively. Heat loads of as low as 120 W (0.02 W/cm²) were tested in the capillary-pumped operations. This wide operating range is a vast improvement over what any capillary or mechanically pumped system previously tested at Goddard Space Flight Center has demonstrated.

The experiment results are most encouraging. The feasibility of a hybrid thermal control system gives us confidence that this technology may be a viable candidate for future space applications, including use on the Space Station Freedom. In fact, a different type of hybrid system has been baselined for the Space Station Freedom core thermal bus. The HPSTM hybrid system is substantially simpler in plumbing than the core hybrid system, and offers some valuable data on this approach to thermal control. The HPSTM is currently undergoing a new series of tests after some modifications were made to further enhance its performance. One objective of these tests will be to demonstrate even higher heat transport potentials of between 75 and 100 kW. Also, TEMP 2C, a hybrid two-phase system, is being scheduled for shuttle flight testing in the near future. The primary goal of that experiment will be to verify the hybrid concept in a microgravity environment.

Contact: Michael McCabe
Code 732

Sponsors: Office of Space Station
United States Air Force
(Wright-Patterson Aeronautical Lab)

Mr. Michael McCabe, who has a BS degree in mechanical engineering is responsible at the Thermal Engineering Branch for the planning and implementation of development activities of advanced spacecraft thermal systems and thermal control components. Mr. McCabe has been with Goddard three years and is interested in thermal control techniques for Space Station Freedom.

STRATOFILM-372: A SECOND NEW BALLOON FILM

One of the objectives of National Aeronautics and Space Administration's (NASA) Balloon Program is to provide a relatively inexpensive, yet reliable program for scientific investigations in a near-space environment. NASA continues to work towards developing materials and vehicles with enhanced capabilities. The balloon film is a highly specialized, very thin material requiring both high strength and elongation at very low temperatures (> -80 degrees Celsius). As a result, very few private companies can or are willing to produce these films. Until this year, only one qualified film existed for NASA scientific balloon use thus placing the NASA Balloon Program in a very tenuous position.

Recent advances in film development by Winzen International, Inc., a NASA contractor, have resulted in a high-quality film now proven in performance by a series of successful NASA test flights. Labeled Winzen Stratofilm-372, this new blown polyethylene film exhibits the combination of low temperature toughness and fabrication properties found necessary for successful balloon flights.

Qualifying a material for use in the fabrication of NASA scientific balloons requires that the material must pass an extensive set of dimensional and mechanical property tests. Physical and mechanical testing includes: film web width, web width profiled thickness, gram weight average thickness, uniaxial strip tensile of both machine direction (MD) and transverse direction (TD) at $+23$ and -80 degrees Celsius, uniaxial crease at $+23$ and -80 degrees Celsius, and cold brittleness (CB) transition point as determined by a "falling ball" similar to a dart impact test.

Manufacturing consistency and repeatability are very important considerations. The film extrusion company must be able to produce the film with consistent physical and mechanical properties over a time period of several weeks or months. The candidate film must "handle" well, lay flat on the production tables and have minimal static charge or blocking. In addition to the above testing, the film must pass a series of fabrication tests which include the ability to heat seal the film while maintaining a large percentage of the film's strength and elongation characteristics (shown in the table). Once heat sealing optimization has been completed by the balloon manufacturer, the film is then fabricated into test balloons and flight tested.

Performance Characteristics of Winzen Stratofilm-372	
Nominal Film Thickness	0.0008 in.
Nominal Web Width	108 in.
MD Ultimate Stress (+ 23 Celsius)	7111 PSI
TD Ultimate Stress (+ 23 Celsius)	6356 PSI
MD Ultimate Strain (+ 23 Celsius)	1020 percent
TD Ultimate Strain (+ 23 Celsius)	1271 percent
MD Ultimate Stress (- 80 Celsius)	10100 PSI
TD Ultimate Stress (- 80 Celsius)	7552 PSI
MD Ultimate Strain (- 80 Celsius)	422 percent
TD Ultimate Strain (- 80 Celsius)	204 percent
CB Point	- 95 Celsius

Twelve balloon flights, lofting payloads weighing as much as 5500 pounds to altitudes of 120,000 feet, have been conducted to date with a 100 percent success rate. The flight testing of the film has been completed and Winzen Stratofilm-372 has been declared a fully qualified and operational NASA balloon film. As a result of this development, the NASA Balloon Program has a second qualified balloon film, thereby resulting in a more flexible and stable program.

Contact: I. Steve Smith, Jr.
Code 842

Sponsor: Office of Space Science and Applications

Mr. I. Steve Smith, Jr. holds a BS degree in aerospace engineering from Texas A&M University. He joined Goddard in 1983 as part of the Balloon Projects Branch at Wallops Island. Mr. Smith has been associated with scientific ballooning for over 14 years and is responsible for the NASA Balloon Research and Development activities.

POLYETHYLENE RESIN BLENDS DESIGNED WITH LOW TEMPERATURE TOUGHNESS FOR USE AS BALLOON FILM

Under a NASA grant a family of tough resin blends has been identified by the Polymer Science Program at Pennsylvania State University. Under the general heading of *Polyethylenes*, polymer scientists identify at least three different types of resin. The energy-to-fracture or toughness is believed to be an important criteria for a balloon film. Mechanical testing showed that better resins than those currently being used are available. Further, blends of different resin types produce mechanical properties which are superior to any single resin type.

From launch to float a balloon experiences different environments and must possess an appropriate range of mechanical properties for survival. Perhaps the most demanding stage in a flight is dynamic loading during passage through the low temperature and wind shear in the tropopause region. Historically, the material of choice for the largest balloons has been *Polyethylene* (PE).

As part of a larger program designed to improve the performance of scientific balloons, a grant has been awarded to Penn State for the purpose of understanding the origin and control of toughness in thin *blown* films. One component of the present study is to identify those resin variables which lead to low temperature toughness. This information should lead to the design of superior resins for balloon applications.

While certain film properties are established during the extrusion stage of film formation, many film properties are largely determined by inherent resin characteristics. PE, as a single material consisting of long chain-like molecules, is a generic term for a whole range of materials. Polymer scientists usually agree that PE can be obtained as distinct resin



types: high density polyethylene (HDPE) consisting of long uninterrupted chains; low density polyethylene (LDPE) containing chains with side arms or branches which are both long and short compared to the overall molecule; and linear low density polyethylene (LLDPE) and ultra low density polyethylene (ULDPE) which are specially prepared copolymers with short branches of known length.

Variations in molecular architecture found in these different PE resin types will control the manner in which resin will form amorphous and crystalline domains and therefore, the mechanical properties of the resulting film.

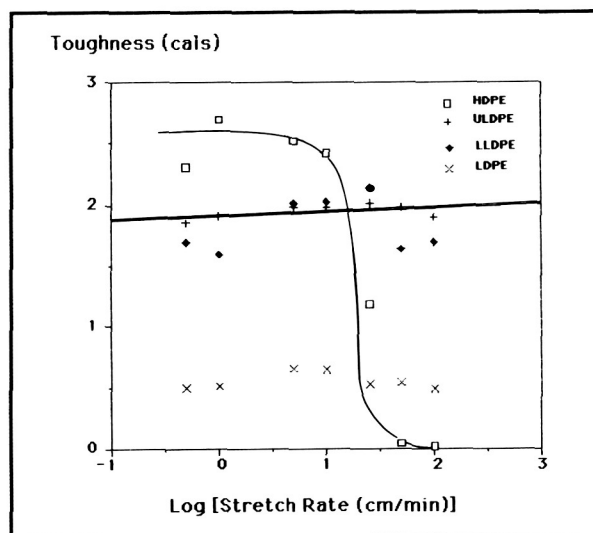
To expedite this study and to avoid experimental difficulties associated with low-temperature tests, mechanical data were taken over a range of test rates. High-rate tests are good indicators of low-temperature responses.

Toughness can be defined in many ways; for the purpose of this study the area under a simple stress-strain curve was employed. Based on the data shown in the first figure, it is apparent that while HDPE is tough at low test rates it rapidly loses that property at high rates. The other polymer types respond differently; LDPE, which is often used in current balloon film is marginally better than HDPE at high rates. LLDPE and ULDPE both have significantly higher values of toughness than either HDPE or LDPE at high test rates (or low temperatures).

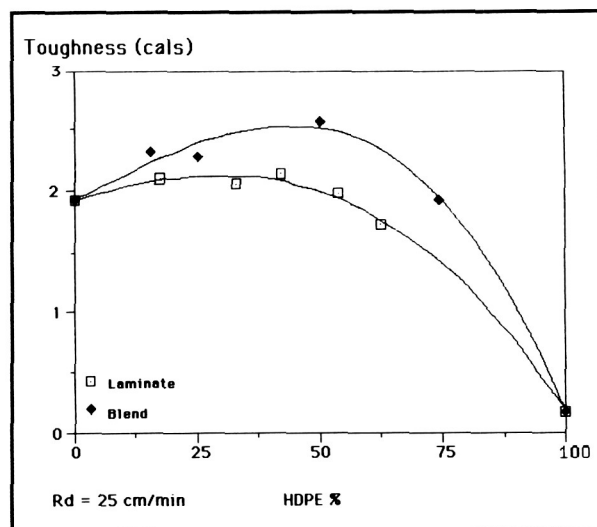
On the basis of toughness, it would appear that if a single resin type is to be used in balloon films then either LLDPE or ULDPE should be the resin of choice. However, at low test rates HDPE is inherently the toughest material. Further, toughness is not the only mechanical requirement. Balloon film should be easily heat sealable and have enough strength and stiffness to be manageable during fabrication at room temperature. Further, the material must survive the dynamics of the launch process. In terms of material properties this latter requirement may translate to film with a higher stiffness or modulus of elasticity, which is less likely to give than the relatively low modulus copolymers.

With these thoughts in mind, the possibility of combinations of HDPE and ULDPE appeared to be very attractive. Polymers can be combined as mixtures or

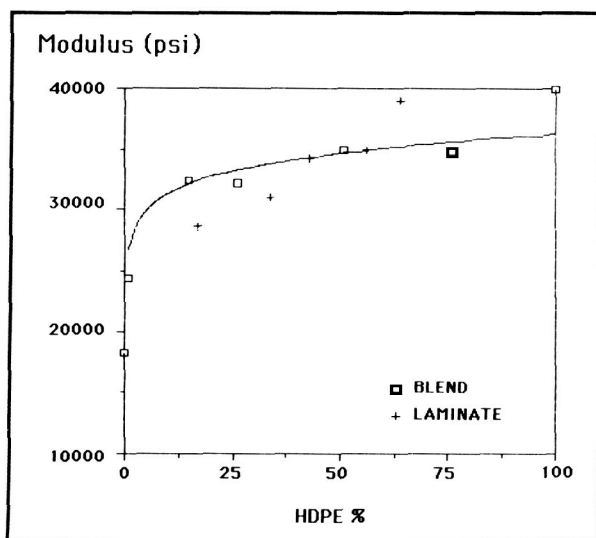
blends, which are analogous to metallic alloys; or as simple laminates of multilayer films composed of layers of film made from different resins. When tested at high rates, where HDPE alone shows poor toughness, both blends and laminates exhibit unique synergistic properties (second and third figures). Those figures show that a 50 percent blend of HDPE in ULDPE has both a higher toughness than ULDPE alone and a modulus closer to that of HDPE (i.e., significantly higher than that of pure ULDPE).



The influence of stretch rate on toughness.



The influence on toughness of blending HDPE with ULDPE.



The influence on modulus of blending HDPE with ULDPE.

At low percentages of HDPE both blends and laminates show similar mechanical response. This observation is surprising since the morphologies of the two systems are quite different. The laminate retains the identity of its constituent resin components, while the blend shows a structure close to that of HDPE alone. Indeed, even a 1 percent loading of

HDPE in ULDPE produces film whose morphology is directed by the HDPE structure.

Work enabled through this grant has demonstrated the importance of resin choice in balloon film manufacture. A family of resin blends and laminates has been identified which possess desirable low temperature characteristics. More importantly, however, the basic concepts of material property design and synergism have been illustrated and offer the hope of similar advances in this and other resin systems.

Contact: L. Dale Webb
Code 842

Sponsor: Office of Space Science and Applications

Dr. L. Dale Webb has a background in physics and holds a PhD degree from Texas A&M University in engineering. He has over 25 years of materials experience and has been associated with balloon-related research for 15 years. Dr. Webb joined Goddard in 1986 as part of the Balloon Projects Branch at Wallops Island and is the Project Engineer for the Balloon Resin and Film Research and Development activities.

SPACE COMMUNICATION SYSTEMS

FLIGHT DYNAMICS/SPACE TRANSPORTATION SYSTEM THREE-DIMENSIONAL MONITORING SYSTEM

During mission operations, a majority of the work performed in the Flight Dynamics Division consists of monitoring a spacecraft's health and safety or determining the cause of any anomalous behavior by that spacecraft. Such efforts require analysts to perform many geometric calculations and mentally assemble these calculations into images of that spacecraft in its surrounding environment. The analysts use these universal pictures to determine possible anomaly causes and remedies. The usefulness of this type of scenario can be seen when anomalies such as the following occur: horizon

scanner interference that occurs only when the Moon precedes the Earth in a scanner sweep, antenna interference due to the shuttle's open cargo bay doors, and invalid sun sensor readings due to Sun reflections off other spacecraft components into the sensor's field of view.

To relieve analysts from the burden of computing and creating these images in their minds a graphics system, the Flight Dynamics/Space Transportation System Three-dimensional Monitoring System (3-D Mon) sample image in the accompanying figure was developed by the Flight Dynamics Division to generate 3-D shaded solid models of the shuttle, Remote Manipulator System (RMS), and other planetary bodies and spacecraft. 3-D Mon computes

ORIGINAL PAGE
BLACK AND WHITE PHOTOGRAPH

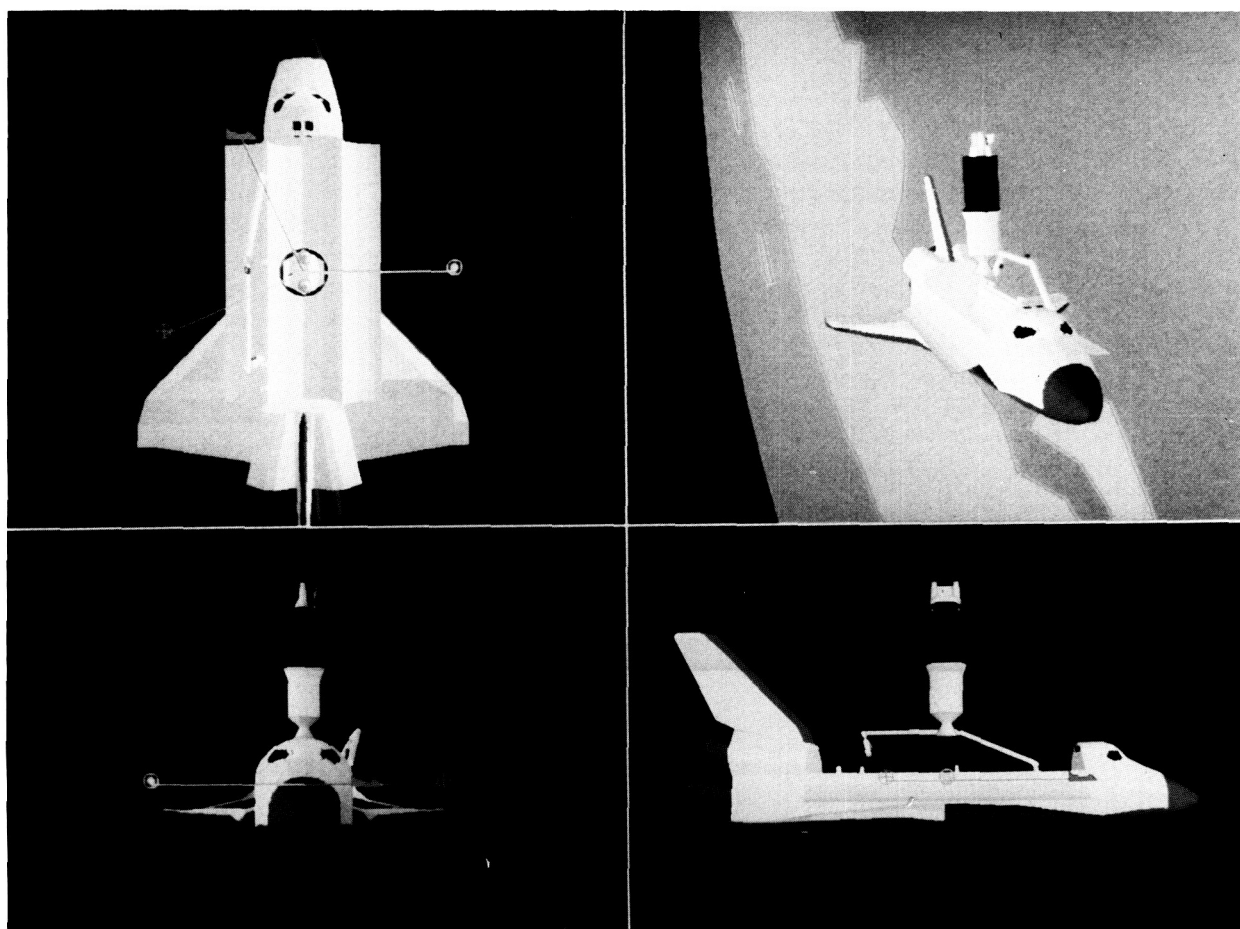


the positions and orientations of these spacecraft using real-time spacecraft orbit and attitude data. The system then provides analysts the capability to interactively move a viewpoint to any location in the universe that may assist mission operation functions. These views may include a look down a spacecraft's x-axis, a look out a sensor's field of view, or a look at a spacecraft from a communications satellite.

3-D Mon is designed to support any spacecraft mission. Needing a premission planning tool, a user can interactively manipulate the attitude of the shuttle and RMS to determine orientation and joint-angle requirements for future payload deployment scenarios. As a mission monitoring utility, 3-D Mon

provides actual spacecraft position and orientation information with accurate solar light modeling from any viewpoint. As a mission analysis aid, 3-D Mon provides playback of previously recorded spacecraft data in slow motion for study of mission anomalies.

To incorporate all these capabilities while updating the graphics images at the same rate that spacecraft data was being received (every 2 seconds), Division staff took many critical design steps. The first step separated 3-D Mon into a distributed processing system. All spacecraft data processing was done on the NAS 8040 mainframe computer and transmitted to a graphics computer for display. The second step selected the Silicon Graphics IRIS 4D/60 Turbo



Deployment of a Tracking and Data Relay Satellite from a shuttle, as displayed in near real time by the FD/STS Three-dimensional Monitoring System. The top right window displays a user-defined view of the deployment. The remaining windows display the scenario as seen along the z-, x-, and y-axes of the shuttle. The arrows represent velocity, Earth, and Sun vectors. The display is driven by real-time spacecraft orbit and attitude data.

graphics workstation as the target computer. The IRIS workstation, executing the UNIX operating system, allowed the graphics workstation software to be broken into three concurrent processes: communications, user interface, and display management subsystem. This breakdown allowed screen images to be generated simultaneously while receiving new data records and supporting user interaction.

Release II of 3-D Mon is currently operational while new enhancements are being incorporated into a third release.

Contact: James F. Jeletic
Code 552

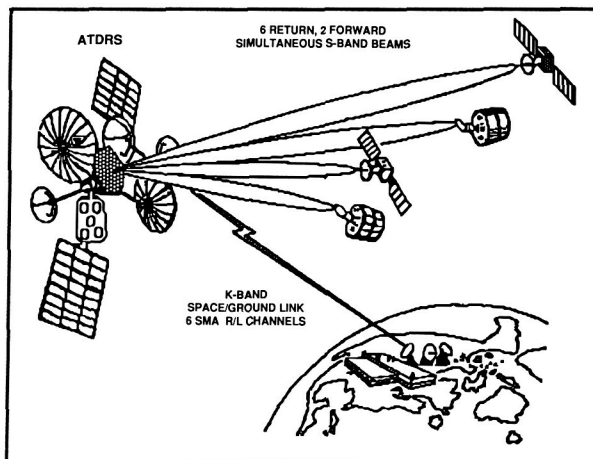
Sponsor: Office of Space Operations

Mr. James F. Jeletic researches, develops, manages, and analyzes flight dynamic computer graphics systems and other mission support software in the Systems Development Branch. He holds a BSE degree in computer science and engineering from the University of Pennsylvania. Computer graphics are a special interest for him. Mr. Jeletic has served Goddard for four years.

ONBOARD BEAMFORMING TECHNOLOGY DEMONSTRATION FOR ADVANCED TRACKING AND DATA RELAY SATELLITE SYSTEM

Goddard Space Flight Center's (GSFC) Tracking and Data Relay Satellite System (TDRSS) provides near-continuous communication coverage for the National Aeronautics and Space Administration's low Earth-orbiting satellites and manned space shuttle missions. To meet the projected communication needs of the 1997 to 2012 time frame, however, an even more ambitious space-based tracking and data relay system—Advanced TDRSS (ATDRSS)—will be required.

One of the challenges of a robust ATDRSS is quality service to a multitude of low-to-medium data rate users (up to 3 Mb/sec) in an era of high data rate users, such as the Space Station, and large orbiting platforms. The key to meeting that goal is an enhanced S-band Multiple Access (SMA) System, shown in the first figure. The projected SMA is built upon an expanded phased-array antenna on board



ATDRSS SMA communication system.

the Advanced Tracking and Data Relay Satellite (ATDRS), featuring a return link gain equivalent to the current TDRS S-band single access dishes.

The improved phased-array gain will require an increase from TDRS's 30 elements to 127 array elements on board an ATDRS. An increase of this magnitude would have a major impact on the current TDRS SMA implementation, which forms each user's beam by first transmitting the output of all array elements to the ground station at White Sands, NM. The huge increase in required frequency spectrum utilization on the Space-to-Ground Link (SGL) for 127 elements makes the current TDRSS approach undesirable for ATDRSS.

An alternative system design is to form each user's beam on board the ATDRS, requiring transmission of only six user channels back to the ground. After study of various design approaches to SMA beamforming, it was determined that onboard beamforming using digital techniques was the most promising. In addition, onboard digital beamforming (DBF) was found to offer other significant benefits in calibration, redundancy, weight, power, and complexity.

To fully understand all of the capabilities and ramifications of performing onboard digital beamforming, and to characterize beamformer design parameters, a hardware simulator was built by the Johns Hopkins University/Applied Physics Laboratory (APL) under contract to GSFC. The lead engineer for this project at APL was Timothy D. Cole.



The second figure presents a functional block diagram of this simulation hardware. The shading in the figure differentiates between support equipment, and those components that would eventually be located on an ATDRS spacecraft.

The simulator included a four-element antenna signal simulator, an Intermediate Frequency (IF) to base-band (or 12.5 MHz) downconverter, a computer-controlled digital beamforming network, a pseudo noise (PN) code despreader, a digital to IF up-converter, demodulator, bit synchronizer, and a bit error rate tester. This hardware configuration permitted full testing of the digital beamforming subsystem to determine the quality of the formed user signals (beams), and to evaluate on-line calibration capabilities. The simulator used four element channels to simulate an antenna array, and provided the capability for the simultaneous generation of calibration and user signals. Each of the subassemblies was specified to operate with signal and noise levels similar to those experienced with the current TDRSS system. The digital beamforming network consists of analog to digital (A/D) converters, digital weighter and combiner logic, digital controller, and an Automatic Level Control (ALC) interface.

Several performance tests were devised and performed to characterize beamformer design parameters. Successful digital beamforming was achieved using four array element signals to produce a user output in both the baseband and the 12.5 MHz

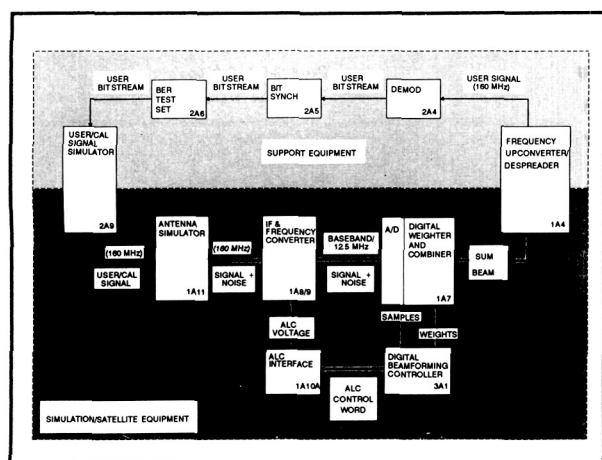
sampling configurations. The simulator performed as expected, based upon theoretical analyses, and demonstrated the feasibility of combining quantized samples of coherently related carrier frequencies using digital phase control.

As a result of the simulations, a number of issues were resolved. Some of these issues are listed below.

- The evaluation of digitally processing phase weights and combining element signals to form a user beam. Phase weighting for the DBF simulator is performed completely in digital logic, unlike those approaches that use digitally controlled phase devices to perform the actual weighting in analog regime, using digital inputs.
- Investigation into calibration algorithms implemented in the digital beamforming controller. It was demonstrated with the simulator that digital beamforming can perform real-time calibration of element channels, possibly using an onboard calibrator, without user service disruption.
- Evaluation of the quality of the simulated user return link as a function of a number of beamformer design parameters.

Results obtained from beamformer tests indicated that satisfactory performance could be readily obtained using table look-up algorithms. This is a simple alternative to approaches dependent upon generalized multiplication to accomplish the complex multiplications involved in beamforming, allowing the use of simpler hardware on board the ATDRS.

The next phase of this program is to extend the simulations to S-band frequencies, add a seven-element helix array for antenna range tests, and augment the electronics to simulate two user signals with simultaneous calibration. A follow-on effort that is to start in Calendar Year 1989 is the evaluating of very large-scale integration/very high speed integrated circuit (VLSI/VHSIC) device technologies, in preparation for developing a beamformer chip set, which in turn should lead to spaceflight qualifiable logic.



Onboard digital beamformer simulator block diagram.

Contact: David J. Zillig
Code 531

Sponsor: Office of Space Operations,
Advanced Systems Program

Mr. David J. Zillig is integration engineer for the Cosmic Background Explorer Navigation Experiment, which is an application of one of the advanced communication capabilities of the Second Generation TDRSS User Transponder developed by Goddard's Telecommunication Systems Branch. Mr. Zillig earned a BS degree in electrical engineering from the Pennsylvania State University. He has served with Goddard since 1966.

AUTOMATING CONTROL CENTERS WITH EXPERT SYSTEM TECHNOLOGY

During a communications event, the Flight Operations Analysts (FOAs) in the Payload Operations Control Center (POCC) will have the responsibility of monitoring and troubleshooting the communications link between the spacecraft and the Tracking and Data Relay Satellite (TDRS). Over 100 real-time performance and status parameters must be carefully analyzed to determine the proper configuration and status of the link. When a problem occurs, it is the responsibility of the FOA to isolate and diagnose it, and to determine the best method of correction. This is a difficult task which, if not handled quickly and properly, could result in poor utilization of TDRS services, inefficient spacecraft operations, and potential hazards to spacecraft health and safety. It is the intent to utilize automation, specifically the services of an expert system, to provide a reliable and efficient system of operations.

The Communications Link Expert Assistance Resource (CLEAR) is a fault isolation expert system to be utilized as an advisory system in the real-time environment of the Cosmic Background Explorer (COBE) Mission Operations Room (MOR). It will run on one of the six AT-class workstations used for console operations in the MOR without hardware modifications, and with the same operating software (e.g., a communication package, graphics routines, and device drivers) used by the other application programs. (The accompanying photo shows the COBE MOR.) Two significant requirements are the quick real-time response required of the expert system, and the mandatory requirement that the effect of CLEAR on the current system of operations be minimal.

These two requirements considered together have generated the concept of the CLEAR expert system attached to the operational system, as if it were an operator's workstation display. This approach, rather than an embedded or in-line system, is expected to reduce the effect of the expert system on the operational system to a minimum, and to meet the response requirement.

The CLEAR system consists of the Expert System and two interface subsystems. The User Interface subsystem generates all of the text and graphics to be displayed on the 19-in. color monitor. The screen display of the CLEAR system will utilize windowing techniques and graphical indicators to provide the current status or values of the communication links, signal strength, and associated systems. (The figure shows the CLEAR User Interface design.) To promote user acceptance, and to make the system as autonomous as possible, required user input is minimal. The user must only initialize the CLEAR system at start-up; virtually no input is required once the event is in progress. The Data Interface subsystem interfaces the Expert System to the Applications Processor (AP) in the Multi-Satellite Operations Control Center (MSOCC). Using the communications software developed for COBE console application software, the Data Interface subsystem buffers the TDRS and COBE spacecraft status data received from the AP, converts it to the required format, and passes it to the Expert System. Both subsystems are coded in the C programming language.

The Expert System is a forward-chaining, rule-based system. It is implemented using the C Language Integrated Production System (CLIPS), an expert system development tool developed at the Johnson Space Center. The knowledge embedded in CLEAR (which enables it to isolate and diagnose problems) was extracted from the COBE Flight Operations Team through an interviewing process, and is represented within the Expert System in the form of rules. Data enters the Expert System as facts (pieces of information); the existence or nonexistence of facts during execution causes rule to fire (execute). When a configuration or communications problem occurs, CLEAR will isolate and diagnose the suspected fault and display the problem, along with advice about how to correct it quickly. In the event that multiple problems are isolated, the system will hierarchically display all problem descriptions, with the uppermost



Cosmic Background Explorer Mission Operations Room.

one designated as the most critical, and the lowest one as the least critical. By default, the system will display the advice for the most critical problem; however, the user may select the problem for which he or she would like advice to be displayed.

To further assist the user, the CLEAR system also includes explanation and event-reporting facilities. The explanation facility provides the user with a more in-depth description of the problem, and an explanation of why the system believes that the problem exists. This is an essential element of an advisory expert system, because it allows the system to explain to the user how and why the problem was isolated. The event-reporting facility logs all expert system activity for postevent analysis. During the communications event, CLEAR will time-tag all identified faults and record the inferences, diagnoses made, and the recommendations offered. After the event, the FOA will be able to trace and analyze the activity of the

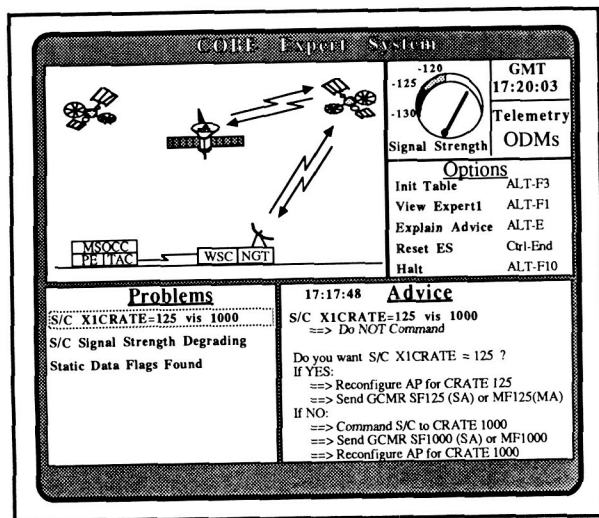
expert system for statistical evaluation of system performance, and to enhance future operations.

It should be emphasized that CLEAR is a passive system supporting COBE real-time operations in an advisory manner. Hence, the ultimate decision concerning which course of action to execute remains the responsibility of the FOA. As more confidence is developed in the utility and applicability of expert systems, this emerging technology will be entrusted to a more active role in monitoring, diagnosing, and possibly operating the control centers.

Contact: Peter M. Hughes
Code 522

Sponsor: Office of Space Operations

Mr. Peter M. Hughes, who works in the Automation Technology Section, received his BS degree in



CLEAR user interface design.

computer science from the College of William and Mary. He is currently pursuing an MS degree in the same discipline at Johns Hopkins University. Mr. Hughes' responsibilities include the design and implementation of the CLEAR Expert System, and he recently co-chaired the 1988 Goddard Conference on Space Applications of Artificial Intelligence.

AN INTEGRATED RECEIVER CONCEPT USING PROGRAMMABLE CHARGE-COUPLED DEVICES

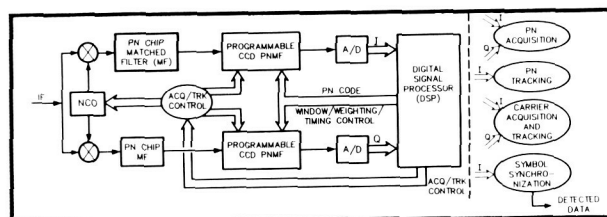
The Goddard Space Flight Center (GSFC) Networks Division (Code 530) is currently involved in the investigation of advanced communications signal processing techniques that are applicable to the Tracking and Data Relay Satellite System (TDRSS) and its planned follow-on, Advanced TDRSS (ATDRSS). One activity is the design and development of a state-of-the-art integrated receiver that utilizes programmable Charge-Coupled Device (CCD) correlator technology as the basis for novel signal processing. This process encompasses extremely rapid pseudo-noise (PN) signal acquisition, as well as PN tracking and carrier/symbol synchronization.

Under a National Aeronautics and Space Administration/GSFC Small Business Innovative Research (SBIR) contract, Stanford Telecommunications, Incorporated (STI) has developed a CCD integrated receiver in laboratory hardware. The programmable

CCD analog-digital correlator can be used to implement a PN-matched filter (PNMF) that can be matched to virtually any long or short PN code, and can provide an effective parallel processing capability to a degree equal to the number of stages. This PNMF flexibility, coupled with its high-level parallel processing capability, makes this CCD correlator attractive for TDRSS signal processing applications—especially for rapid acquisition of PN-coded signals received on power-limited space-to-space communication links between low-Earth-orbiting spacecraft and TDRSS. The proposed CCD integrated receiver shown in the first figure has the ability to apply the same circuitry, and the same signal information, to implement all key PN, carrier, and symbol synchronization functions. The analog CCD correlator outputs are A/D converted, and subsequent digital signal processing is used to implement all acquisition and tracking functions.

The first phase of the STI SBIR effort, which involved the implementation of the rapid PN acquisition feature of the CCD integrated receiver, was recently completed and demonstrated to GSFC. The principal capability demonstrated was the achievement of a 1-second PN acquisition time, at 90 percent probability, under threshold TDRSS signal-to-noise ratio conditions.

The second phase of the SBIR effort, which has also been completed and demonstrated, focused on the remainder of the integrated receiver signal processing functions, including PN, carrier and symbol tracking, and data detection. Also included in the demonstration hardware was the processing required for efficient transition from PN acquisition to stable tracking. Hardware test results indicate that the CCD integrated receiver incurs relatively little implementation loss, and operates within 1 dB of theory. The results of this proof-of-concept effort demonstrate that a lower complexity, high-performance, and

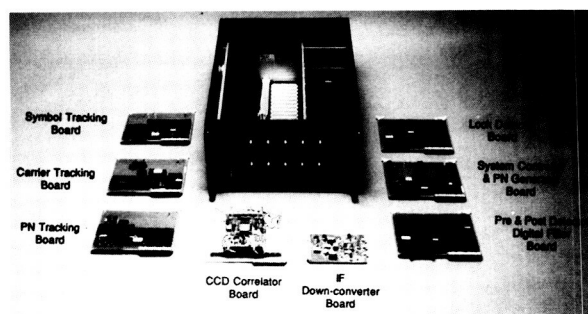


CCD PNMF implementation concept.



operationally flexible (e.g., rapid autonomous reacquisition and reconfiguration, without link interruptions) receiver for TDRSS applications is attainable. Key operational benefits are achieved by the judicious use of digital signal processing, and the application of embedded microprocessors.

The photo shows the CCD Integrated Receiver equipment. The photo highlights the very compact Lincoln Labs' CCD correlator chip (seen at the center of the CCD correlator board) and the highly modular design implementation. A production version of this receiver would probably require no more than 100-200 square inches of electronics. The relatively small weight, power, and size of the receiver make it especially attractive to potential Space Network users.



CCD integrated receiver.

Potential TDRSS applications include user (balloon and spacecraft) transponders, future TDRSS ground station receivers, and Advanced TDRSS (ATDRSS) onboard and ground signal processing applications. Anticipated CCD technology advances over the next few years should be capable of providing these integrated receiver features for all of the TDRSS modes of operation, and data rates of up to at least 10 Mbps.

Contact: Denver Herr
Code 530

Sponsor: Office of Commercial Programs

Mr. Denver Herr is Deputy Project Manager for the Second TDRSS Ground Terminal Project. His professional interests include advanced communications signal processing techniques. Mr. Herr holds an MS

degree in telecommunications from George Washington University, and he has been at Goddard for 22½ years.

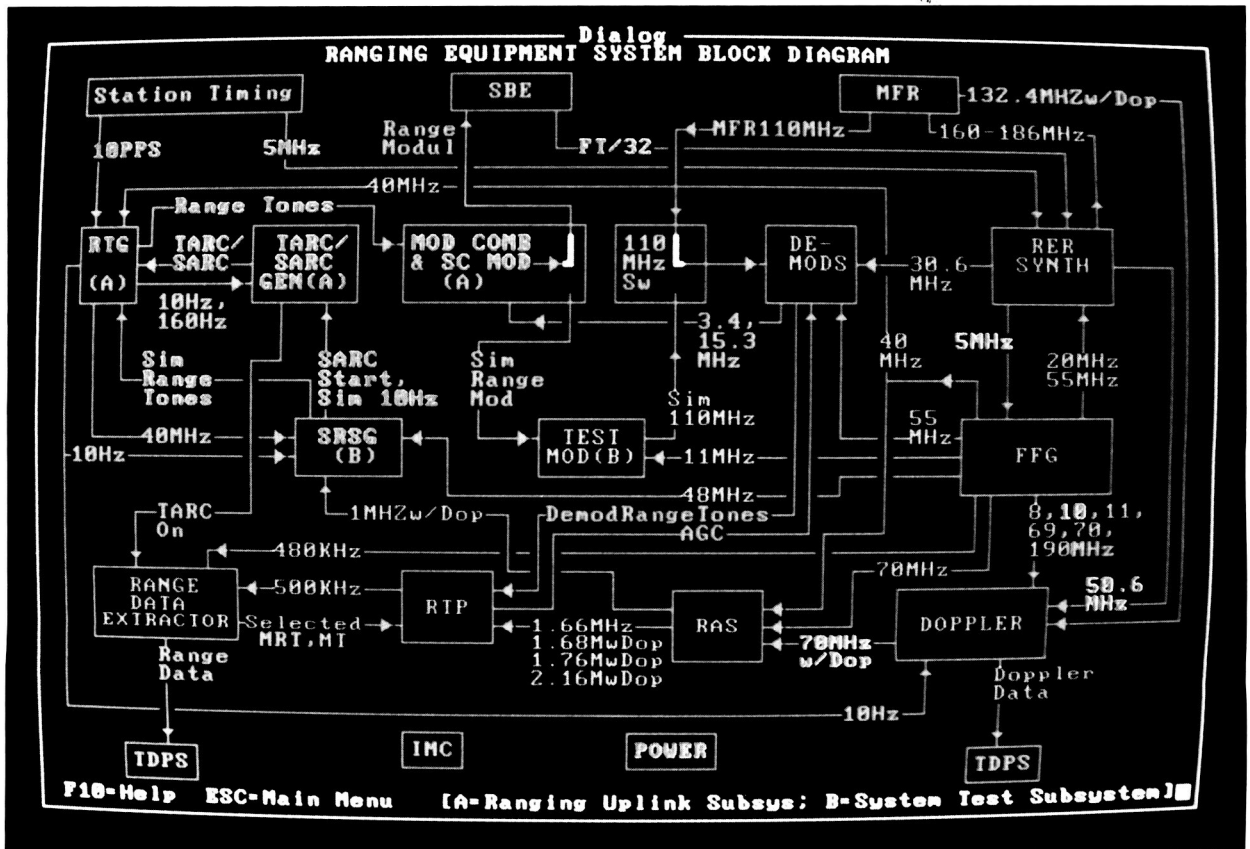
DIAGNOSTIC EXPERT SYSTEM FOR GROUND NETWORK RANGING EQUIPMENT

A new generation of Ranging Equipment (RE) is being installed at National Aeronautics and Space Administration Ground Network (GN) tracking sites to determine range and Doppler for the space shuttle and other spacecraft. The RE is a complex system, incorporating modern electronics technologies for performing high-frequency, low-frequency, and microprocessor-based digital functions. It is comprised of over 50 custom-designed, field-replaceable circuit cards and modules.

When a hardware failure occurs in the RE, the operator must identify the faulty circuit card and replace it with an on-site spare as rapidly as possible, thus restoring the RE to service for mission support. This task is facilitated by an RE internal test point monitoring capability that reports the status of 74 key RE signals. However, the troubleshooting process may take an hour or more, requiring the operator to trace signals and status through several hundred block diagrams and circuit schematics. A major difficulty is that a single fault often causes many test points on numerous circuit cards to stray from their nominal values. The diagnostic troubleshooting process involves reasoning about signal flow and cause-effect relationships in electronic systems. This reasoning process requires knowledge of the available test point values, knowledge of general electronic troubleshooting rules, and specific knowledge of the design and operation of the RE.

To reduce troubleshooting time, a diagnostic expert system has been designed to serve as an assistant to the RE operator. Expert systems have been developed for diagnostic applications in medicine, engine repair, communication networks, and several other fields. Diagnostic expert systems typically consist of a set of "if-then" rules that represent knowledge about how to identify a fault in the domain of interest, and an inference engine that controls the application of these rules.

An advanced prototype, Ranging Equipment Diagnostic Expert (REDEX), has been implemented,



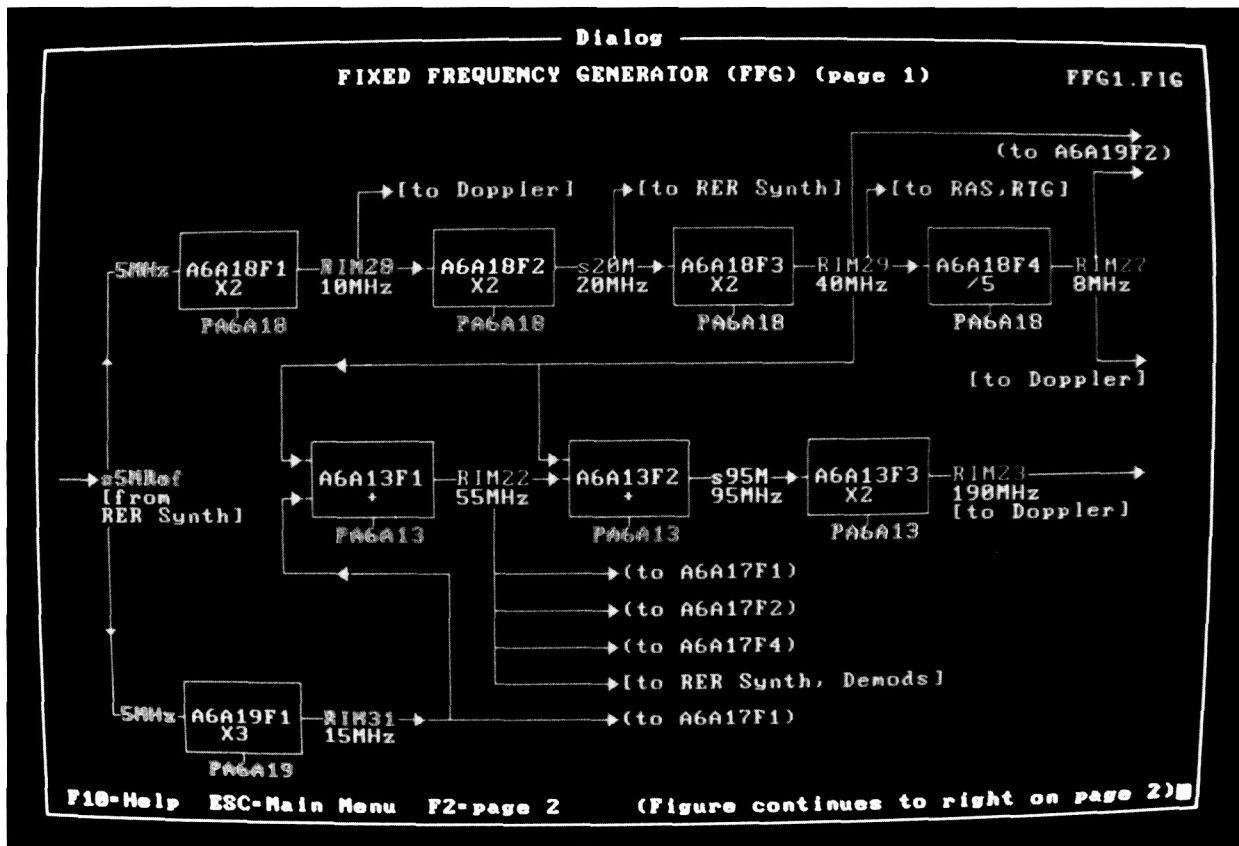
The Ranging Equipment System Block Diagram is color-coded to show good and bad signals. In this example, the effects of a fault in the FFG subsystem (middle right) have propagated into many other subsystems; before diagnosis, the fault location is not obvious.

and is currently undergoing testing and evaluation under the leadership of Computer Sciences Corporation's Edward C. Luczak. When an RE fault is detected at a GN tracking site, REDEX will diagnose the situation, and identify the circuit card or cards that are suspected to be faulty. REDEX will be interfaced directly to the RE to obtain test point status data. REDEX will display the status data and the results of the diagnosis using displays of RE block diagrams, rack-and-drawer layout diagrams, and tabular data.

The troubleshooting knowledge for REDEX was acquired by interviewing an RE troubleshooting expert, and by studying RE design documentation. A semantic network knowledge representation technique was used to model the design structure of the RE. A catalog of generic troubleshooting rules was compiled

to represent "rules of thumb" that are often applied in diagnosing electronic equipment. Additional specific troubleshooting rules were identified to represent diagnostic knowledge that is unique to the RE. Approximately 20 semantic network diagrams, 50 generic troubleshooting rules, and 250 specific troubleshooting rules were derived.

REDEX is implemented in the Prolog language on an IBM PC AT-compatible workstation. Windows, menus, and an on-line help facility make the program easy to use. Block diagram graphics displays such as those shown in the accompanying figures are color-coded to facilitate the display of RE status data and diagnostic conclusions. Signals that have been monitored or inferred to have nominal values are displayed in green, while those out of tolerance are displayed in red. The circuit cards and functions



At the conclusion of the diagnosis, a detailed block diagram of the Fixed Frequency Generator subsystem is displayed. The function "A6A18F2" is flashing, identifying the location of the fault.

diagnosed as faulty are displayed flashing. Over 50 graphic and tabular displays have been implemented.

A hypertext-like scheme is used to allow the user to easily navigate through the space of diagrams and tables. Link "buttons" are defined on each diagram and table. By moving the cursor to one of these link buttons and pressing a function key, a new diagram or table is displayed. These links allow the user to rapidly move up, down, across, and between the hierarchies of block diagrams, layout diagrams, and tabular data.

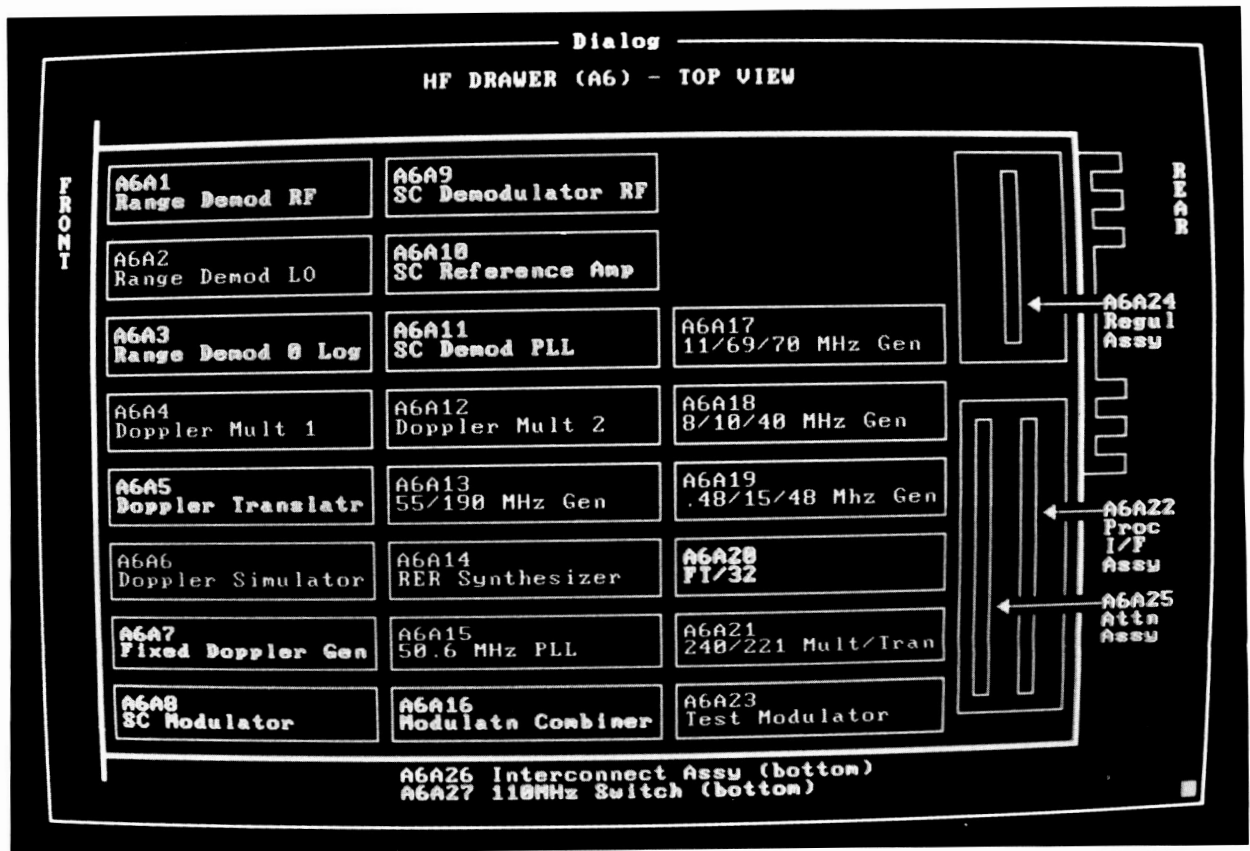
REDEX is currently being evaluated in a stand-alone mode, using simulated RE fault scenarios. It is expected to be a valuable RE troubleshooting training tool in this mode. REDEX will soon be interfaced to the RE, and tested in an on-line environment.

Plans are being made to install REDEX at four or more tracking sites.

Contact: David J. Zillig
Code 531

Sponsor: Telecommunication Systems Branch

Mr. David J. Zillig is integration engineer for the Cosmic Background Explorer Navigation Experiment, which is an application of one of the advanced communication capabilities of the Second Generation TDRSS User Transponder developed by Goddard's Telecommunication Systems Branch. Mr. Zillig earned a BS degree in electrical engineering from the Pennsylvania State University. He has served with Goddard since 1966.



A diagram of one of the circuit card drawers shows that bad signals were found on many circuit card: "A6A18" (middle right) is flashing, identifying the only circuit card needing replacement.

ORBIT DETERMINATION AUTOMATION SYSTEM

The Flight Dynamics Facility (FDF) provides spacecraft trajectory determination for a wide variety of National Aeronautics and Space Administration (NASA) spaceflight missions through the use of Tracking and Data Relay Satellite System (TDRSS) and Ground Spaceflight Tracking Data Network (GSTDN) tracking networks. The FDF trajectory computation system that supports this spectrum of NASA missions is the Trajectory Computation and Orbital Products System (TCOPS). To take advantage of computerized decision-making processes that can be used to control large-scale computational systems like those used in spacecraft navigation, the Orbit Determination Automation System (ODAS) has been designed, developed, and implemented as a prototype system using the TCOPS as the basic spacecraft trajectory determination system (TDS). The main thrust of ODAS implementation has been

to establish and validate the decision-making processes that control the spectrum of computational functions for spacecraft trajectory determination. The three specific subsystems where the decision-making processes have been implemented, tested, and evaluated are: 1) the ODAS driver, which initiates the execution of the ODAS program, and controls its operations; 2) the trajectory determination quality-assurance processor, which monitors and controls the processing of the differential correction; and 3) the ephemeris quality-assurance processor. The addition of these decision-making capabilities to the TDS creates an environment where computational results can be generated with a significant reduction of analyst intervention and computer time, and with a high probability of successful processing.

The ODAS driver is the subsystem that is responsible for the overall initiation and control of computational functions within the ODAS system. This



decision-making subsystem is functionally separated into five major components: 1) the timer, which performs specific functions related to timing of the ODAS operations; 2) the scheduler, which performs the scheduling functions of the overall system; 3) the tracking data sufficiency function, which performs an assessment of tracking data availability prior to the differential-correction job initiation; 4) specific job submission, which in turn creates the control/input data set (CIDS) for orbit determination processing; and 5) a stop function, which suspends or resumes ODAS processing. The ODAS driver subsystem initiates the execution of the ODAS system, and controls its continuous operations. It is the only ODAS subsystem that resides permanently on the mainframe NAS-8063 computers, and is designed to be in continuous execution. It should be emphasized that the ODAS driver monitors all automation functions, effectively synchronizes tasks, and performs TCOPS execution preparation and submission.

The differential correction subsystem, Goddard Trajectory Determination System (GTDS), is a major computational system within the TCOPS environment, and has been used in ODAS without any modifications to its mathematical techniques. The decision-making processes that have been developed and implemented in the differential-correction quality assurance subsystem of ODAS are: 1) an extraction function, which extracts subsets of parameters from the statistical output report of the differential-correction processing for further analyses; 2) a failure detection function, which diagnoses specific differential-correction failures based on computational parameters generated by the differential-correction processing in the statistical output report; 3) a failure recovery function, which initiates a recovery process if a differential-correction process failure has been detected; and 4) a results transmission function, which transmits the decision-making information from the differential-correction quality assurance function to the driver subsystem. The extraction function of the differential-correction quality assurance subsystem works to extract specific parameters that are required for failure detection and recovery processing from the generated differential correction/statistical output report. These generated parameters, such as final-weighted root mean square (RMS) of the differential-correction solution, the atmospheric-density correction estimate, the spacecraft solar radiation estimate, the estimate of the

standard deviation of tracking data residuals, the total change in the state vector between sequential solutions, etc., are selected, transferred, and used by the failure-detection and recovery components of the subsystem.

The failure-detection function through its decision-making processes determines whether or not a differential-correction process or orbit-determination solution has met and passed the acceptance parameters. Based on the intelligence that has been implemented into ODAS, a decision is made as to whether a failure exists. In case of no differential-correction failure, then the differential-correction quality assurance subsystem terminates, thus signaling the execution of the ephemeris subsystem. If a differential-correction failure exists, then the differential-correction quality assurance subsystem activates the failure-recovery component.

For a specific subsystem failure, the failure-recovery component invokes a corresponding recovery procedure, which translates into system control modifications that have been prescribed by expert operators. The recovery function makes use of the following recovery procedures in its decision making processes: 1) extend the tracking data arc in the backward direction; 2) increase the a priori weighted RMS; 3) detect and eliminate the biased or noisy tracking passes from the solution; 4) change the atmospheric density profile; and 5) use the final elements as input parameters. These recovery actions are generated in the differential-correction subsystem, and transferred through the results transmission function of the subsystem to the ODAS driver for further automated decisions.

The ephemeris subsystem is another major computational system within the TCOPS environment that has been used in the ODAS system without any modifications to its mathematical techniques. The decision-making processes that have been developed and implemented into the ephemeris quality-assurance subsystem of ODAS are: 1) an extraction function, which extracts specific parameters from the TCOPS ephemeris comparison results for further analysis, i.e., ephemeris comparison results are the position and velocity difference history over a selected time interval between two sequential ephemerides; 2) a failure detection function, which determines if ephemeris comparisons results meet

specific requirements; and 3) a results transmission function, which transmits the decision-making information from the ephemeris quality-assurance function to the ODAS driver subsystem. The COMPARE extraction function takes the computational parameters for a spectrum of different solutions from the COMPARE results between two sequential ephemerides, and provides that data to the quality-assurance function for further analysis. Then the quality-assurance function of the COMPARE system evaluates the compare parameters from the computations with ephemeris acceptance criteria, and determines that the ephemerides results are adequate. The ephemeris results transmission function transfers the results of the subsystem to the ODAS driver for additional computational decisions.

The design, development, and implementation of decision-making processes for spacecraft navigation in the ODAS system have created an environment where computational results can be generated with significant reductions of external control, analyst time, set up time, and computational time, thus creating a higher probability of success.

Contact: C. E. Doll
Code 554

Sponsor: Office of Space Operations

Mr. C. E. Doll researches and develops mathematical and computational techniques supporting the field of astrodynamics for Goddard's Mission Operations and Data Systems Directorate. Mr. Doll has been at Goddard for 29 years.

REMOTE SCIENCE OPERATIONS CENTER

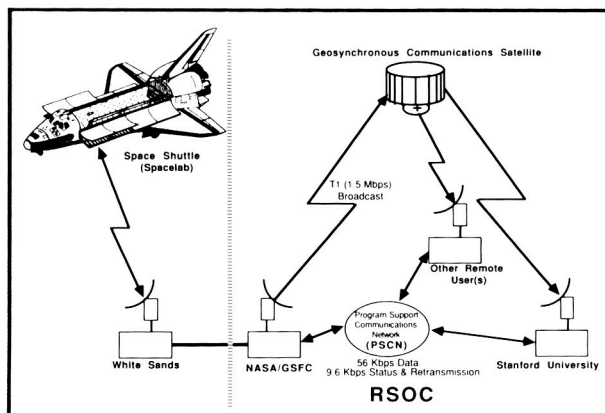
The Remote Science Operations Center (RSOC) is a prototype data communications system developed to demonstrate the feasibility of implementing cost-effective, real-time delivery of experiment data to scientists throughout the United States. The central feature of RSOC is the development and implementation of a protocol with high-speed, half-duplex data transmission via satellite, and error-correcting capability provided by low-speed terrestrial links.

The RSOC prototype demonstrates its viability as a cost-effective, real-time data delivery system. RSOC

is being developed under a cooperative agreement between Goddard Space Flight Center (GSFC) and Stanford University. A full demonstration of the RSOC system is expected to be completed in early 1989.

RSOC has been presented and demonstrated to NASA Headquarters personnel, and to Johnson Space Center personnel. The demonstrations used equipment located at GSFC; local area networks provided all data communications. (The accompanying figure shows RSOC configuration.) Cost benefit results comparing RSOC transmission versus common carrier data transmission were presented. The cost estimate for RSOC satellite transmissions at T1 rates (1.54 Mbps) over a 5-year period is \$200,000 for 1 user, \$600,000 for 5 users, and \$2 million for 20 users. The corresponding figures for common carrier transmission are \$600,000, \$3 million, and \$12 million, respectively.

The RSOC system accepts data from the Spacelab Data Processing Facility (SLDPF), and extracts and creates data packets formatted according to an early version of the Consultative Committee for Space Data Systems (CCSDS) protocol for packet telemetry. For the prototype, the data extraction and formatting process is remotely controlled by information received from the Principal Investigator (PI) at Stanford University. A computer-to-computer link is established between the Stanford host computer and the RSOC host computer (both Vax computers) using a Digital Equipment Corporation Network (DECnet). RSOC host software accepts commands from the PI to start or stop the system, and to select



Remote Science Operations Center Configuration.



the data transmission mode (satellite or backup) and the source of data (either real-time data from the SLDPF, or playback data buffered by RSOC on disk).

The primary data transmission path for RSOC is a half-duplex satellite link originating at GSFC and broadcast to receive-only Earth stations at research facilities throughout the United States. The link operates at 80 Kbps for the prototype, but can be increased to T1 rates, if desired, with no change in ground terminal equipment. The selection of an 80 Kbps rate for the prototype was based on the cost of leasing transponder capacity on a domestic satellite, and on the data requirements of the PI participating in the cooperative agreement.

A secondary, or backup, transmission capability is provided using Transmission Control Protocol/Internet/Protocol (TCP/IP) communications over point-to-point 56 Kbps datalinks. This mechanism can be selected by the PI, who issues commands over the dedicated DECnet control link. Other remote RSOC users are not required to implement backup links. They are notified whenever the transmission mode is switched from satellite to backup via the same low-speed circuits used to request retransmissions.

The functional capabilities of RSOC are as follows:

- Remote users can only access RSOC with authorization.
- Remote users can access the RSOC host via either DECnet or TCP/IP protocols.
- The Principal Investigator can select either satellite or backup links as the primary data transmission mode.
- Remote users are notified of changes whenever the prime user reconfigures RSOC.
- Interactive message passing is supported.
- Retransmission requests are honored.
- Flow control on the rate of retransmission requests processed can be exercised.

Recent technical accomplishments include the following:

- Generic protocol handling software was developed to service a mixture of DECnet and TCP/IP links using either Network Solutions' OPEN-Link or Excelan's EXOS packages.
- VAX asynchronous system traps (ASTs) were implemented to improve the efficiency of full-duplex communications.
- The DECnet control link was implemented and tested.
- Sample applications programs were developed to simulate multiple simultaneous remote users.
- RSOC host and sample applications programs using DECnet were operated to simulate satellite transmission and to verify proper servicing of mode switching commands.
- Authorization and throttling mechanisms were implemented and tested.
- TCP/IP backup links were tested between the RSOC host and external computers located at GSFC and at Stanford.

Contact: Ben Keith
Code 522

Sponsor: Office of Space Operations

Mr. Ben Keith, who earned a BS degree in electrical engineering from Roger William College (Rhode Island), is project manager of Telescience and Telecommunications Projects within the Data Systems Technology Division. Mr. Keith has received several NASA Achievement Awards.

A MAJOR SCIENTIFIC WIDE-AREA NETWORK

The Space Physics Analysis Network (SPAN) continued its phenomenal growth in fiscal year 1988, thus becoming a major scientific wide-area network. SPAN currently has approximately 2500 computer nodes, and is part of an international Digital Equipment Corporation Network (DECnet) internet of well

over 5000 nodes. There are mail gateways connecting SPAN to non-DECnet networks such as the Defense Department's Advanced Research Projects Agency Network (ARPANET); Janet; Computer Science Network (CSNET); and Magnetic Fusion Energy Network (MFENET), providing access to thousands more computer nodes, and X.25 connections to Canada, Japan, and Chile.

The availability of SPAN has changed the way that National Aeronautics and Space Administration (NASA)-funded scientists conduct their research. There is direct access via SPAN to major data centers and data bases across the United States and around the world, to observatories, and to supercomputers at many NASA centers and at supercomputer facilities, such as the San Diego Supercomputer Center. This capability has facilitated the scientists' ability to identify, obtain, and share data/information, in addition to sharing computer resources.

When asked about their use of SPAN, scientists have indicated that they are using it for communications with colleagues, exchange of data and manuscripts among colleagues, and remote data processing. They use SPAN communications to exchange information among members of subgroups, to support collaborations with colleagues, to coordinate work of various NASA-related committees, to coordinate between Principal Investigators in the field and Headquarters project offices, to put together proposals and review them, and to coordinate with editors. With SPAN, scientists' international communications are no longer hampered by 6-hour time differences, or long delays due to various postal systems. Scientists have found SPAN to be extremely valuable for planning and development of future projects, such as International Solar Terrestrial Physics (ISTP) and Galileo. The NASA Ocean Data System (NODS) has taken advantage of the existence of SPAN and linked additional ocean science nodes that were actively managing ocean data into a prototype distributed ocean data management system, or ocean network. SPAN users also are accessing distributed data bases, doing remote interactive modeling on supercomputers, and conducting on-line interactions with ships at sea via the Applications Technology Satellite (ATS).

Contact: Valerie L. Thomas
Code 633

Sponsor: Office of Space Science and Applications

Ms. Valerie L. Thomas, who holds an MS degree in engineering administration from George Washington University, is Project Manager of SPAN. Her professional specialties include wide-area network management, digital image processing, and development of real-time data systems.

THE USE OF SPAN FOR RAPID ACCESS TO INTERNATIONAL ULTRAVIOLET EXPLORER DATA

There are two major wide area National Aeronautics and Space Administration (NASA) networks that are used extensively: SPAN and NSN. SPAN contains over 2050 nodes in the United States and is internetworked with over 6000 nodes in the United States, Europe, Canada, and Japan. Like SPAN, NSN is internetworked with other wide area networks such as ARPANET and the NSFNET, which can reach many thousands of computers. In general, these wide area networks are of relatively low speed; however, they provide a tremendously valuable service for the remote users, allowing access to space and Earth science computer resources and to fellow researchers all across the country. Although a modest amount of data is transmitted over the wide area networks, the bulk of the traffic is informational, such as remote log-on and mail.

With the dramatically increasing ease of electronic access over the last few years, the National Space Science Data Center (NSSDC) has created a major new thrust in "on-line" computer information systems accessible to remote users 24 hours a day. The NSSDC on-line information systems include the NASA Climate Data System (NCDS), the Pilot Land Data System (PLDS), the Crustal Dynamics Data Information System (CDDIS), the Astronomical Catalog Information System (ACIS), the Master Directory (MD), and the International Ultraviolet Explorer (IUE) request system, just to name a few. The use of SPAN has made the IUE Interactive Request System a major achievement in providing rapid access to archived science data and to information about those data.

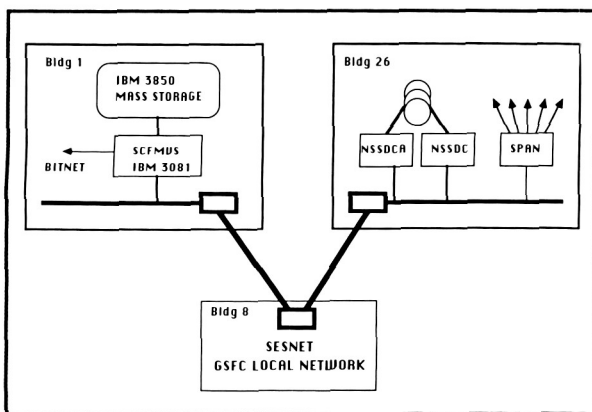
The IUE interactive request system became operational in November 1987; by January 1988, requests



were routinely serviced with this system. The request system consists of on-line mass storage, menu-driven interactive information access software (running on two VAX front-end computers), a high-speed local area network connecting the on-line storage with the interactive front-ends, and the wide area networks, SPAN and NSN.

Rapid access to selected data has been frequently requested by scientists. Since it is not known ahead of time what data will be requested, the NSSDC loaded all the IUE data into the NASA Space and Earth Sciences Computing Center's IBM 3850 Mass Store in order to accommodate the large user demand. It is important to note that the NSSDC typically manages its archive off line. Storing all the IUE data on line was done with full project cooperation and in order to gain valuable experience with highly requested on-line data sets. The IUE data that are currently on line consist of over 61,000 unique star images and spectra.

The IBM 3850 Mass Store device is controlled by an IBM 3081 computer and connected to the NSSDC interactive VAX front-end computers by a high-speed local area network (called SESNET) as shown in the figure showing mass storage data access at Goddard Space Flight Center. The interactive request system



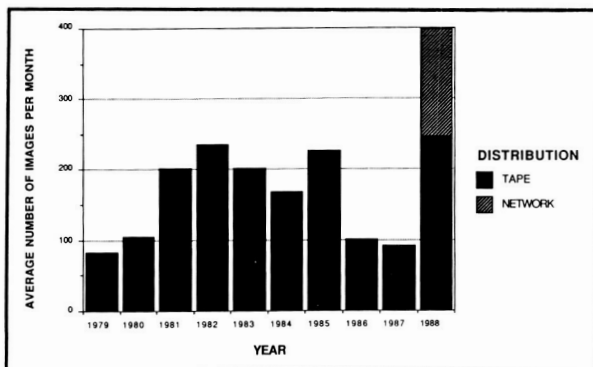
Mass storage data access at GSFC. All the available IUE data are stored in the NSESCC IBM mass storage system. The high-speed local-area network at Goddard Space Flight Center, SESNET, provides connectivity between the IUE Interactive Request System (which resides on the NSSDC interactive VAX front-end computers) and the IBM 3081 and mass storage system.

software runs on the NSSDC VAX computers, allowing a remote SPAN user to log on and order IUE data from the electronic IUE Merged Observer Log. Once the exact data segment requested has been identified, the NSSDC request coordinator networks the IUE data from the Mass Store device through the SESNET network. For requesters desiring a small number of images and spectra, the NSSDC request coordinator can then network the data through SPAN to a specified computer within approximately 24 hours, or else create a magnetic tape to be mailed. Requests for IUE data sent on magnetic tape are easily handled by this system, saving the manual locating of the data. Requests for IUE data also come to the NSSDC through letters and phone calls. (Not all the users are on computer networks.)

The second figure shows the NSSDC monthly averages for IUE image requests from 1979 to 1988. (The NSSDC also sends large amounts of IUE data to other archives not included in this figure.) The solid colored bars in the figure show the number of images sent out on magnetic tape to individual requesters, while the size of the crosshatched bar represents the number of IUE images that have been networked to remote users. From 1979 to nearly the end of 1987, the only service the NSSDC offered was off line; a tape copy of the requested data was produced and sent to the requester. The bar graph also shows the monthly number of IUE images requested in 1988 (an average, computed from data covering the first 8 months of that year).

As can be clearly seen in the second figure, a dramatic increase in the amount of IUE data requested occurred in 1988, reaching approximately 400 images and spectra sent out per month. It is important to note that the IUE Interactive Request System is used by scientists for over 75 percent of all requests. (In August it was 93 percent of all requests.) SPAN is used to deliver, on the average, about 38 percent of the data. (In July 1988, all images requested were networked.) The remaining requests, usually the larger data volumes requested, are satisfied by sending magnetic tapes. Currently, the trend in the use of the IUE Interactive Request System and the reliance on the networks for data delivery continues to increase.

The networked IUE images satisfied requests from many scientists at 15 institutions in the United States, Europe, and Canada (locations serviced by SPAN).



IUE images requested by individuals from the NSSDC archive. This bar chart shows the average number of IUE images requested (per month) for each year since the archive was opened in 1979. Although the IUE Interactive Request System became operational in November 1987, it was not until January 1988 that remote users routinely accessed the new interactive system. The huge increase in the average number of images distributed in 1988 can easily be attributed to the better service that is now provided electronically. The crosshatched bar shows that nearly 40 percent of all images requested are delivered over computer networks.

In addition, care is taken to use SPAN for networking of the IUE data at times of nonpeak network usage. Tests are currently under way in which some IUE data are compressed before being networked to the remote node. Once the compressed data arrive at their destination, they are then decompressed, reducing the communication load on the wide area network.

Since there has been no new funding from NASA Headquarters for increased IUE data analysis, it is clear that the tremendous increase in requested data is due to the convenience this system provides to the user. The following factors are a major part of the user convenience provided by this service: data are loaded to the target system (no tape handling); data arrive in the desired format; no replacement tape need be sent to the NSSDC (currently the network is a "free" service to the users); and rapid turnaround provides the desired data before scientists lose interest.

For the requester to use low-rate communication networks such as SPAN, the size of data requested must

be relatively small. The IUE example is a good one, since the stellar object observed forms a small enough data subset that it can be easily networked. The amount of time required to satisfy a request ranges from 2 to 15 minutes, depending on the communication line rate between the NSSDC and the requester, and the load on the network at the time.

Contact: James L. Green
Code 630

Sponsor: Office of Space Science and Applications

Dr. James L. Green is Head of the National Space Science Data Center, NASA's permanent data archive. Of the numerous awards he has earned, three were Marshall Space Flight Center Certificates of Appreciation, two were Goddard Certificates of Appreciation, and one was a NASA Group Achievement Award. Dr. Green has been with NASA for nine years, of which three have been at Goddard. His PhD degree is in physics.

TUNNELING CALCULATIONS FOR GRADED BAND-GAP STAIRCASE AVALANCHE PHOTODIODES

Very low-noise, high-gain light detectors will be used as receivers in free-space laser communications systems. Currently, silicon Avalanche Photo Diodes (APD) are used to detect light from Aluminum Gallium Arsenide (AlGaAs) semiconductor laser diodes, the kind of laser most likely to be used in optical communications systems developed by the National Aeronautics and Space Administration. These silicon photodiodes presently operate near their theoretical lower bound of multiplication noise. It is desirable to develop photodetectors capable of high-speed, high-sensitivity, and even lower noise operation, to improve the performance of space optical communications systems.

An avalanche photodiode rivaling silicon in speed and sensitivity, but capable of operating with half as much multiplication noise, currently is being developed under the direction of its inventor, Dr. Federico Capasso. This device will be a graded band-gap AlGaAs superlattice, in which the electrons multiply deterministically at each heterointerface, where holes are many times less likely to multiply.



The resulting difference in the degree of amplification of the electron and hole currents is what results in the lower noise operation relative to silicon APDs. Molecular Beam Epitaxy (MBE) is the technique used to grow the stages in the AlGaAs APD. This method permits very close control of layer thicknesses, compositions, and doping levels required to reach the theoretical limits of operation of this device. A ten-stage AlGaAs prototype staircase that displayed the high gain and high ionization ratio of electrons to holes anticipated for this kind of superlattice was recently fabricated in an industrial laboratory. Staircase APDs based on this structure and operating close to their theoretical performance limits are expected within the next 2 years.

In conjunction with development work at an industrial laboratory, researchers are conducting a theoretical study of electronic transport through the conduction band of AlGaAs staircase superlattices at Goddard Space Flight Center's Instrument Electro-Optics Branch. The goal of this study is to perform quantum mechanical tunneling calculations that result in the transmission coefficients and in tunneling current-voltage curves for these superlattices. Resonant energy levels for electrons in the conduction band of the staircase superlattice are calculated as a function of applied and internal electric fields; the effects of composition, and hence the band-gap and effective mass gradients, are taken into account. Previous calculations for semiconductor superlattices have been for step superlattices only: computations of this kind have not yet been reported for graded band-gap superlattices. The information thus provided is made available to researchers for implementation in the design and improvement of the AlGaAs staircase APD.

Contact: Kathrine A. Forrest
Code 723

Sponsor: Office of Aeronautics and Space
Technology

Ms. Kathrine A. Forrest, who has an MS degree in physics, performs applied research in semiconductor physics. She now works with the Instrument Electro-Optics Branch, drawing upon her 8½ years of experience at Goddard.

PERFORMANCE AND RELIABILITY OF AlGaAs TRANSMITTERS

Goddard Space Flight Center leads National Aeronautics and Space Administration (NASA) efforts in free-space laser communications. The laser transmitter will probably be one semiconductor laser diode—or several, combined in a power-summing scheme—whose reliable, stable performance is crucial to the success of any laser communications experiment. In particular, aluminum gallium arsenide (AlGaAs) lasers emitting between 800 and 900 nm have been selected for study as potential transmitter lasers by virtue of high optical output powers that they afford.

The performance and reliability of these AlGaAs laser diodes have been addressed in a comprehensive laser development and testing program that has been underway since 1984. The goal of this program has been to develop, procure, and evaluate reliable, high-power diode lasers emitting at 800 to 900 nm. Researchers' performance requirements are: output powers in excess of 70 mW peak, 35 mW cw; single spectral mode operation; polarization ratios >100:1; single mode far-field patterns with divergences <15° by 25°, and light-current characteristics with low threshold currents (<60 mA) and high efficiencies (slope efficiencies >0.7 W/A). In addition, output beam phase-front aberrations less than one-fortieth of a wavelength are desirable, to minimize diffraction losses through the optical train of the transmitter. Rise and fall times of <≈400 ps are required under high-speed (>100 MHz) modulation, as well as the stability of all the properties listed above. The performance requirements outlined above are extremely stringent, and have presented a considerable technological challenge to the semiconductor laser manufacturer. To add to the challenge, stable operation of candidate lasers with these characteristics must be demonstrated for at least 10,000 hours (a representative mission lifetime), at room temperature.

In industry, the design of the Channeled-Substrate Planar (CSP) diode laser was optimized for emission at 870 nm, resulting in high output powers; single-mode spectra and far-fields; low thresholds; and high efficiencies. Life testing of these lasers at Goddard Space Flight Center and in industry has shown that they have not yet met the goal of long life and stable

operation, however. Future work will be directed towards meeting this goal.

A Buried-Twin-Ridge-Substrate (BTRS) laser, also optimized at 870 nm, was developed in a joint industrial development program. These lasers are currently under life test, and have demonstrated very high performance, as well as impressive stability for operating times in excess of 2000 hours. BTRS lasers that are spectrally stabilized with external etalons have also been developed under this program. Current work in industry entails completing a 4000 hour life test and failure analysis on the free-running BTRS lasers, and measuring the actual spectral stability obtained from lasers with the external etalons.

Commercially available high-power lasers are procured "off the shelf" for evaluation from several manufacturers. A computer-automated laser evaluation facility and laser life test have been assembled at Goddard for the purpose of evaluating these lasers. The life test is capable of in situ measurements of far-field patterns, spectra, output power, polarization ratio, and current drive levels. Diodes on life test can be operated under either constant current or constant power, from room temperature up to 50°C. Diodes are presently being tested at 25°C; 25 mW average, and 50 mW peak power (at constant current); and 200 MHz at 50 percent duty cycle. Results of life testing high-power, 830-nm-wavelength lasers show very good stability of output power, far-field patterns, and polarization ratios for lasers from several manufacturers, with operating times in excess of 6000 hours. This is the first such life test to provide detailed, in situ measurements of these properties for high-performance laser diodes. This information will be used to select flight lasers in future laser communications packages flown by NASA.

Contact: Kathrine A. Forrest
Code 723

Sponsors: Office of Aeronautics and Space
Technology and Office of Space Science
and Applications

EXTERNAL CAVITY PHASED-ARRAY LASER: TIME-RESOLVED PULSED BEHAVIOR

In anticipation of the need for high-power, high-quality laser transmitters for free-space optical

communications, Goddard Space Flight Center's (GSFC) Instrument Electro-Optics Branch has investigated the use of Aluminum Gallium Arsenide (AlGaAs) laser diode phase-locked arrays in optical configurations that take advantage of their high output powers, while seeking to eliminate their undesirable characteristics. In particular, phase-locked arrays in external cavities appear to be promising candidates for future applications.

Most external cavity diode lasers that have been described in the literature use single-stripe lasers with partially reflecting end-cavity mirrors as the active element, coupled with gratings or "Graded Index" (GRIN) rods in arrangements intended to stabilize the spectral output of the laser. The most useful external cavities for the purpose of optical communications use phase-locked arrays, with spatial filters and external optics providing feedback to the laser. This arrangement causes the laser to operate in the fundamental mode, that is, with all the elements lasing in phase with one another. This results in a diffraction-limited output beam, with a very narrow, single-lobed far-field pattern. Although this diffraction-limited operation has been demonstrated in other laboratories for several external cavity phased-array lasers, in most cases the efficiency of the cavity is unreported. Furthermore, little has been reported on their pulsed operation. Stability of the far-field pattern under modulation is required of the transmitter lasers in high-performance optical communication systems.

The goal of the Goddard research on phased arrays in external cavities has been to achieve single-spatial-mode, near-diffraction-limited, high-peak-power (greater than 100 mW) pulsed operation, and to assess their stability under pulsed operation by means of time resolution of their pulsed far-field patterns.

One design adopted in this work uses gain-guided 10-element 100 mW AlGaAs phase-locked arrays as the active element in the external cavity. A partially reflecting flat mirror provides optical feedback to the array via the front facet. The cavity design is such that the output far-field can be adjusted in real time, until the fundamental mode dominates the far-field pattern (or until a diffraction-limited beam $<1^\circ$ wide is obtained). Then the peak and average output powers under modulation are measured, as well as



the time-averaged, and time-resolved far-field patterns. The time-resolved far-field patterns show the changes in the far-field as the external cavity laser is driven up to maximum power. (The time-resolved measurement technique used here was developed at GSFC specifically for evaluating the far-field stability of free-running phased arrays.)

With this cavity, time-averaged single mode operation was obtained. Peak powers of >120 mW were obtained at low pulsed duty cycles (0.2 percent), in a single lobe approximately 0.5° wide. Time-resolution of the pulsed far-field pattern, however, indicated significant competition from higher order array modes at the highest drive levels during the pulse. Future work will aim at improving the discrimination against higher order modes, and raising the pulsed duty cycle, while maintaining or raising the peak powers obtained.

Contact: Kathrine A. Forrest
Code 723

Sponsor: Office of Aeronautics and Space
Technology

THE IN-HOUSE MIXER/PREAMPLIFIER ENHANCEMENT EFFORT

The Microwave Instrument and Radio Frequency Technology Branch has been heavily involved in the integration and test of the Differential Microwave Radiometer (DMR), which is one of three instruments on the Cosmic Background Explorer (COBE) spacecraft. Mixer/preamplifiers (MPAs) are used in the three DMR receivers—31.5-GHz, 53-GHz, and 90-GHz—as part of the frequency down-converters. The original MPA flight units were fabricated by a contractor. The contracted 90-GHz MPAs did not meet the optimistic noise figure specifications of 2.5 dB. Also, time was wasted sending the units to the contractor for any repairs or changes. Because of these concerns, the in-house MPA enhancement effort was initiated. It was felt that some modifications to the original units may yield a required increase in sensitivity. These modifications would be done on MPAs for all three frequencies, emphasizing the 90-GHz units.

The Instrument Microelectronics and Detectors Branch was responsible for preparing the substrates (cutting substrates to the correct size, spinning photo resist, circuit pattern, baking, etching, and mounting diodes) and assembling the MPA units. The Microwave Instrument and Radio Frequency Technology Branch was responsible for coordinating the effort. This included 1) redesign of the mixer blocks and backshorts to include the modifications, 2) specification of the solder, tuning screws, diodes, and tuning tools required for this effort, 3) tuning the backshorts and screws after the MPAs were assembled, and 4) measuring the noise figure and interpreting the results.

Several modifications to the original contracted MPAs were proposed to reduce the noise figure. A major change was to incorporate High Electron Mobility Transistors (HEMTs). Other changes included a two-block mixer housing in place of the three-block housing, noncontacting backshorts, and whiskerless diodes.

Of the modifications listed above, using a HEMT preamplifier instead of the GaAs field effect transistor (FET) preamplifier would provide the most significant decrease in noise figure. The materials in a HEMT are the same as the GaAs FET; however, the structure is slightly different. There are alternating layers of AlGaAs (Aluminum Gallium Arsenide) and GaAs which is called a heterojunction. Because of these layers, the dopant ions are separated from the electrons allowing the electrons to travel more freely and faster from the drain to the source. Consequently, less internal noise is produced in the transistor. The other changes were thought to improve the noise figure slightly.

The first units assembled were the 90-GHz mixer housings with HEMT preamplifiers. In the beginning, several problems were encountered. Eventually these were overcome by improving the assembly and test methods.

After the units were assembled, they were tuned to produce as little internal noise as possible. A test setup was developed that included a noise source at the RF input and a local oscillator (LO) at the LO input. The output of the MPA was followed by an amplifier, a band pass filter, attenuators, and a noise figure meter. The tuning procedure consisted of the

following steps in order: tune LO backshort, tune RF backshort, retune LO backshort, tune the sapphire tuning screws from outside to center, and retune RF and LO backshorts.

Once the MPA was tuned, the output power was measured by placing hot (295 K) and cold (77 K) targets in front of the RF horn at room temperature. By relating the output powers from the hot target, $P(h)$, and the cold target, $P(c)$, the noise figure was calculated. Then a comparison of results was made to those of the original contracted MPAs. Equation 1 is used to solve for the noise temperature, T . Equation 2 converts the noise temperature to noise figure (NF). The loss at the RF input is then subtracted to obtain the noise figure of the MPA.

$$T = \frac{295 - 78 (P(h)/P(c))}{P(h)/P(c) - 1} \quad (\text{Equation 1})$$

$$NF = 10 \log (T/290 + 1) \quad (\text{Equation 2})$$

To perform the noise figure measurements, the 90-GHz MPAs were placed in a Dewar and cooled to 140 K in a vacuum. This was done to simulate the conditions when the MPA is operating in space. One thermistor was located on the MPA and another was attached to the cold plate. The MPAs were cooled with Liquid Nitrogen (LN2). Since LN2 is at 77 K, a temperature controller was used to apply enough heat to stabilize the temperature to 140 K. When the MPA stabilized at this temperature, the unit was turned on for one hour and then the noise figure was measured. Depending on the results, the unit was either prepared for flight use or reworked to get a better noise figure.

Noise figures were being measured within the required specifications (2.5 dB) for the 90-GHz MPAs. This is better than the contracted units by 0.3 to 0.6 dB. In fact, the Microwave Instrument and Radio Frequency Technology Branch has measured the best noise figure ever attained at 90-GHz. The other modifications—whiskerless diodes made at the University of Virginia, noncontacting backshorts, and two-block mixer housings—showed no substantial improvement. 53-GHz MPAs were assembled

with the HEMT preamplifiers and improved the noise figure by 0.1 to 0.2 dB. Several 31.5-GHz MPAs have been built in house replicating the original flight units and had similar noise figure results.

There are currently three in-house mixer/preamplifiers in the DMR receivers. One of the two flight MPAs in the 31.5-GHz receiver was rebuilt in house, due to a failure. The two original contractor units in the 90-GHz DMR receiver have been replaced by in-house MPAs utilizing HEMT technology. All other in-house units will be available as spares. Not only have NASA researchers increased the sensitivity of the 90-GHz receiver; they have developed state-of-the-art mixer/preamplifiers.

Contact: Catherine Long Richards
Code 727

Sponsor: Office of Space Science and Applications

Mrs. Catherine Long Richards, who earned her BS degree in electrical engineering from the University of Maryland, works with the Microwave Instrument and Radio Frequency Technology Branch. Her responsibilities include coordination of the In-house Mixer/Preamplifier Enhancement Effort.

60-GHz INTERSATELLITE COMMUNICATION LINK STUDY

The overall trend in satellite scientific and data collection communities toward use of relay satellites for the return of mission data is expected to continue. The current Tracking and Data Relay Satellite System has intersatellite link capability at S-band and Ku-band. The data rate capacity of these systems is not expected to be large enough to accommodate the projected rates for user spacecraft in the mid-1990s and beyond. The 60-GHz frequency band provides the necessary bandwidth as well as an environment virtually free of terrestrially-generated interference or intercept.

A definition study of 60-GHz intersatellite link capabilities was carried out for the National Aeronautics and Space Administration (NASA) by Ford Aerospace Corporation.



This study considered link parameters for geocentric (GEO) to low Earth orbit (LEO) spacecraft and for GEO-GEO crosslinks. All areas of the system concept were studied including hardware, modulation techniques, orbital parameters and tracking, and RF environment. A set of general ground rules were also established. These were:

- Use 1989 timeframe technology
- Maintain technology commonality among GEO-GEO crosslink and GEO-LEO intersatellite links
- Minimize the burden to GEO user satellites
- Minimize overall power and weight needs in LEO spacecraft

The links were established with a GEO to 3-5 LEO spacecraft simultaneous operation and with GEO to GEO high data rate links. In the course of the study each major configuration component was addressed as a subject of interacting system parameters. Starting with the link parameters, a baseline system was derived and then subjected to iterative development. This system considered present developmental levels and expected improvements as well as evaluating the system concept.

In general, the results show that the crosslink between two geosynchronous satellites with 160° separation is capable of simultaneous transmission and reception of 2-Gbps data through quadrature phase-shift keying (QPSK) modulation using a 10-watt IMPATT diode stable amplifier and a gimbal-mounted 3.2-meter parabolic dish cassegrain antenna with low loss beam waveguide gimbal pointing.

In addition to the GEO-GEO link described above, there are five link packages to provide simultaneous and independent intersatellite links between a GEO spacecraft and low Earth orbiting user satellites having a maximum altitude of 5000 Km. Each forward link (from GEO-LEO) is capable of a 1-Mbps data rate at all times using a 600-mW IMPATT transmitter and a 0.9-M gimbal mounted dish antenna with binary phase-shift keying (BPSK) modulation. Each return link (from LEO user to GEO) is capable of reception of 300 Mbps, forward error correction encoded QPSK information data. For LEO users equipped with a 1.4-M antenna and 7.5-watt

transmitter, the 300-Mbps capability can be maintained approximately 99.95 percent of the time in an equatorial orbit.

This study delineates the evolution of these designs and compares them to alternate methods. The overall baseline design is presented and recommendations for most critical technology development are set forth. Goddard Space Flight Center has begun a developmental program in the areas of high power 60-GHz solid-state amplifiers, low noise 60-GHz oscillators, and beam waveguide flexible joints as a result of this study. It is hoped to have a complete demonstration system ready by the early 1990s.

Contact: Robert B. Jackson
Code 727

Sponsor: Office of Space Operations

Mr. Robert B. Jackson, Head of the Antenna Technology Section, is the antenna engineer for Explorer 12-14, IMP series, UK-1 and UK-2, AE-A and AE-B, IUE, SMM, ISEE, COBE, and other Goddard Projects. He has a BS degree in electrical engineering and 27 years of experience at Goddard.

DESIGNING A SPACEFLIGHT RF SYSTEM WITH MODULAR ANTENNA COMPONENTS

High gain antennas have been developed using a modular concept. Microstrip arrays developed at S- and Ku-band are enabling National Aeronautics and Space Administration (NASA) network users to configure their antenna system to satisfy the best combination of power, weight, and data rate to comply with their requirements.

Solid State amplifiers have been designed for direct coupling to the microstrip subarrays, therefore additional losses from the feed network are avoided and failure of one active component will only slightly degrade the antennas. The subarrays use aluminum honeycomb for a lightweight and thermally dissipative backing material. A waveguide feed network is employed to feed a single amplifier's output to two or more subarrays with minimal losses.

Current multiple antenna modular arrays are being evaluated as complexes of collocated S- and Ku-band

antennas that can be steered with the same gimbal. The effects of mutual-coupling interactions are part of the current investigations as are the thermal, mechanical, and other electrical interfaces.

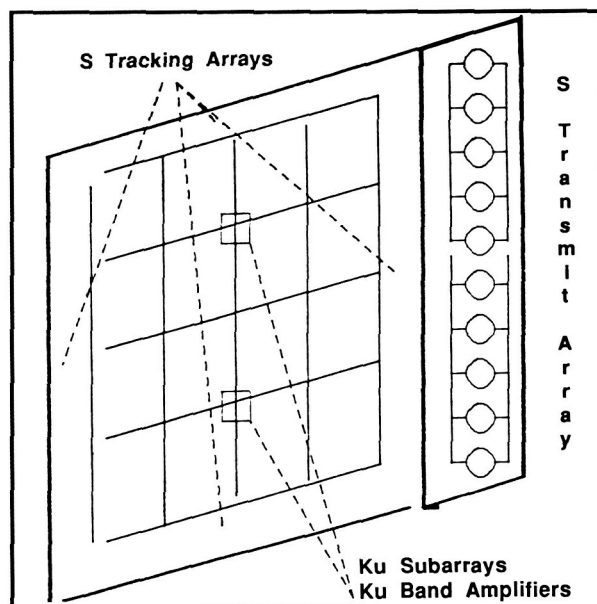
The High Resolution Solar Observatory (HRSO) Project has a demanding 16 Mbps data rate as its primary science link. The goals of the system planner were to find components that would satisfy this primary objective to complement the components used for standard S-band command and telemetry.

To satisfy the free flyer mission the following data rates are required to be supported:

- Ku-band Transmit Single Access—Requires scheduling with TDRSS (16 Mbps)
- S-band Transmit Multiple Access—House-keeping and Telemetry (2 Kbps)
- S-band Receive Multiple Access—Command and Control (1 Kbps)
- S-band Transmit Backup Multiple Access—Deploy/Retrieve/Emergency (100 bps)

The last two links will be supported by the shaped omni antennas which are hardwired into the HRSO radio frequency (RF) subsystem. The omnis will be optimized for the final flight design by changing the size of the baffled ground plane to achieve the best tradeoff of weight, size versus low-angle cutoff. The current baseline is a 2-pound, 12-inch diameter; 4 percent interferometry model omni already tested during the development program. Receive and transmit channels can be switched in to work with our gimbaled antennas. The entire gimbaled antenna is a redundant system to provide additional coverage through Tracking and Data Relay Satellite System (TDRSS) data links. The narrow beam Ku signal will be steered with the NASA Standard Transponder and four S-band arrays on the Ku antenna periphery that sense amplitude and phase differences for auto-tracking. There is no Ku-band monopulse receiver required.

The accompanying figure shows the system block diagram and planar array layout of the best option in the HRSO study. The accompanying table shows the tradeoffs in power, weight, and antenna array



Final HRSO TDRSS antenna concept.

size for three configurations that meet the data rate requirement.

The figure shows a 16 subarray Ku antenna fed by a 20 Mbps data channel. Redundant antenna mounted amplifiers provide full output power right at the antenna feed. The shaped omnis are the default S antennas for deployment and retrieval operations. They are still hardwired in to the S-band network when the tracking antennas are switched off the attenuated lines. The omnis in the figure are also switched to give the user 3 dB additional link margin.

The table indicates combinations of antenna/amplifier weight, size, and power requirements that were traded off for the Ku transmit antenna options that were considered for HRSO.

The 4 ft x 4 ft antenna is the combination currently being used for the HRSO baseline design. A 4 ft x 1 ft S-band transmit array is mounted on the same backplane to provide the Multiple Access Return Link through TDRSS.

Contact: Lawrence M. Hilliard
Code 727

Sponsor: Office of Space Tracking and Data Systems



Combinations of Modular Array Components That Meet HRSO Requirement

Ku Array	Data Rate	# of amps	Total Array* Wt. w/amps	Total dc Power Input	Type of Redundancy
2' x 2'	20 Mbps	4	14.0 lb	142.8 W	½ data rate some degradation
2' x 4'	20 Mbps	2	14.4 lb	75.6 W	¼ data rate some degradation
4' x 4'	20 Mbps	1 (1 spare)	22.4 lb	42.0 W	Requires redundant amp

* Includes weight for source, modulator

Mr. Lawrence M. Hilliard is an electronics engineer in the Antenna Technology Section of the Microwave Instrument and RF Technology Branch. Mr. Hilliard, who has an MEA degree from George Washington University.

DATA RELAY TRANSPONDER

An engineering service experiment has been proposed for the International Solar-Terrestrial Physics (ISTP) satellite for the purpose of relaying scientific data from remote areas of the polar regions. Science-collecting ground stations near the polar regions are not visible by the stationary data-relaying satellites over the Earth's Equator, and moving the collected science data to the occupied areas of the world presents a modern-day challenge. One of the most straightforward methods is to relay the data to a low-orbit polar satellite of opportunity and then to a ground station which has equatorial satellite visibility. The range channel of several satellites is presently being used to relay data from the South Pole station to McMurdo, which has equatorial satellite view.

The ISTP satellite's despun platform offers an opportunity to expand the communication capabilities

to other stations including balloons. The proposed Data Relay Transponder (DRT) will provide two-way service from a fixed station to a balloon, remote site, or another fixed station. The despun platform will provide a continuous view of the Earth, improve the antenna pattern, and maximize the communication channel efficiency. Located in the 400-MHz band, the frequencies were chosen as a compromise in path loss, antenna size, and background noise.

The DRT has been designed as a single-conversion receiver, dual-filter IF, AGC followed by a soft limiter, dual oscillators, and a power out of 5 watts. To facilitate communication with remote sites, a 10-KHz bandwidth option has been included. This narrow bandwidth will allow sites with poor antennas such as balloons to have a low data rate channel available.

The first unit has been completed using conventional components easily located in a typical RF laboratory. However, pending funding, a newer version is planned using microwave integrated circuit (MIC) technology. The MIC will improve the flight criteria of low weight, small size, and low power. A prototype antenna with a diplexer and hybrid feed has been fabricated for evaluation purposes. This arrangement allows polarization selection during the engineering and evaluation phases. The first phase

will evaluate antenna bandwidth, physical size, gain, and beamwidth.

Contact: Lonnie J. Rogers
Code 727

Sponsor: Engineering Directorate

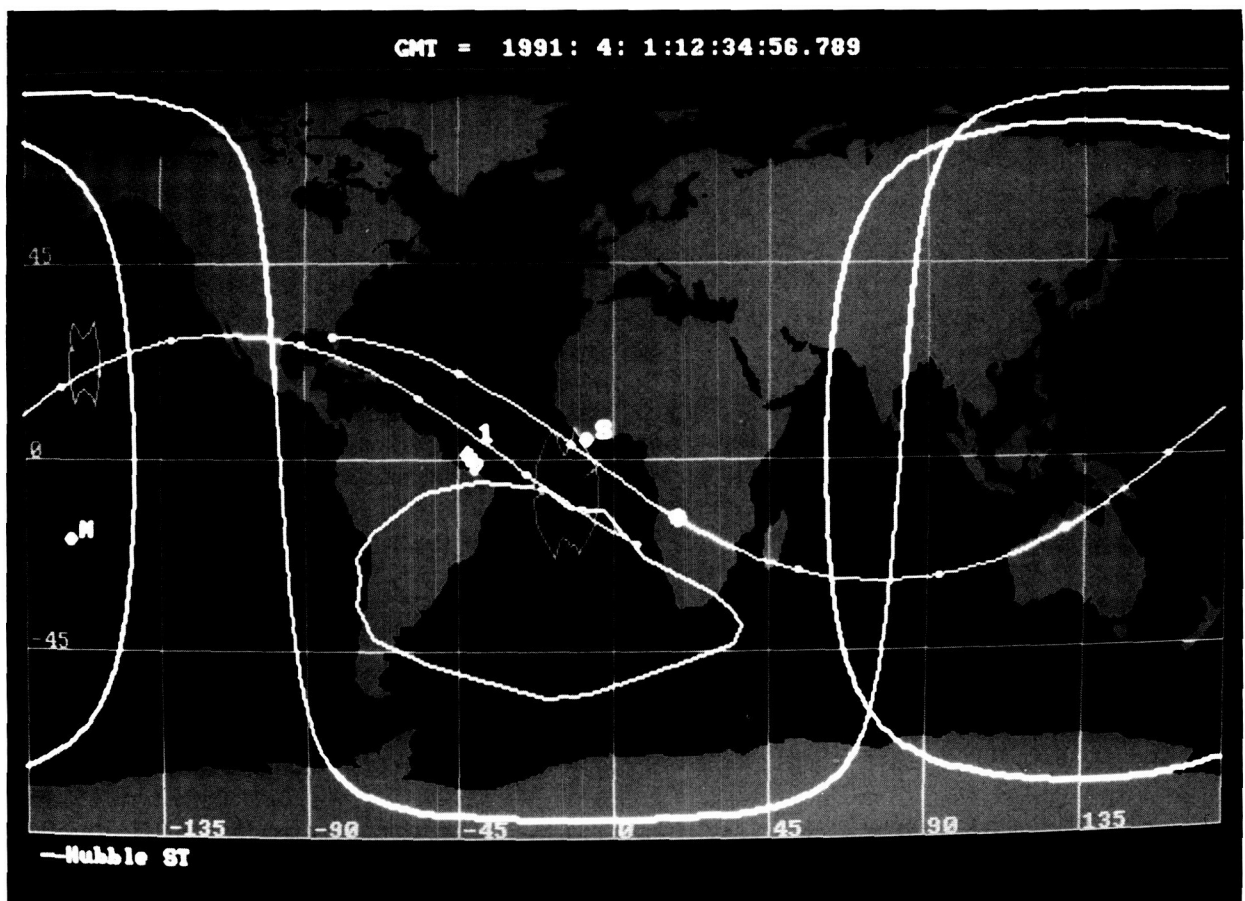
Mr. Lonnie J. Rogers, head of the Microwave Instrument section, provides microwave communication support to the COBE, ISTP, and TRMM projects. He has received Group Achievements for ERBE, Magsat, and IUE. Mr. Rogers holds an MS degree in engineering and has 29 years of experience at Goddard.

SYSTEM AND SOFTWARE ENGINEERING

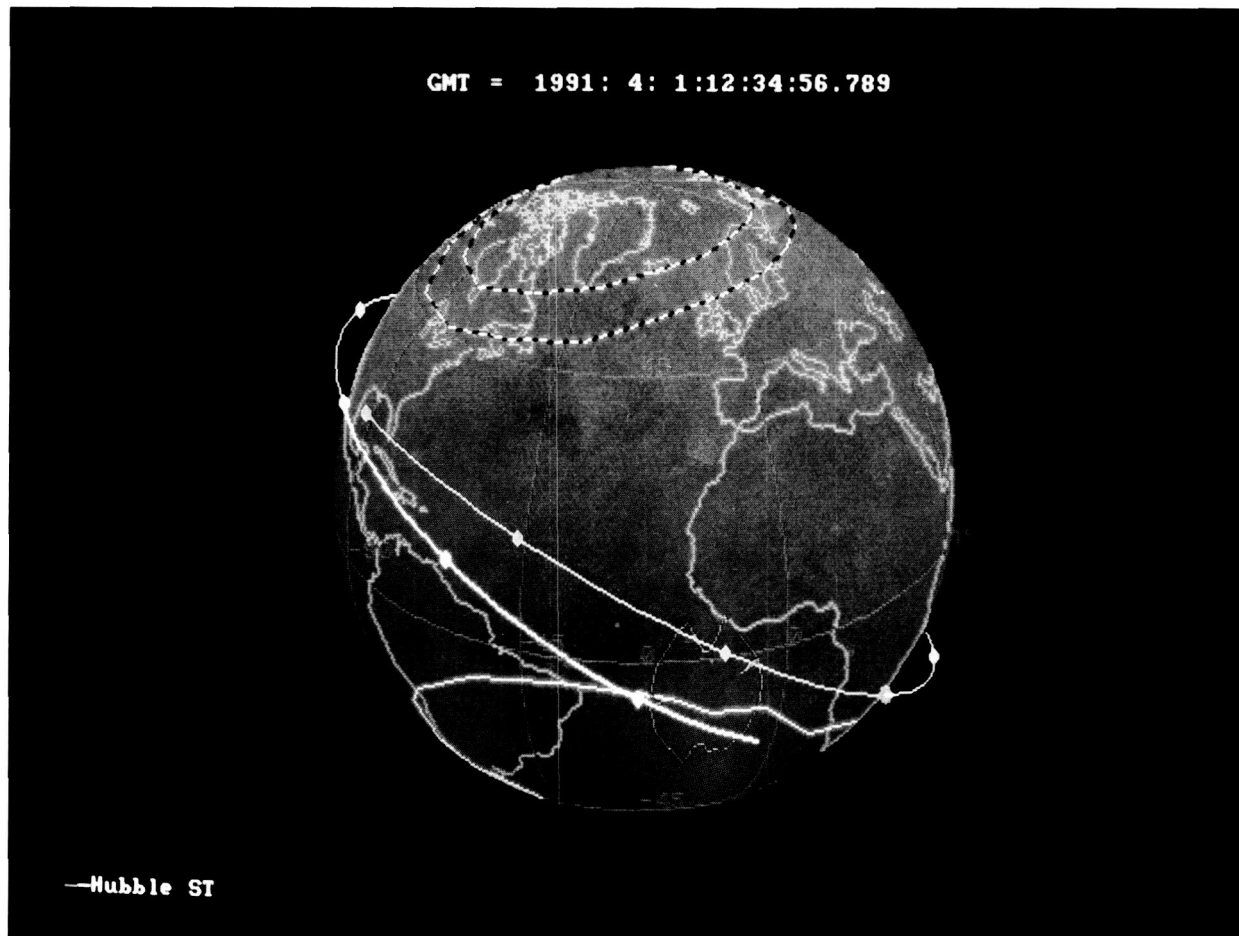
THE PC MISSION PLANNING GRAPHICAL TOOL

Prior to the launch of a satellite or a shuttle attached payload, the Flight Dynamics Division is responsible for several mission planning activities. These activities often require the generation of timelines that

include instrument target availability, acquisition of signal, solar constraint violations, and interference zone intrusion. Information pertaining to this class of constraints can currently be generated by Flight Dynamics systems. This information is presented in tabular form as records that are time incremented and



A two-dimensional world map plot generated by the Mission Planning Graphical Tool. The plot displays Hubble Space Telescope communication coverage over a 130-minute time span.



A three-dimensional world map plot generated by the Mission Planning Graphical Tool. The plot displays electromagnetic interference prediction for a particular Hubble Space Telescope orbit.

contain the data as a series of numbers and flags. Although these data are highly accurate, the presentation format makes quick analysis of trends and time-oriented parameters difficult.

As an aid for these mission-planning activities, the Mission Planning Graphical Tool (MPGT) was developed by the Flight Dynamics Division. MPGT produces two-dimensional and three-dimensional plots of the Earth with time and geometrical data presented as overlays (samples in accompanying figures), which can be toggled on or off, on top of the Earth continents. These overlays include:

- Spacecraft orbit tracks
- Ground station antenna masks

- Tracking Data and Relay Satellite System communication contours
- Interference zone contours
- Instrument field-of-view outlines
- Earth and spacecraft sunrise/set terminator lines
- Solar and lunar ephemeris
- Ecliptic coordinate grid

For cost effectiveness, it was desirable to design MPGT to be mission independent, that is, to eliminate the need for software modifications to satisfy the different requirements of various

spacecraft. To accomplish this desire, developers designed all overlays to be as generic as possible. Communication zone contours and spacecraft terminators were generated analytically, dependent upon the height of the satellite. Interference zone contours, along with their menu names, were specified through data files that could be text edited. These files correspond to mission-related electromagnetic-contamination regions of different altitudes and flux densities. Up to six separate spacecraft orbit tracks could be specified via Keplerian or Cartesian state vectors. Finally, the entire system would be based on a given Greenwich Mean Time that could be altered interactively, automatically varying the positions and orientations of time-related overlays.

Other ideas were also incorporated to increase cost effectiveness of the tool. The system was designed for an IBM PC-compatible microcomputer, executing Disk Operating System (DOS), to allow analyst execution of the utilities in private offices. This eliminated any dependencies on mainframe graphics terminal availability and mainframe response time. All graphics images were produced using a device-independent graphics package, eliminating graphics adapter hardware requirements. These machine-independent characteristics would allow MPGT to be used without constraints by analysts outside of the Division.

Currently MPGT is in the acceptance testing phase of its software development cycle. Future versions of MPGT are anticipated to incorporate new requirements.

Contacts: James F. Jeletic and LaMont Ruley
Code 552

Sponsor: Office of Space Operations

Mr. James F. Jeletic researches, develops, manages, and analyzes flight dynamic computer graphics systems and other mission support software in the Systems Development Branch. He holds a BSE degree in computer science and engineering from the University of Pennsylvania. Computer graphics are a special interest for him. Mr. Jeletic has served Goddard for four years.

Mr. LaMont Ruley has been a summer student in the Flight Dynamics Division for the past two years, the

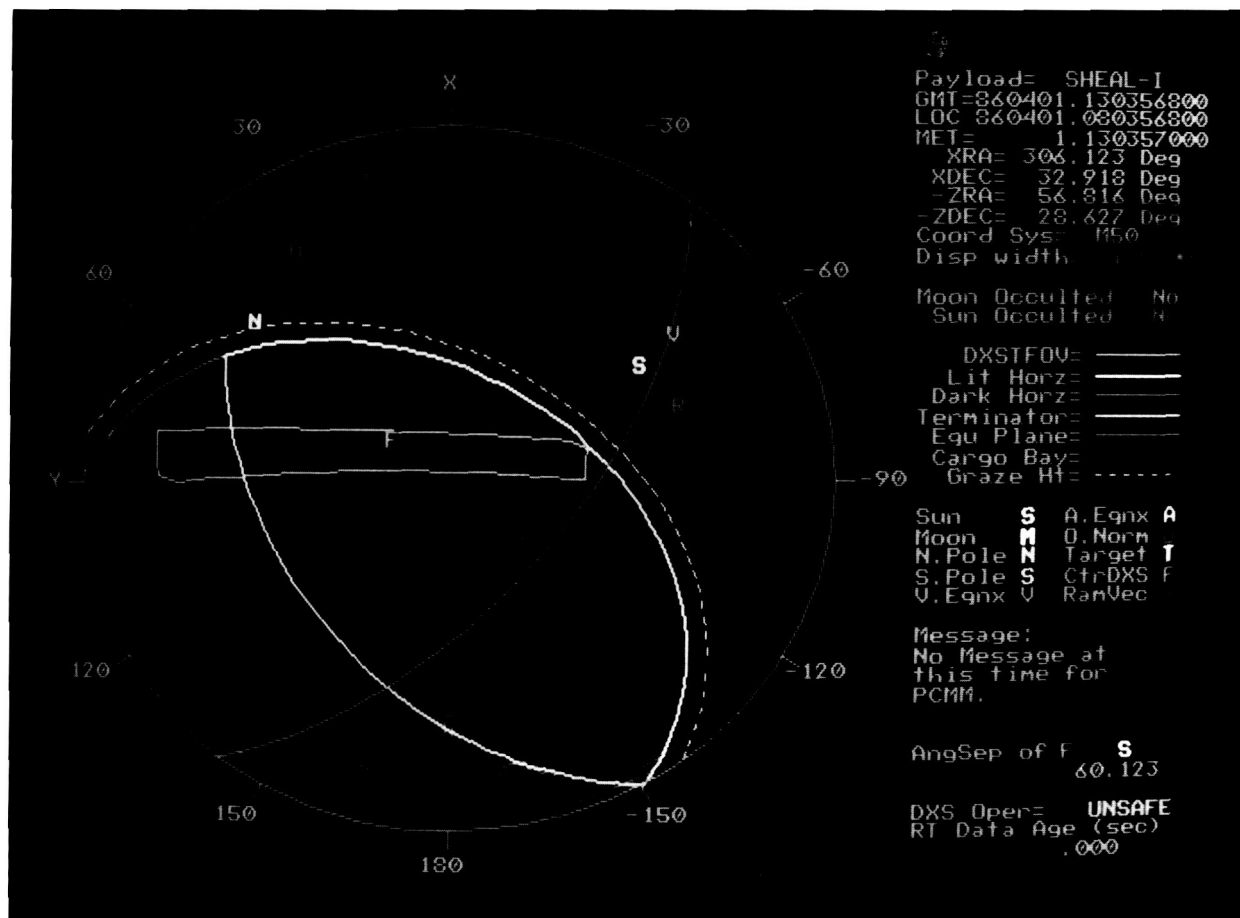
last year as a member of Goddard's Co-Op Program. He is currently working toward a BS degree in mechanical engineering at the University of Maryland.

ATTACHED PAYLOADS MISSION MONITORING SYSTEM

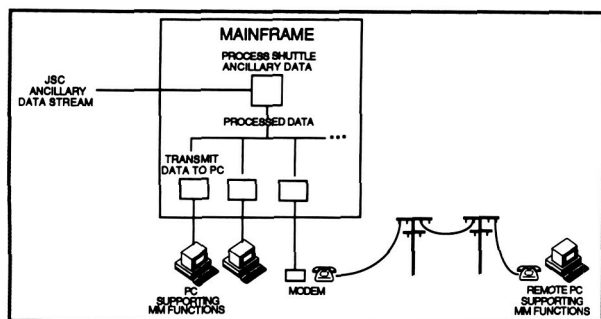
The Attached Payloads Mission Monitoring (MM) System provides near real-time processing of shuttle ancillary data and generation of a variety of graphics displays illustrating the payload state and environment (the first figure shows one such display generated by the MM.) The first release of the system, supporting the Shuttle High Energy Astrophysics Laboratory 1 (SHEAL-1), was completed in 1986. However, the complexity of this system, coupled with the strict performance requirements placed on it, and the limitations of the mainframe-based computational facilities of the Flight Dynamics Division (FDD) on which it executes, resulted in the failure to satisfy project requirements. In addition, a significant performance impact was imposed on the FDD computations environment.

In an attempt to increase the performance of the system while reducing the impact experienced within the operational environment, developers tried to provide the required MM capabilities through a distributed-processing system, utilizing the already available PC AT-class machines located in the FDD. Within the proposed architecture, display-related information, including real-time shuttle orbit and attitude data, is computed on the mainframe. The results of these computations are then transmitted to the PC(s) performing the MM display generation and management functions. The second figure shows a conceptual overview of the system.

After approximately 6 months, the effort resulted in the development of a Fortran-based system, consisting of approximately 20,000 lines of code. The system incorporates commercial communications and graphics packages to support the graphics display generation and management functions of the MM system. Subsequent evaluations of the prototype have indicated a 400 percent increase in performance over the current implementation, and an associated 75 percent reduction in impact on the computational resources within the operations environment. In addition, dramatic increases in graphics display quali-



Celestial Sphere Display generated by the MM prototype system to support the SHEAL-I attached shuttle payload mission. Up to six types of displays are cycled and updated by the MM system, based on user-specified dwell and refresh times. Display generation times of 3-5 seconds have been achieved by the prototype, as compared to 1-2 minutes for the mainframe-based release of the system.



Conceptual overview of proposed MM prototype architecture. Shuttle orbit and attitude data are processed and subsequently transmitted to PCs supporting the MM display generation and management functions.

ty have been achieved, and the ability to support a host of desirable, but previously unattainable, capabilities within the MM System has been demonstrated.

As work continues on the prototype (including the addition of capabilities allowing remote users to access the facility at Goddard Space Flight Center through dial-up telephone lines), the results of the effort to date are forming the basis for software currently being developed to provide MM support for the Broad Band X-Ray Telescope (BBXRT) attached payload mission. The BBXRT mission is currently manifested for a March 1990 flight aboard the Space Transportation System (STS-35).

Contacts: David A. Weidow and Greg Shirah
Code 552

Sponsor: Office of Space Operations

Mr. David A. Weidow, who earned his BS degree in astronomy from the Pennsylvania State University, now works in Goddard's Advanced Technology Section.

Mr. Greg Shirah holds a BS degree in both computer science and mathematics from the University of Georgia. He researches, develops, and analyzes flight dynamics computer graphics systems.

INCREASING ELEVATION RESOLUTION DETECTED FROM STEREO IMAGERY

In any stereo analysis process that determines elevation or depth from a pair of images, one of the fundamental problems is the identification of the corresponding pixels in the two images and to determine the disparities or distances between their locations. For most stereo viewing configurations, the actual elevation or depth is approximately a linear function of the disparity. The automated algorithm for the analysis of stereo imagery implemented on the Massively Parallel Processor (MPP) was developed for Synthetic Aperture Radar (SAR) images. Because one of the dimensions in SAR images is the range from the sensor, disparities measured from SAR stereo pairs are significantly exaggerated in comparison with the disparities that would be measured from optical sensors having the same viewing geometry. For example, disparities of up to 30 pixels were measured for elevation variations on the order of 300 meters from SAR images obtained by the Shuttle Imaging Radar-B (SIR-B) mission. Optical stereo pairs of ground areas with approximately the same elevation variations produce maximum disparities of only 3 pixels. Thus, the algorithm developed for SAR imagery, which gives adequate elevation resolution by detecting the disparity to the nearest pixel, does not give adequate resolution for spaceborne optical sensors. A different technique that obtains the disparity values to subpixel accuracies is required to improve the elevation resolution.

In order to detect the disparity in stereo image pairs, a small neighborhood of pixels is selected from one

image, and used as a template to find the best matching neighborhood in the other. (With stereo imagery, the search can be confined to the horizontal direction within a search area whose size is bounded by a number of pixels related to the maximum elevation variation expected.) At each position of the template neighborhood, the normalized mean and variance cross-correlation function is computed between the pixels in the template and those in the neighborhood below it in the other image. Thus, a correlation measure is computed for each position in the search area, forming a one-dimensional function. If the disparity is computed to the nearest pixel, the position in the search area (relative to the original position of the template) giving the largest value of the correlation measure is the disparity value. However, if subpixel disparities are required, the shape of the one-dimensional correlation measure function must be used to provide the needed information.

Two techniques have been employed to find the subpixel disparity. The first fits a quadratic curve to the values surrounding the maximum peak in the function. The location of the maximum of this curve is calculated, and used as the subpixel disparity value. The second technique finds the centroid of the function values surrounding the peak, which is then used as the disparity. In the first technique, the two function values on each side of the maximum peak, as well as the value of the peak, are used to compute a least-squares estimate of the coefficients of a quadratic equation best fitting the five values. From these coefficients, the maximum of the curve is computed. In the second technique, the centroid of the same five function values is computed.

Initial experiments have been performed with both of these techniques using uniform-contrast, synthetically generated stereo pairs computed from elevation functions of known slope. Results show that both techniques give accuracies within ± 0.1 pixel for low slopes of the elevation function. The curve fitting technique gives a slightly higher accuracy than the centroid technique as the slope increases. The first photo shows a pair of stereo images synthetically generated from known terrain elevation data of the Harrisburg, Pennsylvania region. A Landsat satellite image of the area was superimposed on the elevation data. When viewing this pair with a stereo viewer, the elevation variations shown in the second photo, where brighter areas represent higher



Landsat scene of the Harrisburg, Pennsylvania area. Resolution reduced by 4.3 to match elevation data resolution.



Disparity values detected to nearest integer. Edges are smoothed as part of matching algorithm.



Elevation values for the Harrisburg, Pennsylvania area. Brighter areas represent higher elevations.

elevations, can be seen. The third photo shows the disparity values computed to the nearest pixel value. A smoothing function has been applied as part of the matching algorithm. The fourth photo shows the



Disparity values detected using the curve fitting technique to obtain subpixel resolution.

disparity, computed using the curve fitting technique for subpixel matching. From the model used to generate the stereo pair, the elevation is a linear function of the disparity. Thus, considerably more elevation detail, and a much closer match to the original elevation values, can be seen in the second photo.

Contact: James P. Strong
Code 636

Sponsor: Office of Space Science and Applications

Dr. James P. Strong holds a PhD degree in electrical engineering and computer science from the University of Maryland. Dr. Strong is currently developing algorithms for image analysis and signal processing on the Massively Parallel Processor.

NEW VERSION OF THE LAND ANALYSIS SYSTEM

In the spring of 1987, Goddard Space Flight Center's (GSFC) Space Data and Computing Division (SDCD) released Version 4.0 of the Land Analysis System (LAS). This newest public-domain multi-functioned image processing and analysis software package encompasses all of the functionality of the Version 3.2 release of August 1985, but includes enhancements and corrections to that code. Some improvements are directly visible to the LAS user, while other changes are of interest to the system manager and operations staff at an LAS installation.

Of interest to the user is the addition of 50 new functions, including Fourier transformations in 1 and 2 dimensions, to the original 150 base set. Also of note is the addition of enhanced Geometric Correction capabilities, and expanded documentation for simplified image-to-image and image-to-map registration scenarios. The upper boundary on the numbers of lines and pixels per line in the images handled by LAS has been increased from 8,192 to 20,000.

The dependence of the Version 3.2 functions upon the Floating Point System (FPS) AP180V Array Processor has been eliminated by replacing those functions with non-AP-dependent versions. Under the Version 4.0 release, the SDCCD-developed Display Management System (DMS), which provides image display and graphics capabilities, is an integral part of the configuration. DMS is designed to allow hardware upgrades of display devices with no DMS application software modifications. Another new feature is the use of Catalog Manager (CM) Version 2.8, which allows comprehensive, off-line LAS file management, including tape archival and retrieval. The software has also been improved to allow a single

catalog to be shared by all computers belonging to a VAX cluster.

In addition to the changes in the release that are visible to the user, a dramatic change at the system level has improved the overall package from a system manager's point of view. A one-third reduction in required disk space for the Version 4.0 LAS system, from 60 megabytes to 40 megabytes, has been achieved through the use of the Virtual Memory System (VMS) shareable image. This reduction is even more significant considering the fact that the Version 3.2 system, which contained one-third less application functions, required 50 megabytes. The shareable image allows a shared object library to be included in executable images, thereby reducing disk space and memory utilization by executables. It also permits the update of files (specifically those in the shareable image), without necessitating a relinking of all executable application code. The repackaging of the code has resulted in the ability to install LAS not just through the compilation of delivered source code, as in the past, but also through a relink of the delivered object modules, or through the direct use of the delivered executables. The executable version requires only 16 megabytes! These space requirement reductions mean that LAS is now available for smaller system configurations that do not have compilers. In addition, the smaller memory utilization required by executables allows more simultaneous users.

Efforts to increase user support to the ever-expanding list of user sites (currently at 78 including two United Nations sites located in Geneva and Nairobi) resulted in the publication of a 12-page newsletter "LAS NEWS." Two issues have been released to the community, which now encompasses more than 620 interested scientists, administrators, and system and application programmers. The LAS Support Office (LASSO) duties have been expanded to include referral service for functions in the Contributed Library. That library, also a new feature of the Version 4.0 release, contains an additional 40 application functions. The LASSO library, housed at GSFC, now includes published LAS papers. Tentative plans are being made to host an LAS Workshop in 1989.

In a previous survey of LAS users conducted by GSFC in the spring of 1987, 56.5 percent of the participants indicated a need for the system to be ported



to the UNIX environment. In response to those survey results, efforts to create a prototype portable system commenced in October 1987. Preliminary work included the prioritization of the 150 application functions according to user needs, taking into consideration the typical grouping of the functions in normal use. A prototype system containing 50 application functions should be released shortly.

Contacts: Marilyn Mack, Yun-chi Lu, Philip Pease, and Charles Cosner
Codes 636 and 635

Sponsor: Office of Space Science and Applications

Ms. Marilyn Mack, who holds an MA degree in mathematics from Georgetown University, is Co-Investigator on the Distributed Image Analysis System. Her professional interests include programming, analysis image processing, and computer graphics.

Dr. Yun-chi Lu received a PhD degree in plant physiology from Virginia Polytechnic Institute.

Mr. Philip Pease is Software Configuration Manager for the Computer Systems Research Facility (CSRF) and for the Land Analysis System software development project.

Mr. Charles Cosner is a computer systems programmer for the VAX/VMS-based Computer Systems Research Facility.

ULTRALARGE-SCALE INTEGRATED CIRCUIT COMPONENT FOR ADVANCED MASSIVELY PARALLEL COMPUTER SYSTEMS

Massively parallel systems, those capable of applying 1000 or more processing elements to a single job, are at the frontier of supercomputer research and development. Research activities are underway to develop massively parallel computational components for spaceflight applications. One milestone in this research is the demonstration that ultralarge-scale integrated circuits (ULSI) can be designed and fabricated, enabling massively parallel systems to be implemented with a mere handful of chips. A strong

indication that the needed ULSI technology has indeed arrived is that such chips are currently being developed.

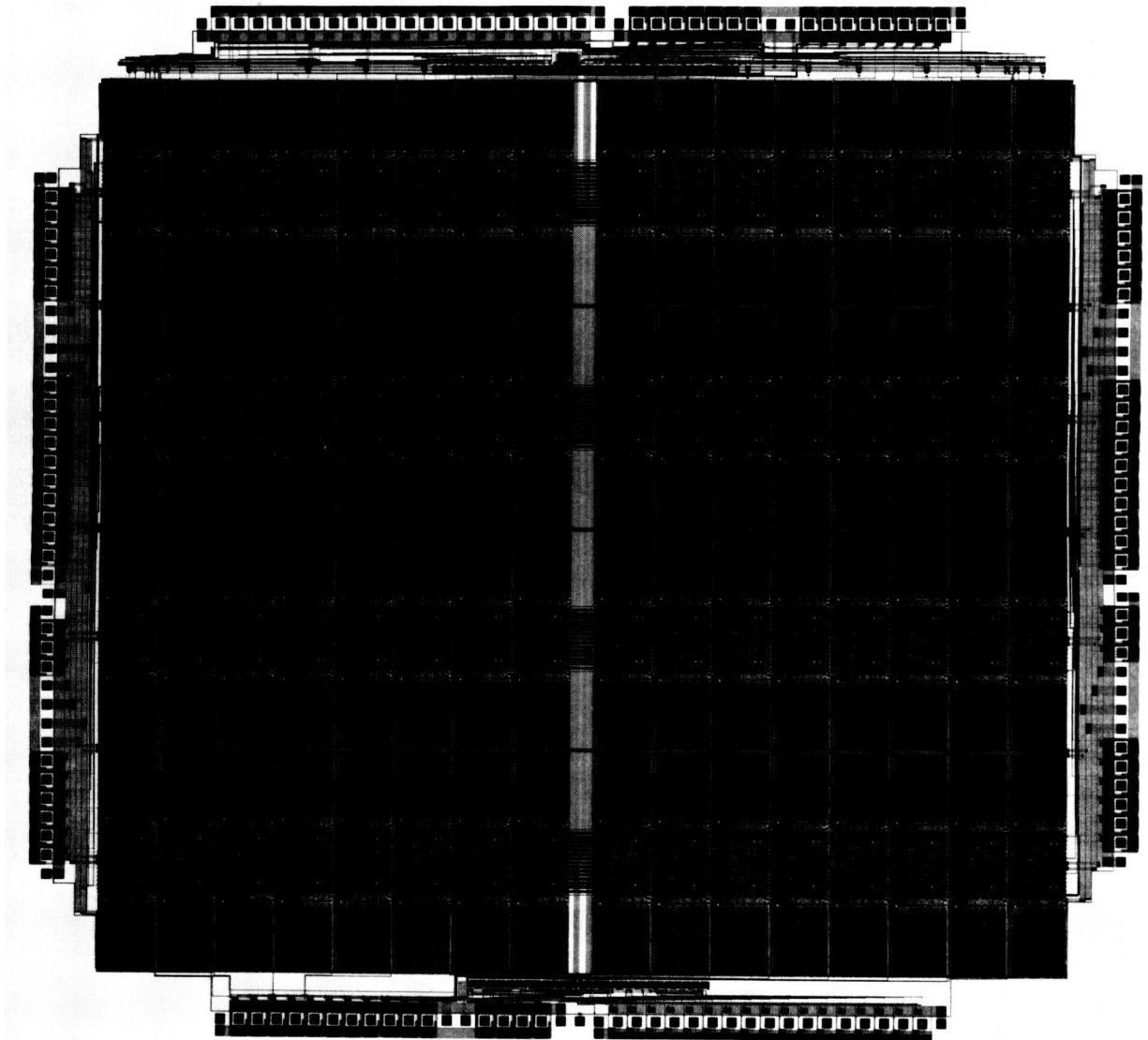
Goddard Space Flight Center researchers developed specifications for design of a 256-processor chip. On the chip, each of the processors would be bit-serial, have its own 256-bit cache memory, and have a 32-bit shift register to accelerate math computation. Such a chip would allow the processing power of a 16,384-processor machine, such as Goddard's Massively Parallel Processor (MPP), to be implemented with only 64 chips, and on a small power budget.

Addressing this specification over the past 2 years, researchers have designed and fabricated through the MOSIS Silicon Foundry a series of progressively more powerful chips, including ones with 64, 96, 160, and 256 processors. These chips were fabricated in complementary metal oxide silicon (CMOS), with line widths of 3, 2, 2, and 1.2 μm respectively. Researchers found that the best current MOSIS foundry process can produce a 256-processor chip; but this chip has only 64 bits of cache per processor, and no shift registers.

Through the Microelectronics Center of North Carolina (MCNC), researchers gained access to a state-of-the-art 1.25 μm design-and-fabrication facility. MCNC undertook the design of a 128-processor chip, where each processor is bit-serial, has its own 1024-bit cache memory, and has a 32-bit shift register. They designed the 1,109,340-transistor Blitzen chip shown in the accompanying figure, which is now in fabrication. It was the largest random logic integrated circuit design ever produced, and is 138 times more complex than the MPP chip that was designed 8 years ago with roughly 8000 transistors.

This research was begun in fiscal year 1986 under the Goddard Director's Discretionary Fund program. It has ongoing support as an element of the Configurable High Rate Processor (CHRP) program, part of the Civil Space Technology Initiative (CSTI) in the Office of Aeronautics and Space Technology (OAST). The goal of the CHRP program is to develop a fault-tolerant, high-rate/high-capacity data system suitable for onboard spacecraft processing of space and Earth sciences sensor data.

ORIGINAL PAGE
BLACK AND WHITE PHOTOGRAPH



Mask layout of the Blitzen Processor Chip: This 1,109,340-transistor CMOS-integrated circuit contains 128 processing elements, each with 1024 bits of local memory. It was designed at the Microelectronics Center of North Carolina, and is now in fabrication.

Contacts: John E. Dorband and James R. Fischer
Code 635

Sponsor: Office of Aeronautics and Space
Technology

Dr. John E. Dorband is a computer scientist with three years of experience at Goddard. He holds a PhD degree in computer science from Pennsylvania

State University, and he is interested in concurrent processing, computer language, and artificial intelligence processing. Dr. Dorband also received a Group Achievement Award.

Mr. James R. Fischer holds a BS degree in electrical engineering from North Carolina State University. He conceptualizes, develops, and implements high-performance parallel computational technologies for researchers in space and Earth sciences.



PARALLEL PROCESSING ALGORITHM RESEARCH

Research is being conducted at Goddard Space Flight Center in advanced parallel supercomputer algorithms. The objective of this work is to perform fundamental research by developing algorithms that map efficiently to computers with very large numbers of processors, and high-speed connections between the processors, for application to NASA problems. The approach taken by developers has been to implement a wide variety of applications on the 16,384 processor single-instruction-stream multiple-data-stream (SIMD) architecture of Goddard's Massively Parallel Processor (MPP), in order to understand the robustness of this type of computer.

During fiscal year 1988, two new algorithms were demonstrated to run in the MPP array unit: hologram computation, and neural network simulation. In addition, two algorithmic approaches first demonstrated in fiscal year 1987 were enhanced considerably: cellular automata, and general ray tracing. The accompanying figure illustrates concurrent processing research on several of these topics. All are extremely compute-intensive, and map very well to the MPP's mesh architecture. The performance of all these algorithms benefits greatly from the bit-serial nature of the MPP processors. The high level languages MPP Pascal and MPP Parallel FORTH were used to implement these algorithms.

- **Hologram Computation:** As an initial step in the development of the hologram algorithm, a 4096-by-4096 hologram of a single point was computed, requiring 7 seconds of MPP time. High-resolution computed holograms may one day give National Aeronautics and Space Administration scientists and engineers the ability to view large amounts of data presented in three dimensions.
- **Neural Network Simulation:** Neural networks were implemented and used to solve clustering problems, and multiple-line-fitting problems. These computationally hard (NP-complete) problems are typical of a class of problems in data fitting, pattern recognition, and computer vision, for which good, but not necessarily optimal, solutions are required. This work was per-

formed in collaboration with the Center for Automation Research at the University of Maryland.

- **Cellular Automata:** In fiscal year 1987, a generalized hexagonal grid-cellular automata for application to magnetohydrodynamic simulations was implemented, and clocked at 850 million site updates per second. During fiscal year 1988, this model was demonstrated to simulate fluid flow around various shaped obstructions. The same simulation runs on a FPS-164 array processor at a rate of 1 million site updates per second, and on the RAP1 (a machine specially designed for cellular automata) at a rate of 40 million site updates per second. This work was performed in collaboration with Goddard's Laboratory for Extraterrestrial Physics.
- **Graphics Generation:** In fiscal year 1987, general ray tracing was first demonstrated on the MPP, based on an algorithm that finds the intersection of light rays and objects in a three-dimensional space. During fiscal year 1988, the approach was enhanced to allow multiple generations of rays. This work was performed in collaboration with Goddard's Laboratory for Terrestrial Physics. Also, a scan line Z buffer graphics generation algorithm was developed on the MPP. The importance of this algorithm is not that the MPP can generate graphics, since that had been shown previously with the ray tracing, but that load balancing can be efficiently performed on the SIMD MPP architecture. Using this method, the MPP was able to render a three-dimensional image consisting of a half million polygons in 1 minute, an effective rate of 8000 polygons per second.

In fiscal year 1989, the parallel ray tracing and neural network simulation techniques will be further optimized and enhanced. Additional graphics and data visualization techniques will be developed. String search algorithms will be demonstrated on the MPP for use in data base searches, or analysis of DNA. The simulation of flow reactors, used to perform molecular evolution simulation, will be implemented.

Contact: John E. Dorband
Code 635

CONCURRENT PROCESSING RESEARCH

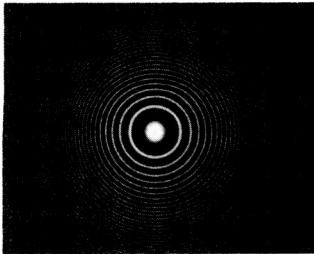
ACCOMPLISHMENTS

Demonstrated running in the MPP array unit:

- Hologram Computation
- Neural Network Simulation
- Cellular Automata (enhanced)
- General Ray Tracing (enhanced)

BENEFITS

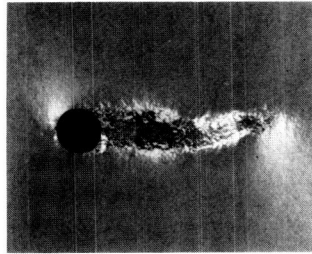
- Scientific Data Visualization
- Solid Modeling
- Thermal Modeling of Spacecraft
- Higher Speed Fluid Simulation
- Foliage Canopy Modeling
- Animated Graphic Generation for Robotics



COMPUTATIONAL HOLOGRAPHY

The hologram of a point.

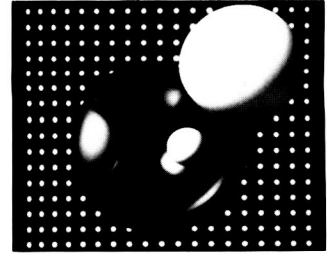
Potential applications include 3-dimensional visualization of engineering and scientific data.



CELLULAR AUTOMATA

Generalized hexagonal grid cellular automata simulating fluid flow. Obstacles inserted in flow produce expected flow effects.

Potential applications include higher speed fluid simulation.



GENERAL RAY TRACING

The enhanced ray tracing algorithm now allows multiple generations of light rays.

Potential applications include foliage canopy modeling and thermal modeling of spacecraft.

Concurrent parallel processing algorithm research on the Massively Parallel Processor.

Sponsor: Office of Aeronautics and Space
Technology

DISTRIBUTED KNOWLEDGE-BASED SYSTEMS

A conceptual basis has been established recently for supporting applied research in the area of distributed knowledge-based systems. This basis includes such components as a blackboard system generator; a semantic network language; a preliminary model of cooperating rule-based systems; and the framework for a test bed in which to demonstrate the applicability of distributed cooperating knowledge-based systems technology to support spacecraft command/control activities.

The blackboard system generator is based on a conceptually simple model of a conference table around which a chair convenes a meeting of agents. Each agent is a specialist in a few subjects; no agent is capable of solving the shared problem in isolation. There are various protocols for guiding the conduct of such meetings. These protocols permit each agent to share viewpoints about the common problem and its possible solution, to be stimulated by the viewpoints of other agents, and to reason spontaneously and opportunistically in attempting to reach a solution. Thus, this model has three principal subsystems: 1) the blackboard, which is a shared global data space that facilitates communication and cooperation; 2) the agents, who are knowledge sources capable of reacting to and modifying the blackboard



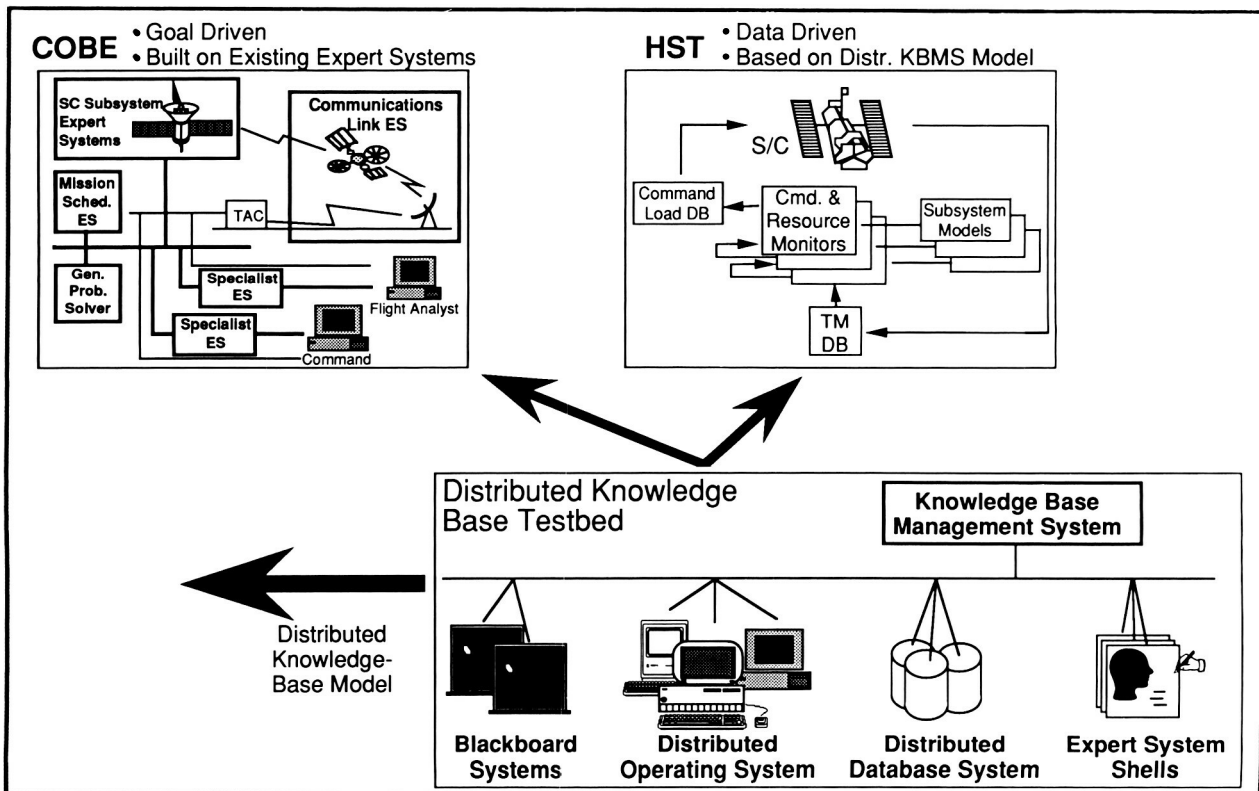
data structures; and 3) the chair who plans agendas and controls the activity of the agents. The information used by the blackboard is organized into a three-level hierarchy of panels that are: 1) a shared information panel that ensures knowledge-sharing among agents; 2) a panel for supporting contract-forming between agents and event scheduling, coordinating, and control; and 3) a panel for meta-level planning and guidance that offers whole situation recognition, top-down reasoning, and adaptive learning.

The semantic network language is an object-oriented knowledge representation language intended to support the construction and management of knowledge bases. The language provides a selected set of knowledge representation services, and has been designed so that this set can be easily extended to accommodate the specific needs of a particular application.

The next component is a model of cooperating rule-based systems. In establishing this model, the

projected role of such systems in spacecraft ground control was analyzed, and the requirements for cooperation among such systems in that environment were derived. From this analysis, clarification of the forms of cooperation that need to be modeled, and an understanding of the various ways that that cooperation might be achieved, allowed a logical model to be developed. This model, in conjunction with the semantic network language and the blackboard system generation concepts, will be used to develop scenarios that will be prototyped, executed, and evaluated in the test bed.

The distributed knowledge base testbed has been configured to include the following components: a knowledge base management system, blackboard systems, a distributed operating system, a distributed data base, and expert system shells. The knowledge base management system component provides a design and implementation methodology for establishing knowledge bases; the blackboard systems support communication among agents involved in distributed problem solving; a distributed operating



Distributed knowledge base research.

system makes available lower-level support for access to distributed heterogeneous systems within the testbed; a distributed data base system provides required data/knowledge storage/retrieval/manipulation capabilities; and the expert system shells provide development frameworks for experimental studies in the testbed. The accompanying figure graphically displays the currently envisioned testbed. Project testbeds, which currently include the Cosmic Background Explorer (COBE) and the Hubble Space Telescope (HST), provide payload operations command-and-control scenarios that are used to develop and evaluate the effectiveness, efficiency, and completeness of the emerging distributed knowledge-based technologies in a simulated operational environment.

This research will produce a comprehensive model of distributed knowledge base management that has been validated in operational environments.

Contact: Walt Truskowski
Code 522.3

Sponsor: Office of Aeronautics and Space
Technology

Mr. Walt Truskowski, a member of the Data Systems Technology Division, holds degrees in mathematics and computer science. His professional interests include the cognitive aspects of human/machine systems, artificial intelligence, and approaches to information exchange.

A USER REQUEST LANGUAGE FOR AUTOMATED PLANNING AND SCHEDULING

Planning and scheduling of spacecraft mission operations will become more complex and challenging in the Space Station era. At present, these operations are performed manually, with varying degrees of computer assistance. In the future, the scheduling process will become more automated and distributed. Goddard Space Flight Center's Data Systems Technology Division has supported the development of a user request language that assists the automation of the planning and scheduling process. (The accompanying figure shows a simple statement in this user request language.) The developers produced a prototype scheduler to evaluate the request language for

use in the distributed scheduling systems of the Space Station Information System (SSIS).

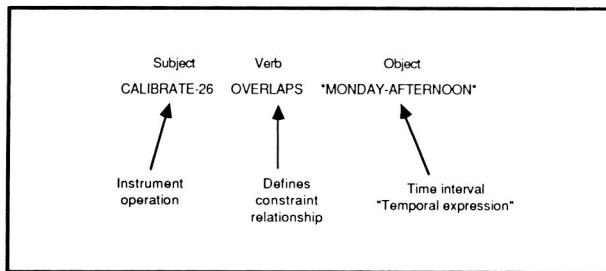
In an automated scheduling system, users need to express their resource requests in a format that computers can understand. Since people use languages to communicate, developers of this user request language planned for users to readily express their resource requests in a language format that computers can process. A language format provides a more direct and expressive method of encoding resource requests than using simple data structures such as data records, tables, and arrays.

For the scheduling of spacecraft mission operations, users communicate their resource requests to the resource scheduler, who processes the requests to produce schedules. The schedules show the timelines of user flight instrument operations and mission activities. The resource scheduler places the user requests on the timeline according to resource availability, mission constraints, and other considerations. For example, a user may request a certain instrument operation to start 10 to 22 minutes after spacecraft sunrise.

Users define their resource requests in a variety of ways. They specify how their requests relate to orbital events, time, mission constraints, and other requests. If their initial resource requests cannot be satisfied, users may request an alternate set of resources. Thus, the resource scheduler may process a complex, flexible request that produces results other than simply indicating whether or not the request was scheduled.

The request language supports many features, such as resource flexibility, temporal expressions, directions, temporal constraints, and alternate requests.

- With resource flexibility, users may specify minimum, nominal, and maximum amounts for each resource. Hence, the resource scheduler may adjust the resource amount so that it may schedule the user request. Also, users may specify minimum, nominal, and maximum time durations of when the resource is needed.
- Temporal expressions allow users to give names to events within their domain such as "week-day" and "spacecraft night." Users may define new temporal expressions by applying



A simple user request language statement.

the UNION, INTERSECT, MODIFY, and SELECT operators to existing temporal expressions.

- Directions allow users to schedule multiple occurrences of an activity with one request. For example, a user may submit a single request to perform a tape recorder dump activity four times a day, or once every four orbits.
- Users may specify temporal constraints with respect to orbital events ("spacecraft night"), calendar events ("weekends"), and other requests ("request A precedes request B"). These constraints are encoded using the request language syntax and temporal expressions.
- Alternate requests allow users to request a different set of resources if the resource scheduler cannot accommodate the initial request. This capability adds flexibility to the scheduling process.

A user request language facilitates the automation of the planning and scheduling process. The developers produced a prototype scheduler to evaluate the request language. The request language proved to be comprehensive, adaptable, and flexible.

Contact: G. Michael Tong
Code 522

Sponsor: Office of Space Operations

Mr. G. Michael Tong received his BS degree in engineering from Tufts University. Currently, he is working on software planning and scheduling concepts for the Space Station Freedom.

THE TRANSPORTABLE APPLICATIONS ENVIRONMENT

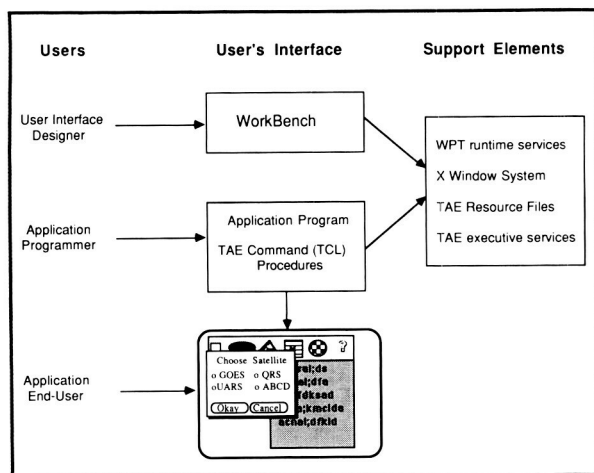
Fiscal year 1988 saw tremendous growth in the Transportable Applications Environment (TAE) project. This growth included an increase in the user community (over 200 installations) and the number of computers on which TAE operates (at least 14 known ports). Functionally, TAE also experienced significant growth. The most exciting development was the expansion of TAE's user interface management capabilities to support the latest interactive high-resolution graphic workstations, and the development of interactive tools for the application user interface designer. Currently, TAE is evolving from a traditional procedural menu and command-oriented system (TAE "Classic") to a graphic-oriented user interface management system (TAE "Plus"). The sophisticated graphic and windowing capabilities of modern workstations provide system developers with the opportunity to rethink and redesign the user interfaces of the National Aeronautics and Space Administration's (NASA's) next generation of software systems. For instance, in a command and control environment, many processes run simultaneously to monitor the state and status of the particular operation and its data. With modern graphic workstations, time-critical information on multiple events can be displayed concurrently on the same screen, organized into different windows, and displayed in a variety of graphical and/or textual presentations. Coupled with the need to prototype and try out different user interfaces (as an effective means of defining and designing new systems), TAE has been undergoing development to provide an environment with sophisticated prototyping capabilities, while retaining the TAE concepts of portability, standard system services, and easy migration from prototype to operational interfaces.

During fiscal year 1988, several significant TAE Plus software releases contributed towards integrating sophisticated user interface design and prototyping functions. The main components of the TAE Plus development are: 1) an intuitive What You See Is What You Get (WYSIWYG) "WorkBench," a tool for prototyping and designing an application's user interface; integrated with 2) tools for efficiently implementing the designed user interface; and 3) effective management of the user interface during an applications' operation. The first figure shows the

components and their relationships to each other and to TAE users.

The WorkBench tool allows the application developer to interactively construct the look and feel of an application screen and manipulate a set of "interaction objects." These objects include buttons, icons, scrolling text lists, pulldown menus, radio button menus, and graphic output workspace areas. The second figure shows a layout of a screen as it is being designed in the WorkBench. Key features of the WorkBench include:

- Easy customization and manipulation of user interaction objects
- Application code generator (a program skeleton is generated with executable user interface code in place; the programmer fills in application specific code)
- Capability to dynamically define connections between interaction objects (i.e., define what happens when the user selects the buttons, menu items, etc.)
- Rehearsal capability to try out sequencing of the user interface design
- Icon editor and support for raster objects
- Scripting support for organized testing of highly interactive applications



Transportable Applications Environment components and relationships.

- Undo capability

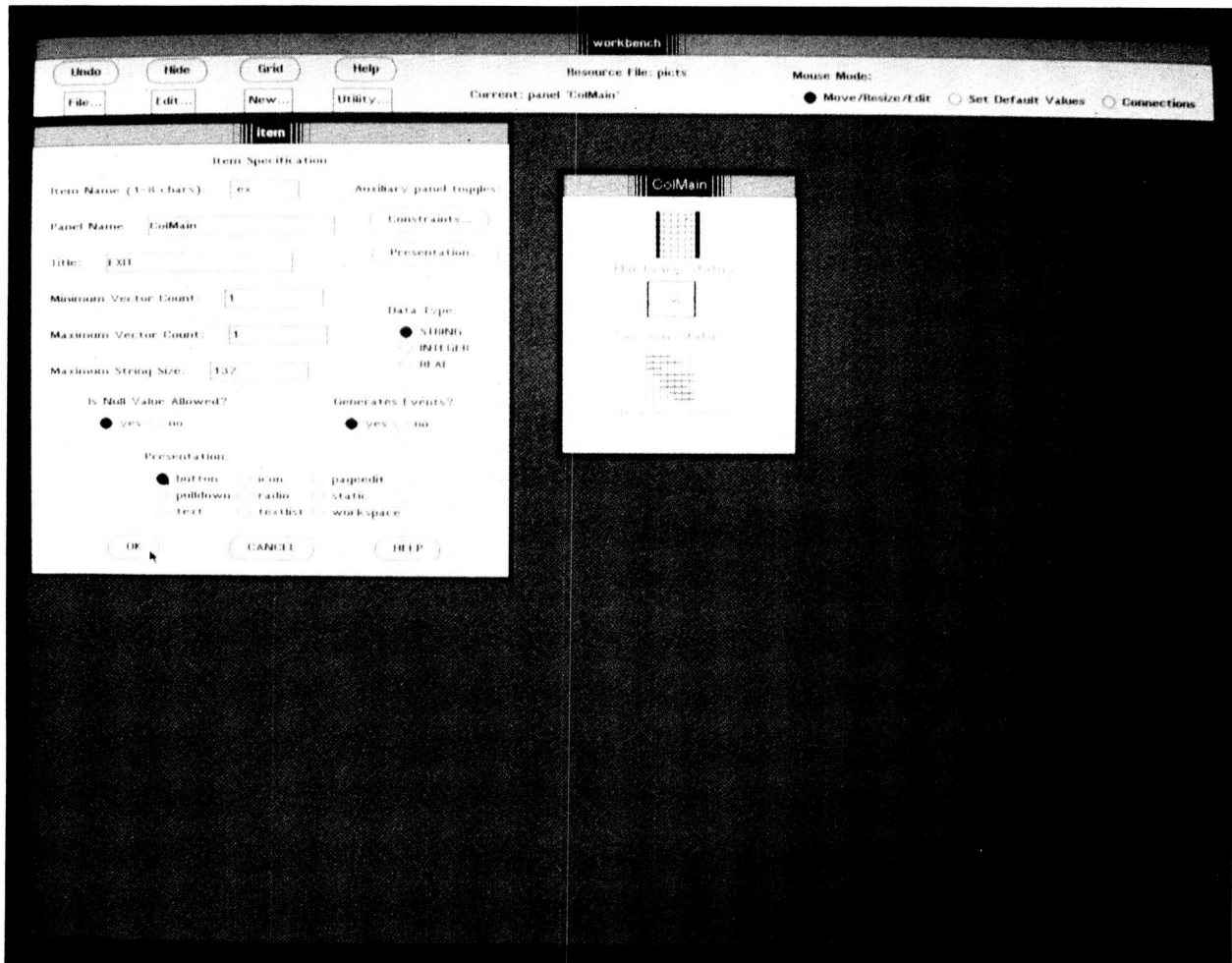
- Help icon/button support (used to build consistent help dialogues for items within an application's user interface)

The WorkBench is written in the object-oriented C++ programming language, and uses the X Window System as the underlying windowing standard. The employment of these state-of-the-art technologies enables developers to evaluate and understand the applicability of object-oriented programming to the user interface management environment, and to analyze portability issues.

Once the application's screens have been designed, the WorkBench saves the user interface details in a resource file. TAE Plus includes runtime services, Windowing Programming Tools (WPTs), that are used by application programs to display and control the WorkBench-designed user interfaces. Since the WPTs access the resource file during execution, the user interface details remain independent from the application code. This allows changes to be easily made in the look and feel of an application, without recompiling or relinking the software. To change the interface or the screen layout, the designer returns to the WorkBench and dynamically makes the modifications; the resource files are automatically updated. The next time the application is run, the modifications will be in effect.

In addition to providing the WPT runtime subroutines, TAE Plus also offers control of interaction objects from the interpreted TAE Command Language (TCL). This capability provides an extremely powerful means to quickly prototype an application's use of TAE interaction objects, and adds programming logic without compiling or linking overhead.

Each year the "transportable" element of TAE becomes more evident, as the number of computers running TAE continues to grow. TAE Classic is currently available for a variety of computers under several operating systems including VMS, ULTRIX, UNIX 4.2 BSD, UNIX System V, and selected hybrid versions of UNIX. The current computer list includes: VAX/VMS, VAXStation II/GPX/VMS; VAX/UNIX; SUN/UNIX; Gould/UNIX; ISI/UNIX; Jupiter/UNIX; Apollo/UNIX; Macintosh with MacWorkStation; CDC/UNIX; HP9000/



Designing an application user interface using the WorkBench.

UNIX; AT&T/UNIX, and Altos/UNIX. TAE Classic is also currently being ported to the IBM VM/CMS environment. The base development of TAE Plus is being done on a Sun workstation under UNIX. TAE Plus is also operating on the Apollo/UNIX, the VAXstation II/ULTRIX, and the Macintosh II under A/UX. Ports to the HP/UNIX and the IBM RT/AIX are under way. A port to the VAX under VMS will begin when Digital Equipment Corporation releases its version of the X Window System.

TAE Plus and the WorkBench are being designed to provide a powerful and much needed tool for developing highly interactive prototypes and operational applications. Future enhancements to TAE Plus will include implementing refinements to the WorkBench,

creating Ada code bindings for TAE interface routines, implementing additional interaction objects, and adding a new class of output objects. These objects will allow the applications developer to define areas of the display that are driven by data from the application, and to dynamically present this information to the user, such as a bar graph that changes when the related application data values change. Feedback and evaluation of the TAE Plus features, architecture, and style will continue to provide guidance towards improving future releases of TAE.

Contacts: Martha R. Szczur and Jay Costenbader
Code 522

Sponsors: Office of Space Operations and
Office of Space Science and Applications

Ms. Martha R. Szczur, who received a BS degree in mathematics from Converse College, is manager of the Transportable Applications Environment Project. Her professional interests include human-factor elements of user interfaces; user interface designer support tools; and the common, standardized user interfaces.

Mr. Jay Costenbader, Deputy Project Manager for the Transportable Applications Environment, is involved in the development of data capture and processing systems at the Data Systems Applications Branch.

RESEARCH AND DEVELOPMENT OF THE SOFTWARE MANAGEMENT ENVIRONMENT

The Software Management Environment (SME) is an integrated set of software tools designed to assist a manager in monitoring, analyzing, and controlling an ongoing software project. During 1988, the research and development of the SME has gone from the conceptualization and architecture of the system to full-scale development of a working version of the environment. This development has proceeded in an iterative manner, by first researching and prototyping a specific feature of the system, and then incorporating suitable results into the overall system.

A major research effort has been the connection of the SME to a historical data base. The data accessed include information on effort, size, computer utilization, and change and error characteristics for both ongoing and past software projects. By interfacing with this data base, the SME has access to profiles of over 70 software projects, thereby giving the system nearly all of the information needed to track project parameters. Establishing this connection has allowed SME users to receive pertinent, up-to-date information on ongoing software projects, and to compare this information to past projects.

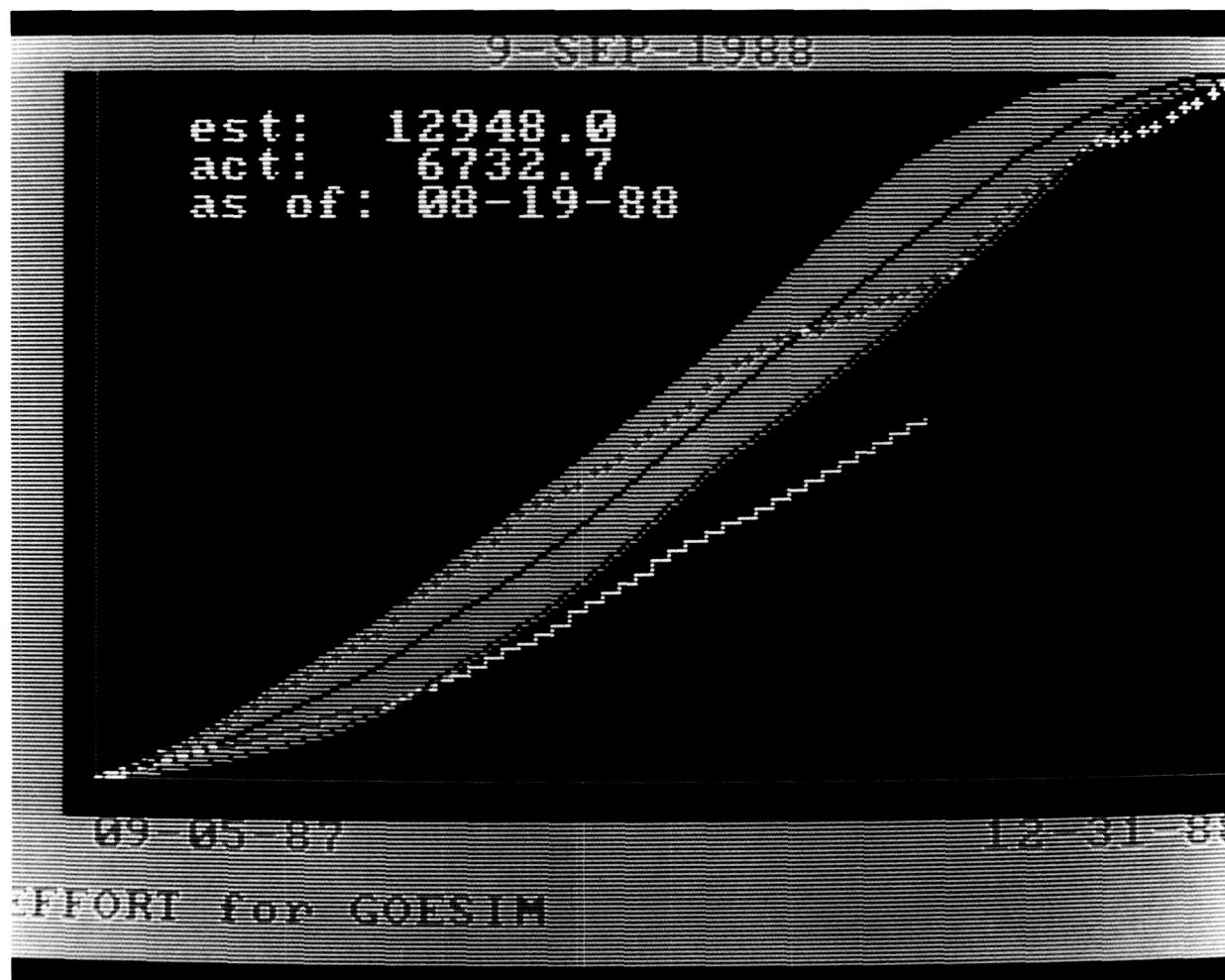
The ability to monitor an ongoing software project is another feature of the SME research. The accompanying figure shows a plot generated by the SME to display information on effort expenditure for project, GOESIM. On this plot, the stepped orange-and-tan line shows the cumulative amount of effort expended on the project on a week-by-week basis. For

comparison, the display also shows a similar project, COBSIM (the line of plus marks), which has already been completed. Using this comparison feature, the researcher can analyze the behavior of the ongoing project as it relates to past projects.

Another portion of the comparison feature is shown by the green band in the figure. This band is a model of the "normal" expenditure of effort within the environment. Recently, models have been completed for all the development parameters used in the SME. The history of past projects from the corporate memory was used in the development of the models; thus, they represent an average of completed projects within the environment. While the actual average is the middle of the model displayed, the band represents one standard deviation from that average. The band is displayed so that the "normal" project will be a range of values, not a single point.

Two other major areas of investigation critical to the completion of the SME are prediction and assessment. Prediction involves automatically analyzing current data to project the future status of development parameters. This feature of the SME will allow the user to estimate the final values of important development parameters such as effort and errors, and will give estimates of the date the project will be completed. Using this data, the manager will be able to reevaluate the project's estimates for key parameters and dates.

In the area of assessment, recent research has focused on improving the system's ability to use "rules" for analyzing deviations of the development parameters. Rules capture the knowledge of experienced software managers in analyzing software projects, as well as the results of empirical studies that have analyzed the chosen software parameters. While these rules have been studied in the past, more extensive research recently has been completed concerning their implementation within the system. A prototype of an expert system has been developed that uses the software rules to analyze deviations, such as the difference between GOESIM's cumulative effort and the model of effort, shown in the figure. When this function is completely implemented, it will give the manager possible reasons for the deviation from the norm of a particular parameter. In this case, analysis of the rules might reveal that the effort's below-normal status has occurred because the project is



Comparison of effort for two Projects.

actually smaller than expected, or because the project is behind schedule. By giving the manager this type of data based on subjective information about the project, the actual deviation, and the values of other measures, the tool provides the manager with some insight into the strengths or weaknesses of a particular project.

Contacts: Jon D. Valett and Susan Ray Valett
Code 552

Sponsor: Office of Aeronautics and Space
Technology

Mr. Jon D. Valett, who specializes in software engineering and artificial intelligence, is involved with the Software Management Environment. Mr. Valett

received an MS degree in computer science at the University of Maryland, and he has five years of experience at Goddard.

Ms. Susan Ray Valett, having earned her BS degree in computer science, has worked for four years at Goddard. At the Project Support Software Section of the System Development Branch, Ms. Valett is responsible for software engineering research, and support to the development of attitude ground support systems.

MISSION ANALYSIS EXPERIMENT WITH EXPERT SYSTEMS TECHNOLOGY

The Mission Analysis Experiment With Expert Systems Technology (MAE WEST) attempts to

develop a prototype mission activity scheduling environment for the Attached Payloads Project. Currently, as many as 5 man-weeks are required to generate a single 4- to 5-day mission activities schedule for an attached payload mission. A mission activities schedule defines the activities (e.g., water dumps, shuttle reorientations, instrument observations, etc.) to be performed during the mission. By providing the capability to define these activities in generic terms, and by automating the scheduling of these activities, MAE WEST attempts to reduce dramatically the effort required to produce a schedule.

To generate a schedule, MAE WEST utilizes a set of mission activities defined in terms of their associated constraints, and a mission timeline that defines the scheduling period. The schedule is produced by stepping through the timeline in chronological order, and evaluating the constraints associated with each activity at each time point. Constraints are evaluated based on the information contained within the mission timeline (this information is generated by existing mission analysis software prior to the scheduling run). All activities whose constraints are satisfied are subsequently evaluated according to a priority system that picks the most appropriate activity or group of activities to be scheduled at a particular time. This process is repeated for all time points within the mission timeline.

A prototype of the MAE WEST system has been developed on an IBM PC AT-compatible under the GoldWorks expert system shell marketed by Goldhill Computers. The major knowledge representation structure is a frame that allows researchers to generically represent the mission activities and the activity schedule. Through these frames, Common LISP (a computer programming language) functions are used to evaluate constraints, and to actually perform the scheduling. The rest of the system is also developed in Common LISP, and consists of an executive, the overall scheduling algorithm, and input/output support functions. By separating the general scheduling support functions, and by using the frames to generalize representation of the mission activities, MAE WEST is designed to support the scheduling requirements of any attached payload.

The results of the prototyping effort are currently being evaluated to determine the applicability of

MAE WEST concepts to actual scheduling operations. Subsequent to the evaluation, numerous enhancements are envisioned. These include the direct interface between the MAE WEST system and other mission analysis software, design and development of an improved user interface for the system, and the inclusion of a more sophisticated scheduling algorithm that will utilize mission objectives to optimize the schedule.

Contacts: Jon D. Valett, Douglas R. Spiegel,
and David A. Weidow
Code 552

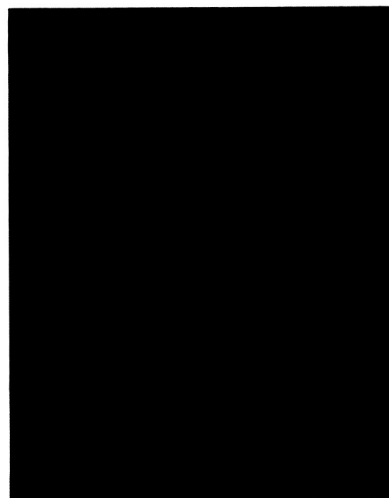
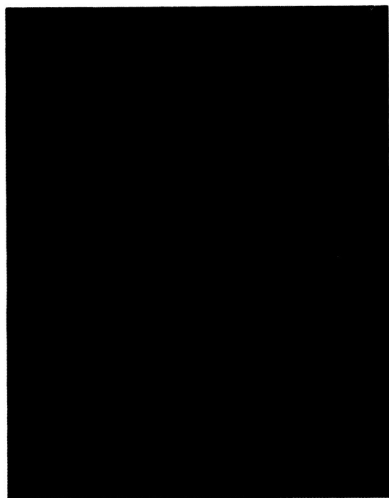
Sponsor: (Internal)

Mr. Douglas R. Spiegel, who holds a BS degree in computer science from Towson State University, performs software engineering and artificial intelligence research for flight dynamics projects.

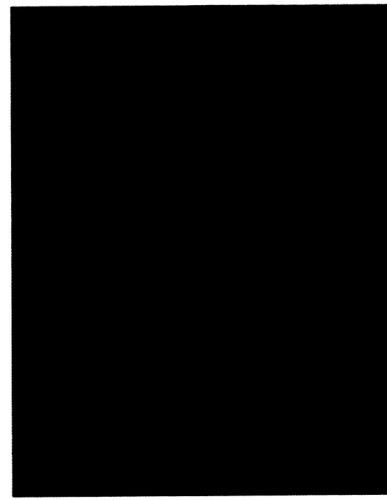
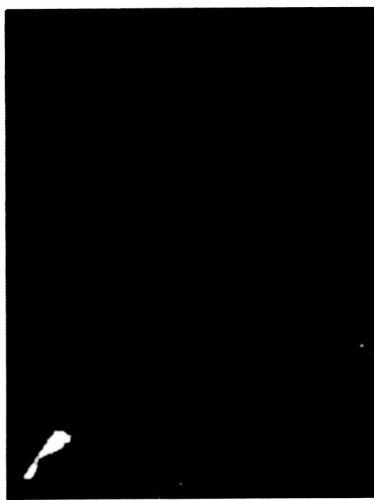
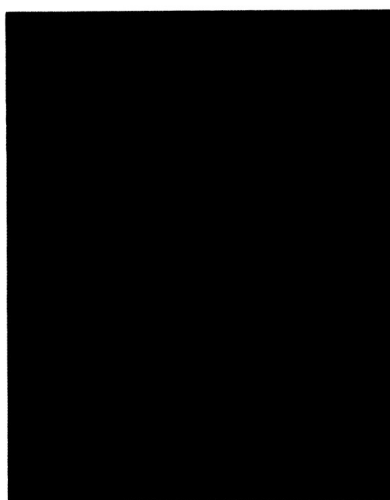
Mr. David A. Weidow earned his BS degree in astronomy from the Pennsylvania State University.

EDGE PRESERVING DATA COMPRESSION FOR SATELLITE EARTH IMAGERY

Satellite data collection rates and volumes expected from the various remote sensing instruments that will be deployed in the upcoming decade will require some form of data volume reduction on board because of the limited down-link transmission bandwidth. Current plans for the High Resolution Imaging Spectrometer (HIRIS) present a most radical example of this limitation, calling for the HIRIS instrument to be turned off nearly 99 percent of the time. A data compression technique that can achieve better than a 10-fold compression on data similar to that to be collected by the HIRIS instrument is now being studied. If this compression technique retains the essential scientific information in the HIRIS data, it could be used to allow the HIRIS instrument to remain operational 10 percent of the time, rather than just 1 percent of the time. This compression technique works equally well for any imaging instrument whose data contains significant spatial detail, such as the proposed Thermal Infrared Multispectral Scanner (TIMS), various Synthetic Aperture Radar (SAR) instruments, the currently operating Landsat Thematic Mapper (TM) instrument, and France's Earth Observation Satellite (SPOT) instrument.



(a) Original TM image. (b) Image created by the reconstruction of image data which was compressed by a factor of 13 using the SCC Segmentation Algorithm.



Pseudo-colored class label maps with water/marsh shown as blue, forest shown as orange, residential shown as grey, and agriculture/domestic grasses shown as green. (a) Bayes classification of the original TM image. (b) Ground truth map. (c) Bayes classification of image created by the reconstruction of image data that were compressed by a factor of 13 using the SCC Segmentation Algorithm.

The image data compression approach achieves compression by encoding a segmentation of the image. The key part of this approach is the image segmentation algorithm, which is called the Spatially Constrained Clustering (SCC) algorithm. The SCC algorithm performs an iterative parallel region growing process in which the best merges in global terms among all pairs of spatially adjacent regions are executed at each iteration. The group of best merges

is obtained as follows. A similarity criterion function value is calculated for all pairs of spatially adjacent regions in the entire image and the best similarity criterion function value noted. The group of best merges is those pairs of spatially adjacent regions with similarity criterion value less than $1 + \epsilon$ times the best similarity criterion value. The similarity criterion function currently being studied is based on minimizing the increase in band variance

normalized mean squared error for each region merge between the original image and the image constructed from region mean values. Other similarity criterion functions incorporating spatial features such as region variance can easily be used with this algorithm.

As a test of this method, a TM image was compressed by a factor of 13. A subjective evaluation of compressed and reconstructed TM images (displayed in the first figure) shows that areas in the original image that are relatively homogeneous, but not necessarily uniform, become completely uniform in the reconstructed images. Low-contrast spatial features are often lost in the reconstructed images, but the higher contrast spatial features, such as edges of regions, are retained very precisely. Even very small spatial features are retained if they have sufficient contrast relative to the surrounding area. Further experiments are needed to verify whether the SCC compression approach effectively retains *all* relevant scientific information in Landsat Thematic Mapper. However, preliminary results seem to indicate that this compression approach retains much of the relevant scientific information. In a first attempt to evaluate the effectiveness of this approach, a classification of the compressed and reconstructed TM image data was performed. The result was compared with a classification performed on the original TM image data. Classification accuracy evaluations and classification maps are shown in the table and the second figure, respectively. The classification accuracies obtained with the data that were compressed

by a factor of 13 are consistently better than the accuracies obtained with the original data!

Contact: James C. Tilton
Code 636

Sponsors: Director's Discretionary Fund and
Office of Aeronautics and Space
Technology

Dr. James C. Tilton is an electronics engineer with the Information Systems Development Facility and chairs the Space Data and Computing Division's seminar committee. His interests center on image analysis approaches that use spatial information. Dr. Tilton, who holds a PhD in electrical engineering from Purdue University, has also received several achievement and performance awards. He has 6½ years of experience at Goddard.

COMPUTER MODELING AND SIMULATION OF THE 20 KHz AC POWER SYSTEM FOR THE SPACE STATION FREEDOM PLATFORM

As a part of Space Station Freedom Work Package 3, Goddard Space Flight Center (GSFC) has the responsibility for the Co-orbiting Space Platform. The platform is envisioned as an unmanned "mini-Space Station" that supports a variety of removable experiments and users. The platform, as well as the Space Station Freedom itself, is baselined as having a 20 KHz power system, which is unique in GSFC's experience. To accurately and optimally design and analyze the power system, GSFC, in cooperation with the Virginia Polytechnic Institute, is developing computer-aided modeling and analysis capabilities for the platform power system.

The need for computer modeling and analysis capability arises because for power systems of increasing size and complexity, it is virtually impossible to ground test the entire power system, or even various components. In this emerging state-of-the-art field, GSFC is taking the lead in power system simulation, and is using this expertise on one of the most complex power systems in GSFC's history.

The modeling capability is made possible and manageable through the utilization of a Boeing Computer Services software program known as

Accuracy comparison (% correct classification)
between classifications of the original TM image
and a reconstruction of 13-fold compression of
the TM image

Class	Classification	
	Original Image	Compressed Image
Water/Marsh	73.7%	79.3%
Forest	74.8%	75.6%
Residential	54.4%	64.9%
Ag./Domestic Grasses	81.9%	83.4%
OVERALL	79.2%	80.9%



EASY-5. EASY-5 allows for the user-friendly creation of small-scale modeling building blocks (or macros) that can represent independent power system components. These component macros can then be linked and organized into a total power system, just as "real-world" components are. EASY-5 will then enable the power system engineer to perform a wide variety of analytical tests on the complete power system. Previous power system simulation programs lacked this flexibility in component and system design, and required significant programming knowledge to alter power system parameters, thus limiting their inherent usefulness. As actual component and system designs are developed, the macros and power system architecture in EASY-5 grow and develop as well, enabling this technique to be utilized all throughout the design, development, manufacture, integration, test, and operation stages. The macros can even be fine-tuned enough to give detailed analysis of subsystem/subsystem interaction (such as power/thermal system interaction). Already, a wide library of power system component macros has been developed, enabling modeling and analysis of a variety of power system designs.

At the present stage of development, a total system simulation of the platform power system has been performed, although a few of the system components were not fully defined, and therefore not modeled in fine detail. The development of these component macros is progressing. In-depth analysis of power system architectures and control schemes will then be performed.

The end results of the effort will be: an invaluable design and analysis tool for the power system engineer; in-house experience and expertise in power system simulation; and a fully functional, highly reliable power system for the Space Station Freedom platform.

Contact: James M. Jagielski
Code 711

Sponsor: Space Station Freedom Project

Mr. James Jagielski, who holds a BS degree in electrical engineering from Johns Hopkins University, has five years of experience in the Power System Design and Analysis Section of the Space Power Applications Branch. Mr. Jagielski is a power system

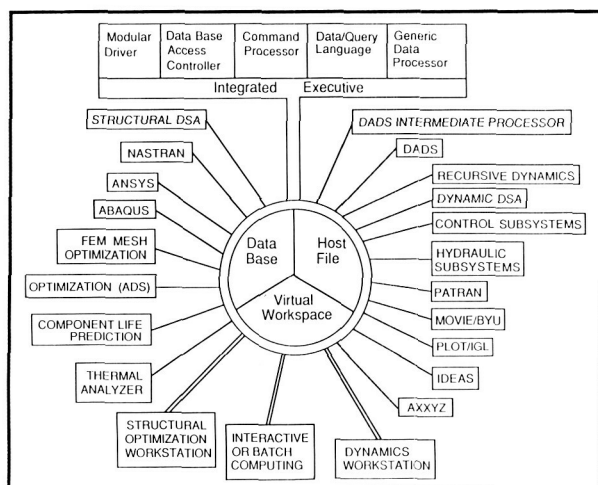
engineer supporting a variety of projects. He is technical monitor for power system modeling of the Space Station Freedom platform.

SIMULATION AND DESIGN OPTIMIZATION OF MECHANICAL SYSTEMS

A joint initiative has been undertaken by the National Science Foundation (NSF), the National Aeronautics and Space Administration (NASA) Goddard Space Flight Center (GSFC), and the United States Army Tank-Automotive Command (TACOM) to exploit recently developed high-speed dynamic simulation methods, parallel processors, supercomputers, high-speed graphics, and emerging network computing methods to create a National Software System for simulation and design optimization of mechanical systems. The foundation for the software system, shown schematically in the accompanying figure is the integrated Analysis Capability (IAC) data base and command processing system developed by NASA/GSFC and the Boeing Aerospace Company.

The IAC serves as the central hub of the software system, providing for interdisciplinary data storage and data communication among applications software, launching interdisciplinary runstreams, and storing data for analysis and design optimization of broad classes of mechanical systems. The spokes on the diagram represent major analysis tools that are executed under IAC control, using workstations that permit interaction with the engineer, providing transparent access via network computing methods to powerful compute servers, such as departmental minisupercomputers, and Cray-class supercomputers.

Development of this National Software System was initiated in September 1987, at the Industry/University Cooperative Research Center for Simulation and Design Optimization at the University of Iowa. In addition to NASA/GSFC and the United States Army Tank-Automotive Command, 20 other industrial and federal participants jointly support and guide the research program toward a new interdisciplinary simulation capability that will support aerospace, automotive, manufacturing, and diverse other forms of mechanical system applications.



A national software system for mechanical system simulation and design optimization.

During the Center's first year of operation, three major new capabilities have been developed. First, software for structural analysis, dynamic analysis, and fatigue prediction have been integrated using the IAC, providing the capability to subject a concept to dynamic simulation, to predict stress and strain time histories, and to predict fatigue life of components of the system, prior to testing the equipment. This new tool offers the potential to use high-powered compute servers, such as Cray supercomputers, to carry out numerical experiments identifying components of machines that are subject to early failure, and correcting such problems prior to fabrication and full-scale testing of a complete prototype.

The second fundamentally new capability developed by the Center is methods for real-time, man-in-the-loop simulation of systems such as automobiles, and space telerobots. Fundamental new algorithms for formulation and solution of the equations of motion of multibody systems are well suited for parallel processor implementation. Applications to date have demonstrated up to a factor of 25 speed-up on a conventional serial processor, and up to a factor of 300 speed-up on parallel computing equipment. Even greater gains are expected as the power of parallel processors expands. Network computing tools and modest-cost high-speed graphics-rendering devices have been integrated by the Center to provide capability for displaying realistic animations of

system dynamic performance, with the operator controlling the simulation as it runs (i.e., man-in-the-loop, real-time simulation). This capability is now being tested with construction equipment by the Center, and will be demonstrated and tested in the Goddard laboratory using space telerobots this coming fiscal year.

The third major development during the Center's first year is creation of a structural design sensitivity analysis and optimization workstation. State-of-the-art finite element structural analysis software, geometric modelers, and design sensitivity computational methods have been integrated in a workstation. The engineer can now define design parameters that size the structure; carry out structural analysis to identify critical stresses, deflections, or natural frequencies; and obtain sensitivity results that show how design variables influence structural performance. The engineer can then interactively modify the structure to obtain a feasible and ultimately optimal design.

Contacts: Harold P. Frisch and Edward J. Haug
Code 712

Sponsors: Office of Space Science and Applications, Office of Aeronautics and Space Technology, and Office of Space Station

Mr. Harold P. Frisch works in the Guidance and Control Branch at Goddard. He has developed many industry standard computer programs used for the design and analysis of spacecraft attitude control systems. He is currently engaged in supporting multidiscipline analysis, in many subject areas, by means of the Integrated Analysis Capability (IAC) program.

Dr. Edward J. Haug is a professor and the Director of the Industry/University Cooperative Research Center at the University of Iowa. He has authored and coauthored 12 books and over 200 research papers in the field of dynamics, optimization theory, and computer-aided design. He is currently striving to create a national software system for mechanical system simulation and design optimization based upon the IAC program.



WORLD MODELING IN SPACE APPLICATIONS

Knowledge of the robotics worksite must be available to operate robots properly. For engineering development work a PUMA robot is currently being used. The following paragraphs address the work being done in the area of world modeling for PUMA. Using things like cameras, torque gauges, and position encoders, it builds a model of its world. This world model, which must be as accurate as possible, is continually updated to reflect changes in its environment.

Actually, PUMA has a lot of help from its sophisticated "back end" team of networked VAXs, which do the high-speed processing necessary to collect data for and maintain PUMA's world model, in addition to controlling PUMA itself.

To Goddard Space Flight Center's (GSFC) Engineering Robotics Team, the hardware and software supporting PUMA are of primary interest in their efforts to develop world modeling software. Starting with a "blackboard architecture" prototype at Carnegie Mellon University, for its Autonomous Land Vehicle Project, the National Aeronautics and Space Administration (NASA) team modified the architecture to support robotic and vision system functions. The aim of this effort is to develop software that will control space-based robots that will perform various assembly and maintenance tasks. To do this the robot must have an extremely detailed model of its environment—including objects it is to manipulate—as well as its own attitude and position.

Cameras, both robot-mounted and environment-mounted, gather data on the position and orientation of objects in the environment. Position switches, mounted on supported surfaces, relay data on the placement of manipulated objects. Data concerning the robot's attitude is gathered by joint position encoders and force/torque gauges. These data are processed by the networked computers and interpreted by robot safety systems, which monitors the current status of the robot's operations. Using this data, a human operator at a remote terminal may monitor, control, or override the operations. This operator may choose to run a preprogrammed set of tasks, or may control the robot directly, using a joystick or set of waldoes.

Presently, the GSFC Engineering Robotics Team's efforts in world modeling has improved PUMA's ability to perform several simple tasks involving the manipulation of objects. Future development will benefit from planned enhancements in the area of real-time performance; sensor processing, development, and correlation; data conflict resolution; and others. The ultimate goal of this effort is to provide an integral part of the National Aeronautics and Space Administration Space Station Flight Tele-robotics Servicer.

Contact: Timothy M. Carnahan
Code 725

Sponsor: Director's Discretionary Fund

Mr. Timothy M. Carnahan earned his BS degree in aerospace engineering from Purdue University and has been working for the Systems Analysis section at Goddard for the last five years. He is now working on simulations of the robot systems for the Space Station Project.

AutoCAD TO GIFTS TRANSLATOR

The power of personal computers (PCs) has increased dramatically in the past few years. Many large engineering programs that, a few years ago, could only be run on large mainframe computers are being adapted to run on PCs. Most engineers now have ready access to PC-based word processing, spreadsheet, drafting, and finite-element programs. Unfortunately, these useful and varied programs rarely provide means to exchange data with each other. Computer aided design (CAD) programs can create three-dimensional models of structures very quickly. The models contain all the basic geometric information needed to create a finite element model of the structure. However, this information is generally not in a form that can be used by finite-element programs. ACTOG (AutoCAD to the graphical interactive finite-element total system GIFTS)) is a program that has been written to bridge the gap between two commonly used engineering programs: AutoCAD, a computer aided design program, and computer aided structural analysis (CASA)/GIFTS, a finite-element analysis program.

ACTOG was developed to facilitate quick generation of small finite-element models using the CASA/

GIFTS finite-element modeling program. ACTOG reads the geometric data of a drawing from the Data Exchange File (DXF) used in AutoCAD and some other PC-based drafting programs. The geometric entities recognized by ACTOG include POINTs, LINEs, ARCs, SOLIDs, 3DLINEs, and 3DFACEs. From this information ACTOG creates a GIFTS SRC file. The GIFTS commands created include KPOINTs, SLINEs, CARC, GRID3s, and GRID4s. The drawing can be created on any CAD system provided the data base can be made compatible to the AutoCAD DXF format. The program has only been run on AutoCAD (Release 9) DXF files, so compatibility with other programs' DXF files is unknown.

ACTOG was designed to be used for cursory analysis of simple structures. The engineer develops a conceptual model of the structure on a DXF-compatible CAD system. The model is selectively written to a DXF file. ACTOG is run and the geometric information contained in the DXF file is converted to a GIFTS SRC format file. Default material and thickness properties are added to the geometric model by ACTOG. (The default properties are included for

convenience and as an example, and are rarely used in entirety.) The SRC file usually will be edited using an American Standard Code for Information Interchange (ASCII) text editor. The file can then be read by one of the GIFTS processing programs, and the model is generated.

Thus, the engineer is able to create a finite-element model, using the CAD model, in just a few minutes. CASA/GIFTS is not currently benchmarked and cannot therefore be used for final analysis, but it can provide accurate conceptual-level analysis quickly. Using ACTOG, multiple iterations of a structural concept can be performed without tying up valuable mainframe computing time.

Contact: Andrew L. Jones
Code 731

Sponsor: Mechanical Engineering Branch

Mr. Andrew L. Jones is a mechanical engineer on EUVE. He received a BS in mechanical engineering from the University of Maryland. Mr. Jones has two years of experience at Goddard.

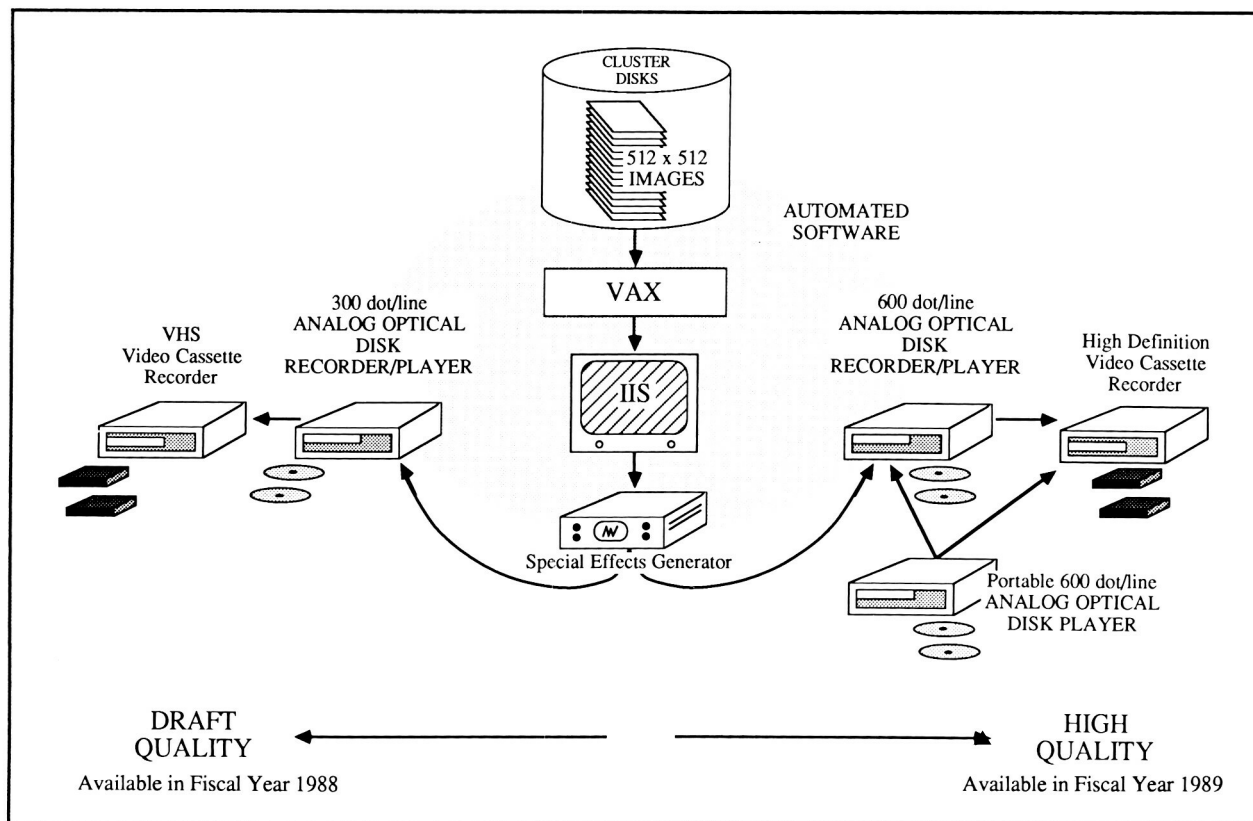
USER SPACE DATA SYSTEMS

NEW COMPUTER MOVIE-MAKING FACILITY NOW AVAILABLE TO GODDARD SCIENTISTS

A new movie-making facility became available to the entire Goddard Space Flight Center scientific community during fiscal year 1988. The facility is located in the Computer Systems Research Facility (CSRF), and is designed for producing movies of computer-generated scientific data, such as graphics, image, or model outputs. In the recent past, the most common way to make movie loops for scientific analysis and presentation was to record all images on 16-mm movie film, using either photographic prints and a copy stand, or Matrix/Dunn cameras attached to computer monitor outputs. The new method used in the movie-making facility employs an analog optical disk to capture and sequence the computer frames into a movie loop viewable on a color video monitor. (See figure.) With this new video technology, se-

quences of color 512 by 512 images can be displayed, instantly recorded, and played back as movies, all within minutes. This system is proving itself to be a valuable tool to scientists, who must rapidly evaluate large amounts of image data. The analog optical disk not only makes it far easier to create a movie loop, but also reduces production costs, and allows video tape (VHS) copies to be made immediately, for use away from the facility (e.g., in the researcher's office, at seminars and conferences, and on television news broadcasts).

In planning for a computer movie-making facility, the CSRF staff evaluated existing commercial movie-making systems, and quickly came to the conclusion that they were not affordable. They then crafted a system around the emerging optical disk technology; a capability that approaches studio quality, but at a fraction of the cost of commercial systems. The



This diagram shows the movie-making process. The scientist provides hundreds or thousands of 512 by 512 gray-scale images that are moved to CSRF's VAX Cluster disks. Each image is displayed in sequence on the IIS image analysis terminal using a color lookup table (pseudocoloring). The process utilizes a graphics package for annotation of the images. The images are then written to the analog optical disk. Once a sequence of images is safely in place and recorded on the optical disk, it can be played by the scientist using a handheld remote control unit. Frame rates vary from 0 to 300 frames per second forward, backward, or in loops. Once the optimal rate of display for the sequence is determined, it can be copied to VHS video tape, and carried away.

analog optical disk recorder/player unit in use by CSRF uses an 8-inch write-once-read-many-times (WORM) disk. The WORM capability is quite adequate for the needs of scientific movie-making. In addition, because each analog optical disk can store 24,999 video images, CSRF is experimenting with using it as an "image notebook," into which a user can instantly and permanently store single images from an image analysis terminal screen. The optical disk is operated from a computer terminal by a system of automated software. Graphics and typesetting routines are also available to provide titles and annotations.

The current optical disk recorder resolves 300 dots per television scan line, which is approximately the

resolution of home VHS videotape. The optical disk industry plans to announce 600 dot per line machines during fiscal year 1989.

Contact: Charles G. Bohn
Code 635

Sponsor: Office of Space Science and Applications

Mr. Charles G. Bohn, who holds an MS degree in geography and Earth sciences, is Manager of movie production at the Computer Systems Research Facility. He also prepares presentations for the facility. Mr. Bohn has received two Group Achievement Awards during his 14 years at Goddard.

NIMBUS-7 CLIMATE DATA SET DEVELOPMENT

Now approaching 10 years of operation, the Nimbus-7 satellite is the last in a series of orbiting observatories that have surveyed the Earth, its atmosphere, and oceans. By mapping land features and water characteristics, as well as observing weather and climate patterns, snow and ice content, and other parameters, the Nimbus series of satellites has served as a test platform for the development of Earth observation techniques that are now used operationally to monitor the Earth's weather, climate, ocean, and land characteristics.

All Level-1 data products from the Coastal Zone Color Scanner (CZCS), covering a period of seven and one-half years, have been transferred to optical disk and archived. A new global ocean chlorophyll processing system has been implemented and tested, and Level-2 and -3 processing of multiyear global data continues. Approximately 3 years worth of global ocean chlorophyll data (1979 through 1982) has been produced.

The Earth Radiation Budget (ERB) solar observations recently entered a second solar sunspot cycle. The instrument has been operating for over nine and one-half years; nearly 9 years of both solar and Earth flux data have been processed and archived. The ERB Earth data subsequent to March 30, 1988, are being processed only to Level 1 and archived, because of budgetary constraints. The solar data are normally processed to Level 1 only.

Over 9 years of Solar Backscatter Ultraviolet (SBUV) ozone data have been processed and archived. SBUV data beyond March 30, 1988, are only processed to Level 1, and then archived, because of instrument malfunction resulting in a degradation of data quality.

Total Ozone Mapping Spectrometer (TOMS) data are still being collected and processed to ozone parameters. Nine and one-half years of total atmospheric ozone data have been archived.

Over nine and one-half years of Scanning Multichannel Microwave Radiometer (SMMR) data have been processed to brightness temperatures and the following derived products: sea ice (multiyear fraction, and sea ice concentration), total atmospheric water

vapor over ocean, sea surface temperature, and sea surface wind speed. The SMMR experiment was turned off on July 6, 1988, because of technical and budgetary constraints.

Eight and one-half years of Stratospheric Aerosol Measurement II (SAM II) stratospheric aerosols in the polar regions have been archived. Data production and validation continue.

A 6-year data set of infrared radiance observations from the Temperature Humidity Infrared Radiometer (THIR) experiment has been archived. Additionally, a 6-year cloud climatology data set, consisting of low, middle, and high cloud amounts derived from a combination of THIR and TOMS data, has been archived.

The table summarizes the operational status of the various experiments on board Nimbus-7.

Operational Status of Experiments On Board Nimbus-7			
Experiment	Current Status	Last Useful Data Date	Final Turn-Off Date
LIMS	Off	05/29/79	06/04/86
CZCS	Off	06/23/86	12/18/86
SAMS	Off	06/13/83	04/09/85
THIR	Off	05/09/85	02/18/86
SMMR	Off	07/05/88	07/06/88
ERB:			
Solar Flux	On*	—	—
Earth Flux	On*	—	—
SAM II	On	—	—
SBUV	On	—	—
TOMS	On	—	—
*Data collection is ongoing, but processing is to calibrated radiances only; the normal solar flux products are Level 1.			

LIMS, CZCS, and SAMS were turned off because of instrument failure. THIR and SMMR have been turned off because of spacecraft power limitations caused by the deterioration of the solar cells and batteries, and because of budgetary considerations.



Contact: Arnold G. Oakes
Code 636

Sponsor: Office of Space Science and Applications

Mr. Arnold G. Oakes holds a BA degree in geology. As Nimbus-7 Manager, Mr. Oakes handles Earth observations data processing and archiving, as well as science data validation and instrument calibrations. He has 19 years of experience at Goddard.

DATA SYSTEMS INTEROPERABILITY

When working in a heterogeneous computational environment, where many applications and resources are tied to specific hardware and/or software environments, a user/developer is often required to absorb an enormous amount of information to effectively utilize each system. Therefore, an easy-to-use mechanism that will enable users/developers to take full advantage of disparate system resources in a transparent fashion is needed. The National Space Science Data Center (NSSDC) Data Systems Interoperability concept is a product of the NSSDC's applied computer science work; it provides a solution for this common problem. The development efforts consist of the engineering of consistent software interfaces for a variety of computational resources available within the Space Data and Computing Division, in order to provide easy-to-use facilities for both data systems users, and developers of these heterogeneous resources. The utilization of this software and similar techniques will help eliminate duplication of effort, and allow users to take full advantage of a variety of system capabilities.

The primary objective of this research is to develop the framework through which consistent interfaces utilizing an open system concept at an applications level can provide a truly heterogeneous, distributed computing environment. This system, which will appear as an extension of a user's/developer's workstation, will transparently provide access to remote files, allow remote execution of procedures, and permit the utilization of resources from multiple vendors. The accompanying figure provides a conceptual view of such a system from a user's perspective.

Within the Space Data and Computing Division there are three different centers, the NSSDC, the National Aeronautics and Space Administration (NASA) Space and Earth Sciences Computing Center (NSES CC), and the Science and Information Systems Center (SISC), which to the outside user community appear as three separate computing facilities. These facilities are composed of their own computational resources, peripherals, and data applications. In many cases, these resources are dedicated to a particular machine. A researcher needs the resources of such facilities, which permit a user to quickly access, acquire, manipulate, and display data.

For a user to take advantage of various resources in the three centers, or to achieve a common goal on different hardware or software systems within a center would require one to utilize each resource separately. For example, if a scientist wanted to scan the catalog and inventory for a particular data set(s) from the tape archive available at the NSSDC, extract the data via the tape processing resources available on the NSES CC IBM 3081, process the data via the SISC Massively Parallel Processor (MPP), and analyze the data via the NSSDC Graphics System (NGS), this would require a specific body of knowledge unique to each of the five resources. Often, the resources of different facilities are available to a user from his or her environment, but the user is required to remotely login across a specific network in order to utilize that environment's local resources. This common situation is frustrating, and wastes valuable time that could be spent on research. Software techniques that utilize extant networks to make remote resources appear as if they are local by means of a common interface can dramatically improve productivity by minimizing the amount of effort required to remotely access valuable systems.

The NSSDC is developing a prototype that will provide a proof-of-concept for an overall interoperable system. One part of the prototype system is currently in place, and another portion is under development. The former integrates the resources available on the MPP with those of the NSSDC Graphics System. This integration will allow the user to rapidly process large, complex, multidimensional data sets using computer graphic techniques for visual representation. The other portion of the prototype helps eliminate the problem of processing very large

numbers of magnetic tapes, a problem that has plagued the NSSDC for a number of years. The NSSDC's DEC VAX-11/780 and 8650 (VMS) computer systems are inherently incapable of supporting large-scale tape processing, a situation that is compounded by the fact that these computers support a number of other NSSDC activities. The NSESCC IBM 3081 running the MVS operating system has proven to be the most efficient method for processing large volumes of tapes. By taking advantage of the tape processing resources available on the IBM 3081, the NSSDC can better achieve its mission of supporting large volumes of data for the NASA scientific community.

The software development effort for the tape processing portion of the prototype consists of porting code that parses specific data set tape formats and the NSSDC Common Data Format (CDF) software to the IBM 3081; modifying the NASA Climate Data System (NCDS) code to submit tape processing jobs to the IBM, rather than the NSSDC VAXs; and implementing the control tools needed to transport information and data via the network (i.e., Interlink) that supports communications between the IBM and the NSSDC VAX 8650. The prototype will allow a user from the NCDS to transparently access magnetic tapes on the 3081, reformat a data set in terms of CDF, and migrate it to the user's directory on the NSSDC VAX for use in NCDS or other VAX-based systems. The software would automatically take care of all remote logins, submittals of job control information, communications protocols, conversion of machine-specific binary formats, etc. These same

techniques also could be adopted by the other VAX-based software systems to transparently utilize the NSESCC facilities.

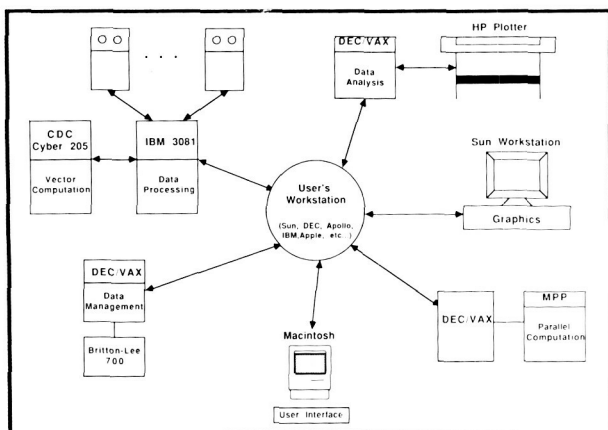
This activity is expected to expand in the future to include other Space Data and Computing Division resources, providing the software developer and ultimately the end user "with the best tool for the job." The utilization of such software and similar techniques will allow one to take full advantage of a variety of system capabilities in a seemingly effortless manner.

Contacts: Gregory W. Goucher and
Lloyd A. Treinish
Code 634

Sponsor: National Space Science Data Center

Mr. Gregory W. Goucher provides technical support for the development and implementation of advanced scientific software applications at the National Space Science Data Center. He has a BS degree in information science and five years of experience as a programmer/analyst at Goddard.

Mr. Lloyd A. Treinish is a data analysis mathematician with nine years of experience at Goddard. He works on the development of advanced data systems for support of scientific applications, as well as studying space and atmospheric phenomena. Mr. Treinish developed the concept of using the Massively Parallel Processor as a computational geometry server. He was the chief designer and developer of the Pilot Climate Data System, and he conceived of the first self-describing data abstraction for the storage and manipulation of multidimensional data, as the Common Data Format. Mr. Treinish has an SM degree in physics from the Massachusetts Institute of Technology and has received four NASA Certificates of Outstanding Performance.



Conceptual view of an interoperable data system.

NASA'S CLIMATE DATA SYSTEM

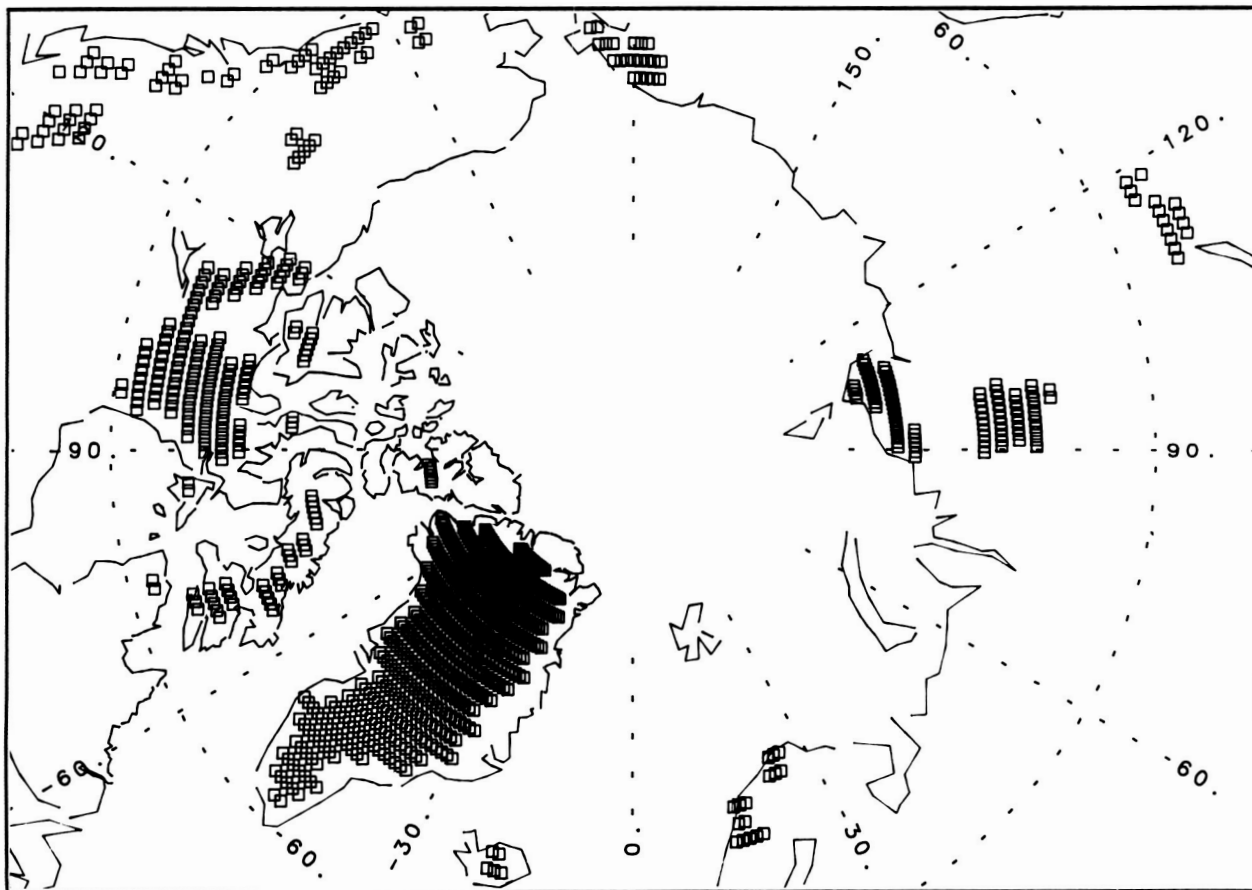
The National Aeronautics and Space Administration's (NASA) Climate Data System (NCDS) is an interactive, scientific information management system designed to locate, access, manipulate, and display climate research data. The Data Management Systems Facility of Goddard Space Flight Center's



(GSFC) National Space Science Data Center (NSSDC) developed this system—and continues to enhance it—to support NASA-sponsored scientists. The collection of data supported by the system continues to expand, and currently consists of over 30 data sets. The user community also continues to grow, with increased access being provided via new nodes on the Space Plasma Analysis Network.

NCDS provides several functions that enable researchers to locate data of interest, preview data using graphical and statistical methods, and extract subsets for further analysis at their own sites. These functions are described below:

- Obtain comprehensive descriptions of a number of climate parameter data sets and the associated sensor measurements from which they were derived.
- Obtain detailed information about the temporal coverage and volume of data sets that are readily accessible via NCDS.
- Access the data sets to order copies; or, for most (but not all) data sets, extract portions using criteria such as time range and geographic location for output to on-line disk files in a special data set independent format.
- Access and manipulate the data in the special data set independent format, performing such functions as combining the data, creating a subset of the data, or averaging the data.
- Create various graphical representations of the data stored in the data set independent format.



Snow coverage plot for July 3, 1983, utilizing data from a recent NCDS acquisition, the International Satellite Cloud Climatology Project (ISCCP) snow/ice data set.

NCDS provides these capabilities through the integration of several general purpose software packages—some commercially available, others developed by other groups within GSFC—with specialized software for reading the supported data sets. The result is a system that is both easy to use and flexible, and that can easily be expanded, either to provide support for additional data sets or to provide additional functional capabilities.

Some of NCDS's fiscal year 1988 accomplishments are listed below:

- Several presentations and papers were prepared using data from NCDS.
- The user support office assisted First International Satellite Cloud Climatology Project (ISCCP) Regional Experiment (FIRE) investigators in placing data in an established exchange format before submitting them to NCDS, the designated FIRE central archive.
- Support was provided for several additional data sets, including several oceanographic ones.
- A new version of the system was released that included several simple enhancements and corrections. This also involved the incorporation of new versions of underlying software packages.
- Consultation was given to a number of other projects, and the system was documented via several presentations and papers.
- The entire on-line catalog was updated, and the data holdings were expanded. Over 800 additional tapes were made available to users.
- Under a memo of understanding developed last year, the University of Maryland continued examining methods for increasing the effectiveness of teaching meteorology using NCDS.

NCDS provides a number of labor-saving utilities, allowing project scientists to perform significant research—even with limited budgets. It also serves as a model for future information management systems in a variety of disciplines.

Contacts: Mary G. Reph and Lola M. Olsen
Code 634

Sponsor: Office of Space Science and
Applications

Ms. Mary Reph is NCDS Project Manager with the Data Management Systems Facility of the National Space Science Data Center. Ms. Reph, who received an MA degree in mathematics from American University, has been with Goddard since 1978.

Ms. Lola M. Olsen oversees the implementation of data sets in NCDS, supports NCDS system users, and writes data set information catalogs. Ms. Olsen has an MA degree from the University of North Carolina/Charlotte and has completed coursework for her PhD degree. She has two years of experience at Goddard.

PILOT LAND DATA SYSTEM

The Pilot Land Data System (PLDS) is a distributed interactive information system intended to provide data access to the National Aeronautics and Space Administration's (NASA) land scientists. This prototype system is in its second year of software development. Currently, there are sites at three NASA centers, Ames Research Center (ARC), Goddard Space Flight Center (GSFC) and Jet Propulsion Laboratory (JPL). The site at JPL has a dedicated computer facility that is used by both the ARC and JPL sites. The PLDS was conceived as a distributed data system, the one feature that sets it apart from the other pilot data systems for climate and ocean. Integration of this concept into the overall design and architecture is a fundamental part of the data system.

The initial focus of the PLDS was to provide information science support for three land science projects—one at JPL, and two at GSFC—rather than to provide access to data of broad interest within NASA's land science community. This focus led to three very distinct information systems, each one focusing on the needs of a specific science project. There was essentially no sharing of software development costs, since the data bases and many other features of the data systems were unique to each project. This trend continues, but efforts are now underway to merge most features. In this way, a significantly smaller software development effort will be



required to add a new data set to the existing structure. The old strategy also tended to produce a data system that was useful only to an expert, someone who used it on a daily basis, and was willing to invest the time and effort necessary to learn the system.

Throughout fiscal year 1988, the PLDS project had two principal objectives: to support the scientific community, and to continue the design and development of the Pilot Land Data System. The PLDS supported the scientific community by adding a new site at ARC to support the community as a whole, and by continuing to support three science projects: Sedimentary Basins (SedBasins), First International Satellite Land-Surface Climatology Project (ISLSCP) Field Experiment (FIFE), and Interdisciplinary Science-Land Surface Climatology (IDS-LSC).

The ARC site provides NASA's entire land science community with access to information about land science data collected by ARC-based aircraft. (ARC serves as NASA's principal site for aircraft-borne sensors.) Once an interesting piece of data is found, it can then be ordered by mail or phone from the archive.

The JPL and GSFC sites, on the other hand, support specific land science projects. The JPL site continued to provide support for the SedBasins science project. Recently, this site has added information about a large quantity of data collected by the SedBasins project, including geological samples, remotely sensed data, maps, and botanical samples. JPL also provides on-line access to a large number of spectra run on the geological samples.

The GSFC site serves as the informal backup location for scientific data collected by the FIFE project. All of the FIFE data are described in the PLDS directory. Portions of the data are also described in the catalog—Advanced Very High Resolution Radiometer (AVHRR) and Thematic Mapper (TM); and inventory (AVHRR and Automated Meteorological Station data). GSFC also holds a complete listing of all physical media received from the FIFE project. This site also provides on-line access to selected portions of the Automated Meteorological Station data.

For the IDS-LSC project, GSFC serves as the principal information system and archival backup. All IDS-LSC data sets are described in the PLDS directory;

eventually, all data sets will be described in both the catalog and inventory. Currently, only the AVHRR, TM, and Multispectral Scanner (MSS) data are described in the catalog. As in the case of the FIFE data, GSFC also holds a listing of all the physical media received from the IDS-LSC project.

Major strides were made recently in several critical areas of the PLDS design and development. First, a proposal for long-term overall system architecture was presented. In conjunction with this proposed system architecture, a companion plan to describe and then build the PLDS system in a modular and layered fashion has been developed. There is a basic system with modular enhancements to that system, making it easier for PLDS sites to customize systems to meet their needs. Developers have decided that the PLDS will be made portable, so that sites can be added to the PLDS system independent of hardware and operating systems.

In the area of software development, PLDS developers added three new functional areas, and substantially improved the functioning of several existing components. Capitalizing on GSFC development efforts for the Master Directory, and the NASA Climate Data System, the PLDS developers provided users with access to a functional directory and catalog at very low cost. A wholly new activity undertaken by PLDS developers to design and build a data base query tool that frees the user from any knowledge of the logical structure of the data base. This new tool allows the user total access to all data available within the data base, with flexibility to pick and choose the information and format of the desired report. This tool will continue to evolve as understanding of the problem increases, and as more powerful user interface tools become available. Major improvements also have occurred in the organization of the PLDS inventory data bases, and within the portion of the data system through which users order data. These components are now substantially easier to use and maintain.

The PLDS inventory now consists of a general purpose segment in which the common attributes of all data (e.g., time and place of collection) are shared across all sites, and a detailed segment that contains information unique to each different kind of data. This concept of a common inventory was first proposed, and is currently used, by the NASA Climate

Data System, and then adopted by the JPL, site of the PLDS.

A new release of the PLDS recently was made available to a select group of scientists for beta-testing, with production release scheduled for the near future.

Contact: Blanche W. Meeson
Code 630

Sponsor: Office of Space Science and
Applications

Dr. Blanche W. Meeson is the Project Manager of the Pilot Land Data System at the Data Management Systems Facility. Her interests include Data Management Technologies, especially the integration of commercially available software products into a coherent system to describe, present, and provide access to scientific data. Dr. Meeson has two years of experience at Goddard.

THE NASA MASTER DIRECTORY

The first operational version of the National Aeronautics and Space Administration (NASA) Master Directory (MD) was released in the fall of 1988. This directory serves as a readily available, on-line system for locating and browsing summary information about space and Earth science data of interest. Data acquired through NASA funding are emphasized, but information about data from other federal agencies, international institutions, universities, state agencies, etc., will also be present if it is of interest to researchers in the space and Earth sciences. The directory also provides information about other data centers and data holding facilities where more specific details about the data may be obtained and/or the data may be accessed.

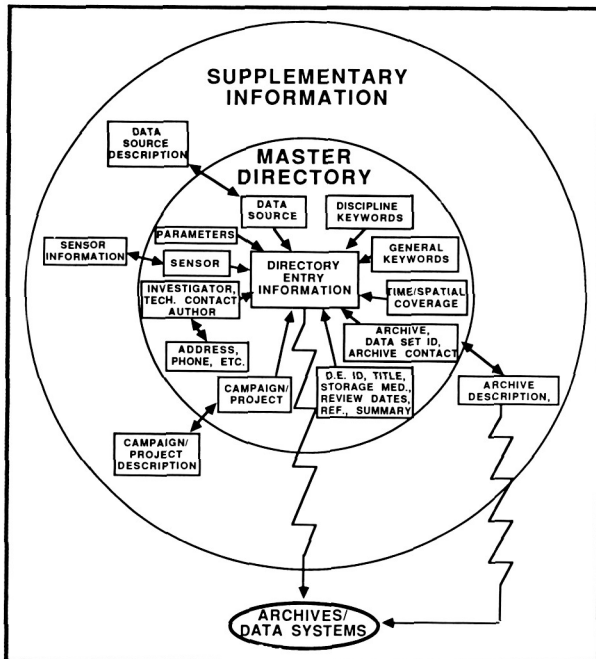
This type of service has been provided by a number of information systems in the past. What distinguishes the MD is that, in many cases, the directory takes advantage of the interconnection of the data centers through computer networks, and provides an automatic link to a number of these facilities upon the user's request. This interconnection has been made possible through the work of the Catalog Interoperability working group. Work is ongoing to test and improve the MD; to provide information about

a wider range of data sets; to include more ancillary information about the data sets; to increase the number of network connections; and to make the overall interlinked network of data information a more uniform environment for the user.

The typical MD user reaches the directory from a computer terminal or personal computer that accesses a computer network or dial-in lines. Upon entry, the user is offered the choice of getting information about archives/data centers, campaigns/projects, or data sets. Since the information on one or more closely related data sets may be combined in the directory, the term "directory entry" is often used in place of the term "data set." If the user chooses to browse through the archives/data centers, he or she is offered a list of archive names from which to choose. Upon selection, the user receives brief descriptive information about the archive (types of data held, ordering information, access costs, persons to be contacted, etc.). If possible, connection is offered to an on-line system at the archive that contains further information. If the connection is invoked, an automatic login is made, and the user is immediately able to continue to search. The user may also choose to look at supplementary information about selected campaigns/projects.

Most users are more interested in data information. If the user chooses to search for particular directory entries, there are a number of ways to narrow the list of potentially useful data. Searches may be made based on one or more of the following categories:

- Discipline (land science, ocean science, space science, etc.)
- Parameters measured (quantities whose values constitute the data)
- Time coverage (first and last dates of interest to the user)
- Spatial coverage (latitude and longitude ranges of interest)
- Location (general names of places, such as Asia, Mars, etc.)
- Data source (satellite name, observing site, ship, etc.)
- Sensor (name of experiment or instrument that gathered the data)



NASA Master Directory organization.

- Investigator (person who led the investigation resulting in the data)
- Campaign or Project (name of organized campaign/project yielding data, if applicable)
- General keywords (any other keywords that may be useful in describing these data)

The result of a search is a title list of applicable directory entries. The user selects a particular title of interest and is offered further information about that entry, including a brief summary describing the data, bibliographic references, names, addresses, and telephone numbers of people to contact for further details, the nature of the medium on which the data are stored, the name of the archive where the data are stored, etc. Supplementary information about the archive, data source, sensor, and campaign/project may also be available (not all of these options are implemented in the current version). If it is possible to link to a system offering further information, data ordering capabilities, browsing of the data, etc. the option to make this connection is offered. If this option is exercised, the user is then automatically logged in at the other archive/data system, and con-

tinues from there. Upon leaving that system, the user is returned to the MD at the place of departure. A summary of the content and organization of the MD can be seen in the accompanying figure.

The information contained in the MD comes directly from the people most knowledgeable about the data. It is submitted via the Directory Interchange Format (DIF), a format developed by the Catalog Interoperability working group. A DIF file is simple to create and use, and is designed to facilitate the transfer of directory information among data systems. The file may be automatically loaded into the Master Directory data base; it provides the core of information about an entry, as shown by the boxes within the inner circle in the figure. A number of other directories and data systems have adopted this format, and the number is continually increasing. Those interested in submitting data information or getting more information on the DIF should request the Directory Interchange Format Manual, National Space Science Data Center publication number 88-19, from the author.

The Master Directory is currently available for use. It is most easily accessed through the Space Physics Analysis Network (SPAN) but connections are possible through Telenet and other network gateways.

Contact: James R. Thieman
Code 633

Sponsor: Office of Space Science and Applications

Dr. James Thieman, who holds a PhD degree from the University of Florida, is Manager of the Master Directory and Catalog Interoperability Projects. His professional interests include astrophysics, specifically planetary radio astronomy and magnetospheric physics, and computer science. Dr. Thieman, a recipient of NASA's Special Achievement Award, has been with Goddard for 11 years.

CRUSTAL DYNAMICS DATA INFORMATION SYSTEM

The Crustal Dynamics Project was formed by the National Aeronautics and Space Administration (NASA) to apply space methods and technology to

advance scientific understanding of Earth dynamics, tectonophysics, and earthquake mechanisms. The Project uses three types of space-age techniques in this study: laser ranging to an artificial satellite or the Moon, very long baseline interferometry (VLBI), and the global positioning system (GPS). As part of its data management, the Project has designed and implemented a centralized Crustal Dynamics Data Information System (CDDIS), shown in the figure. The CDDIS has been fully operational since September 1982. Its main purpose is to store all geodetic data products acquired by the Project in a central data bank and to maintain information about the archiving of all Project-related data. The CDDIS is operational on a dedicated DEC MicroVAX II computer. All authorized Project investigators, staff, and cooperating institutions have access to the system through the Space Physics Analysis Network (SPAN), INTERNet, and the GTE TELENET facilities, as well as through dial-up telephone lines. The menu-driven system provides the user with access to the different parts of the CDDIS; data retrievals or queries are possible with user-friendly interfaces.

The archive of preprocessed laser, raw, correlated VLBI, and GPS data is retained off line in the CDDIS tape library. All other information can be accessed through a data base utilizing the ORACLE data base management system (DBMS). The laser, VLBI, and GPS data sets accessible through the CDDIS fall into four major categories:

- 1) Preprocessed Data. These include catalogs of preprocessed SLR (Satellite Laser Ranging) from 1976 through the present, VLBI data from 1976 through the present, and GPS data from 1985 through the present. Summaries of SLR data from LAGEOS, BE-C, STARLETTE, and EGS satellites are stored on line in a data base; the actual data are archived off line on magnetic tape. The VLBI data consist of on-line experiment listings in the data base and a magnetic tape archive of the actual experiment data. Listings of available GPS data are also contained in the on-line data base.
- 2) Analyzed Data. These include SLR, Lunar Laser Ranging (LLR), VLBI, and combined, analyzed results supplied by the Project's Science Support Groups and other analysis centers, and Project investigators at Goddard

Space Flight Center (GSFC), Jet Propulsion Laboratory (JPL), National Geodetic Survey (NGS), Massachusetts Institute of Technology (MIT), the University of Texas, and many other global institutions. These analyzed results currently span different periods from 1976 through the present and are accessible through the data base management system. They include precision baseline distances, Earth rotation and polar motion determinations, length-of-day values, and calculated station positions.

- 3) Ancillary Data. This information includes descriptions of Crustal Dynamics Project site locations, a priori monument coordinates and calibration data, and a priori star coordinates. These data sets are contained in the on-line data base.
- 4) Project Management Information. This category is accessible through the CDDIS data base to authorized Project personnel only and includes mobile system schedules, occupation information, and configuration control information. In addition, CDDIS operational information is kept in the data base and is accessible to CDDIS staff only. These data include logs of all laser, VLBI, and GPS tapes received from the many global sources, as well as logs of all tapes created by the CDDIS for outside users, and listings of CDDIS backup tapes.

In addition to the on-line, menu-driven user view, the CDDIS is tasked to assist the investigator community with its data requirements. These data services of the CDDIS consist primarily of receiving and archiving Crustal Dynamics-related data on magnetic tape and cataloging these data in the CDDIS data base. All data received by the CDDIS from the many contributing global sites must be verified and often reformatted prior to distribution. The CDDIS is then responsible for the dissemination of these data to authorized investigators of the Crustal Dynamics Project located in the United States and in various global institutions. Efforts are made by the staff to send the data in the most convenient format for the investigators. Data can be made available in the form of printout listings, magnetic tape or floppy disk, or network files.

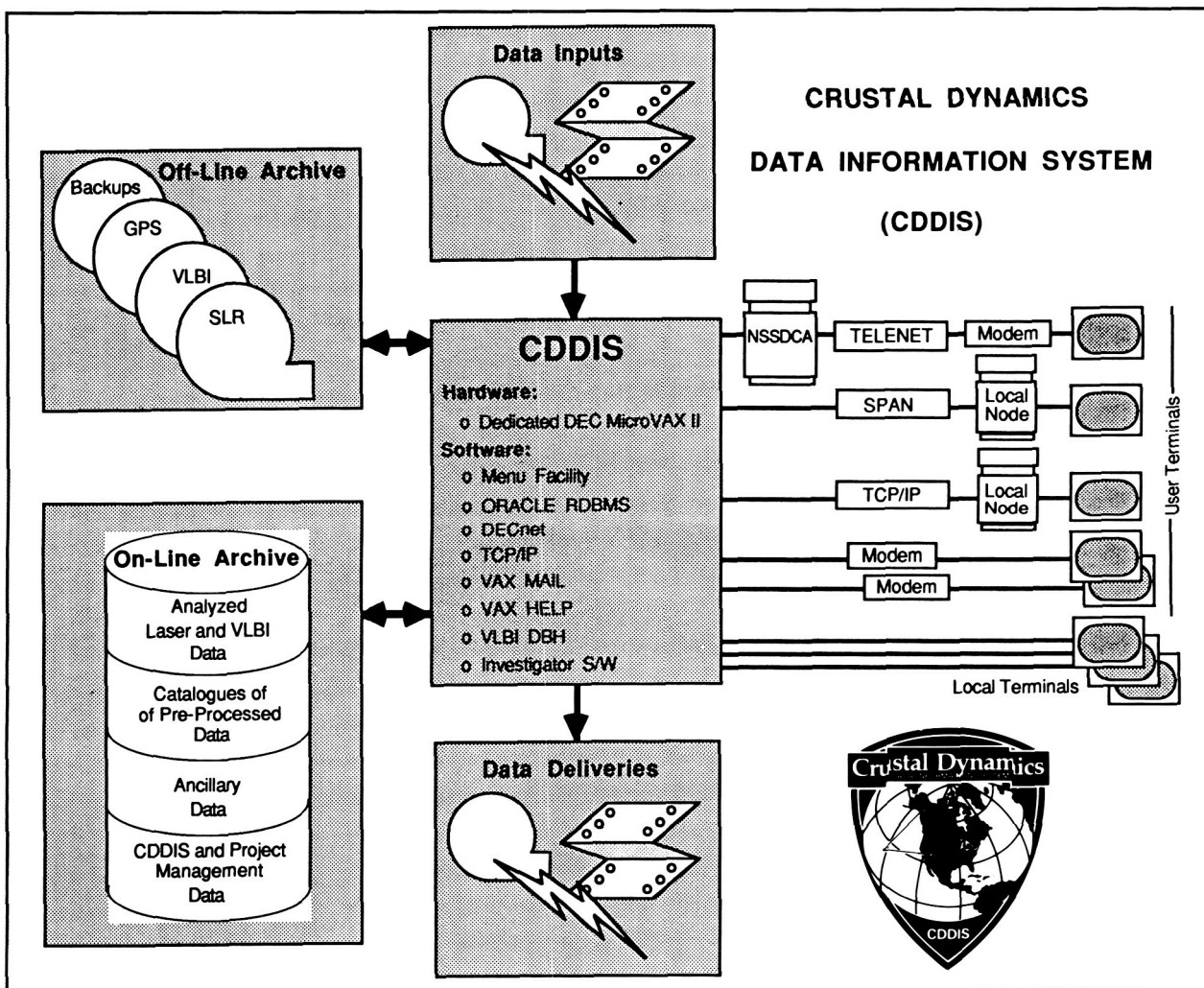
The majority of efforts during fiscal year 1988 concentrated on the transfer of the CDDIS to the dedicated MicroVAX environment. Prior to February 1988, the CDDIS was operational on the NSSDC VAX 11/780 computer. In order to support the increasing requirements of the Crustal Dynamics investigator community, it was decided to migrate the system to a dedicated computer. This accomplishment and others are detailed below:

1) A DEC MicroVAX II computer and various auxiliary hardware and software were procured and installed. Once all computer facilities were functional, the entire CDDIS was ported from the NSSDC's VAX 11/780 to the MicroVAX.

2) Numerous documents for the management, security, and use of the CDDIS MicroVAX were written and distributed to Project and NSSDC personnel.

3) The CDDIS MicroVAX became accessible to users through the SPAN and INTERNET networks. GTE TELENET access is also available but currently routes through the NSSDC VAX 8650.

4) Several new data sets were received from Project affiliates and loaded into the CDDIS data base. These products included revised GSFC fixed and mobile VLBI analysis results, NGS



Crustal Dynamics Data Information System.

mobile VLBI analysis results, GSFC SLR baseline and station position solutions, and monthly sets of International Earth Rotation Service (IERS) polar motion determinations from a variety of sources. The results of the analysis of vertical leveling data were received from Cornell University and are available on magnetic tape.

- 5) A user's guide (*Quick-Look Guide to the Crustal Dynamics Project's Data Information System*) was published and distributed to over 500 users worldwide. A second printing of the document was distributed to potential proposal writers for the LAGEOS II Project.
- 6) The latest version of the document *Crustal Dynamics Project: Catalogue of Site Information* (NASA Reference Publication 1198) was completed and distributed to a worldwide group of the Project's principal investigators and cooperating institutions. The catalogue is designed to provide descriptions of the observing sites utilized by NASA's Crustal Dynamics Project. The information contained in the catalogue is also available on line through the CDDIS.
- 7) The DIS Bulletin continued publication on a regular, bimonthly basis.
- 8) A personnel and networking survey was distributed in order to obtain electronic addresses for Project personnel. The information was entered into the CDDIS data base and was then used to compile a Crustal Dynamics Project personnel and networking directory. The on-line networking service enables Project affiliates to contact each other through computer networks for communication and limited data transfer purposes. Instructions for sending messages between networks are also included in the document and are available in the CDDIS.

Future plans include increasing the archive and cataloguing of GPS data sets. Software for direct GTE TELENET and BITnet network connections will be procured and installed on the CDDIS MicroVAX, thus increasing the connectivity of the system with the worldwide user community. Feasibili-

ty tests will be conducted to determine if optical disk technology will aid in the archiving of preprocessed SLR, VLBI, and GPS data sets in the CDDIS.

Contact: Carey E. Noll
Code 634

Sponsor: Code EEG

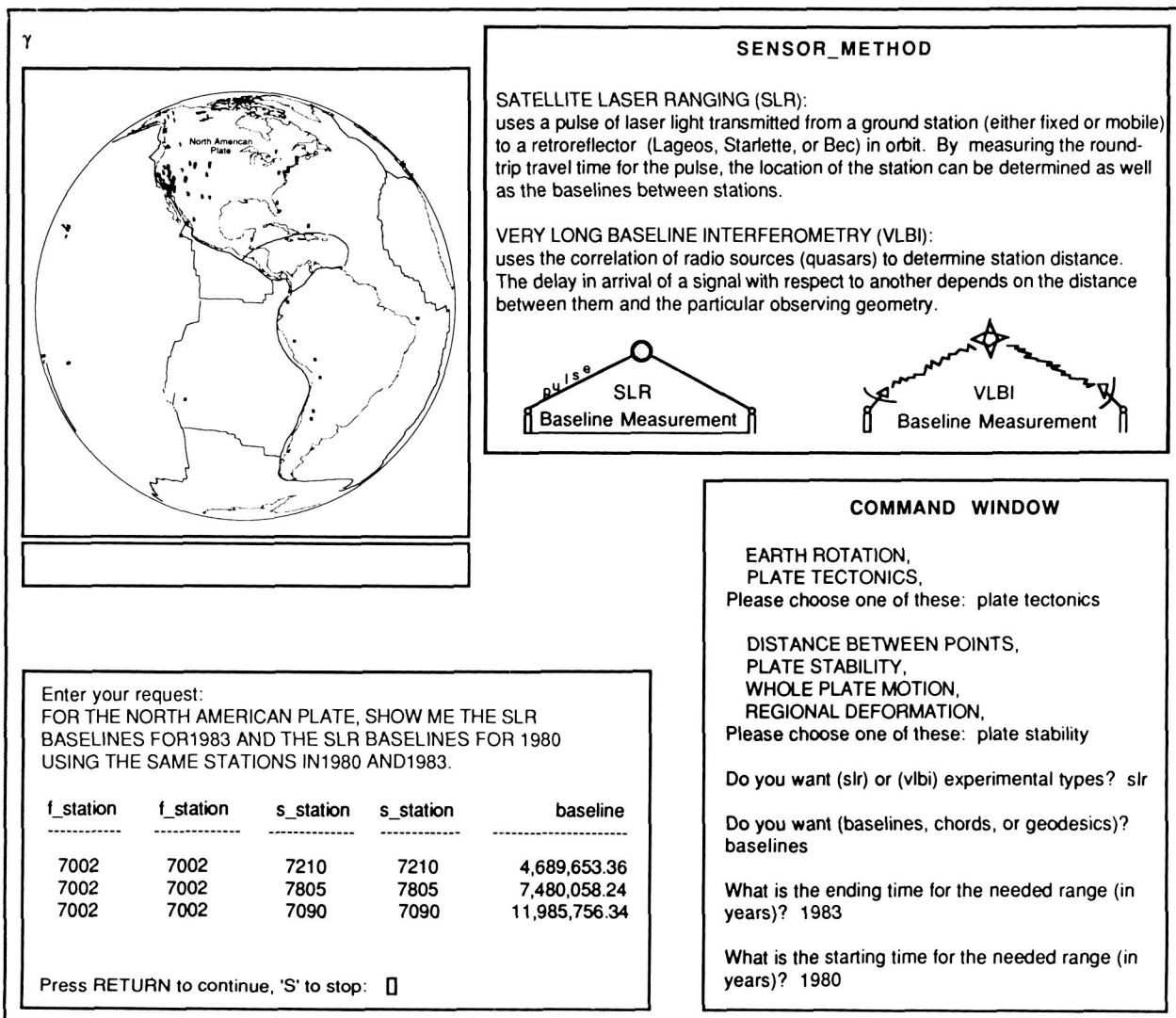
Ms. Carey E. Noll is Data Manager for the Crustal Dynamics Project, overseeing the Crustal Dynamics Data Information System (CDDIS) and the management of the CDDIS MicroVAX computer. Ms. Noll, who holds a BA degree in mathematics from Western Maryland College, has 7½ years of experience at Goddard.

ADDING INTELLIGENCE TO SCIENTIFIC DATA MANAGEMENT

The objective of the Intelligent Data Management (IDM) project was to develop a general capability allowing users to interact with a large operational scientific data base. Utilizing graphics, data, expert knowledge, and knowledge acquisition in an expert system consultation, the user then receives useful spatial data.

Interface designers had two goals: 1) to design and develop a generic interface shell, and 2) to implement and demonstrate a system that allows intelligent interaction with an operational scientific data base. The data base chosen was the Crustal Dynamics Data Information System (CDDIS), which uses the ORACLE relational data base management system (DBMS) at the National Space Science Data Center Computer Facility (NCF).

The first year of research resulted in the development of a moderately capable rapid-prototyped expert system that allows users to graphically interact with spatial objects (for example, crustal plates superimposed on a mercator projection of the Earth). These objects are employed in the reasoning process of the expert system by translating the objects into language symbols. Once sufficient information is gained about a user's data needs, the expert system forms a data base query by constructing an English language question. The English language question is then sent to a natural language query processor (THEMIS by



An example screen from the IUI running on the SUN 3/260 workstation. The individual windows show the dialog with the expert sytem, the dialog of the natural language query processor, the resulting output from the DIS and the 3D graphical spatial data selection.

Frey Associates) on the NCF VAX computer. There it is translated into Structured Query Language (SQL) (a popular relational data base query language) and then dispatched to the CDDIS for data retrieval.

Although the prototype provided for limited access and expansion capabilities and showed a proof of concept, it was limited in size and not transferable to other application domains. Because the goal was to develop a generic interface, an alternative microcomputer workstation (SUN 3/260) was

selected. This workstation contains a state-of-the-art expert system (Automated Reasoning Tool, ART, by Inference Corporation), Natural Language Incorporated (NLI) Data Talker natural language query processor, Sybase DBMS, three-dimensional graphics (Figaro, by Template Graphics Software), advanced spatial data management software, knowledge acquisition of expertise (Advice Taker/Inquirer, the AT/I, by Dr. Robert Cromp, an IDM member), and Unix operation system portability. Unlike its predecessor, this system emphasizes the architecture of a local

scientific workstation connected to a larger, central data management facility. This means that the tools available to the scientist are, in general, the same as in the larger system, except that the nature and amount of data vary. The scientist can capture data into his system allowing him to modify his data, as well as the structure (for example, the domain knowledge) of the interface. Customization of the workstation then means changing the local knowledge base (which is a subset of the central knowledge base), the data base data structures (such as Sybase on the Sun), and the data per se to fit the scientist's needs. Access to information can then be a query to either the local natural language front-end (Data Talker), or the central DBMS natural language front-end (THEMIS). This prototype is illustrated in the figure showing an example screen running on the SUN 3/260 workstation.

To address the customization problem, the AT/I allows the expert user to teach the system the declarative and procedural knowledge necessary for problem solving in his domain. Declarative knowledge is entered into the AT/I by means of an object editor, while procedural knowledge is entered in terms of a very high-level English-like language, which is then compiled into executable code. The code is then used by the operational phase of the AT/I to run the customized expert system.

Because many of the data base objects are spatial in nature, several alternative data management prototypes have been acquired to allow the control and indexing of large numbers of spatial objects and associated attribute information. Such a system will allow the user to assign queries that have inherent spatial relationships. Once retrieved, these spatial objects can be cross-correlated with text data from the relational DBMS and expertise from the knowledge base to complete the scientist's analysis.

In general, this approach to the data management problem emphasizes the integration and customization of many commercial development tools and languages. It attempts to build a *data fusion* system with an intelligent controller manipulating the subordinate, commercial packages (e.g., commercial relational DBMS, spatial DBMS, graphics). As a by-product of this paradigm, the scientific knowledge garnered by each scientist on the system would automatically be codified through the AT/I. In

theory, reducing the costs of data access through intelligent control will facilitate the sharing of specific knowledge, as well as data, among multiple disciplines. Thus, these techniques are expected to meet some of the National Aeronautics and Space Administration's most critical long-term scientific research and operational needs because they will enable managers and scientists to access, modify, and utilize data bases as if they were data base experts.

Contacts: William J. Campbell and
Nicholas M. Short, Jr.
Code 634

Sponsor: Code R

Mr. William J. Campbell is the Manager and chief designer of the National Space Science and Data Center's Applied Artificial Intelligence Laboratory and currently is Space Data and Computing Division's EosDIS System Engineer. He was also the Deputy Project Manager and Systems Engineer and chief designer of the Pilot Land Data System. During his 10 years with Goddard, Mr. Campbell has managed the Eastern Remote Sensing Training Program and served as leading professional in Geographic Information Systems. He was Principal Investigator for the integration of Geographic Information Systems and Remote Sensing Applications. Mr. Campbell holds an MS degree in geography from Southern Illinois University.

Mr. Nicholas Short, Jr. is a member of the National Space Science and Data Center's Applied Artificial Intelligence Laboratory. He was responsible for the design and development of the Crustal Dynamics Data Information System Intelligent User Interface. Mr. Short holds a BA in mathematics and statistics and a BS in systems analysis from Miami University (Ohio), and has two years of experience at Goddard.

DISCIPLINE-INDEPENDENT STORAGE AND MANIPULATION OF DATA

The National Space Science Data Center's (NSSDC) Common Data Format (CDF) is a self-describing data abstraction for the storage and manipulation of multidimensional data. This abstraction, which consists of a software package and a self-describing data structure, is a result of some of the NSSDC's applied



computer science work. Since the CDF is designed to support any scientific application in a discipline-independent fashion, it is a powerful tool for the development of systems that can archive, manage, manipulate, display, or analyze data. For example, the CDF has been used to develop a number of generic data management, display, and analysis capabilities for a wide variety of disciplines at the NSSDC. In addition, CDF is designed to be portable, so that copies can be made available on computer systems outside of the NSSDC, promoting the exchange of both software and data. In fact, over 90 organizations outside of the NSSDC representing various National Aeronautics and Space Administration (NASA) laboratories, research groups, and current and future flight projects, as well as other Government agencies, universities, corporations, and foreign institutions are currently using or have requested the CDF software package. These organizations are using CDF for the development of software to archive, manage, manipulate, display, or analyze data in a variety of disciplines. As a result, the CDF development efforts have become a *standard* method for storing space and Earth science data for a variety of applications.

CDF has been critical to the success of the NSSDC's Coordinated Data Analysis Workshop (CDAW) 8 activity; CDAW 8 participants have produced scientific results from data interpretation and analysis at an unprecedented rate. CDF was used to manage a diverse solar-terrestrial physics data base (more than 50 different data sets) that was a driver for various generic (i.e., CDF-based) data analysis and display tools. CDF will be used to support the upcoming CDAW 9 activity, also in solar-terrestrial physics. In addition, CDF is a key element in the NSSDC's NASA Climate Data System (NCDS), providing a mechanism for climate researchers to work easily with data on line.

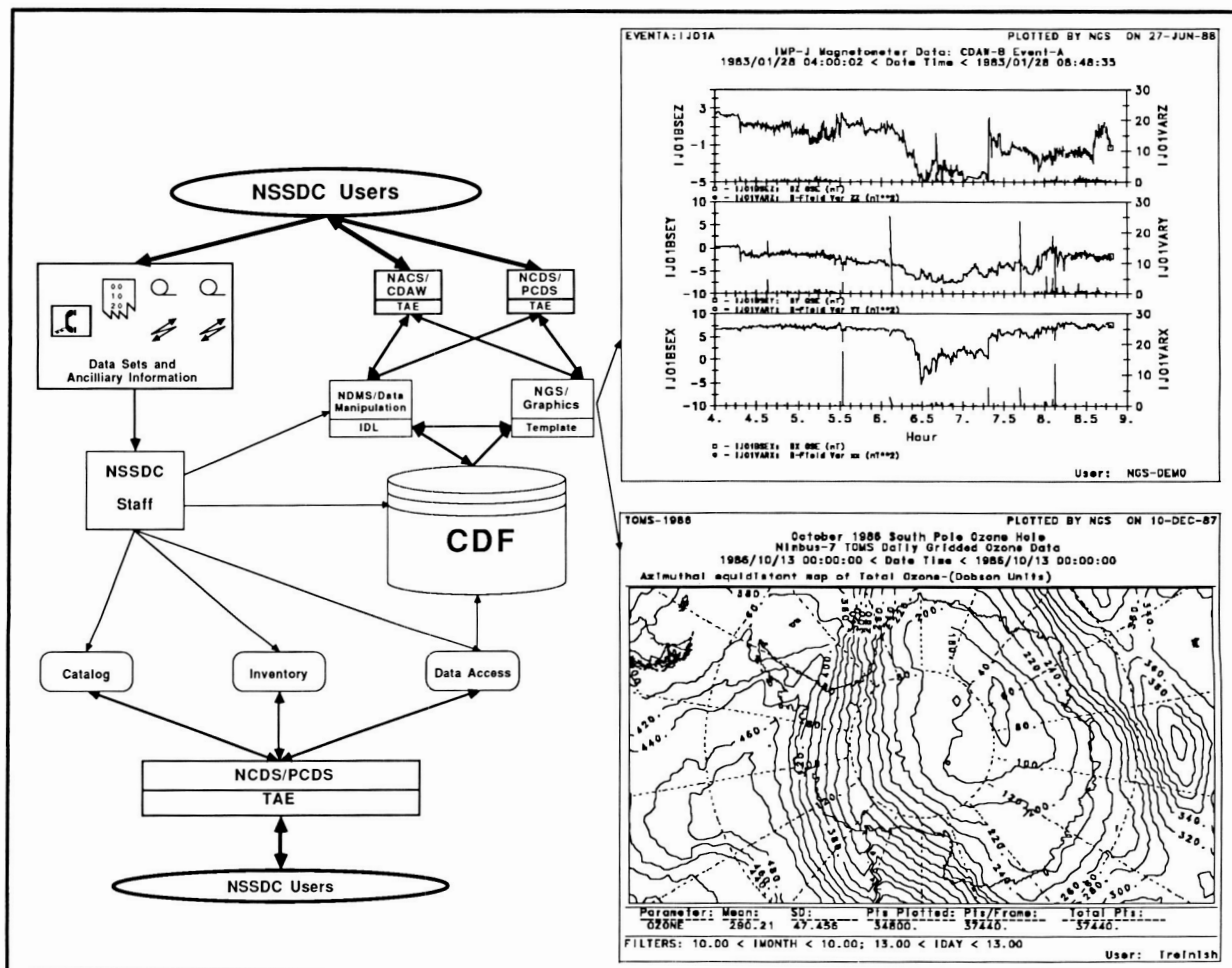
Although FORTRAN language bindings for CDF are now operational on DEC VAX/VMS computer systems, NSSDC's efforts to create generic data storage structures have not stopped. C language bindings have been developed and are being tested for VAX/VMS, IBM MVS and VM, and UNIX (e.g., Sun, AT&T) environments, and coupled with conversion utilities to move the physical files composing a CDF from one computer system to another transparently. For example, software has been im-

plemented to transparently migrate CDFs from the NASA Space and Earth Science Computing Center IBM 3081 to any networked VAX/VMS system (i.e., over the Space Physics Analysis Network, SPAN). These developments will be enhanced for distributed access over local area networks. This Distributed or Network CDF is being developed as part of a joint effort with the Unidata Program, sponsored by the National Science Foundation through the University Corporation for Atmospheric Research. The Unidata Program has adopted CDF as its data storage standard for all applications. Since the implementation of the CDF data abstraction really implies an extension of a conventional programming language for the support of multidimensional data objects, a recasting of CDF into an object-oriented environment such as C++ will be pursued.

The CDF effort involves the integration of various physical science disciplines with the computational sciences. Its goal is freeing the researcher from the need to work with specialized data structures or formats. Such activities will further the use of heterogeneous computer systems to support the management, analysis, and display of any scientific data.

The accompanying figure illustrates the role of CDF in the data systems that support two of the NSSDC's programs, the Coordinated Data Analysis Workshop (CDAW), and the NASA Climate Data System (NCDS). In addition, the sample plots in the figure show the diversity of the data sets that can be supported by CDF. They were generated by a CDF-based application.

The top plot on the right illustrates data about the Earth's magnetic field derived from the Interplanetary Monitoring Platform (IMP)-J spacecraft. These data were among the ensemble of data sets that formed the CDAW 8 data base. This plot is divided into three panels, one each for the x, y, and z components of the magnetic field. Each of the traces is for some five hours of in situ observations by the IMP-J magnetometer on January 28, 1983. The right-hand series of three traces is for the magnetic field components in units of 10^{-9} Teslas, which are marked by a circle. The left-hand traces are for the variance of the components in units of 10^{-18} Teslas².



NSSDC Common Data Format (CDF) Applications and Information Flow.

The bottom plot on the right illustrates data from the Total Ozone Mapping Spectrometer (TOMS) on board the Nimbus-7 spacecraft. The data are available from the NSSDC as daily world grids (37440 cells per grid) from late 1978 through the present; they are supported by the NCDS. These data have become increasingly valuable because they indicate the presence of the so-called *ozone hole* over the south pole. This plot shows the internal structure of the ozone hole for October 13, 1986 projected in an azimuthal equidistant map centered over the South Pole so that Antarctica fills the viewing window. The contour lines of total ozone are incremented every 20 Dobson Units.

Contacts: Lloyd A. Treinish and
Gregory W. Goucher
Code 634

Sponsor: National Space Science Data Center

Mr. Lloyd A. Treinish is a data analysis mathematician with nine years of experience at Goddard. He works on the development of advanced data systems for support of scientific applications, as well as studying space and atmospheric phenomena. Mr. Treinish developed the concept of using the Massively Parallel Processor as a computational geometry server. He was the chief designer and developer of the Pilot



Climate Data System, and he conceived of the first self-describing data abstraction for the storage and manipulation of multidimensional data, as the Common Data Format. Mr. Treinish has an SM degree in physics from the Massachusetts Institute of Technology and has received four NASA Certificates of Outstanding Performance.

Mr. Gregory W. Goucher provides technical support for the development and implementation of scientific software applications at the National Space Science Data Center. He has a BS in information science and five years of experience as a programmer/analyst at Goddard.

A 150 MOPS GaAs 8-BIT SLICE PROCESSOR

Goddard Space Flight Center has engineered the architecture, circuit design, and test results for a gallium arsenide (GaAs) 8-bit slice processor integrated circuit. The device is a high-speed cascable element intended for use in MIL-STD-1750A computers, RISC systems, signal processors, and numerous other applications where high-speed and radiation hardness are required. The bus-oriented architecture features a 31-word by 8-bit, 2-port register file; a fast 8-function arithmetic logic unit; an 8-bit address port; an 8-bit bidirectional data port; and associated shifting, decoding and multiplexing functions. Ancillary logic commonly mechanized in external hardware is included on chip. The 9400-transistor large-scale integration device demonstrates peak performance above 150 millions of operations per second (MOPS) at 9.2 W; a lower power version executes 100 MOPS at 4.2 W.

The concept and design of this GaAs 8-bit slice processor reflect an effort to exploit advances in device technology with new approaches to architecture and circuit design. The bus-oriented architecture and the circuits used to implement it maximize the advantages of the GaAs depletion mode field effect transistor technology and mitigate its limitations. The processor is tailored for the MIL-STD-1750A computer, but due to the flexible microcommand structure a variety of applications are foreseen including reduced instruction set computer and signal processing. The 9400-transistor chip has been successfully fabricated, with working devices executing 150 MOPS.

Contact: Warner H. Miller
Code 728

Sponsor: Office of Aeronautics and Space
Technology

Mr. Warner H. Miller, who received an MS degree in applied science from George Washington University, has been with Goddard since 1961. He designs advanced flight instrument signal processing with the Instrument Electronic System Branch. Mr. Miller's interests include data processing, telemetry, channel encoding, and communications.

PRECISION THERMOMETRY FOR CRYOGENIC TELESCOPE SYSTEMS

The Goddard Space Flight Center engineering staff are currently developing instrumentation to perform high-resolution, high-speed measurements of temperature in the 0.1 °K to 4.4 °K range. Temperatures such as these are required by the newest generation of telescopes that make measurements in the infrared region of the electromagnetic spectrum. In most telescope applications, it is important to know the temperatures that are achieved to better than 0.1 milliKelvin (1/10,000 °K).

The proposed refueling of long-lived cryogenic satellites also places demands on the thermometry system for the determination of the mass and physical state of the cryogen in the tanker Dewar. The Superfluid Helium On-Orbit Transfer Experiment (SHOOT) is a current project of this type.

At these extremely cold temperatures the choice of devices to measure temperatures is severely limited. Sensing is typically done using a small chip of Germanium which is lightly "doped" with impurities. This device, similar to the "cat's whisker" of early crystal radios, is known as a Germanium Resistance Thermometer (GRT). These elements are read out using tiny currents and appropriate processing to extract the resistance signal from the noise. The reading of these voltages at the ends of cables which may be 25 feet long, with temperature-dependent voltages at every contact between dissimilar metals and signal losses in the cables, at a rate in excess of once per second, presents an engineering challenge.

The National Aeronautics and Space Administration has developed a new technique to sense the GRT which combines the best of the two worlds of analog and digital signal processing. The technique is implemented in a compact and reliable system that can survive the space environment.

The method used to read the sensor is based primarily on the classic technique known as synchronous demodulation. The theory can best be explained with the block diagram shown in the figure. A crystal oscillator and a counter chain generate addresses for memory chips at point B. The data in the memories which represent a sine wave at the cycle rate, about 16 Hz, is applied to a digital-to-analog converter (DAC) which produces a sinusoidal output at point C. This output, known as the carrier, is converted by a current source to a balanced differential current of less than 1 microamp root mean square (RMS). A balanced design minimizes errors caused by the cable system.

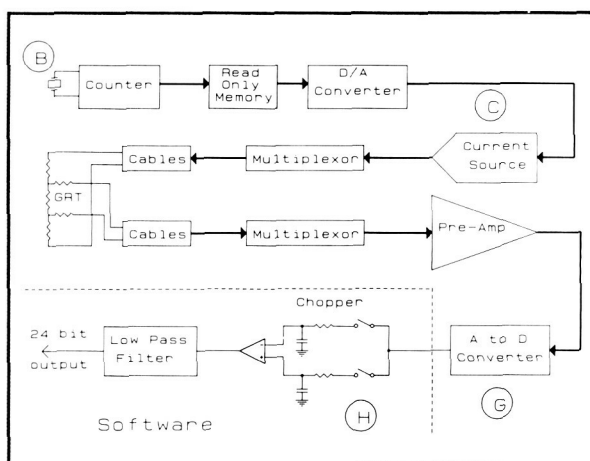
This current drives the GRT, through the cable, at point E. The signal between the two sense leads is selected by the multiplexor and amplified by an amplifier configuration known as an Instrumentation Amplifier, at point F. This preamplifier has a very high input impedance on each input lead on the order of gigaohms and amplifies the voltage differential between the inputs while attenuating the common voltage between the input leads and circuit ground. The ratio of differential to common mode gain is around 120 dB, or about a million to one.

The frequency of the signal is chosen high enough to minimize the effect of one-over-f noise in the preamplifier and low enough to keep the effects of capacitance in the cable system within acceptable limits. $1/f$ noise, sometimes referred to as pink noise, is a noise phenomenon that has a frequency spectrum proportional to the inverse of frequency. It is this noise which is the source of an alternating current (ac) amplifier's superiority over a direct current (dc) amplifier.

At point G, the output voltage of the preamplifier is sampled at the maximum rate of an analog-to-digital converter (ADC), about 10 kiloHertz. A digital simulation of the function of a synchronous demodulator is performed in software. It is desired to measure only the component of the returned signal

that is at the same frequency and in phase with the excitation signal. All other signals represent contamination by capacitance and external noise. Since the timing of this signal is stable and precisely known, a narrow bandpass filter can be applied at the carrier frequency. This is accomplished digitally in software. It is represented schematically at point H in the figure by a relay, resistor, and capacitor chopper. Since the simulated capacitor shows no soakage, we have effectively eliminated a problem that limited the accuracy of previous designs. Precise phase shifts can be programmed to provide optimum measurement of the magnitude and phase of the signal in the presence of systematic phase shifts caused by the cable capacitance and resistance. Since all state variables are under software control, the low-pass filter is essentially presettable (that is, each measurement has no memory of any previous measurement). This means that settling time, a major issue in previous designs, is now a nonissue. The bandwidth of the synchronous demodulator is limited only by the allowable integration time, thereby allowing an almost arbitrary signal-to-noise ratio. An integration time of 1 second has been chosen for SHOOT. Missing code problems in the ADC are eliminated because the system output represents the result of a large number of individual conversions at different places within the converter's range.

The result of this measurement process is a high-precision, 24-bit digital word which is generated rapidly compared to other designs.



GRT measurement block diagram.



A key component of the system is a real-time dynamic calibration process that uses the output of calibration channels to form a correction to the raw data. The accuracy of the system can be enhanced by a factor of 10 over that obtainable without correction. A mathematical algorithm could be executed in real time in the ground control equipment, the on-board aft flight deck computer, or conceivably in the measurement system itself. With this algorithm, the system will work up to its full potential over the severe ranges of ambient temperatures found in the space shuttle cargo bay.

Recent tests have shown a temperature resolution of 7.7° microkelvin over a range of 3°K . Stability is limited by the stability of the calibration resistors. Construction of a flight unit is underway for the SHOOT project.

Extension of the techniques described herein are expected to enhance the precision and speed of the system. The need for precision thermometry at lower cryogenic temperatures is expected to increase in the future. Space and power may be reduced considerably if the entire thermometry system is fabricated on a single chip. There is also interest in production of circuits that could work inside the Dewar at very cold temperatures. This would eliminate the bulk of the delicate wiring and long cables between the readout electronics and the sensors.

Contact: Christopher E. Woodhouse
Code 728

Sponsor: Office of Space Flight

Mr. Christopher E. Woodhouse is an electronics engineer in the Instrument Electronic System Branch with four years of service at Goddard. He received his MS degree in electrical engineering from the Georgia Institute of Technology, and is currently involved in instrumentation for Goddard payloads including COBE, SHOOT, and XTE.

CUSTOMER INTERFACE ADAPTER FOR THE STAR*BUS

The STAR*BUS is a brassboard 100-Mbs fiber optic local area network (LAN) targeted for advanced flight data systems. The Customer Interface Adapter

(CIA) provides a means of connecting standard user data interfaces into the high-rate STAR*BUS LAN. These interfaces include digitized video (RS-170), digitized audio, analog signals, high-speed serial data (RS-422/449), TTL level discretes, relays, RS-232 serial protocol, and a parallel data bus (IEEE 488). The CIA is utilized to collect, convert, and transport data to host computers, other CIAs or through gateways or bridges to other LANs. Expected users of the CIA are payloads, sensors, actuators, and workstations.

One requirement of the CIA architecture is to utilize as much off-the-shelf hardware as possible, to minimize engineering development costs. The CIA architecture utilizes a Motorola 68020 microprocessor developed in a VMEBUS backplane. This high-power microprocessor allows the CIA to achieve a 10-Mbs full duplex data rate while providing a low latency. The utilization of the VMEBUS backplane renders a very modular design for the CIA, allowing the addition of other standard interface modules as desired.

The results of a tradeoff study conclude that, in order to increase throughput of the CIA, *smart* user interfaces are required. To that respect, several of the high processing requirement interfaces have their own microprocessors in order to prevent the overloading of the 68020 system microprocessor. This allows us to support Consultative Committee for Space Data Systems (CCSDS) proposed data packetization standards with the CIA.

The CIA interfaces with the STAR*BUS through a High Speed Interface (HSI) with the STAR*BUS's Bus Interface Units (BIUs). This port on the BIUs transmits and receives serial data at a burst rate of 32 MHz. This is the only custom board in the CIA and additionally provides multiple data packet buffers for data transmission and reception.

The CIA and the STAR*BUS are being tested to provide information for Space Station and Platform contractors for identification of early technological risks in data management systems.

Contact: Kenneth A. LaBel
Code 735

Sponsor: Office of Space Station

Mr. Kenneth A. LaBel is a graduate of the Johns Hopkins University with a BES degree in electrical engineering. Mr. LaBel has been at Goddard since 1983, working on both ground and flight data

systems. He has also worked at the University of Maryland as a special student and is currently working on a Masters degree in electrical engineering at the Johns Hopkins University.

TECHNIQUES

STRENGTH TESTING OF GLASS AND CERAMIC MATERIALS

The increasing size of optical components made from glass and ceramic materials requires that these components also be used as structural members. These materials are brittle, and are selected for properties other than their structural qualities. Parameters needed for design with these materials are: the strengths associated with inherent and machining flaw populations, and the environmentally dependent crack growth rate. The determination of these parameters is critical for predicting the lifetime of these components.

The configuration commonly employed to test glass and ceramic materials is a rectangular specimen loaded in three- or four-point flexure. The disadvantage in using rectangular specimens is that they often fail from edge flaws that are not representative of the flaw population under interrogation. A recently promoted alternate test configuration is ring-on-ring loading. This test configuration is desirable because the specimen edge is well away from the maximum bending stress; edge failures are thus eliminated. An additional advantage of the ring-on-ring specimens is that the manufacturing costs are much lower than those of the rectangular bend specimens. Problems associated with the ring-on-ring configuration occur due to uncertainties in the surface stress, caused by variations in fixtures between test facilities. A test program was implemented to validate this test technique, in preparation for the acquisition of design parameters to support flight projects.

Researchers verified that the actual maximum surface stress on the specimen agreed with that predicted by theory by monitoring surface strain through strain gauges. The actual surface strain was then compared

to that predicted by theory, calculated using the applied load, and fixture geometry.

Results of the verification testing indicated that commonly used test techniques can give rise to large errors in test results. It was found that a small piece of tape, placed on the compressive surface to hold the specimen together after fracture, causes a 5–10 percent greater-than-predicted surface stress. Analysts feel that this increase in stress is due to the tape's creation of a smaller effective loading diameter.

A ball bearing with a ground face is commonly used to apply the inner ring load to the specimen. It was found that using the ground ball bearing also causes a 5–10 percent greater-than-predicted surface stress. The degree of error is dependent on the aspect ratio between loading and support diameters. This discrepancy can be alleviated by using a small thrust bearing as the loading ring.

The qualification of the testing procedures will ensure the acquisition of accurate data that will then be used to predict the lifetime of components on spacecraft.

Contact: Michael J. Viens
Code 313

Sponsor: Office of Safety, Reliability,
Maintainability, and Quality Assurance

Mr. Michael J. Viens of the Materials Branch has an MS degree in mechanical engineering. With two years of Goddard experience, Mr. Viens is responsible for mechanical testing of ceramic, metallic, and polymeric materials and for subsequent evaluation of test results. He is also involved in ultrasonic



(nondestructive) evaluation of materials and inductively coupled plasma spectroscopy.

AN AUTOMATED PARTICLE-COUNTING SYSTEM

The aerospace industry is very concerned about the destructive potential of contamination. There are a host of documented cases of contamination-related loss or degradation of spacecraft instruments. As a result of this experience the National Aeronautics and Space Administration's (NASA) Centers have established control programs to safeguard spacecraft components from destructive contamination.

Monitoring of spacecraft assembly and integration areas is an essential aspect of the contamination control program. To this end, "witness plates" are frequently placed in clean areas. These mirrors are examined for contaminants after a specified period of time. Military Standard 1246A established surface cleanliness standards for two classes of contaminants: Nonvolatile residue (NVR), and particulates. One technique for determining surface cleanliness is the



NASA/GSFC automated particle-counting system prototype.

manual counting of particles by an operator with a microscope. This process is repetitive, tedious, and a good candidate for automation.

An automated system for the assessment of particulate contamination would improve the contamination control process. Automated particle-counting systems do exist, but many have price tags exceeding \$50,000. The system that was developed using existing NASA/Goddard Space Flight Center hardware could serve as a prototype for a microcomputer-based system and would be significantly cheaper. The accompanying photo shows the prototype.

The particle-counting system consists of the following components: a laminar flow bench, a microscope with computer-controlled stage, a vidicon television camera, a minicomputer-based image-processing system, and a PC XT-compatible computer. The first figure shows a schematic of the system.

The microscope system provides magnified images (roughly 195 times the original size) of particulates on a silicon wafer. Particles appear as bright, white objects against the dim, featureless background of the silicon wafer. The microscope is housed in a Class 100 tabletop laminar flow bench to prevent "post-witnessing" contamination of the wafers. The microscope's stage can be commanded remotely (via a serial communication port on a controlling unit) to travel over a 2 in. by 4 in. range. A vidicon television camera is mounted on the microscope, and provides an RS-170 composite video signal for the image processor. (RS-170 is a video signal standard.)

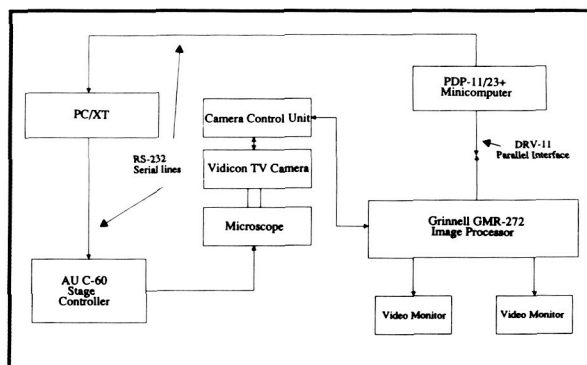
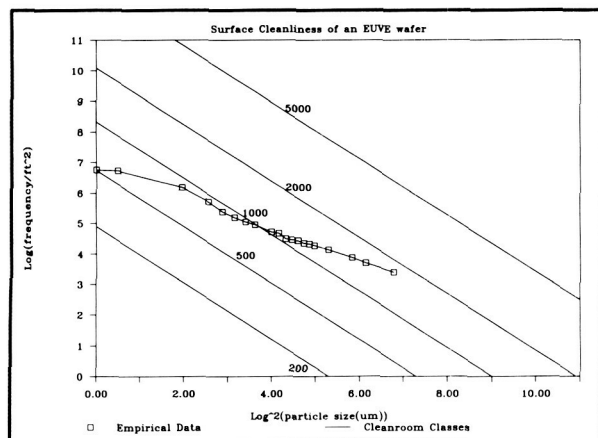


Diagram of automated particle-counting system.



Military Standard 1246A surface cleanliness data.

The image-processing system consists of a Grinnell GMR-272 digital image processor connected to a DEC PDP-11/23 + minicomputer. The PDP-11 controls the image processor completely, by way of Fortran-callable subroutines. The particle counting and sizing is performed by custom software, written in Fortran for the PDP-11. Both the cross-sectional area and apparent size of particulates are determined (minimum detectable particle size is about $5\mu\text{m}$). The PDP-11 sends these data to the PC XT, which stores it, and sends commands to the stage controller.

The particle-counting system produces Military Standard 1246A data from silicon wafers used as "witness" mirrors. The second figure shows sample data of this type. The system determines surface cleanliness by examining a portion of the wafer surface. The process is less labor-intensive, and less tedious, than the manual method. The only operator intervention required is occasional adjustment of microscope focus. The system has been configured so that a microcomputer-based imaging system can replace both the Grinnell image processor and the PDP-11 minicomputer. This upgrade of the system offers the potential of faster, and more sophisticated processing. An autofocus mechanism is also a possible upgrade, since it would reduce the need for operator intervention.

Contact: J. Timothy Van Sant
Code 313

Sponsor: Office of Flight Assurance

Mr. J. Timothy Van Sant, with a BS degree in electrical engineering, works in the Materials Branch. Mr. Van Sant investigates the materials applications of image processing. Throughout his three years at Goddard, he has also been involved in the automation of materials testing.

FRACTURE TOUGHNESS OF SiC/A1 METAL MATRIX COMPOSITES

Researchers of the Materials Branch at Goddard Space Flight Center recently conducted a study evaluating the fracture toughness of SiC/A1 metal matrix composites (MMC). The materials were 12.7-mm thick extrusions of 6061 aluminum alloy, with 40 volume percent SiC particulate. They were tested in the T6 temper. Specimen configuration and test procedures conformed to the American Society for Testing and Materials (ASTM) E399 Standard Test Method for Plane Strain Fracture Toughness of Metallic Materials for compact tension specimens.

Researchers found that special procedures were necessary in the preparation of precracked specimens for the MMC materials to obtain fatigue cracks of controlled lengths. Initial efforts failed to produce the precrack by conventional methods, because once the fatigue crack started, it would instantly propagate throughout the entire specimen. To avoid this problem, fatigue loading with both minimum and maximum loads in compression was used to start the precrack. The initial precracking would stop by self-arrest. Afterwards, the precrack could be safely extended to the desired length by additional cyclic tension loading.

Test records of the specimens were analyzed according to ASTM Standard E399. The results met practically all of the criteria for the calculation of plane strain fracture toughness of the materials. A valid K_{Ic} value of the SiC/A1 composites was established as

$$K_{Ic} = 8.9 \text{ MPa } \sqrt{\text{m}}$$

Fractographic examination was performed on the specimens using a scanning electron microscope. In the area of precrack, there was more extensive plastic deformation due to cyclic tension than to compres-



sion loading. The fracture surface consisted of fine dimples, indicating that fracture occurred by the micromechanism of void coalescence.

Contacts: Yury Flom, Bradford H. Parker, and
H. P. Chu
Code 313

Sponsor: General Electric (Aerospace Division)

Dr. Yury Flom received his PhD degree in materials engineering from the University of Maryland. Dr. Flom is involved in materials engineering, testing, evaluation, and failure analysis services provided to Goddard and other NASA facilities.

Mr. Bradford H. Parker received a BS degree in chemical engineering from Virginia Polytechnic Institute and State University. He is currently a materials engineer in the Materials Branch working in the areas of scanning electron microscopy, failure analysis, materials characterization, and nondestructive evaluation.

Dr. Huai-Pu Chu has served as senior metallurgist with the Materials Branch since 1982. He provides technical support to flight programs in the areas of fracture, fatigue, creep, and stress corrosion of metals; and testing and evaluation of materials for spacecraft applications. He holds a PhD degree in metallurgy from the Colorado School of Mines.

REACTION TORQUE MINIMIZATION TECHNIQUES FOR ARTICULATED PAYLOADS

Articulated payloads on spacecraft, such as antenna systems and robotic elements, impart reaction torques back into the vehicle that can significantly affect the performance of other payloads. This disturbance can degrade the quality of the data obtained by other onboard experiments and systems.

To minimize the reaction torques of articulated payloads through command-shaping algorithms and unique-control implementation, a Dynamic Offset Gravity Balance (DOGB) facility (shown in photo) has been developed. This facility is the culmination of a multiphase development effort to evaluate control techniques and implementations to minimize

reaction torques. The DOGB will allow full up testing of articulated systems by offloading gravity effects to the experiment under test and measuring the actual reaction forces and torques under various operational maneuvers. Measuring capability of the DOGB allows post processing of the reaction torque data to predict on-orbit disturbances with given structural models of the spacecraft.

The need to measure and predict torque disturbances of articulated payloads is best realized by experiences encountered on past missions. One example is the LANDSAT-4 satellite. The LANDSAT-4 payloads include a Thematic Mapper (TM) and a Multi-Spectral Scanner (MSS). Both sensors are imaging instruments, sensitive to onboard disturbances, which collect spectral radiation data of (lighted) land masses. A typical attitude deviation response in the roll axis during a Tracking and Data Relay Satellite (TDRS) antenna program track startup, is greater than 400 arc seconds, peak to peak. This operation is a slew type maneuver to point the antenna and acquire the satellite and produces a relatively large deviation that can affect the data.

To provide autonomous gravity offloading capability over the relatively large excursions of articulated systems, the DOGB employs three active control loops. These loops track payload horizontal motions and maintain a constant vertical gravity offloading force on the payload.

This active gravity offloading technique finds particular application in testing and evaluating articulated payloads such as gimballed antenna pointing systems. By selectively determining the payload attach point and cable tension based on the mass properties of the payload and intermediate gimbal structures, the net gravity-induced torques at each gimbal are cancelled. This allows the system to be tested over nearly full operating excursions in a 1-g environment.

To measure reaction forces and torques of the system under test during operational maneuvers the DOGB facility incorporates a six-degree-of-freedom Force Measurement System (FMS) mounted on the floor beneath the DOGB fixture. The FMS is composed of a wide range dynamometer and control electronics package. The dynamometer consists of four 3-component force measurement sensors which are

ORIGINAL PAGE
BLACK AND WHITE PHOTOGRAPH



DOGB fixture with simulated planar array antenna, gimbal pair, and force measurement system.

used to provide three axes of force and three axes of torque measurement capability.

With the given offloading and reaction force and torque measurement capability the DOGB system allows better dynamic interactions and performance predictions to be for articulated systems prior to in-flight operation.

The current status of the DOGB facility is a full size working demonstration unit with a simulated payload and gimbal pair for offloading verification. These simulated gimbals are in an elevation/lateral configuration and are based on those used for High Gain Antenna System on the Solar Maximum Mission satellite. Also included is an active gimbal pair for control law verification and later DOGB integration.

The active gimbal pair are digitally controlled and in an elevation/azimuth configuration. In this configuration the azimuth gimbal requires no gravity offloading in its degree of freedom and the elevation gimbal can be counterbalanced with weights to over-

Some of the current dynamic properties of the DOGB facility are given in the table.

Dynamic Offset Gravity Balance Characteristics	
Payload Weight	5 to 100 pounds (can be upgraded)
Static Balance	< 5% gimbal torque capability
Z Force Loop Bandwidth	> 20 Hz (3 dB closed loop)
Z & Y Position Loop Bandwidth	> 5 Hz (3 dB closed loop)
Payload Motion (X,Y,Z)	> ± 2 feet

come gravity induced torques. This allows control law testing of the gimbal without the DOGB fixture.

As an overall effort to measure and improve reaction force and torque disturbances on spacecrafts, the DOGB study contract is also evaluating unique control law implementations. These evaluations include adaptive slew maneuver control and static/slow-moving tracking type reaction control.

Contact: Roberto M. Alemán
Code 727

Sponsors: Code T and Office of Space Operations

Mr. Roberto M. Alemán, who has a BS degree in biology and electrical engineering, works in the Antenna Technology Section of the Radio Frequency and Microwave Technology Branch. His interests include antenna gimbal and control systems. Mr. Alemán has one year of experience at Goddard.

DEVELOPMENT OF GUIDELINES FOR ROBOTICALLY SERVICEABLE HARDWARE

The use of robots to perform on-orbit autonomous servicing and assembly of spacecraft will greatly increase the productivity and safety of working in



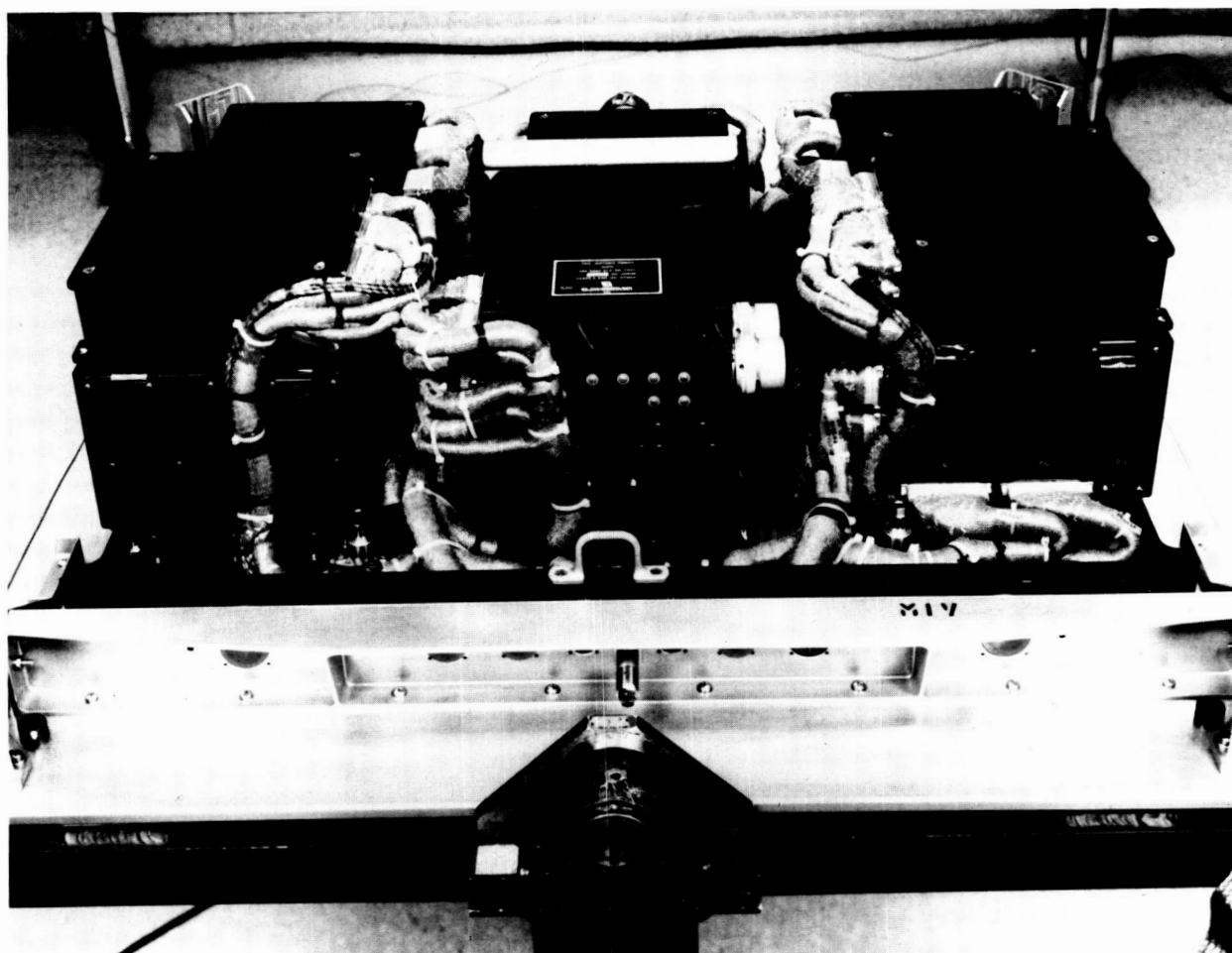
space. The capability for autonomous robotic servicing requires the development of robots that can make real-time decisions about how to implement the tasks assigned to them. It also requires spacecraft that have been designed for servicing in such a way as to exploit the strengths and minimize the weaknesses of those robots.

The research being conducted at Goddard Space Flight Center is an attempt to examine the inter-related issues of "intelligent" robot systems and robot-friendly spacecraft design. One side of this research is therefore directed at the development of path-planning software which can determine the robot motions required to perform a given task. The other is focused on the development of guidelines for the design of spacecraft hardware that can be serviced by robot systems using the path-planning soft-

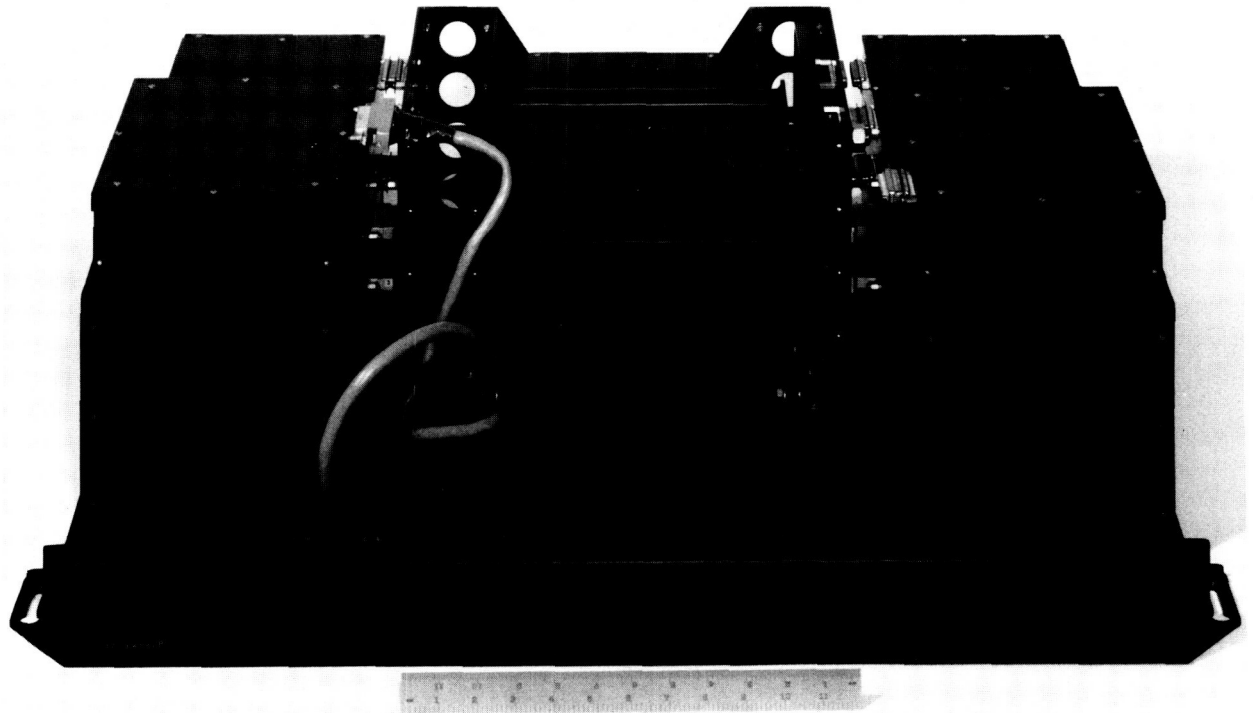
ware. Based on these efforts, a mockup has been developed which represents the application of the identified design guidelines to an existing spacecraft system in order to make it robotically serviceable. The mockup will provide a means of evaluating the design guidelines and serve as a realistic test of the capabilities of the path-planning software.

The design guidelines represented by the mockup were derived from the requirements of servicing a spacecraft in a zero-g environment using two force-feedback robots that are driven by the path-planning software. The guidelines are as follows:

- All components are constrained during servicing.
- Two-handed servicing operations are allowed.



SIC&DH module used on the Hubble Space Telescope.



SIC&DH mockup developed for robotics research.

- All fasteners must be captive.
- Standard hardware must be used where possible.

The mockup is based on the Scientific Instrument Command and Data Handling (SIC&DH) system of the Hubble Space Telescope. The actual SIC&DH (shown in the first photo) consists of 17 electronics modules mounted to a structural tray and interconnected by a wire harness. The SIC&DH was selected because servicing this system would involve both mechanical and electrical connections and would be complex enough to provide a wide variety of servicing operations. The mockup developed for this research (shown in the second photo) maintains the physical layout and dimensions of the original SIC&DH system as well as uses the same type of electrical connectors in order to accurately represent the conditions that might be encountered in robotically servicing the SIC&DH.

Three methods for servicing the electronics modules which meet the design guidelines have been incorporated into the mockup. The bus method involves

plugging the electronics modules into a fixed-bus structure and then securing the modules to the structural tray. The mechanism method uses a worm-and-wheel gearbox to mate a group of connectors once the modules have been secured to the tray. The harness method utilizes a specially designed locking connector shell to allow the wire harness to be plugged in once the modules have been mounted to the tray. All of the above servicing methods make use of captive screws to attach modules to each other as well as to the structural tray. The captive screws eliminate the need to manipulate the screws independently of the modules, an elimination which greatly reduces the number of steps required to perform a servicing task.

Currently work is underway to develop the tooling required to service the mockup using two Cincinnati Milacron T3 robots. The T3 robots will be running the path-planning software against a computer-aided design generated model of the mockup and using real-time force feedback to make decisions about discrepancies between the real world and the



computer-aided design model. The tooling will consist of a gripper that can support interchangeable fingers and a bolt spinner that can operate the captive screws on the modules.

This robotics research provides a link between the development of robot technology for space use and the design of serviceable spacecraft. The design guidelines were derived from the requirements of the robot hardware, the path-planning software, and the servicing environment. The mockup represents how well these guidelines can be applied to an actual spacecraft system. Servicing the mockup will test out the planning software as well as highlight limitations to the design guidelines. The mockup will serve as a test bed to develop and enhance the capabilities for servicing spacecraft robotically.

Contact: Scott A. Gordon
Code 731

Sponsor: Office of Aeronautics and Space
Technology

Mr. Scott A. Gordon is an aerospace engineer in the Mechanical Engineering Branch, with over four years of experience at Goddard. He holds a BS degree in mechanical engineering from the University of Maryland, where he is now pursuing an MS degree in aerospace engineering. Currently, he designs robotic and spacecraft hardware with computer-aided design (CAD) techniques and develops and implements new CAD and computer-aided engineering (CAE) tools for mechanical design.

MYOELECTRIC MAN-MACHINE INTERFACE

This project is being performed to explore the possibilities of using the small electrical currents generated in human muscles during contractions as a source for signals that could be used to control robotic devices. This new man-machine interface would directly, electrically couple the human body to a robotic manipulator. The theory is that the human brain would now be more capable than a slower computer of accurately handling the complex calculations of positioning in three-dimensional space, including velocity and acceleration. The advantage is gained by allowing the brain to use previously learned motor patterns refined since birth.

This more natural control scheme would attempt to eliminate the awkwardness of conventional cybernetic links and require much shorter learning times. Removing these calculations from the computer and placing the brain in the loop would, hopefully, yield a faster, more precise and more easily controlled system.

The basic control and operation of any device is limited by the man-machine interface. Whether the operating device is a joy stick, track ball, or mini-master in a master-slave controller, the result is the same. The operator must spend enough time using the controls to feel comfortable. Only then does the awkwardness seem to disappear and the operator begins to feel in harmony with the device.

But what if the operator could become part of the device from the start? Then his own brain's impulses would control that device directly. Work in the area of prosthetics and reanimation using myoelectric signals has been going on for years. Why not apply this approach for man-machine interfaces?

First one needs to understand myology. One type of nerve is called an efferent nerve. Efferent nerves reach from the brain to a muscle and control contractions. In an efferent nerve the end effector is called a motor unit end plate. A single muscle fiber may be connected to 20-50 different motor units. When the efferent neuron receives enough energy to exceed its threshold, it fires. Firing entails an influx of positively charged sodium ions into the negatively charged axon in order to rectify the chemical imbalance that was generated. This chemically balancing ion flow propagates lengthwise down the axon and generates an electrical impulse-myoelectrical signal. The positive ions are almost immediately pumped out of the axon, and the neuron is ready to fire again. This myoelectrical signal produces an electromagnetic field which can be detected and measured. It is this signal which causes the contraction of the muscle. The impulse conduction velocity of a muscle is slow, at 2-6 meters/second, compared to the neural conduction velocity of 30-75 meters/second. As neural impulses from 20-50 neurons reach a muscle they pile up or superimpose to give an increased amplitude pulse in the muscle. This spacial-temporal superpositioning of pulses is referred to as the motor unit action potential. This is the potential



Signals coming from the human arm, displayed on the left screen, are processed and used to control the robotic arm. The right screen is a graphical representation of arm position.

that is obtained by surface electrodes and used for electromyoelectric (EMG) control.

The approach taken was to concentrate on one degree of freedom, as an example the elbow joint in the axis of elbow flexion/extension. The intention was to also collect data from other degrees of freedom as a basis for a latter expansion, understanding that expansion is not a linear relationship.

On April 15, 1987, a 1-year research grant entitled *The Efficacy of Using Human Myoelectric Signals to Control the Limbs of Robots in Space* (NAG 5-895) was initiated with the University of Maryland. The Principal Investigators for the University were Dr. Jane Clark, Dr. Sally Phillips, and doctoral candidates Jody Jensen and Pam Russell. The expertise of the University was employed in the area of physiology.

The results of the grant provided large amounts of data for different joints and muscle groups of the

arm and shoulder under different specified conditions. Primary interest was in concentric isotonic contractions of the main elbow flexors (i.e., brachialis, brachioradialis, and the biceps brachii) in the sagittal plane. Data collected from surface electrodes showed repeatable EMG signals indicative of the ongoing movements.

These signals are collected through a hybrid amplifier connected directly to the surface electrodes. (See photo.) The signals then pass through an analog rate-of-change correlated adaptive myoelectric filter. Digitalization of these signals is then performed by an analog-to-digital converter (ADC) interfaced to the personal computer (PC) model AT. Because the majority of the energy in the EMG signals is contained below 1 kHz, conversion rates of 5,000–10,000 samples per second, which are readily available for the AT, are more than adequate. The AT can display these signals real time, give a graphical representation of human arm position, or command a robot



to obey these inputs. Software support for these functions is partially provided by Tony Conrad (Code 733).

A custom Andronics Corporation prototype robot containing specially patented Air-Over-Hydraulic actuators was developed for use in this research. This robotic arm complete with five fingers and a 32-bit microcontroller is in turn controlled by the AT and is used to demonstrate the true feasibility of the project.

The actual implementation with all the hardware including the recently received robot is still in the early stages. Currently limited one-degree-of-freedom robotic motion via myoelectric control can be accomplished but is being refined. Complex microcontrollers, communications protocols, and software execution times slow the loop servoing rates with the robotic controller. An upgrade to an Intel 386-based machine is being developed to increase feedback loop rates and thereby improve the response of the system.

This Goddard Space Flight Center Directors Discretionary Fund project has achieved these results with less than \$40,000 of financing, covering both the research grant and all hardware purchases.

Contact: I. Joseph Burt
Code 733

Sponsor: Directors Discretionary Fund

Mr. I. Joseph Burt handles ground-support systems for COBE and is also working on the Flight Telerobotics Servicer Project. He has a BS degree in electrical engineering from the University of Maryland and is currently earning his masters degree from Johns Hopkins University. Mr. Burt has been with Goddard for three years.

PROCEDURAL SAFETY SYSTEM FOR TELEROBOTIC OPERATIONS

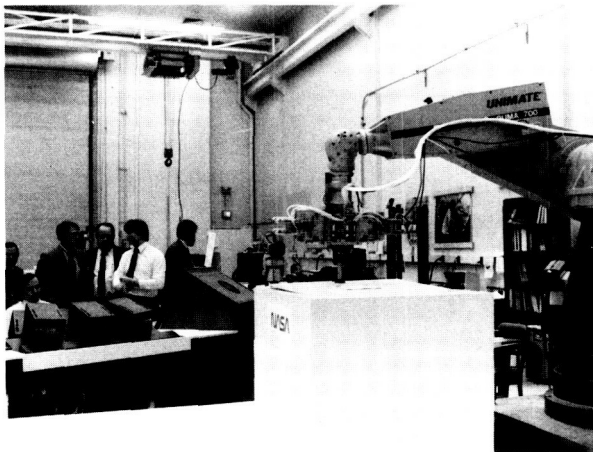
One of the efforts that is currently being made in the Telerobotics Laboratory is the research, design, and development of a safety system for telerobotic operations. Telerobotic operations involve both autonomous and teleoperated control of the robot. The

Flight Telerobotic Servicer (FTS) will be tasked to perform a wide variety of tasks such as refueling a satellite, repairing a satellite, and assembling the trusses for Space Station. These types of tasks incorporate both autonomous and teleoperated control utilizing a great deal of sensing capabilities, thus requiring sophisticated safety systems to ensure the safety of humans, the robot, and the objects in the robot's environment.

There exist several levels of safety for telerobotic control. One level, which is referred to as the Watchdog Safety System (WSS), monitors servo level robot data such as robot joint positions, motor currents, and joint torques to ensure that these readings are within safe limits. This level of safety is concerned mainly with the health of the robot arm and knows nothing about the present step of the task. The safety level that has been implemented in the Telerobotics Laboratory is the Procedural Safety System (PSS). The PSS exists in a higher level of telerobotic control, requiring knowledge of the task that is being performed. It monitors sensor data such as forces and torques at the end effector and gripper status to ensure that the data are within safe operational limits for the present step of the task. The PSS, unlike the WSS, ensures the safety of humans and of the robot environment.

The PSS is presently used in an Orbital Replacement Unit (ORU) demonstration in the Telerobotics Laboratory. (See photo.) The task of replacing an ORU, a generic housing for an experiment on Space Station, is one of the functions that the FTS will be required to perform. The ORU demonstration involves using a PUMA robot to move an ORU from one position on a platform to a second position. The robot then opens the door of the ORU, allowing the robot to repair or replace submodules within the ORU. Prior to implementing the PSS, the ORU demonstration incorporated very few safety checks. The burden of ensuring that the task was operating safely was placed on the operator. The PSS relieves this burden by monitoring sensor data and commands to ensure that the sensor data lie within safe operational limits and reporting anomalies to the operator.

PSS was implemented using the expert system shell NEXPERT OBJECT, which is an object-oriented, rule-based expert system shell. NEXPERT OBJECT



Demonstration of an Orbital Replacement Unit changeout in the Flight Telerobotic Servicer Laboratory.

allows knowledge about the task to be represented in a rule format and reasons about this knowledge to solve a problem. During each safety cycle, NEXPERT OBJECT evaluates and executes only those rules which contain objects, in this case the objects are the sensor data, which pertain to the state of the world. For example, if the force in the X direction exceeds the safe operational limit for a step in the ORU task such as grasping the ORU handle then the rules which contain that object will be evaluated. Currently, the PSS demonstration is limited by sensing capabilities provided by the ORU demonstration. PSS receives force/torque data, end effector status, and ORU position data and joint encoders. If PSS detects an unsafe condition it notifies the operator both visually and audibly. Visual information is provided in a dedicated window on the terminal screen. If, however, the operator is concentrating on the camera monitors and is not looking at the screen, audio information is provided via a voice synthesizer.

The PSS that has been implemented in the Robotics Laboratory has enabled us to begin looking at safety for telerobotic operations. The PSS has made the ORU demonstration easier and much safer to operate. PSS relieves a great deal of the operator load enabling the operator to concentrate on performing the task without being required to monitor the sensor information.

Contact: Maureen O'Brien
Code 735

Sponsor: Office of Space Station

Ms. Maureen O'Brien is an electrical engineer at Goddard. Her current work at the Flight Data Systems Branch emphasizes safety for telerobotic operations. She received her BS degree from Loyola College (Baltimore) in 1986, at which time she joined Goddard.

ALGEBRAIC EDGE-DETECTION THROUGH COMPACT POLYNOMIALS

The objective of this ongoing research has been to develop a comprehensive mathematical model for image processing using algebraic techniques to support the docking tasks of the Goddard Robotics Laboratory. An algebraic approach has been used to represent and manipulate grey-level images for machine vision. Researchers at Goddard Space Flight Center have developed an efficient algebraic edge-detector which is based on simple concise polynomials in two variables, and they are currently formulating algebraic image processing algorithms for feature extraction, pattern recognition, and object identification.

An image A may be represented by

$$A = \{(x,y) \in Z \times Z \mid u_A \in [0,1]\},$$

where $u_A(x,y)$ denotes the grey-level of pixel (x,y) and grey-level has been normalized between 0 and 1.

Addition of binary images A and B may be defined as the *exclusive - or* operation:

$$A + B = (A \cup B) \cap (\bar{A} \cup \bar{B})$$

where \bar{A} and \bar{B} are the respective inversed images. This definition of addition to grey-level images A and B is extended as follows:

$$\begin{aligned} A + B &= \{(x,y) \in A \cup B \mid u_{A+B}(x,y) \\ &= \min [\max(u_A(x,y), u_B(x,y)), \\ &\max (1 - u_A(x,y), 1 - u_B(x,y))]\} \end{aligned}$$



The multiplication of grey-level images A and B is defined to be:

$A * B$

$$= \{ \sum (x_1 + x_2, y_1 + y_2) \mid u_{A*B}(x_1 + x_2, y_1 + y_2) \\ = \min [u_A(x_1, y_1), u_B(x_2, y_2)] \}$$

$(x_1, y_1) \in A$

$(x_2, y_2) \in B$

where \sum denotes the addition operation defined above.

Thus, with addition and multiplication operations defined, one may represent an image A by the polynomial

$$A = \sum_{(m,n) \in A} u_{mn} x^m y^n$$

where m and n are arbitrary integers u_{mn} = grey-level of pixel (m,n) and summation is the addition operation defined previously.

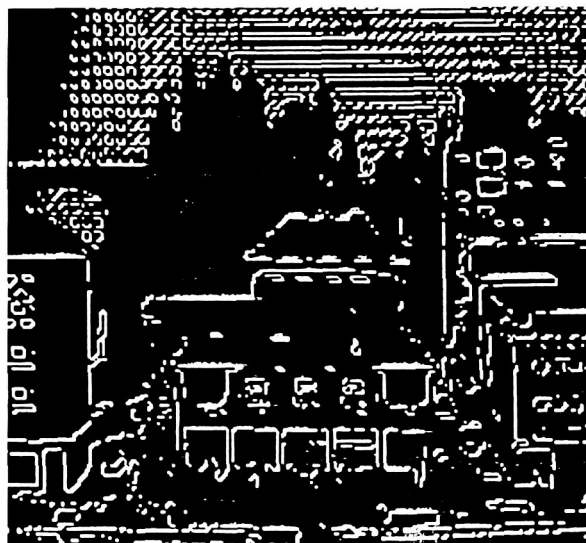
The classical two-dimensional differential operator may be defined as $D_1 = (1 + x)(1 + y)$. If D_1 is applied to a grey-level scene A, then contour-like regions are produced. Images are then thresholded at $u = 0.5$ since the definition of grey-level addition gives 0.5 as a natural threshold value.

A variation of the classical differential polynomial, $D_2 = (1 + xy)$, has been used to achieve improved contour-enhancement of grey-level scenes, and has yielded substantially better edge-detection capability. The two figures depict the action of D_2 on a typical building scene.

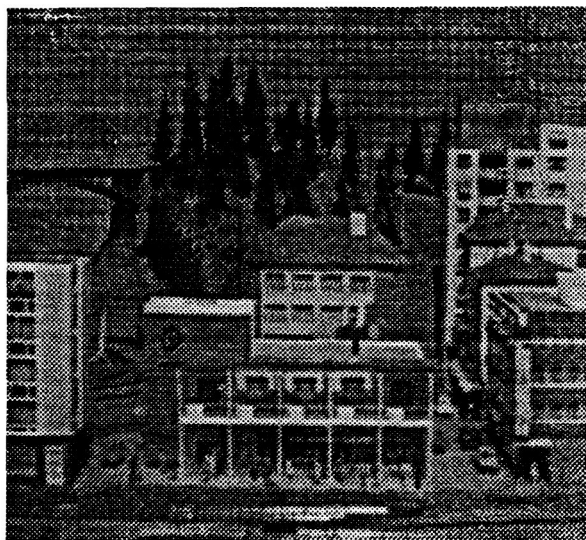
Contacts: Bao-Ting Lerner and Hans Thomas
Code 735

Sponsor: Office of Space Station

Dr. Bao-Ting Lerner is assigned to the Robotics Laboratory at Goddard and is an Associate Professor of Mathematics at the United States Naval Academy. For the past year, as a Visiting Research Professor



Building scene A.



$D_2 A$ thresholded at $u = 0.5$.

at the Robotics Laboratory, she has directed research projects on computer vision and multivalued logic applications to expert system development. Dr. Lerner earned her PhD degree in mathematics from George Washington University. In 1987 and 1988, she was an American Society for Engineering Education Summer Faculty Fellow.

Mr. Hans Thomas, a student at Carnegie-Mellon University, has been a student-intern and consultant

at Goddard for four years. He is currently working at the Robotics Laboratory developing autonomous vision algorithms.

MAXIMUM ENTROPY SUPERRESOLUTION IN FOURIER TRANSFORM SPECTROSCOPY

Traditional estimates of the power spectral density have followed the methods of Blackman and Tukey, which have been modified to take advantage of the Fast Fourier Transform (FFT). However, these techniques, which employ a smoothing of the autocorrelation function by a time domain window, or a smoothing of the squared magnitude of the Fourier Transform, do not design windows based on the true spectrum. Two immediate consequences of this are sidelobe leakage in the transfer function of the smoothing window, and a limit on resolution.

In 1957, Edwin T. Jaynes published his Maximum Entropy formalism, in which he derived statistical mechanics on the basis of information theory. Shannon had introduced the concept of information to communication engineering; its mathematical form is essentially identical to that of entropy in the statistical mechanics of Boltzmann and Gibbs. Jaynes' Principle of Maximum Entropy can be stated as: "If data D are given concerning the outcome of a random experiment, then predictions about the outcome should be based on that distribution (p_1, p_2, \dots, p_n) , which maximizes the Shannon missing information measure, subject to the constraints

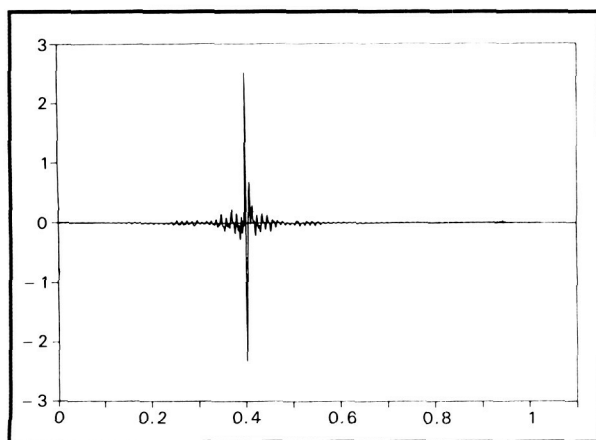
imposed by D ." The Maximum Entropy Method (MEM) for power spectrum estimation was introduced in 1967 by John Burg. Given the first few error-free lags of an autocorrelation function (ACF), the basic idea is to find the infinitely long ACF that maximizes the determinant of the ACF matrix. Since the Shannon entropy of a time series is proportional to this determinant, maximizing the latter is equivalent to maximizing the Shannon entropy. Burg also showed that the Maximum Entropy extension can be obtained simply by solving the modern Yule-Walker equations for the reflection coefficients, and then using the modern Levinson recursion to find prediction error coefficients. The power spectral density, $P(f)$, is obtained by evaluating the expression

$$P(f) = \frac{P_{n+1} \Delta t}{|1 + \sum_i a_i \exp(2\pi j f i \Delta t)|^2}$$

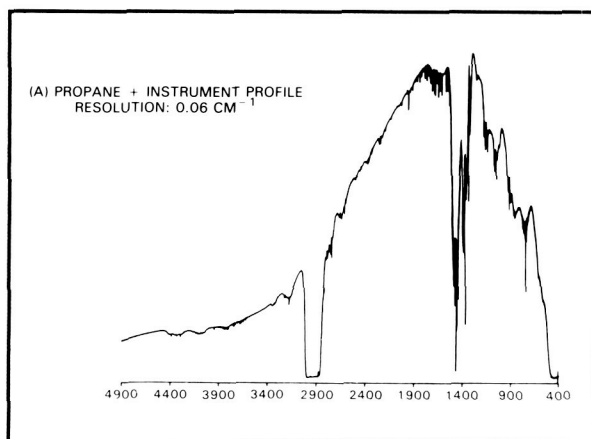
Thus, the Maximum Entropy power spectral density can be considered as simply the Fourier Transform of the infinitely extended ACF.

The term superresolution refers to the effort of estimating a solution with a resolution in excess of a physically imposed limit. This study was undertaken to determine if MEM would produce large improvements in the analysis of propane interferogram signals corresponding to line spectra. Preliminary work had indicated strongly that MEM works very well for these signals. One reason is its ability to perform high resolution spectroscopy, with an efficiency far superior to that of conventional techniques. The resolution limit in Fourier Transform spectroscopy is primarily determined by the maximum permissible path of two beams in the interferometer used to measure the interferogram.

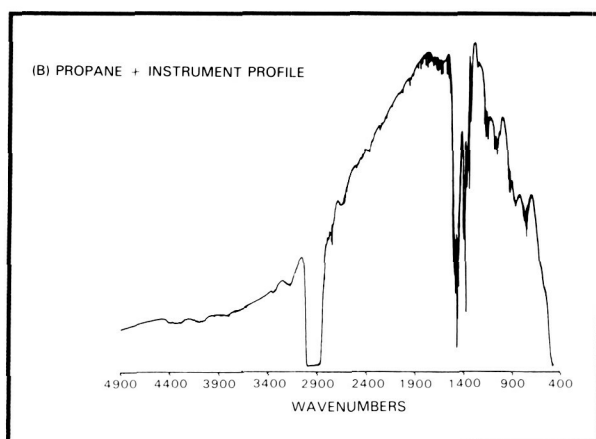
In an experiment performed by the Optics Branch, the Nicolet 8000 Fourier Transform spectrophotometer was used to measure the propane transmittance spectrum. This instrument is a Michelson interferometer with a maximum mirror travel of 16.6 cm, which gives a maximum unapodized resolution of 0.03 cm^{-1} . For this measurement, a global source at approximately 900°K , and a Mercury Cadmium Telluride (HgCdTe) detector operating at 77°K were used. The beamsplitter was a 5-cm diameter potassium bromide (KBr) crystal coated with a thin film of germanium (Ge). A 10-cm-long gas cell with



Propane interferogram (compiled from Nicolet data).



Power spectrum from the Fast Fourier Transform, using 2^{18} data samples.



Power spectrum from the Maximum Entropy Method, using 2^{10} data samples.

cesium iodide (CsI) windows bevelled to eliminate multiple reflections was placed in the infrared beam. The pressure of propane gas in the cell was 103.6 T; 1000 scans at maximum resolution were averaged to produce this spectrum. Data samples numbering 2^{18} were recorded using a Nyquist frequency of 7899 cm^{-1} . The interferogram and Nicolet FFT propane power spectrum were produced by Dr. J. B. Heaney and K. P. Stewart of Code 717.1, Optical Research. These are shown in the first two figures. The second figure shows the full FFT resolution using 2^{18} (262,144) data samples, while the third figure shows the MEM-generated spectrum from only 2^{10} (1024) samples.

Although the length of the interferogram available for MEM estimation in the third figure was 256 times shorter than that in the second figure, there appear to be neither spurious peaks, nor peak-position shifts in the third figure. It is estimated from the data that the resolution increase by the MEM is between 2^4 and 2^7 , and that the resolution in the spectrum estimated by the MEM exceeds the limit of the interferometer spectrometer. To determine the resolution gain more precisely, the study is presently concentrated on a narrow (45 cm^{-1}) band, in which the MEM reflection coefficients, prediction error power, and power spectrum are to be estimated, and then compared to individual lines in this same band using the full 2^{18} data sample FFT. In this case, the MEM will extend the autocorrelation from given values to all the values that lie outside the data range. It is known that the limit on this extension is imposed by the presence of noise in the data. Since the autocorrelation size is directly proportional to the length of mirror travel, with the Maximum Entropy Method, a small, inexpensive Fourier Transform spectrometer may gain a capability comparable with that of a larger, high resolution instrument.

Another important issue to be examined is the effectiveness of noise on corrupting MEM spectra, since it may actually change the signal model. For example, by merely adding noise, an autoregressive process (AR) can be converted to an autoregressive moving average (ARMA) process as a source for the signal. The MEM can compensate for this by increasing the filter order, or number of reflection coefficients. Knowledge of the signal model is important for proper implementation of MEM.

Contact: Dr. N. L. Bonavito
Code 636

Sponsor: Office of Space Science and Applications

Dr. N. L. Bonavito is a physicist with the Information Systems Development Facility. Dr. Bonavito, who earned a PhD degree in physics from The Catholic University of America, is interested in statistical physics, stochastic processes, neural networks, and fractal dynamics. He has been with Goddard for 27 years. During his military tour of duty, he served as a First Lieutenant of the U.S. Army's Guided Missile Center at Fort Bliss, Texas.

Space and Earth Sciences





Satellite Laser Ranging and Very Long Baseline Interferometry allow Crustal Dynamics Project observers to determine in relatively short periods of time the intersite distance between two observing stations to a level of several centimeters, even if the two sites were separated by thousands or tens of thousands of kilometers. This international capability has made direct measurement of the motion of tectonic plates and of the deformation of the Earth's crust in active plate boundary regions possible for the first time.

TERRESTRIAL, LAND, CLIMATE

MEASURING CONTEMPORARY CRUSTAL MOTIONS WITH SPACE GEODETIC TECHNIQUES

In the early and middle 1970s, two new space-based geodetic techniques became available that offered unprecedented accuracy in the measurement of distances over long baselines. Satellite Laser Ranging (SLR) and Very Long Baseline Interferometry (VLBI) allow observers to determine in relatively short periods of time the intersite distance between two observing stations to a level of several centimeters, even if the two sites were separated by thousands or tens of thousands of kilometers. Therefore, the motion of any one site with respect to another can be monitored at the level of better than a 1 cm/year. This made direct measurement of the motion of tectonic plates and of the deformation of

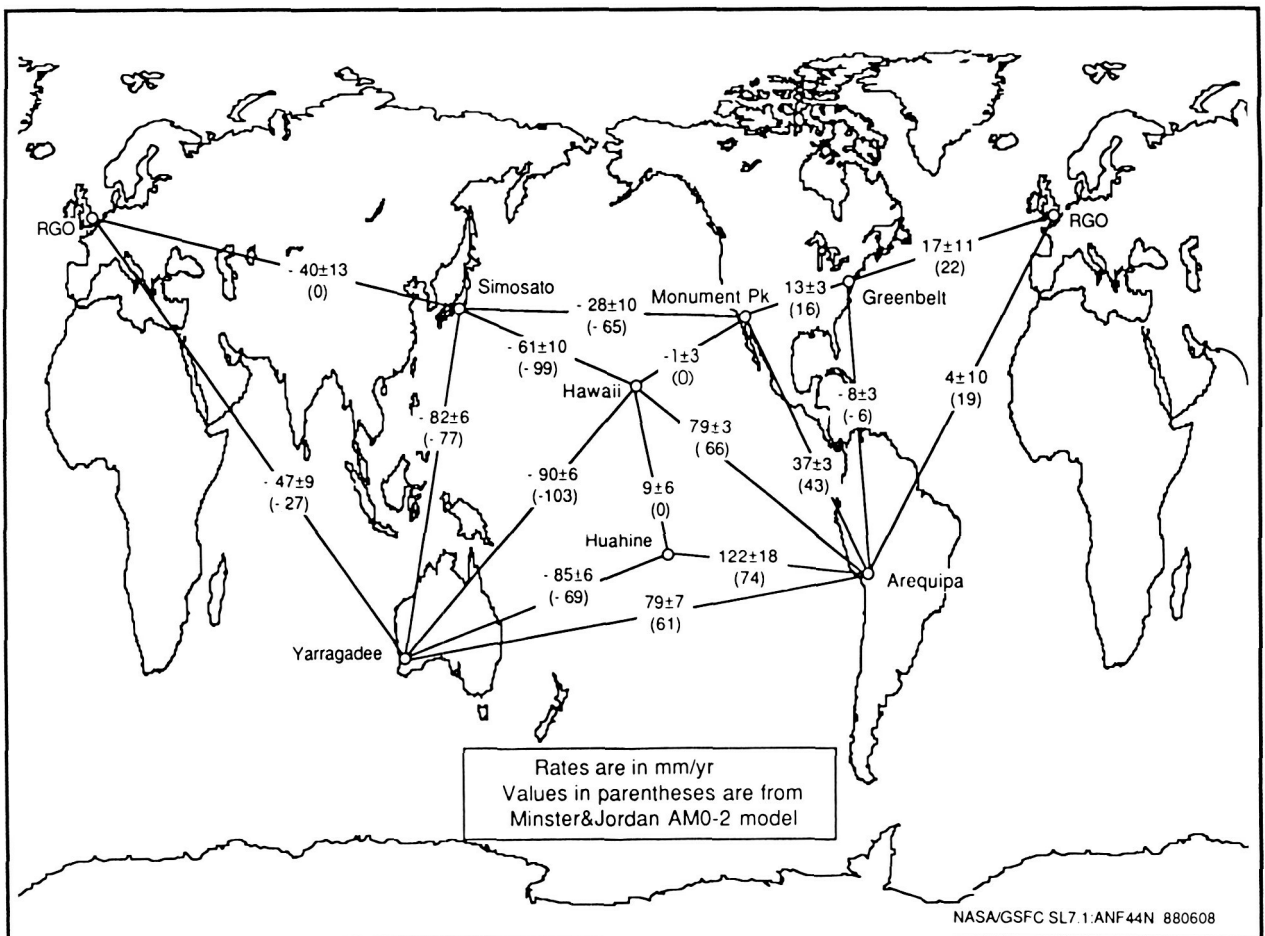
the Earth's crust in active plate boundary regions possible for the first time. The National Aeronautics and Space Administration formed the Crustal Dynamics Project in 1979 to further develop the SLR and VLBI techniques, to implement global networks of stations with the cooperation of many different countries, and to conduct measurements of plate motion and regional deformation. This Project has grown into an international effort to collect information directly relevant to understanding the threat of earthquakes and the way the crust and upper mantle of the Earth actually work.

The observing program of the Crustal Dynamics Project is guided by the Project's scientific objectives. Most of the Project's effort is put into understanding the motions occurring in California and Alaska, situated along the plate boundary in western North

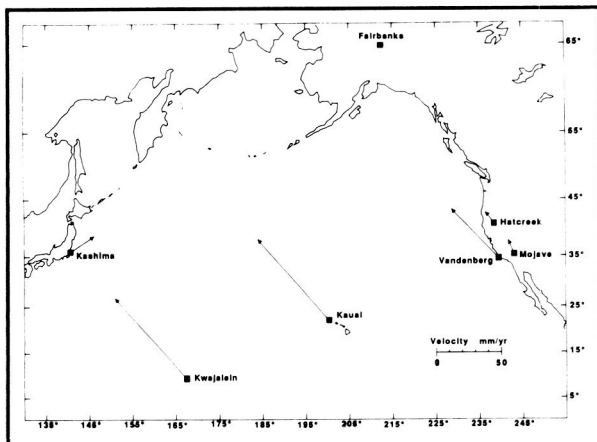
- ◀ *A three-channel Geostationary Operational Environmental Satellite (GOES East) (subsattellite point 75° West) full Earth image taken on September 1, 1985 at 1500 Greenwich mean time. At that time Hurricane Elena was approaching the Florida Panhandle. The visible, 6.7- μm and 11.0 μm , channels are displayed using the red, green, and blue guns of the display system, respectively. Therefore bright, high (cold) cloud systems like the hurricane's central dense, overcast area; tropical cloud clusters; and severe thunderstorm tops appear white. Subsidence areas (e.g., subtropical highs and the region just north of the hurricane) appear pink. The southern part of the subtropical high off the coast of Chile has a green cast to it due to upper-level moisture detected by the 6.7- μm channel. Finally the unilluminated region, west of the terminator at approximately 130° West, appears blue-green. The continents are masked in the 6.7- μm band so that they can still be seen in the visible and 11.0- μm window channels.*

America. Another involvement is the determination of plate motion, especially with respect to North America. The distribution of presently occupied sites in the global SLR network provides a basic framework for the determination of plate motion. This is augmented by VLBI observations, especially between North American sites and those in the northern Pacific and Eurasia. In terms of regional deformation observations, it is the VLBI systems that carry the load in western North America. Elsewhere, scientists have begun a long-term set of SLR measurements in the complicated Mediterranean region under a joint program between the Crustal Dynamics Project and a consortium of European countries.

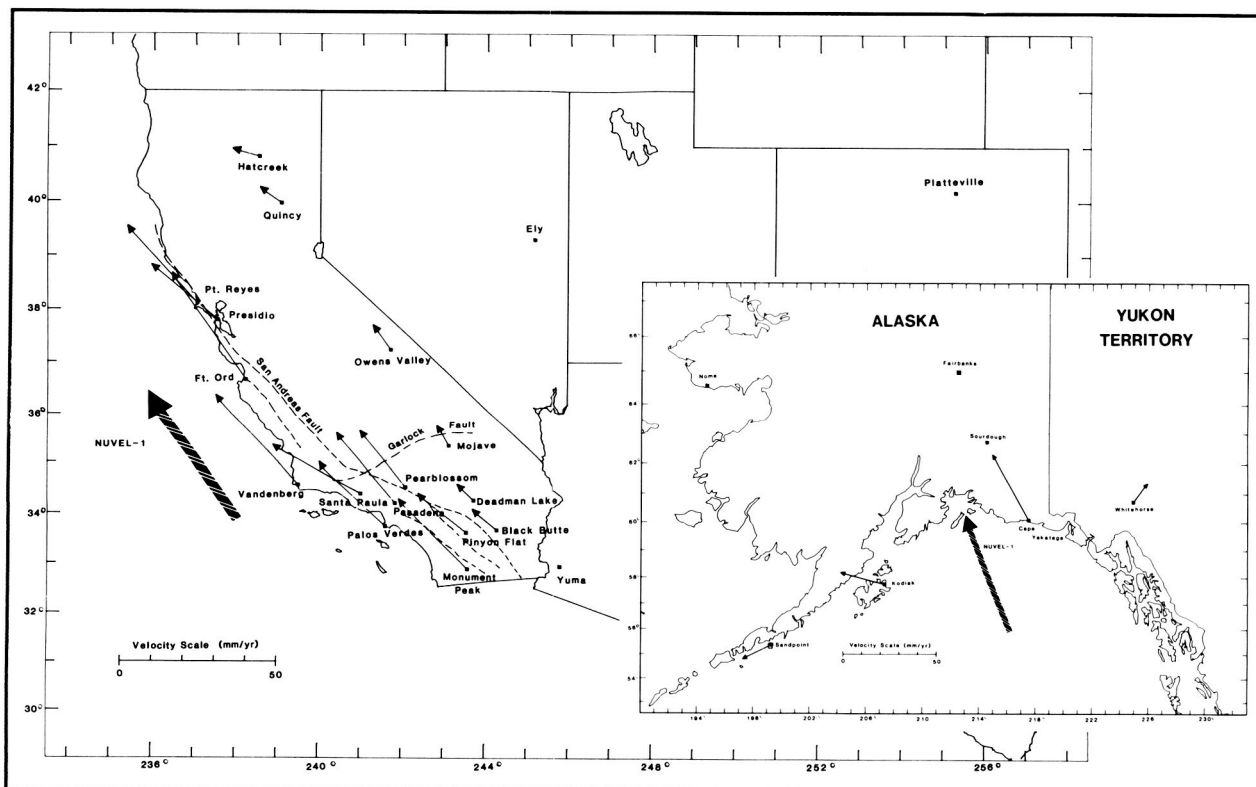
Global plate motion studies using data provided by both SLR and VLBI systems have largely confirmed the expected motion for most plates, even though this expected motion was based on geologic data averaged over several million years. The first figure shows recent measurements of plate motions along specific baselines, as determined from SLR systems. The second figure shows a similar result for VLBI observations in the Pacific, represented this time as motion of the individual sites with respect to the stable interior of the North American plate. These direct determinations of plate motion are important: they provide the first demonstrated proof that the plates move as the theory of plate tectonics suggests, and



Rate of change of baseline lengths from Satellite Laser Ranging data for selected baselines between North America, Eurasia, and the Pacific. Rates are in millimeters per year, in a reference system where the motions are with respect to the underlying mantle. In parentheses are the "predicted" rates based on long-term geological averages.



Observed motions of Very Long Baseline Interferometry (VLBI) sites in the Pacific. Motions are calculated with respect to a North American plate site at Fairbanks, Alaska, assumed fixed. The observed motions for Vandenberg, Kauai, and Kwajalein are very close to the predicted motions based on long-term geological averages, and clearly show how the Pacific plate is sliding northwestward past the North American plate.



Motion of VLBI sites along the North American-Pacific Plate boundary in (a) California and (b) Alaska. For comparison, the predicted motion of the Pacific Plate with respect to North America is shown, based on a recent plate motion model (NUVEL-1). Note the departure of the motion of Kodiak and Sand Point in Alaska from the expected plate motions.

that the motion over short time scales is similar to that determined from long-term geologic averages.

Both VLBI and SLR systems are engaged in measurement of the relative motion between the North American and Pacific plates near the plate boundary in California. Observations from both systems show that, along baselines that almost certainly lie within the boundary zone, the motion between the plates is less than that measured far from the boundary zone by the global network. The third figure shows vector site motions in the western United States with respect to interior North America, as measured by VLBI. For reference, the long-term velocity of the Pacific plate relative to the North American plate as determined by the Northwestern University Velocity Model 1 (NUVEL-1) plate motion model is shown. The data indicate that the velocities measured near the plate boundary are several tens of mm/year less than those predicted for the plates as rigid bodies (>50 mm/year). This difference between far-field motion and near-field motion has potentially important implications for the earthquake hazard problem in California, as it may be related to how stress is distributed and stored within boundary zones between two large moving plates.

Another result determined by the Crustal Dynamics Project has to do with motions in the deformation boundary zone in Alaska, where the Pacific plate converges upon, and is consumed under, the North American Plate. The third figure also shows vector site motions in Alaska and the Yukon Territory with respect to interior Alaska, as determined by VLBI. For reference, the long-term velocity of the Pacific plate relative to the North American plate offshore of southern Alaska, as given by the NUVEL-1 plate motion model, is shown. It is clear that several of these sites show relatively large motions of 30–40 mm/year, which may be related to the seismic potential of this area. Several of these sites are located in “seismic gaps” where large earthquakes have *not* occurred in recent times, despite the prolific seismicity in the surrounding areas.

Contacts: Herbert V. Frey and John M. Bosworth
Codes 622 and 601

Sponsor: Office of Space Science and Applications

Dr. Herbert V. Frey, Assistant Project Scientist on the Crustal Dynamics Project, also conducts research on the nature of MAGSAT crustal magnetic anomalies and the crustal evolution of Mars. He has received numerous Achievement Awards for his work on a variety of NASA Projects. Dr. Frey has a PhD degree in astronomy.

Mr. John M. Bosworth, Project Manager of the Crustal Dynamics Project, directs the Project's technical activities, including projectwide planning, resource management, international coordination, and engineering development.

EXCITATION OF THE EARTH'S ROTATIONAL VARIATIONS

The Earth's rotation varies slightly in both its speed (the length-of-day, or LOD, variation) and the orientation of its rotational axis (the polar motion). Under the law of conservation of angular momentum, any mass motion/redistribution on or in the Earth can cause the rotation to vary; identification of these excitation sources has been a long-standing problem in geophysics.

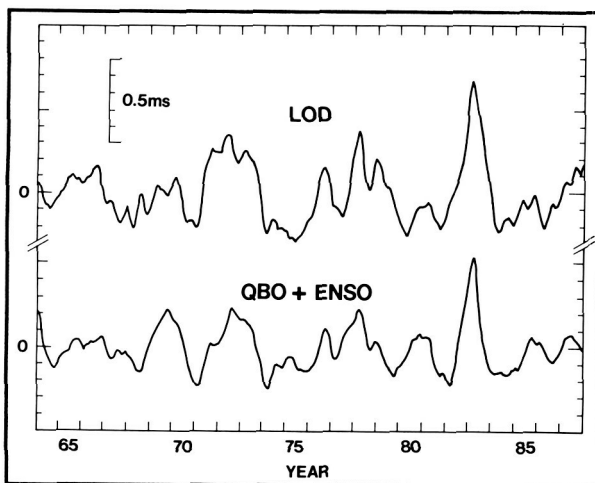
Researchers have been studying the effects of some atmospheric and hydrological phenomena, as well as earthquakes, on different aspects of the Earth's rotational variations:

- 1) Atmosphere versus LOD: The atmospheric angular momentum variation has been known beyond any doubt to be the major cause of LOD variations on seasonal (mostly annual and semiannual) and shorter time scales. Based on that knowledge, researchers investigated the atmosphere-LOD connection on the interannual scale (nominally 1 to 10 years). The most prominent interannual atmospheric fluctuations are El Niño/Southern Oscillation (ENSO) in the Pacific-Indian Ocean troposphere, and the Quasi-Biennial Oscillation (QBO) in the equatorial stratosphere. Analysts use the time series of the Southern Oscillation Index as a proxy for ENSO, whereas they calculate the axial angular momentum time series for QBO. The observed interannual LOD variation is then compared with the combination of ENSO + QBO in both time and frequency domains. A



strong correlation is evident. The first figure shows a time domain comparison with a correlation coefficient as high as 0.75. Considering the uncertainties in each data series, this indicates that ENSO and QBO can account for most, if not all, of the interannual LOD variation.

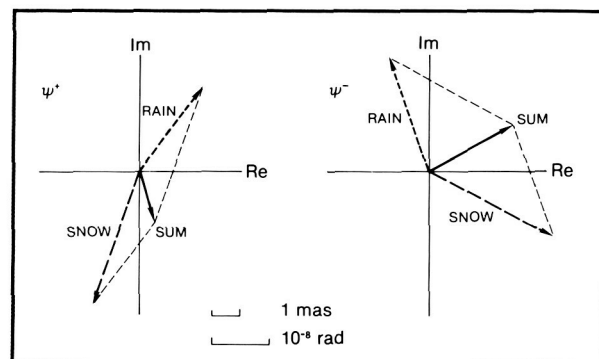
- 2) Hydrosphere versus polar motion: While the hydrological mass redistribution is only of marginal importance in changing LOD, it can contribute significantly to the excitation of the polar annual wobble. Researchers have studied the two major components in continental water storage, snow, and rain. For snow mass, they use the time series derived from the remote-sensing Scanning Multichannel Microwave Radiometer instrument on board the Nimbus-7 satellite for the period of 1979–1985. For rainfall and the accompanied evapotranspiration, they use the mean monthly values compiled by Willmott et al. (1985) using conventional meteorological data collected over many decades. They found that, although individually having a magnitude of about 30 percent of the observed annual wobble excitation, the two contributions largely cancel each other, as



A time domain comparison of the observed interannual length-of-day variation with the combined effects of the El Niño/Southern Oscillation, and the Quasi-Biennial Oscillation, the latter in terms of their equivalent length-of-day in milliseconds for the period 1964–1987. The correlation coefficient is 0.75.

shown in the second figure. Physically, this occurs because of their reverse seasonal polarity, and the similar amount of water mass involved. In addition, researchers have also studied the hydrological reservoirs, whose effect is ignored in the above studies for simplicity in the modeling. This serves to correct the results in the second figure.

- 3) Earthquakes versus LOD and polar motion: An earthquake produces a global deformation field that in turn can change the Earth's rotation, as well as its gravitational field. Researchers calculated these geodetic effects caused by some 2000 large earthquakes that happened during 1977–1985, using a normal mode summation scheme. Since no truly large earthquakes happened during this period, the calculated effects were, in general, two orders of magnitude too small to account for the observed effects. Nevertheless, researchers found that the earthquakes had a very strong tendency to make the Earth rounder and more compact; earthquakes definitely tend to decrease LOD, and the Earth's oblateness. In addition, earthquakes are found to make the pole drift towards the direction of 150°E, roughly opposite to the direction inferred from observations. These findings, as well as the geophysical questions they raise, presumably can only be explained in terms of, and in conjunction with, the dynamics of plate tectonics.



Estimates of the surface water-induced annual wobble excitation (for the prograde and retrograde components relative to January 1). RAIN designates the contribution of rainfall and evapotranspiration, SNOW that of snow, and SUM their vector sum.

Contact: Benjamin Fong Chao
Code 621

Sponsor: Crustal Dynamics Project

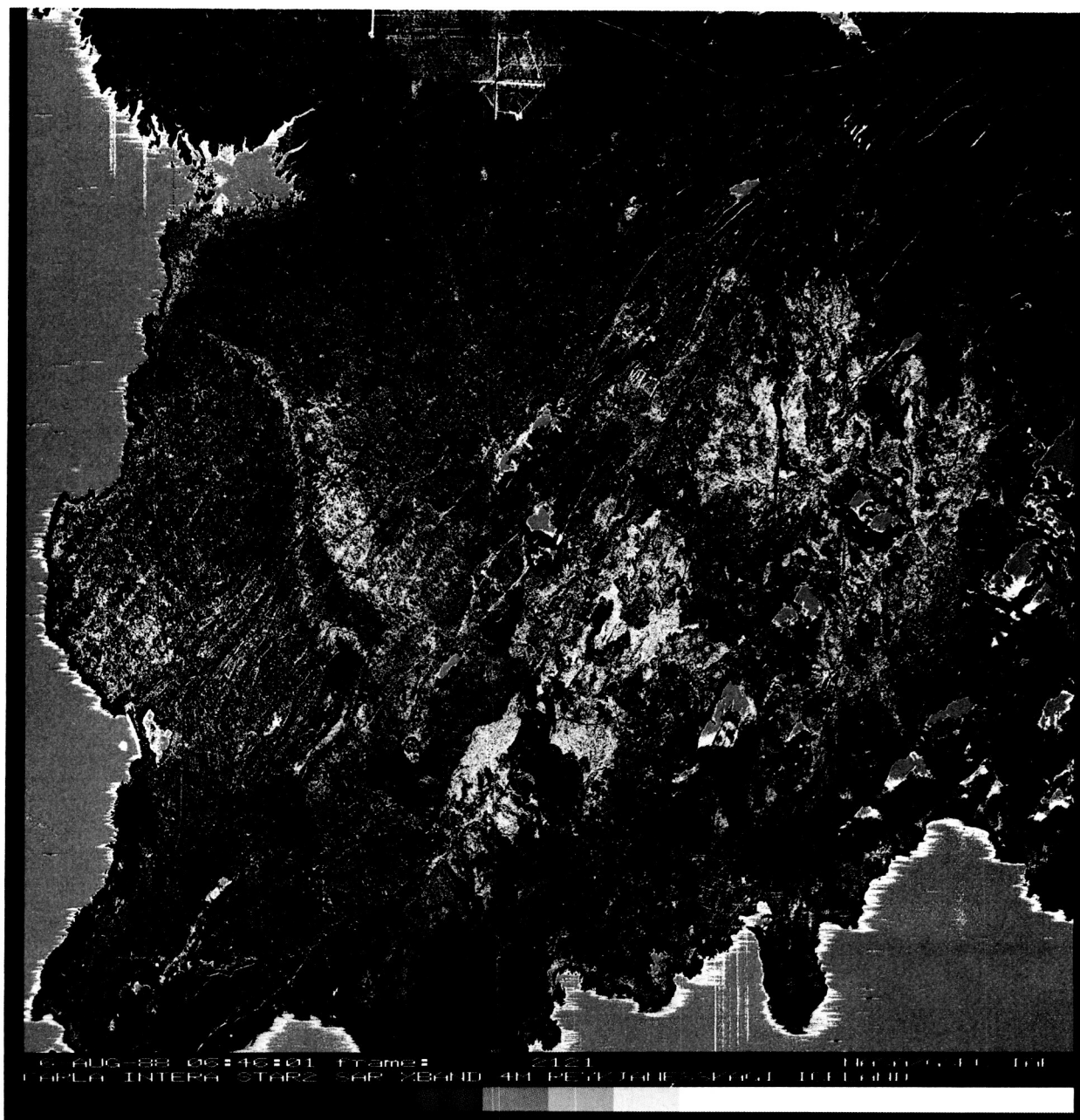
Dr. Benjamin Fong Chao is a research geophysicist with the Geodynamics Branch of the Laboratory for Terrestrial Physics. Having earned his PhD degree in Earth sciences from the Scripps Institution of Oceanography of the University of California, San Diego, he now conducts research in Earth/Planetary dynamics and gravitational fields. Dr. Chao is most interested in rotational dynamics, theoretical seismology, and numerical methods.

GEOLOGIC REMOTE SENSING OF THE REYKJANES AREA OF ICELAND

The Earth as a planet relies on midocean-ridge volcanism (MOR) as an important mechanism for lithospheric heat transport, and the global system of midocean ridges provides insights into this fundamental terrestrial geologic process. The subaerial expression of MOR volcanism is a rarity on Earth, making synoptic investigation of this process very difficult. However, the Mid-Atlantic Ridge (MAR) system propagates onto land in extreme southwestern Iceland in a region known as Reykjanesskagi, and this is perhaps the one relatively pristine example of recent MOR volcanism in a subaerial setting. Reykjanesskagi is also an ideal setting from which to explore volcanic eruption styles and their products by means of high-resolution remote-sensing techniques because of the paucity of vegetation and relative absence of erosion. In fact, many varieties of pristine volcanic constructs occur in this region, including simple lava shields, fissure eruption source vents, volcanic pit crater chains, large systems of channelized lava flows, and scoria cones. The following paragraphs highlight preliminary results in the characterization of basic MOR volcanic landforms and deposits by means of high-resolution imaging radar data together with airborne laser altimeter profiles. The intent is to establish unique microtopographic and radar textural signatures for the primary volcanic terrain types; and to develop models for the formation, emplacement, and modification histories of on-shore MOR volcanic zones. These results may have bearing on other unique subaerial volcanic settings on Earth such as the Afar region in Eastern

Africa. A final objective in this ongoing study is to attempt to retrospectively infer lava rheologies from the remote sensing data in order to develop improved models for the lava emplacement process.

Airborne synthetic aperture imaging radar (SAR) data were acquired at very high resolution (~8 m per pixel) for southwestern Iceland in a cooperative effort with the National Aeronautics and Space Administration (NASA) by INTERA Technologies using an X-band system with a radar incidence angle of 75°. The first figure provides an example of a small section of this digital data set that illustrates the extreme southwestern tip of Reykjanesskagi; this is where the propagation of the MAR onto land occurs. The ubiquitous linear features in this region are unique to Iceland (but may be common on the ocean floor in MOR zones) and represent purely tectonic fissures due to extension of the uppermost crust. This pervasive extension is related to thermal uplift due to near-surface magma storage regions in this part of Iceland. These features occur in swarms (local zones of crustal weakness perhaps due to thinning). It is important to note that these fissures are *not* volcanic in origin, a contrast to the volcanic fissure eruption systems that are common in the same region. The airborne imaging radar illuminates the terrain from the bottom (from the south looking due north) in an oblique sense, and radar shadows are produced behind topographically prominent landforms. The higher standing volcanic features in this image are related to volcanic eruptions under ice, and date from the time of the last Ice Age. Many of them are made up of a material termed hyaloclastite, which resembles a welded or cemented ash. Perhaps the most interesting landform in the image is the small Icelandic lava shield (just left of center), with its summit crater and radiating pattern of lava flows. This monogenetic shield, called Sandfellshaed, is unlike the more well-known hot-spot volcanic shields of Hawaii. These primitive Icelandic shields are more like those expected to be abundant on the volcanic plains of the planet Venus. The Sandfellshaed shield is cut by a series of tectonic fissures which postdate its formation; however, only about 50 percent of these features can be seen in the radar image. This restriction is a consequence of the fixed-radar viewing geometry and a common problem known as "look-azimuth biasing." All of the fissures on the northwestern part of the lava shield "step down," and hence cannot be seen with the north-looking



Airborne synthetic aperture imaging radar image of Reykjanesskagi obtained with the 8-m resolution INTERA Technologies STAR-2 (X-band) instrument in May 1987. The look direction is to the north, and the incidence angle averages 75°. False coloring has been used to enhance geologically significant structures.

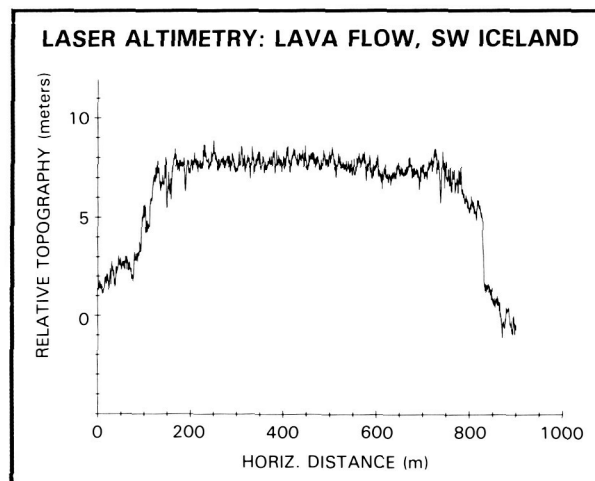
viewing geometry of the image. Most of the recent (e.g., in the past 10,000 years) eruptions in Reykjanesskagi have been of the fissure-fed variety. The landforms that result are often subtle, except when crater chains later develop along the strike of the fissure.

Just to the east of the radar scene previously discussed is an area in which a series of lava rivers (i.e., channelized lava flows) were erupted in the 11th century. This area, called the Ögmundarhraun lava flow field, is made up of more than 10 individual eruption episodes. Since the entire Reykjanesskagi region

has been geologically mapped at very high resolution, it is possible to compare results derived from remote sensing with well-established field relationships as depicted in the geological maps. For the Ögmundarhraun flow field Goddard Space Flight Center researchers seek to establish the local eruption sequence and later check it in the field.

The late-stage channelized lava flow units within the Ögmundarhraun lava field were profiled using a Goddard Space Flight Center airborne laser altimeter in May 1987. The horizontal resolution of the laser topographic profiles is ~33 cm, with a vertical precision of 15 cm after removal of aircraft motion. Researchers have been using the laser altimetry data as a tool for improving general understanding of the way lavas are emplaced and their subsequent deformation histories, which are related in part to local topography, composition, and cooling history. The second figure illustrates a perched lava channel approximately 700 m in width, which appears to represent one of the latest stage eruptions in the sequence that formed the Ögmundarhraun lava field. By measuring the height, width, and local slope across this flow unit, the effective yield strength of the lava can be retrospectively determined. Researchers have assumed a Bingham-Plastic rheology for the lava, which has been shown to be realistic to first order for basaltic materials on the inner-solar system planets. A yield strength of 1350 (± 150) pascals was derived for this flow unit, which suggests very fluid behavior, at least when compared with similar data for the lavas in Hawaii. One of the key questions is whether severe local slopes may have influenced the inferred flow behavior of channelized flow units such as that shown in the second figure.

In summary, the combination of airborne laser altimeter topographic profiles with high-resolution SAR imagery offers new opportunities to quantify MOR volcanic processes in a subaerial setting as exemplified by extreme southwestern Iceland. During the latest stage of Earth geologic history, the mid-ocean ridges have been the most consistently active volcanic regions; yet most are hidden beneath kilometers of seawater and inaccessible with airborne or spaceborne remote sensing instruments. Iceland offers a unique opportunity to study MOR volcanic processes on land in a setting well suited for synoptic remote sensing, and may provide an important



High-resolution laser altimeter profile across a single lava flow unit (a channelized basaltic flow); the horizontal resolution is ~30 cm, with a >20-cm vertical control. This flow unit is perched and represents one of the late-stage eruption products in the area (an 11th century eruption).

“training site” for Eos-era remote-sensing studies of active volcanic regions.

Contact: James B. Garvin
Code 622

Sponsor: NASA Geology Program

Dr. James B. Garvin, a planetary geophysicist with the Geophysics Branch, studies the quantitative topographic properties of volcanic and impact landforms, as well as the quantitative sedimentology of Mars, Venus, and Philos. He is also Co-Investigator on the Mars Observer Project and Principal Investigator on the Iceland Project. Dr. Garvin received his PhD degree in geological sciences from Brown University.

CHARTING RAPID COASTAL PROCESSES: NILE DELTA, EGYPT

In the geological sciences, major changes occur on a relative large time scale. One exception to this generalization is the changes happening along some coast lines. Charting these rapid variations with conventional surveying techniques is costly and time-consuming. Remote sensing methods, especially those



using Landsat, SPOT, and SAR data, offer the ability to precisely chart these shoreline modifications on a regional scale.

For the last 100 years, there has been a diminution in the flow of the Nile River into the Mediterranean Sea. This resulted from a general decline in river flow, which was accelerated by the construction of two dams; the largest, finished in 1964, was the Aswan High Dam. Now the reduced water volume of the Nile can no longer resupply sediment in sufficient volume to offset the significant coastal erosion along the Mediterranean. This erosion process is complicated by eustatic sea level variations. The main erosional agent, the eastward-tracking coastal and near-shore Mediterranean currents, has been the major agent for sediment removal along the Nile Delta coast and redeposition in the more easterly regions of the Mediterranean basin. These coastal changes have threatened major economic harm to nearby arable lands, fresh water, and coastal lakes.

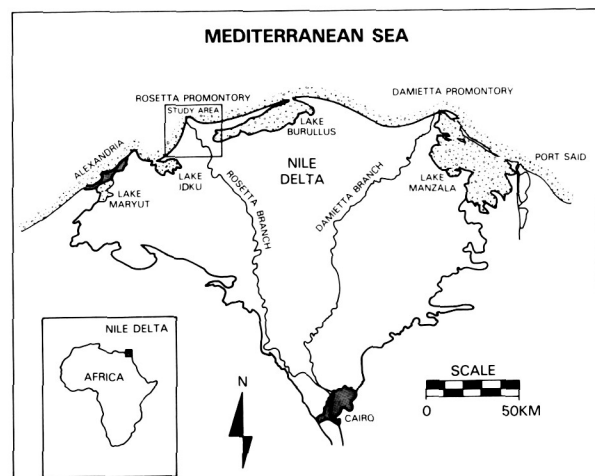
This report discusses preliminary results of applying Landsat data to monitor rapid coastal changes (both erosion and deposition) along the southeastern Mediterranean coast at the mouth of the Rosetta Branch of the Nile, the area shown in the first figure. This project is a part of the major study of the evolution of the Nile Delta being conducted by the Smithsonian Institution (Museum of Natural History), under the direction of Dr. Daniel J. Stanley.

Landsat data acquired at two different times that illustrate the character of the coastal variation along the promontory of the Rosetta branch of the Nile River were used in this study. The second figure shows two Landsat subscenes (scenes 1039-07592 and 1900-38038) covering the same section of the lower Rosetta Branch of the Nile. The earlier image was constructed from data acquired August 31, 1972, and the more recent data were collected on December 23, 1976. These data were registered to Defense Mapping Agency (DMA) 1:50,000 scale topographic maps. Thirteen coincident control points were established for each Landsat subscene. These coregistered data sets were digitally differenced, with the 1976 water/land contact changes being subtracted from the 1972 contacts. The resulting differenced image, shown in the third figure, exhibits regions of erosion and deposition.

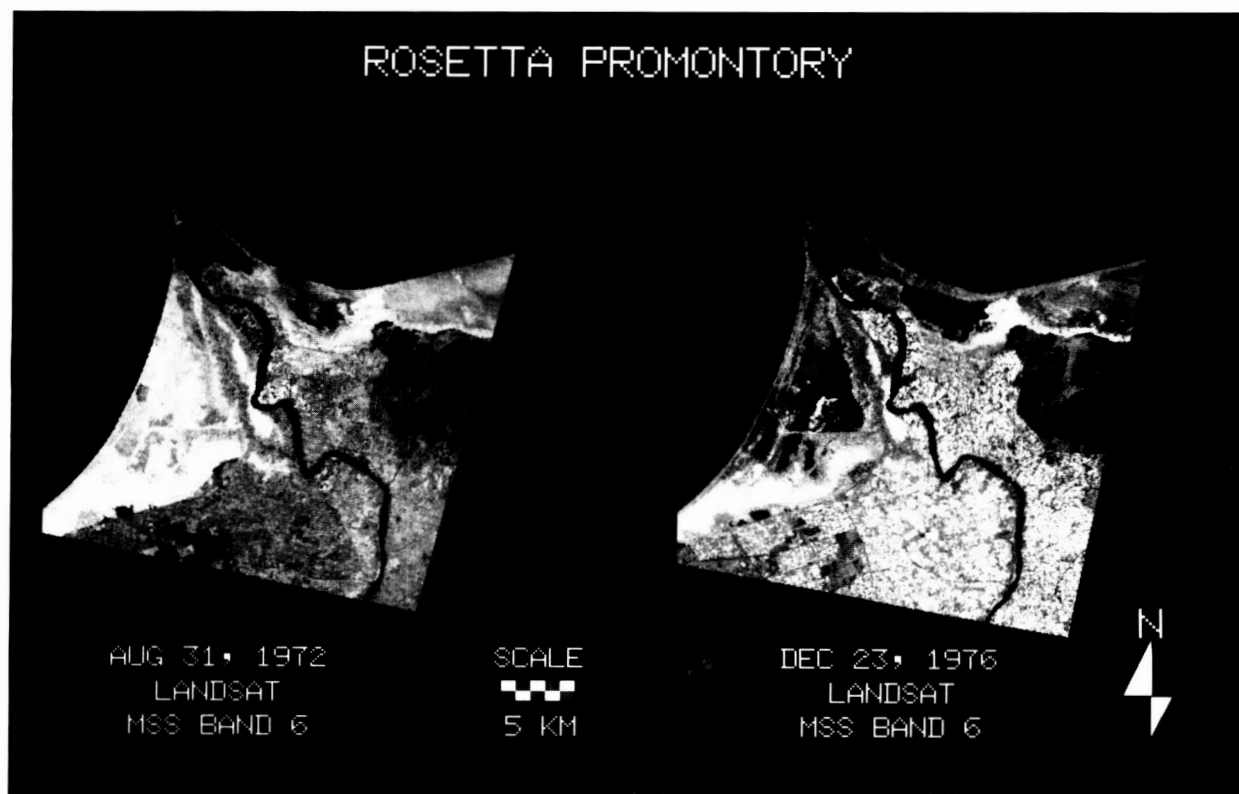
For purposes of analysis, this part of the Rosetta Branch has been divided into three sectors. The promontory at the mouth of the Nile, located in sector 1 of the figure has undergone the greatest amount of erosion per length of coast line. Sector 2 displays the next largest erosion, and sector 3 the least erosion per length of coast line. Sector 3 shows the greatest buildup of shore area by sediment deposition, while sector 2 displays only a small amount of land increase, and sector 1 shows no deposition.

At sector 1, 1.1 km² of sediment have been removed in 52 months. Since only the areal extent of erosion is being observed, there is no indication of volume of sediment removed; using existing bathymetric charts, however, some very generalized estimates may be possible. To the east, in sector 2, 2.1 km² of sediments have been eroded along the 20 km coast line by eastward flowing along-shore currents. Sector 3 is the only region where deposition has exceeded erosion: 0.4 km² were eroded and 0.5 km² were deposited, a net addition of 0.1 km². There are some 25 km of coast line in this sector. The pattern of erosion revealed by these Landsat images is consistent with the measured easterly movement of the Mediterranean coastal currents. The promontory of the Rosetta branch of the Nile River has been most affected by erosion.

The figure shows several other regions of both extensive erosion and deposition; in particular, an apparent displacement of the Nile River channel. Areas



Reference map showing the study area (Rosetta promontory) in relation to the Nile Delta.



Two Landsat subscenes used to obtain erosion/deposition rates around Rosetta promontory of the Nile River.

designated "A" on the third figure are of low relief, and are locally below mean sea level. A comparison with the second figure suggests that the region received significant precipitation just prior to the 1976 observation date. Runoff filled the topographic depressions behind the slightly elevated coastal strands on the north and east, and also flowed into Lake Burullus on the west. This runoff created temporary lakes in the "A" designated areas. The westernmost lobe of Lake Burullus includes low mud flat areas subject to inundation. In the 1976 scene, area "B" shows inundated areas covered by shallow waters containing some clay in suspension. The resultant complex spectral pattern produces an erroneous display of terrestrial surfaces lost and gained during the time period considered. This interesting erosion deposition pattern requires further research to establish its veracity. Along the Rosetta Nile, erosion has occurred along the southern bank, while deposition occurred along the northern one.

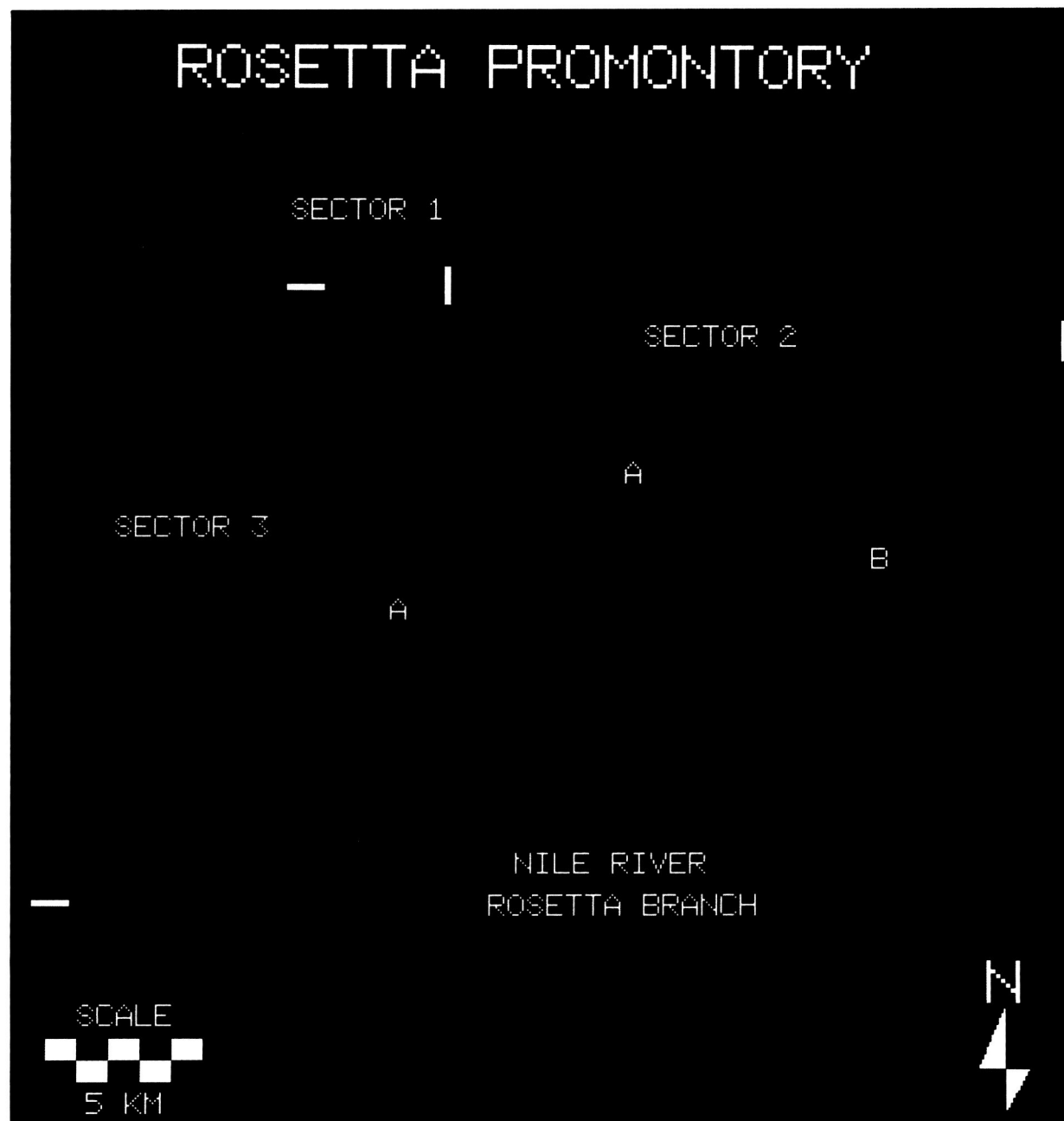
This erosion pattern, of course, was only for the period from 1972 to 1976 and may represent an arti-

fact caused by differing Sun angles of the two subscenes. Study of the coastal dynamics of the Nile Delta region eastward to the Damietta promontory and Port Said will be continued. Interpretation of these data will be aided by the field work being conducted by Smithsonian staff members and associated workers in Egypt.

Contact: Patrick T. Taylor
Code 622

Sponsor: Land Processes Branch

Dr. Patrick T. Taylor, who received a PhD degree in geophysics from Stanford University, conducts geological interpretations of Magsat and other remote sensing data. Working with the Geophysics Branch, Dr. Taylor also contributes to scientific planning for future NASA missions. He has received a Performance Award during his 10-year tenure at Goddard.



Map of Rosetta promontory showing results of subtracting the latter Landsat subscene from the former.

Eos GEODYNAMIC LASER RANGING SYSTEM

Knowledge of the strain surrounding regional and local fault zones is fundamental to the understanding of crustal movements. A precise and viable method for measuring strain can now be achieved due to ad-

vances in laser technology, and to the ability to range with lasers from a stable platform in space. A variation of this method can be applied to acquire altimetry topographical data for studies in several Earth-sensing disciplines. Some examples are ice sheet volume in oceanography, rift valley delineation in

geomorphology, and cloud-top heights in meteorology. The ranging and altimetry techniques are combined in the Geodynamic Laser Ranging System (GLRS), a spaceborne laser ranging system for the Earth Observing System (Eos). The GLRS is a facility instrument being developed by Goddard Space Flight Research Center to fly on an Eos platform as part of the cooperative program involving the National Aeronautics and Space Administration, the European Space Agency, and the Japanese Space Agency.

The GLRS will perform geodetic quality observations to determine the intersite distance and relative height between fixed retroreflector targets arrayed about fault zone surfaces, and to measure vertical height to the Earth surface along the nadir orbital track. In the first mode, when the platform comes into view of hundreds of targets various distances apart in a typical fault zone area, the laser beam points at individual targets in order. Range time from the generation of the laser pulse to the return of the pulse after it reflects off the target is measured to 10 picoseconds (ps), or roughly $\frac{1}{3}$ cm traveled. A second ranging pulse timed relative to the first with a 2-ps precision corrects for atmospheric variations. The altimetry profiling is similar, except that it requires no correction; the beam is diffusely reflected off the surface, and the waveform of the return pulse is electronically analyzed. The observational quality of the GLRS will be significantly better than current laser ranging systems. To achieve this, new technological designs that represent engineering advances have been incorporated in the laser, receivers, pointing, and gimbal design of the GLRS.

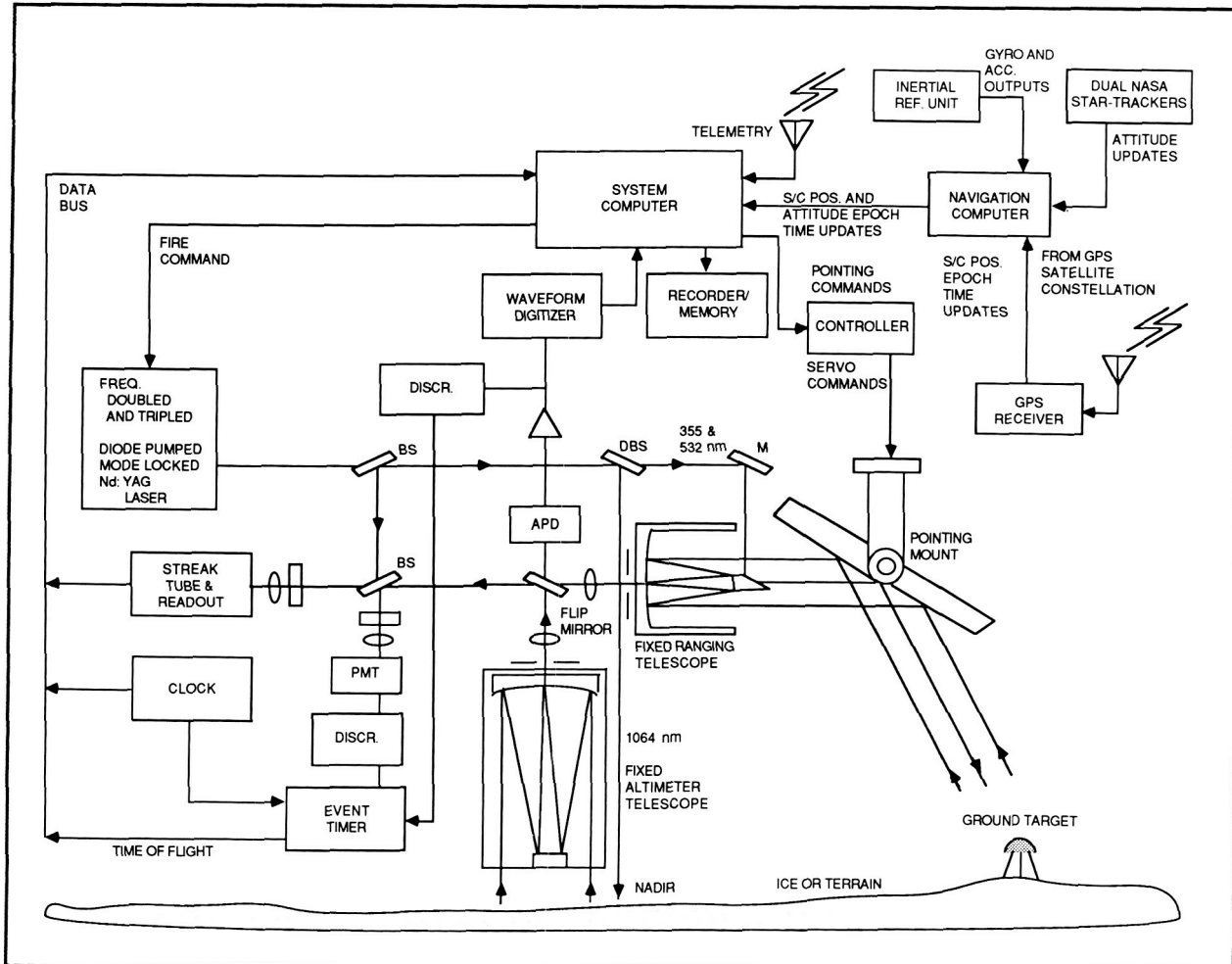
A conceptual diagram for the GLRS is shown in the accompanying figure. The laser transmitter generates three different colored pulses at the rate of 40 pulses per second, with a divergence of 0.1 to 0.2 milliradians. The 1064 nm infrared pulse is used for altimetry. The 532 nm green pulse and the 335 nm ultraviolet pulse are used for ranging. When operating with a yearly duty cycle of 20 percent for 5 years, the GLRS will expend over 1 billion shots. Current lab tests indicate that the device's expected lifetime exceeds 3 billion shots. Laser ranging to a retroreflector target begins when the pair of range pulses trips an event timer. The pulses are aimed at the target with the pointing mirror. They travel to the target, are reflected, return in a wide pattern to intercept the instrument, and are then relayed by the pointing mir-

ror into the 18 cm receiving telescope. The angle and light intensity of a portion of the green return pulse are detected by an angle tracker for feedback to the controller, which directs the gimbal motion of the beam pointing mirror. When the green light is detected by a photomultiplier, or PMT, it stops the time-of-flight measurement. Some green light along with the 355 pulse is also detected in the streak tube. The streak tube measures the pulse separation of the 532 nm and 355 nm pulses. This relative time is a correction to the absolute event time, making the range distance more accurate, and eliminating the need for ground-based atmospheric error correction sensors.

The altimetry pulse at 1064 nm is directed downward, reflecting off the underlying terrain. The return is collected by the 50 cm telescope of the altimetry receiver. A high-speed avalanche photodiode (APD) detects the focused light and relays the signal into a constant fraction discriminator/time interval unit. Accuracy of the time-of-flight measurement is 300 ps, or 4.5 cm for ice and land measurements, and 0.5 microseconds for cloud-top measurements. The APD signal enters the two digitizers and is stored as waveshape data. These waveform data provide knowledge of the combined surface roughness and slope of the terrain, or location of the cloud top.

As ancillary components, GLRS will have star-trackers, a three axis gyro, and a global position system (GPS) receiver to provide position and attitude information for the pointing system and to locate the altimeter pulses on the nadir track to 5 arc seconds. Ranging measurement data, target location data, control commands, and software programs for operation are handled by the system computer. The data rate with both the altimetric and ranging modes operating is less than 1 Mbit/sec.

Simulations have been conducted to derive the accuracy with which baseline lengths, heights, and orbital parameters can be determined using typical GLRS retroranging data. Equations of satellite motion are solved simultaneously by quasi-dynamic data reduction techniques to find the satellite trajectory and ground target locations. Noise in the observations and imprecision in the force model—which includes the gravity field, drag, solar radiation pressure, solid Earth and oceanic tides, Earth rotation and polar motion, third body attractions, etc.—are the major sources of error. To reduce errors,



Eos Geodynamic Laser Ranging System.

short orbital arcs are taken to derive the intersite distances while computing independent satellite orbital parameters. Noise-limited calculations indicate uncertainties of 2 to 3 mm for a typical target grid; the noise-plus-bias uncertainty is less than 1 cm for distances up to 250 km, with vertical accuracies better than 1.5 cm. By tuning the orbital parameters, the orbit can then be found with an error of less than a few tens of centimeters over a 3 to 16 day period. The orbit-determining capability supports other sensor data collected from the platform.

Conceptual design studies are now underway. More detailed engineering design studies have begun. The GLRS is scheduled to be placed into orbit aboard the Eos platform in 1997. This instrument, the first ranging facility to fly, will serve an international com-

munity of scientists seeking to understand the solid Earth.

Contact: Kenneth S. Brown
Code 625

Sponsor: Eos Project

Mr. Kenneth S. Brown is Study Manager for the Eos GLRS facility. He has studied, designed, and managed instruments for extraterrestrial and Earth physics applications during his 19 years at Goddard. Prior to that, Mr. Brown was lead mechanical engineer on two IMP spacecraft. He received a BS degree in mechanical engineering from Purdue University in 1957.

MEASUREMENT OF GLACIER MASS BALANCE CHANGE BY ANALYSIS OF REFLECTANCES DERIVED FROM LANDSAT THEMATIC MAPPER DATA

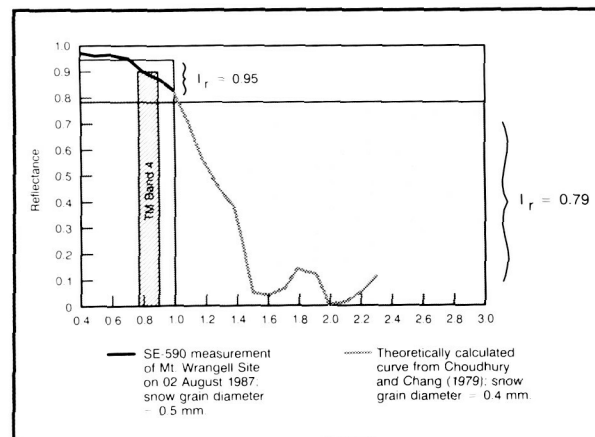
Research has shown that up to 50 percent of the observed sea level rise over the past 100 years may be attributable to the melting of the small glaciers of the world. Small glaciers (i.e., all glaciers and ice caps, with the exclusion of the Greenland and Antarctic Ice Sheets) are sensitive indicators of short- and long-term climate change, and climatic effects are often observable on decadal time scales. These glaciers represent a key to understanding the existence and rate of global climate change.

Detailed study of the reflectance characteristics of ice and snow has been conducted using satellite and ground measurements on glaciers in Greenland and Alaska. On an unnamed glacier in Alaska's Wrangell Mountains, the reflectance integrated over discrete parts of the reflective range of the electromagnetic (EM) spectrum, or integrated reflectance, I_r , was computed using in situ reflectances (for the visible part of the spectrum) and theoretically derived reflectances (beyond the visible part of the spectrum) according to the following equation:

$$I_r = (\sum SE * R) \div \sum SE$$

where R is the surface reflectance of the target or feature, and SE is the incident solar energy in a specified part of the EM spectrum. I_r for the part of the spectrum from 0.40–1.0 μm was computed to be 0.95, while I_r over almost the entire reflective range of the spectrum (0.40–3.0 μm) was 0.79, as shown in the accompanying figure. This example demonstrates the importance of using the full spectrum reflectance for computing snow and ice albedo, and for calculating energy and mass balance parameters.

In terms of glacier mass balance, reflectance has been computed using Landsat Thematic Mapper (TM) band 4 data (0.76–0.90 μm). The data were corrected for atmospheric effects using a multiple scattering atmospheric correction model, and compared with in situ measurements taken at a nadir-viewing angle. To ensure that the TM-derived reflectances represent physically meaningful values, field research was conducted on valley glaciers in Greenland in 1986, and Alaska in 1987. Results showed that after atmospheric



Integrated reflectance of snow derived from spectrometer measurements on a glacier on Mount Wrangell and theoretically calculated values.

corrections were applied, TM-derived reflectances matched in situ reflectances, obtained with a hand-held spectrometer, to within 6 percent using TM bands 1–4 on the glacier in Greenland. At the same time, TM band 4-derived reflectance matched the in situ reflectance to within 1 percent on an unnamed glacier in the Wrangell Mountains of Alaska.

I_r may be computed using the six reflective bands of Landsat TM data that cover parts of the EM spectrum from 0.45–2.35 μm . Computation of I_r for glacier zones provides a more meaningful representation of energy balance changes between years, and thus energy absorption, than does computation of the reflectance using only a discrete part of the reflective spectrum.

A glacier or ice sheet may be divided into two major units, an ablation and an accumulation area. Expansion of the ablation area, along with retreat of the glacier terminus and glacier thinning, indicates that a glacier is in a state of negative mass balance. This can be detected by detailed, in situ, field study. Also, the glacier terminus retreat and expansion of the ablation area can be detected using Landsat TM-derived reflectances.

Retreat of the Pasterze Glacier of the Grossglockner glacier system in the Austrian Alps has been monitored in situ for more than 100 years. Landsat TM band 4 reflectances, computed for the entire glacier basin, have shown a reduction of reflectance



from 60.2 to 50.2 percent from an August 3, 1984 TM scene, to an August 9, 1986 TM scene. This reduction in reflectance is due primarily to expansion of the Pasterze Glacier's ablation area that resulted from reduced snowfall, and warmer spring and summer temperatures in 1986, as opposed to 1984. When data saturation in TM bands 1-3 is not a problem, then I_T can be calculated from TM data for an entire glacier system and compared between years.

This method of studying glacier mass balance change utilizing satellite reflectances may be applied to glaciers on a regional scale, and may thus be used to study changes in glacier energy and mass balance over a period of years. These changes can then be related to changes in regional and global climate conditions.

Contacts: Dorothy K. Hall, Alfred T. C. Chang,
James L. Foster and Robert A.
Bindschadler
Codes 624 and 671

Sponsor: Hydrological Sciences Branch

Dr. Dorothy K. Hall has been working with visible and near-infrared satellite data to devise techniques to measure mass balance change in small glaciers.

Dr. Alfred Chang works in the Hydrological Sciences Branch. Pursuing his interests in radiative transfer and microwave interactions, he studies microwave interactions with snow, soil, vegetation, and precipitation.

Mr. James Foster conducts research on snow properties with microwave radiometry and albedo measurements.

Dr. Robert Bindschadler is a glaciologist in the Ocean and Ice Branch, studying the dynamics of ice sheets and their role in global climate.

ESTIMATING SOIL SURFACE TEMPERATURES AND HEAT FLUXES FROM PROFILE TEMPERATURE AND FLUX MEASUREMENTS

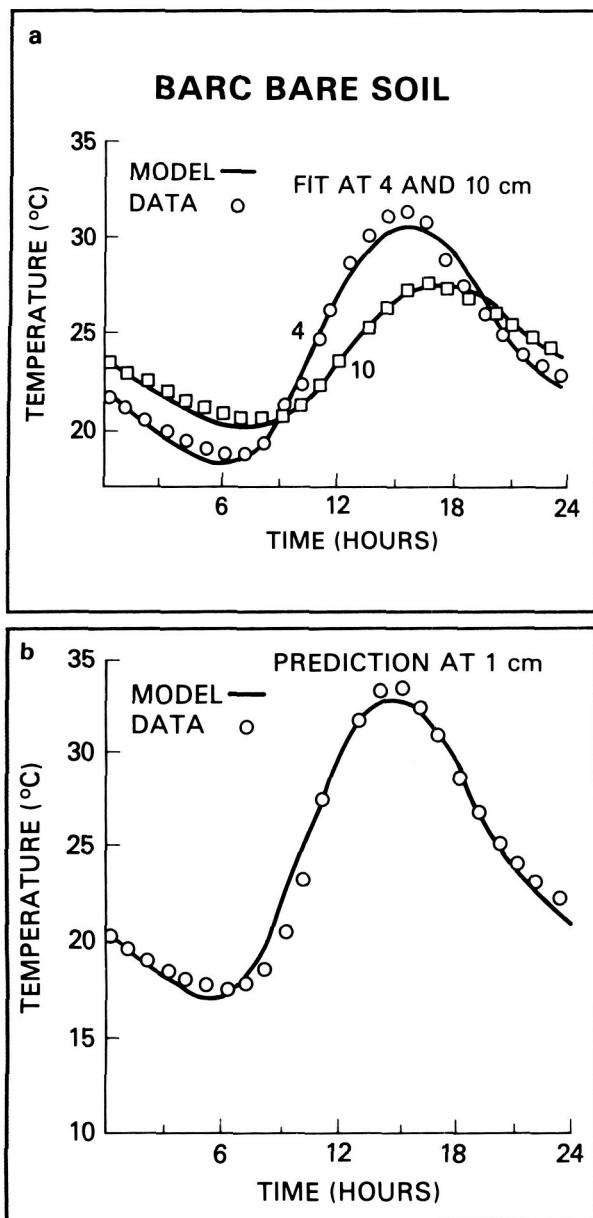
Energy and moisture balance studies of the Earth's surface frequently require estimates of the soil heat

flux and temperature at the soil surface, for intervals of an hour or less. These estimates are needed for bare soils and those under vegetation when calibrating multilayer energy balance models. The surface flux cannot be measured directly, and the soil surface temperature can be measured radiometrically only if there is no vegetation. Goddard Space Flight Center (GSFC) scientists have developed a method to estimate the surface temperature and flux from just a few subsurface temperature measurements.

The most recent methods fit the soil temperature data to the Fourier series solution of the heat flow equation (Carslaw and Jaeger, 1959). The surface flux can be computed in this way by fitting a daily time series of hourly temperatures at two or more depths to the Fourier series and then evaluating the analytical derivative at the surface (Horton and Wierenga, 1983). This method also requires independent estimates of the thermal conductivity and heat capacity.

GSFC staff have extended that work by fitting the Fourier series with less data and with physically identifiable fitting parameters. This will extend the usefulness of the method to situations in which only a few measurements are available. For example, some U.S. Weather Service stations routinely measure daily maximum and minimum temperatures at a fixed soil depth. If these measurements can be supplemented with remotely sensed soil surface temperatures near sunrise and the daily maximum, these four data points could be used to estimate the four model parameters and then to calculate the soil surface temperature throughout the day. This approach would be very useful for regional energy-balance studies. It may also be possible to estimate values for one or more of the parameters, further reducing the number of temperature measurements needed.

This model assumes that the surface soil heat flux is constant at night and varies sinusoidally during the day and that the Fourier coefficients are computed analytically. The fitting parameters are the constant nighttime and maximum daytime fluxes; soil thermal conductivity and heat capacity; and a constant temperature offset, which is the daily mean surface temperature. The temperature and flux equations therefore have five unknown parameters. These unknowns reduce to four if only temperatures are predicted and used for calibration.



Comparison of modeled and estimated soil temperatures for the BARC bare soil plot. Curves are labeled with depth in cm. Panel a compares the data at 4 cm (circles) and 10 cm (boxes) to the model fits (solid line), and Panel b compares the data at 1 cm (circles) to the model predictions (solid line).

The first test uses data from a field experiment performed at the Beltsville Agricultural Research Center (BARC) in Beltsville, Maryland, during the summer of 1985 (Camillo et al., 1986). The data used here

were taken on August 5 and consist of half-hourly measurements of soil temperature at depths of 1, 4, and 10 cm in bare soil. Soil heat fluxes were not measured, and concurrent surface and subsurface temperatures were not available due to instrument problems. The two deepest temperatures were used to estimate the model parameters, which were then used to predict the temperatures at 1 cm.

The results are summarized in panels a and b of the first figure and the first line of the table. Panel a shows the fit of the model to the 4 and 10 cm data, and the first line of the table gives the parameter values and the root mean square error (RMSE) of the fit in panel a. The mean and RMSE of the predicted minus measured values from panel b are in the last column.

This analysis was repeated on data taken during an experiment near Phoenix, Arizona in March 1971 (Jackson, 1973) using soil heat fluxes and temperatures at 5 cm. These data were available only when the surface soil moisture changes over the day were large, so the profile could not be considered homogeneous. This data set demonstrates how to fit using temperatures and fluxes together and provides a test of how well the model performs when the assumption of a homogeneous profile is violated. Line 2 of the table shows the parameter values. The second figure shows the temperatures and fluxes.

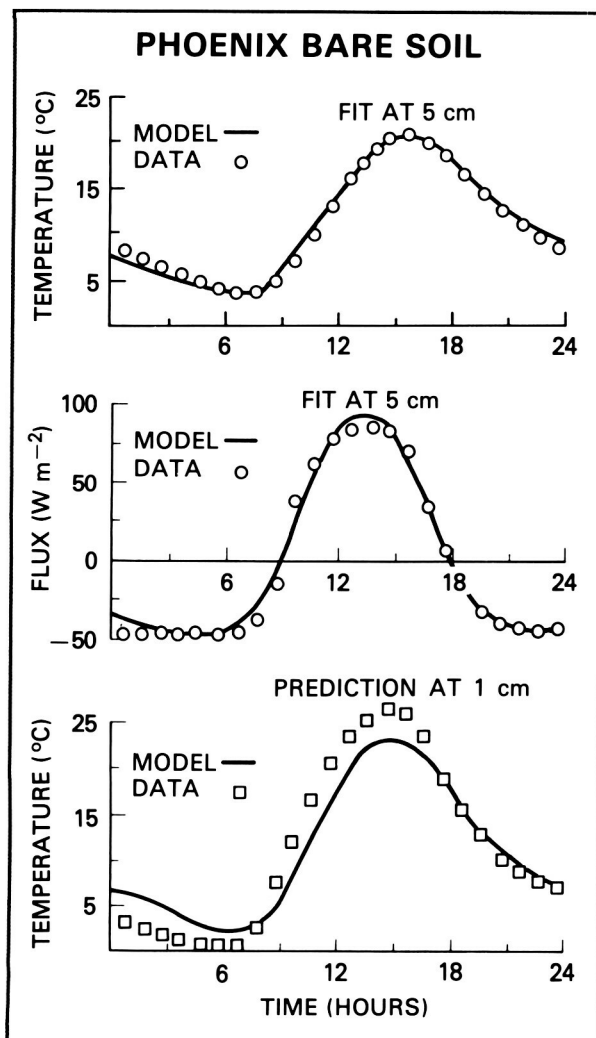
The size of the RMSEs relative to the expected measurement errors is a good indication of how well the model represents the data. The accuracy of the temperature data is about 0.2°. Comparing this data to the fit RMSEs of the table (column 6) shows that the model errors are about two to four times this size. On the other hand, the smallest RMSE in model extrapolations to other depths (column 7) is 1°, about 5 times the expected measurement error. Clearly the model extrapolations are not as good as the fits, but the errors are small enough so as to be useful in most energy-balance studies. The fact that the extrapolations to the surface have a very small bias is particularly appealing. And even though the RMSEs are larger than what one would expect from a point measurement, they are still on the order of the surface temperature spatial variability one would measure in a natural environment.



Summary of the Model Inversions Using the BARC and Phoenix Data

Data Source	G_0/G_1	G_1/λ $^{\circ}\text{C}/\text{m}^{-1}$	λ/c $10^{-6}\text{m}^2\text{s}^{-1}$	T_a $^{\circ}\text{C}$	G_{1-2} Wm^{-2}	Fit RMSE $^{\circ}\text{C}$	Predicted Bias, RMSE $^{\circ}\text{C}$
BARC	-0.497	1140	0.592	24.3	—	0.46	0, 1.0
Phoenix	-0.420	951	1.65	11.1	122.4	T:0.7 $^{\circ}\text{C}$ G:6.8 Wm^{-2}	-0.1, 2.2

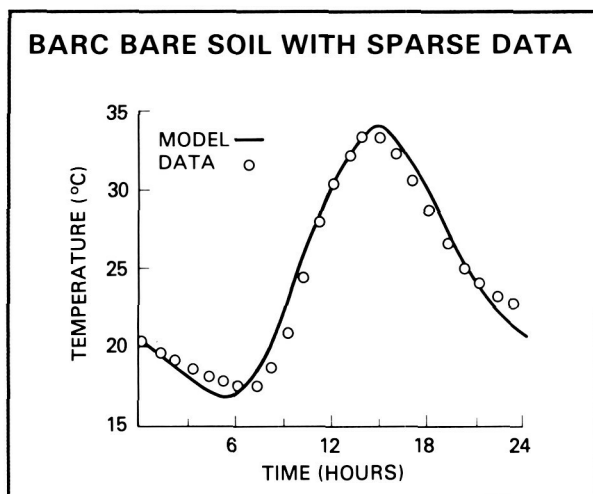
* Column 1 shows the field, columns 2-6 show the parameter values, and column 7 is the RMSE of the fit. The last column shows the bias and RMSE when comparing predicted and measured near-surface temperatures.



Comparison of modeled and measured temperatures and fluxes for the Phoenix data when fitting on temperatures and fluxes at 5 cm. Panel a shows the measured (circles) and fit (solid line) temperatures at 5 cm. Panel b is the same for the fluxes at 5 cm, and Panel c shows the comparison between measured (boxes) and predicted (solid line) temperatures at 1 cm.

The model has only four or five parameters and may be applied with fewer data points than have been used so far, so it is important to test the inversion with sparse data. In any situation data selection will depend on data availability. Remote sensing instruments on Earth-orbiting spacecraft routinely provide estimates of surface radiances at time intervals ranging from days to hours. The Earth Observing System (Eos) will provide frequent surface temperature measurements. It is useful to test the model with a couple of measurements at the depth where one wants to estimate the diurnal variations, and a couple of deeper measurements. The third figure shows the results of using only the maximum and minimum temperatures at 1 and 4 cm. The agreement is as close as in panel b of the first figure, which used half-hourly data from 4 and 10 cm. It appears that daily maximum and minimum temperatures at the surface and a few cm below it could represent surface temperatures throughout the day.

The model equations for the outlined estimation method are the usual Fourier series solution to the



Comparison of measured (circles) and predicted (solid lines) temperatures at 1 cm for the BARC bare soil data when fitting the maximum and minimum temperatures at 1 and 4 cm.

heat flow equations, but with analytical expressions for the coefficients calculated by assuming a function for the surface heat flux. The equations depend on only four or five physically identifiable parameters, the number depending on whether or not soil heat flux data are used in the calibration. Tests show that the model can be fit to subsurface temperatures and heat fluxes to an accuracy two to four times the expected measurement errors. Using this calibration, the model may then be used to predict temperatures and fluxes at other depths, the most useful being at the surface, with a degraded but still acceptable accuracy. The best results were found when calibrating with either temperatures at two depths, or temperatures at one depth and heat fluxes. While the data were sparse, the accuracy of the predictions appears to be as high as for predictions made with half-hourly temperature measurements.

Contact: Robert Gurney
Code 624

Sponsor: Office of Space Science and Applications

Dr. Peter Camillo, who did this work, had 10 years of experience at Goddard. He was responsible for the numerical modeling of physical systems at the Hydrological Sciences Branch. Dr. Camillo had a

PhD degree in physics from the University of Virginia. He died in October 1988.

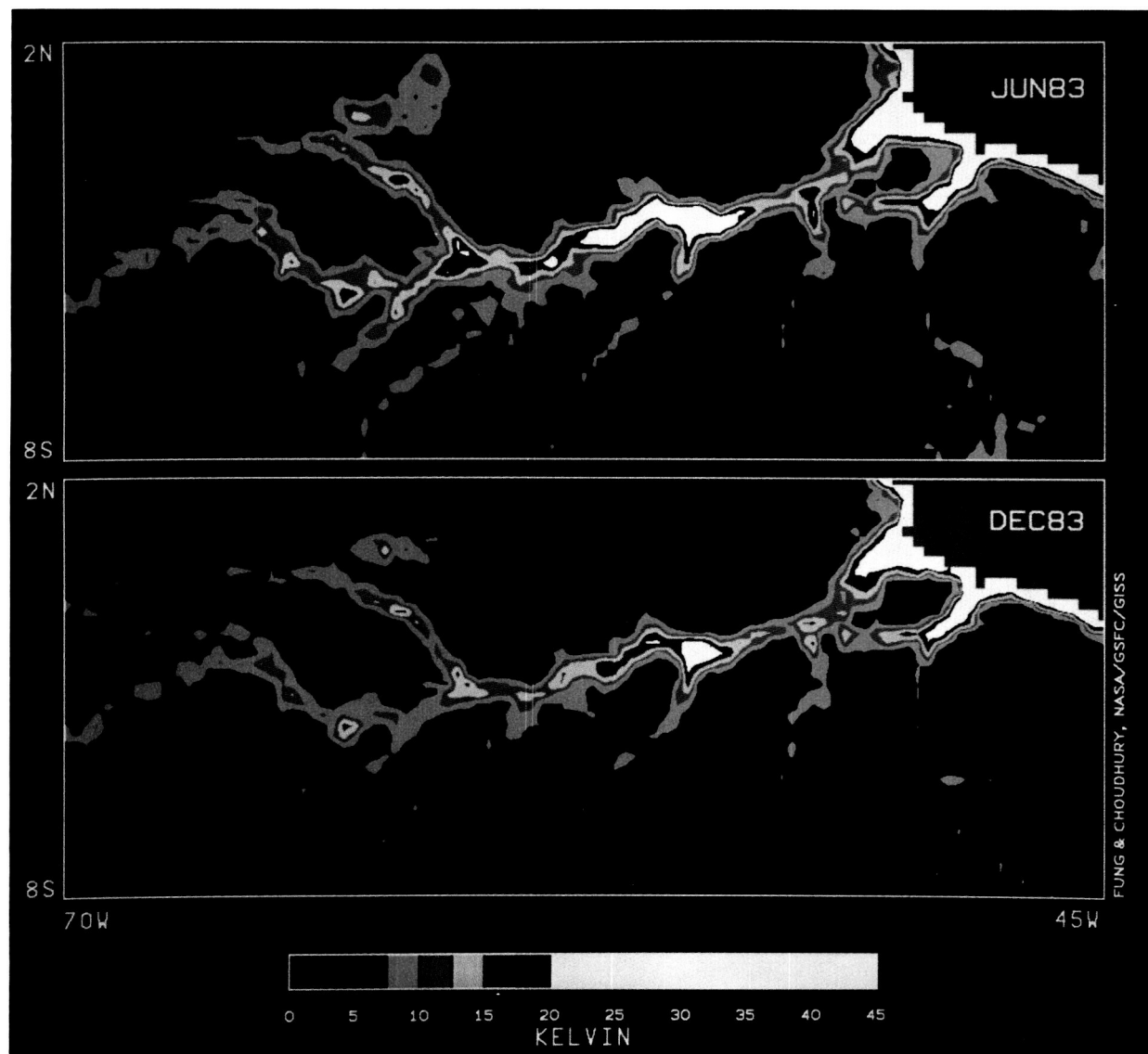
SATELLITE OBSERVATIONS OF AMAZONIAN INUNDATION

Methane, a major greenhouse gas that is active in tropospheric chemistry, is produced under anaerobic conditions of flooded soils. Although natural wetlands and rice paddies are estimated to contribute up to half of the global source of methane, the distribution and magnitude of the emissions are highly uncertain because of the difficulty of direct observations. The inundation area and duration of flooding, among other factors, affect both the magnitude and seasonality of the methane flux to the atmosphere.

At microwave wavelengths, the dielectric constant of liquid water is higher than that of dry soil by about a factor of 25, resulting in an emissivity of ~ 0.95 for dry soils and <0.6 for wet soils. Because of this sensitivity of the emissivity to the water content of the soil, remote sensing in the microwave spectrum has been demonstrated to be successful for monitoring soil moisture.

Seven consecutive years of monthly microwave data for the globe have been processed and analyzed. The data are the dual-polarized brightness temperatures at 37 GHz obtained by the Scanning Multichannel Microwave Radiometer (SMMR) aboard Nimbus-7. The global coverage is accomplished in about every sixth day, with Equator crossing at 12.00 and 24.00 hours, local solar time. The weekly values were composited to minimize the effects of cloud and rain on the microwave brightness temperature.

The difference between vertically and horizontally polarized brightness temperatures at 37 GHz (PD), has been computed from the SMMR data. PD is high ($\sim 40^\circ\text{K}$) in desert and dry regions. It decreases rapidly as the surface gets covered by vegetation, but increases to 60°K for open water. The first figure displays the SMMR 37 GHz PD for the Amazon Basin for June and December 1983, at the height of the wet and dry seasons, respectively. A striking feature is the expansion, during the wet season, of the region of $\text{PD} > 8^\circ\text{K}$ in the vicinity of the Amazon River and its tributaries, representing the inundated

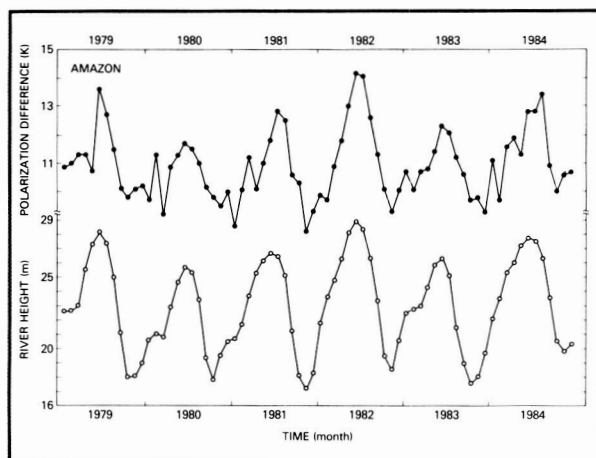


PD (in Kelvin) for the Amazon Basin (8S-2N, 70W-45W) for June 1983 (upper panel) and December 1983 (lower panel). The areas of high PD values correspond with the Amazon River, its tributaries, and floodplains from its headwaters in Peru to its mouth in the Atlantic Ocean (the grey area in the upper right corner of each panel).

forests (varzeas and igapos) of Amazonia. Also evident is the large expanse of igapo forest near the confluence of Rio Branco and Rio Negro during the rainy season. This seasonality contrasts with that of the rainforest, where PD is $\sim 5^\circ\text{K}$, with small seasonal variations.

The time series of PD averaged for the Amazon Basin shows good correspondence with the time series of

river height at Manaus, Brazil, an indicator of the streamflow of the main stem. The relationship is shown in the second figure. The interannual variations of the peaks in both the PD and river height data are in step with measured rainfall fluctuations for the region. Such correspondence supports the use of PD as a monitor of seasonal inundation of the Amazon Basin. Using $\text{PD} > 8^\circ\text{K}$ as a criterion for inundation, scientists can obtain a first estimate of



Comparison of PD averaged for the Amazon Basin (upper panel) and the river height data at Manaus (lower panel) for 1979–1984.

a seasonally inundated area of $\sim 75,000 \text{ km}^2$. This estimate is slightly higher than, but of the same order of magnitude as, the areal estimate collated from asynoptic surveys. While much research is still required to improve estimates of inundation using microwave data, the ability to describe monthly fluctuations of Amazonian inundation is an important first step towards long-term monitoring of natural wetlands and their role in the global carbon cycle.

Contacts: Inez Fung and Bhaskar Choudhury
Codes 640 and 620

Sponsor: Office of Space Science and Applications

Dr. Inez Fung has been studying the global carbon cycle through a combination of global modeling, remote sensing, and synthesis of field observations. Dr. Fung received her ScD degree from the Massachusetts Institute of Technology.

Dr. Bhaskar Choudhury is a solid-state physicist with the Hydrological Sciences Branch. Dr. Choudhury received a PhD degree from American University.

CONSTRAINTS ON MEASURING BRDF FROM A POLAR ORBITING PLATFORM

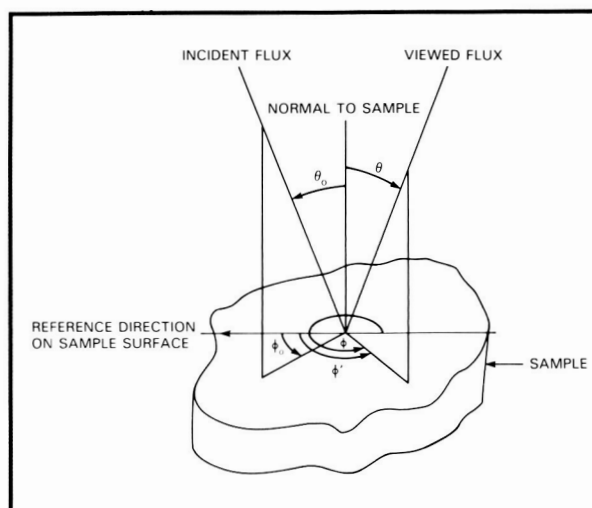
The Bidirectional Reflectance Distribution Function (BRDF) is a fundamental property describing the

reflection characteristics of a surface. It is denoted by ρ , and defined by the following equation:

$$\rho = L(\theta, \phi) / E(\theta_0, \phi_0)$$

The angles θ_0 , ϕ_0 refer to the direction of the radiating source (the Sun), and the angles θ , ϕ refer to the direction of the sensor, as shown in the first figure. In this definition, the term L ($\text{W}/\text{m}^2 - \text{sr}$) is the reflected radiance at the surface of the Earth in the direction θ , ϕ produced by the incident irradiance E (W/m^2) of a well collimated beam (parallel rays) from the direction θ_0 , ϕ_0 . The angles θ and θ_0 lie in the range 0 to $\pi/2$, and the angles ϕ and ϕ_0 lie in the range 0 to 2π . In addition to permitting identification of land surface features, the BRDF allows for a more complete description of the radiative boundary condition at the Earth's surface. In principle, remotely sensed radiance data could be utilized periodically along with an atmospheric model to estimate the BRDF on a grid over the Earth's surface. The globally estimated values of BRDF could then be utilized to provide the radiative boundary condition at the Earth's surface in a global energy-balance model. Errors in estimated hemispheric reflectance as high as 45 percent have resulted when using nadir views only.

In order to estimate the radiance L at the surface of the Earth from the radiance measured by the sensor on board a satellite, the effects of the atmosphere must be removed by use of an atmospheric model.



Bidirectional reflectance geometry.

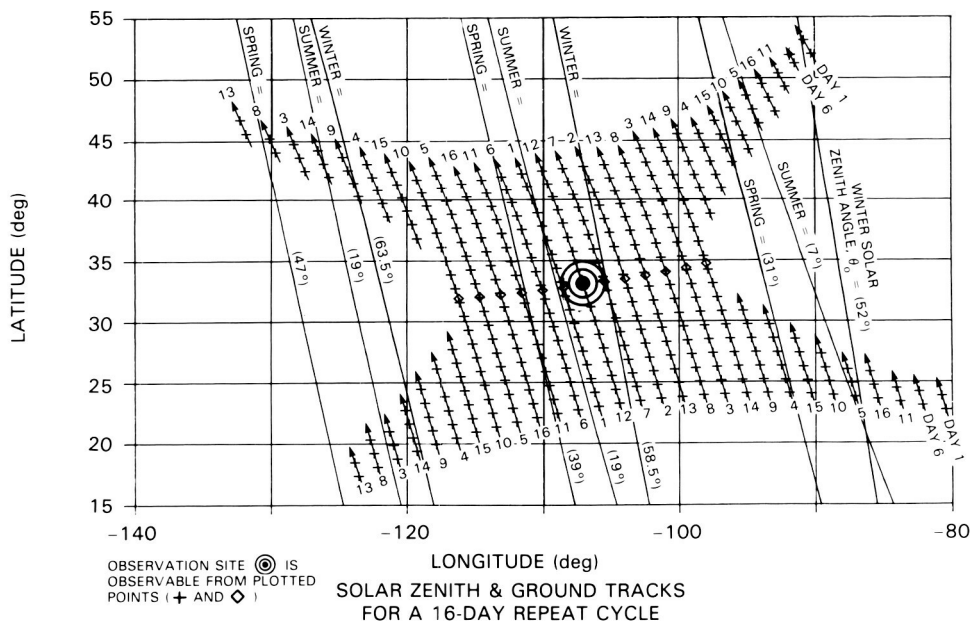
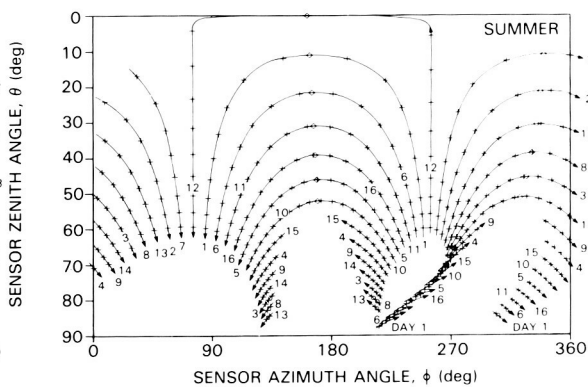
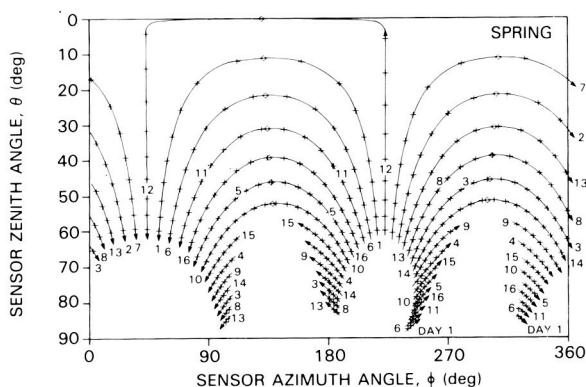
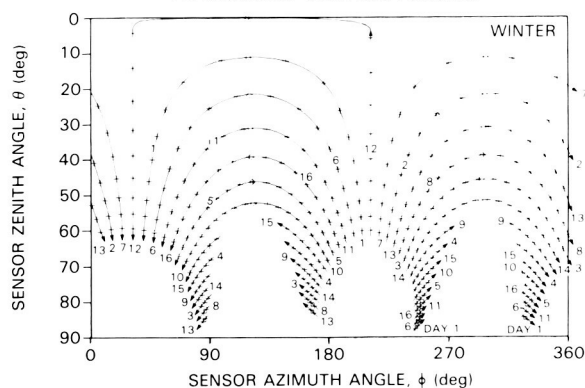


BRDF GEOMETRICAL CONSTRAINTS

OBSERVATION SITE: WHITE SANDS, NM
 LONGITUDE: 107 W
 LATITUDE: 33. N

LEGEND: + MODIS-T
 ◇ MODIS-N

ATTAINABLE VIEWING ANGLES



Ground tracks of a polar orbiting satellite and corresponding BRDF angle trajectories for a typical ground observation point.

In this activity, the available range of values of θ and ϕ for which reflected radiances can be measured from a polar orbiting platform has been determined. The second figure presents the trajectories of BRDF angles (i.e., θ versus ϕ) for nominal Eos ground tracks for a typical ground observation point. The observation point is located at 107°W longitude and 33°N latitude, which is White Sands, NM. At the bottom of this figure are shown, all the points along the typical ground tracks for which sensors, such as MODIS-N and MODIS-T, can see the observation point. MODIS-N has a one-degree-of-freedom cross track scan angle of $\pm 45^\circ$ about nadir, and MODIS-T has a two-degree-of-freedom scan that includes the $\pm 45^\circ$ cross track scan and an orthogonal $\pm 50^\circ$ tilt along track. In order to realize all the MODIS-T observations shown in the figure, the scan mirror angles would need to be programmable. Lines of constant solar zenith angle at the observation point for winter, spring, and summer are shown on the ground track plot. At the top of this second figure are the MODIS-T BRDF angle (θ versus ϕ) trajectories for winter, spring, and summer, corresponding to the ground tracks shown at the bottom of the figure. The attainable MODIS-N BRDF angles (only one value of θ versus ϕ for each ground track) are also shown on the trajectory plots.

Contact: Harry Montgomery
Code 620

Sponsor: Eos Project

Dr. Harry Montgomery, in the Sensor Concepts and Development Branch, develops preliminary designs of new sensors from new starts, through subsequent Phase A (feasibility) investigations, and through Phase C/D (hardware) development. He is the Instrument Study Manager for the Eos MODIS-N facility instrument. Remote sensing and information extraction from observations are his primary interests. He has won the Group Achievement Award for VAS demonstration. His PhD degree is in aerospace engineering.

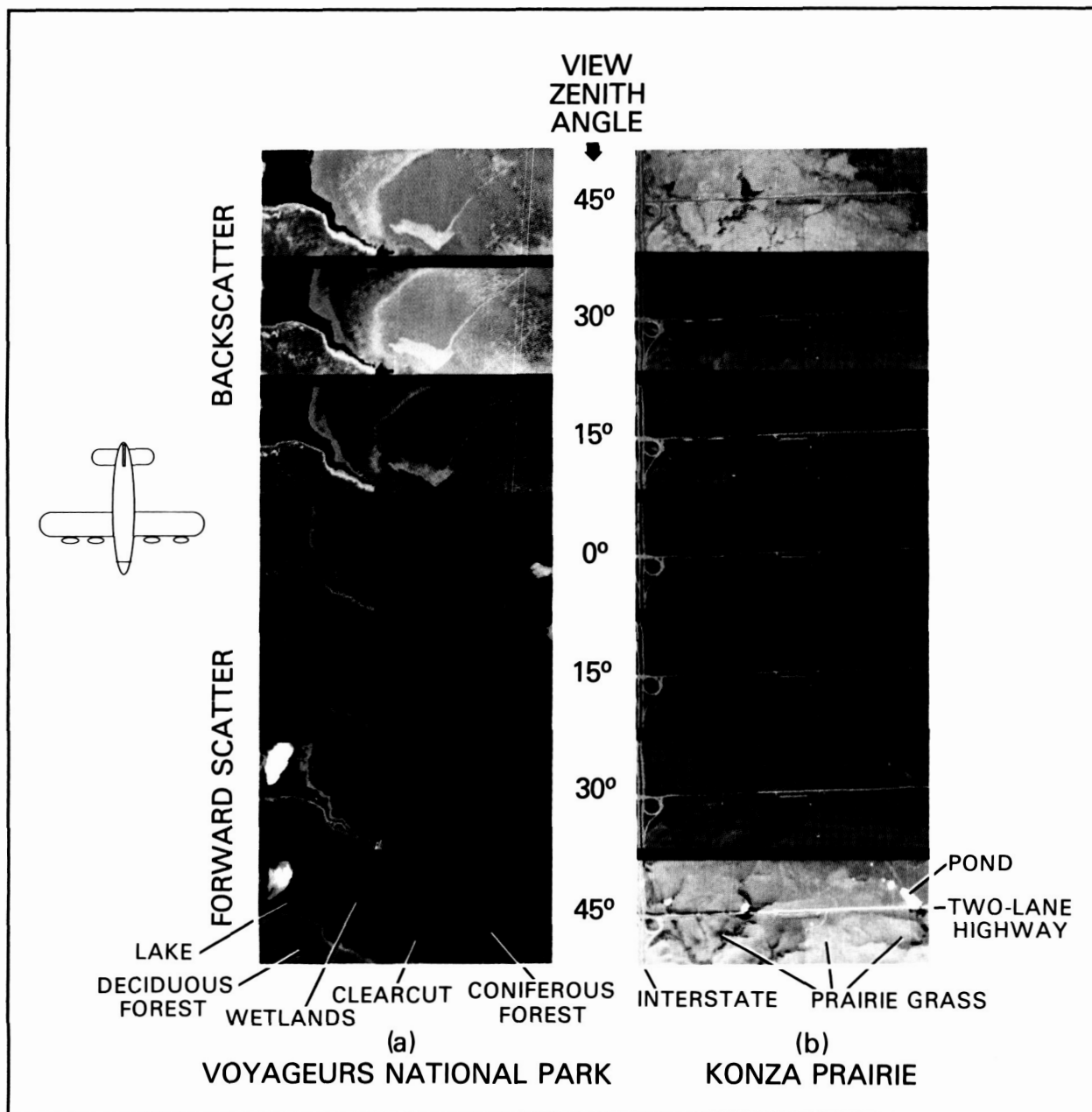
FOREST AND GRASSLAND ECOSYSTEM STUDIES USING THE ADVANCED SOLID-STATE ARRAY SPECTRORADIOMETER

One of the advantages offered by area detector array technologies is the capability to build imaging sen-

sors having compact optical heads with no moving parts. In addition to the obvious benefits of reduced payload size, weight, and complexity, a compact optical head facilitates the off-nadir pointing of the sensor field-of-view. Pointing capabilities are planned for at least two sensors, the Moderate Resolution Imaging Spectrometer-Tilt (MODIS-T) and the High Resolution Imaging Spectrometer (HIRIS), aboard the Earth Observing System (Eos). In advance of the Eos, scientists and engineers at Goddard Space Flight Center (GSFC) have been conducting terrestrial ecosystems research with a pointable airborne sensor called the Advanced Solid-State Array Spectroradiometer (ASAS).

ASAS employs area detector array technology to acquire digital image data in 30 visible and near infrared spectral bands, with a spectral resolution of 15 nm. When installed aboard the National Aeronautics and Space Administration (NASA)/Ames C130 or NASA/Wallops Skyvan aircraft, a gimbal-mounted mounting bracket allows ASAS to be pointed up to 45° off-nadir either fore or aft of the aircraft. ASAS is able to track and image a target site through a sequence of seven or more fore-to-aft view angles as the aircraft approaches and flies past the site. ASAS is calibrated, maintained, and operated by GSFC.

The value of acquiring data from multiple-view directions for ecosystem studies stems from the anisotropic nature of reflectance from land surfaces. Reflectance from land surfaces varies not only with the wavelength of observed radiation, but also varies with the view direction relative to the direction of illumination from the Sun. Observations of these reflectance variations provide information on the composition and geometric structure of such land features as plant canopies and soils. Varying the sensor view direction from a remote platform also varies the atmospheric path length through which the reflected energy is transmitted; multiple-direction data can therefore potentially provide information on atmospheric optical thickness and related conditions. Furthermore, multiple-direction observations can improve remote estimations of surface albedo (the total solar energy reflected in all directions) relative to estimates derived from single-direction observations. Measurement of albedo is critical to understanding the disposition of intercepted solar energy, which drives terrestrial processes within and across ecosystems.



Sequences of ASAS images from seven fore-to-aft view directions, showing the anisotropic reflectance characteristics of two ecosystems: (a) images acquired over a forest ecosystem in Voyageurs National Park, Minnesota, on June 26, 1988, with a solar zenith angle of 34°; (b) images acquired over a prairie grass ecosystem near the Konza Prairie, Kansas, on July 11, 1987, with a solar zenith angle of 48°. The platform aircraft flew in the solar principal plane (i.e., directly into or out of the Sun) over both sites. Backscatter indicates the observation of solar radiation scattered back towards the Sun, while forward scatter indicates the observation of radiation scattered towards the direction of specular reflection. Note the specular glint from water bodies at the forward-view zenith angles closest to the solar zenith angles. Data from a near-infrared spectral band, a red band, and a green band were coded as red, green, and blue, respectively, to create the images.

During the past year, ASAS data were acquired for two ecosystem studies. The accompanying figure shows ASAS images from the two studies. One is from an ongoing study of a prairie grass ecosystem called the First International Satellite Land Surface Climatology Program (ISLSCP) Field Experiment (FIFE). The study site is the Konza Prairie Long Term Ecological Research area near Manhattan, Kansas. FIFE is an extensive study, involving investigators from a number of Earth science disciplines and research institutions, with NASA as the lead agency. The objectives of FIFE are: to better understand the role of vegetation in interactions between the atmosphere and the land surface, and to investigate the use of satellite observations to infer climatologically significant land surface parameters. ASAS data were acquired over several instrumented sites within the study area during four 2-week periods that were spread over the 1987 prairie grass growing season. The goals of the ongoing data analyses are: to relate spectral and directional distributions of prairie grass reflectance to phenology, biomass, and leaf area; and to demonstrate improved estimates of prairie grass albedo from multiple-direction observations.

The other current study involving ASAS is the Forest Ecosystem Dynamics Project at GSFC. This project is designed to investigate the use of remote sensing data in modeling interactions between forest vegetation, soil, and radiation environments. ASAS data were acquired for the project in June 1988 over northern coniferous forests in Minnesota. These data are intended for analyses of forest canopy structure, as well as for analyses of directional reflectance distributions and estimates of forest canopy albedo. Plans call for further acquisitions of ASAS data over coniferous forests in Maine during 1989.

Plans for 1989 also include ASAS flights over White Sands, New Mexico, and flights over several simulated aircraft crash sites. Multiple-direction reflectance observations of the gypsum sands of White Sands are needed to support the use of the area as a calibration target for satellite sensors such as the Eos MODIS-T. Flights over the simulated crash sites are planned in support of a GSFC Search and Rescue Mission investigation into the feasibility of using pointable imaging sensors to locate downed aircraft from satellites. These planned missions demonstrate the diversity of investigations that can benefit from

multiple-direction reflectance observations acquired by sensors such as ASAS.

Contacts: James R. Irons and Frederick G. Huegel
Codes 623 and 725

Sponsor: Office of Space Science and Applications

Mr. James R. Irons works in the Earth Resources Branch to measure and model light scattering from terrestrial surfaces, with an emphasis on soil surfaces. He has also received several Achievement and Performance Awards. Mr. Irons is currently earning a PhD degree at the University of Maryland.

Mr. Frederick G. Huegel, an instrument systems engineer in the Instrument Systems Branch, is especially interested in remote sensing instrumentation. Currently, he is involved with the Moderate Resolution Imaging Spectrometer-Tilt. He holds a BS degree in electrical engineering. Awards that he has earned include the Quality Increase Award in 1985 and the Special Achievement Award in 1986.

RELATIONSHIPS OF SOILS AND VEGETATIVE GROWTH IN SOUTH AMERICA USING SATELLITE IMAGERY

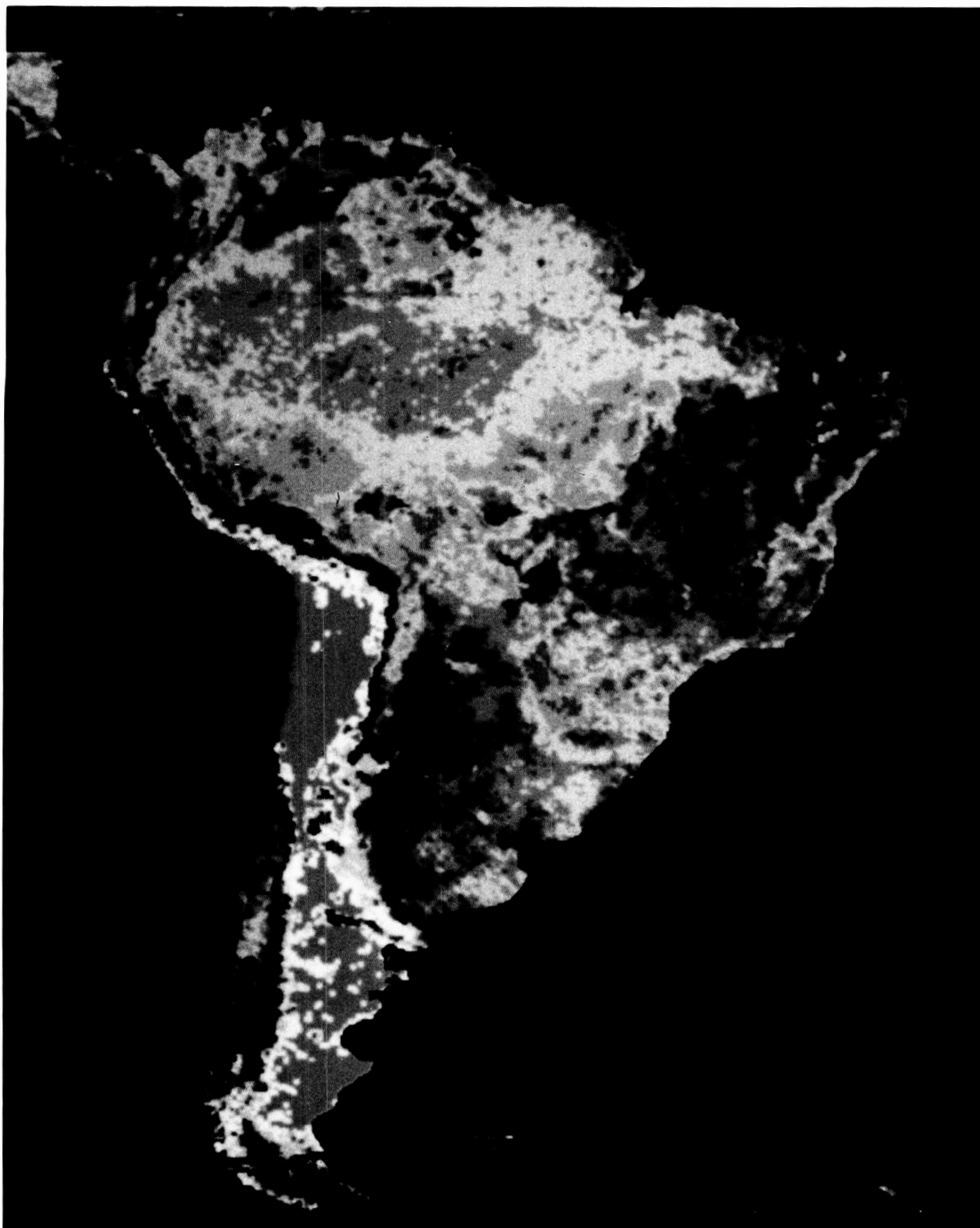
The soil profile is a critical component of the biogeochemical cycle that determines the productivity of vegetation on Earth. Properties and processes that occur within the soil determine moisture, temperature, density, and nutrient availability, all of which relate directly to potential for plant productivity. Thus, vegetative properties such as greenness, senescence, water or metal stress, or nutrient deficiency may be controlled by the condition of a given soil and its potential to act as a suitable substrate for plant growth. Because of this intimate relationship between vegetation and soil properties, the spectral response of vegetation should reflect the status of soil conditions at a given time.

The Normalized Difference Vegetation Index (NDVI) is an index of greenness that has been correlated with known patterns of vegetation seasonality and variability across major biomes and thus may be related to net primary productivity of vegetation. The NDVI is computed as follows:

$$NDVI = (NIR - VIS)/(NIR + VIS) ,$$



A digital representation of a soil map of South America, provided by the UNEP in Geneva, Switzerland. The map was prepared on a 1:5,000,000 topographic base and displays soil association mapping units that are distinguished by color.



Annual integrated image produced from NDVI monthly measurements over the April 1982 to March 1983 time period (NASA/GSFC/Global Inventory Monitoring and Modeling Studies).



where NIR refers to near-infrared wavelength measurement, and VIS refers to visible wavelength measurement. These wavelengths are used to separate vegetation signals from variations in background brightness, and to emphasize the unique reflectance spectrum of photosynthetically active vegetation of low reflectance in the visible (0.4–0.7 μm) spectral region, and high reflectance in the near-infrared (0.7–1.3 μm) spectral region.

Visual comparison of the UNEP-GRID-FAO* map of South America shown in the first figure with the map of NDVI derived from satellite imagery shown in the second figure uncovered similarities between soil mapping units and patterns of vegetative growth. These mapping units represent soils that exhibit common properties and provide a similar source of substrate for vegetative growth. In order to quantify the visual relationships observed between vegetation (as determined by NDVI) and soil properties on the continent of South America, field data from individual soil profiles were collected and statistically compared to NDVI values.

Satellite imagery from the Advanced Very High Resolution Radiometer (AVHRR) on board the National Oceanic and Atmospheric Administration (NOAA) series of polar-orbiting meteorological satellites was used in this study. Monthly composited satellite images of South America were produced to minimize cloud contamination, as well as to reduce the effect of off-nadir imaging by the satellite. These 12 monthly images were then integrated using a trapezoidal approximation to produce an annual pattern of vegetation activity. The final output provided NDVI values for an annual integrated image over the continent of South America for the period between April 1982 and March 1983. Each integrated value represented a 15 km pixel area.

Soil characterization data from 257 soil profiles across the continent of South America were used to correlate NDVI values with soil parameters. Soil variables chosen for analysis were: carbon/nitrogen ratio, nutrient status, pH, bulk density, particle size distribution, and water-holding capacity. In order to account for variability of soils with depth, a separate,

weighted value for each of these variables was obtained for individual soil layers (horizons).

Each of the 257 soil profiles was also assigned a climate classification based on the Koppen system, according to their geographic location. For the profiles used, two general climate types were identified: tropical and temperate. These are further divided by Koppen according to the presence of a dry season, its length, and when it occurs (summer or winter). This resulted in 12 climate groups for South America, into which soil profile data were clustered.

Results of correlation analysis showed that within a given climate group, NDVI was related most to nutrient status (base saturation, acidity, or content of individual cations), pH, silt content, and water-holding capacity of soils. Results varied by climate, depending upon patterns of temperature and rainfall. In addition, correlations were more significant for certain soil horizons than others, which may be due to more intensively weathered soils in particular areas, or to variations in rooting depth of different types of vegetation.

Despite the coarse resolution of AVHRR, and therefore of NDVI, and considering the use of point soils data to represent the large area covered by NDVI pixels, these preliminary correlations indicate that relationships between soils and vegetative growth can be observed using satellite imagery. Weighting and clustering of soil data gave stronger correlations with NDVI than when soil profiles were analyzed individually, because this grouping emphasized common properties of soils over large regions.

Contacts: Elissa Levine and Arlene Kerber
Code 623

Sponsor: Director's Discretionary Fund

Dr. Elissa Levine, a physical scientist with the Earth Resources Branch, is responsible for the modeling of soil genesis processes and for interfacing soil models with remote sensing. She has a PhD degree in soil genesis (agronomy) and has 2½ years of experience at Goddard. In addition, Dr. Levine received the 1988 Peer Award.

*United Nations Environment Programme-Global Resource Information Database-Food and Agricultural Organization

Ms. Arlene Kerber, a physical scientist with the Earth Resources Branch, is currently studying the use of AVHRR imagery of South America for vegetation parameters. She is also interested in better understanding interactions of vegetation, climate, and soil on a continental level. Ms. Kerber has received three Special Achievement Awards.

CLIMATE VARIABILITY IN THE TWENTY-FIRST CENTURY

The global climate is expected to warm during the coming decades as a result of the greenhouse effect of carbon dioxide and other trace gases being added to the atmosphere. The projected climate warming may well have a large impact on societal activities including agriculture, forestry, and general water resource availability. In this regard, the first order effect of changes in mean temperature and precipitation are expected to be important. However, for many biological processes, changes in the degree of climate variability will determine the full extent of its impact. The study described below was conducted to provide a first estimate of changes in future variability.

Researchers used the Goddard Institute for Space Studies general circulation model to simulate the current climate and the climate for the next 100 years. These model runs were then used to assess changes in variability for temperature and precipitation on three time scales: interannual, day-to-day, and diurnal. The model variability for the current climate was also compared with the observed variability for various locations.

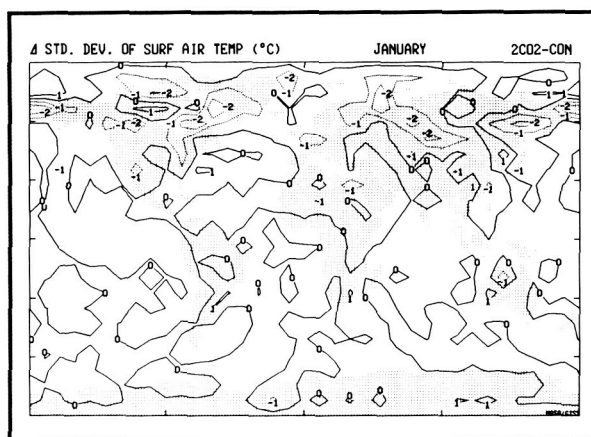
The results show that temperature variability generally decreases in the future on all three time scales. The decrease is often not significant on a local (grid box) scale, although the number of grid boxes that do show the decrease is significant. The general decrease in the interannual standard deviation of surface air temperature in the winter hemisphere between the doubled CO₂ climate and the current climate is shown in the figure. Reduced temperature variability is associated with a decrease in the latitudinal temperature gradient and increased greenhouse gas trapping of radiation. With reduced latitudinal temperature contrasts, air advected into a region from the north or south is of a more uniform

character, diminishing the interannual and day-to-day variability. With increased greenhouse gas absorption, nighttime radiative cooling is reduced, limiting the amplitude of the diurnal cycle.

Precipitation variability generally increases as the climate warms. With a warmer climate, there is more evaporation from the ocean, and more rainfall. With higher absolute rainfall totals, there is greater range for variability, meaning that the absolute magnitude of the variation increases. There is thus a correlation between the sign of the change in the average precipitation and the sign of the change in its absolute variability. Again, the changes are often not significant at a grid box level, although the percentage of locations that experience the increase is significant.

Approximately 60 percent of extratropical locations experience a decrease in temperature variability and an increase in precipitation variability; thus the changes noted above are not experienced everywhere. The magnitude of these changes is often on the order of 10 to 20 percent, large enough to conceivably affect ecosystems and their disturbance frequency. The impact of this change in variability must ultimately be compared with the rapid change in the mean values of temperature and precipitation forecast for the next century.

Contact: David Rind
Code 640



Change in the interannual standard deviation (a measure of variability) of the surface air temperature between the double CO₂ climate and the current climate for January.



Sponsor: NASA Climate Office and EPA

Dr. David Rind, who does research into past and future climate changes, is also interested in climate and middle atmosphere modeling. He has a PhD from Columbia University and eight years of experience at Goddard.

PALEOCLIMATES AT HIGH LATITUDES: IMPLICATIONS FOR FUTURE CLIMATE CHANGE

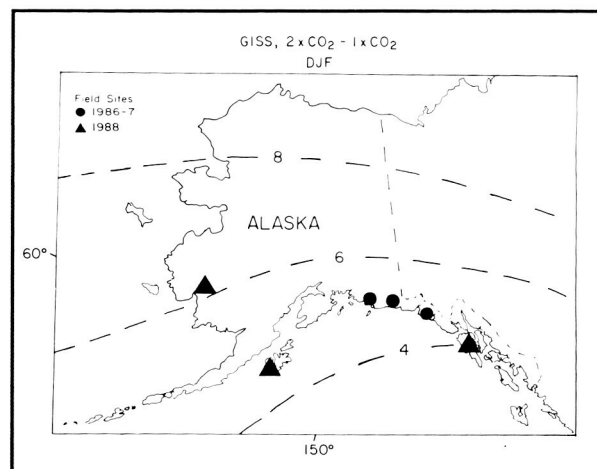
Ice cores from Greenland and Antarctica indicate that rapid and extreme reversals in climate characterized intervals of the last 30,000 years. These reversals are unexplained by Milankovitch insolation cycles, which explain only the gradual glacial to interglacial changes. Thus, the processes and feedbacks involved in global climatic change remain unclear. These include changes in carbon dioxide concentrations, global ice cover, sea level, and ocean circulation. Advancing our knowledge about the mechanisms of climate change requires detailed documentation of paleoclimatic events at various sites of geographical interest. In particular, it is important to document the timing of vegetational and climatic change at sites from different continents and oceans, so that mechanisms in climatic change may be elucidated. Model simulations of paleoclimatic time intervals such as the last ice age may also then be tested against the data.

High latitudes are not only sensitive reflectors of global climatic changes (see global climate model projected temperature increases for increases in carbon dioxide in the accompanying figure), but also play a major role in driving them. Land and sea ice, ocean circulation, and high latitude vegetation are all interactive parts of the ocean-atmosphere-biosphere linkages. Recently several groups have suggested that future climatic changes may be dependent upon these regions. For example, high latitude peat bogs have been proposed as an important source of methane, a greenhouse gas, to the global atmosphere. At present, the type, depth, and age of formation of these peat bogs are unknown. In the light of impending environmental oscillations, the need to provide a historical perspective from the biosphere is clear.

Arctic and subarctic regions such as Alaska are ideal areas for research on global climate change. Peat

bogs and lakes contain stratigraphic sequences of fossil pollen and macrofossils that record vegetational and climatic changes over thousands of years. The climate research group at the Goddard Institute for Space Studies (GISS) is currently investigating the climatic history of various Alaskan sites through analysis of fossil peat and lake sediments. Data from Yakutat, Icy Cape, and Cordova (1986-7) span the last 10,000 years; they indicate that major climatic changes have taken place along the eastern Alaskan coastline. A warmer, drier climate characterized the early Holocene, approximately 7000-9000 years ago. Peat formation began shortly afterward, and high deposition rates, particularly about 3500 years ago, indicate a much wetter environment. Storm activity was presumably much more intense. Climatic cooling in more recent millennia (3500 years to the present) is indicated by the appearance of more montane species in the fossil record.

In 1988, 5 weeks of field research in the Kodiak, Bethel, and Juneau regions of Alaska yielded eight new lake and bog cores. The stratigraphy of fossil pollen, spores, and plant fragments will be used in connection with radiocarbon dating and glacial geology to reconstruct the climatic history at these various locations. Preliminary glacial evidence from western Kodiak Island indicates that marine ice recession was followed by alpine ice advances during the



Winter air temperature change in the GISS climate model for doubled atmospheric carbon dioxide (°C). Location symbols indicate Alaskan sites of paleoclimatic investigation spanning the last glacial to interglacial transition.

transition from glacial to interglacial conditions. Numerous deposits of volcanic ash in the cores also point to the dominant role that volcanism has played in coastal western Alaska over the last 12,000 years.

The timing of glacial-interglacial climate changes in the North Pacific is important for comparison and correlation with documented changes in the North Atlantic region and the southern hemisphere. Questions of particular interest concern how rapidly the climatic changes occurred, their magnitude, and the relationship of the changes in glacial extent to vegetational change. Implications for future climatic changes are derived from a defined historical perspective of past changes, along with a better understanding of the mechanisms and feedbacks within the climate system. Global circulation model simulations

are interactively used to further test hypotheses about causes and processes in climate sensitivity and climate change.

Contact: Dorothy M. Peteet
Code 640

Sponsor: Director's Discretionary Fund
Climate Group at GISS

Dr. Dorothy M. Peteet, working at the Goddard Institute for Space Studies, does paleoclimatic research using fossil pollen and seeds and compares global climate model results with paleoclimatic data. She received her PhD in biology from New York University and has been with Goddard four years.

ATMOSPHERES

TROPICAL RAINFALL MEASURING MISSION PROGRESS

The Tropical Rainfall Measuring Mission (TRMM) is a proposed space system for measuring tropical rainfall and its variations. Such measurements are critically needed for progress in our knowledge of the overall Earth system. Evaporation of water vapor into the atmosphere and its condensation to produce rainfall are at the heart of the Earth's hydrological cycle, which is, in turn, essential for life on the planet. The placement of human settlements has been dictated more by the availability of an ample water supply than by any other factor. The nature of the Earth's vegetative cover is controlled to a very large extent by moisture conditions, and particularly by rainfall. The nature of this heat release, coupled with the resulting motions in the atmosphere, concentrates rainfall in the tropics in a thin latitude band called the intertropical convergence zone. It is now known that year-to-year variations in the latent heat released in this region are a leading cause of global climate variations, including the El Niño/Southern Oscillation (ENSO) phenomenon.

In July 1988, the National Aeronautics and Space Administration (NASA) and the Space and Technology Agency of Japan each successfully completed a 1-year study of the feasibility of implementing TRMM as a joint space mission with the goal of obtaining improved measurements of rainfall over the global tropics and subtropics. A basic product would be a data set of 30-day average rainfall and its vertical distribution over 5° by 5° areas.

The quantifying of global or regional rainfall is a major challenge, due to rainfall's high temporal and spatial variability. Moreover, most of the rain in the tropics falls in regions that are relatively inaccessible to in situ measurements. The quantitative distribution over the tropical oceans is uncertain to a multiplicative factor of about two.

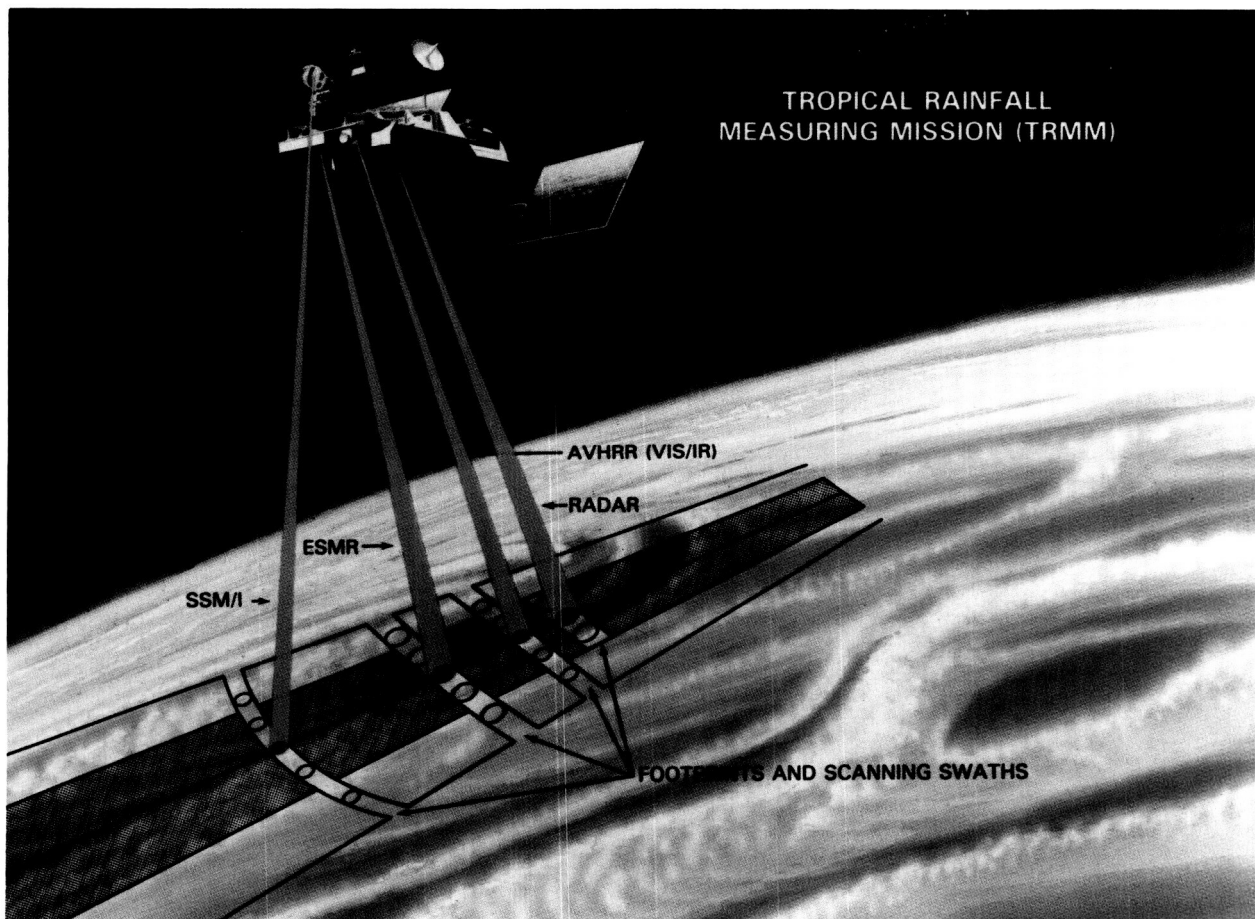
Remote sensing from space has already been helpful in studying rainfall; it promises to be the only useful and economical means of obtaining such measurements worldwide in the future. Spaceborne measurements of outgoing long-wave radiation currently provide our best climatological estimates of rainfall over the tropical oceans. These measurements have been aided by passive microwave measurements from the



electronically scanning microwave radiometer on Nimbus-5, from the scanning multichannel microwave radiometer on Nimbus-7, and since 1987, from the Special Sensor for Microwave Imaging on the Defense Meteorological Satellite. These microwave measurements have all been obtained from polar Sun-synchronous orbits. As a result, they do not give representative estimates of the daily rainfall at low latitudes, owing to the very large diurnal variations of rainfall in the tropics. The same will be true for the microwave measurements to be made on the Eos polar platforms. Present microwave measurements are also more reliable over oceans than over land, where differences in surface emissivity complicate data interpretation.

TRMM will carry three principal instruments. (See first figure.) One is a cross-track scanning multichannel passive microwave radiometer, which will

give good rainfall measurements over the oceans. In addition, TRMM will be the first space mission to include a precipitation radar (14 GHz), which will scan across a narrower track. Use of passive microwave results to constrain the radar equation will permit vertical profiling of rainfall over both land and sea. Vertical rain profiles are important because they may be used with cloud models (developed mainly at Goddard Space Flight Center) to derive vertical profiles of latent heat release. General circulation models and theory have shown that the height distributions of latent heating are vital for understanding and modeling the impacts of tropical rain variability on large-scale atmospheric circulations such as the hemispherewide "teleconnections" associated with an ENSO event. The third instrument is an advanced very high-resolution radiometer (AVHRR) with two or three channels (visible and infrared and an added nighttime visible channel, if



Tropical Rainfall Measuring Mission.

resources permit). When compared with rainfall measurements from the passive microwave and radar instruments, data from this device can be used to better interpret and calibrate visible/infrared rain estimations from past and future operational satellites, which will be of great value to the World Climate Research Program (WCRP).

The TRMM orbit will be circular at an altitude of 350 km and at an inclination of 35° . This orbit will give intensive coverage in the tropics. (See second figure.) It has been shown that if the instruments were perfect, the error due to rain sampling would be less than 10 percent. The 35° inclination causes the orbit to precess, so that it passes over each 5° by 5° box at a different local time each day, allowing the diurnal cycle in rainfall to be documented. The instruments' field of view will extend to latitudes as high as 37° ; this is particularly valuable for the Japanese owing to the large percentage of Japan's rainfall that occurs from the "Baiu front" found at that latitude in spring and summer. An advantage of the relatively low orbital altitude is a smaller instrumental "footprint" and hence higher spatial precision, allowing determination of rainfall variations over smaller spatial scales. As the second figure indicates, an extensive "ground truth" or validation program is underway for testing the remote sensing algorithms. Both the orbit inclination and altitude would permit recovery of the TRMM payload by a shuttle for refurbishment and later deployment on the Space Station.

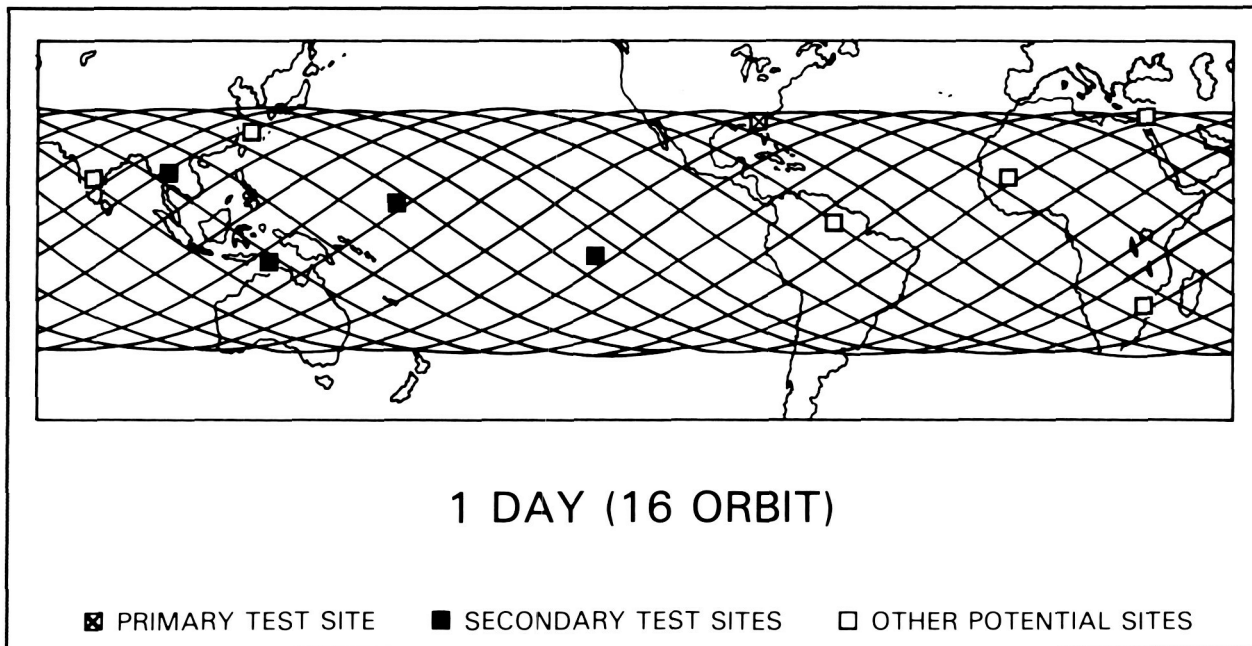
The possibility of a joint U.S./Japanese mission to measure tropical rainfall was proposed in September 1986 in a letter from the NASA Associate Administrator for Space Science and Applications to the Commissioner of Space Activities of Japan. The resulting feasibility studies concluded that a shared mission promises to be both possible and useful. Japan would build the rainfall radar and launch TRMM on its new H-2 rocket. The U.S. would provide the spacecraft, the passive microwave instrumentation, and the AVHRR, and would supply the TRMM data system. With this division of tasks, a TRMM mission seems possible beginning as early as 1994; thus, these data would be available during the later stages of the Tropical Oceans and Global Atmosphere (TOGA) program. Japan has agreed to provide initial funding for the radar, and has tentatively manifested TRMM for a 1994 launch. The

American portion of TRMM is included in NASA's Office of Space Science and Applications budget plan. TRMM is expected to be a candidate for a fiscal year 1990 new start as an early component of the new Earth Probe program (a series of small, specialized Earth science satellites).

In early 1987 NASA selected 20 scientists distinguished in Earth sciences, tropical meteorology, rain processes, and microwave remote sensing as the TRMM Science Steering Group. This group met twice at the Goddard Space Flight Center and once more in connection with a special Symposium on Tropical Precipitation that was held in Japan in October 1987. The group's completed report on the scientific aspects of TRMM was submitted with the engineering reports at the end of the joint feasibility study in July 1988. The report, which is being published as a NASA Reference Publication, reflects major advances made in the scientific bases for the mission since the pre-TRMM research was initiated.

Real progress has been demonstrated in algorithms to calculate rain amounts and vertical profiles from signals produced by the onboard instruments planned for the spacecraft:

- An algorithm called Height Area Rain Threshold (HART) has been developed from earlier surface radar-rainfall studies. If the area of rain above a specifiable threshold rate is determined, as well as the height of the rain layer within that area, a very accurate estimate of rain amount can be made. The estimate is insensitive to possible errors in the radar reflectivity-rain rate relationships. This new algorithm extends the usefulness of TRMM results to mesoscale studies, since rainfall may be determined fairly accurately along individual swathes of the rain radar without requiring averages of many satellite passes (as had been initially anticipated).
- Encouraging progress has been made using cloud models to derive latent heat profiles from TRMM-determined precipitation profiles. These models have also been used to simulate real cloud fields in experiments developing and testing rain retrieval methods.
- Important early steps demonstrate that vertical precipitation profiles can be obtained under most conditions with the single frequency radar.



Tropical Rainfall Measuring Mission ground track for 35° orbit with ground truth verification sites.

Results from the passive microwave instruments are used to constrain the radar equation.

- An overall error analysis estimates that if instrumental and retrieval biases are uncorrelated with rain rates, TRMM errors in monthly rainfalls over the 5° by 5° areas will probably be considerably lower than the discrepancies likely to be found among the various validation methods! Over oceans, the combined errors are estimated at about 13 percent (1.2 mm/day in high rain areas), while over land, the estimate is about 20 percent (1.7 mm/day). The largest component of these errors is due to sampling; this component would be greatly reduced by the presence of a single polar orbiting rain-measuring satellite.

It is well known that the most carefully calibrated ground-based radar rain measurements rarely agree to within 13-20 percent of estimates made from dense networks containing as many as 100 rain gauges surrounding the radar site. Thus, it is not a wild dream to suppose that one day, not too distant, space measurements of rainfall in the tropics will be used to validate and calibrate those of surface techniques rather than the other way about!

Contacts: Marvin A. Geller and
Joanne Simpson
Code 610

Sponsor: Office of Space Science and
Applications

Dr. Marvin A. Geller, Chief of the Laboratory for Atmospheres, received his PhD degree from the Massachusetts Institute of Technology. Interested in atmosphere dynamics and the upper atmosphere, he is a Fellow of the American Meteorological Society. Dr. Geller has worked for nine years at Goddard.

Dr. Joanne Simpson, a member of the National Academy of Engineering, is the Chief Scientist for Meteorology at the Laboratory for Atmospheres and Study Scientist for the Tropical Rainfall Measuring Mission. She has recently been selected as one of the initial Goddard Senior Fellows. She received her PhD in meteorology from the University of Chicago. Dr. Simpson has received numerous awards, including NASA Exceptional Scientific Achievement Award; and has nine years of experience with Goddard. Dr. Simpson is the incoming President of the American Meteorological Society.

RAINFALL ON OIL RIG 50 MILES OFFSHORE IN THE GULF OF MEXICO

Rainfall data measured 50 miles offshore in the Gulf of Mexico are presented for the period October 1985 to June 1987. The following paragraphs describe the tipping bucket rain gauge, its installation on pumping platform Eugene Island Block 322, and the method of formatting and collecting the data via Geostationary Operational Environmental Satellite (GOES). Features of the rainfall data are presented in the table.

The purpose of installing a rain gauge on an oil pumping platform 50 miles offshore in the Gulf of Mexico was to obtain a record of rain rate and annual rainfall at a location as far offshore as practical, for a period of 1 year or longer. This installation would provide a new rainfall record which may be useful in planning the Tropical Rain Measurement Mission (TRMM) to be flown on a spacecraft in the 1990s.

The Sutron Model AH GOES Transmitter includes a data collection system which has a 16-bit increment-

ing counter, and a processor for formatting the data and programming the operation of the transmitter. Each 0.01 inch of rainfall caused the rain gauge bucket to tip and send an electrical pulse to the 16-bit counter. Every 2 minutes the contents of the counter were sampled and stored as a formatted three-byte binary message in a buffer. Every 3 hours the contents of the buffer (90 messages of three bytes each) were transmitted to GOES with an appropriate header.

A data block consists of Platform identification (ID), Julian Day, Greenwich mean time (GMT) in hours, minutes, and seconds; B for Binary Data; and D@ for housekeeping. These symbols are followed by 90 groups of three bytes each, where each group represents the contents of the 16-bit incrementing counter sampled every 2 minutes. The six least significant bits (LSBs) of the least significant byte represent the contents of the six LSBs of the 16-bit counter. The next byte represents the contents of the next six bits of the counter. The four LSBs of the most significant byte represent the contents of the four most significant bits of the 16-bit incrementing

Rainfall 50 Miles Offshore in the Gulf of Mexico						
	1985		1986		1987	
	inches	days ¹	inches	days ¹	inches	days ¹
January	—	—	5.70	10	6.93	9
February	—	—	1.49	9	4.80	10
March	—	—	0.99	6	3.44	11
April	—	—	0.59	6	0.72 ³	4
May	—	—	0.18	2	0.45	5
June	—	—	0.67	7	5.97	15
July	—	—	5.07	10	3.22	11
August	—	—	3.51	11	—	—
September	—	—	5.12 ²	15	—	—
October	6.47	11	4.23	10	—	—
November	1.60	5	6.35	13	—	—
December	2.73	6	5.62	10	—	—
Total	10.80	22	39.52	109	25.53	65
¹ 0.01 or more inches of rain during the day. ² 2.50 inches of rain in 1 hour and 42 minutes on September 8, 1986. ³ No rain for 18 days between April 14, 1987 and May 2, 1987.						



counter. Every time the rain bucket tips, the contents of the incrementing counter increase by one count, where each count represents 0.01 inch of rain.

The design of the data format yields rainfall in increments of 0.01 inch with a time resolution of 2-minute intervals, and a capability to record rain rates from 0 inches of rain for days to several inches of rain per hour. Most of the data indicate that there was no rain and are therefore redundant. Their transmission to the GOES satellite could be suppressed with a sophisticated controller processor in the transmitter. It may be useful to review these data to determine if additional offshore installations of rain gauges should be made.

Contact: Jan M. Turkiewicz
Code 675

Sponsor: Office of Space Science and Applications

*The installation and operation of the rain gauge were made possible by the AMOCO Production Company, with assistance by Mr. Don Romero, Operations Foreman.

Mr. Jan M. Turkiewicz is Acting Branch Head for the Microwave Sensors and Data Communication Branch and Project Manager for the Wide Band Data Collection System. He has a BS degree in electrical engineering, and has received several Special Achievement and Group Awards for the Orbiting Astronomical Observatory, Advanced Technology Satellite (ATS-F), and Search and Rescue Satellite Aided Tracking projects. Mr. Turkiewicz has 28 years of experience at Goddard.

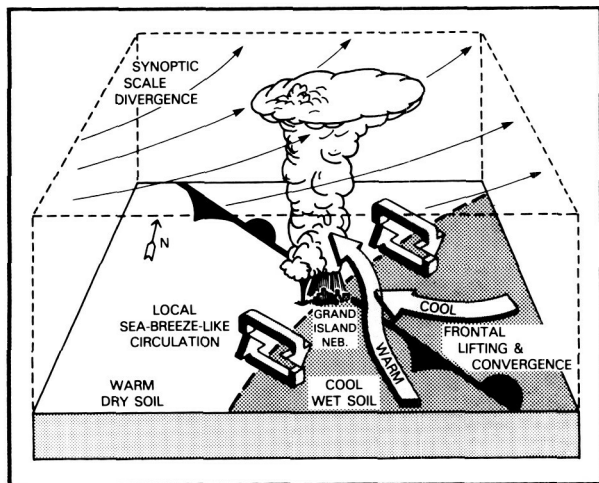
THE INFLUENCE OF THE SURFACE ENERGY BUDGET AND HYDROLOGICAL BUDGET ON THE DEVELOPMENT OF MESOSCALE RAIN SYSTEMS

To study the effects of spatial variations of soil moisture and vegetation coverage on the evolution of a prestorm environment, the formulation for the surface energy budget and a hydrological budget parameterization have been modified to incorporate an evapotranspiration model. Soil moisture contents of both top soil and root zone layers are estimated from an antecedent precipitation index (API) that integrates daily precipitation data. Fractional vegeta-

tion coverage is estimated from a composite image of a normalized difference vegetation index (NDVI), which is a remotely sensed parameter related to green biomass. The case chosen for study, June 3-4, 1980, is particularly interesting because of an isolated tornado-producing convective complex developed near Grand Island, Nebraska, during a period of relatively weak atmospheric forcing. The figure shows the hypothesized mechanism for the formation of this isolated storm. The storm required the combined influence of favorable conditions on three scales of atmospheric motion. On the large (continental) scale, a generally favorable pattern of divergence at upper levels existed. On the mesoscale, a stationary front provided an additional lift to the low-level moist air. And, on the local scale, a boundary between dry and wet soil developed a sea-breeze-like flow from the cool, wet soil towards the warmer, dryer surface due to differential preceding rains. This small-scale circulation fine tunes, or pinpoints, the location of greatest atmospheric instability.

Three numerical experiments were conducted with an updated version of the Goddard Mesoscale Atmospheric Simulation System (GMASS) at the Goddard Space Flight Center. The first two experiments compared a surface with an observed distribution of vegetation cover and soil moisture with an otherwise identical surface without vegetation. A third simulation run without spatial variations was made by assuming relative soil moisture at 60 percent of saturation, and fractional vegetation coverage at a uniform 28.5 percent throughout the model domain.

Results show that the crucial positioning and orientation of the stationary front, on which the storm was triggered, were primarily determined by the orientation of the soil moisture gradient upwind of Grand Island. In the run without spatial variations, this surface front never formed. In the run without vegetation, only a weak front was maintained, and surface temperatures were much higher than observed. The run that included vegetation and soil moisture produced the best agreement with the observations, manifesting a strong frontal boundary, a significant sea-breeze-like component of the low-level flow, and a compensating return flow at jet stream level. All of these elements combined to produce an environment conducive to the development of deep, intense convective storms such as those actually observed.



Cooperation of Three Scales of Motion in Initiating an Isolated Severe Thunderstorm.

Contacts: Peter J. Wetzel and Jy-Tai Chang
Code 612

Sponsor: Office of Space Science and
Applications

Dr. Peter J. Wetzel, with the Severe Storms Branch, is currently working on models that describe the interaction between land surfaces containing large variability and the lower atmosphere. His interests include mankind's impact on the heat and water exchanges between land surfaces and the atmosphere. Dr. Wetzel has eight years of experience at Goddard.

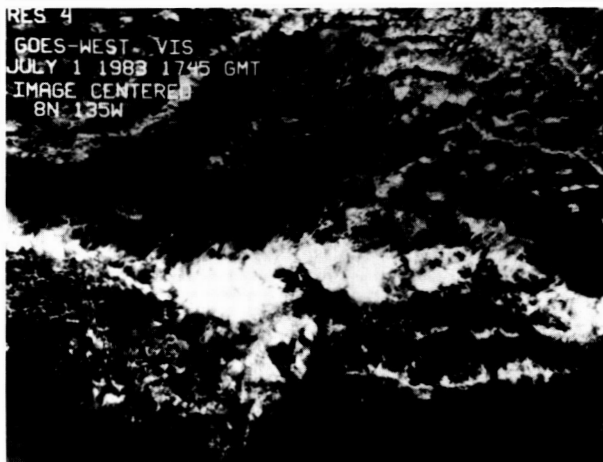
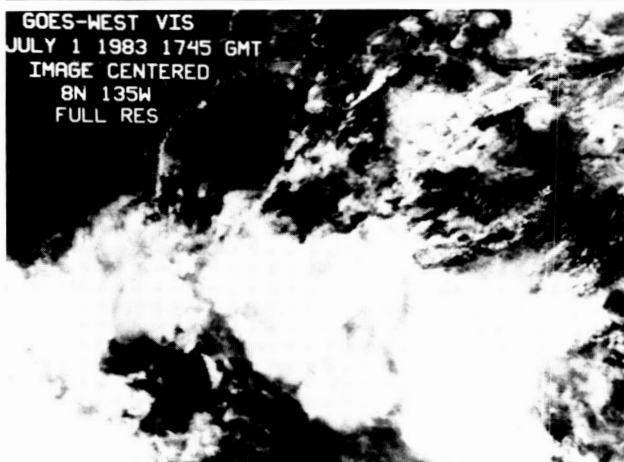
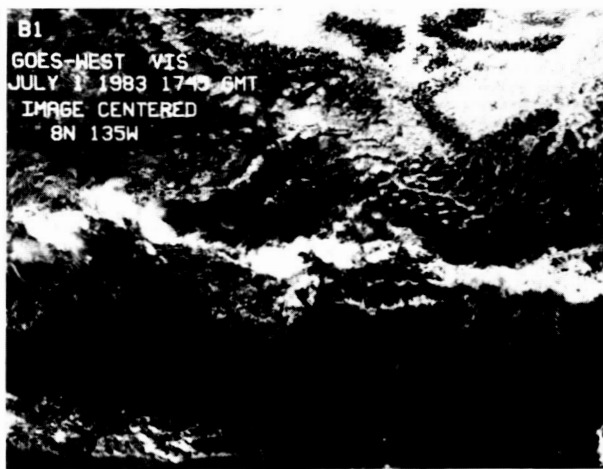
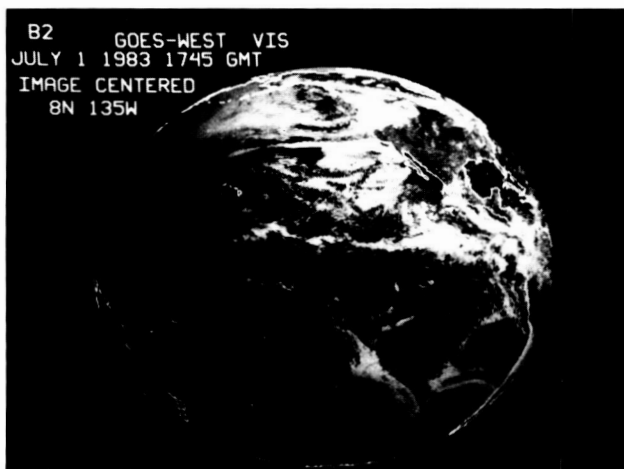
MEASURING CLOUDS AND RADIATION FROM SPACE

Satellite observations of clouds have been utilized in atmospheric research ever since the first satellite images were returned, but systematic progress in obtaining a quantitative understanding of global cloudiness has been slow. There are many ways to observe cloud properties and behavior; however, only satellites provide the overview of cloud systems at the scale of the synoptic weather systems in which they form. Moreover, satellites can directly observe the effects of clouds on Earth's radiation balance at the top of the atmosphere, the fundamental forcing of the atmosphere system. A key obstacle to a determination of the climate's sensitivity to perturbations

is lack of understanding of the nature of cloud-radiation feedbacks; hence, a global survey of cloud properties is a key objective of climate research programs in this decade.

The simultaneous collection of several types of data presents an unprecedented opportunity to tackle the problem of cloud-radiation interactions. These data include several global cloud climatologies, such as the International Satellite Cloud Climatology Project of the World Climate Research Program (ISCCP), Nimbus-7 (a National Aeronautics and Space Administration research satellite project), and ground-based weather observations. Additionally, the Earth Radiation Budget Experiment (ERBE) and Nimbus-7 provide two global radiation budget data sets. The United States First ISCCP Regional Experiment (FIRE), International Cirrus Experiment (ICE), and Japanese Northwest Pacific Cloud Radiation Experiment (NWPCRE) also provide detailed data sets for studying cloud properties. The multispectral, multiscale, multidirectional observations contained in these data sets, when combined in a comprehensive analysis, allow for a thorough examination of the relations between satellite-observed radiances and cloud properties (remote sensing problem), and between cloud properties and radiation budgets (climate model problem).

The basic steps in the analysis of satellite observations of clouds are three: detection, radiative modeling, and statistical characterization. The first step is the process of isolating those measurements that have any clouds or particular types of clouds in them. In developing a cloud detection method, researchers must define the observable quantities that discriminate between cloudy and clear scenes, determine the amount of contrast present in these quantities (their range), and select the values of these quantities that divide cloudy from clear conditions. Clouds can be detected by radiance variations in wavelength, space, time, or some combination of these. Recent studies have begun to examine the systematic variations of cloud properties to define better cloud-clear discriminators; a quantitative intercomparison of nine methods led to the design of the algorithm for ISCCP. Developing better analysis methods is interactive, because the results of the analysis and its validation lead to refinements, and to an improved analysis. Significant progress has occurred in the development of cloud detection methods.



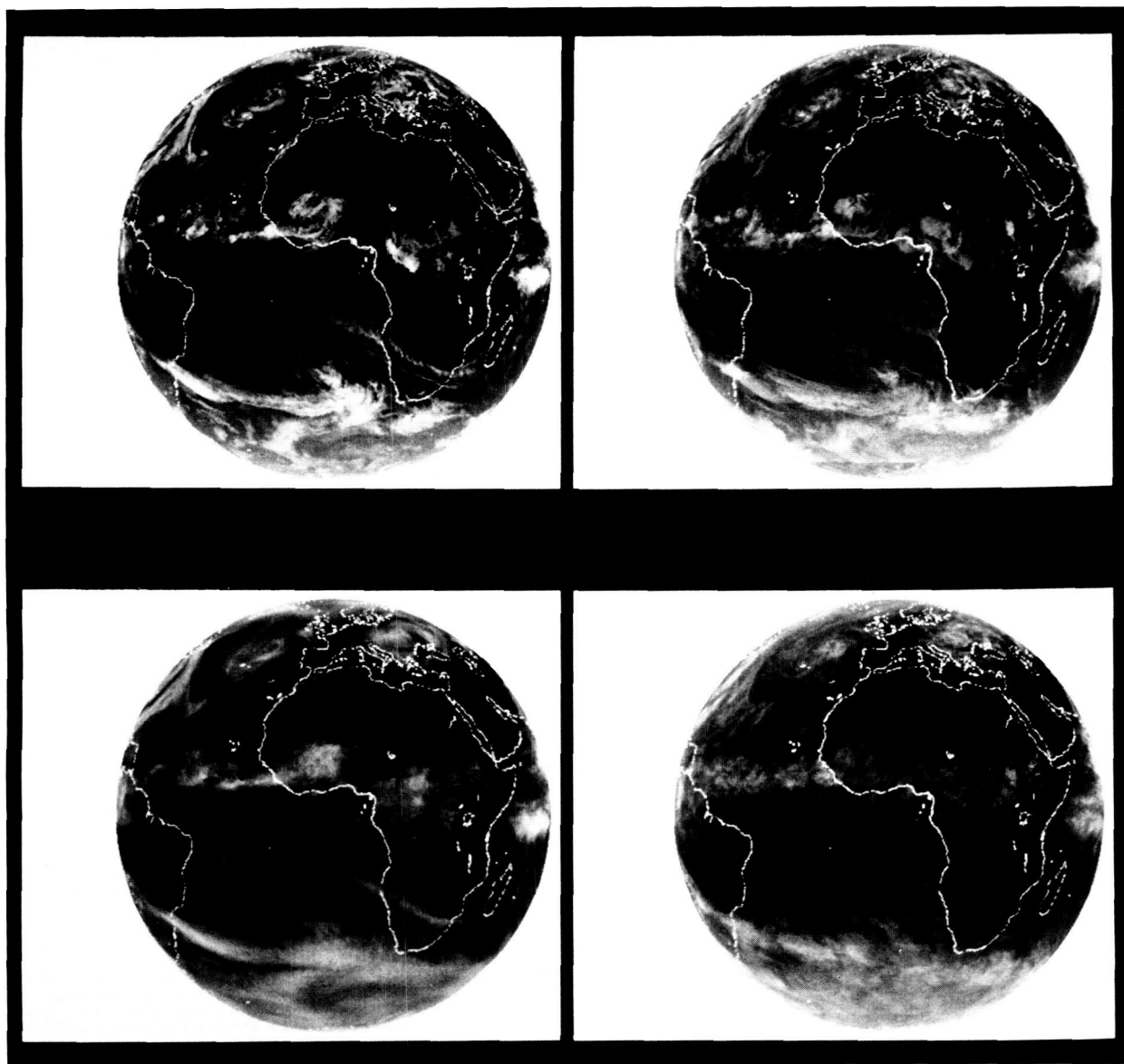
A single visible image from Geostationary Operational Environmental Satellite-4 (GOES-4) (WEST) on July 1, 1983, displayed at four spatial resolutions: 32 km (upper left), 8 km (upper right), 4 km (lower right), and 1 km (lower left). Each image shows a progressively smaller portion of the same region centered at 8°N latitude and 135°W longitude.

The second step in analysis involves removal of other effects from the radiative measurements, isolating the cloud contribution, and the inference of specific cloud physical properties from the measured spectral radiances. The success of this step depends on the fidelity of the radiative transfer model used to analyze the data; the most important open issue is how to account for the effects of small-scale cloud vertical and horizontal inhomogeneities on the measured radiation. The results also depend on the accuracy of specifying the other properties of the atmosphere and surface that also affect the satellite radiances. Usually, only a few of the relevant parameters needed for a complete analysis are available or measurable in a particular data set because it is

limited to a small number of wavelengths. Although several instrument combinations have flown (e.g., the current National Oceanic and Atmospheric Administration—NOAA—polar orbiters carry a narrow-band, multichannel imager, a temperature-humidity sounder, and broadband, scanning, radiation budget radiometers) that contain more information, no complete multi-instrument analysis has been tried. The ISCCP analysis procedure represents the closest approach to implementation of this strategy so far; the analysis results of the NOAA polar orbiter sounder system, called Television Infrared Operational Satellite (TIROS) Operational Vertical Sounder (TOVS), are used to specify the atmospheric temperature and humidity profiles in the analysis of the

NOAA Advanced Very High Resolution Radiometer (AVHRR)—and other satellite—imaging data. Studies are underway to compare broadband radiation fluxes calculated from ISCCP results with those measured directly by ERBE. Further development of such comprehensive multi-instrument data analysis techniques will be required to attain the objectives of the Earth Observing System.

The third step in analysis of satellite cloud observations is defining and determining statistical measures of cloud behavior that lead to better conceptual understanding of the spatial patterns, and their time evolution seen in the satellite data. The most important statistics are those that characterize the predominant time and space scales of cloud variations, and consequent radiation flux variations. This step is, in



Visible images from METEOSAT-2 at four time resolutions: 30 min (single image from July 12, 1983, upper left), 1 day (average of two images at the same time of day, one day apart, upper right), 2 days (lower right), and an average over the diurnal cycle (lower left). The spatial resolution is 30 km near image center; all images are taken at local noon in the upper panels and in the lower right panel.



fact, linked to the first two, since measures of the same statistical quantities can be used to signal the presence of clouds in the data with more reliability, and to define the most crucial radiative parameters for calculating the radiative fluxes. A key research objective is to improve the treatment of smaller scale cloud inhomogeneities in calculations of their radiative effects.

The accompanying photos illustrate the effects of different space and time resolutions on observed cloud variations. The impression conveyed in the first series of photos is that at the largest and smallest spatial scales there are large regions of relatively uniform optical properties (usually thought of as cloudy and clear conditions), though some smaller scale variations are still apparent at the highest resolution. At intermediate spatial scales, there is a mixture of larger scale areas composed of a statistically uniform set of smaller elements, producing the characteristic texture of different cloud types. The second series of photos shows that the smaller spatial-scale features and their precise locations vary rapidly in time, producing a reduction in contrast between cloudy and clear conditions, and generally "smoothing out" the small spatial-scale structure of the clouds. This "smoothing" is even more noticeable when images are averaged over the diurnal cycle; this reduces contrast much more than does averaging over several days at the same diurnal phase. Nevertheless, the positions and characteristics of the *larger* scale features are remarkably constant in time when viewed at global scale. This suggests that a large-scale statistical representation of the small-scale cloud and radiation variations may be possible. In the coming years, the combination of data from several instruments, from several detailed field studies, and from several cloud and radiation budget climatologies that are now available should produce major advances in scientists' understanding of the role of clouds in the changing climate.

Contact: William B. Rossow
Code 640

Sponsor: Office of Space Science and Applications

Dr. William B. Rossow is responsible for research in planetary atmospheres, atmospheric dynamics, cloud physics, radiation and remote sensing, and climate. He is Head of the FS CCP Global Process-

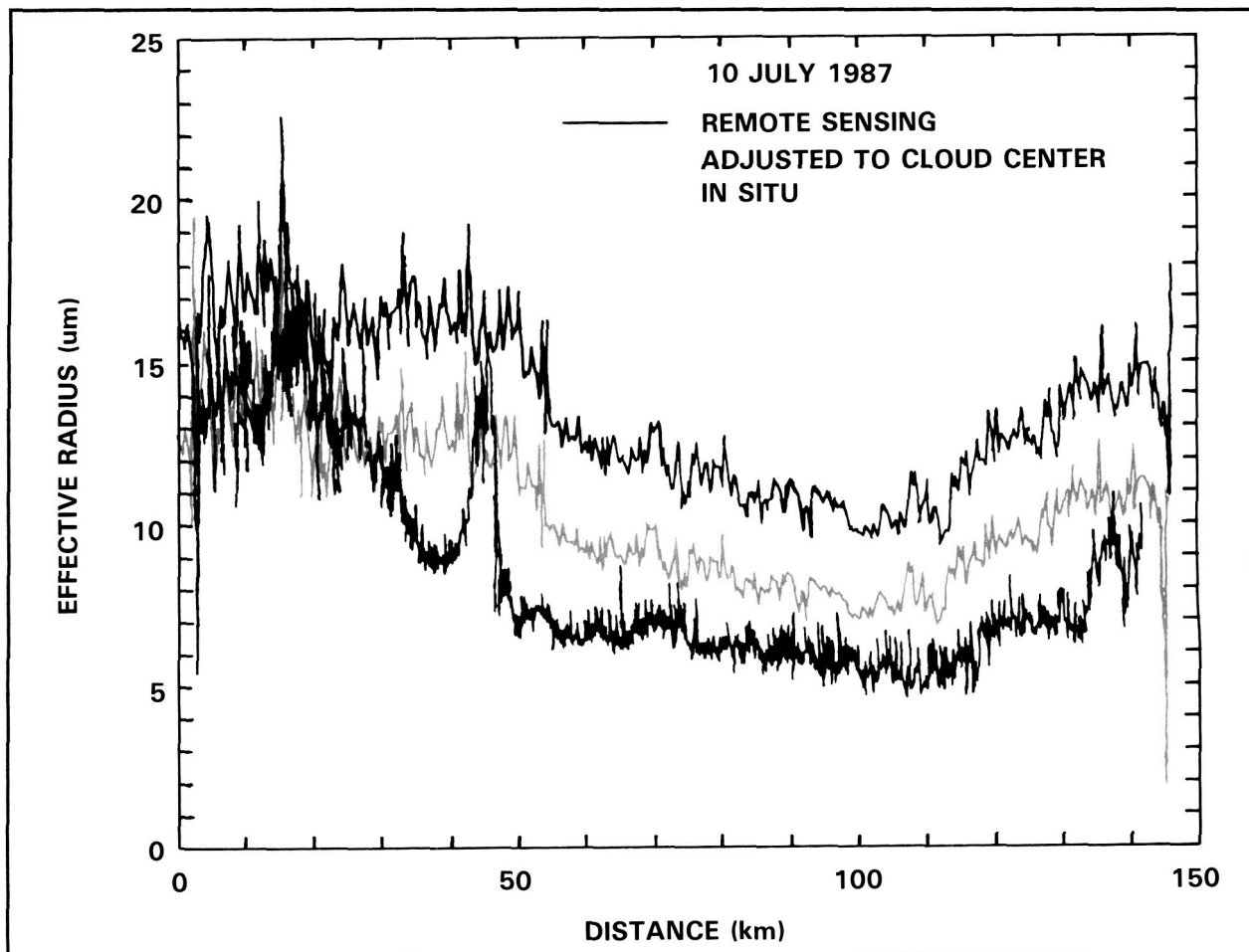
ing Center, and serves on NASA planetary and Earth sciences projects. Dr. Rossow has a PhD degree in astronomy from Cornell University.

CLOUD RADIATIVE AND MICROPHYSICAL PARAMETERS

During the last 10 years, two spectral scanning radiometers have been developed at Goddard Space Flight Center for the purpose of determining cloud radiative and microphysical parameters from aircraft platforms. The motivation behind developing these instruments for remote sensing of cloud radiative properties is the large uncertainty that clouds play in the energy balance and redistribution of energy in the Earth's climate system, and the promise that cloud radiative and microphysical parameters can be determined globally from future space platforms, such as the Earth Observing System (Eos).

The first of these radiometers, primarily flown on the National Aeronautics and Space Administration's high-altitude (19 km) ER-2 aircraft, utilizes the spectral reflectance of clouds to infer the cloud optical thickness, thermodynamic phase (ice or water, clouds or snow), and effective particle radius of cloud droplets (or ice particles). This multispectral cloud radiometer flew during the marine stratocumulus intensive field observation component of the First ISCCP (International Satellite Cloud Climatology Project) Regional Experiment (FIRE), conducted off the coast of San Diego, CA, during July 1987. An important test of the remote sensing technique for obtaining cloud particle radius was thus provided by the simultaneous in situ measurements of cloud particle radius obtained from the University of Washington Convair C-131A cloud physics aircraft.

On July 10, 1987, the C-131A flew a tightly coordinated mission with the ER-2 aircraft consisting of continually flying 145-km legs. The C-131A was primarily making cloud radiation and cloud microphysics measurements deep within the cloud layer, whereas the ER-2 was flying well above the cloud. The first figure illustrates a comparison of the effective (cross sectional area weighted) particle radius as a function of distance for this section of marine stratocumulus cloud. The curve labeled "in situ" was derived from the Particle Measuring Systems (PMS) probes aboard the C-131A aircraft, which was



Comparison of the effective particle radius as a function of distance as derived both from high altitude measurements of the reflectance spectrum, and from in situ measurements within the cloud. The measurements were obtained in a marine stratocumulus cloud off the coast of San Diego on July 10, 1987.

primarily flying in the middle of this 450-m thick stratocumulus cloud layer. From the scanning radiometer images of the reflectance spectra, it was possible to derive images of the particle radius 35 km in width, in contrast to the in situ measurements, which were restricted to the central location of the C-131A aircraft.

The curve labeled "remote sensing" in the first figure represents the results of the remote sensing analysis of the reflectance spectra for the nadir portion of the image. In general, it shows that the remote sensing-derived particle radius is similar in shape to that derived from the in situ measurements, but is noticeably larger in magnitude. Since the particle radius derived from the reflected solar radiation measure-

ments arises primarily from multiple scattering in the upper portion of the cloud (a region where the particles are larger than those lower in the cloud), an adjustment was made to the remote sensing results to correct them to the midlevel of the cloud, where the C-131A was flying. This correction, also shown in the figure, makes a substantial adjustment to the remote sensing-derived particle radius, but does not account for the entire bias that is observed. Although the explanation for this bias is not yet fully understood, it does not seem possible to account for its magnitude solely from calibration uncertainties.

The same algorithm that was applied to the aircraft flight line shown in the first figure has also been applied to Landsat-5 Thematic Mapper images of



marine stratocumulus clouds. These images are presently being compared to in situ microphysics measurements in a manner similar to that presented in the figure, and are a useful prelude to anticipated measurements from the Moderate Resolution Imaging Spectrometer-Nadir (MODIS-N) on Eos.

A second airborne multiwavelength scanning radiometer has been developed for measuring the angular distribution of scattered radiation deep within a cloud layer. The purpose of this instrument is to provide measurements from which the similarity parameter of clouds can be derived as a function of wavelength, where the similarity parameter is a function of cloud single scattering albedo and asymmetry factor. The cloud absorption radiometer also flew on the University of Washington's C-131A aircraft during the marine stratocumulus intensive field observation component of FIRE.

The cloud similarity parameter is defined as $s = [(1 - \omega_0)/(1 - \omega_0 g)]^{1/2}$ where g is the asymmetry factor, and ω_0 the single scattering albedo. The determination of s is based on measurements of the ratio of the nadir to zenith intensity within the diffusion domain of an optically thick cloud. As such, it is neither dependent on an absolute calibration of the radiometer, nor on the solar zenith angle, because

the relative angular distribution inside an optically thick cloud is independent of solar zenith angle.

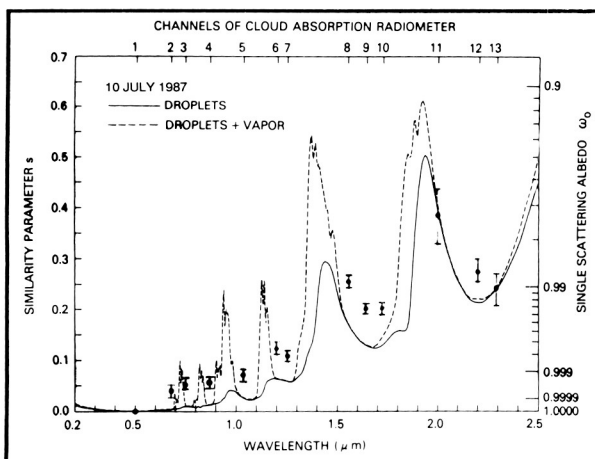
The motivation for studying the spectral absorption properties of marine stratocumulus clouds arises from the following considerations: 1) large discrepancies have been observed between the total short-wave absorption measured and predicted for stratiform cloud systems; 2) various hypotheses proposed to account for this "anomalous absorption" of clouds have different consequences for different wavelength regions; and 3) remote sensing results based on the optical properties of water droplets and water vapor may be in error, due to some unexplained absorbing component. Item 3, for example, could be used to partially explain the discrepancy presented in the first figure.

The second figure illustrates the similarity parameter as a function of wavelength obtained from aircraft measurements of the cloud absorption radiometer on July 10, 1987. These results were obtained in the central portion (48–95 km) of the marine stratocumulus cloud system presented in the first figure. The second figure also illustrates the similarity parameter as a function of wavelength for a model cloud composed of water droplets only (solid curve), and droplets plus saturated vapor at 10.3 °C (dashed curve). The size distribution of the cloud droplets used in the calculations was obtained from measurements aboard the C-131A for this portion of the cloud, so this figure presents the first simultaneous comparison of measured and theoretically predicted similarity parameter (or, alternatively, single scattering albedo, shown on the right-hand scale) as a function of wavelength. These results show little difference between theory and experiment in the 2 μ m region, but a small enhanced absorption in the visible portion of the spectrum. This bias can possibly be explained by enhanced absorption in the cloud droplets themselves (dirty water), or by absorbing interstitial aerosol.

Contact: Michael D. King
Code 613

Sponsor: Office of Space Science and Applications

Dr. Michael D. King is responsible for the development and application of algorithms for the remote



Similarity parameter as a function of wavelength for water droplets alone (solid line), and drops plus vapor (dashed line). The measurements obtained from the 13 channels of the cloud absorption radiometer were obtained in a marine stratocumulus cloud off the coast of San Diego on July 10, 1987.

sensing of cloud radiative and microphysical parameters from airborne spectral radiometers. His interests include multiple light scattering, radiative transfer, remote sensing of clouds, aerosols, Earth radiation budget, inversion methods, and radiation instrumentation. Dr. King has received several Achievement Awards and the NASA Exceptional Service Medal.

DIURNAL VARIATION OF CLOUDINESS IN THE MARITIME CONTINENT AND SUMMER MONSOON REGIONS

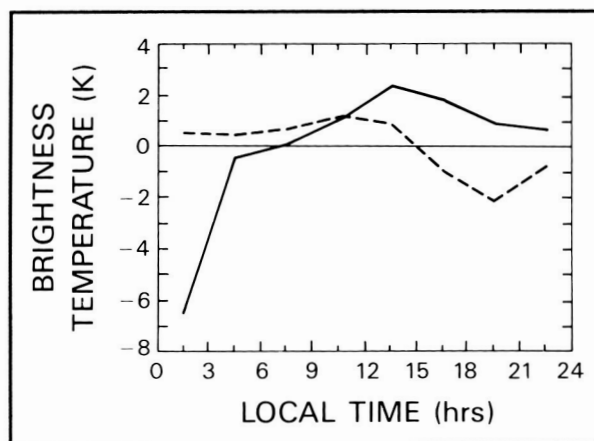
Radiation and latent heat are two of the most important energy sources that force the circulation of the atmosphere. Global distributions of these sources can be best derived by measurements from space. One of the major difficulties in interpreting these measurements is the inadequate temporal coverage of most meteorological satellites. The twice-a-day coverage of the polar orbiting satellite is expected to cause bias in estimating radiative and latent heat budgets. This bias can be reduced if there is information on the cause and pattern of the diurnal variation of cloudiness, which can be inferred from the satellite-measured brightness temperature. In addition, the diurnal variation of cloudiness can provide information on the interaction of radiation and precipitation with large-scale atmospheric circulations.

The diurnal variation of brightness temperature, which reflects cloudiness in tropical and monsoon regions, was studied in the maritime continent Inter-Tropical Convergence Zone (ITCZ) and the eastern Asian monsoon region for the month of July 1983 using the International Satellite Cloud Climatology Project (ISCCP) Geostationary Meteorological Satellite (GMS) infrared data. Analyses of the GMS data show that the large-scale diurnal variations of brightness temperature in the maritime continent and the Asian monsoon regions have coherent patterns. It was found that the radiative heating and cooling of land have a dominant effect on the diurnal variation, while the nighttime cloud-top cooling plays a moderating role.

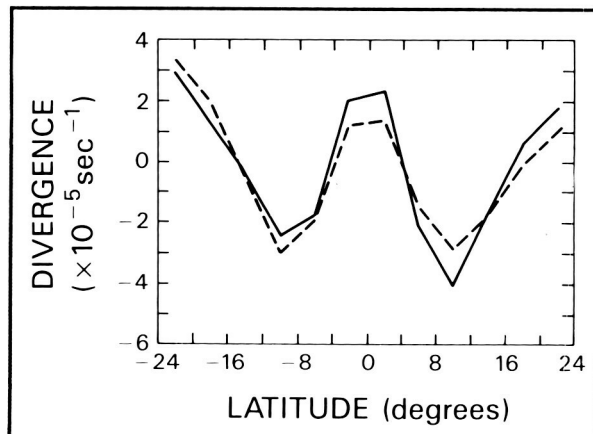
The first figure shows diurnal variations of brightness temperature (with the mean removed), longitudinally averaged (from 120°E to 172°E) along the northern (dashed) and southern (solid curve) borders of the ITCZ. The latitude bands are from 12°N to

16°N for the northern branch and from 4°S to 8°S for the southern branch. There are two distinct patterns of diurnal variation. The brightness temperature attains a minimum (corresponding to a cloudiness maximum) in the afternoon in the northern branch of the ITCZ and the monsoon regions, and in early morning in the southern branch of the ITCZ. These patterns are consistent with the diurnal change in wind divergence. The second figure shows the latitudinal distribution of the wind divergence averaged from 114°E to 168°E for 0000 and 1200 GMT, which correspond, respectively, to $\approx 10:00$ a.m. and 10:00 p.m. local time in the maritime continent region. Convergence increases during the daytime (solid curve) in the region between 4°N and 16°N, and at night (dashed curve) in the region between 14°S and 4°N. During the daytime, the solar heating of the maritime continent reduces atmospheric stability and strengthens the northern trade wind. Convergence increases in the region from 4°N to 16°N, indicating a late afternoon cloudiness maximum. At night, the strong cooling of the Australian desert intensifies the trade wind, which enhances the wind convergence in the ITCZ between 14°S and 4°N. Thus, a nighttime maximum in cloudiness can be expected in the southern branch of the ITCZ.

The infrared radiative cooling at cloud top has long been suggested as a factor causing a nighttime maximum in cloudiness. This theory is based on the cool-



Diurnal variations of brightness temperature (with the monthly mean removed) longitudinally averaged (from 120°E to 172°E) along the northern (dashed) and southern (solid curve) borders of the ITCZ for the month of July 1983.



Latitudinal distribution of the zonally averaged (from 114°E to 168°E) wind divergence for the month of July 1983. The solid curve is the divergence at 0000 GMT ($\approx 10:00$ a.m. local time at 140°E), and the dashed curve at 1200 GMT ($\approx 10:00$ p.m. local time).

ing difference between mesoscale cloudy regions and the adjacent clear regions. At night, the cloud-top cools at a much faster rate than the air at the same level in the adjacent clear regions, but the region below clouds cools at a slower rate than the adjacent clear region, since clouds act as a shield for thermal radiation. Thus, temperature gradients are set up. These gradients could induce a circulation that would intensify convection in the cloudy region, and increase subsidence in the adjacent region. Besides the horizontal temperature gradient induced by the cloud-top radiative cooling, the cloud-top instability induced by nocturnal radiative cooling is also important in enhancing deep convection. Because the effects of cloud-top and surface radiation are in phase in the southern branch, but out of phase in the northern branch, the amplitude of the diurnal variation is larger by about a factor of three in the south than in the north (shown in the first figure).

Although large-scale wind is suggested as the main factor affecting the diurnal variation of brightness temperature, it is reasonable to expect that topography also plays a role in moderating the amplitude of the variation. The large diurnal cycle in central Borneo and southern Indochina is an example of this type. The monthly mean diurnal range is greater than 25°K in these regions, with a maximum at noon and a minimum in the evening. The

solar heating of the land and the subsequent strengthening of the trade wind in the late afternoon cause an increase in cloudiness that is further enhanced by the effect of topography.

Contact: Ming-Dah Chou
Code 613

Sponsor: Office of Space Science and
Applications

Dr. Ming-Dah Chou, who holds a PhD in meteorology from New York University, is responsible for the development of surface radiation retrieval methodologies in the Laboratory for Atmospheres, Climate and Radiation Branch. Dr. Chou, with nine years of experience at Goddard, received the GSFC Exceptional Performance Award in 1981.

OBSERVATION OF THE GLORY OF CLOUDS AT NEAR-INFRARED WAVELENGTHS

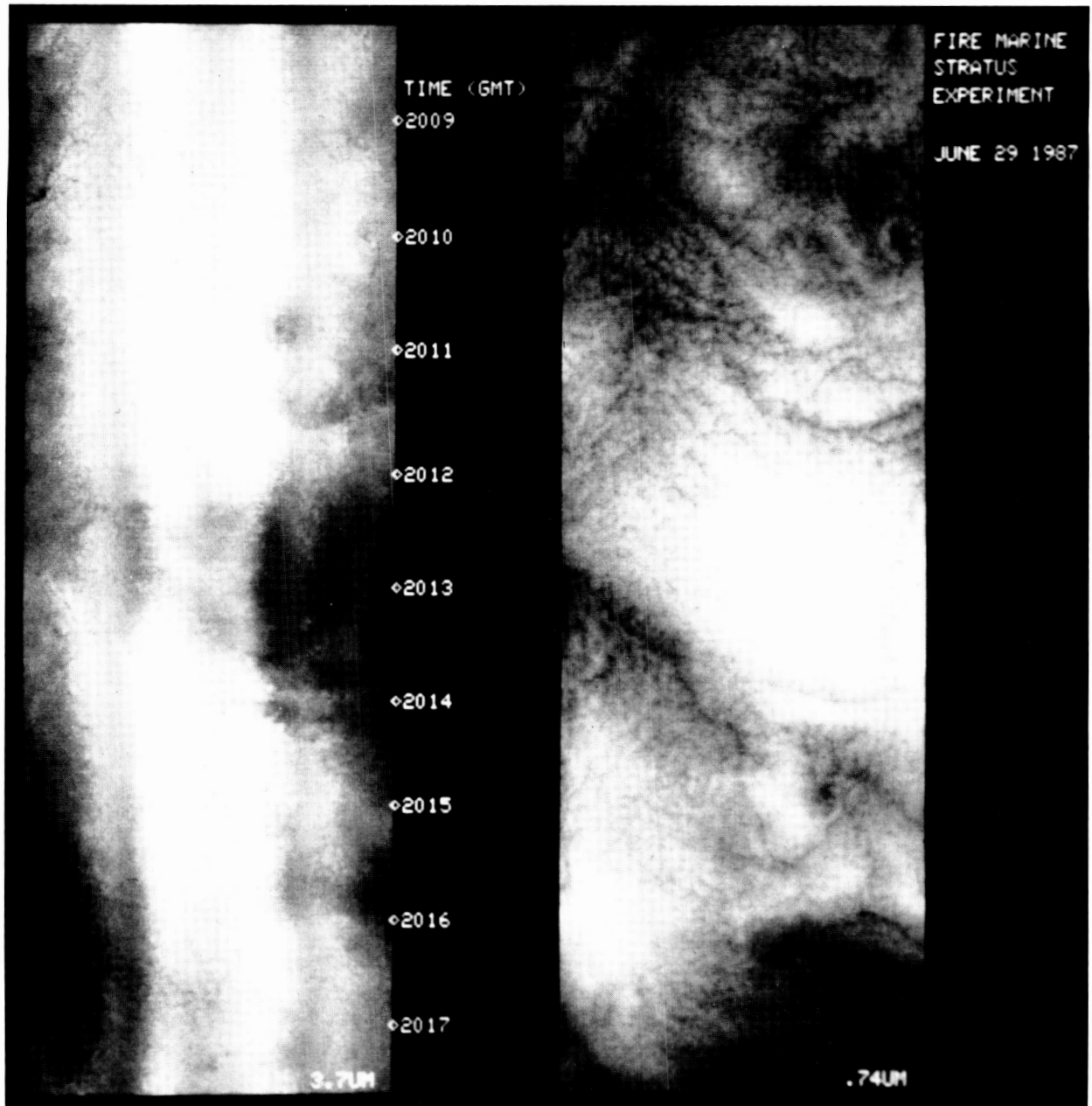
An atmospheric optics phenomenon that is occasionally observed is the cloud glory. The glory is typically observed by aircraft passengers as a bright ring surrounding the shadow of the aircraft on cloud tops. The cloud glory is a single scattering phenomenon; it is typically washed out in the visible by cloud multiple scattering, and thus rarely seen. However, recent observations from the National Aeronautics and Space Administration (NASA) ER-2 research aircraft indicate that at near-infrared wavelengths the cloud glory is a much more dominant phenomenon.

Extensive observations of the spectral reflectance for marine stratocumulus clouds were acquired during the ISCCP (International Satellite Cloud Climatology Program) marine stratocumulus field experiment of June-July 1987. The observations were acquired by cross-track scanning spectral radiometers on board the NASA ER-2 aircraft. Radiometrically accurate cloud top images were built up within a 45° view angle along the aircraft flight track. The observations were acquired at 11 visible channels, 3 infrared window channels, and 4 near-infrared channels of 3.7, 2.1, 1.6 and $1.36 \mu\text{m}$.

The overflights of extended marine stratocumulus were made on 10 experiment days. A very pronounced pattern was frequently observed in the

spatial reflectance data for the near-infrared wavelengths. The feature was not found for visible channels. An example of the data results appears in the accompanying figure, which shows a cloud top image at $3.7\text{ }\mu\text{m}$, and at a visible wavelength. A pronounced linear brightness feature is visible at the $3.7\text{ }\mu\text{m}$ wavelength.

An analysis of the pattern indicated that a single scattering cloud glory was being observed. The backward scattering angles for the intensity peak were larger than would be expected for a visible wavelength glory. At the $3.7\text{ }\mu\text{m}$ wavelength, a typical scattering angle was 12° . Distinct variations of the scattering angles occurred; they are thought to result from



Coincident image of a marine stratus cloud derived from cross-track scanning at 3.7 and $0.86\text{ }\mu\text{m}$ wavelengths. The near infrared glory is seen as the linear brightness feature.



changes in the cloud droplet size distribution. The entire data set of stratus observations was surveyed for all cases wherein the solar elevation angle was sufficiently high for the appropriate scattering angles to be observed. In all cases, the glory at near-infrared wavelengths was clearly apparent. It is thus concluded that the glory of clouds in the near infrared is a consistent feature. An explanation of the observations based on spectral cloud absorption has been developed. Radiative transfer calculations derived from simultaneous droplet measurements made within the stratus clouds have been compared to observations; the results may lead toward improved cloud parameter remote sensing, and aid the interpretation of satellite radiance data.

Contact: James Spinhirne
Code 617

Sponsor: Office of Climate Research

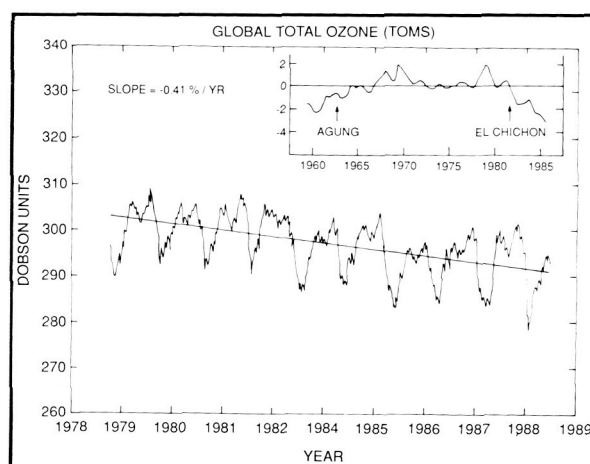
Dr. James Spinhirne, who holds a PhD degree in atmospheric science from the University of Arizona, is Principal Investigator for the ER-2 cloud experiment. His scientific specialty is atmospheric remote sensing and instrumentation. Dr. Spinhirne has served with Goddard for nine years.

LONG-TERM MEASUREMENTS OF OZONE

There is considerable observational evidence that the atmospheric concentrations of numerous gases important in controlling atmospheric ozone are rapidly increasing on a global scale, due largely to human activities. This has led to a search for long-term changes in stratospheric ozone that might be caused by such human activity. The search is not an easy one. The first figure shows the change in the total column ozone from 1979 to 1987, inferred from data obtained by the Total Ozone Mapping Spectrometer (TOMS) on the Nimbus-7 spacecraft. The insert on the figure shows the total column ozone measured by a ground-based instrument (Dobson) over the period from 1959 to 1986. It is obvious that much of the trend seen by TOMS could be ascribed to normal fluctuations of the atmosphere. If researchers are to link causes and effects of man's activities on stratospheric ozone, the natural fluctuations themselves must first be ascertained.

A future ozone data base must possess two attributes. First, the data base must be long-term and continuous; second, it must have a precision of close to 1 percent per decade because researchers are looking for changes on the order of a few percent.

How is this achieved? No single instrument, whether ground-based or satellite-borne, can provide continuous data collection with such a high degree of precision. No matter how well designed, every instrument has its own systematic errors that can lead to erroneous trend detection. Comparison of data from different instruments leads to detection of these systematic errors. Ground-based instruments are an essential part of an ozone-observing system, since they can be continuously calibrated against absolute standards. However, ground-based instruments do not provide the essential coverage in latitude or longitude needed to detect ozone trends, as opposed to simple redistribution. The second figure shows a global picture of the change in the total ozone derived from TOMS data for the months of October 1979/1980 to 1986/1987. The change in ozone is not uniform with latitude or longitude, meaning that global coverage is required to obtain a true global average. Satellite instruments can provide this global coverage, but the long-term calibration of these instruments is difficult. In the end, it is not the precision or accuracy of each instrument that will determine the reliability of the observed trends, but agreement between many different instruments.

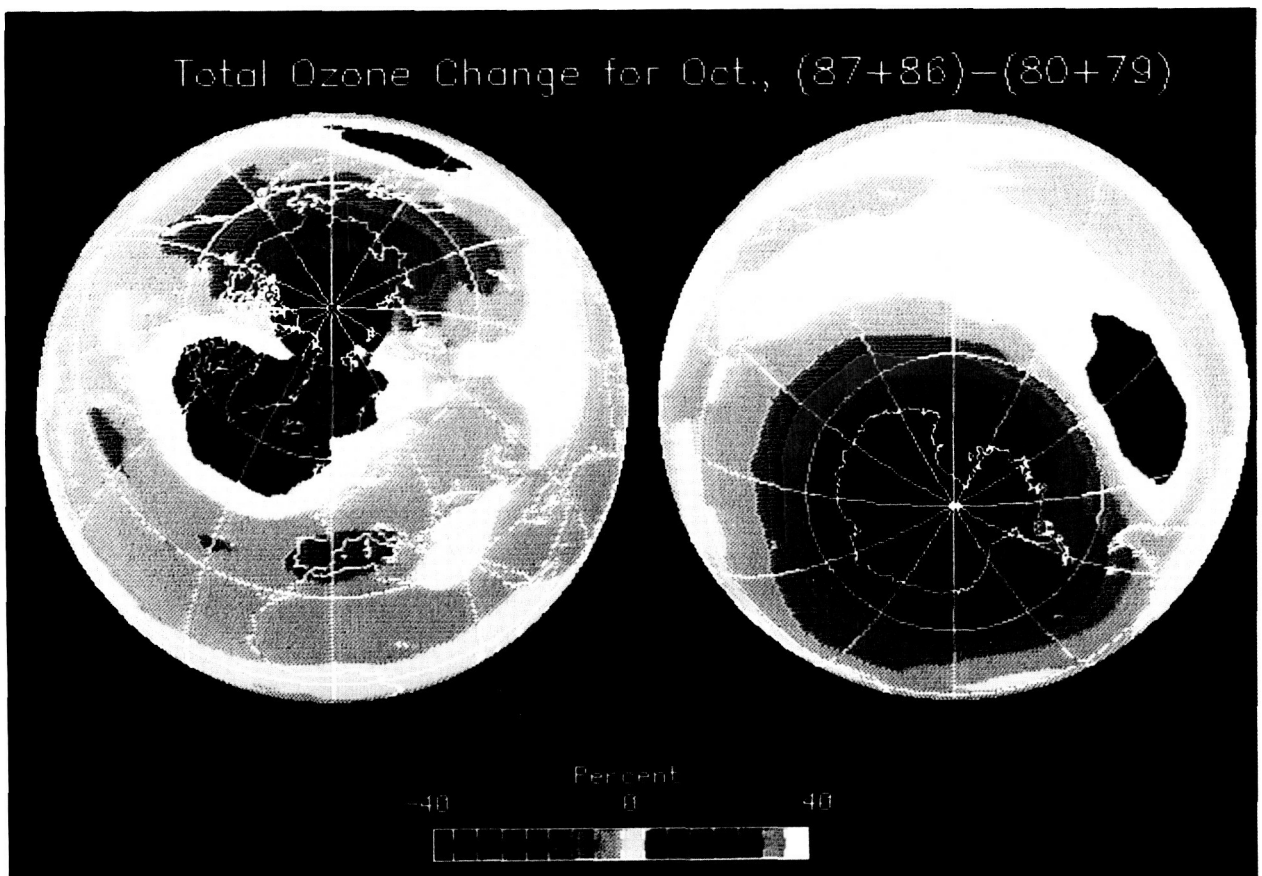


Change in global total ozone obtained by TOMS, 1978 to 1988. Insert shows changes measured by the Dobson instrument from 1960 to 1986.

Goddard Space Flight Center (GSFC) has an extensive program to obtain precise, long-term ozone trends. Both TOMS and its sister instrument, the Solar Backscatter Ultraviolet (SBUV) spectrometer were conceived and built by GSFC. These instruments are still producing data after their introduction in 1978. The conceptual design for the follow-on to SBUV, the National Oceanic and Atmospheric Administration (NOAA) SBUV/2, was performed at GSFC, which also has the overall management responsibility for the production and calibration of the instrument. GSFC also assumed responsibility for the analysis of the data from the SBUV/2 instruments as the instruments are placed on standby as part of the NOAA operational program. In this way, the different instruments can be intercompared and their precision improved. An SBUV for flight on the space shuttle (SSBUV) was developed; the first launch was scheduled for February 1989. The instru-

ment package contains onboard calibration devices, and can be absolutely calibrated both before and after flight. When the data from SSBUV is compared with data from the SBUV/2 instruments over several flights (SSBUV is scheduled to fly on missions at nine-month intervals), it should be possible to follow any calibration drifts of the SBUV/2 instruments, and to improve the precision of the SBUV/2 data.

At the same time as this in-house data base is being assembled, in-house data are beginning to be compared with that from ground-based and other satellite-borne instruments. The immediate goal is to produce a composite data base that reflects the best estimate of the trends of the ozone data over time. The final goal, however, is to use this data base along with theoretical models to separate the changes in atmospheric ozone due to human activities from those caused by natural variability.



Change in total ozone for the months of October 1979/1980 to 1986/1987, as a function of latitude and longitude.



Contact: Robert D. Hudson
Code 616

Sponsor: Office of Space Science and
Applications

Dr. Robert D. Hudson, Head of the Atmospheric Chemistry and Dynamics Branch, specializes in experimental physics and atmospheric science. Dr. Hudson, who holds a PhD degree from the University of Reading (United Kingdom), has been at Goddard for 12 years.

THREE-DIMENSIONAL SIMULATION OF STRATOSPHERIC CHEMISTRY

Space-based instruments have provided valuable information about the distribution of several important trace constituents in the stratosphere. For example, on the National Aeronautics and Space Administration's (NASA's) Nimbus-7 satellite the Limb Infrared Monitor of the Stratosphere (LIMS) instrument provided daily maps of the concentrations of ozone (O_3), nitrogen dioxide (NO_2), water (H_2O), and nitric acid (HNO_3) for a 7-month period (November 1978 to May 1979). Several other satellite- and shuttle-borne instruments have measured trace constituent amounts in the stratosphere, but provided less than complete geographical coverage.

The space-based data are complemented by ground-, balloon-, and aircraft-based measurements. These measurements do not have the spatial and temporal coverage of the satellite data, but provide information on many more constituents. For instance, there are no global measurements of any chlorine-containing constituents in the stratosphere, and there will be none until the launch of NASA's Upper Atmosphere Research Satellite (UARS), currently scheduled for 1991. Since chlorine-containing species are believed to play a crucial role in anthropogenic ozone depletion, this is a serious lack of information.

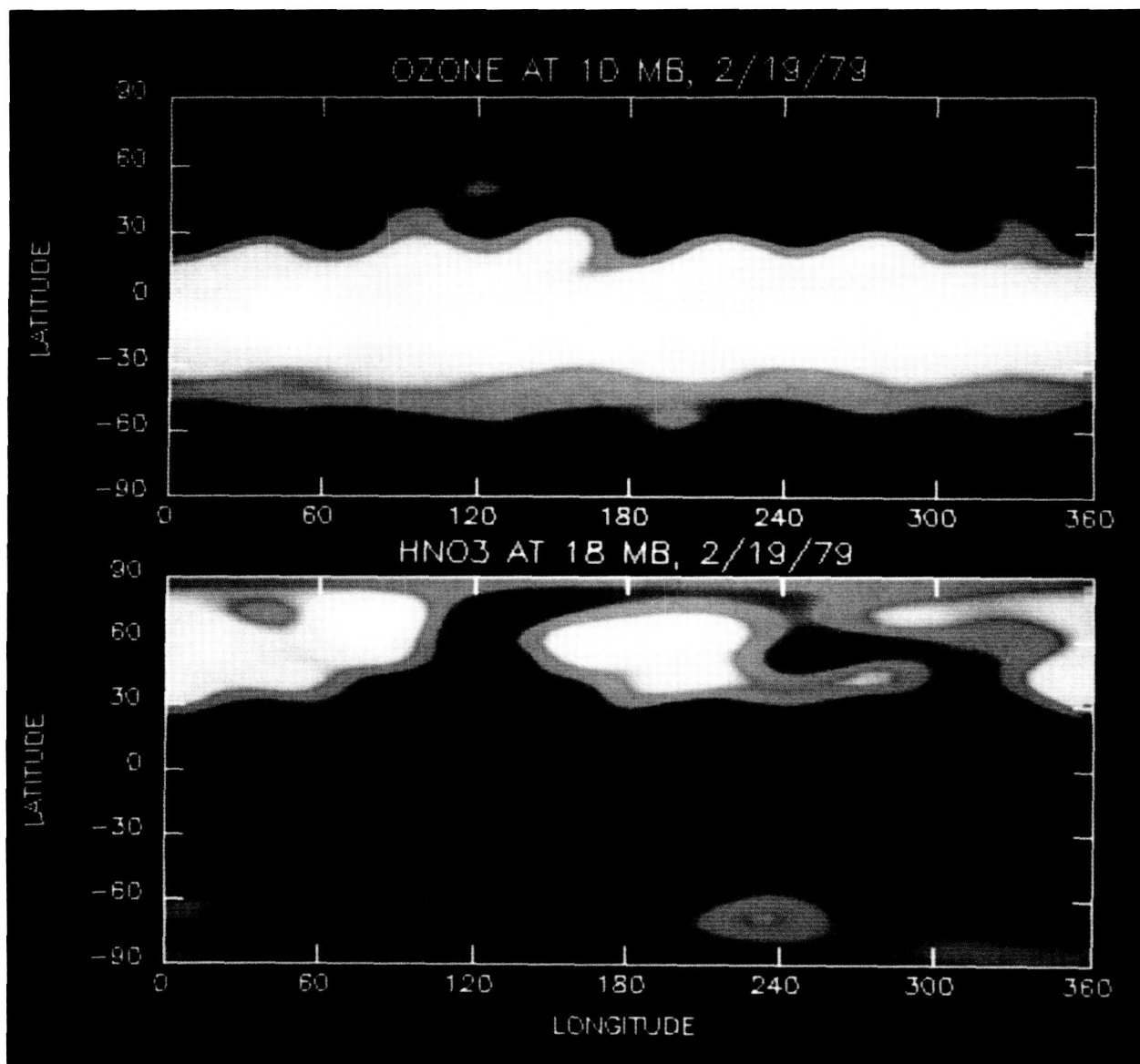
Knowledge of the spatial and temporal variability of trace constituent amounts is important for understanding exactly how representative the individual measurements are. Furthermore, it is necessary to know both the natural variability of constituent

fields, and the effect of atmospheric motions on atmospheric chemical composition, in order to confidently extract long-term trends in trace constituent amounts.

The three-dimensional (3-D) chemistry/transport model under development in the Atmospheric Chemistry and Dynamics Branch (Code 616) has the potential to lead to dramatic increases in scientists' understanding of these issues. Using wind fields generated as part of the data assimilation project in the Global Modeling and Simulation Branch (Code 611), the simultaneous effects of chemistry and transport may be studied for most important stratospheric trace constituents, including those containing oxygen, hydrogen, nitrogen, and chlorine. Early efforts in this direction have focused on the time period in which the LIMS instrument on Nimbus-7 was operating, so that model calculations can be compared with satellite data.

Simulations performed for February 1979 indicate that the structure of the computed constituent fields qualitatively agrees with LIMS observations. The temporal variance, caused largely by transport, is accurately represented. The good agreement between model computations and global observations leads to the conclusion that the variability of unobserved (or less frequently observed) species has been properly simulated.

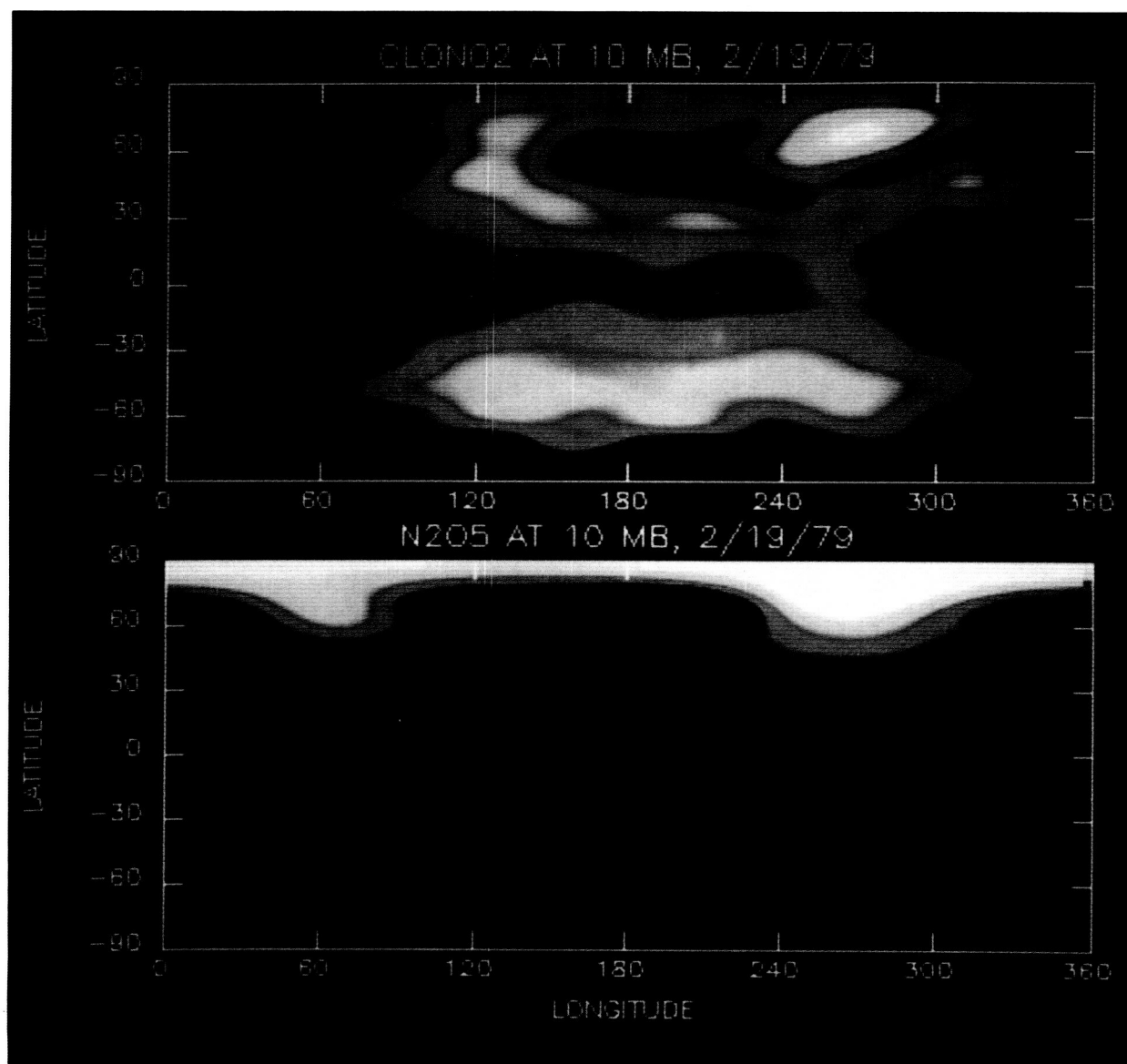
Some of the longitudinal variability calculated may be seen in the first figure, in which contours showing the O_3 distribution at 10 mb (top, 30 km) and the HNO_3 distribution at 18 mb (bottom, 27 km) are plotted in a color scheme in which yellow is high, blue is low, and red is in between. Both O_3 and HNO_3 are long-lived constituents at these pressure levels, especially at middle and high northern latitudes, so that dynamical processes should be reflected in their distributions. The high correlation between O_3 and HNO_3 in the northern hemisphere indicates that the horizontal structure of the wind field is several kilometers deep. The transport of high- O_3 and low- HNO_3 air in a northward direction to the west of the region near $180^\circ E$ and $60^\circ N$ and in a southward direction to the east of the region is clearly visible. There is little longitudinal variation in the Southern (summer) Hemisphere, where the stratospheric waves are small.



Contour plots showing the distribution of O_3 at 10 mb (top) and HNO_3 at 18 mb (bottom) as a function of latitude and longitude. The color scheme runs from blue (low) to red (moderate) to yellow (high) to white (highest).

Results for species for which there are only very limited satellite-based observations are shown in the second figure. Chlorine nitrate ($ClONO_2$) and dinitrogen pentoxide (N_2O_5) are shown in the top and bottom panels, respectively. The distributions are shown for the 10 mb (30 km) pressure level, where, except at high latitudes (polar night and polar day), both species undergo important diurnal variation (they maximize at night and minimize in the day, due

to solar ultraviolet photolysis). The distributions are thus expected to reflect both diurnal photochemical and dynamical variations, and both may indeed be seen. In the $ClONO_2$ field, the diurnal variation is shown most clearly in the high (yellow) values near 180°E and 60°S, while the dynamical variation is shown by the crescent-shaped region of high (yellow) $ClONO_2$ air around the region of lower values. For N_2O_5 , high values associated with the diurnal



Contour plots showing the distribution of ClONO_2 (top) and N_2O_5 (bottom) at 10 mb as a function of latitude and longitude. The color scheme is as in the first figure.

photochemical variation are shown centered near 240°E over all but the most northern latitudes, while dynamical variations can be seen at high northern latitudes by the two regions of enhanced values centered near 60°E and 270°E .

The 3-D chemistry model with winds from the assimilation provides the best quantitative tool currently available for understanding constituent variability. It is anticipated that the model will prove

invaluable for interpreting UARS data. Furthermore, the model is being used as part of the Airborne Arctic Stratosphere Expedition (AASE, January/February 1989) to determine expected variability and the potential global effects of localized heterogeneous chemistry, which has been suggested to be important in ozone depletion.

Contacts: Jack A. Kaye and Richard B. Rood
Code 616

Sponsor: Office of Space Science and Applications

Dr. Jack Kaye is a space scientist assigned primarily to the Stratospheric General Circulation with Chemistry Modeling Project. His professional interests include atmospheric chemistry, chemical kinetics and reaction dynamics, planetary atmospheres, and theoretical chemistry. Dr. Kaye, who holds a PhD degree from the California Institute of Technology, has almost five years of experience at Goddard.

Dr. Richard B. Rood, with a PhD from Florida State University, is responsible for model development and interpretation of past and future satellite data at the Laboratory for Atmospheres. His interests include development of models of the Earth's atmosphere and the use of data assimilation to study constituent transport. Dr. Rood has six years of experience at Goddard. He has also received two Performance Awards.

OZONESONDE MEASUREMENTS OF ANTARCTIC OZONE DEPLETION

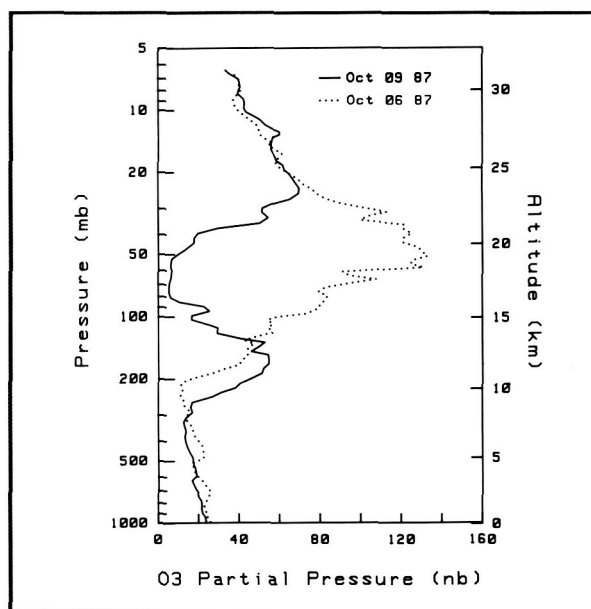
The sudden and dramatic decreases in stratospheric ozone over Antarctica that have occurred each austral spring for the past decade have stimulated much interest within the scientific community. Total ozone overburdens drop by up to 50 percent from August to October; over 90 percent of the ozone disappears at certain altitudes. These losses are largely confined to the polar vortex, a region of air circulating about the pole having relatively little interaction or exchange with the surrounding air. Although a recovery in ozone amounts is noted around November, the changes have worsened during the years.

The behavior of ozone over Antarctica affords observers a unique opportunity to test theoretical understanding of atmospheric processes against experimental observations. In contrast to global ozone depletion, which is slow and difficult to quantify, changes over Antarctica are easily measured and occur on a regular basis. Attempts to explain these changes have implicated a combination of anthropogenic chlorofluorocarbons and the relatively unique Antarctic meteorology, which promotes the formation of polar stratospheric clouds. The latter

is believed to enhance the rate of ozone destruction by chlorine chemistry.

Both the National Aeronautics and Space Administration (NASA) and the National Science Foundation (NSF) sponsored expeditions in 1987 to study the Antarctic ozone problem. In a cooperative effort between these two ventures, Goddard Space Flight Center/Wallops Flight Facility conducted a series of 52 balloon-borne measurements of vertical ozone profiles over the NSF research facility at Palmer Station, Antarctica (64°S, 64°W) between August 9 and October 24, 1987. The measurements were made with electrochemical ozonesondes that were coupled to meteorological radiosondes for data transmission to a ground receiving station.

A progressive depletion of ozone occurred within the 13–23 km altitude range from August to October. The region of maximum ozone loss was centered around 17 km. The ultimate magnitude of this loss is illustrated in the accompanying figure, which shows two vertical profiles of ozone measured 3 days apart. The October 6 profile is a “normal” profile,



Vertical ozone profiles over Palmer Station, Antarctica, measured when the polar vortex boundaries were poleward of Palmer (October 6) and when the vortex boundaries had expanded to include Palmer (October 9). Virtually all of the 17–20 km ozone had disappeared within the vortex.



measured on a day when the boundary of the polar vortex was poleward of Palmer Station. This is similar to the profiles observed within the vortex during early August, before significant changes occurred. By October 9, meteorological dynamics expanded the vortex boundary to include Palmer. As can be seen in the figure, a large portion of the stratospheric ozone peak was lost by this date within the vortex. Almost no ozone remained between 17 and 20 km.

Total ozone overburdens sometimes exceeded 300 Dobson units (DU) in early August. By early October, this quantity had fallen to values as low as 150 DU.

The Palmer experiment will be repeated during 1988, with the objective of characterizing the changes in depth and vertical extent of the ozone depletion. Following the Antarctic measurements, a series of soundings will be conducted at a high northern latitude site as part of NASA's study of possible ozone depletion in Arctic regions.

Contact: Arnold L. Torres
Code 672

Sponsor: Office of Space Science and
Applications

Dr. Arnold L. Torres develops analytical techniques for trace-gas measurements at the Observational Science Branch. He has a PhD from the University of South Carolina and has 10 years of experience at Goddard.

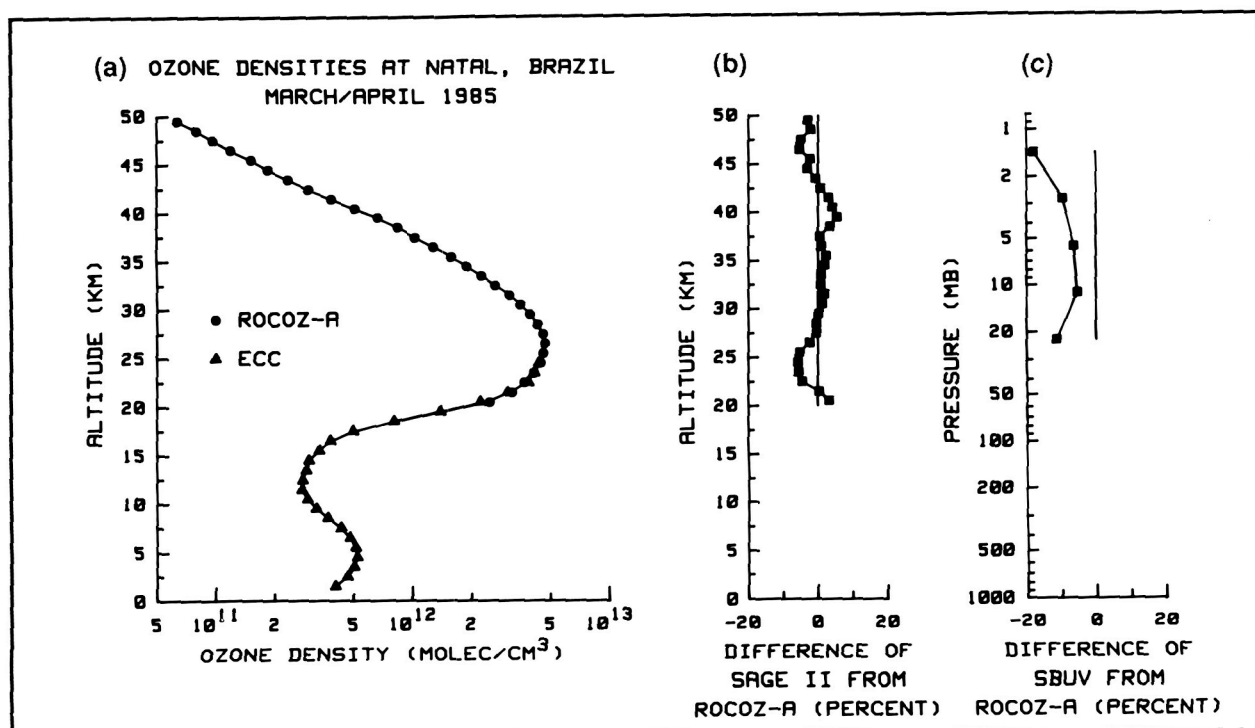
THE ROCKET-OZONESONDE (ROCOZ-A) LINKS SATELLITE OZONE PROFILER DATA SETS

In the fall of 1986 an interagency Antarctic Ozone Expedition Team spent the months of August to November in Antarctica. They conducted a coordinated series of ground and balloon observations to study the disappearance of stratospheric ozone reported previously by the British Antarctic Survey. Their results verified that the ozone level was diminished by as much as 90 percent at some altitudes, and that the reduction is increasing every year. At the same time, unpublished reports were circulated stating that the ozone amount around the

globe is decreasing by about 1 percent per year. It is known that an ozone decrease can be linked to an increased risk of skin cancer in humans. Consequently, the Antarctic and global ozone reports heightened interest in ozone trend detection. The National Aeronautics and Space Administration, in conjunction with the World Meteorological Organization and the United Nations Environment Program, initiated a major review of the subject of ozone trend detection. An Ozone Trends Panel composed of eminent scientists from federal agencies, industry, and universities, was formed. The Goddard Space Flight Center's Correlative Measurements Program at the Wallops Flight Facility was represented on the Satellite-to-Satellite Intercomparisons Working Group. Rocket Ozonesonde (ROCOZ-A) and Electrochemical Concentration Cell (ECC) balloon-borne sensors have been used through the years to measure the vertical profile of ozone in the stratosphere. Comparisons are then made with the data products of orbiting satellite ozone profiler instruments, such as the Solar-Backscattered Ultraviolet (SBUV) on Nimbus-7, the SBUV-II on the National Oceanic and Atmospheric Administration (NOAA) polar orbiting series, the Stratospheric Aerosol and Gas Experiment (SAGE-II), the Solar Mesospheric Explorer, the Limb Infrared Monitor of the Stratosphere, and others. The particular data sets of interest to the Ozone Trends Panel were collected at Natal, Brazil.

During an experiment at Natal in March and April of 1985, it was found that the atmospheric variability over a short time span is negligible. Therefore, a small number of ROCOZ-A vertical ozone profiles can be compared with high precision with a larger number of satellite ozone profiles compiled in that region during the same time frame *without* exact time coincidence. This reduces the cost of the field campaign, and reduces the complexity of the launch schedule. The Natal area in March and April is an ideal location to use rocket profiles to tie together various satellite ozone profiler instruments.

The major results produced for the Ozone Trends Panel are shown in the figure. The ROCOZ-A average ozone density profile is plotted with respect to altitude in graph (a). ECC ozonesondes were used for the portion of the profile below 20 km, the lower limit for ROCOZ-A. In graph (b), the difference between SAGE-II and ROCOZ-A average density profiles is shown. Between 25 and 50 km, these differ-



Major results produced for the Ozone Trends Panel.

ences are sometimes negative and sometimes positive; they never exceed 5 percent, and the average is about -1 percent (the ROCOZ-A values are slightly higher). In graph (c), the difference between ROCOZ-A and the SBUV results from Nimbus-7 is plotted. This comparison is made in terms of ozone layer amount versus Umkehr layer, the primary ozone data product from the SBUV. For all layers, the SBUV values are less than ROCOZ-A. The difference is 18 percent in layer nine and 5 percent in layer six. The implication of this Natal data set and other findings of the Ozone Trends Panel is that the SBUV vertical profile data are of questionable value for ozone trends detection. Instrumental effects in the SBUV that are inadequately accounted for may be responsible for some of these measured differences. The Panel's report does concur, however, in finding that an ozone decrease on the global scale is real. The earlier reports of a decrease were considerably exaggerated because of the SBUV instrument problem, but concern about anthropogenic alterations to the ozone layer is justified. Routine monitoring of the ozone vertical profile is, therefore, an absolute requirement for the future. ROCOZ-A is now being used to measure the stratospheric ozone layer to validate ground-based lidar profiling, the technique

scientists are developing to monitor future changes in the ozone.

Contact: Chester L. Parsons
Code 672

Sponsor: Office of Space Science and
Applications

Mr. C. L. Parsons, RTOP Manager of the Advanced Sensor and Principal Investigator of the Correlative Measurements Program, is interested in radar instrumentation, microwave backscattering, and ozone measurements. Mr. Parsons has an MS in geoscience from Purdue University, eight years of experience at Goddard, and 20 years of experience at NASA.

BALLOON- AND ROCKET-BORNE MEASUREMENTS OF TEMPERATURE: IMPROVEMENT AND APPLICATION

Global satellite monitoring coverage of atmospheric temperature provides useful information, and the newer lidar techniques can provide detailed vertical



profiles; however, continued in situ measurements from radiosondes and rocketsondes are still required for calibration and verification of the remote measurements. The present operational satellites, and even the research instruments, are not stand-alone means of obtaining information; they depend upon in situ temperature measurements for validation and calibration. Not only are these in situ measurements essential, but enhanced knowledge of their accuracy and precision is equally important.

Early on in the application of rocketsonde it was recognized that temperature measurements were being seriously influenced by a number of external factors. Among these factors were aerodynamic heating of the sensor, radiation, thermal lag, and sensor emissivity. The most serious of these turned out to be aerodynamic heating and radiation, together these account for about 90 percent of the measurement error. Temperature corrections were then developed that could be applied operationally. However, recent investigations of global temperature trends established that the corrections, although optimal for a uniform launch time at all of the launch sites, are deficient at most other times during the day (nor do all launches occur at a uniform time). It should be noted that nighttime corrections do seem to be adequate.

Rather than undertake a costly and lengthy study to improve the corrections, researchers began an investigation of the inflatable sphere technique already in use at many launch ranges. These spheres have the intrinsic property of providing rather accurate temperatures, readings influenced only by vertical winds, which appear in the reduction as perturbations in density and temperature. Comparisons between sphere-derived temperatures and in situ rocketsonde temperature sensors have revealed that the rocketsonde and sphere temperatures are in excellent agreement below 50 km. Between 50 km and 70 km (the upper limit of the in situ sensor), the direct sensing technique provides temperatures that are too warm by up to 12–15 °C.

While corrections for rocketsonde measurements were of major concern during the 1960s, little to no effort was made to isolate radiosonde errors that were known to exist. Differences between radiosonde and remote measurements of 1–3 °C make it imperative

for accurate radiosonde temperatures to be obtained. Radiosondes were flown equipped with multiple thermistors coated to respond differently to long- and short-wave radiation, allowing scientists to determine the radiation error of the thermistor. Since three coatings (thermistors) were used, three heat transfer equations (one for each coating) were solved simultaneously to derive the actual, or ambient, temperature. The difference between the thermistor-measured temperature and the ambient temperature represents the radiosonde's temperature measurement error.

Results from approximately 100 radiosonde observations indicate that daytime thermistor measurement errors reach 1.0 °C at about 30 hPa (hecto pascal) for solar elevation angles of 30–60 degrees, and then decrease to 0.5 °C at 10 hPa. On the other hand, the nighttime error is negative from the surface to 10 hPa, being –0.2 °C at 100 hPa and –1.4 °C at 10 hPa. Apparently, the decrease in daytime error at levels above 30 hPa results from the influence of the dominant and increasingly larger long wave error with increasing altitude. The magnitude of the error also appears to be influenced by the temperature lapse rate and the underlying surface or cloud-top temperature.

In spite of the longevity of the present radiosonde system used in the United States, recently there has been a proliferation of instruments from different manufacturers. These radiosondes operate on different principles and use different sensors. Unless data are adjusted to a known standard (not currently possible), the upper-air data base will be biased and contain large variances. Development of a reference standard will insure that adjustments of the various radiosondes to a standard baseline can be accomplished. The multiple thermistor radiosonde has the potential of providing this reference standard. Periodic comparisons will still be necessary to guard against drift of the various sensors and the occurrence of differences between the instruments.

Although rocketsonde is an accepted technique for temperature measurement, very few measurements are available for ground truth (~55 per week in 1974 and ~10 per week in 1988). Those measurements that are available provide highly reliable temperatures to 50 km. In order to monitor rocketsonde reliability,

comparisons are made with radiosondes. Radiosondes are the basic measuring tool of the atmospheric research community and promise to be widely used for many of the National Aeronautics and Space Administration's present and future programs.

Contact: Francis J. Schmidlin
Code 672

Sponsor: Office of Space Science and Applications

Mr. Francis J. Schmidlin handles investigations of instrumental compatibility, accuracy, and precision for the Observational Science Branch. He has a BS in meteorology from Pennsylvania State University.

IONIZATION RESULTING FROM SPACE SHUTTLE THRUSTER FIRINGS

One of the prime concerns of scientists working on the space shuttle is how and to what degree this spacecraft system perturbs the ambient atmospheric and ionospheric environment. Contaminant gases are introduced into this environment by outgassing, off-gassing, water releases, and thruster firings. The snowplowing action of the large, fast-moving body also has a pronounced effect on ambient particle distributions in the immediate vicinity; this is demonstrated by the existence of a plasma wake behind the vehicle that is more depleted than in any other hitherto-observed spacecraft wake. Several shuttle missions carried contamination monitors, but it was not until the Spacelab 2 mission that a specific scientific package, the Plasma Diagnostic Package (PDP), was employed with specific shuttle operations to provide a measure of the plasma distribution about the spacecraft under controlled conditions. One of the problems encountered was the plasma disturbance introduced by complex sequences of thruster firings that cannot be inhibited for long periods of time if strict attitude control is to be maintained. An understanding of how these firings impact the plasma was therefore necessary. For this purpose, an extensive post-mission study was made of Goddard Space Flight Center-supplied ion mass spectrometer measurements on the PDP, made at different locations and attitudes about the shuttle during firings of the small vernier thruster engines.

When scientists concentrated on simple sequential firings of the vernier thrusters as one or (at most) two of the six engines fired for several continuous seconds, they found that ionization effects around the shuttle were dependent upon not only the location of the vernier fired, but also upon the attitude of the spacecraft with respect to the ambient magnetic field. Ionization enhancements associated with the firings were composed of molecular species that are not present in the atmosphere at these altitudes. Water ions were typically the most prominent non-ionospheric ion species introduced, but other molecular ions such as NO^+ , which was a minor ambient ionospheric constituent, also originated from the thrusters. These contaminant ion enhancements persisted seconds beyond the cutoff of the engine firings. This demonstrated that the thruster plume had an impact on the ambient medium far from the immediate vicinity of the shuttle, and that ionization produced in the thrust chamber itself was not the prime source of the contaminant ion species seen. The neutral gas of the plume was ionized by charge transfer with ambient ionospheric ions, and the resulting ions were captured by the local ambient magnetic field as the shuttle moved through the resulting plasma cloud. The thruster neutral gas emissions also reduced the flux of ambient ions flowing towards the shuttle through the ion-neutral particle chemical reactions responsible for the production of the ambient ions, and through collisional scattering. The importance of the latter effect was seen in the wake of the shuttle, where normally unpresent ambient ions were detected during the thruster firings. Although this phenomenon is a nuisance with regard to measurements of the ambient plasma in the vicinity of the space shuttle, study has shown that the shuttle's short-lived and spatially restricted thruster plumes provide a well-defined and useful source for the investigation of neutral plasma interactions in a rarefied media.

Contact: Joseph M. Grebowsky
Code 614

Sponsor: Office of Space Science and Applications

Dr. Joseph M. Grebowsky performs research in thermal plasma environments of Earth, Venus, and spacecraft at the Planetary Atmospheres Branch. He



was also a Co-experimenter on the Plasma Diagnostic Package and was responsible for the ion mass spectrometer experiment. Dr. Grebowsky has 20 years of experience at Goddard.

INFLUENCE OF SOLAR PROTON EVENTS ON CONSTITUENTS IN THE MIDDLE ATMOSPHERE

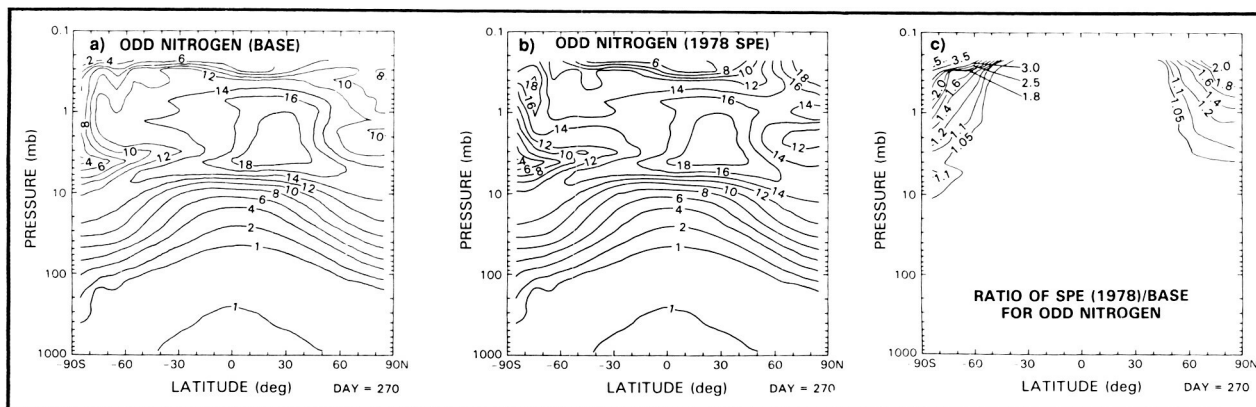
Scientists are relying increasingly on atmospheric photochemical models to predict atmospheric change due to anthropogenically produced chlorofluorocarbons. Because these model predictions can influence government policy, the models used in predictions should be developed to include as many natural atmospheric perturbations as possible. Since solar proton events (SPEs) are an integral part of every solar cycle and provide natural atmospheric perturbations, the quantifiable SPE effect on minor constituents in the atmosphere should be included for more accurate model computations.

SPEs produce HO_x (H , OH , and HO_2) and odd nitrogen (N , NO , NO_2 , NO_3 , HNO_3 , HO_2NO_2 , N_2O_5 , and ClONO_2), both of which can decrease ozone. The HO_x species have lifetimes of only hours in the middle atmosphere, while odd nitrogen can remain for several days to several months, depending on its altitude of formation and transport after formation. Because of its long lifetime, the odd nitrogen

produced by SPEs has the most significant influence on long-term atmospheric change and must be analyzed in more detail.

The initial study investigated the production of odd nitrogen by SPEs during 1978 and 1979, dates chosen because 1978 was the most proton active year and 1979 a rather quiescent year of the last solar maximum. The proton data compiled by Thomas Armstrong and colleagues from the University of Kansas was used in an energy deposition code that resulted in an ion pair production computation used to derive an odd nitrogen production.

The figures compare two-dimensional model simulations for day 270 of year 1978 for (a) the odd nitrogen in ppbv from the background model experiment (labeled BASE), which includes no SPEs; (b) the odd nitrogen in ppbv from the perturbed model experiment (labeled SPE), which includes the observed SPEs; and (c) the ratio of the SPE to the BASE case. The SPEs cause odd nitrogen enhancements of 20 percent to over 100 percent at altitudes above 2 mbar for the polar latitudes. The model simulations also indicate that the SPE-produced odd nitrogen during 1978 and 1979 enhanced odd nitrogen in the upper stratosphere and mesosphere for up to 2 to 3 months past the SPE, depending on the season. The SPE-produced odd nitrogen had a longer atmospheric influence on the background atmospheric odd nitrogen in winter or late fall than it did in summer or late spring.



Comparison of the two-dimensional odd nitrogen model distribution on day 270 of year 1978 for (a) the background model experiment (labeled BASE), (b) the perturbed model experiment which includes solar proton events (labeled SPE), and (c) the ratio of the SPE/BASE odd nitrogen distributions for the two model experiments. Units of odd nitrogen are in ppbv (parts per billion by volume).

Work is continuing on SPEs and their influence on constituents in the atmosphere. The model now includes proton flux data from 1963–1985 (over two solar cycles). In this next study, scientists will not only be looking at SPE effects on odd nitrogen, but the corresponding influence on ozone as well.

Contact: Charles H. Jackman
Code 616

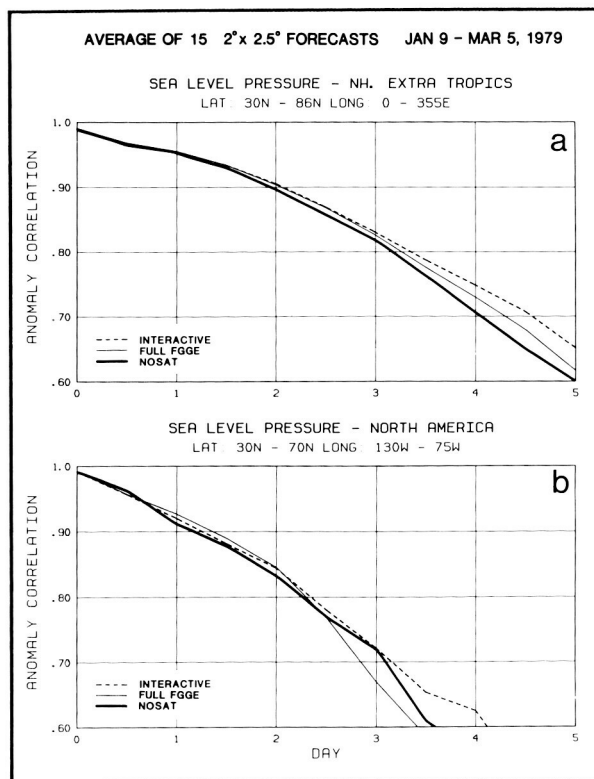
Sponsors: Office of Space Science and
Applications and the Upper Atmosphere
Theory and Data Analysis Program

Dr. Charles H. Jackman researches the Earth's stratosphere and mesosphere with the use of a two-dimensional photochemical model. His special interests include investigating the interaction of charged particles on the Earth's atmosphere. Dr. Jackman has a PhD from the University of Florida and has eight years of service with Goddard. He recently received the Peer Scientific Achievement Award from the Laboratory for Atmospheres.

IMPROVING SATELLITE IMPACT ON FORECASTING SKILL

Recent research at the Goddard Space Flight Center (GSFC) Laboratory for Atmospheres has resulted in the demonstration of a considerable improvement in the impact of satellite data on weather forecast skill. Prior to this result, it was generally thought that use of satellite data had little, if any, beneficial impact on forecast skill in the Northern Hemisphere because of the existence of an extensive conventional observing system of rawinsondes, ships, planes, etc. The conventional wisdom was based primarily on experience with operational temperature soundings produced using data from the low Earth orbiting operational sounding instruments, High Resolution Infrared Sounder 2 (HIRS2) and Microwave Sounding Unit (MSU), analyzed by National Oceanic and Atmospheric Administration (NOAA) National Environmental Satellite Data and Information Service (NESDIS) using regression-based techniques. The improved satellite impact has resulted from the use of the Goddard Laboratory for Atmospheres (GLA) physically based interactive forecast-retrieval-analysis system, coupled with high-resolution forecasts.

The GLA interactive forecast-retrieval-analysis system is an end-to-end processing system which simultaneously produces self-consistent fields of satellite- and model-derived geophysical parameters and appropriate analyses. GSFC scientists have used this system to process data from the HIRS2 and MSU operational sounding instruments in an interactive mode in conjunction with the GLA Fourth Order General Circulation Model (GCM) and an objective analysis scheme. In each 6-hour period, the interactive cycle starts with the 6-hour forecast field generated by the GLA $4^\circ \times 5^\circ$ Fourth Order GCM. The 6-hour forecast temperature-humidity profiles are used as an initial guess for all soundings occurring in the interval 3 to 9 hours from the forecast time. An analysis is then performed using the satellite temperature soundings and all other information measured in the time interval (such as radiosonde and



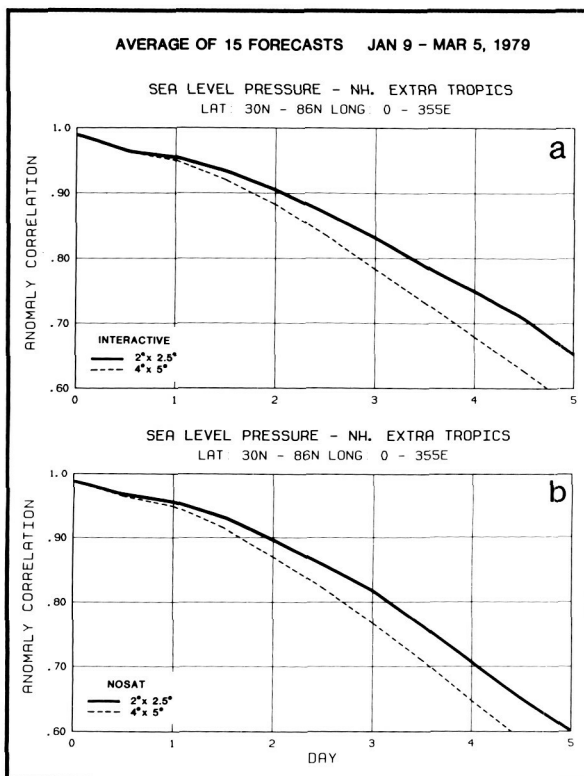
Average anomaly correlation coefficients of sea level pressure for ensembles of fifteen 5-day forecasts, produced with the GLA $2.0^\circ \times 2.5^\circ$ resolution GCM, starting from three different sets of analyses. a) Verified over the Northern Hemisphere extratropics. b) Verified over North America.



ship reports). Using the same 6-hour forecast field as a first guess for the retrievals and also as initial conditions for the analysis is advantageous not only for the retrievals (because the first guess is accurate) but also for the analysis and subsequent forecast (because the modifications to the first guess from the point of view of the analysis are small and allow for a better dynamic balance in the initial conditions for the next 6-hour forecast).

GSFC scientists have recently tested the accuracy of different analyses by conducting forecasts from these analyses during the 1979 First Global Atmospheric Research Program (GARP) Global Experiment (FGGE) year and verifying them against the analyses

produced by the European Centre for Medium-Range Weather Forecasting (ECMWF). These sets of forecasts were run from the $4^\circ \times 5^\circ$ analyses produced using 1) NOSAT (no satellite data) conventional data only; 2) the full FGGE data set including conventional data and the satellite soundings produced by NOAA NESDIS; and 3) the interactive analysis which used the same data as full FGGE but with GLA interactive retrievals in place of the NESDIS soundings. Two sets of forecasts were run from each analysis. In the first set, the same $4^\circ \times 5^\circ$ version of the GLA GCM used to produce the analyses was used to generate the forecasts. In the second set, the $2.0^\circ \times 2.5^\circ$ version of the GLA GCM was used to generate the forecast. The $4^\circ \times 5^\circ$ analyses were first interpolated to the $2.0^\circ \times 2.5^\circ$ grid before the forecasts were run. The first figure shows average anomaly correlation coefficients for sea level pressure over an ensemble of fifteen 5-day forecasts, run every fourth day from January 9, 1979 to March 5, 1979, using the $2.0^\circ \times 2.5^\circ$ model. The anomaly correlation coefficients in the first figure are verified against ECMWF analyses over the entire Northern Hemisphere extra tropics (top) and over North America (bottom). Higher correlations of forecasted anomalies with observed anomalies are indicative of more skillful forecasts. An anomaly correlation coefficient of 0.6 or greater is an estimate of useful forecast skill.



Average anomaly correlation coefficients of sea level pressure, verified over the Northern Hemisphere extratropics, for two ensembles of fifteen 5-day forecasts, from either the GLA $2.0^\circ \times 2.5^\circ$ resolution GCM or the GLA $4^\circ \times 5^\circ$ resolution GCM. a) Forecasts made starting from the interactive analyses. b) Forecasts made starting from the NOSAT analyses.

The top graph in the first figure shows that the limit of skill of the NOSAT forecasts for the Northern Hemisphere is about 5 days. The average skill, over the entire winter, of the Full FGGE forecasts appears to be greater by about 3 hours than that of NOSAT. The GLA interactive forecasts are more skillful than NOSAT by at least 12 hours. The bottom graph shows that the average skill of all sets of forecasts for North America is somewhat less than that of forecasts for the entire Northern Hemisphere. Nevertheless, an improvement of skill of the interactive forecasts, compared to the NOSAT forecasts, of more than 12 hours is observed. This improvement contrasts sharply with the 3-hour negative impact of the Full FGGE forecasts compared to the NOSAT forecasts over North America.

In general, the $2.0^\circ \times 2.5^\circ$ forecasts were more skillful than the $4^\circ \times 5^\circ$ forecasts run from the same analyses, but the degree of improvement depended on the nature of the data used. The top graph in the second

figure shows the improvement in skill, due to model resolution, of the interactive forecasts of sea level pressure verified over the Northern Hemisphere extra tropics, to be about 20 hours on the average. The bottom graph shows the improvement in skill, due to model resolution, of the NOSAT forecasts verified over the same region to be only about 12 hours. In general, forecasts from the Full FGGE analyses showed intermediate levels of improvement, between that of NOSAT and of the interactive forecasts, when model resolution was increased. This finding, which also held in other geographical areas, is a result of the higher resolution model being more sensitive to the initial conditions and the quality of the data entering into them. Consequently, increasing spatial resolution of the model increases the impact of

satellite soundings on the forecast skill, especially if the soundings are compatible with the model.

Contact: Joel Susskind
Code 611

Sponsor: Office of Space Science and Applications

Dr. Joel Susskind is Senior Research Scientist with the Global Modeling and Simulation Branch of the Laboratory for Atmospheres. Dr. Susskind is responsible for the development of improved techniques for utilization of operational satellite data and for research involving improved satellite instrumentation. He received his PhD in physical chemistry from the University of California at Berkeley. Dr. Susskind has 11 years of experience at Goddard.

OCEAN

A NEW THEORY OF EL NIÑO AND THE SOUTHERN OSCILLATION

Every few years anomalously warm sea surface temperatures cover the equatorial Pacific, extending over roughly one-fourth of the Earth's circumference, from the dateline to the South American coast. These oceanic events, called El Niño, occur typically at intervals of 3 to 4 years, but can be separated by only 2, or by as many as 7 years. During the height of an El Niño, sea surface temperatures can be 3–4°C above normal along the Equator, and even warmer along the South American coast.

Associated with the El Niño phenomenon in the ocean are a host of events occurring in the tropical atmosphere. These are often referred to as the Southern Oscillation. The name derives from the observed large-scale seesaw in atmospheric sea level pressure between the eastern and western Pacific, which is one of the outstanding and earliest documented atmospheric responses to El Niño. Also part of the atmospheric response is warming of the entire tropical atmosphere, major changes in the distribution of precipitation over the Pacific, and changes in atmospheric circulation patterns produced by the anomalous precipitation regimes.

Over the last 10 years, El Niño and the Southern Oscillation have come to be regarded as a single phenomenon—ENSO. This view goes beyond recognizing that the two are related—for example, the idea that the causes of variability are inherent in either the ocean or the atmosphere with the other element merely a passive one. Rather, it is now clear that neither system on its own could produce ENSO, and that it is only through sympathetic interactions between the two that large, long-term ENSO variability occurs.

The view that ENSO is a coupled phenomenon has been bolstered greatly by work with numerical models of the ocean and atmosphere. These models allow researchers to perform experiments on the computer that they cannot perform with the real system. Some examples are sensitivity experiments, in which atmospheric models are programmed with the anomalous sea surface temperatures observed during El Niño events and are then made to produce a prediction of changes in atmospheric circulation. Experiments like this have been performed with many different atmospheric models by several research groups. The results are conclusive: given the tropical sea surface temperature anomalies, the responses obtained from the atmospheric models are very similar to the



behavior of the tropical atmosphere during actual El Niño events. This does not mean, however, that the ocean plays the dominant role. Similar sensitivity experiments have also been performed in which the anomalous atmospheric circulation patterns observed during ENSO events are used to force ocean models. Again the results are conclusive: given the atmospheric forcing, the responses obtained from the ocean models are very similar to the observed behavior of the ocean during El Niño events.

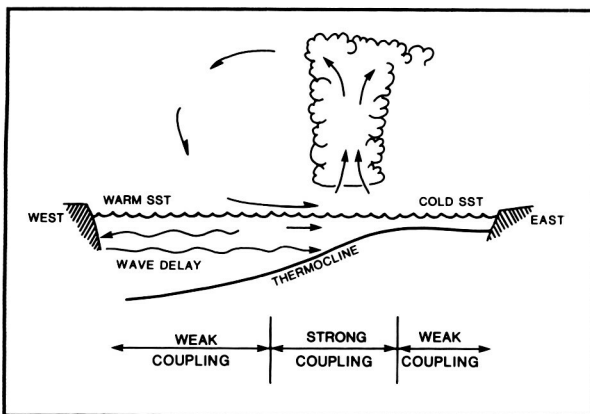
The symmetry of these calculations is perhaps the most forceful argument for the coupled nature of ENSO. Since neither system can be considered as dominant, the variability must arise from their interaction. The work at Goddard Space Flight Center has been devoted to understanding how this occurs. Again, computer models of the atmosphere and ocean have been used to perform "coupled" experiments rather than "sensitivity" experiments. In these experiments, no inputs of observed ENSO conditions are supplied. In fact, no observations whatsoever are used, and no time-dependent forcing is applied. The two models are coupled, started from rest, and, using a steady forcing that mimics the energy input from the Sun, are allowed to spin up for several years, producing their own oceanic and atmospheric general cir-

culations. Long-term experiments (30 to 40 years) are then performed, during which the behavior of the two models is monitored.

The results of the first coupled calculations (published in the Journal of Atmospheric Sciences in 1988) showed that, for appropriate choices of parameters, such as the degree of coupling between the two systems, the models produce large-scale variability very similar to ENSO. Solutions consist of irregular vacillations of sea surface temperature and atmospheric circulation with characteristic periods of 30 to 40 months. To show that the coupling is fundamental to producing these self-sustained oscillations, a series of idealized uncoupled experiments was also performed. In one, the ocean model was run, forcing it with time-mean conditions from the atmospheric model; in another, the atmosphere was run over time-mean ocean conditions and its history used to force the ocean. In all cases, the system settled to a nearly steady state with no sign of the ENSO signal.

When these results were analyzed, researchers concentrated on trying to explain the typical period of the vacillations. No time-dependent external forcing was applied, so 30 to 40 months, the period of the vacillations, had to be a natural time scale of the system. This is particularly interesting because there is no obvious natural frequency in this range, in either the ocean or the atmosphere. The theory proposed to explain the model's frequency selection relies on a subtle interplay between the two systems, and on the properties of oceanic signals propagating east-west along the Equator.

Briefly, the theory is as follows: as sea surface temperatures rise in the central and eastern Pacific during an El Niño event, atmospheric precipitation patterns shift, tending to overlie the warm temperatures. This anomalous latent heat release then modifies the low level atmospheric circulation, producing anomalous westerlies along the Equator. (The figure shows a schematic of these processes.) In this theory, the anomalous winds have two important effects. First, they tend to maintain the warm surface temperature anomalies that produced them, closing a positive feedback loop between the ocean and the atmosphere. (This feedback has been recognized for some time as an essential ingredient of ENSO



Schematic of the main processes thought to produce El Niño. Above-normal sea surface temperatures produce increased precipitation and changes in atmospheric circulation. These tend to maintain the warm temperatures by driving oceanic currents. Some of these effects are immediate; others act after the forced signal reflects from the western boundary and returns to the region of strong coupling.

theories.) The second effect is more subtle. In addition to forcing oceanic motions that maintain the temperature anomalies in the east, the wind anomalies also excite oceanic, equatorial Rossby waves, which propagate westward and eventually reflect from the western boundary. However, the phase of these westward propagating signals is opposite to that of the growing disturbances east of the wind anomalies. Thus, when they return to the center of the basin after reflecting from the western boundary, they have a cooling effect, and mitigate the positive feedback. But because they act on a time delay (the time needed to travel to the western boundary and back), they can turn the system around and begin a cold phase or anti-El Niño. The action then repeats, but with all signs changed, as a new set of signals propagates to the western boundary and back.

The theory thus predicts that the time scale of ENSO should depend on the time it takes oceanic signals to propagate from the region of strong coupling to the western boundary and back. From these simple arguments, the period is expected to be no less than twice this time. It can also be argued that the period is several times longer. These and other predictions made by the theory now need to be tested by analyzing the observational record in this light, and by experimenting with more detailed models.

It is important to emphasize that the coupled calculations that led to these arguments were highly idealized. For example, only the upper ocean layers were modeled, and these were contained in a rectangular ocean basin similar to the tropical Pacific only in size. The atmosphere also was highly simplified, and processes that unquestionably have a large impact on real ENSO, such as the seasonal cycle, were neglected. A new generation of coupled models, now under development, addresses most of these deficiencies. The hope is that by studying more detailed and realistic models, it will be possible not only to test the theory, but to begin to predict this important mode of inter-annual variability of the Earth's climate.

Contacts: Max J. Suarez and Paul S. Schopf
Codes 611 and 671

Sponsors: Atmospheric Dynamics and Radiation
Branch/EET and
Oceanic Processes Branch/EEC

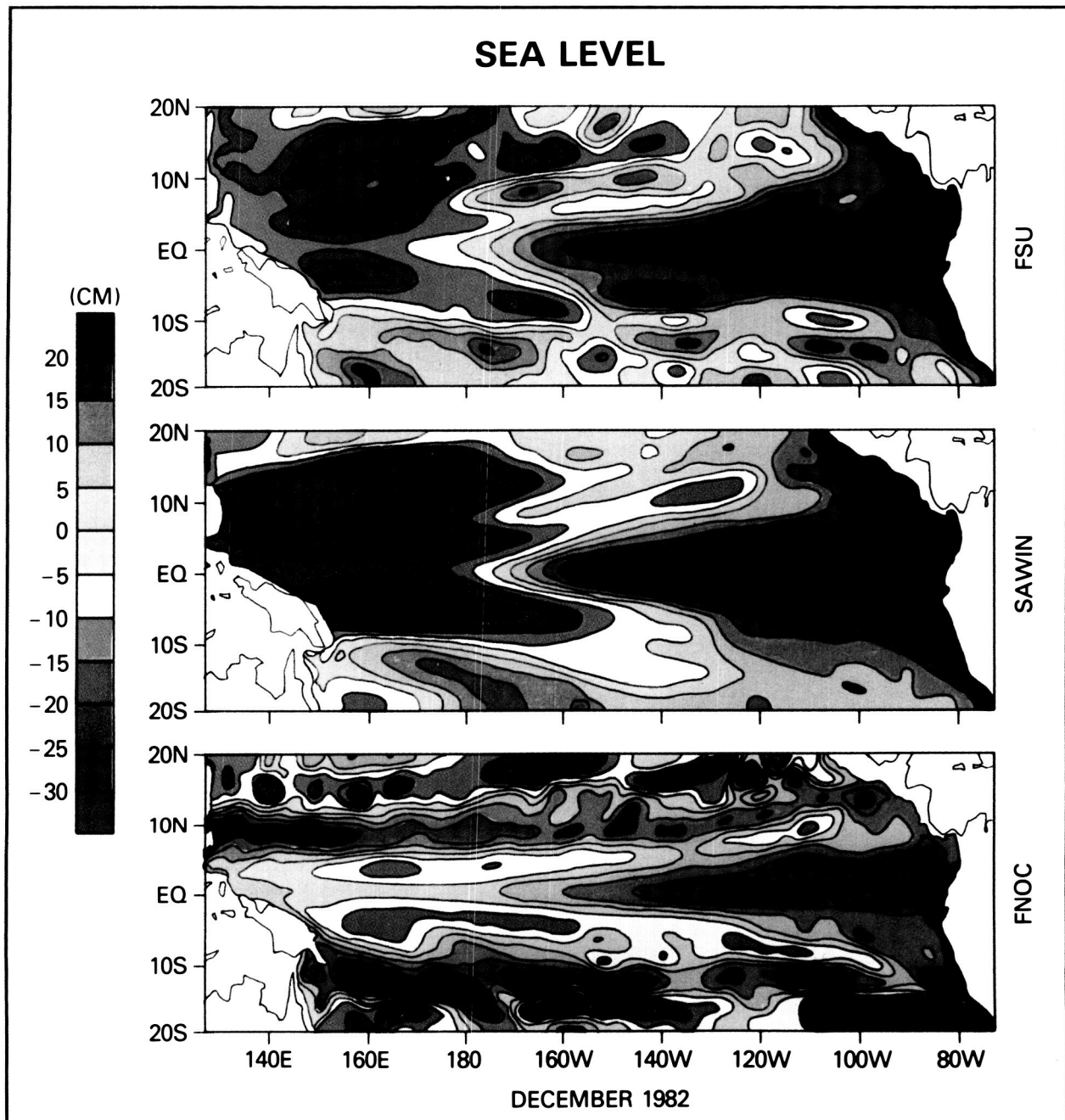
Dr. Max J. Suarez, who is with the Modeling and Simulation Branch, is primarily interested in atmospheric general circulation modeling, ocean-atmosphere interactions, and climate modeling. Currently he develops numerical models of the atmosphere for weather prediction, data assimilation, and climate studies. His PhD degree is from Princeton.

Dr. Paul S. Schopf, who earned his PhD degree at Princeton University, is a research oceanographer with the Oceans and Ice Branch. He is interested in ocean circulation and climate, particularly numerical and theoretical modeling of the ocean's role in climate.

WIND-FORCED SIMULATIONS OF TROPICAL PACIFIC SEA SURFACE TOPOGRAPHY

Over the next decade, the approach to ocean science will be altered radically by the availability of global satellite observations of the sea surface. In the past, the lack of global coverage of ocean surface variables such as surface wind stress, sea level, and sea surface temperature has severely limited our understanding of ocean circulation and, in turn, the role the oceans play in determining world climate. Uncertainties in observations of the surface wind field imply uncertainties in the description of the dominant forcing function for ocean circulation. Asynoptic coverage of the ocean topography implies an incomplete monitoring of the horizontal redistribution of mass and heat in the ocean. Sporadic measurements of the sea surface temperature permit only a fragmented view of a principal link between the ocean and the atmosphere.

With all the promise afforded by scatterometers, altimeters, and radiometers, such global measurements of the surface wind stress, sea level, and sea surface temperature, respectively, return only information about the skin of the ocean, as it were—a very thin surface layer. In order to fully monitor and understand the four-dimensional circulation of the world's oceans, these satellite measurements will be utilized in concert with in situ ocean measurements and numerical ocean models. In preparation for these satellite measurements, numerical ocean models are currently being used to study the upper-ocean response to wind stress estimates; to identify regions of important variability in the surface wind field; to



Three sea level solutions near the height of the 1982–1983 El Niño, from a linear ocean model forced by three different analyses of conventional observations of the surface wind field. Top: Response to a subjective analysis of ship wind observations from the Florida State University. Middle: Response to a subjective analysis of satellite-observed, low-level cloud motion vectors, ship wind observations, island wind observations, and buoy wind observations by the University of Hawaii. Bottom: Response to an objectively analyzed operational wind product from the United States Navy's Fleet Numerical Oceanography Center.

analyze the associated oceanic response; to demonstrate the applicability of remote sensing of wind stress, sea level, and sea surface temperature; and to illustrate the limitations of conventional observations of ocean variables.

A prime example of study is the tropical oceans. Roughly half of the world's oceans are in the tropics. Tropical oceans are regions of significant heat content, air-sea heat exchange, and advective heat transport and mixing, and thus play an important role in climate. Most notable is the tropical Pacific Ocean, with a width one-third the circumference of the Earth. Yet, even over this great expanse, wind energy input into the ocean in the far western Pacific can have its influence felt in the eastern tropical Pacific 75 to 90 days later through the propagation of internal equatorially trapped Kelvin waves. These time and space scales provide a very nice laboratory to test current theories of ocean circulation. However, considering the cost of a research vessel at \$10,000 to \$20,000 per day; it is often financially and logistically impossible to mount the monitoring programs needed to observe the pertinent ocean variables. As a result, routine surface observations in the tropical Pacific are limited to point measurements at approximately 30 islands, and those from merchant vessels plying the major shipping lanes.

The limitations of this restricted coverage are illustrated in a recent joint model/data analysis of the variability of the tropical Pacific Ocean on seasonal and interannual time scales for 1979–1983. This period was chosen for study because of the extreme El Niño event of 1982–1983, which was preceded by 3 years with a fairly regular seasonal cycle. Moreover, three different conventional descriptions of the surface wind field were available for this same period, and were used to quantitatively evaluate ocean model simulations of the tropical Pacific sea surface topography.

The accompanying figure shows three model sea level simulations, near the height of the 1982–1983 El Niño. For the top panel, a linear, numerical treatment of the shallow water wave equations was forced by a Florida State University subjective analysis of ship wind observations. In the middle panel, the same model was driven by another subjective analysis of

satellite-observed, low-level cloud motion vectors, ship wind observations, island wind observations, and buoy wind observations from the University of Hawaii. In the third panel, the model was forced by an objectively analyzed operational wind product from the United States Navy's Fleet Numerical Oceanography Center.

Twenty to thirty centimeters differences in the sea level solutions are present throughout the tropical Pacific basin, and are due solely to the differences among the three wind products. Comparisons with in situ ocean measurements indicate that the two solutions forced by subjective analyses of the wind field are in best agreement with the observations. These top two panels describe an oceanic state in response to a dramatic collapse of the trade wind system during El Niño. The resulting redistribution of mass from west to east is effected by Kelvin waves, causing a 30–40 cm increase in sea level in the east- and westward-propagating Rossby waves responsible for the drop in sea level in the west.

The magnitude of the signal, and errors within these sea level solutions, are well within the altimetric measurement capabilities of the future joint United States/France ocean topography experiment, TOPEX/POSEIDON. Together with remote sensing of the surface wind field, these measurements will allow an enhancement of our ability to discriminate the dominant physical processes in ocean circulation studies from uncertainties due to improper physical parameterizations and poorly specified forcing functions. Ultimately, in situ and ocean satellite data will be used to validate and assimilate into global ocean models, thereby contributing to the development of a predictive and operational monitoring capability for the world's oceans.

Contact: Antonio J. Busalacchi
Code 671

Sponsor: Office of Space Science and Applications

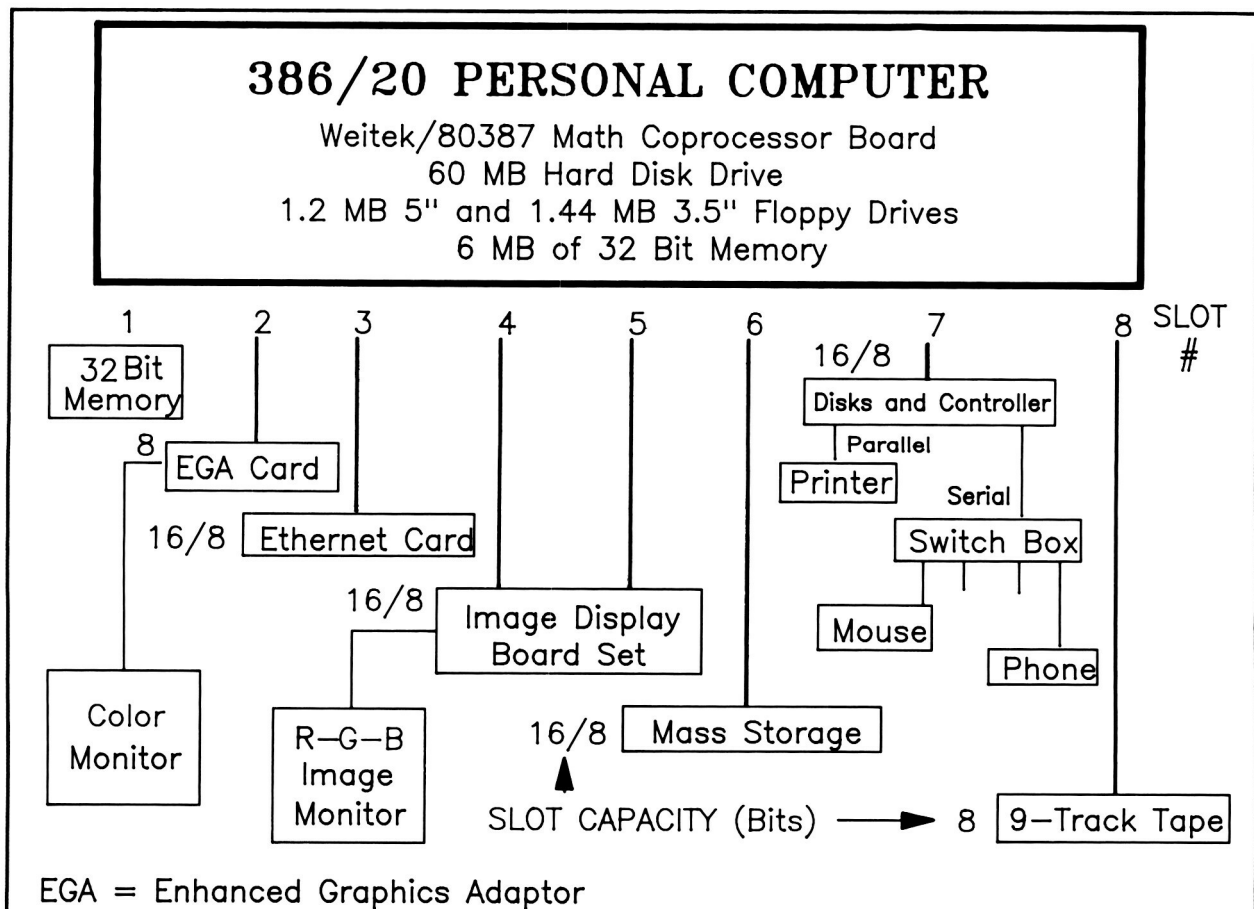
Dr. Antonio J. Busalacchi, who has a PhD degree in oceanography from Florida State University, studies ocean circulation. Dr. Busalacchi has received several Awards and honors for his work.



SEAPAK: AN ANALYSIS PACKAGE FOR OCEANOGRAPHIC RESEARCH

SEAPAK is a user-friendly oceanographic data analysis package developed at the National Aeronautics and Space Administration (NASA)/Goddard Space Flight Center (GSFC) during the past 7 years. Its primary applications are for analyzing Nimbus-7/Coastal Zone Color Scanner (CZCS) and National Oceanic and Atmospheric Administration (NOAA)/Advanced Very High Resolution Radiometer (AVHRR) data, but modules for the analysis of meteorological and hydrographic data sets are also included. The code has been written in Fortran-77 for the Digital Electronics Corporation's VAX line of central processing units. The display system used with SEAPAK is the International Imaging Systems (IIS) Model 75 (512 x 512 pixel display), supported

with the IIS System 575 software. The user interface is the Transportable Applications Executive (TAE). This interface is menu driven with on-line help for all programs and input parameters. SEAPAK complements other environmental data analysis packages such as GEMPAK (General Meteorology Package) and LAS (Landsat Analysis System), which were developed at NASA/GSFC under the same hardware/software environment. In fact, the meteorological analysis component of SEAPAK's ENVIRO module utilizes some of GEMPAK's subroutines. (See table.) In order to analyze gridded data fields from sources such as the NASA Climate Data Center (NCDC), the National Ocean Data Center (NODC), and National Center for Atmospheric Research (NCAR), a comprehensive toolbox for the creation and analysis of Common Data Format (CDF) files has been implemented. The CDF



Hardware configuration for the personal computer-based satellite image analysis workstation, for which the PC-SEAPAK software is designed.

concept is an outgrowth of archiving activities at the NASA Space Science Data Center. Several NODC file formats are supported; hydrographic station data are generally stored as index files that can be queried by location, time, and parameter.

SEAPAK currently contains over 140 interactive programs that are organized into several categories in the menu system. The table illustrates the root menu. Most programs allow user interaction not only through the standard TAE interface, but also through use of the IIS trackball cursor to define pixels or areas of interest, and the IIS keypad, from which sub-processes may be executed in any order and any number of times without exiting the main program. Hard copy support includes a Matrix camera and dicomed tape output for photographs of image data, a Hewlett-Packard 7550 plotter (a queued device) for line plots, and the system line printer for outputs of selected data values. Most programs for statistical analysis and data extraction also provide for ASCII file output so that data can be downloaded to microcomputers for further analysis and display using the wide variety of commercial software packages available.

Finally, SEAPAK is being ported to a 386/20 class IBM AT compatible personal computer (explained in accompanying figure), where most of the user friendliness, flexibility, and versatility of the VAX/IIS system will be duplicated.

SEAPAK Root Menu

- | | |
|--------------|--|
| 1. CZCSIN | Satellite and aircraft data tape ingest programs |
| 2. REMAP | Image remapping and registration |
| 3. CZCSL2 | CZCS Level 2 product generation |
| 4. OVERLY | Graphics overlay generation |
| 5. DATA | Geophysical data extraction |
| 6. FUNCTIONS | Image transformations |
| 7. STAT | Statistical analysis |
| 8. UTIL | Utility programs |
| 9. IMAGING | IIS refresh memory and graphics plane management |
| 10. MIAMI | University of Miami DSP file format conversion |
| 11. ENVIRO | Ancillary environmental data analysis |

Contact: Charles R. McClain
Code 671

Sponsor: Ocean Processes Branch, NASA
Headquarters

Dr. Charles R. McClain, with a PhD in physical oceanography, conducts research in physical and biological oceanography for the Oceans and Ice Branch of the Laboratory for Oceans. Dr. McClain has been with Goddard 10 years and has received several achievement awards. He is also interested in the development of hardware and software systems for the analysis of oceanographic data.

OCEAN DATA ACQUISITION SYSTEM

National Aeronautics and Space Administration (NASA) research has shown the utility of remotely sensed radiance for measuring chlorophyll plant pigment concentration for oceanic research programs. Between the demise of the Coastal Zone Color Scanner in June 1986, and the flight of a follow-on sensor in the early 1990s, scientists are dependent upon aircraft sensors for contemporary data. While several research ocean color instruments are available within federal laboratories, there is currently no simple, commercially produced instrumentation available for routine scientific use.

The Ocean Data Acquisition System (ODAS) is a low-cost instrument with potential commercial application. It is easily mounted on a small aircraft and flown over the coastal zone ocean to remotely measure sea surface temperature and three channels of ocean color information. From this data, chlorophyll levels can be derived for use by ocean scientists, fisheries, and environmental offices. Data can be transmitted to shipboard for real-time use with sea truth measurements, ocean productivity estimates, and fishing fleet direction.

The aircraft portion of the system has two primary instruments: an infrared radiometer to measure sea surface temperature, and a three-channel visible spectroradiometer for 460, 490, and 520 nm wavelength measurements from which chlorophyll concentration can be derived. The outputs of both instruments are fed into a data system where they are digitized to 12-bit resolution, formatted, recorded on board, and transmitted to a receiving (shipboard)



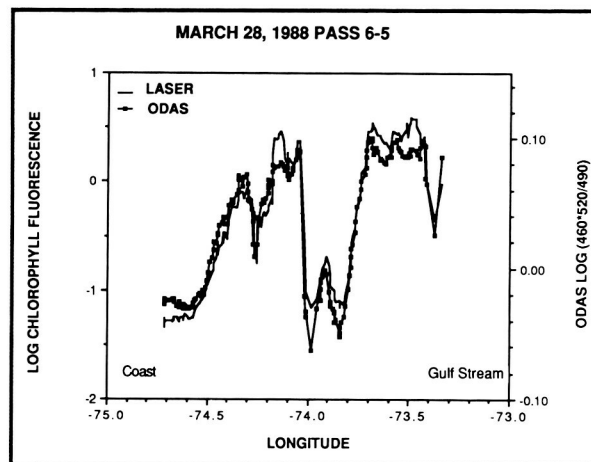
system for processing. The aircraft package contains Long Range Navigation-C (LORAN-C) equipment for aircraft location information, clock, on-board data processor and formatter, digital cassette tape recorder, packet radio terminal controller, and radio transceiver for data transmission to a ship. From the measurement altitude of 500 ft, the line-of-sight transmitter range to a ship is about 30 miles. The very high frequency (VHF) transceiver can also be used for voice communication, and for coordination between aircraft and ship.

The shipboard package contains a transceiver packet terminal controller, data processing capability, cassette tape recorder, and printer. Both raw data and chlorophyll concentrations are available for real-time analysis.

To keep down the cost of reproducing the instrument system in the future, commercially available subsystem components are used. Good-quality camera lenses for the optical systems, amateur radio packet controllers, modified amateur transceivers (modified to Federal Communications Commission-assigned Ocean Data Acquisition System frequencies) for the data transmission systems, and rack-mountable personal computers for the data systems are examples.

The Ocean Data Acquisition System (ODAS) was tested on the Wallops P3-A Orion aircraft during development on a series of four missions including the Arctic Ocean Expedition in May 1987. Comparison of ODAS observations with simultaneous NASA Wallops Flight Facility (WFF) Airborne Oceanographic Lidar values is shown in the figure. The correlation coefficient (r) for the chlorophyll signals in the example was 0.97. These data were obtained between the Gulf Stream and the Atlantic coast off Wallops Island, Virginia in March 1988.

In July and September 1988, the ODAS was used by investigators from the Virginia Institute of Marine Sciences (VIMS), The Chesapeake Bay Institute, and University of Delaware, and the National Oceanic and Atmospheric Administration to overfly portions of the Chesapeake and Delaware Bays. The objectives of these flights were to test ODAS performance in the more turbid estuarine waters, to demonstrate ODAS utility as an operational sensor in the Chesapeake Bay monitoring program, and to demonstrate a transfer of technical capability from



Comparison of simultaneous ODAS and NASA WFF Airborne Ocean Lidar data taken in the Atlantic Ocean between Wallops Island, Virginia and the Gulf Stream.

NASA to academic investigators. The ODAS was flown on the VIMS aircraft, a DeHaviland Beaver, and was operated by the investigators themselves. About 25 megabytes of data from the flights are presently under analysis at the three institutions.

Contacts: Wayne E. Esaias and
Bertrand L. Johnson, Jr.
Code 670

Sponsors: Office of Commercial Programs,
Office of Space Science and Applications,
and National Oceanic and Atmospheric Administration

Dr. Wayne E. Esaias, Project Scientist for SeaWiFS ocean color sensor on Landsat-6, analyzes Global Coastal Zone Color Scanner data for the Laboratory for Oceans. Especially interested in spectral radiometry, he holds a PhD degree in biological oceanography. Dr. Esaias has received two Group Achievement Awards.

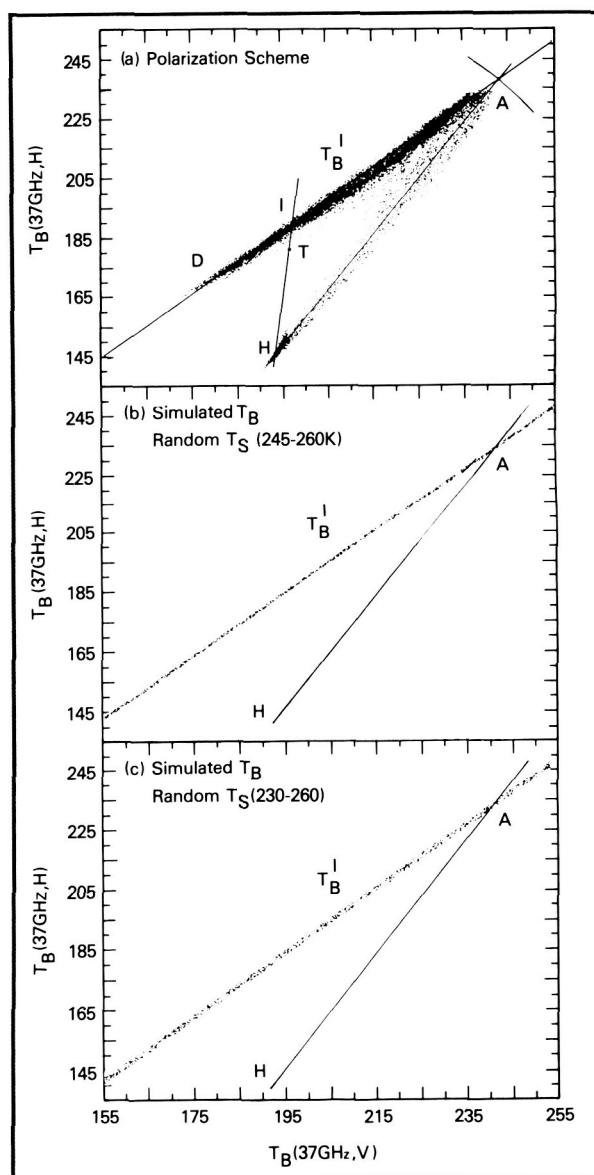
Mr. Bertrand L. Johnson, Jr., is Instrument Manager of the Mars Observer Laser Altimeter. As a member of Goddard's Laboratory for Oceans, Mr. Johnson has received several awards in connection with his work leading the Space Shuttle Ocean Color Experiment team. He has been with Goddard for 26 years.

MICROWAVE REMOTE SENSING OF ARCTIC SEA ICE

Satellite microwave sensors have been known to be very effective for monitoring temporal and spatial variations of global sea ice cover. The geophysical parameters of interest are sea ice extent, actual ice cover, and areal cover of the different ice types. Because of the large contrast in the emissivity of sea ice and open ocean at some frequencies, the determination of ice extent can be derived from the microwave data with reasonable accuracy. Accuracy is limited mainly by the resolution of the sensor (about 30 km). The determination of actual sea ice cover, which requires calculation of ice concentration within each sensor field of view, and the determination of ice type are significantly more complicated. The complications have been mainly due to spatial and temporal variations of microwave emissivities of sea ice. The microwave emissivity of sea ice varies with temperature, thickness, age, snow cover, structure, salinity, and overall surface conditions. Thus, first-year ice that is saline, about one-to-two meters thick, and has snow cover, would look radiometrically different from the thicker, and less saline, multiyear ice. Also, the emissivity of ice during its early stages, i.e., from grease ice to pancake ice, to nilas, and then to young ice is not constant, and changes significantly from one stage to another. Furthermore, melting and wet surface conditions make the material very opaque, and the emissivity very high.

The capabilities of multispectral microwave sensors like the Scanning Multichannel Microwave Radiometer (SMMR) in unraveling some of these problems have been studied using bootstrap and cluster analysis techniques. It is apparent from the analysis that, indeed, the signature of consolidated sea ice varies considerably, especially at 37 GHz and higher frequencies. The observed wavelength dependence of the emissivity is also consistent with the expected effects of internal scattering of the microwave radiation within the ice and snow cover. In much of the Central Arctic ice pack, the emissivity of sea ice at 37 GHz with vertical polarization, while largely variable, was discovered to exhibit a strongly linear relationship with that of 37 GHz, horizontal polarization. This phenomenon is illustrated in a scatter plot in the first figure, part (a), showing brightness temperature data at one polarization versus that of the

other. In this plot, data from consolidated sea ice regions are represented by data points along the line labeled AD, while data from ice-free areas or open



(a) Scatter plot of horizontally polarized 37 GHz SMMR brightness temperature data versus the vertically polarized data at the same frequency and schematics for ice concentration determination, (b) sensitivity of data to variations in physical temperature of the ice from 250° to 265°K, generated at random, and (c) sensitivity to variations in physical temperature from 240° to 265°K, generated at random.

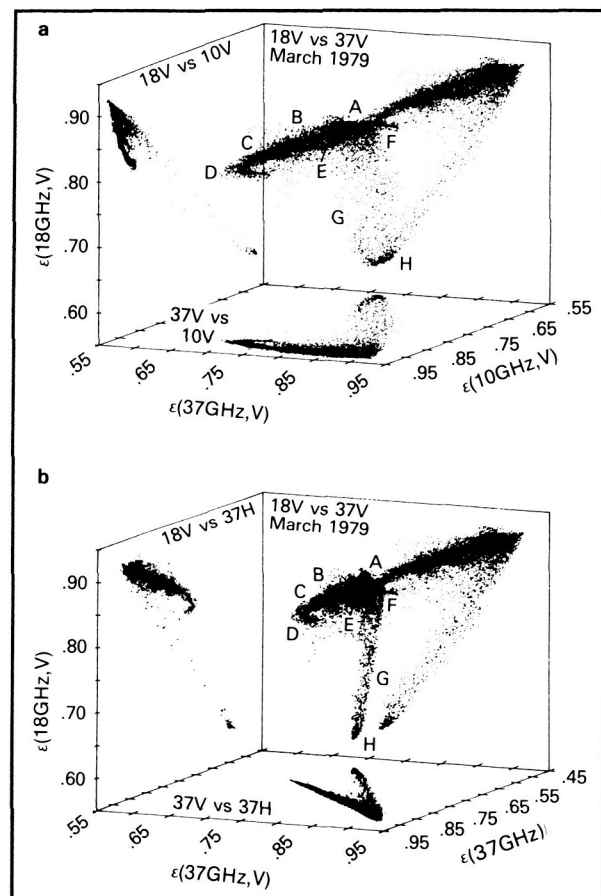


ocean are clustered together and labeled H. The plots in parts (b) and (c) of the figure are results of a simulation; they show that variations in physical temperature over consolidated sea ice cause the data points to shift, but along the same consolidated ice line. The scatter plot thus illustrates the power and potential use of two polarizations in deriving ice concentration.

Using the basic radiative transfer equation in conjunction with a simple mixing algorithm, scientists can calculate ice concentration from the 37 GHz dual polarized data. In simple terms, given a data point, such as T in part (a), the ice concentration is the ratio of HT with that of HI, where I is the intercept of the line HT with the consolidated ice line. The remarkable thing about this technique is that the slope of the consolidated ice line does not vary with time or location, and is approximately equal to 1. Thus, the technique can be generalized easily to apply to any ice condition. Also, the standard deviation about the ice line is less than 3 K, which would correspond to about 3 percent error in ice concentration. This is significant because within the ice pack, ice concentration has been observed to be about 95 percent or higher, and a precision of about 3 percent would make it possible to detect leads and small polynyas. Some complications arise near the marginal ice zone because of persistently bad weather conditions and the presence of some ice types (mainly new ice) which do not fall along the line AD in part (a). A scatter plot of 18 GHz versus 37 GHz at vertical polarization shows that the effect of weather near the marginal ice zone and in open ocean regions is predictable and can be minimized with the use of a thresholding technique. The problem with new ice has not been resolved and usually causes underestimates in ice concentrations.

To illustrate the capability of various SMMR channels and a combination thereof in identifying ice types, three-dimensional scatter plots of emissivities and two-dimensional projections of the components are shown in the second figure. These plots show information content of data from different frequencies and polarizations, and the utility of different frequencies in the detection of radiometrically different surfaces represented by different clusters (i.e., A, B, C). Unsupervised cluster analysis done in collaboration with Drs. Yun-chi Lu and H. Ramapriyan of the National Aeronautics and Space Administra-

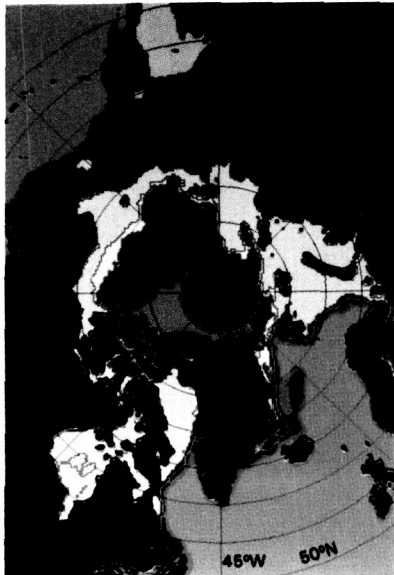
tion/Goddard Space Flight Center, using as many as six different SMMR channels at a time, has revealed that there are indeed several radiometrically distinct and persistent surfaces in the Arctic region, especially in winter. These distinct surfaces are believed to represent real physical features, or structures within the ice. A set of color-coded cluster maps, using different combinations of channels and up to six SMMR channels showing geometrical locations of the data that are bunched in different clusters, is shown in the third figure. The set of images shows that the data set is really three-dimensional, and that almost the same information could be obtained from a set of three, as compared to six, channels. Much of the seasonal ice region tends to be represented by one set of data points belonging to a cluster, and has been



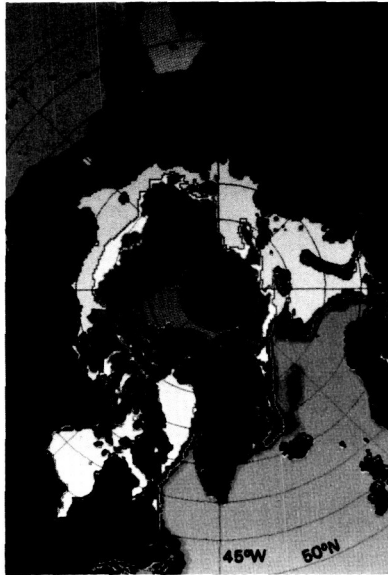
Three-dimensional scatter plot of (a) 10 GHz versus 18 GHz versus 37 GHz at vertical polarizations, and (b) 18 GHz versus 37 GHz, both at vertical polarizations, versus 37 GHz at horizontal polarization.

EMISSIVITY CLUSTERS (MARCH 1979)

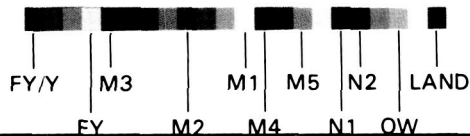
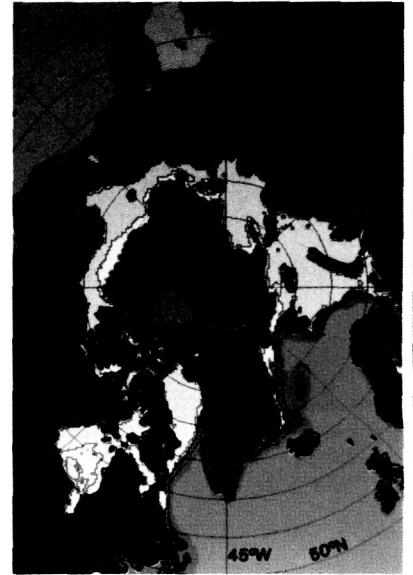
ALL 6 CHANNELS
(10, 18, 37 GHz)



VERTICAL
POLARIZATION CHANNELS



HORIZONTAL
POLARIZATION CHANNELS



Color-coded images of geographical locations of clusters derived using emissivities from (a) all six channels (37 GHz, 18 GHz, and 10 GHz, at vertical and horizontal polarizations), (b) three vertical polarization channels (37 GHz, 18 GHz, and 10 GHz), and three horizontal polarization channels (37 GHz, 18 GHz, and 10 GHz).

labeled FY because this region is a predominantly first-year ice region. In the marginal ice zone, the regions labeled as NI and Y are likely covered by new ice and young ice, respectively. The other areas of the Arctic are expected to be covered mainly by multiyear ice, but are represented by several clusters indicating several distinct signatures. The existence of several clusters is consistent with different history, and therefore structural characteristics for different areas of the Arctic region, as predicted by models using several years of buoy data.

Some processes, such as flooding, intrusion of sea water into the snow ice interface, and wetness on the surface change the signature of multiyear ice to that of first-year ice. In fact, these processes might be a

lot more prevalent than expected, because a comparison of summer minimum ice cover with that of multiyear ice cover calculated for the subsequent winter shows that the latter is less by about 50 percent. Even the sum of the areas represented by the various multiyear ice clusters is 15 percent less than the summer ice cover. This strongly suggests that the sensor may not effectively account for all the multiyear ice in the Arctic region during winter. Several experiments have been conducted to better understand these phenomena, including an overflight over the Arctic basin concurrently with a submarine mission in 1987, to obtain a unique, three-dimensional observation of the sea ice cover, and field programs from ships. More concrete answers are expected in the near future.



Contact: Josefino C. Comiso
Code 671

Sponsor: Office of Space Science and Applications

Dr. Josefino C. Comiso, who received a PhD degree from UCLA, is interested in the physics of microwave emission from sea ice, and in polar oceanography. Dr. Comiso has developed new techniques for deriving geophysical sea ice parameters from multispectral passive microwave data.

MULTIMODE AIRBORNE RADAR DEVELOPMENT SUPPORTS Eos RESEARCH AND OPERATIONAL MAPPING MISSIONS

Following the TOPEX/POSEIDON collaborative radar altimeter mission in the early 1990s, satellite radar altimeters will be developed with the capability to measure the Earth's surface topography over a wide swath of coverage, rather than just at the satellite's nadir. Operation at off-nadir angles creates new and challenging technological issues. A flexible, airborne radar instrument system is being developed to study these problems and to define solutions for them. Intended for initial deployment on the Goddard Space Flight Center P-3 research aircraft, the Multimode Airborne Radar Altimeter (MARA) will be used first to study the operation of simultaneous multiple radar beams, with each beam producing precision range tracking measurements. At issue is the amount that tracking precision will degrade as the off-nadir angle increases. Optimum techniques will be sought for maintaining TOPEX quality satellite topographic measurements in space for off-nadir angles of up to 4 degrees.

In addition to this multiple beam mode, the MARA contains a scanning beam mode. This configuration of the MARA will serve as an improved version of the Surface Contour Radar, a dependable but antiquated aircraft radar instrument that has been used for over 10 years to map the wave structure of the ocean. From the resulting measurements of wave topography, directional wave spectra will be derived and used to remotely monitor the state of the sea.

A final mode of the MARA is intended to study the interferometric technique planned for use in the advanced altimeter system proposed for the Earth

Observing System (Eos). Researchers will investigate the stability of interference lobes as backscattered waveforms in a tracking radar system. Also, the MARA will be used to collect backscattering cross-section (power) measurements at 36.0 GHz for a variety of land, ocean, and ice surfaces and for a range of environmental conditions; this frequency will also be used by the Eos instrument.

All three modes share the same Radio Frequency (RF) hardware and the same data system. Differences occur in the antenna design and in the software used to operate the systems in flight. For the multibeam mode, five beams are produced by splitting the transmitted 36.0 GHz RF signal evenly and transmitting from five fixed-position feedhorns through a dielectric lens. For the scanning beam mode, the RF signal is transmitted by a single feedhorn and reflected from a scanning plane mirror through the same dielectric lens. Two feedhorns, boresighted to the same off-nadir footprint and fed by 36.0 GHz signals of equal magnitude, form the antenna system for the interferometric mode.

The key reason for the flexibility of the MARA is the distributed, multiple central processing unit computer system. Each single-board processor used in the system has specific responsibilities; communication with the other units is achieved through bus interfaces. With this modular design, the total functioning of the radar system is under computer control. Software modules specific to a particular MARA mode can be installed in the system easily, making the transition between one mode of operation and another straightforward. This ease of operation makes the MARA a unique tool for a variety of radar altimeter applications, especially those involving measurements at off-nadir angles.

Contact: Chester L. Parsons and
Edward J. Walsh
Code 672

Sponsor: Office of Space Science and
Applications

Mr. C. L. Parsons, RTOP Manager of the Advanced Sensor and Principal Investigator of the Correlative Measurements Program, is interested in radar instrumentation, microwave backscattering, and ozone measurements. Mr. Parsons has an MS in geoscience

from Purdue University, eight years of experience at Goddard, and 20 years of experience at NASA.

Dr. Edward J. Walsh is presently designing with the Observational Science Branch an improved Surface Contour Radar, which will settle questions about the open ocean directional wave spectrum. Dr. Walsh, who holds PhD and BS degrees from Northeastern University, has eight years of experience at Goddard and 21 years with NASA.

AT THE OUTSET OF THE OCEAN TOPOGRAPHY EXPERIMENT

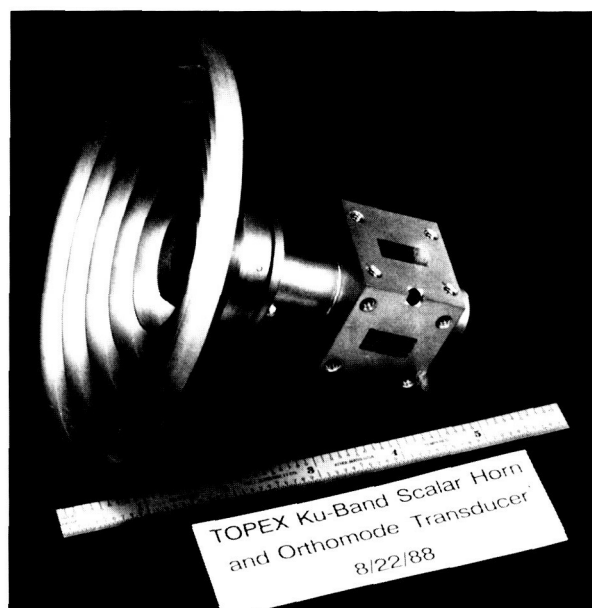
With the approval of the Ocean Topography Experiment (TOPEX) mission in fiscal year 1987, those activities associated with the development of the flight TOPEX Radar Altimeter were initiated in earnest. The Johns Hopkins University Applied Physics Laboratory (APL) was assigned the role of developing the necessary hardware under the sponsorship and direction of Goddard Space Flight Center (GSFC) in support of GSFC's role in the Jet Propulsion Laboratory's TOPEX Mission. The Applied Physics Laboratory, having had the opportunity to complete a laboratory bench unit (Advanced Technology Model—ATM) Radar Altimeter proving that the engineering designs could successfully measure ocean topography from space to <2 cm precision, was thus provided an orderly phase-in to the flight hardware program. Their initial efforts focused on the configurational aspects of the flight system, while also strengthening certain subsystem designs developed under the ATM effort where appropriate.

Among the subsystems further defined and evaluated by APL are the antenna feedhorn subsystem that must operate with two Ku-band frequencies and one C-band; the Ku-band microwave transmission unit (MTU) necessary to couple transmitted and received RF-power to the Radar Altimeter antenna; and the microprocessor selected for incorporation in the Radar Altimeter's adaptive tracker unit subsystem.

With respect to the feedhorn, the design has been completed for a corrugated configuration. To achieve the necessary isolation (minimum 30 dB, with a goal of 40 dB) between the two Ku-band frequencies—one of which will be used by the French Space Agency (CNES) Poseidon Radar Altimeter System—an

Orthomode Coupler has been incorporated into the design. This Orthomode coupler must also present a low insertion loss for these Ku-band frequency signals. The Ku-band portion of this feedhorn design is shown in the first figure. Tuning screws and mode filters (in the form of thin vanes perpendicular to the electric field vector) will reduce the coupling between the input ports to an acceptable level. Initial pattern testing of this hardware has been accomplished at APL. When the complete feedhorn is integrated with the engineering model antenna system, it will be tested at the GSFC Antenna Range.

With regard to the Ku-band microwave transmission unit, some functional design differences were incorporated into the design of the flight microwave transmission unit, distinguishing it from the MTU design used in the ATM. Active component redundancy was incorporated for increased reliability. Series cross-guide couplers in the transmit path were replaced with a single cross-guide coupler and power divider (this configuration was used in the C-band MTU of the ATM effort, proving successful at that frequency). Switching circulators were added, since there will be two independent Radar Altimeters (Side A and Side B) feeding a common antenna/microwave transmission unit combination. The transmit power monitor amplifier was redesigned (dc instead of ac

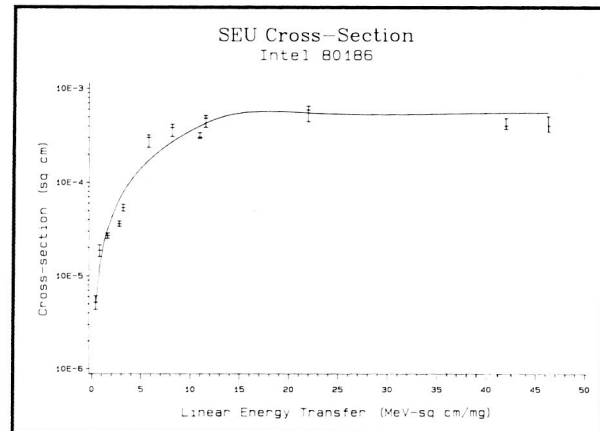


TOPEX Ku-band Scalar Horn and Orthomode Transducer.



coupling proved better suited for the higher TOPEX pulse repetition frequency (PRF), also improving size and decreasing power drain). The brassboard of this MTU system is shown in the second figure.

In the area of space qualification of the Intel 80186 microprocessor selected for the TOPEX Radar Altimeter's adaptive tracker unit, it was paramount that its susceptibility to single event upsets (SEUs) be understood early in the development of the Radar Altimeter; if the microprocessor proved susceptible to latch-up caused by energetic particles, the necessary redesign needed to be effected as early as possible. While SEUs are not typically permanently damaging to the type of device selected for the TOPEX Radar Altimeter, they can increase the noise in the data stream and introduce logic errors into the system, affecting both operations and data quality. APL assessed the susceptibility of the Intel 80186 by configuring their test article so that while the microprocessor was tested within a beam of bombarding ions, an external controller dynamically exercised the device. In this fashion, the sensitivity of the major segments of the chip design such as the executive unit, the bus interface unit, the direct memory access (DMA) controllers, and the interrupt controller were observed. The test objectives were: to measure the device SEU cross section as a function of linear energy transfer (LET), to test the angular dependence of the cross section, to study the effect of higher operating temperatures on the error rate, to determine the frequency dependence of the cross section, and to identify the most sensitive areas of the microprocessor die design. This testing was performed at the Brookhaven National Laboratory SEU test facility under the auspices of the code 600-managed National Aeronautics and Space Administration/Department of Defense Consortium. The third figure is a plot of the cross section of the 80186 as a function of LET. For the TOPEX Mis-



SEU cross section.

sion orbital altitude at solar maximum, this equates to an upset or error rate of one upset every 3.3 days, with a worst case estimate of one every 5 hours during an anomalously large solar flare event. These error rates are not considered a problem for the TOPEX Radar Altimeter; however, "Watchdog Timer" and "Bit Error Detection" schemes will be incorporated within the Radar Altimeter's onboard flight software to preclude potential deleterious effects that might occur during the mission.

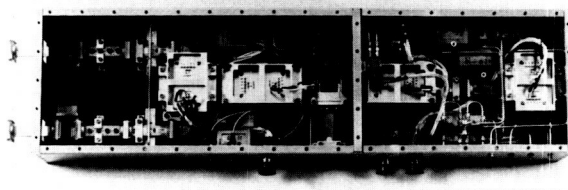
Contact: Laurence C. Rossi
Code 672

Sponsor: Office of Space Science and
Applications

Mr. Laurence C. Rossi is currently Topography Experiment, Radar Altimeter Project Manager. He was also Project Manager for the GEOS-3 and Orbiting Frog Otolith Projects and received a Group Achievement Award for GEOS-3. Mr. Rossi, who has a BS in electronics engineering from Northrop Institute of Technology, has eight years of experience at Goddard and 25 years with NASA.

EVALUATION OF PROPOSED SEAWIFS AND JAPANESE OCTS SATELLITE BANDS FOR CHLOROPHYLL AND PHYCOERYTHRIN PIGMENT RECOVERY IN CONTINENTAL SHELF WATERS

A new satellite ocean color sensor designated SeaWiFS has been recommended to replace the



Brassboard of MTU system.

Coastal Zone Color Scanner (CZCS) that operated until the summer of 1986. The proposed visible and near infrared bands are: 443, 500, 565, 665, 765, and 867 nm. Likewise, the Ocean Color Temperature Scanner (OCTS) has been under study by Japanese scientists for independent launch during the same general time frame. The Japanese space agency has narrowed their band selection for OCTS to two different but similar plans. Plan A provides bands at 412, 443, 490, 520, 565, 665, 765, and 867 nm, while Plan B moves the 490 nm band to 500 nm and the 520 nm band to 620 nm positions. Note that the SeaWiFS bands are the same as the OCTS/Plan B, except that the U.S. sensor at the time of this writing has no 412 nm and 620 nm bands.

These new bands have been under study using airborne active-passive correlation spectroscopy (APCS) methods. In APCS applications, oceanic surface truth was obtained with an airborne active, or laser-induced fluorescence system operated simultaneously during the acquisition of the requisite passive ocean color data. Passive band combinations were then tested for chlorophyll pigment recovery by regressing them against the laser-induced chlorophyll fluorescence. The effectiveness of algorithms for the recovery of the photosynthetic accessory pigment phycoerythrin was tested in the same way, using the concurrently obtained laser-induced phycoerythrin fluorescence and passive upwelled radiances. APCS has proven to be a highly sensitive technique that easily detects subtle constituent-driven variations in the airborne ocean color spectrum. During postflight analysis, all possible passive radiance ratio combinations from the instrument's 32 available passive color bands were used to compute independent chlorophyll concentration estimates. Each of the resulting radiance ratios was then linearly regressed against the Airborne Oceanographic Lidar (AOL) laser-induced and water-Raman-normalized chlorophyll fluorescence for each sampling point along the flight line. High regression coefficients (>0.80) revealed those regions of the spectrum where the ocean color spectral variability is strongly correlated with the chlorophyll fluorescence. Only those flight lines that provided a reasonably wide range of chlorophyll concentration and were free of sun glint were selected. From these, only passes that contained distinct sections where the concentration of chlorophyll was found to be noncoherent with the concentration of phycoerythrin were considered for analysis. This

precaution was adopted to assure that the chlorophyll algorithms were not responding to phycoerythrin, which often covaries with chlorophyll. Passes were also selected which exhibited some small-scale variability or patchiness and which contained no sun glint.

Four AOL missions in the Atlantic from Long Island to about Cape Hatteras were analyzed. Most of the data were taken in Case II waters (wherein the optical properties are not determined solely by the chlorophyll pigment and its derivatives). Approximately 25,000 active or laser-induced spectra were analyzed in conjunction with 25,000 passive solar induced spectra obtained concurrently.

Both two-band radiance ratios and three-band curvature algorithms were evaluated for their effectiveness in recovering chlorophyll (or phycoerythrin) pigment. The table summarizes results from the analysis of the 50,000 active-passive ocean color waveforms. For coastal waters, curvature algorithms yielded better overall results than did the radiance ratio algorithms. The data in the table show that the 443/500/565 nm and the 443/490/565 nm algorithms produced the best correlation for the

<i>RADIANCE RATIO/CURVATURE COMPARISON</i>			
RANK	SENSOR	ALGORITHM	CORR.
1.	B,S A	443/500/565 443/490/565	= 0.93
2.	B B	412/443/620 500/620/665	= 0.91
3.	A	520/565	= 0.90
4.	A,B	412/443/665	= 0.90
5.	B	443/620/665	= 0.88
Legend:			
A = OCTS Plan A Bands			
B = OCTS Plan B Bands			
S = SeaWiFS Bands			



recovery of chlorophyll. Only the 520/565 nm radiance ratio algorithm ranked in the top five when the entire set of 50,000 paired spectra were considered.

The top figure shows the performance of the 443/500/565 nm curvature algorithm in an along-track profile comparison with the laser-induced and water-Raman-normalized chlorophyll fluorescence. These data were taken on a flight mission conducted along the Virginia coastline across the Chesapeake Bay mouth and into Case I waters northeast of Cape Hatteras. The corresponding 520/565 nm radiance ratio chlorophyll estimate is shown in the comparative profile plot in the bottom figure. The correlation coefficient of the algorithm when regressed against the laser-induced and water-Raman-normalized chlorophyll fluorescence is shown within each figure.

For the chlorophyll pigment, numerous other results were also found during the analysis of the entire 50,000 paired-spectra data set: 1) the 412 nm and the 775 nm bands were ineffective within radiance ratios but did contribute as "anchor" bands in curvature algorithms; 2) the 520 nm band was found to play no significant role in the curvature algorithm for either the OCTS or the SeaWiFS sensor bands; and

3) curvature algorithms showed potential for higher accuracy than radiance ratios since the overall in-water correlations were higher (these conclusions can also be seen in the data shown in the table).

Regarding the phycoerythrin pigment, it cannot be consistently recovered with the present OCTS or the SeaWiFS band configurations. Two-band radiance ratio algorithms proved ineffective in the recovery of phycoerythrin. Curvature algorithms were effective, but only in the 600 nm spectral region. Thus, it was concluded that a curvature algorithm with a center band at 600 nm is required for recovery of the phycoerythrin pigment. It was suggested that the Japanese OCTS 620 nm band be moved to the 600 nm position, permitting recovery of phycoerythrin as well as the other constituents originally sought with this particular band.

The 443/500/565 nm curvature algorithm was tested for sensitivity of the placement of the 500 nm center band. It was found that this band is precariously placed near the edge of a correlation maximum. Accordingly, any future movement of the prescribed SeaWiFS bands should allow a shift of the 500 nm band only towards shorter wavelengths. The excellent chlorophyll recovery of the 443/500/565 nm could be spoiled by any movement of the 500 nm band toward redder wavelengths. Similarly, it was found that the 412/443/565 nm algorithm will only allow the shift of the 565 nm band to redder wavelengths; a shift to bluer wavelengths would cause the correlation to suffer significant degradation.

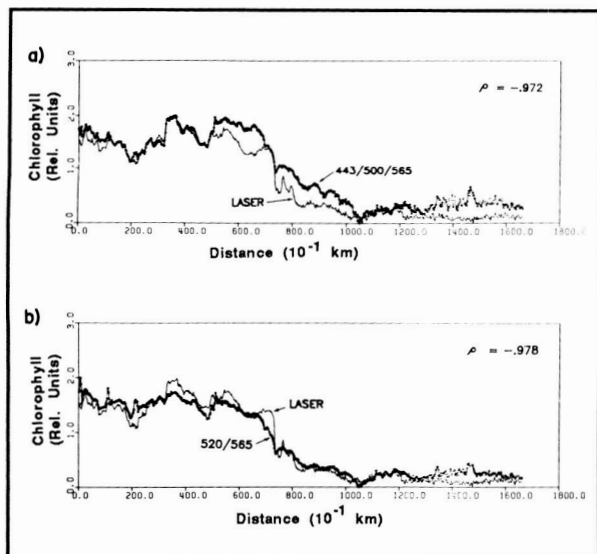
Contact: Frank E. Hoge
Code 672

Sponsor: Office of Space Science and
Applications

Dr. Frank E. Hoge, Project Scientist for the Airborne Oceanographic Lidar, is interested in active and passive ocean color spectral variability studies. He has seven years of experience at Goddard, and 21 total years with NASA.

RAIN EFFECTS ON MICROWAVE SCATTERING FROM THE SEA

Fair weather observations and active microwave data form the foundation of empirical algorithms that are



The chlorophyll retrieval performance of the (a) 443/500/565 nm curvature algorithm and (b) 520/565 nm radiance ratio algorithm as revealed by comparison with the laser-induced and water-Raman-normalized chlorophyll fluorescence.

used to relate various geophysical parameters associated with the ocean's surface to measurements from satellites. Many of these algorithms are inaccurate during rain; suspect data can be identified by using radiometer data to quantify rainfall rates. Discarding measurements in foul weather areas is the solution that is appropriate for some parameters. This solution, however, is not always viable, because it can overlook areas of interest or can bias data sets. For example, global wind velocity estimates are needed to validate ocean circulation models used to enhance climate forecasts. Yet even after corrections for atmospheric effects, rain causes satellite scatterometer wind estimates to be anomalous. Because rain also alters sea surface geometry and air-sea interaction processes, these effects need to be quantified if we are to advance our measurement capability.

Sea surface roughness controls microwave scattering from the sea. It is usually produced by wind generation of surface waves, which tend to align in the wind direction. Rain alters sea surface roughness by three physical processes: 1) raindrop impact on the sea generates isotropic short-waves (local effect); 2) as drops penetrate the surface a vortex of fluid descends through the top few centimeters of water, causing mixing that attenuates existing wind waves (larger rainfall area); and 3) stratification of fresh rain water over saline sea water changes momentum transfer from atmosphere to ocean. The relevance of each of these factors must be quantified.

The research objective is to upgrade microwave remote sensing algorithms so that they will provide accurate data during rain. Data quantifying changes of radar response caused by the physical processes occurring at the air-sea interface during rain are nonexistent because: 1) field conditions are so complex that researchers have avoided the problem, and 2) wind-wave tank facilities have lacked radar systems and rain simulators.

Radar systems and rain simulators are currently being developed for laboratory use so that researchers can establish a better understanding of the physical processes in a controlled environment. Experiments are being conducted at the Goddard Space Flight Center/Wallops Flight Facility wind-wave tank; its dimensions are 19.3 by 1.2 by 0.9 m. Normal water depth is 0.7 m. The height of the air column for wind is 1.5 m, and the maximum wind speed is 20 m/s.

Some preliminary findings of microwave signal changes due to rain-generated short waves on a wind-wave surface, along with research plans for the future, are summarized below.

A 36 GHz (8 mm wavelength) radar system was designed and assembled for these experiments. A Gunn oscillator generates 150 mw, which is video modulated at 1 kHz and transmitted through a 6 degree horn/lens system. The transmit assembly is designed to provide linearly polarized, planar wave fronts at short range. The receiver system consists of a 30 degree horn, a detector, and a video to dc demodulator/amplifier, which removes the 1 kHz. The radar assembly typically is located in the wind-wave tank at 13 m downwind and situated 1 m above the water surface. Transmit and receive horns can be positioned at various inclinations; the initial position is at 30 degrees inclination, pointing up-wind, with vertical-vertical polarization. This configuration provides a scatterometer that is sensitive to sea surface roughness.

Rain is simulated by 1.4 to 2.8 mm diameter water drops produced from nozzles located above the water surface. To study the radar response to rain-generated waves, the rain simulator size is 20 cm by 30 cm, with 10 nozzles that generate 2.8 mm diameter drops. In later attempts to study physics associated with raindrop-generated turbulence, researchers will employ a 50 cm by 500 cm rain simulator with 1500 nozzles. The number of nozzles is derived from a need for uniform distribution of low rainfall rates (0 to 12 mm/hr). The maximum rain rate of the experiments corresponds to typical saturation levels for satellite-based radiometer rainfall rate estimates. Naturally occurring drop sizes for these rainfall rates are 1 to 3 mm.

A systematic series of laboratory experiments were conducted in which data were obtained for all combinations of six wind speeds (2 to 6 m/s) and six rainfall rates (0 to 12 mm/hr). The data products and deductions are summarized as follows. For the cases with no rain, radar return power increases as wind speed increases, as is typical of scatterometers. The wind plus rain cases show that radar return power increases as wind speed increases; for each wind speed, radar return is greater as the rainfall rate increases. The power level difference between no rain



and rain conditions diminishes as wind speed increases, so the response is nonlinear. For this data set, it was demonstrated that rain effects can be parameterized and included in one of the scatterometer algorithms. The data confirm that radar functions in a laboratory wind-wave tank; thus, it may indeed be possible to model rain effects so as to improve remote sensing algorithms.

Contact: Larry F. Bliven
Code 672

Sponsor: Office of Space Science and
Applications

Dr. Larry F. Bliven develops improved active microwave algorithms for satellite systems. He is also interested in the physics of air-sea interaction as well as the remote sensing of atmospheres and oceans. Dr. Bliven, who has a PhD in marine sciences from North Carolina State, belongs to the American Meteorological Society and American Geophysical Union. He has three years of experience at Goddard.

SURFACE CONTOUR RADAR OBSERVATIONS LEAD TO NEW INSIGHTS IN OCEAN WAVE GROWTH

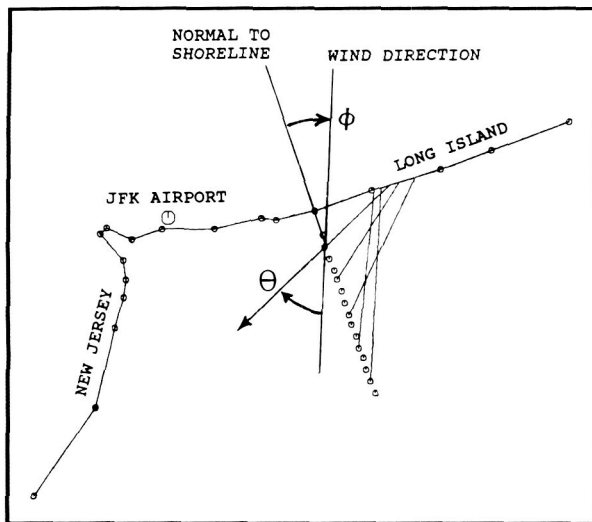
Observing fetch-limited wave growth, the phenomenon of waves being generated by an offshore wind so that the sea state varies as a function of the fetch (distance from shore), provides important information in refining our knowledge of how waves grow. The Surface Contour Radar (SCR) is a Goddard Space Flight Center (GSFC) 36-GHz computer-controlled airborne radar that routinely produces ocean directional wave spectra with much higher angular resolution than pitch-and-roll buoys. Its ability to obtain contiguous directional wave spectra over a 300-km fetch in less than an hour permits insights on wave growth to be obtained from a single data set. This is in sharp contrast to the way that in situ experiments are conducted, wherein a few point observations from many different days, or even experiments, are combined in a nondimensional fashion for various wind speeds to arrive at the growth of the wave field. SCR fetch-limited observations have led to the discovery of a constraint between the rate of growth of wave energy and the rate of growth of wave length with fetch.

Researchers Donelan, Hamilton, and Hui demonstrated that if an elongated closed body of water has a steady wind blowing at some angle to the shore, the rapid increase of fetch as the direction deviates from that of the wind may more than offset the reduced effectiveness of the wind; thus, the largest waves approach the observer from some direction other than that of the wind. The three researchers observed waves in Lake Ontario propagating as much as 50° off the downwind direction; they predicted the propagation direction with great accuracy by assuming that waves in a given direction were generated by the component of the wind in that direction.

The figure shows an outline of the southern Long Island and northern New Jersey shorelines. A GSFC P-3 aircraft flew offshore from the middle of Long Island during a cold air outbreak to collect SCR data. The offshore circles show the centers of SCR data spans used to generate directional wave spectra; radials extend from some of them in the reciprocal of the measured wave propagation direction until they intersect the shore of Long Island.

The five wave propagation directions documented in the figure provided an excellent opportunity to see if the procedure developed by Donelan, Hamilton, and Hui could predict how much the wave propagation direction would deviate from the downwind direction along a straight shoreline. For example, the near shore effective wind was blowing from about 2°, so that ϕ , the angle between the effective wind direction and the perpendicular to the shoreline, was about 20°. The angle θ , constructed between the wave propagation direction and the downwind direction, was about 38°. A simulation was performed that demonstrated that the algorithm developed by Donelan, Hamilton, and Hui correctly predicted the propagation direction variation in the figure, even though the growth rates of wave energy and wave length observed by the SCR were significantly different from those reported by the algorithm's developers.

If a constant, homogeneous wind blows at some angle to a straight shoreline, waves can only propagate one way. Analysis of data obtained using the SCR showed that the prediction of wave propagation direction was uniquely tied to the growth rates of wave energy and wave length. This result presented a challenge: how could the algorithm correctly



Outline of the southern Long Island and northern New Jersey shorelines and offshore circles indicating the centers of Surface Contour Radar data spans used to generate directional wave spectra during a cold air outbreak. The wave propagation direction (indicated by radials extending from some circles) was not in the downwind direction, which led to new insights into ocean wave growth.

predict the propagation direction using the *incorrect* growth rates, while the *observed* growth rates produced absurd predictions for propagation direction? Further analysis resolved the quandary, demonstrating that growth rates for wave energy and wave length should not be independently assigned when attempting to determine them from a set of observations.

The algorithm parameterization developed by Donelan, Hamilton, and Hui has been generalized to allow other wave growth models to predict the same propagation direction in asymmetrical fetch situations. The generalization results in an additional constraint in determining the best overall match of a growth rate model to the data. Valid combinations of the growth rates must result in the same rate of change of wave steepness with fetch as those reported by Donelan, Hamilton, and Hui. When considering angles well off the wind direction, the present model suggests a significantly reduced effectiveness for the wind.

Contact: Edward J. Walsh
Code 672

Sponsor: Office of Space Science and Applications

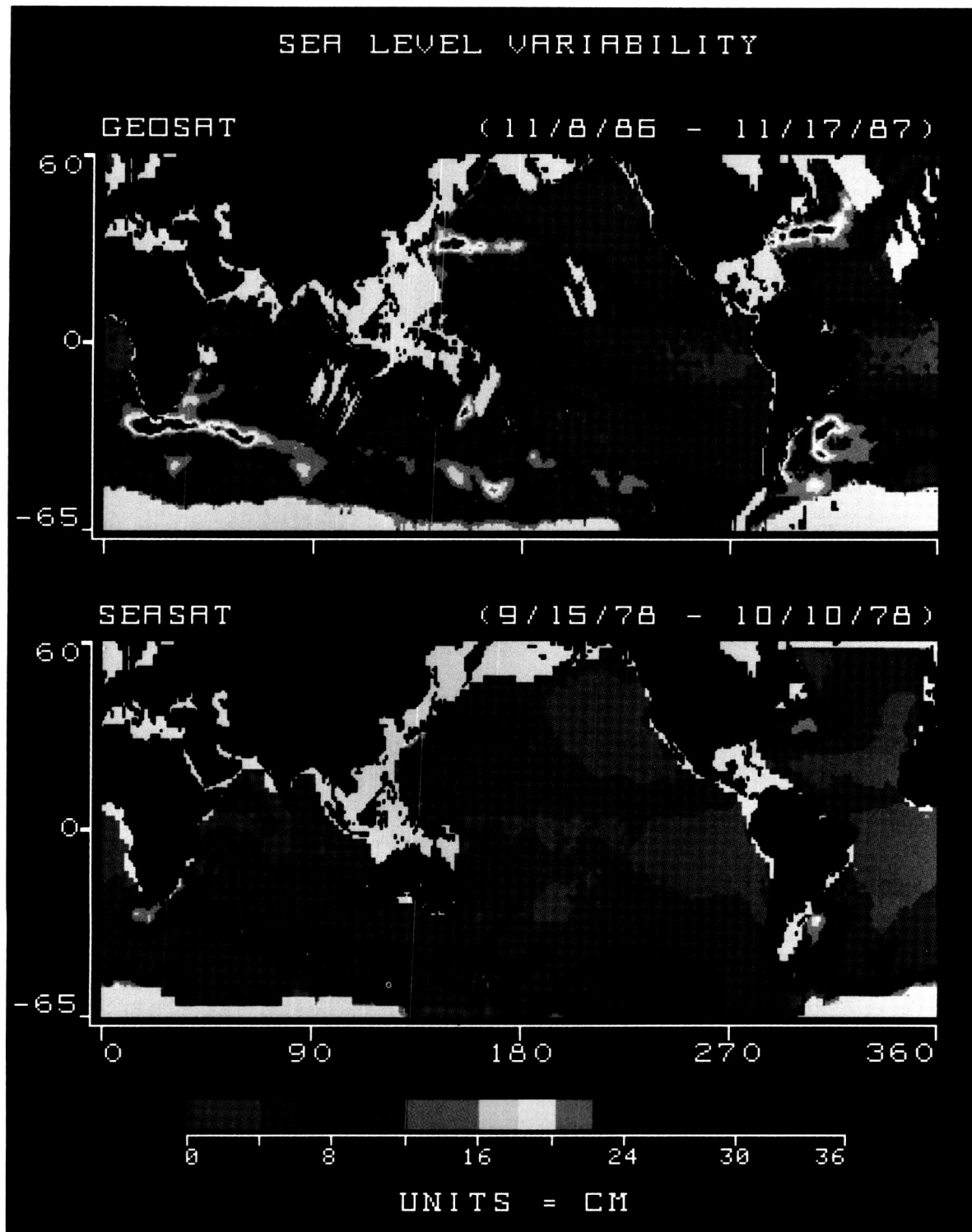
Dr. Edward J. Walsh is presently designing with the Observational Science Branch an improved Surface Contour Radar, which will settle questions about the open ocean directional wave spectrum. Dr. Walsh, who holds PhD and BS degrees from Northeastern University, has 8 years of experience at Goddard and 21 years with NASA.

SEA LEVEL CHANGE

For the first time, a long-term global view of sea level change is available to the ocean science community. The United States Navy's Geodetic Satellite (GEOSAT) altimeter satellite has been measuring ocean surface topography with unprecedented precision since March 1985. The measurement of sea level is an important variable for the determination of ocean circulation. Sea level slopes reflect the surface pressure gradients that force large-scale (>25 km) currents. GEOSAT measurements make a significant contribution to our understanding of ocean circulation, and represent a dramatic improvement over previous altimeter observations.

The figure shows a determination of global mesoscale (50 to 1000 km) sea level variability from two different satellite altimeter missions. The lower portion shows an estimate of the root-mean-square (RMS) variability derived from the National Aeronautics and Space Administration's Sea Satellite (SEASAT) project, covering the 25 days from September 15, 1978 to October 10, 1978. The upper portion shows a recent estimate derived from GEOSAT for the 1-year period from November 8, 1986 to November 17, 1987. The analysis depicts the variations in sea level caused by wavelengths between 35 and 1500 km. Longer wavelength variations are presently contaminated by inaccuracies in the orbit determination of both satellites. Shorter scale variations are dominated by instrument noise. In this figure, land has been masked in black, and shallow water or data void areas are masked in grey.

This figure shows the dramatic improvement in resolution that is being provided by the GEOSAT mission. This is the result of both a longer time series and higher spatial resolution. GEOSAT repeats its



Both the U.S. Navy's GEOSAT and NASA's SEASAT satellite altimeters have observed sea level variability over horizontal scales of 50 to 1000 km during the last decade. The figure shows estimates of sea level change from these two missions in terms of the root-mean-square.

orbit every 17 days, resulting in orbital tracks that are separated by only 164 km at the Equator, whereas SEASAT repeated its orbit every 3 days, resulting in equatorial orbit separations of 951 km. Consequently, the amplitude of the sea level variability derived from GEOSAT is much larger than that derived from SEASAT, resulting in a better definition of both the primary ($\text{RMS} > 15 \text{ cm}$) and secondary ($7.5 < \text{RMS} < 15 \text{ cm}$) regions of mesoscale sea level change.

The primary regions of mesoscale sea level fluctuations are found in the vicinity of the strongest current systems (i.e., Agulhas, Kuroshio, Gulf Stream, Brazil/Falkland, East Australian, and Antarctic Circumpolar Current), and result from dynamic instabilities in these currents. The instabilities cause meanders in the current systems, as well as the formation of detached vortices. The largest variability is found in the Agulhas Current, where sea level RMS over 1 year exceeds 50 cm at some locations. Ship observations have found the most energetic isolated vortices in the world in the vicinity of the Agulhas retroflection, which is located southeast of the Cape of Good Hope, at the southern tip of Africa. The Antarctic Circumpolar Current (ACC) is the only nonboundary current where sea level change greater than 15 cm RMS is found. In this current, for the first time, GEOSAT clearly resolves several regions of high variability in the vicinity of remote topographic features, such as the South Tasman Rise, the Campbell Plateau, the East Pacific Rise, the Atlantic-Indian Ridge, and the Kerguelen Plateau. Unlike the boundary currents, the instabilities of the ACC appear to be closely linked to topography.

GEOSAT observations have revealed a number of secondary regions of sea level variability that were not resolved by SEASAT. These regions are principally in the equatorial current systems and subtropical regions of both hemispheres. This variability is, most likely, the result of current instabilities or frontal meanders. For example, the region of sea level change between 6 to 8 cm RMS off the coast of California is known from ship and satellite radiometer observations to be a turbulent region with large (200 km-diameter) isolated vortices. Most of the areas of secondary variability in the equatorial regions and in the Northern Hemisphere have been known at least qualitatively from ship observations. However, the delineation of extensive regions of secondary variability in remote locations of the

Southern Hemisphere, as shown in the figure, is a new discovery.

Unfortunately, some of the geophysical corrections applied to the GEOSAT altimeter data are not well known (e.g., sea-state bias, atmospheric range delay, and tides). Consequently, some of the variability in the GEOSAT observations is related to inaccuracies in these corrections. For example, the fluctuations over the Patagonia Shelf and in the Gulf of Alaska could be the result of poor tidal estimates. Likewise, some of the secondary variations in the equatorial regions and subtropics (primarily in the vicinity of the South Pacific Convergence Zone) could be caused by inaccuracies in the wet-tropospheric-range-delay correction. Work to improve these corrections is in progress.

Contact: Chester Koblinsky
Code 621

Sponsor: Office of Space Science and
Applications

Dr. Chester Koblinsky, a physical oceanographer, studies large-scale ocean circulation processes with satellite altimeters and scatterometers. He has a PhD degree in physical oceanography from Oregon State University.

PRODUCTION AND ARCHIVAL OF A GLOBAL OCEAN BASIN CHLOROPHYLL DATA SET

Phytoplankton, the microscopic plants that grow in the upper, sunlit regions of the oceans forming the base of the marine food web, require light and nutrients to grow. An understanding of their distribution and abundance is critical for many branches of marine ecology and fisheries science. In addition, since the fixation of carbon in the ocean by photosynthesis is about equal in magnitude to that occurring on land, a knowledge of the temporal and spatial distributions of phytoplankton biomass and primary production is necessary to better assess the role of the ocean in the global carbon cycle.

As phytoplankton and their associated chlorophyll pigments become more abundant, ocean color shifts from blue to green. Taking advantage of this fact, the National Aeronautics and Space Administration



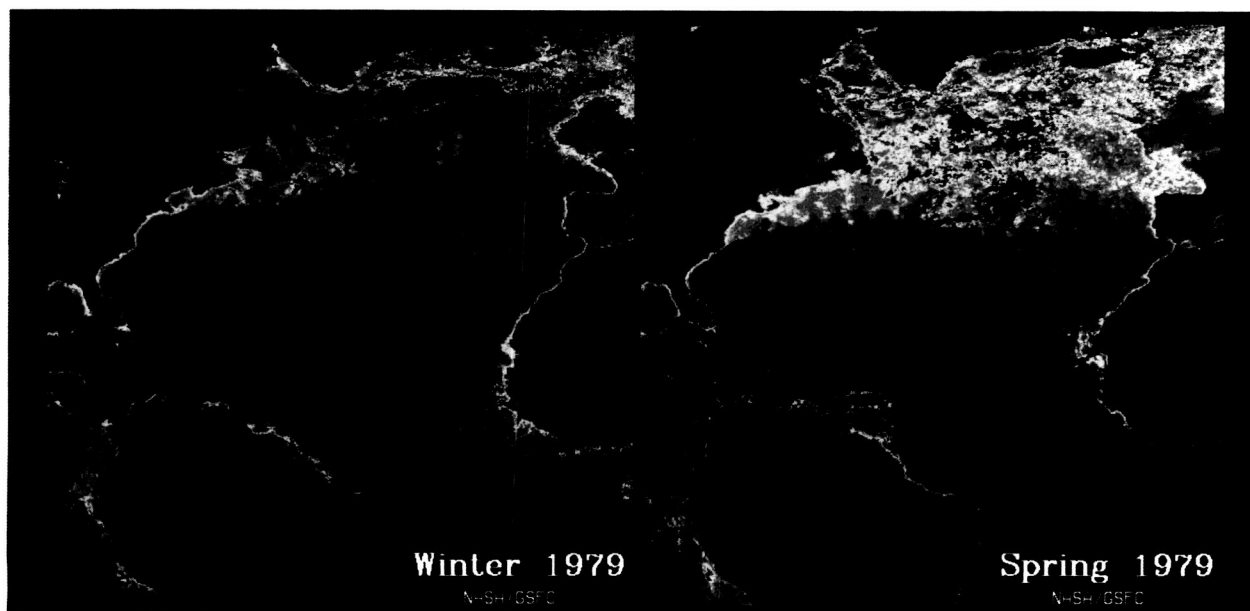
(NASA) developed the Coastal Zone Color Scanner (CZCS), which was launched on the Nimbus-7 satellite. During its lifetime (October 1978 through June 1986) CZCS acquired nearly 66,000 images (825 gigabytes of data). This data set, using a consistent sampling strategy and single processing technique, represents the most comprehensive source of ocean color measurements to date, and has made possible scientists' first synoptic view of the distribution and abundance of phytoplankton over the global oceans. More importantly, it has provided researchers with the ability to monitor how these patterns change both in time and space.

The Nimbus Project Office, in collaboration with the Laboratory for Oceans and the University of Miami/Rosenstiel School of Marine and Atmospheric Science, has undertaken to process all the CZCS imagery to produce a Global Ocean Basin Chlorophyll Data Set and to provide easy access to the data products by the oceanographic community through NASA's National Space Science Data Center (NSSDC).

An image processing/analysis system utilizing recent advances in data base management and digital optical disk storage technology has been developed, and is now operational in a full-production mode. Approximately 3000-4000 CZCS images are being processed each month, with the data products being ar-

chived on digital optical disk. The transfer from magnetic tape to optical disk has a number of advantages. For instance, a significant reduction in data storage media has been achieved. Approximately 150-200 1600 bpi tapes containing the original Level-1 CZCS data can now be stored on a single 12-inch optical disk platter. With the incorporation of an optical disk autochanger (jukebox), the system will have on-line access to nearly 160 gigabytes of data, which will facilitate the flow of data through the system, and greatly alter the way in which scientific research can be done. As of August 1988, nearly 70 percent of the entire data set had been transferred to optical disk.

NSSDC will be the central archive and distribution facility responsible for providing copies of the digital global CZCS data set to the research community. In addition to archiving the original Level-1 data (1 km resolution), the NSSDC archive will contain the Level-2 data products of derived geophysical parameters at reduced resolution (4 km) in satellite swath coordinates, and the Level-3 Earth-gridded global products of these parameters. Composites of the key parameters (phytoplankton pigment concentration, diffuse attenuation coefficient, water-leaving radiances, and aerosol radiance) at daily, weekly, monthly, seasonal, and annual time scales will also be archived, along with the relevant compositing statistics. In addition to the digital data, an analog



CZCS data, colors represent phytoplankton concentration.

optical disk browse and data-order capability has been developed to run on either VAX, IBM PC, or Apple Macintosh computer systems.

The accompanying figure represents the kind of temporal and spatial variability that can now be viewed for the first time. From the temperate regions to the poles, the nutrient supply of the upper ocean is replenished through the deep vertical mixing driven by surface cooling and the strong winter winds. As the seasons progress from winter to spring, the amount of sunlight available for phytoplankton growth increases. This period of rapid growth and accumulation of phytoplankton biomass in the upper waters is referred to as the "Spring Bloom." Its development and intensity are shown in these two seasonal composites of CZCS data, acquired during the winter (January–March) and spring (April–June) of 1979. Areas rich in phytoplankton are shown as orange-red (greater than 1 mg/m³) progressing through yellow, green, and blue, with purple (less than 0.1 mg/m³) representing areas with the lowest chlorophyll concentrations.

While the amount of data shown here is several hundred times more than oceanographers have been able to gather from ships, large regions of the central Atlantic are still blank, since the CZCS could operate only intermittently. Still, the bloom's intensification with time and broad spatial extent is clearly evident. More continuous high productivity of the coastal zones and major fisheries grounds is also seen. The spring bloom of phytoplankton in the North Atlantic converts a significant fraction of atmospheric CO₂ into particulate material through photosynthesis. A major focus for oceanographers in the next decade is to understand the dynamics responsible for this global phenomenon, and to place it in perspective with the atmospheric CO₂ increase and its projected effects on climate.

Contact: Gene Carl Feldman
Code 636

Sponsor: Office of Space Science and Applications

SN 1987A

GAMMA-RAY LINES FROM SUPERNOVA 1987A

Supernova 1987A is one of the most exciting events in astrophysics in this century. The Gamma Ray Imaging Spectrometer (GRIS), one of a new generation of powerful high-resolution germanium spectrometers, was rushed to completion in time to observe this source near the predicted peak of its emission of gamma-ray lines from the decay of ⁵⁶Co produced in the explosion. GRIS is the first of the new generation instruments, specifically designed and optimized for astrophysics, to fly and has provided the most sensitive observation to date (5 sigma) of the 1238 KeV line from the supernova. The observation of the lines from the radioactive decay of ⁵⁶Co by several groups is a historic confirmation of the standard model of nucleosynthesis in supernovae and ranks with the detection of neutrinos from the supernova. The direct observation of freshly synthesized elements in the supernova ejecta confirms theories

that suggest most heavy elements in the universe are produced in supernovae.

High-energy resolution measurements, on the contrary, show the line shape to be inconsistent with any of the models of the expanding supernova ejecta previously proposed. During the same flight the galactic center 0.511 MeV line was observed at the 7 sigma level. This result should provide new information on the spatial distribution of the line source as well as a possible detection of the three-photon continuum from this source. In one flight, this instrument has made significant measurements of two of the three confirmed gamma-ray line sources outside our solar system. Most of the GRIS instrument remains in Alice Springs, Australia. The Low Energy Gamma Ray Group (part of Goddard Space Flight Center's (GSFC's) Laboratory for High Energy Astrophysics) and its collaborators at AT&T Bell Labs and Sandia labs are preparing for a second



balloon flight this fall to observe the evolution of this line as a result of radioactive decay and expansion of the supernova ejecta.*

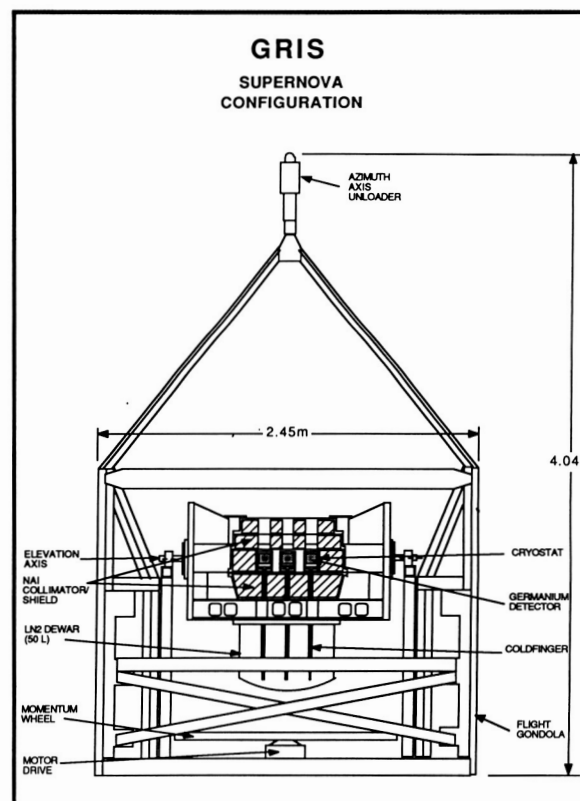
The GRIS gondola is illustrated schematically in the first figure. GRIS incorporates an array of seven very large cryogenically cooled germanium detectors for high-energy resolution gamma-ray spectroscopy. This array includes many of the largest n-type germanium detectors ever produced including four detectors with efficiencies of approximately 70 percent (compared to a 3" x 3" NaI detector at 1.33 MeV). Other features contributing to the high sensitivity of this instrument include a very heavy active NaI shield of 15 cm minimum thickness and a custom cryostat design, fabricated at GSFC, which minimizes the passive material introduced inside the active shield.

A unique feature of GRIS, packaging each detector in the array in its own cryostat, has greatly facilitated the difficult process of procuring and maintaining a large array of germanium detectors. The present inventory for GRIS includes nine detectors, and the replacement of individual detectors can be accomplished in the field in a matter of hours. Planned upgrades of the GRIS system include a coded aperture imaging system (which has nearly completed fabrication but was not relevant to the supernova observations), segmentation of the germanium detectors to provide improved background rejection, and procurement of larger detectors as they become available. GRIS should remain one of the premier instruments for spectroscopy of astrophysical sources until it is superseded by a spacecraft instrument with similar design such as the Nuclear Astrophysics Explorer.

The supernova was observed during a balloon flight of 27.7 hours duration launched from Alice Springs, Australia at 19:58 Universal Time (UT) on April 30, 1988. The supernova observation was divided into approximately 36 20-minute segments. Source segments were alternated with background segments. Background was taken at the same elevation as the source, but the azimuth was changed, typically by 180°. Observations of the galactic center region were made in a similar manner during the time the supernova was too low in elevation to be observed. Dur-

ing the flight, a degradation of the resolution was observed that was not detected in ground testing. The problem was caused by very large (>200 MeV) saturating pulses due to charged particle events, and resulted in a pair of peaks separated by 0.8 percent for each gamma-ray line. This problem has been simulated on the ground using a custom-designed pulser, and the electronics design has been corrected for the next flight.

An empirical model of the instrument response during the first flight has been developed using background and calibration lines. This model is completely consistent with our understanding of the electronics problem and can be used to correct for the effects of resolution degradation during the flight. Fortunately the supernova line at 1238 keV was very broad (indicated in the table), and as a result the degradation of the instrument response did not significantly effect the results for this important observation. At the 847 keV line (also from ^{56}Co),



Schematic drawing of the GRIS experiment in the supernova configuration.

*The second flight was also successful, and preliminary data analysis confirm these expectations.

1238 Line Fits				
Model	$\chi^2\text{min}$	Flux 10^{-4} (ph/cm ² – s)	Peak Energy (keV)	Width FWHM (keV)
Gaussian	23.4	10.9 ± 2.3	+ 2.1	+ 6.2
			1235	25
			– 2.3	– 5.5
Rectangle	22.8	9.2	+ 1.4	+ 5.6
			1235	26
			– 1.6	– 2.6
dof = 23 Fits are to source segments only with linear continuum. Errors are one sigma ($\chi^2\text{min} + 1$).				

a strong 844 keV background line from aluminum is smeared out by the resolution problem with a resulting increase in background for the broad supernova line. Except for this problem, the instrument performed almost faultlessly on its maiden voyage to the credit of all those who struggled to rush the project to completion.

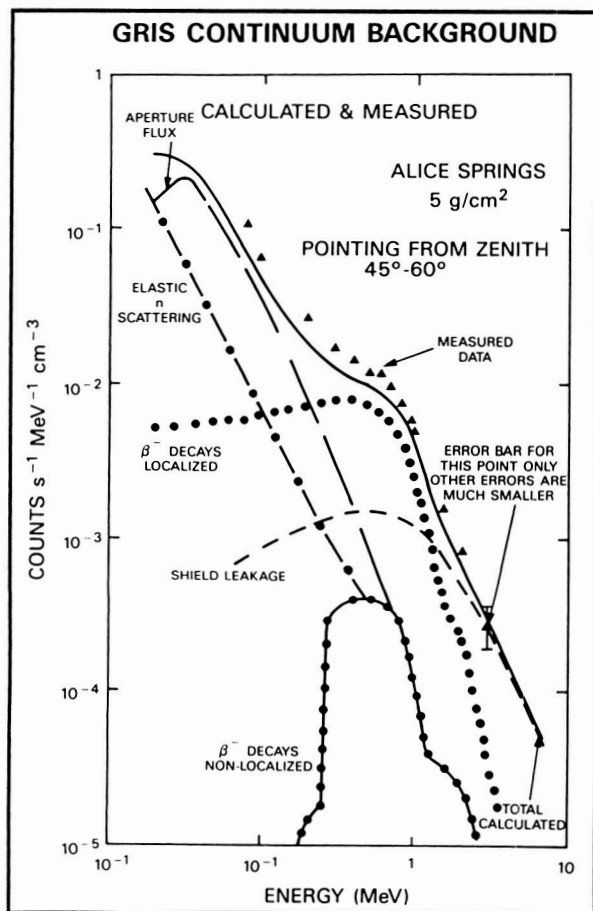
An important aspect of the design of this instrument was the development of an accurate model of the background which could be used to optimize the design and to evaluate the merit of various proposals to improve the sensitivity. Gamma-ray instruments generally operate in the regime where signal-to-background ratio is small and are, therefore, very sensitive to design features which effect the background. A sophisticated model using Monte Carlo techniques and numerical integrations was constructed to predict the background. This model attempted to derive the components of the background due to all known sources without resort to adjustable parameters and was successful at modeling the background in the previous balloon instruments from GSFC and Bell/Sandia. The second figure shows the background calculated for the supernova observation with GRIS and the contributions of each individual component. Also shown is the measured background from the first flight which is in remarkably good agreement with the prediction. Of particular importance is the hump in the region from 200 keV to 2 MeV, which is attributed to localized beta decays.

It is this component that would be eliminated by detector segmentation, and its elimination should result in a factor of two improvement in sensitivity in this important region. Unfortunately this technology was not available for the supernova, but detectors of this type have been manufactured. It should be possible to reprocess our current inventory of detectors to incorporate this technique when the technology becomes more readily available.

An analysis of the supernova lines is in progress to provide rapid results to the large community of observers and theorists interested in Supernova 1987A. Because this analysis is not complete, all the work presented here must be considered preliminary. Two procedures have been used to extract the line information. In the first procedure each background segment is subtracted from the adjacent source segment, and the difference is corrected to the top of the atmosphere. A weighted average of these corrected difference spectra is constructed, taking into account the significance of the measurement in each spectrum at each energy, and the average is corrected for livetime and detector efficiency to produce a flux. The resulting source spectrum can be fit to a line model using the instrument response function. At 1238 keV there is an apparent broad line feature with a flux of $(8.1) \pm (1.7) \times 10^{-4}$ ph cm⁻² s⁻¹. At 847 keV there is no statistically significant evidence of a line feature, but a 17 keV window, scaled from the width of the 1238 keV line, yields a flux of $(4.8) \pm$



$(2.2) \times 10^{-4} \text{ ph cm}^{-2} \text{ s}^{-1}$, which should be considered an upper limit on the line flux as it may include source continuum. An examination of the background spectrum in the region of the 1238 keV line shows no statistically significant features. The same is true for the sum of all the galactic center data. If we assume that the continuum in the source segments can be fit with a smooth function, then there is no need to subtract background. Eliminating the background subtraction effectively reduces the uncertainties by a factor of $\sqrt{2}$, allowing a more precise fit to the line shape.

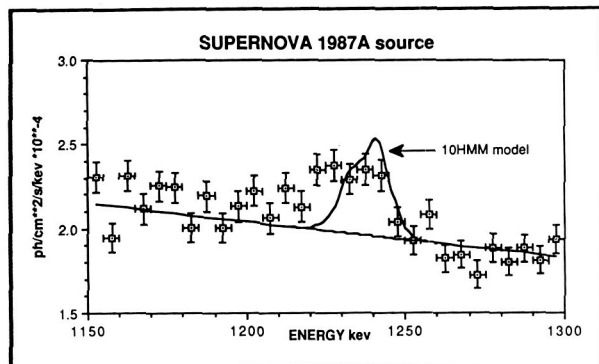


Instrument background predicted by modeling is confirmed by flight data. The low level of the 0.511 MeV background line is also confirmed (predicted $7.8 \times 10^{-5} \text{ ph cm}^{-2} \text{ s}^{-1}$, observed $9.1 \times 10^{-5} \text{ ph cm}^{-2} \text{ s}^{-1}$). Confirmation of accurate modeling suggests that improvements in sensitivity, predicted for detector segmentation, will be achieved.

This alternate analysis procedure takes the sum of all the source segments and fits this raw counts spectrum with a line plus a smooth continuum. By fitting the continuum with a smooth function, both background and any residual continuum from the source are removed from the line. Flux is calculated from the fit parameters using the average value of the atmospheric correction. The table shows the results of fits to the 1238 keV line with a linear continuum and two different line models. The flux derived in this procedure is statistically consistent with the previous value.

The 1238 keV line flux and the 847 keV flux limit are in reasonable agreement, given the systematic uncertainties, with the values measured by other experiments and with the supernova models designed to fit those measurements. The line profiles predicted by these models are all qualitatively similar. Every model predicts a blue shifted line, due to absorption of the line photons from the receding side of the supernova ejecta. This attenuation is necessary to explain an observed flux which is only 12 percent of the total line flux produced by ^{56}Co in the supernova. The total amount of ^{56}Co is well determined by the optical output of the supernova as the decay of radioactive elements is the dominant source of heating after the explosion. Some radial mixing of layers in the ejecta has been included to explain the early appearance of lines and their flat light curves. These models produce peaks in the range 1241 keV to 1244 keV and a line width of 8 keV to 11 keV full width, half maximum (FWHM) at 400 days (near the time of this observation). Clearly the observed line is significantly broader and shows no indication of a blue shift.

A more direct comparison of the model and observed data is illustrated in the third figure. Data from source segments have been summed in 5 keV bins (no background subtraction). A linear fit to the background has been added to the 10HMM model of Pinto and Woosley and smeared with the detector response function. From this data set one can derive a probability that the difference between the observed data and the model is due to a statistical fluctuation. The model was binned in 5 keV bins and the value of chi-squared was calculated for the 15 points nearest the observed peak. The corresponding reduced chi-squared of 2.9 for 15 degrees of freedom has a probability of less than 0.1 percent. Models



The sum of all source segments is displayed without background subtraction. For comparison a linear fit to the background has been added to a standard model for the 1238 keV line profile. The probability that the observed data is consistent with the model is less than 0.1 percent.

more consistent with the observed line profile can only be created by dropping the assumption of spherical symmetry in the expanding ejecta so that the observer can see through holes in the ejecta to the receding back side. The large width of the observed line requires that material from the inner shell where nucleosynthesis occurs be accelerated to velocities (6000 km/s) much greater than the bulk motion predicted for this shell. In short, a new class of significantly more complex models will be required to explain these results.

Contact: Jack Tueller
Code 660

Sponsor: NASA SRT Project

Dr. Jack Tueller, working with the Low Energy Gamma Ray Group of the Cosmic Ray Branch, serves as Co-Investigator on both the Gamma Ray Imaging Spectrometer balloon experiment and the Nuclear Astrophysics Explorer.

INFRARED OBSERVATIONS OF SN 1987A: PROBING THE EJECTA AND ITS SURROUNDING MEDIUM

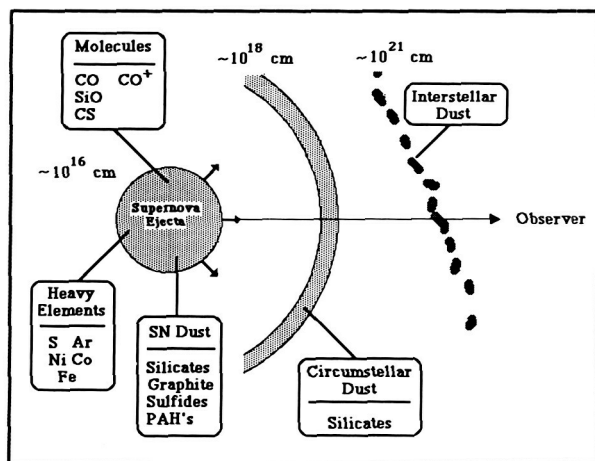
The extremely rare occurrence of a relatively nearby supernova, SN 1987A, provides astronomers with a unique opportunity to conduct a detailed multi-wavelength analysis of this event and its effect on the

ambient medium. Looking inside the supernova, astronomers are getting their first unbiased view of the composition of the expanding ejecta. The infrared (IR) region of the spectrum can carry the signature of products ranging from heavy elements, synthesized during the early phases of the expansion, to molecules and dust formed after the ejecta underwent significant cooling. Probing the ambient medium, IR observers can gain information on the presence and distribution of dust in close proximity (\sim pc) to the supernova (SN), and on the interaction of the SN blast wave with the surrounding dusty medium. At larger distances from the SN, scientists can set constraints on dust properties in the scattering dust layers detected at distances of \sim 120 and \sim 330 pc from the supernova. The various IR emission sources and the regions from which they arise are shown schematically in the figure.

Infrared observations of the SN revealed a spectrum dominated by strong spectral lines rising from a nearly flat continuum. The lines are hydrogen high-n transitions and fine structure transitions from heavy elements (Fe, Co, Ni, Ar, and S) that were synthesized in the explosion. The line strengths, their ratios, and profiles can be used to determine the elemental abundances, physical conditions (density and temperature), the dynamics of the explosion, and the degree of mixing among the various layers of the ejecta at the time of the IR observations. The continuum is most likely free-free emission arising from the expanding supernova ejecta.

Infrared observations also revealed the presence of CO and SiO molecules in the spectrum of the supernova. Various spectral features suggest the presence of CO^+ and the electronically excited CO^* ($a^3\Pi$) metastable state of CO as well. Furthermore, an unidentified broad feature at $3.9\ \mu\text{m}$ may be due to the presence of CS in the ejecta. The CO observations suggest that the expansion velocity of the emitting material is $< 2,000\ \text{kms}^{-1}$. This velocity is comparable to the slowest moving hydrogen, which suggests that the CO may have formed in the metal-rich layers (mantle) of the ejecta.

In several novae, scientists found that CO emission was followed by the appearance of a broad thermal emission component arising from dust formed in the nova ejecta. To date, there has been no evidence for any thermal emission from supernova-condensed



The figure (not shown to scale) depicts the various sources of infrared emission from SN 1987A, and the regions from which they arise.

dust, or for preexisting dust in the surrounding medium of SN 1987A. The detectability of any SN-condensed dust depends on the existence of radiation sources (trapped ultraviolet, underlying pulsar, energetic particles) at the epoch of dust formation. Preexisting dust, located about 1 pc from the supernova, is heated by its ultraviolet-visual light curve, and may give rise to a detectable IR echo. The absence of such an echo at day ~ 390 after the explosion sets limits on the amount of dust that may be present around the supernova.

Thermal IR emission may also arise from the dust layers that are located at distances of ~ 120 and ~ 330 pc in front of the supernova, producing the observed arcs of reflected light around the SN. With current instrumentation, the flux is below, or, at best, close to the $50\text{--}100\text{ }\mu\text{m}$ detection limit. However, these echoes will remain accessible for many years, and future combined infrared, visible, and ultraviolet observations of these arcs will provide more detailed information on the dust properties along the line of sight to the supernova.

Contact: Dr. Eli Dwek
Code 680

Sponsor: Internally Sponsored

Dr. Eli Dwek received a PhD degree in astrophysics from Rice University. Dr. Dwek serves on the COBE

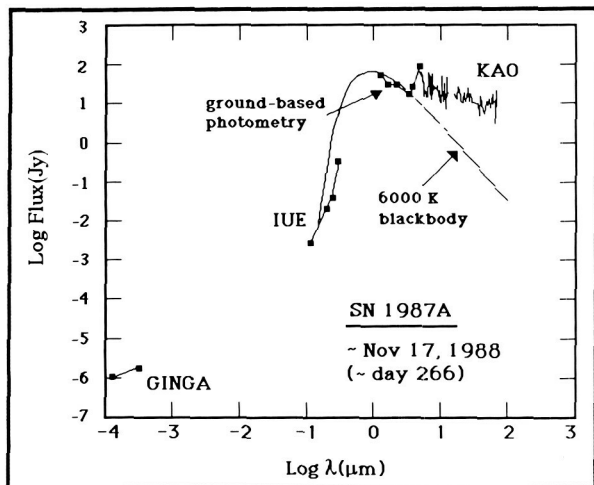
project and is a member of NASA's Supernova 1987A Science Working Group.

ELEMENTAL ABUNDANCES AND PHYSICAL CONDITIONS IN SUPERNOVA 1987A

The extremely rare occurrence of a nearby supernova (SN) provides astronomers with a unique opportunity to conduct the most detailed multi-wavelength analysis of this event and its effect on the ambient medium. The first figure shows the spectrum of this supernova, SN 1987A. Infrared (IR) observations of SN 1987A can provide information on the chemical composition and kinematics of the ejected material, the physical conditions in the ejecta, the formation of dust in the outflow, and the interaction of the supernova blast wave with the surrounding dusty medium.

Since supernovae are believed responsible for creating and returning to the interstellar medium almost all the heavy elements in the universe, the determination of the abundances of such elements synthesized in stellar interiors and explosions is a highly coveted goal in astronomy. Far-infrared (FIR) observations of the supernova have several distinct advantages over other wavelength regimes in probing the elemental abundances in the ejecta. The FIR portion of the spectrum contains many fine structure lines of heavy elements, such as Co, Fe, S, Si, and O, that are synthesized in massive stars and SN explosions. Many of these lines can be detected with high signal-to-noise ratios, and their analysis is relatively uncomplicated by radiative transfer effects and line blending. The fine structure lines can therefore be used to determine elemental abundances without substantial sensitivity to the adopted physical conditions.

In their early development, supernovae are powered by the radioactive decay of elements arising from the stellar explosion itself. In the initial phases of the supernova explosion, a strong shock wave is generated by the hydrodynamic bounce of the collapsed core. This outgoing shock wave compresses and heats the overlying stellar layers, giving rise to explosive nucleosynthesis in these regions. It is by this process that much of the important nucleosynthesis in supernovae occurs. One of the elements created in this process is ^{56}Ni , which is a radioactive isotope with a half-life of 6 days. The Ni decays to ^{56}Co ,



The spectrum of SN 1987A as observed around day 266 from the X-ray through the far-infrared. The X-ray measurements were made with the Japanese GINGA satellite. The ultraviolet measurements were made using the International Ultraviolet Explorer (IUE). The infrared measurements were all made using NASA's Kuiper Airborne Observatory (KAO).

which has a half-life of 78 days, decaying to stable ^{56}Fe . It is the energy released in these decays that powers a supernova in its first years. To produce the observed brightness of the supernova, $0.075 M_{\odot}$ of radioactive ^{56}Ni must have been synthesized in the explosion, which quickly decayed to ^{56}Co , of which $0.063 M_{\odot}$ will have decayed to stable ^{56}Fe by the time of our first observations.

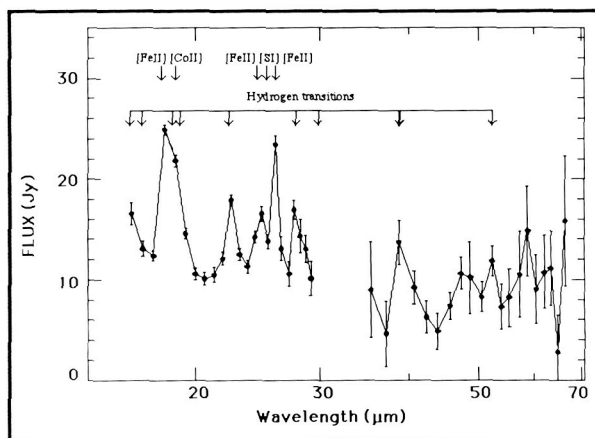
On November 17 and 19, 1987, the first far-infrared spectrophotometric observations ever made of a supernova were carried out. The observations were made aboard the Kuiper Airborne Observatory (KAO) flying out of Christchurch, New Zealand, with Goddard Space Flight Center's 24-channel grating spectrophotometer.

The second figure shows the $16\text{--}30 \mu\text{m}$ and $35\text{--}66 \mu\text{m}$ spectra of SN 1987A. The short wavelength region of the spectrum is characterized by strong emission lines, which account for about 20 percent of the emission in this wavelength region. A continuum at a level of about $8\text{--}10 \text{ Jy}$ dominates emission at the longer wavelengths, with excess emission at the wavelength of strong H-recombination lines.

The strengths of many of the lines of heavy elements observed are excellent indicators of the mass of those elements in the supernova. The mass of iron and cobalt has been determined. The total mass of iron is determined to be 0.021 solar masses, assuming the lines are optically thin. Since the total amount of Fe measured from these infrared observations is substantially lower than that expected on the basis of the decay of Co, it is likely that the strong $[\text{Fe II}]$ lines are optically thick. Therefore, only a part of the total iron that is present in the ejecta can be seen. As the ejecta expand, and the spectral lines become more transparent, increasingly accurate mass estimates are expected. The mass of Co, derived from the strength of lines that are optically thin, is close to the $0.0073 M_{\odot}$ expected from the radioactive decay of an initial mass of $0.075 M_{\odot}$ of ^{56}Co after 270 days.

Lines of different ionization states and excitation levels of some elements fall in our spectral range, and the presence (or absence) and relative strength of these lines provide us with an excellent picture of the ionization state and electron temperature in the metal-rich ejecta. We find that Fe is almost all singly ionized, and that the electron temperature is $6000 (+2000, -1000) \text{ K}$.

All of the observed infrared emission can be explained as either free-free or line emission from the



The far-infrared spectrum of SN 1987A as measured on November 17 and 19, 1987. The spectrum shows continuum emission of $\sim 10 \text{ Jy}$, with strong spectral lines of H, Fe, S, and Co.



expanding ejecta. Therefore, no evidence is seen for thermal emission from dust, either in the expanding ejecta, or in the circumstellar shell around the supernova.

The unique opportunity to study this rare and important event has provided new insight into the supernova phenomenon, and has shown that the infrared region of the spectrum offers some of the most powerful diagnostics of physical conditions and elemental abundances inside the supernova. The new observations have shown the basic theory of the supernova process to be remarkably accurate in general, and have allowed theoreticians to develop increasingly complete models of these events, which dominate the chemical evolution of the universe.

Contacts: Harvey Moseley, Eli Dwek, and
Robert Silverberg
Code 685

William Glaccum (Appl. Res. Corp.)
James Graham (Downs Lab.)
Robert Loewenstein (Yerkes Observ.)

Sponsor: NASA Airborne Astronomy Program

Dr. Eli Dwek received a PhD degree in astrophysics from Rice University. Dr. Dwek serves on the COBE project and is a member of NASA's Supernova 1987A Science Working Group.

Dr. Robert Silverberg, currently heading a balloon-borne experiment to study Cosmic Background Radiation, is also Co-Investigator on the Cosmic Background Explorer Project.

ANTARCTIC SUPERNOVA GAMMA-RAY BALLOON FLIGHT

A high-altitude balloon was launched on January 1988 from Williams Field near McMurdo Station, Antarctica, carrying aloft the GRAD (Gamma-Ray Advanced Detector) telescope spectrometer. The major goals of the GRAD Antarctic balloon flight mission were: to measure the Cobalt-56 (56-Co) emission from the Supernova SN 1987a; to study the induced activity in the Bismuth Germanate (BGO)/Germanium (Ge) detector system; to study the operation of an active particle/gamma-ray shield in sup-

port of the Mars Observer Gamma-Ray Spectrometer (GRS) program; and to demonstrate the feasibility of launching large balloons from the Antarctic. All of these goals were accomplished.

The scientific investigation team consisted of Principal Investigator, A. C. Rester, University of Florida, and co-investigators R. L. Coldwell, F. E. Dunham, and G. Eichorn, University of Florida; J. I. Trombka, Goddard Space Flight Center; Richard Starr, Catholic University of America; and G. P. Lasche, Defense Advanced Research Projects Agency (DARPA). Major support for the project was provided by DARPA; the National Science Foundation; the Air Force Geophysics Laboratory; and the National Aeronautics and Space Administration's Solar Systems Exploration Division.

Astronomical observations of Supernova SN 1987a were first obtained in February 1988. These observations indicated that the supernova occurred in the Large Magellanic Clouds, the closest supernova to the Earth seen in the last 300 to 400 years. Measurements made throughout the electromagnetic spectrum held great promise for yielding information on the nature and dynamics of such a spectacular astrophysical phenomenon. In particular, gamma-ray spectral observation would yield information about nucleosynthesis believed to occur in the core of stars and during supernovae. Elements lighter than iron are formed under normal conditions within stars; it has been further theorized that the shock waves and extremely high temperatures of a supernova explosion would lead to the formation of the majority of elements that are heavier than iron. The most intense discrete line gamma-ray emissions are expected to be from the decay of 56-Co and iron-56 (56-Fe). Furthermore, Doppler shifts in the discrete line energy spectrum are caused by matter moving towards or away from an observation point providing information on the dynamics of the explosion.

Because gamma rays are absorbed in the Earth's atmosphere, measurements must be made at altitudes that can be achieved with large balloon flights. SN 1987a can be seen only in the Southern Hemisphere; because of the low intensity expected of the gamma radiation, long-duration flights are desirable. Early in the evolution of the event, the high density of debris around the supernova did not allow the gamma radiation to escape. About two to three hundred

days after the initial explosion, the cloud of debris dispersed enough to allow gamma radiation to escape. Based on these factors, it was determined that a balloon flight carried out during the 1987–1988 Antarctic summer would be most suitable for performing gamma-ray observations of SN 1987a.

The GRAD detector was launched on a $3.3 \times 10^5 \text{ m}^3$ balloon from Williams Field on January 8, 1988, at 0015 UT. The instrument reached and maintained a float altitude of 36 km, following the 78° south parallel eastward, until it was brought down some 320 km east of the Soviet Antarctic base at Vostok on January 10, 2345 UT. It was recovered from the Antarctic plateau on January 14.

The lines characteristic of the 56-Co decay were observed at 847 keV, 1238 keV, and 2598 keV from the direction of the supernova. Doppler broadening was observed, indicating an expansion velocity from 2000 to 3000 km/sec. Measurements were made with the active particle/gamma shield disabled, partially disabled, and enabled. The data have been used to

simplify significantly the Mars Observer GRS design. Extensive measurements of background produced in the near-space environment were made; this information will allow better detector design for future space flight and balloon missions. Finally, the successful launch, flight, and recovery of the GRAD demonstrated that Antarctic long-duration balloon flights are feasible.

Contact: Jacob I. Trombka
Code 682

Sponsor: Office of Space Science and Applications

Dr. Jacob Trombka is Project Scientist for the Mars Observer Gamma-Ray Spectrometer and for the X-Ray/Gamma-Ray Remote Sensing Spectrometer for the Planetary Observer Missions. Dr. Trombka, who holds a PhD degree from the University of Michigan, is a recipient of the John Lindsay Award and the NASA Exceptional Scientific Achievement Medal, as well as several Group Achievement Awards.

ASTRONOMY

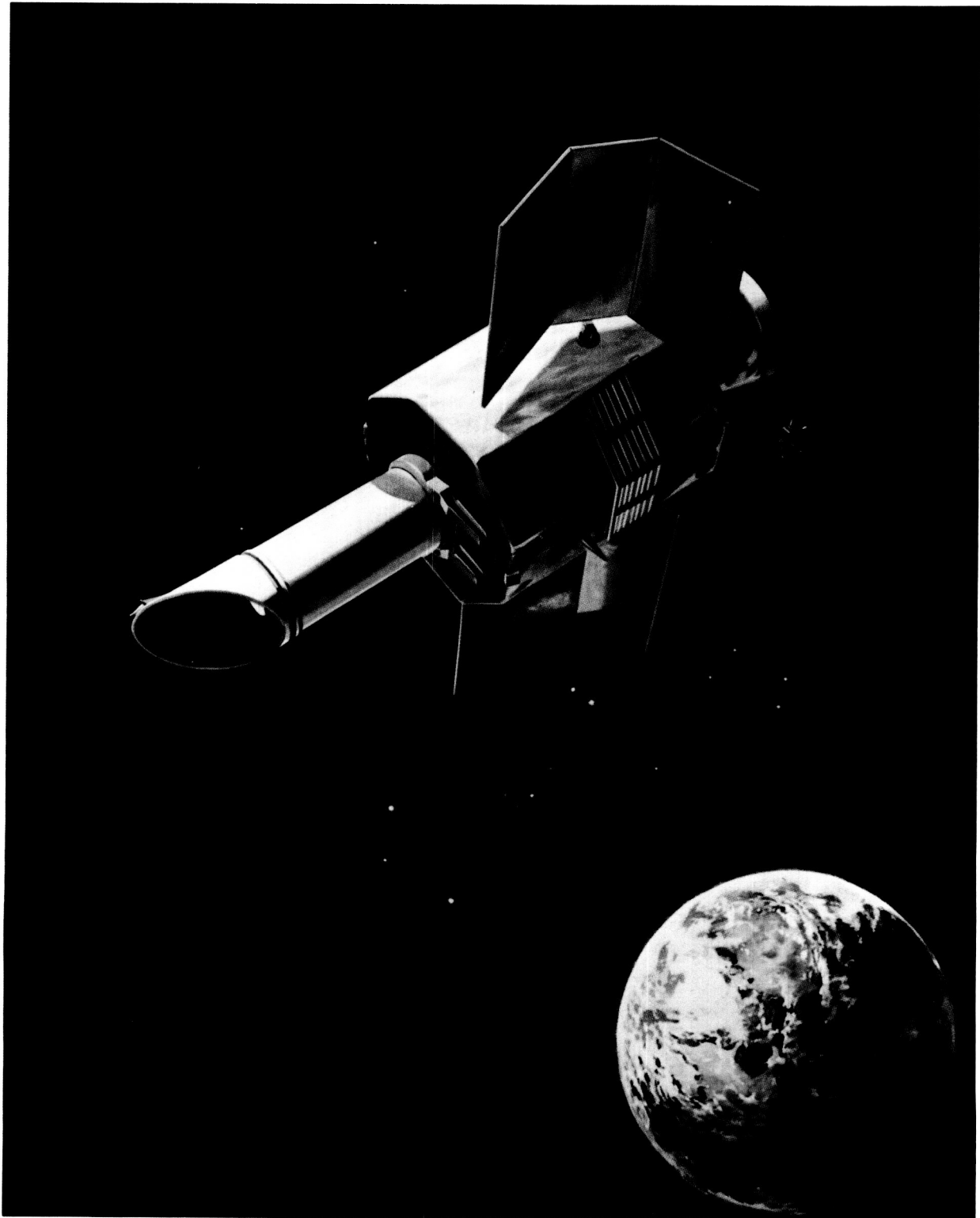
A DECADE OF ULTRAVIOLET ASTRONOMY WITH THE INTERNATIONAL ULTRAVIOLET EXPLORER SATELLITE

The International Ultraviolet Explorer (IUE) satellite shown in the first figure was launched into a geosynchronous orbit over the Atlantic on January 26, 1978. It is a joint program of the National Aeronautics and Space Administration, the European Space Agency (ESA), and the British Science and Engineering Research Council. Thanks to its geosynchronous orbit, the satellite is operated 24 hours a day without interruption, 16 hours a day from the science operations center at Goddard Space Flight Center (GSFC), and 8 hours a day from the ESA Villafranca ground station near Madrid, Spain.

The IUE is an observatory designed to obtain astronomical spectra in the ultraviolet. Its mid-

ultraviolet spectrograph provides data in the 1900–3200 Å range, and its far-ultraviolet spectrograph in the 1150–2000 Å range, with a high resolution of 0.1–0.3 Å and a low resolution of 6–7 Å.

The satellite was originally designed to last 3 years but is still operating successfully after the tenth anniversary, celebrated earlier this year. At launch, the IUE was equipped with six functioning gyros; three gyros are necessary for normal operation of the satellite in three-dimensional space. When the fourth gyro failure occurred in 1985, the satellite was operated with only two gyros, thanks to the two-gyro system that had been developed for such an eventuality with the innovative support of GSFC engineers. The same engineering team has designed a one-gyro system that can be put into operation, should it become necessary.



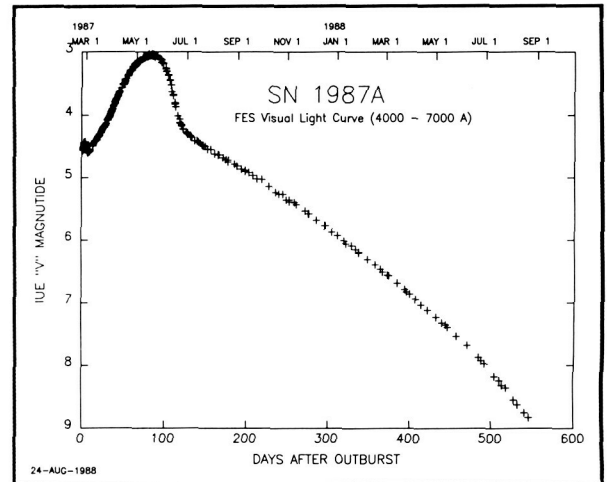
An artist's conception of the IUE satellite in geosynchronous orbit.

Its longevity is not the only remarkable thing about the IUE. The quality of scientific research performed with it, and its productivity measured in terms of scientific papers published in refereed journals are the most notable achievements of this satellite observatory. At the end of 1987, several weeks before the tenth anniversary of its launch, the total number of refereed papers published using IUE observations stood at 1561 articles, for which the satellite has become known as "the most productive telescope in the solar system."

From the outset, the IUE satellite has been operated as a guest observer facility, the very first of its kind. The opportunity to observe with the IUE has been open to all astronomers of the world. Indeed, astronomers from all of the five continents have come to use the IUE, including nations such as the Soviet Union, the People's Republic of China, India, Australia, South Africa, and Argentina, not to mention practically all of the European countries, Canada, Mexico, and Japan. Over 1600 astronomers have used GSFC and ESA facilities. More than half of the active research astronomers in the United States have used the IUE at one time or another.

The themes of research with the IUE have ranged from solar system objects, such as planets, satellites, asteroids, and comets, to the interstellar medium, practically all types of stars, novae, and supernovae, external galaxies, and quasars. Just about every conceivable astronomical source has been a subject of IUE research. Highlights of the IUE research over the past decade, include the following:

- 1) **Mass Loss from Stars.** The most effective way to study the mass loss from stars is through their ultraviolet spectra; the temperatures and densities of the outflowing gas are such that its spectral features are most clearly observable in the ultraviolet. Rocket, balloon, and earlier satellite observations have shown that some evolved hot stars are losing matter at copious rates. The IUE has extended the study of mass loss to stars of all kinds. Mass loss is usually observed as Doppler-displaced (towards the shorter wavelengths) absorption. Evidence of mass loss has been observed in evolved cool stars, unevolved main-sequence stars, pre-main sequence stars, and even in some white dwarf stars that are at the end of stellar evolution. It



The visible light curve of the Supernova 1987A as observed with the Fine Error Sensor of the IUE.

is expected that this ubiquitous mass loss phenomenon, when fully digested, will significantly improve scientists' understanding of stellar evolution, and the replenishing of the interstellar matter.

- 2) **Chromospheres and Transition Regions.** The study of the stellar chromospheres and transition regions, the latter being located above the former and below the hot coronae, has come of age with the IUE. The chromospheric temperatures range up to some 20,000 °K, and the temperatures of the transition regions from 20,000 to 200,000 °K; the spectral signatures of the rarified gas are most readily observable in terms of the resonance lines of ionized atoms in the ultraviolet. Among the significant results are the following: A) Upper stellar atmospheres may be divided into *solar* types and *nonsolar* types, the former having hot transition regions, and the latter massive, cool stellar winds. The *nonsolar*-type stars are usually cooler than spectral-type K1 giant. There are hybrid stars whose transition regions are hot (in the 100,000 °K range), but with strong winds. B) The heating of the chromospheres of stars hotter than spectral-type mid-F apparently involves acoustic heating, whereas the heating for stars cooler than mid-F seems to involve primarily magnetic fields. C) We have begun to understand how stellar dynamos work.



- 3) Evolutionary Processes in Interacting Binary Stars. Over half of all stars are estimated to be members of double- or multiple-star systems. Since most of the fundamental parameters for stars such as the mass and the radius are obtained from observations of binary stars, it is important to understand the evolutionary processes involved. In addition, the majority of the most intriguing stellar sources appear to involve binary systems. Examples include X-ray binaries, and cataclysmic variables. Because of the temperatures and densities of gas involved, the ultraviolet spectra provide the best opportunity to study the mass flow in binaries. The results from the IUE show: A) Virtually all binaries observed show evidence of mass loss. B) A fraction of the mass flowing out of the mass-losing component is accreted by its companion, while the remainder escapes from the binary system. C) In the cases of some binary systems, such as a nova, where the mass-accreting star is a compact (planet-sized) white dwarf, a quasi-stable accretion "disk" may form. D) After the more massive of the two stars has evolved and reached the critical Roche equipotential surface, the out-flowing plasma may form an optically thick envelope around the less massive companion, obscuring its nature.
- 4) The Interstellar Matter and the Galactic Halos. Current knowledge of the physical conditions and morphological features of the interstellar matter has made major advances with the IUE. This is because 24-hour observing capabilities have enabled observations of fainter and more-distant sources, against which interstellar absorption can be studied in detail. The large spectral coverage at a good resolution also has made it possible to study a number of different ionic species. Some of the significant results are: A) A detailed mapping of the amorphous local interstellar cloud (about 10–20 light years across) through which the Sun is moving presently at some 20 km per second has been conducted with the IUE satellite. This local cloud is surrounded by an extensive, tenuous, hot gas. B) Elemental depletions in the interstellar medium have been studied in much greater detail than had been the case previously. C) Detailed mapping of the interstellar dust extinction, with a

peak absorption/scattering at 2175 Å, has been performed. D) The discovery of the galactic halos was made with the IUE, and the study of its morphology and physics has been carried out. E) The elemental abundances in the Magellanic Clouds have been studied and the results show lower metal abundances in the Clouds.

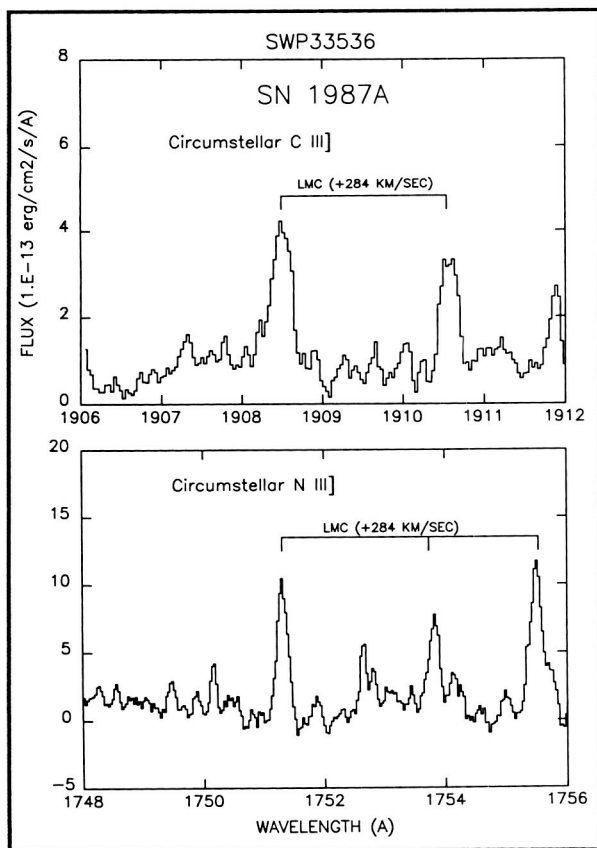
- 5) Active Galactic Nuclei, including BL Lacertae Objects and Quasars. The IUE observations of the active galactic nuclei have closed some of the gaps between the visible-light and X-ray observations. Since the shape of the continuum provides a key to the nature of the *energy machine* within, a more complete knowledge thus obtained is quite valuable. Some of the interesting results include the following: A) Most of these objects are known to be variable; hence, simultaneous observations in multiple wavelength regions are essential for unraveling the mysteries of these sources emitting a great deal of energy. Indeed, the first multifrequency observations of the BL Lac object Markarian 501 were made in 1978 at the initiative of an IUE observer using the HEAO-1 X-ray satellite, the IUE, the 5-meter telescope at Palomar Mountain (visible), the 2.5-meter telescope (IR) at Mt. Wilson, the 46-meter Algonquin radio telescope, and the 92-meter radio telescope at Greenbank. These observations have provided information crucial in constraining theoretical models, e.g., the relativistic jet model. B) Quasars emit mostly in the ultraviolet and extreme ultraviolet, which makes the IUE region extremely important. The shapes of the continua in the extreme and far ultraviolet for quasars of low-to-intermediate red shifts have become observable with the IUE. While the ultraviolet continua of highly red-shifted (hence quite faint, and very distant) quasars may be studied in the visible region from the ground, the ultraviolet continua at the source are often contaminated by the Lyman series absorption caused by the intervening intergalactic clouds; it is difficult to discern the ultraviolet continua at the source from ground-based data. C) The time lags observed in the variations of the ultraviolet emission lines, and of the continua, have yielded valuable information on the size of the line-emitting region. Such information

has been obtained for Seyfert galaxies Fairall 9 and NGC 4158.

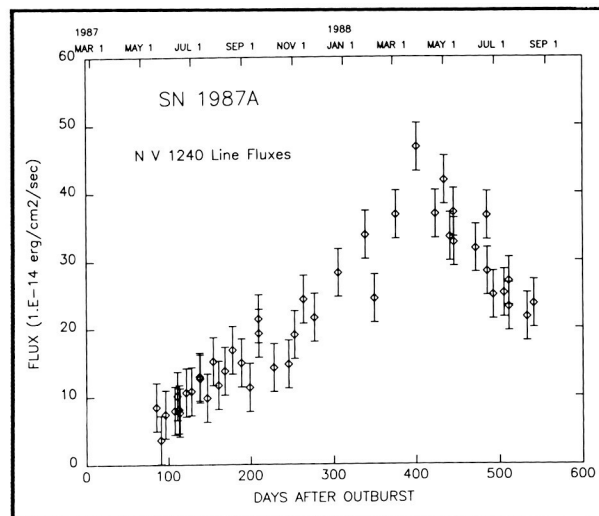
- 6) Supernova 1987A. This brightest supernova since Kepler's observation of the galactic supernova in 1604 has provided invaluable insight into this cosmic cataclysm. The visible light curve of the Supernova 1987A is shown in the second figure. The IUE observations were crucial to the identification of the supernova's progenitor as a blue supergiant. Continued observations of SN 1987A have shown that the emission lines shown in the third figure, which originated in the circumstellar shell that was

ejected from the progenitor thousands of years ago, peaked about 400 days after the initial outburst, an event shown in the fourth figure. Since the emission lines are excited by the light from the supernova, the radius of the circumstellar shell, shown in the fifth figure, appears to be less than about 400 light days. This provides additional evidence that the blue supergiant was once a red supergiant that had lost its outer envelopes in the form of stellar wind.

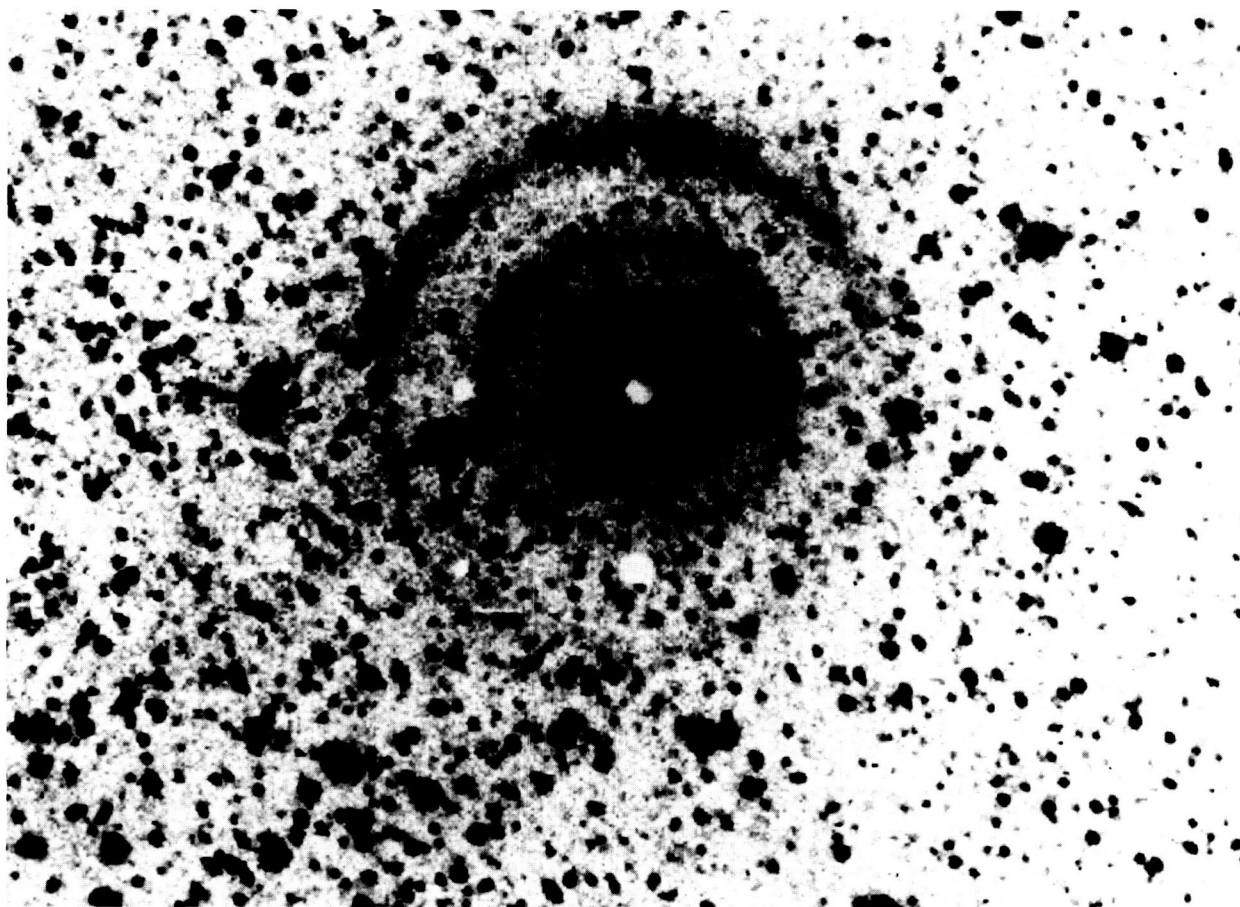
The highlights given above are but a few examples of the exciting research that has been or is being performed with the IUE. Scores of other topics could have been included. For example, a year-long series of observations of Halley's Comet yielded a significant improvement in our understanding of this comet, also providing important support to flyby missions, i.e., Giotto, Sakigake, Suisei, Vega 1 and 2, and ICE. The continued monitoring of the Jovian satellite Io's volcanic activities has shown its ejecta's intricate interactions with the Jovian magnetic field. More comprehensive discussions of the highlights of the IUE may be found in *Exploring the Universe with the IUE Satellite* by Kondo, et al., 1987. A total of 294 participants from all over the world took part in the tenth-year celebratory symposium held at



The twice-ionized carbon (C III) and twice-ionized nitrogen (N III) emission lines arising from the circumstellar shell of SN 1987A observed on May 15, 1988. The Doppler-shifted radial velocity (+284 km/s) of the multiple emission lines corresponds to that of the Large Magellanic Cloud. The shell was formed by the matter carried by winds thousands of years ago from the progenitor of the supernova.



The rise and fall of the emission lines in the spectrum of SN 1987A. Note the peak strength in the emission lines near Day 400. It indicates a radius of less than about 400 light days for the circumstellar shell.



The circumstellar shell observed from ground as it reflects the intense light from the supernova. It was observed on March 19, 1988, about 400 days after the initial outburst.

GSFC in April 1988. Its proceedings have been published.

Contact: Yoji Kondo
Code 684

Sponsor: Office of Space Science and Applications

Dr. Yoji Kondo is Project Scientist for the International Ultraviolet Explorer, as well as an Adjunct Professor of astronomy and astrophysics at the University of Pennsylvania and President of the International Astronomical Union Commission on Astronomy from Space. He specializes in interacting binary stars, the local interstellar medium, active galactic nuclei, supernovae and white dwarfs. Dr. Kondo received his PhD degree from the University of Pennsylvania.

FIRST ASTRONOMICAL RESULTS FROM THE NEW 58 x 62 INFRARED ARRAY CAMERA SYSTEM

A new infrared array camera system designed and built by the Infrared Array Group has produced excellent results during the first two observing runs on the 3.0 m National Aeronautics and Space Administration/Infrared Telescope Facility (IRTF) at Mauna Kea, Hawaii. A variety of infrared astronomical sources were observed, including Jupiter, several dust shell stars, the Orion BN/KL complex, the planetary nebula NGC 7027, and the Galactic Center. In addition, a series of $5\ \mu\text{m}$ speckle interferometry observations were made on IRC + 10216 that clearly shows resolved source structure on the 0.3 arc sec scale. The results are the highest spatial resolution, most sensitive images yet obtained of these objects at $10\ \mu\text{m}$.

The new array camera system uses a 58 x 62 pixel Si:Ga (gallium-doped silicon) DRO (direct readout) photoconductor detector array sensitive from 5–17 μm , manufactured by Hughes/Santa Barbara Research Center (SBRC). The array and optical assembly are operated at 10° Kelvin. The simple off-axis mirror, circular variable filter wheel, and cold aperture stop optical design produces diffraction-limited images with undetectable distortion. Out-of-band rejection is better than 99 percent. The system noise equivalent flux density (NEFD) = $0.05 \text{ Jy min}^{-1/2} \text{ pixel}^{-1}$, with a circular variable filter (CVF) wheel spectral bandwidth $\Delta\lambda/\lambda = 4\%$, 0.28 arc sec pixels, operating at a frame rate of 30 Hz. The camera electronic system architecture is divided into three subsystems: 1) high-speed analog front end, including 2-channel low noise preamp module, timing generator, low noise bias power supplies; 2) two 16-bit, 2.5 microsec per conversion Analogics Corporation ADAM 826-1 analog-to-digital converters interfaced to a Mercury ZIP 3216 arithmetic array

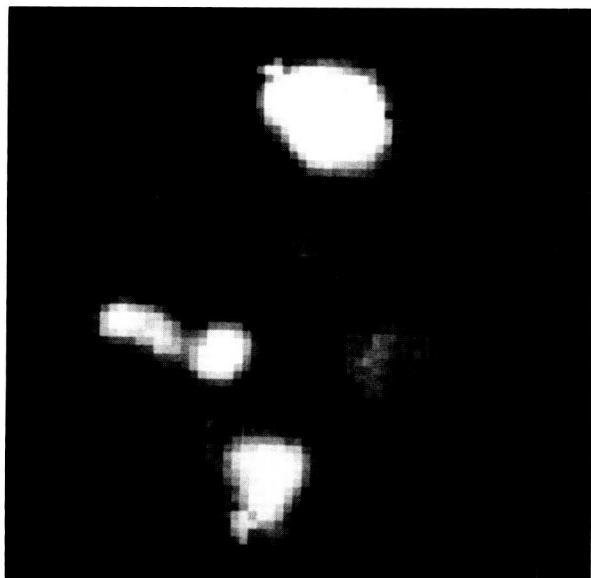
processor; and 3) an LSI 11/73 camera control and data analysis computer.

Seeing-limited images of the central 1 par sec (~ 20 arc sec) of the Galactic Center, shown in the first figure, reveal that there is a strong similarity (with notable discrepancies) between the extended 11.6 μm emission component and the highest resolution (sub-arc sec) 2- and 6-cm continuum very large array (VLA) maps and Brackett α emission in the Sgr A West core region. However, near the nonthermal point source Sgr A*, there is a distinct difference in the 11.6 μm and VLA/Br α distributions. Careful comparison of the ionized gas and dust emission shows that there is a systematic tendency for the ionized gas to peak closer to Sgr A*, along the inside of the curved ridge. In contrast, the 11.6 μm compact dust peaks are displaced typically ~ 2 arc sec away from Sgr A*, along the outside of the curved ridge. Considering the high intrinsic relative astrometric accuracy of the array images, the radial displacement seen is significant. The enhanced ionized gas brightness along the inside of the ridge can be interpreted as emission from regions that are relatively hotter and depleted of dust in comparison with the adjacent 11.6 μm bright regions. While there is no evidence for 10 μm emission at the position of Sgr A* or IRS16, this enhancement of the ionized gas emission as compared to the warm dust suggests the influence of a central luminosity source near Sgr A*.



An 11.6 μm image of the central 1 par sec of the galactic center (about 20 arc sec square field of view) taken with the new 58 x 62 infrared array camera system, showing the curved ridge of emission and bright compact sources surrounding the nonthermal point source Sgr A (not visible, located in the dark area at the center of the image, to the right of the bright source, IRS 1). This 1-minute exposure has better spatial resolution and sensitivity than previous results with 30 minutes of integration time.*

The 12.0 μm images of the Orion BN/KL infrared cluster shown in the second figure have revealed sub-arc second structure in IRC2, the infrared source that plays a central role in the current model for the energetics of region. Orion BN/KL is one of the best studied infrared source complexes, and is considered a prototype for the process of star formation in molecular clouds. In this new infrared array imaging result, cluster member IRC2 (which was previously thought of as a single, highly luminous young source) has been resolved into three point-like objects. One is the 20 μm source IRC7, the second is the true IRC2 source, and the third is a new, compact object, partially resolved 1 arc sec from IRC2, at the nominal Orion SiO maser position. The SiO maser is apparently associated with the new infrared source, but not with a high luminosity star formation region, as previously had been thought. The dominant luminosity sources for the region now appear to be IRC7



A 12.0 μm image of the Orion BN/KL infrared complex, showing the Becklin-Neugebauer object at the top, the Kleinmann-Low nebula at the bottom, and the IRC2 cluster at left. The compact source to the right in the cluster is actually the 20 μm source IRC7, the peak to the left is IRC2, and the partially resolved compact source next to IRC2 between the two is the new infrared object at the SiO maser position. This is the first two-dimensional infrared image resolving these objects.

(rather than IRC2), possible internal sources in KL, and the BN object itself.

Contact: Daniel Y. Gezari
Code 685

Sponsor: Office of Space Science and Applications

Dr. Daniel Y. Gezari received his PhD degree in astronomy from Stony Brook University. Currently, he specializes in the development of infrared array detector imaging systems for study of star formation and galactic structure.

INTERCOMPARISON OF SOLAR TOTAL IRRADIANCE DATA FROM RECENT SPACECRAFT MEASUREMENTS

The total radiation from the Sun received by the Earth's atmosphere and ocean system is the most im-

portant parameter in meteorology and climatology. Various modeling studies have predicted the occurrence of variations in mean global surface temperature with variations in solar total irradiance. A sustained solar constant change of 0.1 percent would be sufficient to have an effect on global climate. Monitoring the energy received from the Sun, and extending the monitoring to several solar cycles is essential for understanding the temporal variations in solar irradiance and its effects on weather and climate. Solar total irradiance measurements obtained in recent years utilizing electrically self-calibrating pyrheliometers on board spacecraft platforms have yielded solar constant data of high accuracy and precision. The results discussed below are based on a comparative study of the solar constant data derived from solar total irradiance measurements made by self-calibrating pyrheliometers of the Earth Radiation Budget Experiment (ERBE) on board the National Aeronautics and Space Administration (NASA) Earth Radiation Budget Satellite (ERBS) and the National Oceanic and Atmospheric Administration (NOAA) Satellites NOAA-9 and NOAA-10; the Earth Radiation Budget (ERB) on board Nimbus-7; and the Solar Maximum Mission Active Cavity Radiometer Irradiance Monitor-1 (SMM ACRIM-1).

The accompanying figure shows the multiyear solar constant data derived from the ERBS ERBE, the NOAA-9 ERBE, the Nimbus-7 ERB, and the SMM ACRIM-1 missions. The ERBS ERBE and NOAA-9 ERBE measurements cover a period of 26 and 24 months respectively, while the SMM ACRIM-1 and the Nimbus-7 ERB data span a period of 74 and 100 months, respectively.

During the period from October 1984 to January 1987, ERBS ERBE made solar total irradiance determinations on 63 days, while NOAA-9 ERBE made measurements on 49 days. Both the ERBS ERBE and NOAA-9 ERBE measurements yielded a mean value, 1364.90 W/m² for the solar constant. The spread of the ERBS ERBE data is 1.80 W/m², from a low of 1364.20 W/m² to a high of 1366.0 W/m². For the NOAA-9 ERBE, the spread of the data is 2.50 W/m², from a low of 1363.60 to a high of 1366.1 W/m². The standard deviations are 0.40 W/m² (0.029 percent), and 0.62 W/m² (0.045 percent) of the mean solar constant value from the ERBS ERBE and the NOAA-9 ERBE, respectively.



a better understanding of the systematic biases in the measurements, and the realization of a reference value to link successive solar total irradiance measurements into a long-term data base significant for climatological applications.

Yearly mean solar constant data derived from all four solar monitors (ERBS ERBE, NOAA-9 ERBE, Nimbus-7 ERB, and the SMM ACRIM-1) show a slow but steady decline between the launches of the spacecraft and the third quarter of 1986. A systematic, long-term decrease of 0.08 percent and 0.09 percent in the solar constant data derived from the Nimbus-7 ERB and the SMM ACRIM-1, respectively, can be observed between 1980 and mid-1985. A decrease in the solar constant of 0.02 percent and 0.04 percent is evident in the results derived from the ERBS ERBE and NOAA-9 ERBE, respectively, between the launches and the end of 1986.

The Nimbus-7 ERB yearly mean value remained nearly constant for 1984, 1985, and the third quarter of 1986. Similar constancy can be observed in the SMM ACRIM-1 data for 1985 and 1986. A small upturn in the average solar constant data is evident in both the Nimbus-7 ERB and ERBS ERBE towards the beginning of 1987. Analysis of the data sets spanning the time period of solar cycle 21, from late 1978 to mid-1987, indicates the solar total irradiance variability on time scales ranging from minutes to years. Solar irradiance variability is a subject of great interest to scientists mainly because of its potential for affecting the radiation balance of the Earth-atmosphere system.

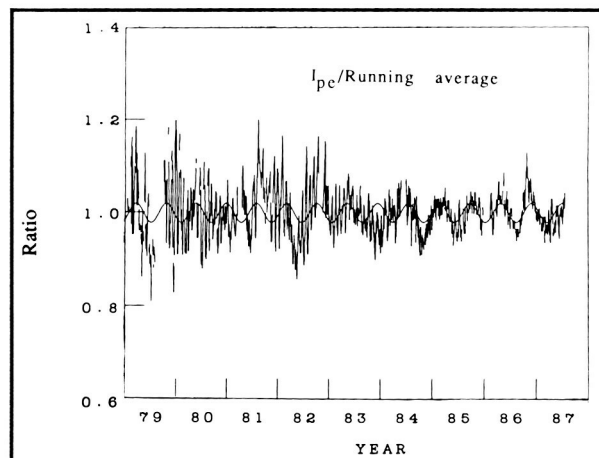
Contact: Ann T. Mecherikunnel
Code 670

Sponsors: Office of Space Science and Applications
and EET

Dr. Ann T. Mecherikunnel, Principal Investigator in the ERBE Science Team, is responsible for analysis of ERBE data from ERBS, NOAA-9, and NOAA-10 spacecraft. As a member of the Ocean Data Systems Office, Dr. Mecherikunnel is also responsible for the development of satellite data direct readout capability for Earth observation applications programs. She has received several Achievement Awards.

A SEVEN-MONTH SOLAR CYCLE OBSERVED WITH THE LANGMUIR PROBE ON PIONEER VENUS ORBITER

A 7-month solar cycle has been observed in the photoelectron current measured over the time period from 1979 through 1987 by the Langmuir probe on the Pioneer Venus Orbiter. The probe photoelectron current, I_{pe} , is obtained when the spacecraft is outside of the Venus ionosphere; the measured current is due primarily to photoelectron emission caused by solar extreme ultraviolet (EUV) radiation in the wavelength range from about 30 nm to 121.6 nm. About one half of I_{pe} is due to solar Lyman alpha emission. One I_{pe} measurement is made each Earth day, except when Venus is at superior conjunction. The daily I_{pe} data were normalized to remove the long-period, 11-year solar maximum-to-minimum trend by dividing it by the 400-day running average. The normalized data are shown in the first figure. Three periods can be prominently seen: the envelope due to the maximum-to-minimum trend; the rapid, 29-day solar rotation; and a less-well-known 7-month cycle. The 1984 through 1987 data are dominated by the 7-month cycle, although the cycle is present in all of the data. A sine wave, fit to the 1979-1987 data using a period of 216 days, is shown in the figure as a solid line.



Ratio of daily Pioneer Venus Orbiter I_{pe} data divided by 400-day running average for 1979 through 1987. I_{pe} is in units of 10^{-9} amps. A least-square fit sine wave at the 7-month period (216 days) is plotted as a solid line.

The power spectrum of the I_{pe} data is shown in the second figure. The method of analyzing data that has arbitrary data spacing was devised by Deeming. The Deeming power spectrum is the convolution of a true Fourier transform with a spectral window that characterizes the data spacing. The strongest observed cycles are (in order of decreasing power): 216-, 29-, 156-, 112-day, and other weaker cycles. The first and third cycles are 7-month and 5-month cycles, respectively.

The 2800 MHz solar radio flux, observed from Earth over the same time range, exhibits a similar 7-month cycle at about 233 days that is less dominant than a strong, 5-month (155-day) cycle. Solar Mesosphere Explorer (SME) Lyman alpha observations from mid-1981 through mid-1988 also exhibit 5- and 7-month cycles. Since the 7-month and 5-month cycles are observed from Venus (I_{pe}) and from Earth (2800 MHz radio flux and SME Lyman alpha), they must be intrinsic enhancements involving a wide range of solar longitudes, rather than narrow (rotational) beacons, which would produce distinct synodic periods when observed from the two planets.

The 7- and 5-month cycles are believed to be caused by long-lived flux enhancements from nonlinear interactions of global oscillation modes in the Sun's convective envelope (r-modes) and radiative interior (g-modes). An analysis of the frequencies of these (rotational) oscillations and their (intrinsic) nonlinear beat frequencies shows that: 1) the $L = 1$ r-mode is the only rotational source of the 7-month cycle

(observed from Venus); 2) the $L = 1$ r-mode produces a 12-month cycle observed from Earth; 3) the intrinsic sources of the 7-month period are due to beats of r-mode $L = 3$ with $L = 6$, and g-mode $L = 3$ with $L = 10$; and 4) the 5-month cycle is due to beats of g-mode $L = 2$ with $L = 3$, and r-mode $L = 4$ with g-mode $L = 6$.

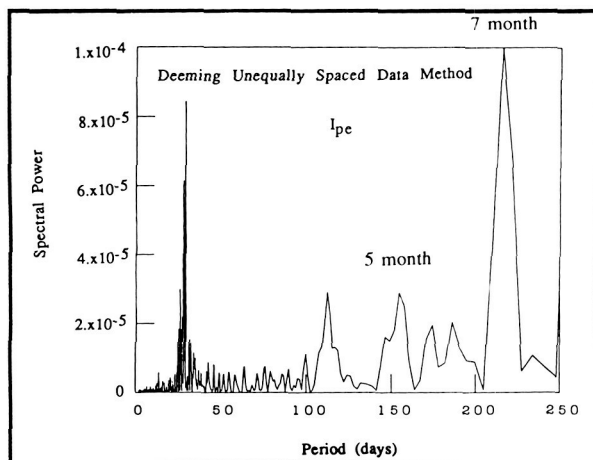
Future research will investigate mechanisms for the generation of the intrinsic mode beats from the r- and g-mode nonlinear interactions, and will study the amplitudes of the beats using the observed amplitudes of the r- and g-modes. The amplitude information may provide some insight into the physics of the r- and g-mode interactions.

Contacts: Walter R. Hoegy and
Charles L. Wolff
Code 614

Sponsor: Office of Space Science and Applications

Dr. Walter R. Hoegy is a physicist in the Planetary Atmospheres Branch Laboratory for Atmospheres. He is also Co-Investigator for the Dynamics Explorer. Dr. Hoegy, who holds a PhD degree from the University of Michigan, has been a part of Goddard for 20 years.

Dr. Charles L. Wolff, who received his PhD degree in physics and astronomy from the University of Illinois, studies variability of the solar output. Working in the Solar Radiation Office, he has 27 years of experience at Goddard.



Power spectrum of the data of the first figure using the Deeming power spectrum.

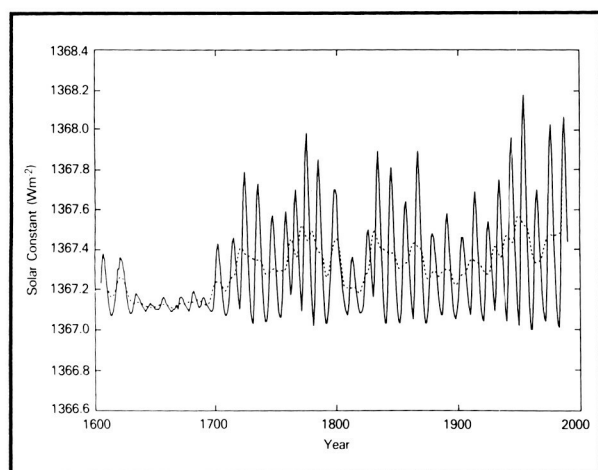
SOLAR CONSTANT SECULAR CHANGES

A recent model for solar constant secular changes suggests that over extended time intervals a positive correlation of the solar constant with solar activity (sunspot number) takes place. This occurs despite the observed several-day-long decrease in the solar constant associated with the passage of an active region across the solar disk. The positive correlation in this model is associated not with the direct activities of the Sun's active regions, which are thought to be in a close "energy balance" over their lifetime, but rather with global features-bright faculae, which exist as both polar and network features on the solar disk.



Recent solar constant observations showing a downward trend for the last half of solar cycle 21, followed by an upturn in the solar constant (associated with the onset of high-latitude faculae) in the beginning of cycle 22, support the model's general predictions for the recent solar constant behavior. Using this model, a "proxy" solar constant has been calculated. Calculations of a proxy solar constant for the past four centuries are based upon the sunspot record. Calculations for the previous nine centuries are based upon C^{14} observations and their relation to solar activity. Predictions for the next decade are based upon a dynamo theory model for the solar cycle. The proxy solar constant data may be useful for climate modelers studying global climate changes. For example, it would be helpful in disentangling solar influences from any anthropogenic changes associated with trace gas increases in the terrestrial atmosphere.

This subject is of particular interest because of the recent work of climate modelers, who have demonstrated a startling trend in the atmospheric global temperature. As suggested by "greenhouse" theories of the atmospheric temperature structure, a small but highly significant rise in the Earth's atmospheric temperature (on the order of 1°C) associated with the accumulation of trace gases (CO_2 , CH_4 , N_2O , etc.) will take place during the



This figure shows the modeled solar constant from 1610 to the year 2000, based upon the solar constant model. The dashed line shows the 33-year smoothed running mean of the modeled solar constant. The depressed values in the 17th century correspond to the Maunder minimum time period.

1990s. Its effect is expected to be at least three standard deviations above the climatology of the 1950s. These atmospheric models do not consider solar variability, which has time constants (from the 11-year solar cycle to the 80- to 100-year Gleissberg cycle) comparable to those being studied in climate modeling. Although the changes associated with the rise in trace gases are likely to be of greater significance than the solar activity variations, it is important to understand the influence of the latter. This model illustrates the effects of known solar influences upon the solar constant.

To better understand the influence of anthropogenic changes on the atmospheric temperature structure, one must understand those sources of temperature change associated with natural variability. These include volcanic dust veils, as well as solar activity. Thus Goddard Space Flight Center modelers updated the understanding of the influence of solar activity upon the solar constant.

In preparing the model, the influences of solar activity upon the solar constant were reviewed. There are several well known, as well as some disputed influences that were categorized as follows: 1) active region influences (sunspots and faculae); 2) global contrast features; 3) global size and shape changes; and 4) other unknown changes that may affect the solar constant (temperature variations in the quiet photosphere, etc.). The solar constant model, published recently, incorporates the last few hundred years of sunspot data. The figure shows this modeled solar constant versus year from 1610 to the year 2000. The dashed line shows the smoothed 33-year running mean of the modeled solar constant, demonstrating the secular trend. A reduction in the solar constant can be clearly observed during the Maunder minimum (the period in the 17th Century when there were virtually no sunspots). Following this depressed period, there has been a general rise in the modeled solar constant, with slight depressions near the turn of the last two centuries. This 80- to 100-year undulation is referred to as the Gleissberg cycle, although it appears to be more of a persistency than a true periodic cycle.

It is highly unlikely that the general rise in the modeled solar constant over the last few hundred years is the actual source for the recent global climate warming trend. This conclusion is supported by two

observations: 1) the observed heating trend follows the trace gas heating curve closely; and 2) the recent values for the modeled solar constant have not been increasing in the last 3 decades. (The largest solar cycle to date has been cycle 19, which peaked in 1957.) Thus, it does not appear that natural solar variability caused the recent global atmospheric warming.

Contact: Kenneth Schatten
Code 610.1

Sponsor: Office of Space Science and
Applications

Dr. Kenneth Schatten, who holds a PhD degree from the University of California at Berkeley, is a solar physicist with the Solar Radiation Office of the Laboratory for Atmospheres. Dr. Schatten has been with Goddard since 1969 and has received several awards for his scientific achievements.

MONOLITHIC CRYOGENIC BOLOMETERS FOR BROADBAND DETECTION OF MICROWAVE RADIATION

Some microwave applications require detection of radiation over a very broad frequency range to study weak continuum sources. The high-frequency spectral coverage of existing coherent techniques is limited by the narrow bandwidth of various receiver components. Incoherent detection can, in principle, achieve a noise temperature much lower than current coherent receivers operating near 100 GHz. To pursue this advantage, a very wideband incoherent receiver using a cryogenic bolometer as the sensing element is being developed.

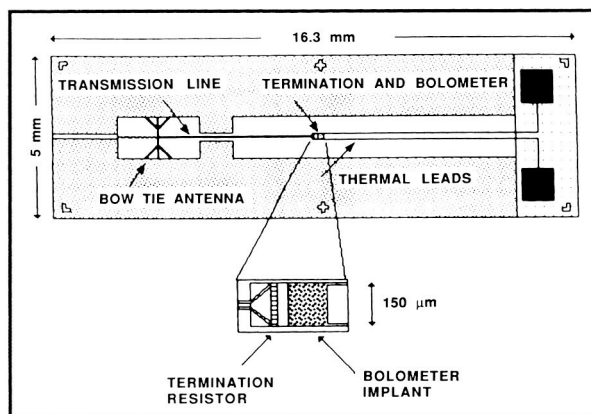
A bolometer is a heat sensor. It consists of a radiation absorber to convert the incident radiation to heat, a low thermal-conductance structure to thermally isolate the very low heat-capacity element that is heated by the incident radiation, and a very sensitive thermometer to sense a tiny change in temperature. For high sensitivity, low temperatures are required, both for the very small heat capacities that can be obtained and the excellent thermometers that are possible. Monolithic silicon technology offers high accuracy in the construction of the small-scale components needed, and the ability to build extremely low-volume, high-strength structures. For

these reasons, construction of a monolithic cryogenic bolometer is now being attempted for use in a balloon-borne cosmology experiment to study details of the 3K radiation left behind by the Big Bang.

The monolithic sensor being built is adapted for operation at 90 GHz. A small waveguide antenna, which is part of the monolithic bolometer structure, is placed in the waveguide to absorb the radiation. (See accompanying figure.) The broadband antenna couples to the incident radiation, and is connected via a transmission line formed by two of the long thin legs of the bolometer to a terminating resistor. This structure provides efficient coupling and conversion of the incident radiation into heat. The transmission line components are also the low thermal conductance legs required to thermally isolate the bolometer from the reference temperature bath. The transmission line is terminated by a small gold film resistor whose resistance is matched to the antenna and transmission line impedance. The matching condition assures that about 50 percent of the power incident on the waveguide antenna is dissipated in the resistor.

This power heats the tiny, thin piece of silicon containing an ion-implanted thermometer, which has a very large temperature coefficient of resistance. The other two thin support legs are highly doped silicon to allow the silicon legs to be both thermal isolators and electrical conductors. This allows electrical monitoring of the thermometer's resistance.

A model of this type of detector has been operated at 1.5°K to test the concept; the results agree with



Schematic diagram of cryogenic monolithic silicon microwave bolometer. Element sizes are not to scale.



the calculations of expected performance at this temperature. The monolithic bolometer being built is designed for operation at 90 GHz, with up to a 30 GHz bandwidth. For the balloon-borne experiment, the signal source is coupled to the detector by a microwave horn feeding a waveguide. The monolithic detector will be operated in the experiment in a waveguide cooled to 0.1 °K, where the much higher sensitivity permitted by this low temperature is required for successful operation of the experiment.

Contacts: Robert Silverberg, Sam Petuchowski,
and Harvey Moseley
Code 685

Sponsor: Director's Discretionary Fund

Dr. Robert Silverberg, currently heading a balloon-borne experiment to study the Cosmic Background Radiation, is also Co-Investigator on the Cosmic Background Explorer Project. Working with the In-

frared Astrophysics Branch, Dr. Silverberg has received two Quality Increase Awards. He has a PhD degree in astrophysics and has been with Goddard for 14 years.

Dr. Sam Petuchowski works with molecular spectroscopy of interstellar regions and develops sub-millimeter astronomical instruments in the Infrared Astrophysics Branch. He holds a BS degree, an MS degree, and a PhD degree. Dr. Petuchowski has been with Goddard for five years.

Dr. Harvey Moseley, who holds a PhD degree from the University of Chicago, is Co-Investigator on the Cosmic Background Explorer Project; Principal Investigator of the Kuiper Airborne Observatory Instrument Program; Co-Investigator on the AXAF XRS instrument; and Instrument Scientist on the SIRTf IRAC. Dr. Moseley has received the NASA Exceptional Service Medal.

HIGH ENERGY ASTROPHYSICS

GAMMA RAY OBSERVATORY

The Gamma Ray Observatory (GRO) is currently in the integration phase, i.e., the spacecraft subsystems are being placed on the structure, and the electrical interconnections are being validated. The photo shows the scientific instruments being placed onto the observatory, a task scheduled for completion in January 1989, when testing of the observatory will commence. Launch of GRO is scheduled for 1990.

The major effort in fiscal year 1988 was to get the observatory ready for instrument installation. The structure had to undergo load testing to assure that it was strong enough to support the payload during shuttle lift-off and landing. Testing of the spacecraft's electrical subsystem had to be finished, and the harnesses for the spacecraft had to be built, tested, and installed. The largest harness weighed about 340 pounds, and had about 300 connectors. Testing and calibration of the scientific instruments had to be completed.

The Gamma Ray Observatory is one of four major National Aeronautics and Space Administration (NASA) missions (called the "Great Observatories") planned for launch during the next decade. The Hubble Space Telescope (HST) and GRO are scheduled for launch within the next 2 years. The Advanced X Ray Astrophysics Facility (AXAF) and the Space Infrared Telescope Facility (SIRTf) are planned for later in the 1990s. These space observatories will cover the electromagnetic spectrum, from infrared to high-energy gamma rays. GRO, a 35,000-lb satellite, will carry a complement of four large instruments to make synergistic measurements over a wide range of energies, from 0.02 MeV to over 10,000 MeV. The sensitivity of the GRO instruments will enable detection of sources that are at least 10 times fainter than those found on earlier missions. In addition, source positional information will be improved by a factor of five, which will permit searches for optical, X-ray, or radio counterparts. During the first year of the mission, GRO will undertake a complete sky survey. Once the survey is completed, selected targets of interest will be studied in detail.

The investigation will include a variety of sources, including: steady-state and time-variable discrete sources; diffuse regions, such as giant molecular clouds; the Milky Way galaxy, as well as external galaxies; and the diffuse, presumably universal gamma-ray background. The most energetic phenomena in the universe radiate a significant fraction of their energy in gamma rays. In order to understand these sources, it is necessary to determine the intensity, energy distribution, and temporal variations of their gamma-ray emissions. Gamma rays make ideal tracers of astrophysical phenomena, for, in contrast with lower energy photons, they are not easily absorbed by the interstellar medium.

Modern astronomy has revealed a variety of exotic, compact sources such as pulsars, supernovae, black holes, neutron stars, and X-ray binaries. Matter in the vicinity of these objects is subjected to extreme temperatures and pressures, and to extreme magnetic fields. By observing features in the energy spectra over more than five orders of magnitude, and by measuring the temporal variations to a resolution of

1 millisecond, insight will be gained into the nature of these extraordinary objects and the physical phenomena that power them. Two of the instruments on GRO will be capable of measuring nuclear lines over the entire nuclear spectroscopy range, from 0.1 to 10 MeV. The detection of line emission from radioactive nuclei and electron-positron annihilation in, for example, regions of recent supernovae, molecular clouds, or accreting objects, provides researchers with the opportunity to study nucleosynthesis in such objects, and to investigate the properties of collapsed celestial objects. A detailed gamma-ray map of the Milky Way will provide information on a variety of topics.

The interaction of cosmic rays with diffuse matter, such as interstellar gas and dust in the Milky Way or in molecular clouds, produces gamma rays, whose intensity is proportional to the density of the matter and cosmic rays. The high angular resolution of the GRO instruments will provide scientists with the capability to make maps of the matter distribution to far greater detail than in past experiments. These maps will provide valuable information for understanding the structure and dynamics of the Milky Way and nearby galaxies. Nuclear lines from radioactive nuclei are also produced through a variety of phenomena. For example, experiments on NASA's High Energy Astrophysics Observatory (HEAO-3) and Solar Maximum Mission (SMM) satellites have provided evidence for Aluminum-26 (Al-26) and electron-positron annihilation radiations from the general region of the galactic center. The survey obtained by the instruments on GRO, with sensitivity and angular resolution improvements by a factor of five (or better) than the previous missions, will provide detailed maps of these emissions, and thereby distinguish between the candidate sources, e.g., supernovae, novae, compact objects, massive stars, etc.

One instrument on GRO is specifically designed to detect gamma-ray bursts from any direction in the sky, and to identify their directions, time profile, and energy distribution. The other instruments also have capabilities of gathering information about these bursts. Bursts appear to be unique phenomena, capable of emitting extreme amounts of energy within fractions of a second. A network of satellites, using precise timing, has enabled several burst directions to be identified to arc minute accuracies. GRO will



The Gamma Ray Observatory during assembly prior to the installation of the scientific payloads.



add greatly to this network, owing to its sensitivity and measuring abilities.

The capabilities of GRO will permit studies of sources beyond the Milky Way. The so-called "active" galaxies emit extraordinary amounts of energy. They appear to be powered by huge black holes. Based on preliminary observations of several nearby active galactic nuclei, it appears that gamma-ray emission may dominate the luminosity of these objects. Almost certainly, the features of their gamma-ray energy spectrum will provide important information for theoretical models. Observations of the spatial structure of the universal diffuse gamma radiation will be an important test of the idea that large-scale regions—the size of galaxies—might exist in both matter and antimatter which, in the case of a collision, would produce gamma rays by annihilation.

The gamma-ray region of the electromagnetic spectrum has been largely neglected, in part due to the difficult nature of the observations, and in part because of the large, complex instrumentation needed for the task. The launch of GRO portends an era of exciting discovery on the questions of the most energetic phenomena that are occurring in the universe.

The scientific payload of GRO consists of the following four instruments:

- The Oriented Scintillation Spectrometer Experiment (OSSE) will observe line and continuum gamma-ray sources in the 0.1- to 10-MeV range, and solar gamma rays and neutrons above 10 MeV.
- The Imaging Compton Telescope (COMPTEL) will perform a very sensitive celestial survey in the 1- to 30-MeV range, with a wide field of view, good angular resolution, and low background noise.
- The Energetic Gamma Ray Experiment Telescope (EGRET) will search for diffuse and discrete gamma-ray sources from 20 MeV to 30 GeV, and will measure the intensity, energy spectrum, position, and time variations.
- The Burst and Transient Source Experiment (BATSE) will monitor the entire unocculted sky

for transient events and bursts, and will provide burst trigger signals to the other instruments. BATSE is optimized for the 0.06- to 0.6-MeV range.

Contact: David L. Bertsch
Code 662

Sponsor: Office of Space Science and Applications

Dr. David L. Bertsch of the Gamma Ray Astrophysics Branch serves as Assistant Project Scientist on the Gamma Ray Observatory and as Co-Investigator on the Energetic Gamma Ray Experiment Telescope.

CASCADE MODEL OF GAMMA-RAY BURSTS

Gamma-ray bursts are transient sources of gamma rays having remarkably little of their emission below 1 keV. They were discovered by the Vela satellite in 1969, though they were not recognized as events of cosmic origin until 1973 during a search for gamma-ray transients correlated with supernovae. Early spectra showed smooth shapes which resembled the emission of tenuous, hot plasmas with temperatures of a few hundred keV. Since then, each new generation of gamma-ray detectors has discovered more bursts and has revealed new and unanticipated characteristics of these sources. The Soviet KONUS experiments on the Venera satellites observed a large number of bursts, many of which showed evidence of absorption and emission lines. The absorption dips occur around 20–40 keV and are interpreted as cyclotron absorption or scattering in magnetic fields of $2\text{--}5 \times 10^{12}$ gauss. The reality of these features has been recently confirmed by detectors on the GINGA satellite. Emission features observed by KONUS at energies around 400–450 keV may be electron-positron annihilation radiation, redshifted in the gravitational field of a neutron star. The discovery of a very intense burst on March 5, 1979 that had a rise time less than 0.2 ms, restricting the source size to less than 60 km, and that showed 8-second pulsations, reinforced the suspected link to magnetized neutron stars. The spectrum of this source also showed the strongest annihilation feature observed to date. Since 1981, the Gamma-Ray Spectrometer on board the Solar Maximum Mission (SMM) satellite has discovered that nearly all gamma-ray bursts

have significant emission above 1 MeV, with some of these bursts having hard power law spectra extending to 50 MeV.

Many of the models proposed to explain gamma-ray bursts following their discovery have failed to account for new features in the data. Progress in understanding these sources has been very slow, and consensus on the energy source of the bursts and on the type of emission mechanism(s) operating has yet to be achieved. One outstanding theoretical problem has been the difficulty of energizing the gamma-ray emitting particles fast enough to overcome the very rapid radiation losses in neutron star magnetic fields. If the emission occurs in magnetic fields greater than 10^{12} gauss, there should be absorption above 1 MeV by magnetic pair production, making the hard power law spectra observed by SMM difficult to explain.

In an attempt to resolve some of these problems, A. K. Harding of Goddard Space Flight Center's High Energy Astrophysics Theory Group, P. A. Sturrock of Stanford University, and J. K. Daugherty of the University of North Carolina have investigated an electron-positron cascade model of gamma-ray burst emission. In this model, electrons are accelerated to energies of 10^{11} – 10^{12} eV by an electric field parallel to the magnetic field several stellar radii above a strongly magnetized neutron star. As the electrons stream along the curved dipole magnetic field toward the neutron star, they radiate gamma rays which can produce energetic electron-positron pairs, leading to a cascade of gamma rays and pairs. This process, which is also believed to occur in radio pulsars, results in some 10^4 electron-positron pairs from each accelerated primary electron and a power law gamma-ray spectrum extending as high as 100 MeV. The pairs from the cascade stream along the magnetic field and decelerate when they reach the neutron star surface, annihilating there to produce the red-shifted emission lines. Numerical simulations of these cascades yield spectra which provide good representations of observed gamma-ray burst spectra and enough pairs to account for observed annihilation lines, in particular the strong line observed in the spectrum of the March 5, 1979 burst. The electric field required to accelerate primary electrons in this model may originate from magnetic field reconnection, as in a solar flare, or by induction from an infalling comet or asteroid moving through the equatorial magnetic field of the neutron star.

Contact: Alice K. Harding
Code 665

Sponsor: Office of Space Science and Applications

Dr. Alice K. Harding is an astronomer who specializes in theoretical high-energy astrophysics. Her professional interests include pulsars, gamma-ray bursts, processes in strong magnetic fields, and UHE gamma-ray and neutrino sources. Dr. Harding holds a PhD degree from the University of Massachusetts.

GAMMA-RAY SIGNATURES OF COSMIC-RAY SOURCES

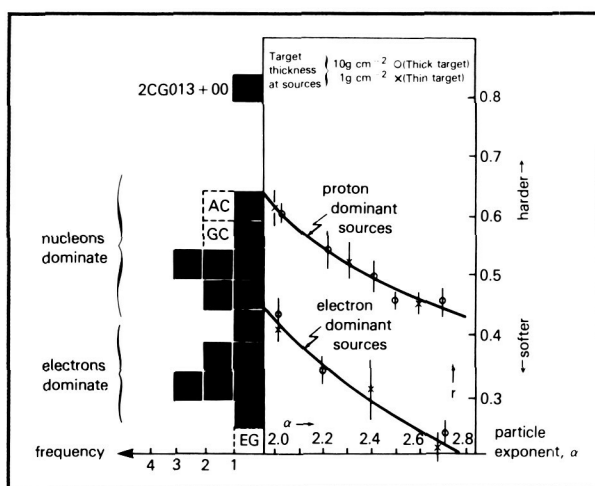
Scientists have long anticipated that gamma rays would play for cosmic-ray nuclei the role that synchrotron radio emission plays for cosmic-ray electrons in pinpointing their sources. Indeed, European Space Agency's satellite gamma-ray experiment COS-B's gamma-ray sky maps—the most extensive skymaps available—reveal the existence of a number of “spots” along the galactic plane significantly brighter than their surroundings. A comprehensive list of such spots, also known as the 2CG catalog (the second catalog of gamma-ray sources), contains 25 “objects,” only three of which are presently identified. Crab and Vela pulsars were discovered by NASA's Small Astronomy Satellite 2 (SAS-2) through their unmistakable time signatures. The object 3C273, the only extragalactic source, is identified by its positional coincidence in an uncrowded region of sky. The rest, sometimes called the UGO (unidentified gamma-ray objects), are still awaiting association with known, more conventional sources. Could these be the long-expected sites of cosmic-ray acceleration standing out on the gamma-ray sky? If so, what would be the identifiable gamma-ray signatures of such cosmic ray sources when observed with a COS-B type, low spectral resolution instrument?

Observational and theoretical studies indicate that, at their sources, cosmic rays should be characterized by power law spectra (in momentum p) of the type $dN/dE \propto p^{-(2.0+\epsilon)}$ (where ϵ reflects the strength of the shocks believed to accelerate them). This characterization is consistent with the standard leaky-box model of cosmic-ray propagation. In this model the cosmic-ray spectra at their sources are harder than near the Earth because higher energy particles would



have shorter residence times in the galactic disk tangled with magnetic fields. Data on cosmic rays also suggest that such sources should be surrounded by a shroud of material (of about 1 g/cm^2) and, therefore, would reveal themselves as localized sources of gamma rays.

For a quantitative assessment of these converging ideas, Monte Carlo techniques have been used to model these sources. The results are compared with the parameters of the reported gamma-ray objects in the 2CG list.



COS-B spectral parameter r (corrected for the E^{-2} input spectral shape used in COS-B estimations), for proton and electron dominated cosmic-ray sources as a function of particle spectral exponent α . A possible separation of ranges of r -values for two particle populations is evident. No separation of sources could be made, however, on the basis of thickness of target material at sources. Superimposed on the horizontal axis is the frequency of sources with the same spectral parameter values from the 2CG catalog. Bimodal frequency distribution in r -values correspond to the nucleon- and electron-dominated sources of simulations. The boxes with broken lines and designations GC, AC, and EG represent the spectral parameter values for the galactic center, anticenter, and extragalactic diffuse gamma-ray emissions derived from their reported spectra. One source, 2CG013+00, is significantly separated from the rest of the population by its extremely hard spectral parameter value. Its shape can only be simulated by a virtually monoenergetic beam of protons with energies 100 GeV or higher.

It appears that, among the variables that can be used in modeling the cosmic-ray sources such as the target thickness, the particle spectral exponent, and the composition (i.e., domination by nucleons or electrons), COS-B data seem especially sensitive to the latter variable. The relevant simulation results are summarized in the accompanying figure. The spectral parameter values that the COS-B instrument would register from such hypothetical cosmic-ray (gamma-ray) sources are shown as a function of spectral exponent of the particles. Note the differences between the spectra produced by electrons and that produced by nucleons in the source. It can be observed that only the softest nucleon sources would be confused in gamma-ray output with the hardest electron sources. Also superimposed on the same figure is the frequency distribution of 2CG sources in terms of the gamma-ray spectral parameter values reported. Here the gamma-ray sources are treated as a population independent of their identities. (Since most of the sources are UGOs, this treatment is highly justifiable!) It seems that even this meager spectral information provided by COS-B observations as the ratio of higher energy photons to the majority of gamma rays (formally formulated as the ratio of intensities above 300 MeV to those above 100 MeV) was unexpectedly useful in identifying the possible dominant types of particles in these gamma-ray sources. More detailed data expected from NASA's Gamma Ray Observatory (GRO) will truly help to resolve many of the problems encountered at the intersection of cosmic-ray and gamma-ray astrophysics.

Contacts: Mehmet E. Özel and
Jonathan F. Ormes*
Code 662

Sponsors: National Academy of Sciences/
National Research Council

Dr. Mehmet E. Özel is responsible for hardware and software development, as well as data analysis and interpretation, at the Gamma Ray Astrophysics Branch for Goddard's double-Compton balloon X-ray experiment. He received his physics degrees from the Middle East Technical University (Ankara, Turkey) and worked at the Max Planck Institutes for

*Internally sponsored

Extraterrestrial Physics (Munich) and Radioastronomy (Bonn, West Germany).

Dr. Jonathan F. Ormes is interested in particle astrophysics. The current focus of his work is on the development of Astromag, a superconducting magnet spectrometer for Space Station Freedom. He received the NASA Exceptional Service Medal in 1986.

ANTIMATTER IN COSMIC RADIATION

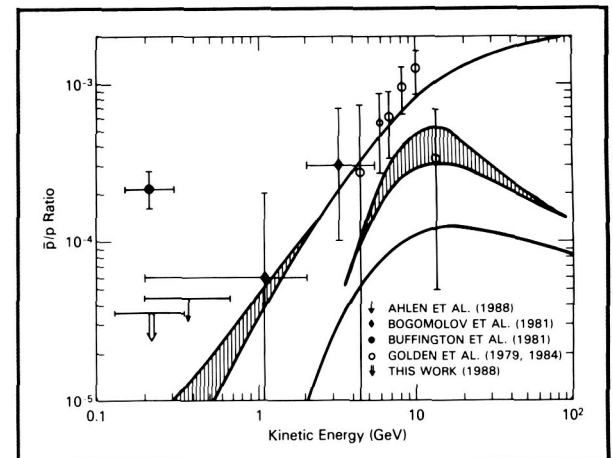
The discovery by Robert Golden (1979) of antimatter in the cosmic radiation interested both the experimenter and the theorist. However, it was a measurement made in the few hundred million electron volt (MeV) energy range by Buffington (1981) that excited the cosmic ray scientific community. This experiment reported an antiproton flux several orders of magnitude higher than expected. For the next few years, theories explaining the antiproton excess abounded. These theories included the evaporation of primordial black holes, the annihilation of super symmetric particles, and the existence of antimatter galaxies.

Recognizing the need for a definitive measurement of the antiproton spectrum, Goddard Space Flight Center (GSFC) became involved in an experiment to measure antiprotons in the cosmic rays over the 100-MeV to 1-GeV energy range. With collaborators Dr. Robert Golden from New Mexico State University (NMSU) and Dr. Ted Bowen from the University of Arizona (UA), GSFC experimenters have successfully carried out the Low Energy Antiproton experiment (LEAP). LEAP, a balloon-borne experiment, was launched from Prince Albert, Canada and spent 22 hours at a float altitude of 119,000 feet. The experiment utilized a superconducting magnetic spectrometer, a time-of-flight detector, and a Cherenkov counter to collect and analyze hundreds of thousands of cosmic rays incident on the apparatus. Currently, the LEAP experiment has been able to establish a new lower limit on the antiproton-to-proton ratio of 3.5×10^{-5} in the 100–360 MeV energy range, a result nearly an order of magnitude smaller than the ratio reported by Buffington. This measurement challenges the validity of the Buffington result and places strict constraints on the models used to explain the apparent excess of low-energy antiprotons. Stan-

dard galactic propagation models are also constrained by this result. (See figure.)

In addition to the information on the antiproton flux, the data from LEAP will likely shed light on several astrophysical questions. One of the questions pertains to the abundance of antihelium in the cosmic rays. The antihelium measurement is important because of its relevance to baryon symmetric cosmological theories. These theories postulate that matter and antimatter were initially created in equal abundances and that there exist regions of the universe comprised of antimatter. The existence of antihelium is a strong indication of the existence of antimatter galaxies. The data from LEAP will allow new limits to be set on the antihelium abundance.

Another question concerns the abundances of the light isotopes: hydrogen, deuterium, helium-3, and helium-4. The LEAP isotopic composition measurements will provide information which will check theories that suggest that hydrogen and helium have different origins and histories from that of the heavier



*Antiproton/proton ratio versus energy. This figure shows the present state of both experimental results and theoretical calculations for the antiproton/proton ratio in the cosmic radiation. The limit labeled **THIS WORK** refers to the experiment undertaken by GSFC in collaboration with NMSU and UA. The three curves are, top to bottom: the closed galaxy model as calculated by Protheroe; the calculation by Simon et al. with a range of reacceleration parameters; and the leaky box as calculated by Protheroe.*



nuclei. Since deuterium and helium-3 are produced in collisions between cosmic rays and matter, their spectrum will contain information pertaining to the density and distribution of matter traversed by cosmic rays in the galaxy. The isotope measurements will also help in understanding the production of antiprotons as secondaries.

Additional collaborators in this work are: Ms. Ann Moats, Dr. Jeremy Lloyd-Evans, Dr. Jonathan F. Ormes, Dr. Vriddhachalam K. Balasubrahmanyam, and Dr. S. Alfred Stephens.

Contacts: Robert Streitmatter and Steve Stochaj
Code 661

Sponsor: Office of Space Science and Applications

Dr. Robert Streitmatter, an astrophysicist, received a PhD degree in physics from the University of Chicago. He is interested in the experimental measurements of cosmic ray spectra and theoretical work on cosmic ray origins.

Mr. Steve Stochaj received an AB degree in physics from Franklin & Marshall College and is working towards a PhD degree from the University of Maryland. He has worked on all phases of the LEAP Project, from experiment design to data and analysis.

A SEARCH FOR X-RAY EMISSION FROM THE GREAT ATTRACTOR

Recent optical measurements of the peculiar velocities of elliptical galaxies have led to the discovery of large-scale streaming motion in nearby parts of the universe. This streaming appears in addition to the general expansion of the universe, and it has been interpreted to be the result of the gravitational attraction of 5×10^{16} solar masses (1 solar mass = 2×10^{33} gm) at a redshift of 0.014 (corresponding to a distance of about 86 Mpc; 1 Mpc = 3×10^{24} cm). This mass concentration has been nicknamed the "Great Attractor" (Lynden-Bell et al., 1988; Dressler, 1987). The nominal galactic coordinates of the Great Attractor are $l = 310$, $b = 10$. The Great Attractor could be a quite extended object; the distribution of redshifts measured from more than 1000 galaxies distributed over a steradian of the sky in this general direction shows a peak at a redshift

corresponding to the distance of the Great Attractor. Since these measurements suggest that the Great Attractor may have a radius of 20° or more, it is reasonable to assume that the Great Attractor is extended along the line of sight, perhaps with redshifts from ~ 0.011 to 0.017.

Goddard Space Flight Center (GSFC) scientists have searched the High Energy Astrophysics Observatory 1 (HEAO-1) A2 data base for X-ray emission from clusters of galaxies which might be associated with the Great Attractor. The search is based on the hypothesis that the Great Attractor is a supercluster of galaxies. Superclusters are the only known concentrations of luminous matter with total mass comparable to that inferred for the Great Attractor. If the Great Attractor is a normal supercluster, a significant fraction of the mass will be contained in smaller concentrations of mass: clusters of galaxies. Clusters of galaxies are always bright X-ray sources (with X-ray luminosities in excess of 10^{42} ergs s^{-1}), and X-ray surveys can provide a sensitive way of searching for either optically obscured or previously unknown clusters of galaxies.

The result of the search, described in the following paragraphs, is negative: there is no evidence that the Great Attractor is composed of normal clusters. Therefore, the Great Attractor, if real, is an unusual object with the mass of a supercluster but without bright member clusters (the characteristic which has previously defined superclusters).

The medium- and high-energy detectors of the HEAO-1 A2 experiment were designed to measure surface brightness in the 2–60 keV X-ray band, had a quantum efficiency over 50 percent between 3 and 17 keV, and surveyed the entire sky twice beginning in 1977. The field of view was mechanically collimated to $1.5^\circ \times 3^\circ$ full width, half maximum (FWHM).

The data were collected by scanning great circles along lines of constant ecliptic longitude. The experiment performed one complete revolution each 33 minutes if; at 12-hour intervals, the spin axis, which was always pointed approximately at the Sun, was moved 0.5° in ecliptic longitude. In this manner the entire sky was surveyed in 6 months. The sky coverage is relatively uniform, except that areas at high ecliptic latitude were in the field of view for a

larger number of consecutive days. The sensitivity threshold to point sources is about 1.5×10^{-11} ergs $s^{-1} cm^{-2}$ in unconfused regions. The data from one 6-month period of the experiment have been used to create a map of the sky binned by 0.5° in ecliptic longitude and 0.25° in ecliptic latitude. The data in each bin are statistically independent although the angular resolution of the experiment is much coarser.

Since rich clusters of galaxies are strong X-ray sources, with luminosities greater than 5×10^{42} ergs s^{-1} , an X-ray survey with the flux limits of the HEAO-1 A2 experiment is an efficient way of finding nearby clusters. Although many known clusters are undetected in X-ray surveys, there is no evidence that any concentration of mass which meets the definition of a rich cluster does not have an X-ray luminosity in the range 3×10^{42} to 3×10^{45} ergs s^{-1} . The undetected clusters in general have large redshifts ($z > 0.07$). At the distance of the Great Attractor an object with luminosity of 1×10^{43} ergs s^{-1} produces a flux of 1.2×10^{-11} ergs $s^{-1} cm^{-2}$. Clusters with a modest luminosity of a few times 10^{43} ergs s^{-1} would thus be detectable by the HEAO-1 A2 experiment if they were at the distance of the Great Attractor.

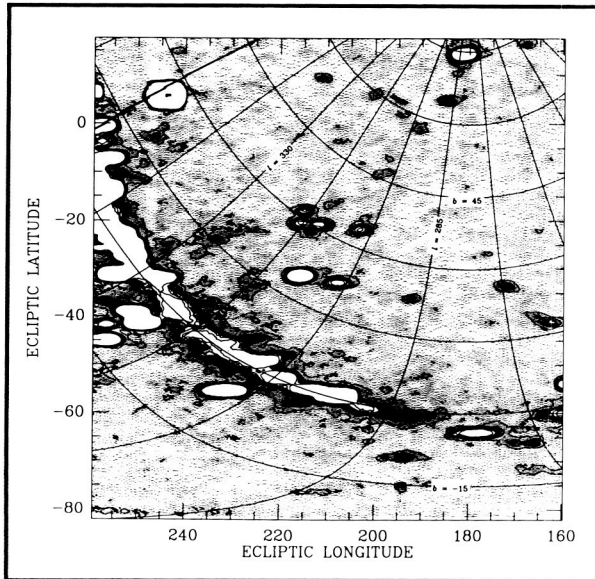
Assuming that the baryonic mass of a typical galaxy is 10^{11} solar masses, the number of rich clusters contained in the Great Attractor is $5 \times 10^5 f_1 f_{rc} / N_{rc}$ (where f_1 is the fraction of the gravitational mass which is luminous, f_{rc} is the fraction of the luminous mass contained in rich clusters, and N_{rc} is the average number of galaxies per rich cluster). For f_1 of 0.1 (appropriate for normal clusters), f_{rc} of 0.1 (which is probably low according to recent estimates), and N_{rc} of 75 (consistent with the definition of rich clusters) one predicts that the Great Attractor contains about 70 clusters. Using the cluster luminosity function of Piccinotti et al. (1982) and the space density of Abell clusters estimated by McKee et al. (1980) one can estimate that about 30 percent of all clusters have luminosities greater than the 8.5×10^{43} ergs s^{-1} of the Centaurus cluster.

The Centaurus cluster is used as a standard candle because it has a relatively high flux and is a cluster of galaxies in the general direction of the Great Attractor. The Centaurus cluster, however, is also participating in the general gravitational infall. It has a larger infall velocity than the Milky Way, and the

Great Attractor hypothesis does not allow it to be considered among the dominant mass concentrations of the Great Attractor. If the Centaurus cluster were at the distance of the Great Attractor, it would produce a flux of about 9×10^{-11} ergs $s^{-1} cm^{-2}$. At this flux level one can search for unidentified point sources even within the plane of the Milky Way, where confusion due to the presence of galactic sources and diffuse emission associated with the galaxy obscure the faintest detectable sources. Assuming then that the Great Attractor is composed of clusters described by the Piccinotti et al. luminosity function, GSFC scientists predict about 20 clusters with flux in excess of 9×10^{-11} ergs $s^{-1} cm^{-2}$ associated with the Great Attractor. The luminosity distribution for clusters is not well determined much below the luminosity of the Centaurus cluster. However, if clusters associated with the Great Attractor have a normal luminosity distribution, the data are consistent with the idea that more than half would have flux in excess of 4×10^{-11} ergs $s^{-1} cm^{-2}$. Of course if the ratio of dark to luminous matter in the Great Attractor is large compared to the ratio measured in clusters, the expected number of clusters would be reduced significantly.

The figure presents a contour map of the X-ray sky surface brightness covering more than a steradian of the sky, centered near the Great Attractor. The data are presented in the natural coordinates of the experiment, and the overlay grid shows galactic latitude and longitude. Although presented on a $0.5^\circ \times 0.25^\circ$ grid, the data have been smoothed over a 5 pixel by 5 pixel grid with a pyramidal weighting scheme. The smoothing thus includes data over an area similar to but slightly smaller than the formal $3^\circ \times 1.5^\circ$ resolution element. The smoothing broadens the width and reduces the apparent peak intensity of point sources by two thirds.

Contours are drawn at intervals corresponding to 0.33×10^{-11} ergs $s^{-1} cm^{-2} deg^{-2}$ above the mean X-ray sky brightness in source-free regions. (The conversion is approximate and depends on the spectral characteristics of the X-ray emission.) For point sources, which appear with pyramid shape of the collimator, each contour represents a peak (unsmoothed) source flux of 2.2×10^{-11} ergs $s^{-1} cm^{-2}$. The grey scale, which is shown only at the lower flux end of the scale, is chosen to emphasize the fact that even in "source-free" regions there is a nonzero



The X-ray sky surface brightness in the vicinity of the Great Attractor. The data are taken from the HEAO-1 A2 experiment. The contours have linear spacing. The average value in source-free regions, indicated by the gray scale, is one interval below the lowest contour. The nominal ecliptic coordinates of the center of the Great Attractor are (220, -35).

X-ray flux (the average intensity about 1.3×10^{-11} ergs $s^{-1} cm^{-2} deg^{-2}$). The apparent fluctuations in this diffuse flux are real and are generally believed to be the consequence of statistical fluctuations in the number and intensity of unresolved point sources within each resolution element.

Immediately visible in the figure is X-ray emission coincident with the galactic plane as well as a number of point sources. Point sources at higher ecliptic latitudes appear to extend farther in ecliptic longitude due to the Mercator projection.

Sources within a few degrees of the galactic plane (i.e., $|b| \leq 10$) will be considered separately from those at higher latitude. The reason for this separation is two-fold: first, the low latitude sources are primarily galactic; and second, the X-ray sky is more crowded and difficult to interpret in the galactic plane.

Sources with luminosities greater than the Centaurus cluster, subject to the assumption that they are at the distance of the Great Attractor, must have four or

more closed contours. Outside the galactic plane in the figure there are eight such sources. All have been previously identified: Sco X-1 (at $\sim 245, 6$), coincidentally the brightest source in the X-ray sky, is a galactic binary; Centaurus A ($\sim 217, -31$) is an active galaxy with a redshift $z = 0.0016$; the Centaurus cluster itself ($\sim 208, -33$) with a redshift of 0.0118 is a candidate, although as discussed earlier it cannot be associated with the main part of the Great Attractor; Ex Hya ($\sim 203, -22$) is a galactic cataclysmic variable source; M87 ($\sim 181, 14$) is a cluster (Virgo) with a redshift of 0.0037; and three other sources (near $\sim 210, -20$) include a distant cluster ($z = 0.073$), and an active galaxy and a cluster with redshifts appropriate for the Great Attractor (i.e., near 0.014). Of these eight sources, two (Centaurus A and the Centaurus cluster) are within 10° of the nominal position of the Great Attractor; four are about 20° away; and the other two are more than 40° away. The identifications allow us to make a strong statement: outside the galactic plane there is no evidence for any more than one cluster associated with the Great Attractor with luminosity greater than the Centaurus cluster. (Note that this one cluster is 20° away from the nominal position of the Great Attractor.) At flux levels above 4×10^{-11} ergs $s^{-1} cm^{-2}$ (two closed contours) there are seven additional sources. Of these sources, the two that are clusters are both relatively far, in angle, from the nominal position: A1060 ($\sim 172, -34$) has $z = 0.0114$ and is about 30° from the nominal position of the Great Attractor, while A1367 ($\sim 170, 18$) at $z = 0.019$ is about 60° away. The other sources are galactic (one supernova remnant and one binary) or are active galaxies at incompatible or unmeasured (in one case) redshift. Excluding A1367, our catalog of clusters with flux in excess of 4×10^{-11} ergs $s^{-1} cm^{-2}$ contains only two objects (compared to a prediction of ~ 40).

Inside the galactic plane it is not possible to search so thoroughly for objects with flux below 9×10^{-11} ergs $s^{-1} cm^{-2}$. However, all of the emission within the fourth contour is consistent with its origin in galactic sources. The sources have been identified as galactic through optical identification, or in a few cases are assumed to be galactic due to the time scales of their intrinsic variability. There is thus no evidence for any of the 20 predicted cluster sources within the "boundaries" of the galactic plane. The peak intensity is so bright inside $l = 330$ that such sources could

be hidden; the obscured area, however, is relatively small and is 30 or more degrees from the best predictions for the center of the Great Attractor. It is unlikely that 20 bright clusters are concealed within this region.

The Great Attractor, if it exists, must therefore not be composed of ordinary clusters of galaxies. Assuming that the Great Attractor is real, this result could be explained by allowing the Great Attractor to contain a much larger fraction of nonluminous matter than inferred for typical clusters. The result could also be explained by assuming that the luminous matter is more uniformly distributed than that in typical superclusters and has not condensed to form clusters of galaxies. A possible consequence of the second alternative is that nonclustered baryons (i.e., luminous matter) are in equilibrium with the gravitational potential of the Great Attractor and therefore are at X-ray emitting temperatures. If this were the case, the Great Attractor might be detectable as an enhancement in the diffuse X-ray sky surface brightness. Research is currently in progress to set limits to this hypothesis. While the X-ray sky is about 2 percent brighter in source-free areas in this general direction than for the region 180° away (where the comparison can be made in the most systematics-free way), it is not trivial to separate galactic and extragalactic effects.

The individuals who have contributed to making this work possible are too numerous to mention individually. The efforts of past and current members of GSFC's Laboratory for High Energy Astrophysics who have lent their skills to this enterprise and the efforts of all who contributed to the success of the HEAO-1 program were essential.

Contact: Keith Jahoda
Code 666

Sponsors: National Academy of Sciences
and HEAO Data Analysis Program
(Code E supported)

Dr. Keith Jahoda, a National Academy of Sciences/National Research Council Resident Research Associate, participates in the analysis of archival data from the High Energy Astrophysics Observatory 1 A2 experiment. He received his PhD degree from the University of Wisconsin.

MEASURING THE SIZE OF AN X-RAY SOURCE FROM ACCRETION SPRAY

A simple approach to determining the size of an X-ray source is possible if it is eclipsed either totally or partially by opaque material. This approach is used to determine the radii of binary normal stars and the radii of some degenerate dwarf stars, such as the companion of the K star in V471 Tauri. The ingress or egress of a 10-km neutron star should only take tens of milliseconds, and an accurate measurement has not been made.

The neutron stars with small mass companions (less than one solar mass) probably have magnetic fields of 10^9 – 10^{10} gauss, relatively small compared to the fields of the young neutron stars in high-mass binaries. The magnetosphere, or surface where the gas accreting in the disk starts leaving the disk and following magnetic field lines, should be small, perhaps 10 neutron star radii. The X-ray data from these sources have demonstrated that there can be distinguishable structure in this region, with separable emission components ascribed to the neutron star surface and hot gas in the magnetosphere or inner disk. Spectra have been an important source of information. In sources which show quasi-periodic oscillations, the frequencies and other characteristics of the modes may lead us to a clear quantitative picture of this region. In the meantime there are a few sources which offer a possibility of geometric measurement of the size of the X-ray emission region when it is occulted by obscuring material.

The first *dipper* discovered (using data from the satellite), was the rather low-intensity Uhuru source XB1916-05. Drops in intensity which are irregular occur approximately every 50 minutes. If one observes the binary orbit at an inclination angle of about 85° (or 15° off the plane) and a stream of gas flowing from the companion feeding mass to the neutron star splashes where it joins the accretion disk, this material could appear high enough out of the disk plane to interrupt the line of sight to the neutron star region. The irregularity of the light curves would be understandable in terms of turbulent interaction of the stream with the disk.

The transitions in the light curve during dips look sudden on time scales of 2–20 seconds, which could



be examined with High Energy Astrophysics Observatory 2 (HEAO 2) experiments. On those time scales the X-ray source size is unresolved. The proportional counters on the Japanese satellite Ginga observed the source with three times as much effective area (2400 cm²), which can resolve times in tenths of seconds. In a collaboration with the Japanese Institute for Space and Astronautical Science, it was possible to use this data to study questions about the central source and the absorber.

When the source is occulted by a body of material more extensive than itself, the transition time reflects the source size. The data show that such ingresses and corresponding egresses take about 0.5 second, implying a source size of $v \times (0.5 \text{ second})$, where v is the velocity of the occulting edge across our line of sight. On the other hand the data also show many short dips of intensity which imply a small cloud has moved over the source. These dips imply small clouds of about $v \times (0.2 \text{ second})$ in size. Thus most of the temporal structure is resolved on a scale in tenths of a second.

In deducing sizes from measurements of time, there is uncertainty in the velocity of the clouds. The physical model of the formation of the clouds is uncertain. A simple picture, extrapolated from studies of U Geminorum type cataclysmic variables, is that the accretion stream impacts at some angle with respect to the line of centers of the two components of the binary system and that this configuration rotates with the binary period. This picture would give the occulting material a velocity of a few hundred kilometers per second, depending upon how close to the neutron star the stream impacts the disk. However, if the clouds are formed in shocked material joining the disk, they could pick up the Keplerian velocity of the disk. This could be as fast as 2000 km s⁻¹.

With this uncertainty in velocity, the X-ray source could be as small as 80 km or as large as 1000 km. These measurements are larger than a thermal scale height of the neutron star and precisely the region expected for the magnetosphere or inner disk. They are consistent with interpretation of the spectra and suggest that the conversion of energy of accretion to X-ray luminosity takes place out at some distance from the neutron star, rather than all at the neutron star's surface.

Part of the source could still be the neutron star itself. While the statistical accuracy of the data is not sufficient to resolve effects as short as 20–50 msec in individual events, an autocorrelation function is sensitive to the cumulative effects of many events. There is evidence for a correlation time scale of 20 msec in addition to the longer time scales.

The X-ray source is occulted by a spray of small clouds, with corresponding typical dimension of 10–200 km, depending on the model of their configuration in the system. The energy dependence of the absorption of the X rays by the clouds during the dips implies the clouds are cold enough that elements like iron (for which the absorption edge is observed), silicon, and oxygen are not very ionized. The absorption and the size together determine a range of density of the clouds. The parameters appear to be in agreement with a recent thesis that small clouds should form in the shocked material under the influence of the central X-ray source.

The source XB1916-05 is an X-ray *burster* (discovered by data from the Cosmic X-ray Spectroscopy Experiment on OSO-8). The Ginga experiment observed one burst which appeared to begin simultaneously with the end of a dip. Occultations of a source undergoing a thermonuclear flash, when the neutron star is very luminous, could provide a good measurement of the size of the neutron star itself. However, for this source the short binary period means a binary semimajor axis of only half a solar radius, and theoretically the impact of the accretion stream occurs only a twentieth of a solar radius from the neutron star. The clouds are formed so close to the neutron star that, when the thermonuclear flash luminosity peaks during the first half a second, the star can evaporate them. This is likely to have happened to the clouds occulting the source when the burst observed by Ginga began.

Contact: Jean H. Swank
Code 666

Sponsor: Laboratory for High Energy Astrophysics

Dr. Jean Swank, who earned her PhD degree at the California Institute of Technology, now works with the Laboratory for High Energy Astrophysics. She studies X-ray astronomy, especially that of galactic

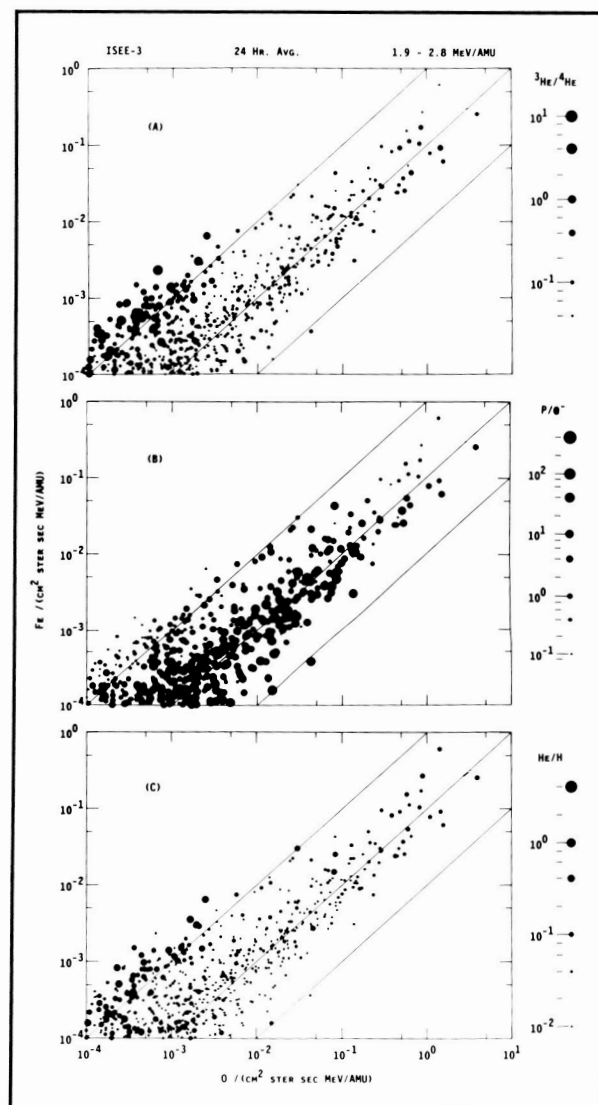
X-ray sources such as compact binaries and normal stars. Dr. Swank has served at Goddard for 13 years.

A NEW PERSPECTIVE ON ELEMENT ABUNDANCES IN THE ENERGETIC PARTICLES FROM THE SUN

The cosmic abundances of the elements and isotopes are a record of nuclear processes in the early universe and in the evolution of stars. The most complete record of those abundances, by far, is obtained from measurements in the solar system. However, each sample of material studied is also affected by a unique set of physical and chemical processes that alter its abundances, a fact that complicates the determination of the original abundances but also provides a valuable tool to study the physics of the processes involved.

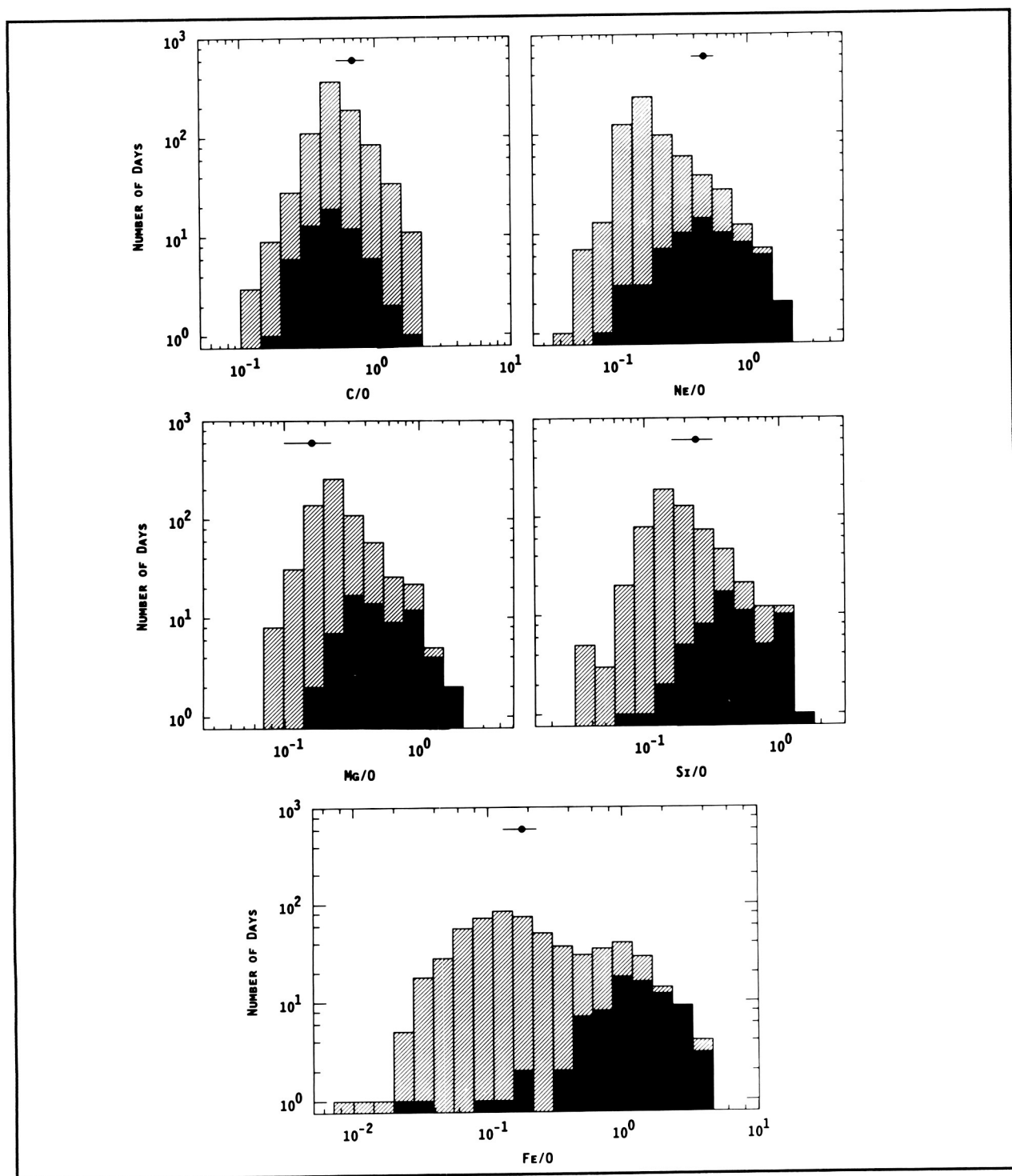
Studies of the element abundances in the solar wind and in solar energetic particles (SEPs) from large flares provide information on element abundances in the solar corona where these particles were derived. Each of these samples of coronal material is observed to vary from time to time or from flare to flare, revealing variations in the underlying acceleration processes. The SEP abundances are also punctuated by small but numerous events, called ^3He -rich events, in which abundance of the isotope ^3He is enhanced by as much as four orders of magnitude relative to its neighbor, ^4He . Heavier elements, such as iron, are also enhanced.

During the last few years it has been possible to distinguish two classes of solar particle events with different acceleration mechanisms that give rise to two different populations of energetic particles in space. The most recent evidence comes from a study of particle abundances during an 8-year period with the Goddard Space Flight Center energetic particle experiment on the International Sun-Earth Explorer (ISEE-3). When the intensity of iron ions is plotted as a function of that of oxygen ions, the two particle populations are seen as clusters of points along diagonal lines representing Fe/O ratios of 0.1 and 1.0. These two populations are emphasized when the points are highlighted by varying the symbol size according to the $^3\text{He}/^4\text{He}$, proton/electron, or He/H ratios as seen in the first figure.



Each panel shows the daily averaged intensity of iron versus that of oxygen for all days with measurably large intensities during an 8.5-year synoptic study of solar energetic particles. The symbol size at each point varies with the value of the parameter shown to the right of the plot. The parameters are the $^3\text{He}/^4\text{He}$ ratio in panel A, the proton/electron ratio in panel B, and the He/H ratio in panel C. These parameters highlight the differences of two populations of particle events.

Studies of the individual solar events that contribute to these observations have shown that the enhanced abundances come from impulsive solar flares that



The histograms show the distribution in frequency of occurrence of various particle abundance ratios in the daily averaged measurements. The blackened regions of the histograms are the subset of days when $^3\text{He}/^4\text{He} > 0.1$. The filled circle near the top of each histogram shows the value of the ratio derived in a gamma-ray line flare.

often occur in sequences from the same active region. In contrast, the "normal" abundances occur in large events that are accompanied by coronal mass ejections and by coronal and interplanetary shock waves. Separate observations have shown that the iron ions that arrive during the enhanced events are also more highly ionized, indicating that they are derived from material that has been heated to high temperatures. Thus, the degree of enhancement depends upon the flare temperature.

It is now clear that the particles from impulsive flares are drawn from material that has been directly heated by the flare, while the particles in the other population are accelerated from ambient coronal material by a shock wave expanding outward through the corona and through interplanetary space. The actual enhancements in the impulsive flare population are produced through selective heating of the particles by resonant interactions with plasma waves that are generated in the flare.

So it seems that the anomalous ^3He -rich events that were once considered to be rare and unusual are, in fact, associated with the flares that are seen daily on the Sun. The plasma processes that cause the abundance enhancements cannot be seen in the radio, optical, X-ray, or gamma-ray emission from the flares but are only evident in the particle abundances themselves. It is important to understand these processes in the Sun since it is likely that they also modify the observed element abundances in other regions of the galaxy where particle measurements are not possible.

The distributions of other elements in the SEP measurements are shown by the histograms of the daily averaged measurements in the second figure. Days on which the $^3\text{He}/^4\text{He}$ ratio exceeds 10 percent are shown in black. The progressive enhancement of increasingly heavy elements can be seen in the figure. Also shown at the top of each panel in the figure are abundance values derived from gamma-ray line intensities observed on the Solar Maximum Mission. With the exception of neon, the gamma-ray line abundances agree with the large-flare abundances and, thus, with the coronal abundances. The agreement of the neon abundance in gamma-ray line measurements with that in impulsive flare particles suggests that the neon abundance in the Sun might be as much as a factor of 3 higher than previously thought. It is not possible to measure neon in photospheric spectra or in meteorites.

Contact: Donald V. Reames
Code 661

Sponsor: Office of Space Science and Applications

Dr. Donald V. Reames, an astrophysicist in the Nuclear Astrophysics Branch, specializes in astrophysics of energetic-particle acceleration. He received his PhD in physics from the University of California at Berkeley and has been with Goddard since 1964. Dr. Reames is also Chairman of the C-Language Working Group of the Laboratory for High Energy Astrophysics and belongs to several professional societies.

SOLAR SYSTEM

REMOTE OBSERVATIONS OF MERCURY: SURFACE PROPERTIES AND SOLAR WIND INTERACTIONS

Mercury is the least studied and least understood of the terrestrial planets. Its interior and subsurface properties are still largely unknown. A surprising result of the Mariner 10 mission in 1973 and 1974 was the discovery that Mercury possessed a relatively strong intrinsic magnetic field, with an estimated

equatorial surface field strength of 300–400 nT, and a well-developed magnetosphere. Signatures were found in the Mariner 10 data of a strong bow shock, and a sharp magnetopause boundary. Using the magnetic moment and local solar wind conditions at 0.4 AU, the bow shock and magnetopause at Mercury scaled very consistently with analogous structures on Earth. The origin of Mercury's magnetic field remains an unsolved mystery, and naturally relates to the interior structure.



Determination of the overall distribution of the surface and subsurface temperature of Mercury on the dayside, the nightside, and especially at the day-night terminator contributes to a better understanding of the thermal inertia of Mercury's surface materials and of the physical composition of the crust. Also, the actual global heat flow is needed to understand the physics of the interior, and to evaluate the total heat production of the planet. This information would be helpful in determining whether the core is fluid, and hence capable of generating the magnetic field by a dynamo process. The measurement of microwave radiation from the Hermean regolith, where at a wavelength of 6 cm, the electrical skin depth of Mercury is about 70 cm, is an essential part of finding out the heat flow.

The Mariner 10 data suggested that Mercury's magnetosphere episodically extracts energy from the solar wind flow. A major fraction of this energy may be precipitated onto the surface of Mercury, producing possible heating effects. But these effects may be quite small ($\leq 1^\circ\text{K}$), so that the thermal properties must be determined before particle heating can be discerned.

Researchers recently have been attempting to use complementary ground-based radio and infrared observations to study the surface and subsurface emissions from Mercury. Observations at radio frequencies using the Very Large Array (VLA) interferometer can probe the long-term heating of the regolith by the Sun, to set limits on any internal sources of heat, and to measure the surface thermal, electrical, and geometrical properties of Mercury. Observations in the infrared can be used to provide an important constraint on the thermal properties of the top surface layers, and to set boundary conditions for the heat flow. Taken together, these ground-based observations will extract substantial new information about the intrinsic physical properties that may help to define new spacecraft observations of Mercury.

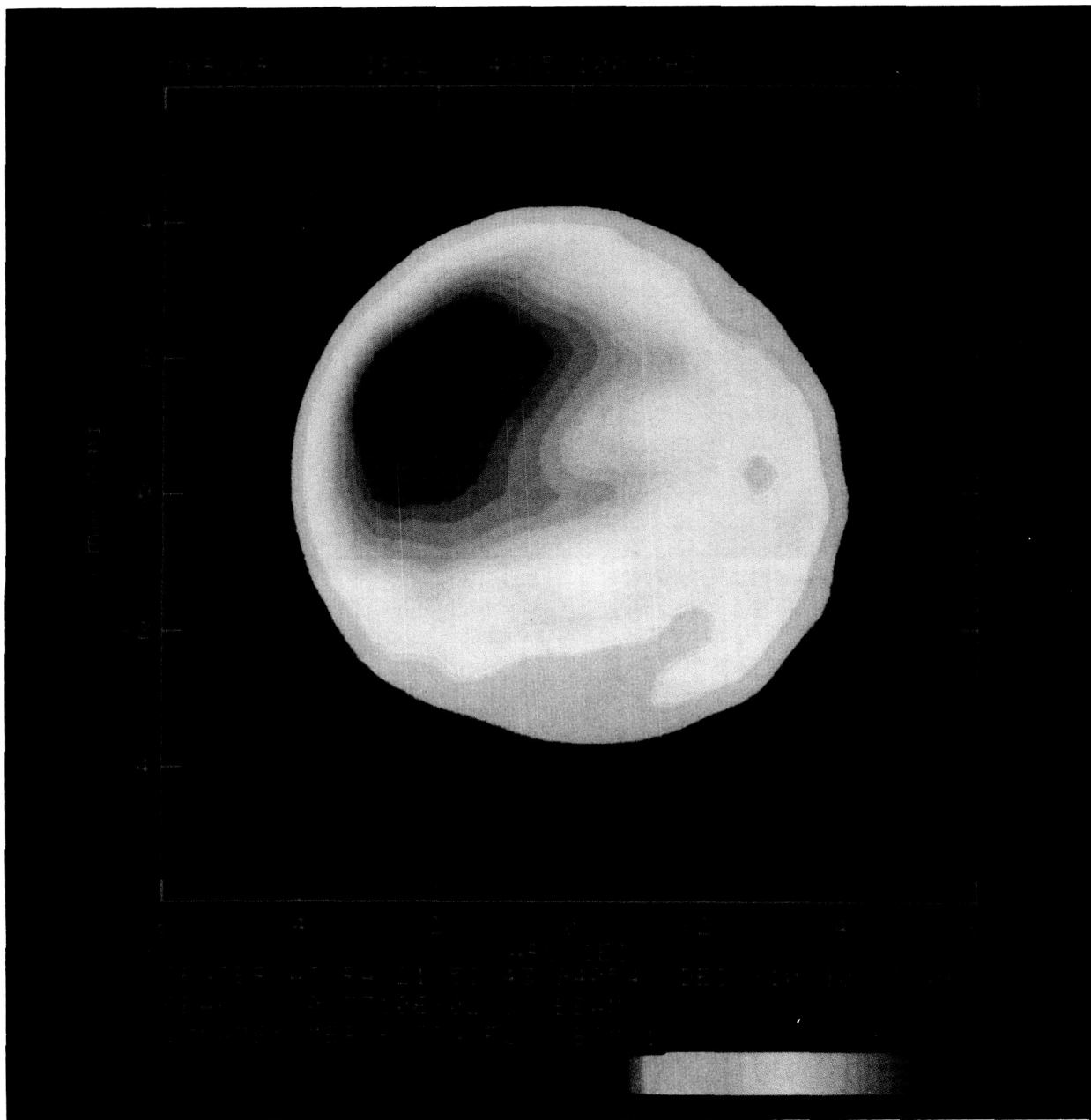
Knowledge of the subsurface layers of Mercury has remained stagnant for about a decade, because neither higher resolution ground-based radio observations nor space-based observations (Mariner 10 did not carry a microwave radiometer) have been undertaken. Recently, scientists have taken a major step forward by performing VLA observations at 6 cm,

the first observations to significantly resolve the planetary disk. Researchers mapped the distribution of both total and polarized intensities from the planet's subsurface layers.

These VLA observations were the first to detect one of the two "hot poles" along the Hermean equator, one at 0° longitude. Analysts have modeled the observed distribution of emission as simple blackbody re-radiation from solar diurnal heating, modified by the effects of surface orientation with respect to the line of sight. The peculiar circumstances of Mercury, namely a highly eccentric orbit and tidal phase locking in a 3:2 spin-orbit resonance, give rise to the unusual heating pattern from the Sun, in which two hotter longitudes (at 0° and 180°) stand out above the rest of the cooler regolith, a difference visible in the accompanying figure. Unlike shorter wavelength observations, the microwave data constrain the long-term heating pattern of Mercury. With these first VLA maps, researchers can rule out thermal models of Mercury that have an internal heat source producing in excess of $10\text{--}20^\circ\text{K}$ at the surface.

VLA observations also led to the first map of the distribution of polarized emission from Mercury. The observations, too, add significant new information on the electrical properties of the regolith. The fractional polarization is found to peak near the limb of the planet, at about 12 percent, and to decline to 0 percent near the center of Mercury. Scientists are able to understand the distribution of polarization in terms of the dielectric properties of the Hermean surface. The initially randomly polarized thermal radiation from the subsurface is modified by the change of refractive index between the surface and the planet's atmosphere. A net linear polarization of the refracted radio waves is produced, with an expected increase in the fractional polarization towards the limb of the planet. Using a simple model for the planet (approximated by a smooth dielectric sphere), researchers were able to set a lower limit on the surface dielectric constant of 1.55.

Radio frequency observations probe the subsurface layers of Mercury down to a depth of perhaps 0.5–1.0 m. Infrared observations, on the other hand, sample a thin surface layer, a few millimeters deep, with small thermal mass, and fast response times to changing external conditions. In addition to interpreting the new radio interferometric observations,



False color representation of the thermal properties of Mercury. The image was made from Very Large Array (VLA) radio interferometer data taken on February 2, 1988, at 6 cm wavelength. The bright red region is the subsurface "hot pole" region described in the text. This region is tens of degrees Kelvin warmer than the surrounding planetary regolith.

researchers are also producing near-infrared two-dimensional imaging that aims at a better understanding of the thermal properties of the surface. Such observations have never been done for Mercury.

The thermal properties of the surface can be inferred by infrared observations across the terminator onto the nightside of the planet. With sufficient angular resolution (1 arc-sec or better, limited by seeing), it



will be possible to map the temperature gradient from day to night. No such map of Mercury's surface exists; the Mariner 10 infrared radiometer only scanned narrow bands across the planet. The Mariner 10 did detect some *hot spots* on the nightside, where temperatures were 5–10°K above the average. Researchers should be able to detect such features in the near-infrared using ground-based observations with an infrared array detector.

The observational program is intimately connected to theoretical models. The thermal modeling on Mercury is basically driven by the planet's orbital and rotational properties. The spin orbit phase-locking is such that three sidereal rotations are completed in two orbits about the Sun, so that the local day endures for two full orbits, or 176 Earth days. The high eccentricity of the planet's orbit ($e=0.2$), together with this phase-locking, implies that some parts of the surface are heated much more strongly than other parts. At a typical place on the planet, the Sun shines for 88 Earth days, during which the surface is heated to a temperature in excess of 650°K. After sunset, the surface rapidly cools off, reaching a temperature of about 110°K. Just beneath the surface, heat transport is downward during the day, and upward at night. Deeper into the crust, the violent thermal swings of the surface are damped by the thermal inertia of the material. At some depth (a few meters, depending on the material properties), the temporal swings are fully damped, and the temperature is roughly constant with time (though it depends on longitude and latitude). The temperature at depth *must* be determined by the long-time-scale average of the local solar insolation, plus whatever contributions there may be from internal heating. Assuming no internal heating, analysts can easily construct a two-dimensional model for the unchanging temperature at depth; they have done so.

This work is being done by GSFC researchers in conjunction with several colleagues: Professors Jack O. Burns and Michael Zeilik (both at the University of New Mexico), and Drs. Galen Gisler and Joseph E. Borovsky (both at Los Alamos National Laboratory). Continued observation, analysis, and modeling using modern astrophysical tools may provide clues to unlocking the secrets of one of the most enigmatic—and most critical—members of the solar system family of planets.

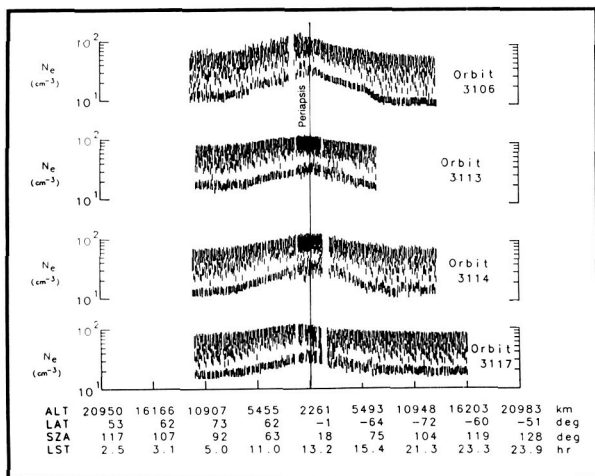
Contact: Daniel N. Baker
Code 690

Sponsors: University of California, United States
Department of Energy, and Director's
Discretionary Fund

Dr. Daniel N. Baker is currently Chief of the Laboratory for Extraterrestrial Physics. His research interests include solar-planetary relations, magnetospheric physics, plasma astrophysics, cosmic particle acceleration, and magnetosphere-atmosphere coupling. Dr. Baker holds a PhD degree from the University of Iowa.

A HOT ION PRECURSOR TO THE VENUS BOW SHOCK

The Langmuir probe on the Pioneer Venus Orbiter (PVO) has discovered that significant enhancements in both the electron and ion flux occur just upstream of the Venus bow shock, an area where one might have expected only solar wind plasma to be present. This region of increased flux is called the Venus Precursor. The first figure shows the raw spin modulated electron density profiles from a series of such upstream passages that occurred in 1987. These unique profiles of the precursor were made possible by an accidental coincidence between the configurations of the shock and orbit at this time, permitting the orbit to closely parallel the shock during the near noon passages. Both the orbit and the shock are elliptical in cross section in the subsolar region. Periap- sis was at the Equator at this time, and its altitude just happened to be coincident with the typical nose distance of the shock. The measurements shown in the figure occurred on those days when the shock formed planetward of the orbit, thus permitting essentially latitudinal profiles of the precursor to be taken at a small distance (order of 100 km) ahead of the shock. The precursor is approximately centered on the subsolar point, and extends in latitude up to solar zenith angles of about 80°, ahead of nearly the entire dayside shock. The electron flux is enhanced by a factor of about 1.6 at the nose, and the ion flux (not shown) is also increased. Note that the precursor profiles change little from orbit to orbit; their stability suggests that this phenomenon is not very sensitive to the often variable solar wind, or to interplanetary magnetic field conditions.



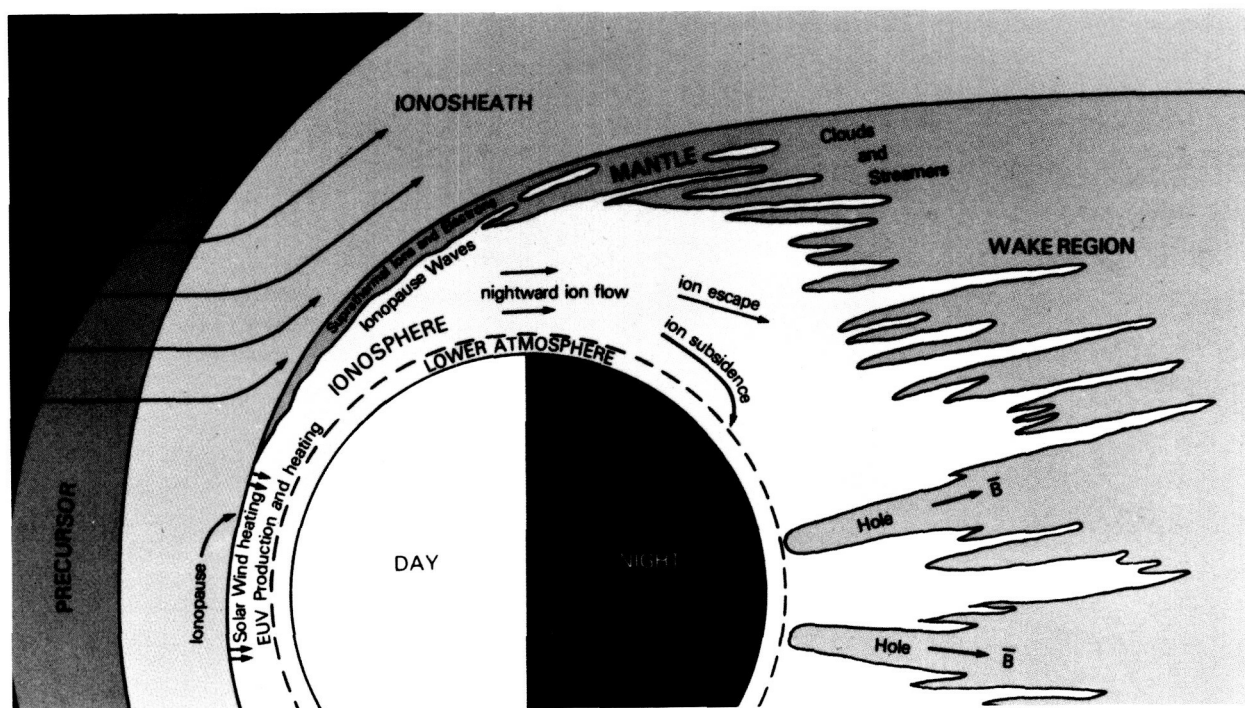
Four spin modulated N_e profiles of the precursor from selected near-noon orbits of May 1987, orbits that passed parallel to the bow shock and within a few hundred km upstream. Only minor orbit-to-orbit variations are apparent, which suggests that the precursor is relatively insensitive to solar wind conditions.

These and other traversals of the precursor suggest that it may have the spatial configuration illustrated by the cartoon shown in the second figure. The many other features of the Venus plasma environment shown in the figure have been discussed elsewhere. It is suspected that the electron and ion flux enhancements in the precursor represent the effects of an unexpectedly large population of hot ions (and perhaps electrons) in this region, probably produced by solar wind interactions with Venus at the underlying bow shock. This pre-shock feature may be unique to unmagnetized planets, at least in its large amplitude.

Contact: Larry H. Brace
Code 614

Sponsor: Office of Space Science and Applications

Mr. Larry H. Brace, head of the Planetary Atmospheres Branch, is Principal Investigator for DE and PV Langmuir probe experiments. He has a BS



A cartoon indicating the apparent configuration of the Venus Precursor and its relationship to the bow shock. Other aspects of the Venus plasma environment are also shown. The precursor may be caused by fluxes of energetic electrons and ions produced by solar wind interactions at the underlying bow shock nearby.



in physics from the University of Michigan and 26 years of experience at Goddard. Mr. Brace has also authored over 165 publications in refereed journals.

THE CLOUDS OF VENUS

Venus is constantly shrouded by an extensive, unbroken cloud system that has a pale yellow appearance in the visible spectrum and exhibits features at near ultraviolet (UV) wavelengths. It is now well established that the principal component of the extensive cloud system on Venus is concentrated sulfuric acid droplets. Since concentrated sulfuric acid is transparent in the blue and near ultraviolet range, another agent must be responsible for the absorption that gives the clouds the yellow coloration and produces the UV cloud features. The identity of the requisite absorbing material(s) remains a subject of considerable speculation. At present, elemental sulfur seems to be the favored candidate, but that thesis is based on limited inferential evidence and depends on having an appropriate admixture of the metastable allotropes S_3 and S_4 with the normal orthorhombic sulfur S_8 . In addition, the optical constants of the various sulfur forms are not well known, so the spectral behavior of such a model is qualitative.

An interesting alternative to elemental sulfur is croconic acid, $C_5O_5H_2$, dissolved as a contaminant in the concentrated sulfuric acid droplets. Several strong and relatively broad absorption bands in the blue and near ultraviolet impart an intense yellow color to croconic acid and croconate solutions. To pursue this possibility, researchers have examined a range of cloud models with varying degrees of croconic acid contamination, and vertical location of the contaminated layer. The wavelength dependent spherical albedo for each model is calculated using multiple scattering techniques previously developed at the Goddard Institute for Space Studies for the analysis of ground-based and spacecraft remote sensing of clouds. These models employ optical constants based upon the absorption coefficients for a very dilute solution of croconic acid in sulfuric acid recently measured at the University of California in San Diego. A 2.5 percent contamination of the sulfuric acid droplets over an 8-km altitude range somewhat below the top of the 30-km thick Venus cloud system has been found to be capable of producing a wavelength dependent spherical albedo in good agree-

ment with observations. This degree of contamination corresponds to a volume mixing ratio for croconic acid of 20 ppb for that region of the atmosphere. A possible mechanism for producing the croconic acid in the cloudtop region of the Venus atmosphere involves an acid-catalyzed polymerization of carbon monoxide. While the actual existence of croconic acid in the cloudtop region of Venus cannot be demonstrated, it seems plausible that such a mechanism is operative, and capable of yielding the relatively small amounts required to produce the absorption observed in the clouds of Venus.

Contact: Larry Travis
Code 640

Sponsor: Office of Space Science and Applications

Dr. Larry Travis is Associate Chief of the Goddard Institute for Space Studies and Principal Investigator on the Pioneer Venus Cloud Photopolarimeter Experiment. He received his PhD from Pennsylvania State University. Dr. Travis has received the NASA Exceptional Scientific Achievement Medal.

NEW TECHNIQUES TO MEASURE THE ELECTRIC FIELD SPECTRUM OF IONOSPHERIC PLASMA TURBULENCE

From the solar corona to Jupiter's magnetosphere to the Earth's ionosphere, plasma turbulence is ubiquitous in solar system space plasmas. The most accessible natural "laboratories" with which to conduct detailed investigations of plasma turbulence and instabilities in space are the Earth's own unstable auroral and equatorial electrojet current systems. Electrojets occur primarily in the altitude range of 95–120 km. The main drivers of electrojet plasma waves are the Farley-Buneman and gradient drift instabilities. The linear growth rate of the former produces mainly meter-scale waves, while the latter creates a broad spectrum of waves, with scales ranging from kilometers to meters. The entire system then undergoes nonlinear wave-wave interactions and develops as a turbulent medium.

Rocket-borne electric field probes provide ideal means with which to study electrojet plasma turbulence. Because the two-stream wave spectrum includes growth at scale lengths of tens of centimeters,

electric field experiments must be designed to measure the true amplitudes of these waves without attenuation. This attenuation is created when the wavelength (λ) is on the order of, or smaller than, the boomlength (d), as seen in the expression of measured potential by an electric field double probe:

$$\phi = \delta \underline{E} \cdot \underline{d} \frac{\sin(\underline{k} \cdot \underline{d}/2)}{(\underline{k} \cdot \underline{d}/2)}$$

where \underline{k} is the wavevector ($k = 2\pi/\lambda$). Thus, instead of the usual requirement that the boomlength be as long as possible, these science objectives dictate that electric field receivers with *short* boomlengths be flown, in order to correctly parameterize the wave amplitudes and spectrum.

To achieve these objectives, a rocket experiment was developed with multiple electric field boom dimensions, as shown in the first figure. Included are boomlengths ranging from 0.6 m to 5.5 m. Not only will several boomlengths enable the wave amplitudes to be discerned, but the situation can be turned around so that the booms are used as spatial filters, enabling the wavelengths to be ascertained. The payload was designed and built at the National Aeronautics and Space Administration's Wallops Flight Facility.

On April 9, 1988, the rocket payload described above was launched from Esrange, Sweden, into a strong auroral electrojet. The rocket flight was almost flawless, and the electric field experiment returned excellent data. A spectrogram of the waves and turbulence detected in the electrojet on the downleg is shown in the second figure. In the two-stream region, the largest wave amplitudes were indeed observed by the shortest booms, confirming the short-wavelength nature of the oscillations. The results influenced several theories about the nature of the Farley-Buneman wave spectrum and its effects on plasma heating and wave-wave interactions.

Another key question involves the phase velocity (V_ϕ) of the waves. Besides theoretical interest in this parameter, knowledge of the phase velocity is essential in order to relate the measured fluctuations to wavenumbers. The predicted two-stream velocities are on the order of the acoustic velocity and/or the $\underline{E} \times \underline{B}$ velocity that may be comparable to typical

rocket velocities. In order to sort out the Doppler shift, which is given by

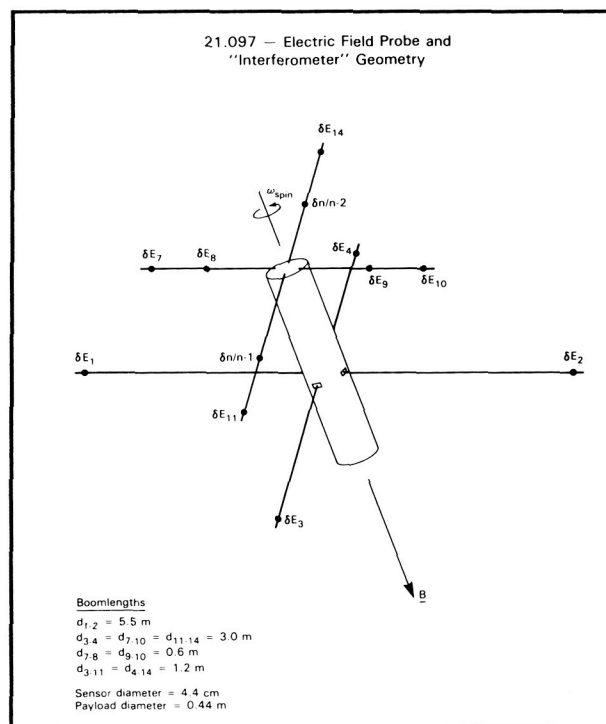
$$\omega_{\text{meas}} = \underline{k} \cdot \underline{V}_{\text{rocket}} \pm \underline{k} \cdot \underline{V}_\phi$$

the same rocket payload was equipped with spaced receivers (sometimes called "interferometers" in the literature) to measure the Doppler-shifted wave velocity in the rocket frame. This was accomplished by spacing the two small (0.6 m) electric field probes along a 2.4 m baseline, in order to measure the phase shift, or time lag, as the waves propagate past the probes. The collected data promise to yield the first rest-frame k spectrum of two-stream turbulence in a space plasma.

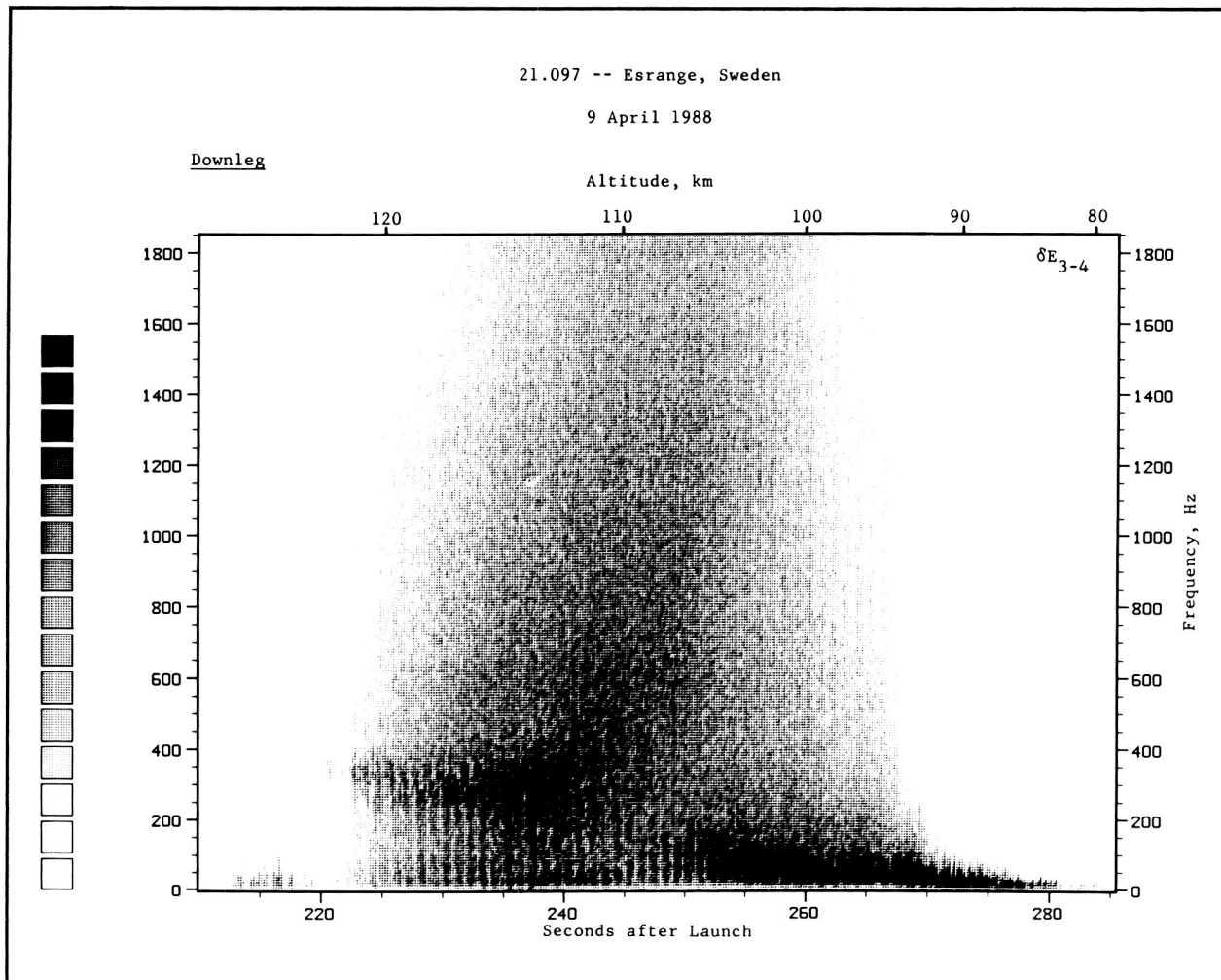
Contact: Robert F. Pfaff, Jr.
Code 696

Sponsor: Office of Space Science and Applications

Dr. Robert F. Pfaff, Jr., works in Goddard's Laboratory for Extraterrestrial Physics investigating



Rocket payload showing multiple electric field boomlengths designed to measure short-scale plasma waves and their phase velocities.



Sonogram showing rocket measurements of plasma wave electric fields in the auroral electrojet over Esrange, Sweden. The grey scale covers over 30 dB of dynamic range with black indicating the strongest amplitudes.

the nature of dc and wave electric fields in space. Dr. Pfaff is especially interested in electric fields, space flight instrumentation, and plasma waves.

THE ZONAL CIRCULATION OF JUPITER AS A CONVECTIVE EIGENMODE

Among the planets in our solar system, Jupiter reveals one of the most intriguing and complex atmospheric circulations observed. In the visible clouds of Jupiter, zonal wind velocities have been traced in ground-based and spacecraft observations. Relative to the rotation of the planetary interior—inferred

from modulation of the magnetic field—zonal wind velocities up to about 100 m/sec are observed. These winds show narrow jets that alternate direction with latitude. The largest and broadest jet is seen in the equatorial region. Such a pattern is also observed on Saturn, but not in any other planetary atmosphere. At the cloud level, Jupiter's atmosphere rotates at a mean rate faster than the planetary interior (super-rotates), a feature common to all planetary atmospheres.

It is instructive to compare Jupiter's circulation with that of Venus. On Venus, the zonal circulation varies slowly with latitude. In the visible clouds, the winds

are also about 100 m/sec; but they do not alternate their direction. They are always positive, and form a broad jet at midlatitudes. Why are the circulation patterns of these two planets so different? Clearly, the differences in size and rotation rate must be important. Venus is rotating slowly, having a 243-day period. Jupiter is much larger and is rotating rapidly in a 10-hour period. But there is a more fundamental difference. Being close to the Sun, Venus' atmosphere is driven entirely by the absorbed solar radiation; its potential temperature tends to increase with altitude (convectively stable). In contrast, Jupiter is far away from the Sun and, somewhat like the Sun, this giant planet is gaseous and emits its own energy, an amount comparable to that received from the Sun. Its potential temperature must decrease with altitude (convectively unstable).

It is suggested that the complex behavior of Jupiter's circulation can be explained as a convective eigenmode.

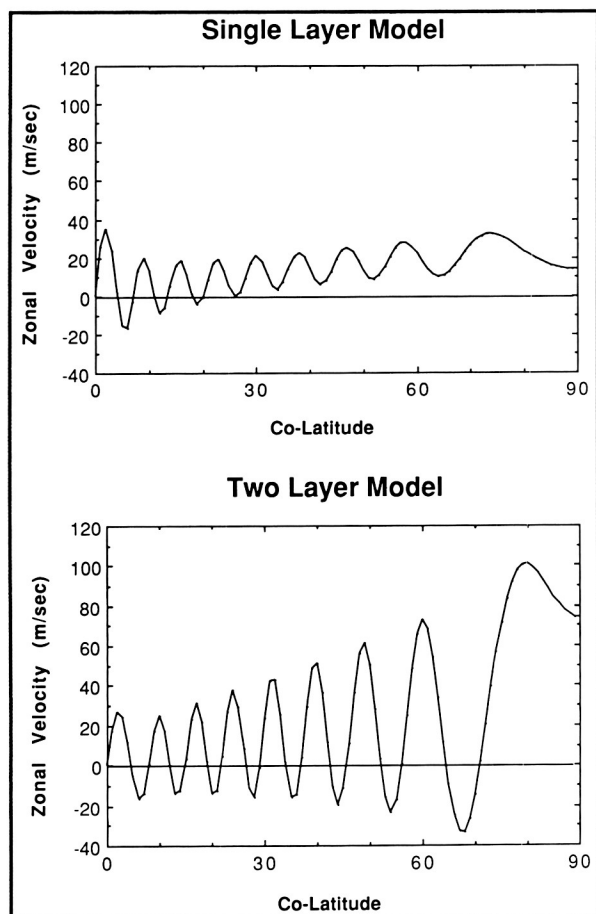
Jupiter's atmosphere is considered as a heat engine driven by solar radiation preferentially absorbed at the Equator. In such an atmosphere, a large-scale meridional circulation is driven, transporting energy and momentum. At the same time, transient eddies develop. The simplifying assumption is made that these eddies tend to dissipate energy and momentum, and can be described in terms of anisotropic eddy-diffusion coefficients. As a result of both transport processes, latitudinal temperature and pressure variations are established that are balanced by the Coriolis force (geostrophic balance); this force requires the large zonal wind velocities that are observed. The question is, how are these temperature (pressure) variations established?

For the atmosphere of Venus, which is convectively stable, the energy advection by the meridional circulation will redistribute (dissipate) the external energy from the Sun. This process tends to go in the same direction as eddy diffusion, providing a stable balance to the external heat source driving these motions.

For the convecting atmosphere of Jupiter, whose potential temperature decreases with altitude, the upward motions (near the Equator, for example) driven by the external source do not remove energy, but instead accelerate the upward flow of energy, causing

heat to accumulate. The two transport processes—diffusion and energy advection—tend to cancel each other, instead of balancing the external heat input. The efficiency of the meridional advection changes with the horizontal-scale size of the circulation. Thus, the critical balance between diffusion and meridional advection will favor a particular scale size, a “convective eigenmode.” Considering the boundary conditions on the globe, such an eigenmode is characteristic of a multicellular meridional circulation, with alternating zonal jets similar to those observed on Jupiter.

Researchers have developed two-dimensional models to describe the Jovian circulation, and this analysis leads to the following conclusions: 1) In a super-adiabatic atmosphere, the energy transported by the meridional circulation can balance the diffusive heat transport. The response to an external heat source is amplified, depending on the latitudinal structure of the circulation. A banded wind field with equatorial jet is then excited, representing a convective eigenmode that has a resemblance to the zonal circulation observed on Jupiter. 2) The latitudinal structure of the circulation depends on the magnitude of the convective instability, estimated to be on the order of $-10^{-1}^{\circ}\text{K/km}$. 3) The observed magnitudes in the zonal wind velocities require that the vertical eddy diffusion coefficient be on the order of $3 \times 10^5 \text{ (cm}^2\text{/sec)}$, which in turn is consistent with the observed outward flux of energy from the planetary interior. This diffusion rate is also of the right magnitude to obey mixing-length theory. 4) The ratio between the adopted horizontal- and vertical-eddy diffusion coefficients is of critical importance. If it is too large ($>>10^5$), differential rotation and superrotation cannot be maintained; if it is too small ($<<10^4$), the Equator tends to corotate. The intermediate value, 5×10^4 , is again consistent with mixing length theory (a conclusion similar to that derived for Venus). 5) With the above constraints on the transport coefficients, the flow is geostrophic, and the meridional winds are much smaller than the zonal winds, consistent with observations. 6) The computed meridional circulation is multicellular, of the Ferrel-Thomson type, with alternating vertical velocities that may be related to the cloud striations observed on Jupiter. 7) In the stratosphere at higher altitudes, an area which is convectively stable, a single Hadley cell develops with positive zonal jets at midlatitudes, resembling the circulation observed on



Computed zonal velocities for one- and two-layer models that apply to an atmosphere which is convectively unstable (Jupiter-like). Note the weak polar vortex in the two-layer model, which comes about because of interference between two different convective eigenmodes that can develop in a deeper atmosphere.

Venus. This analysis suggests that the convective instability of the Jovian atmosphere, required to transport heat out of the interior, is the key ingredient distinguishing its zonal circulation from that of Venus.

This convective eigenmode is characterized by a wind field with alternating zonal jets resembling the observations. However, the model also generates large polar vortices which are not seen. Under geostrophic conditions (which apply to Jupiter), the latitudinal scale length of the circulation depends on the planetary rotation rate, the temperature, and the

potential temperature gradient, and the latter two vary considerably with the depth below the cloud layer. In a recent study, this variation was accounted for with a two-layer model. Researchers show that "superposition" of two convective eigenmodes excited in a deep atmosphere can bring about a cancellation of the large polar vortices that blemished the earlier results. The accompanying figure shows this comparison. The magnitude or absence of high-latitude jets thus may reflect upon the depth of a particular atmosphere, and this may have bearing on the differences between the observed circulations of Jupiter and Saturn. Based on temperature and wind measurements from the Voyager spacecraft (Hanel et al., 1979, 1981), the circulation of Saturn is believed to extend to greater depth than that of Jupiter. In such a case, more mode superposition can occur. Indeed, Saturn's circulation is characterized by a larger equatorial jet and a more rapid fall off in the zonal velocities toward higher latitudes when compared with Jupiter's.

Contacts: Hans G. Mayr, Isadore Harris, and Kwing L. Chan
Codes 610 and 614

Sponsor: Office of Space Science and Applications

Dr. Hans G. Mayr is an atmospheric scientist with the Dynamics Explorer and Pioneer Venus projects. Dr. Mayr, who holds a PhD degree from the University of Graz, has 20 years of experience with Goddard.

Dr. Isadore Harris, who received a PhD degree from Northwestern University, is a planetary astronomer with 28 years of service with Goddard.

Dr. Kwing L. Chan, a computational astrophysicist with Applied Research Corporation, is involved with solar radiation and convection research. Dr. Chan received a PhD degree in physics from Princeton University.

EVOLUTION OF SATURN'S RINGS

The Voyager 1 and 2 Saturn encounters of 1980 and 1981 provided a wealth of information regarding the origin and evolution of Saturn's rings. The ring

system has long been regarded as a relic of the circumplanetary accretion disk that formed out of the primitive Saturn nebula about 4.5 billion years ago. According to this cosmogonic view, the present day rings represent a failed attempt at satellite building, a remnant of a primordial accretion disk that produced no satellites. As such, the rings are regarded as a microcosm of solar system formation, providing a visible example of the accretion disk that formed in the solar nebula from which the planets grew. However, studies of the newly acquired Voyager observations suggest that the rings are relatively young in comparison to the age of the solar system. Thus, an alternate view now gaining acceptance is that the rings are the remains of a recent formation event, such as the catastrophic disruption of an inner satellite. In this view, the rings are evolving quickly, victims of a plethora of erosional processes and dispersive effects.

One such erosion process, studied in detail by Northrop and Connerney, appears capable of eroding the rings on a time scale of a few tens of million years. This mechanism works by removing from the rings small (submicron) bits of ring particles that acquire an electrical charge, becoming confined to motion along magnetic field lines. The particles themselves can acquire a charge in many ways, but it appears that the most likely process involves charging by impact plasma resulting from micrometeorite bombardment of the rings. Once charged, the particles move along field lines under the influence of gravity, centrifugal force, and the magnetic mirror force. The variation of these forces with radial distance in the ring plane leads to separate regions in which these particles behave quite differently. In the innermost region, corresponding to the optically thin C ring, the particles cannot be stably confined to the ring plane. They accelerate along the field line and are ultimately lost in Saturn's atmosphere. In the optically thick B ring at greater radial distance ($r > 1.525 R_s$, $1 R_s = 60,330$ km), however, these charged particles return to the ring plane. The net result is mass loss, or erosion of the rings inward of $1.525 R_s$, and relative stability, or long life, of the rings outward of that boundary. This explains the present day structure of the rings, with a dearth of small particles in the C ring, and the sharp transition to an optically thick B ring just beyond the stability boundary at $1.525 R_s$.

The eroded mass, largely water ice in composition, eventually travels to the planet's surface along magnetic field lines that originate at midlatitudes. The enhanced influx of water at latitudes linked magnetically to the rings is responsible for a cataclysmic depletion of Saturn's ionosphere at these latitudes. Water from the rings may also play an important role in the visible appearance of the planet and the chemistry of the upper atmosphere. Narrow dark bands that appear in Voyager images of Saturn's midlatitudes may be due to the localized depletion of stratospheric hazes by downward diffusing water.

The electromagnetic erosion mechanism is capable of eroding the rings in an estimated 4 to 67 million years. This is consistent with an estimated lifetime of 30 million years, based on the photochemical model of Saturn's ionosphere; a 4 to 20 million year lifetime, based on the radial evolution of the small ring moons; and a 10 to 100 million year estimate, based on atmospheric chemistry. Thus, it appears that the rings are relatively young and evolving quickly compared to the 4.5 billion year old solar system.

Contact: J. E. P. Connerney
Code 695

Sponsor: Office of Space Science and Applications

Dr. J. E. P. Connerney is Co-Investigator for Voyagers 1 and 2, the Mars Observer, and the Tethered Satellite Magnetometer and has received the NASA Medal for Exceptional Scientific Achievement. Dr. Connerney, who received a PhD degree in applied and engineering physics from Cornell University, specializes in magnetospheres, planetary magnetic fields, and geophysics.

IMPULSIVE SOLAR-WIND DRIVEN EMISSION FROM URANUS

On January 24, 1986, the Voyager 2 spacecraft flew by Uranus, providing scientists with the first detailed look at the planet. Analysis by the planetary radio astronomy team members following the Voyager 2 encounter has shown that the planet's emission morphology is complex, more complicated than the Earth's or Saturn's, comparable instead to the rich



emission phenomena seen at Jupiter. It is now recognized that Uranus' magnetosphere supports at least six separate radio components which can be distinguished by their polarization, time variability, and bandwidth. In total, Uranus radio emission covers the band of frequencies from about 5 kHz to 850 kHz.

One of the radio components, in fact the first Uranus emission to be seen—just a few days before encounter—was so unusual in character that analysts raised serious concerns that the signals were not planetary in origin at all, but were only some form of spacecraft-related noise. Subsequent analysis has shown, however, that the signals did indeed originate at Uranus. Goddard Space Flight Center scientists showed that the signals repeated with a periodicity equal to the 17.24-hour period of the planet's rotation, a period that was not known before the encounter took place. The phase of the emission's rotation modulation suggests a probable source for these bursts above the north magnetic polar region, on open field lines. What makes the waves unusual is their extraordinary narrowbandedness. Intense signals occurring at one frequency might not be seen on receiver channels only a few kHz away. Naturally occurring signals with bandwidths of only a few kHz have never been detected previously.

Once the distinguishing characteristics of the bursts were fully appreciated, data records taken well before the encounter were examined for evidence of predisccovery events. Many signals identical in character to the narrowband bursts were found in both the radio astronomy data and in the Voyager plasma wave data. Discovery of events predating the encounter by more than 1 month indicated that the bursts were organized into two major ≈ 10 -day long episodes. One episode occurred just before and up to the time of encounter, and an earlier episode occurred from late December 1985 to early January 1986. These episodes turned out to be simultaneous with times of enhanced solar wind levels at Uranus, giving the first evidence of a solar wind driven radiation at Uranus. It is hoped that further analysis of these signals will provide information on the nature of the solar wind interaction with a highly unusual planetary magnetosphere.

Contacts: Michael D. Desch and
Michael L. Kaiser
Code 695

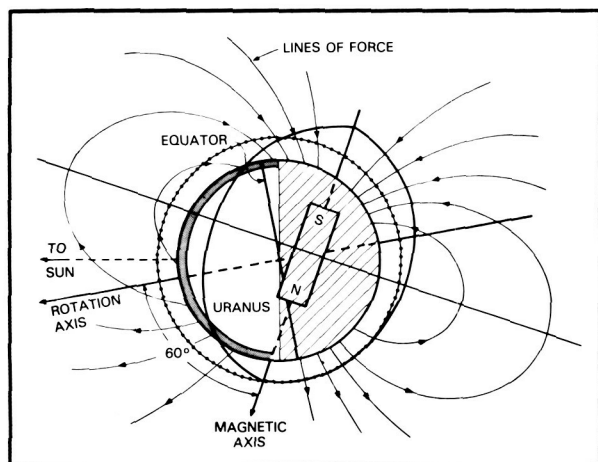
Sponsor: Office of Space Science and
Applications

Dr. Michael D. Desch is involved in the analysis of Voyager spacecraft radio astronomy data of Jupiter, Saturn, and Uranus. Dr. Desch received a PhD degree in astronomy from the University of Florida, and he has been with Goddard for eight years.

Mr. Michael L. Kaiser, who analyzes Voyager data from the outer planets, is ISTP Project Scientist for Data Systems. He holds an MS degree in astronomy from the University of Maryland. In his 19 years at Goddard, Mr. Kaiser has received an Exceptional Scientific Achievement Award and an award for saving Goddard over \$1,000,000 in costs.

A LOWER UPPER ATMOSPHERIC TEMPERATURE AT NEPTUNE

Jupiter, Saturn, and Uranus all share a common characteristic: temperatures in the uppermost parts of their atmospheres, their exospheres, by far exceed what we would expect on the basis of solar heating alone. Instead of recording exospheric temperatures in the 200–300° K range, the Voyager spacecraft observed temperatures in the 800–1000° K range. One hypothesis explaining these anomalously high exospheric temperatures is that the precipitation of energetic particles from the planetary magnetospheres into the planets' auroral zones provides the heating source. The estimated amounts of precipitation appear sufficient to explain the high exospheric temperatures of Jupiter and Saturn. However, the exospheric temperature of Uranus cannot be explained by auroral precipitation alone. There is not sufficient energy available, a shortfall of about an order of magnitude. An additional source of heating at Uranus is due to the offset and tilt of the magnetic field, shown the accompanying figure. Unlike Jupiter and Saturn, where the magnetic field dipoles (shown as the bar magnet in the figure) are tilted only at small angles with respect to the axes of rotation, and are approximately centered in the planets, Uranus possesses both a large tilt and offset. Hence, particles that mirror freely on the nightside of Uranus are rapidly lost as they drift to the dayside.



The offset, tilted magnetic field of Uranus. The bar magnet shows the location of the equivalent dipole magnetic field. The hatched region indicates the Uranus nightside. The football-shaped solid line perpendicular to the magnetic lines of force indicates the mirror positions of trapped particles. Note that trapped particles that mirror well above the nightside atmosphere appear deep in the atmosphere as they drift to the dayside.

Such a magnetic field configuration is most likely unique to Uranus; Neptune will not have this additional source of heating, and will only have auroral input. Since the magnetic field of Neptune is expected to be similar in strength to that of Uranus, the auroral energy input will also be similar, and, like the auroral input at Uranus, will be too weak to maintain a high exospheric temperature. As a result, the Neptune exospheric temperature is expected to be only about 200 °K, as compared with 800 °K at Uranus.

A direct consequence of the expected low exospheric temperature on Neptune is that electroglow, the anomalously intense ultraviolet radiation observed at Jupiter, Saturn, and Uranus, may be suppressed at Neptune. This conclusion is based on the temperature dependence of the processes that are presently believed to underlie electroglow. To date, observations of Neptune made by the International Ultraviolet Explorer indicate that electroglow at Neptune is much weaker than that at Uranus, if indeed it exists at all.

Contact: Steven A. Curtis
Code 695

Sponsor: NASA Program for Research in Planetary Atmospheres

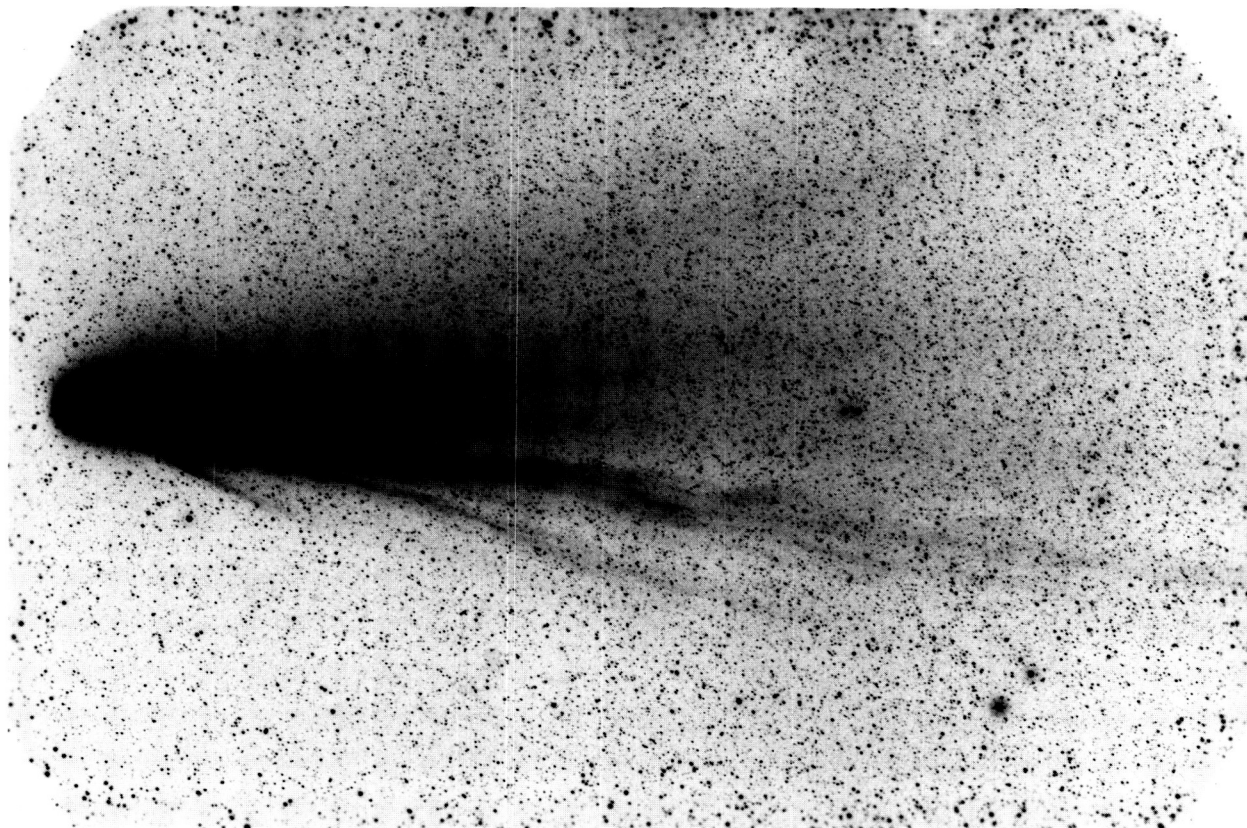
Dr. Steven A. Curtis, who holds a PhD degree from the University of Maryland, is branch head of the Planetary Magnetospheres Branch at the Laboratory for Extraterrestrial Physics. He is particularly interested in the coupling of planetary atmospheres and magnetospheres. Dr. Curtis received an Exceptional Achievement Award for the correct prediction of Uranus' nonthermal radio emissions.

ARCHIVING OF WIDE-FIELD IMAGES OF HALLEY'S COMET

Although Halley's Comet has receded to such a large distance from Earth as to render it invisible to all but the largest telescopes, interest in the comet continues at a very high level. Questions concerning the rotation of the 15-kilometer icy nucleus and about the physics of plasma tails tens of millions of kilometers long (to name but two areas of scientific inquiry) remain incompletely answered. Perhaps the primary reason for this state of affairs is that the Halley data, taken both on the ground at hundreds of observatories worldwide, and by the international Halley spacecraft, are so voluminous as to require years to digest and analyze fully.

The International Halley Watch (IHW) is a National Aeronautics and Space Administration (NASA)-sponsored program that has as its goal the creation of a permanent archive containing as much ground- and space-based Halley data as possible. Such an archive would represent a uniquely large and complete source of data with which to answer scientific questions about comets in general, and Halley specifically.

The IHW consists of eight distinct worldwide networks, or disciplines, each of which represents a different method of observing comets. NASA/Goddard Space Flight Center is the center of the Large-Scale Phenomena (L-SP) Discipline, whose data type is wide-field (usually photographic) imagery. The principal scientific target of interest to this discipline is the interaction of cometary plasma tails with the solar wind, and in particular the mechanisms by which transient disturbances such as "disconnection events" occur.



Spectacular plasma tail and prominent ray activity are apparent in this March 16, 1986 photograph of Halley's Comet taken on Easter Island by William Liller.

The accompanying photo shows plasma, one of two types of cometary tails (the other being dust), which is composed of ionized molecules such as carbon monoxide and water spiraling around magnetic field lines captured from the solar wind. The solar wind itself is a very tenuous, hot supersonic gas continuously flowing out from the Sun, and the magnetic field it contains is primarily responsible for the formation of plasma tails. Because the solar wind and its magnetic field are highly structured, the plasma tails of comets exhibit variable behavior. The objective of plasma tail/solar wind studies is to understand what features in the solar wind are responsible for the different classes of plasma-tail structures.

At the present time, the L-SP Discipline Team has received over 2000 images from 50 observatories around the world; the best of these are being converted to digital form by a process known as micro-

densitometry. These digital images will later be deposited on video compact disks (CDs), along with the digital data resulting from the other seven disciplines. At present, about 20 CDs are envisioned as necessary to store all the IHW data. Copies of this CD library will be sent to the hundreds of observers worldwide who contributed the data.

Contact: Malcolm B. Niedner, Jr.
Code 684

Sponsor: Office of Space Science and Applications

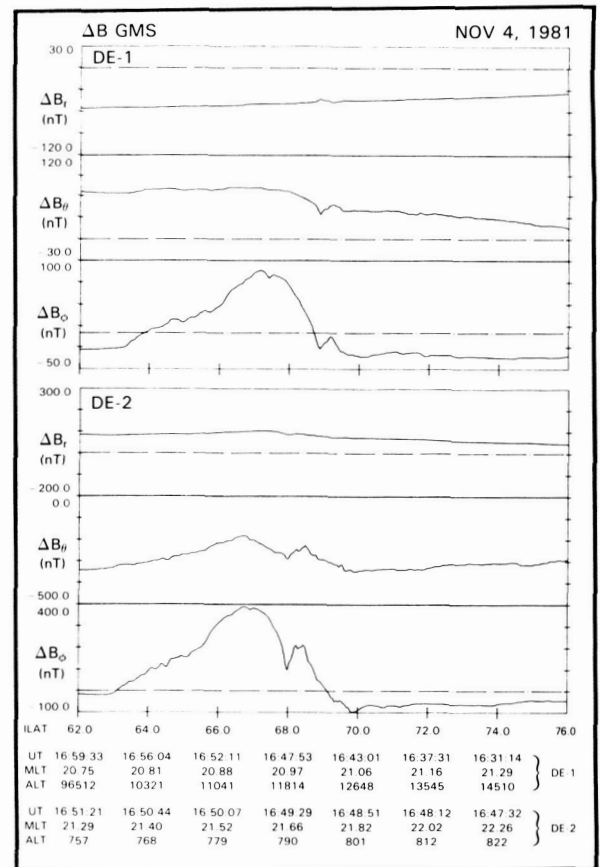
Dr. Malcolm B. Niedner, Jr., an astrophysicist with the Laboratory for Astronomy and Solar Physics, has received two Outstanding Performance Awards at Goddard. He works on cometary plasma/solar-wind problems, also archiving wide-field images for the International Halley Watch.

MULTIPOINT MEASUREMENTS OF FIELD-ALIGNED CURRENTS IN THE EARTH'S MAGNETOSPHERE: DYNAMICS EXPLORER-1 AND -2 OBSERVATIONS

The interaction of the solar wind with the geomagnetic field gives rise to the Earth's magnetosphere, a large, blunt-nosed, cylindrical magnetic cavity (terminal diameter is equal to 60 Earth radii) containing highly time-varying and spatially structured regions of high- and low-beta plasma (beta is equal to the ratio of thermal to magnetic pressures). The low electrical resistivity along magnetic lines of force embedded in collisionless space plasmas gives rise to a situation wherein large amounts of energy can be transferred from high altitudes (10^4 – 10^5 km) within the magnetosphere down to the ionosphere (altitude $\sim 10^2$ km) through field-aligned currents, (FACs). First detected by magnetometers on low, earth-orbiting spacecraft in the late 1960s, the Poynting flux of electromagnetic energy associated with these currents (total $J = 10^6$ A; total $P = 10^{11}$ – 10^{12} W) is believed to be the principal energy source for the anti-sunward motion of ionospheric plasma and thermospheric winds at high latitudes.

A primary science objective of the Dynamics Explorer (DE) mission is to investigate the relationship between electric fields, currents, and charged particle motion over the altitude range of 10^2 – 10^4 km. For this purpose two spacecraft, DE-1 and DE-2, with apogees of 23,000 and 1,000 km, respectively, were launched into coplanar polar orbits. Using the magnetometers on these two spacecraft, it has been possible to examine the altitude dependence and, in some cases, the time dependence of FACs, as illustrated in the accompanying figure. The upper and lower sets of panels display the DE-1 and DE-2 magnetic field measurements, respectively, as a function of invariant latitude (ILAT) for a crossing of the nightside auroral oval on November 4, 1981 (i.e., ILAT = 63–70°). The coordinate system is based upon a dipole model of the Earth's magnetic field, with positive B_r directed outward, B_θ positive toward the south, and B_ϕ (the east-west component) completing the right-handed system. The delta in front of each quantity indicates that a Magsat reference field model has been subtracted from the DE observations.

The perturbation fields shown in the figure are associated with currents flowing exterior to the Earth. They display very similar features at both DE-1, altitude 10,000–13,000 km, and DE-2, altitude 750–800 km. The nature of the electrical currents can be deduced from examination and modeling of the magnetic field measurements. As shown, there is essentially no radial, and only very weak north-south perturbation magnetic fields. Application of Maxwell's equations ($\text{curl } \mathbf{B} = \mathbf{J}$) indicates that the electrical current must, therefore, flow predominantly along the geomagnetic field lines (i.e., having large-ly radial direction at these altitudes) to produce the



Dynamics Explorer-1 and -2 magnetic field measurements (after subtraction of a Magsat reference field) are displayed for an evening passage through the auroral zone. The field coordinates are Geomagnetic Spherical (GMS) and the units are nanotesla (nT). For both spacecraft, high time field measurements (16 samples/sec) have been averaged into 0.05°-wide invariant latitude bins.



strong 10^2 – 10^3 nT east-west perturbation magnetic fields observed. Hence, the term “field-aligned” is indeed appropriate for these currents. The observations charted in the figure are typical in that they indicate the downward/upward flow of current on the low/high latitude side of the auroral zone for this evening sector pass. However, they are remarkable in that the two spacecraft were magnetically conjugate (i.e., simultaneously occupying the same magnetic flux tube, at different altitudes) at the time of the FAC observations.

Recent examination of conjugate FAC measurements by the Dynamics Explorer-1 and -2 Magnetometer Experiments has shown that: 1) FAC spatial structure as a function of invariant latitude is frequently altitude independent (e.g., the November 4 case displayed in the figure); 2) FAC current sheet intensity decreases with altitude as $r^{-3/2}$, consistent with conservation of total current within a given flux tube; and 3) individual FAC events can be time-stationary over intervals at least as long as 10 minutes, and highly variable on scales at least as short as several minutes. Ultimately, these findings may contribute significantly to the final description of how the solar wind and magnetosphere combine to drive the many auroral electrodynamic phenomena observed at high latitudes.

Contact: James A. Slavin
Code 696

Sponsor: Office of Space Science and
Applications/Space Physics Division

Dr. James A. Slavin, who received his PhD degree from UCLA, currently works in Goddard's Laboratory for Extraterrestrial Physics. Dr. Slavin is the lead Co-Investigator for the Dynamics Explorer Magnetometer investigation, and Co-Investigator for several other Magnetometer investigations, among other duties.

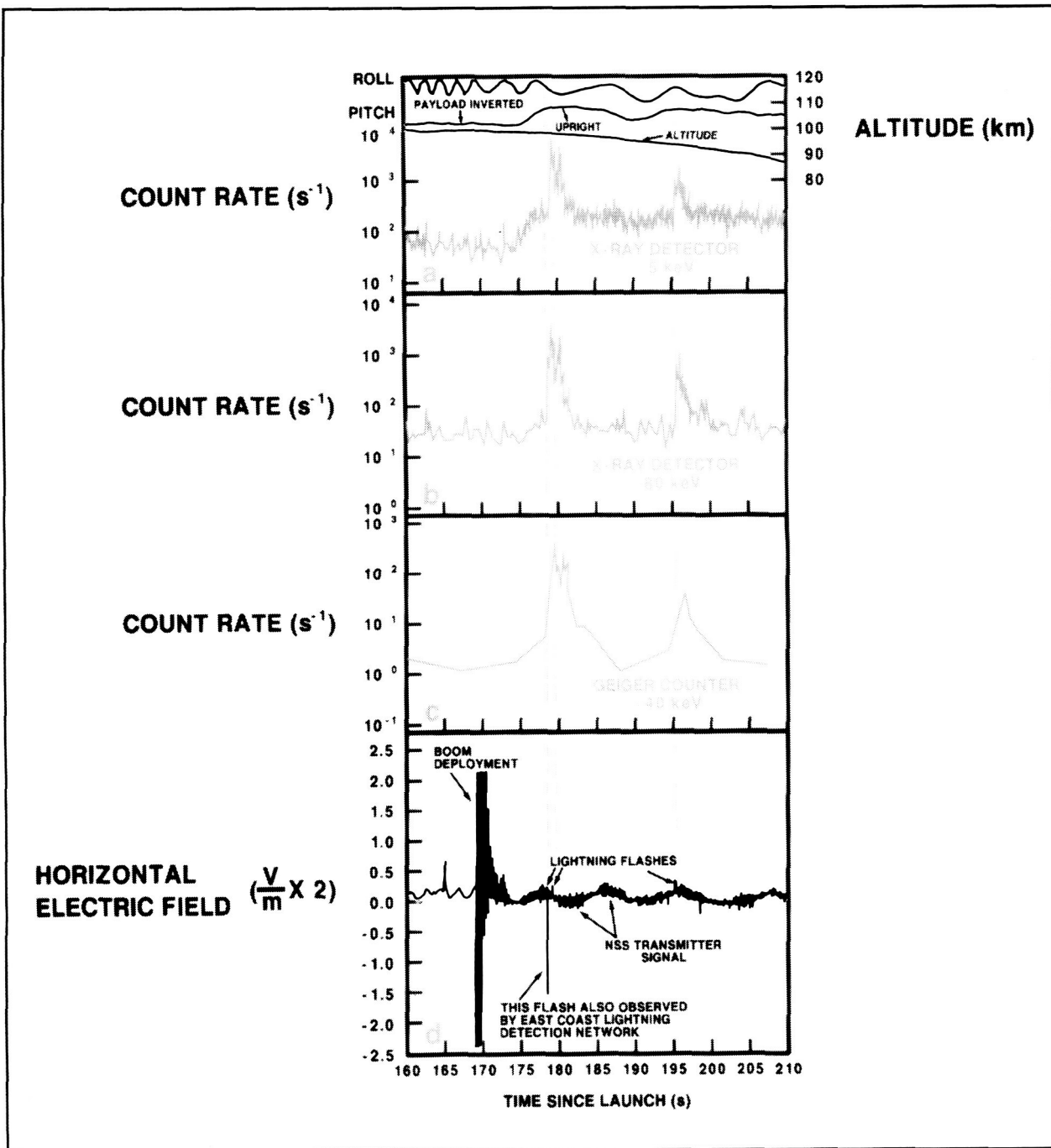
MAGNETOSPHERIC ELECTRON BURSTS INDUCED BY LIGHTNING

Radio waves, particularly in the Very Low Frequency (VLF, 3–30 kHz) range, are capable of inducing magnetospheric electron precipitation. Because of the possibility that this electron precipitation might alter

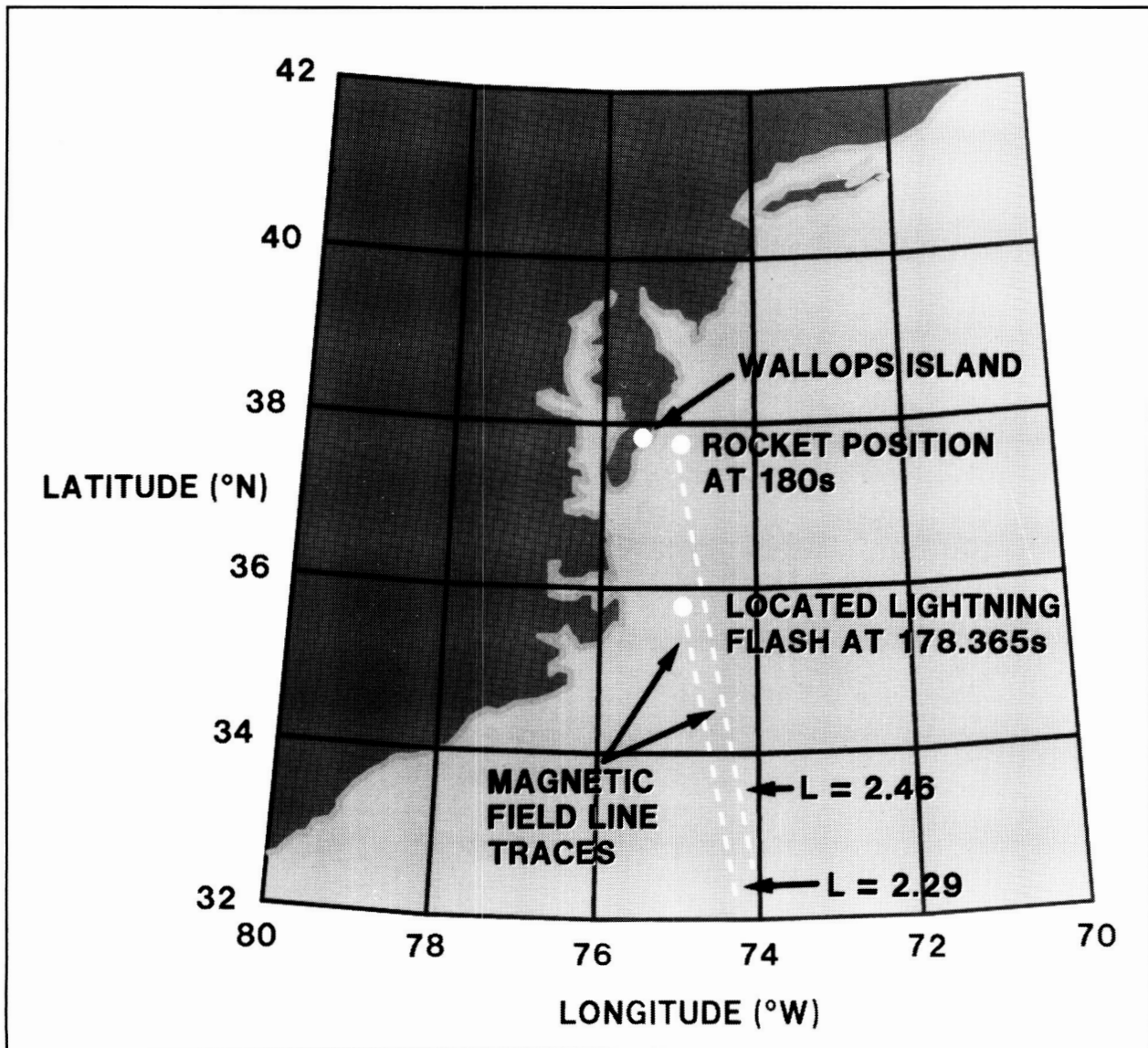
the lower ionosphere, thus affecting the propagation of radio waves used in communications and satellite control, the role of lightning as a VLF radio source for electron precipitation in the magnetosphere has been the subject of numerous theoretical and experimental studies during the last 2 decades. On a global basis, lightning is a frequently occurring phenomenon. At any instant of time, approximately 2000 storms are in progress, each producing a lightning flash every few seconds, or about 100 flashes per second worldwide. According to theory, the lightning produces VLF radio waves that travel to the base of the magnetosphere, where they can then be ducted along magnetic field lines toward the Earth's magnetic equator. Upon arrival at the magnetic equator, most theories predict that these waves, commonly referred to as whistlers, can alter the loss cone for high-energy electrons attempting to escape from trapping in the magnetosphere through a process known as electron cyclotron resonance. When caused by lightning flashes, the induced electron precipitation should appear as pulses of electrons, detectable in the upper atmosphere by various platforms such as satellites and rockets.

There is currently an active experimental program using sounding rockets to study the electron precipitation, to evaluate the magnetospheric wave/particle interactions, and to ascertain how lightning-induced VLF waves reach the base of the ionosphere for conversion to whistlers. The first and only direct observation of electron pulses induced by known lightning flashes occurred off the coast of Wallops Island, Virginia, on a Nike-Orion rocket payload flown in August 1984. The first figure (panels a, b, and c) shows three separate lightning-induced electron pulses, as observed by two channels of a zenith-viewing x-ray scintillator detector also sensitive to energetic electrons, and simultaneously by a side-mounted Geiger tube detector. These electron pulses were observed at altitudes above 90 km, where atmospheric absorption of the detected energetic electrons (>135 keV) is not a serious problem. Also shown (panel d) are the lightning flashes responsible for the electron pulses as measured by electric field probes on the same payload.

Through comparisons with data provided by the East Coast Lightning Detection Network, it was determined that the lightning flash responsible for the first observed electron pulse was a large cloud-to-ground



(a) Scintillator ($<5 \text{ keV}$ energy loss channel) count rates (left scale) versus time from 160 seconds to 210 seconds after liftoff. The trajectory (right scale) and payload aspect (arbitrary units) are also given. The pitch angle is used to indicate when the payload is in an upright position following a parachute deployment; (b) Scintillator ($<80 \text{ keV}$ energy loss channel) count rates for the same interval; (c) Geiger tube count rates for the same time interval; (d) Horizontal electric field for the same time interval showing lightning flashes under consideration.



Map of the East Coast of the United States, showing locations of Wallops Island, Virginia, the located lightning flash at 178.365 seconds after rocket liftoff, and the payload position at nearly the same time. The magnetic field line traces intercepting the payload and the lightning position at 100 kilometers are also indicated.

flash located approximately 200 km southeast of the payload. The precise time and location of the lightning flash (cf. the second figure), coupled with the high time resolution of the data (0.5 msec) permitted a detailed analysis of this event. This verified the interaction described by the electron cyclotron resonance process through kinematics describing the wave and particle transit times to and from the magnetic equator; it also provided the first experi-

mental evidence for a second, highly competitive process probably involving magnetospheric acceleration mechanisms.

Additional rockets were launched from Wallops Island in 1985 and 1987 with the intention of isolating and describing the newly discovered "acceleration" process. These flights were launched with more sensitive detectors into a more favorable thunderstorm

environment, within which large quantities of lightning were observed in close proximity to the payload. Furthermore, the payloads reached much higher apogees, permitting energetic electron observation times of nearly 5 minutes in comparison to the 20-second observation time on the first flight. In spite of the more ideal conditions for these latter flights, no further observation of large electron bursts associated with individual lightning flashes has been observed during these or other rocket flights.

The question of whether or not lightning generates electron precipitation on a regular basis can now be answered through the latest analyses of the available data. On the most recent flight launched from Wallops Island in July 1987, measurement was made of the timing configuration of electron counts following a lightning flash, as determined through the signal-to-noise averaging of electron count data from 43 independent lightning-induced events. A similar analysis was performed on data acquired on the early flight reported above, but at a time following the period of large electron bursts. During both of these periods, electron precipitation was too weak to be observed on an individual event basis; however, the accumulated time sequences of electron count rates were found to compare favorably with the single-event patterns observed during the large electron bursts discussed above. The similarity among the signatures for counts versus time in this comparison provides convincing evidence that electron precipitation occurs following every lightning event; however, in most cases it is simply too weak to be observed with current measurement techniques. A null result would have implied that the process only occurs under very specialized conditions, which would have been far more difficult to understand.

There are several problems relating to future progress in this research. First, researchers must determine under what conditions the very large electron bursts are generated, a determination critical to the design of future experiments. Second, researchers must design new detectors capable of observing the details of even the weak bursts, an understanding of which is probably required to answer the first question.

Contacts: Richard A. Goldberg and
Steven A. Curtis
Codes 696 and 695

Sponsor: Office of Space Science and
Applications

Dr. Richard A. Goldberg studies solar-terrestrial relationships at the Laboratory for Extraterrestrial Physics. His study emphasizes middle atmospheric electrodynamics and coupling processes. He also has been Principal Investigator for more than 50 rocket payloads. Dr. Goldberg, who holds a PhD from Pennsylvania State University, has received several achievement awards. He has 25 years of experience at Goddard.

Dr. Steven A. Curtis, who holds a PhD degree from the University of Maryland, is branch head of the Planetary Magnetospheres Branch at the Laboratory for Extraterrestrial Physics. He is particularly interested in the coupling of planetary atmospheres and magnetospheres. Dr. Curtis has 20 years of experience at Goddard, and he received an Exceptional Achievement Award for the correct prediction of Uranus' nonthermal radio emissions.

ELECTRODYNAMIC PATTERNS IN THE POLAR REGION DURING PERIODS OF EXTREME MAGNETIC QUIESCENCE

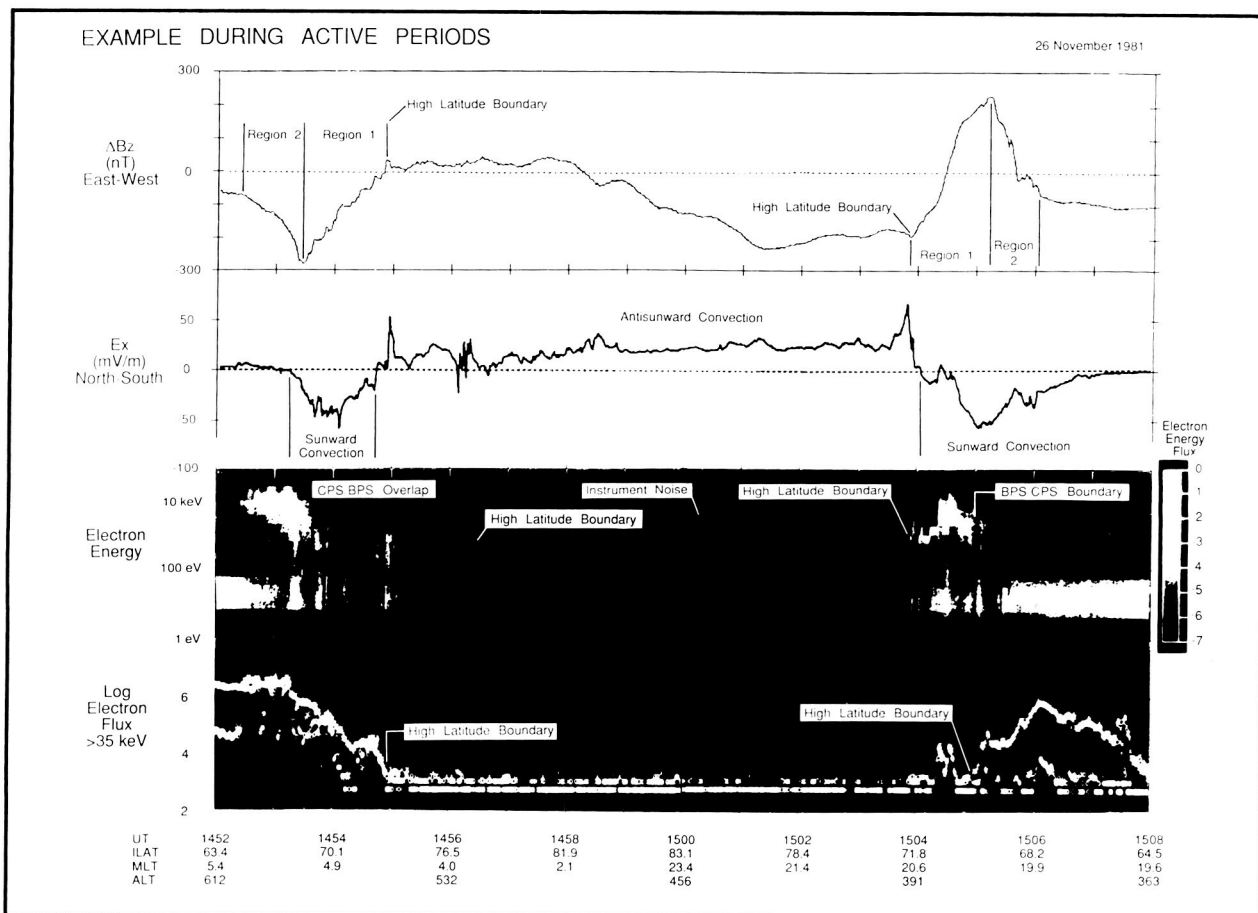
Electrodynamic patterns in the Earth's polar regions at ionospheric altitudes during periods of extreme magnetic and auroral quiescence are considerably different from those that are observed during periods of magnetic and auroral activity. Data published from instruments on low-altitude polar-orbiting satellites have generally pertained to the latter periods because of the difficulty which scientists experience in identifying truly quiescent conditions.

In the past, analysis of magnetograms from ground magnetic observatories has provided good indications of periods of low-level magnetic activity. However, the distribution of these observatories over the polar region is insufficient to positively identify periods of extreme quiescence. Now, with the availability of global auroral images from the spin-scan auroral imager flown on the Dynamics Explorer-1 (DE-1) satellite, by Dr. Louis A. Frank of the University of Iowa, scientists have been able to identify periods of extreme auroral quiescence that also had extremely low levels of magnetic activity.



To contrast the differences in electrodynamic patterns over the polar region between active and quiet periods, the first figure shows data from a pass of the Dynamics Explorer-2 (DE-2) satellite across the polar region during a period of magnetic activity. In this dawn to dusk pass, the top panel contains the east-west component of the perturbation magnetic field (measured field minus model Earth's field). The gradients near each end of the panel (slightly below 70° invariant latitude—ILAT) are due to large-scale electric currents along the magnetic field lines. The region 1 current on the dawn side is downward, the region 2 current is upward, with opposite polarities on the dusk side. The second panel contains the north-south component of the electric field, which indicates the direction of the convection of the ionosphere (the convection is perpendicular to both

the electric field and magnetic field). A classical two-cell convection pattern is observed from the dayside to nightside over the polar cap, with return flow (sunward convection) at auroral latitudes. The third panel contains an electron spectrogram showing the energy flux of electrons precipitating into the atmosphere as a grey scale versus log energy from 5 eV to 30 keV as a function of time. At dusk, a typical electron precipitation structure was observed—an inverted-V—characterized by an intensity maximum (upper whitish band) that rises in energy to 10 keV and then falls. It is generally thought that these electrons are accelerated by an electric potential along the magnetic field. These electrons are important charge carriers of the dusk side region 1 field-aligned current. On the dawn side, at the lowest latitudes, electrons of energies extending above 30 keV typically



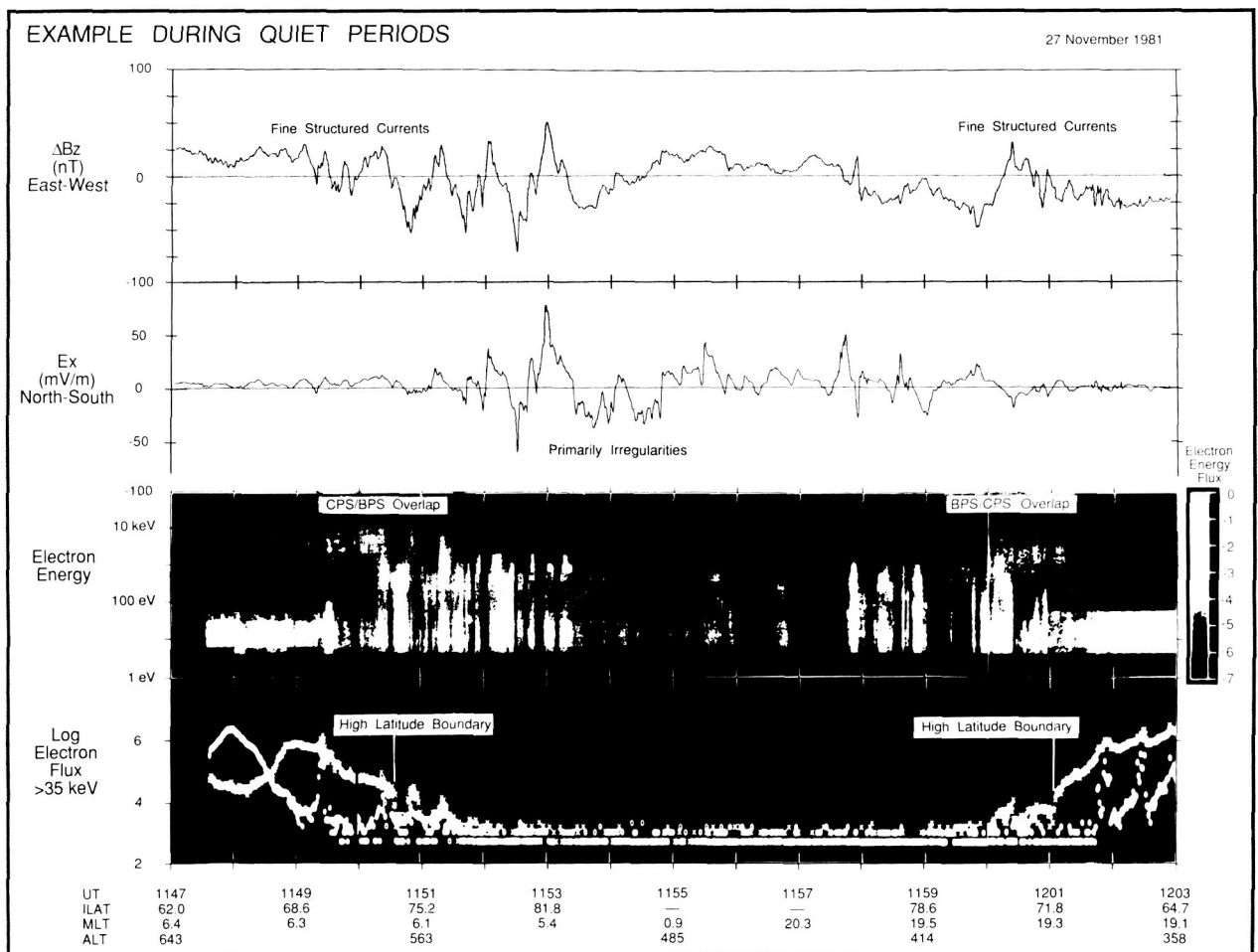
Data from the Dynamics Explorer-2 satellite in a dawn (left) to dusk (right) pass in late November 1981, during a period of magnetic activity. UT is universal time, ILAT is the invariant latitude, MLT is magnetic local time, and ALT is the altitude of the satellite in km. The data panels are explained in the text.

precipitate in a rather structureless band, followed at higher latitudes by highly structured, usually very narrow inverted-Vs. Over the polar cap, no electron precipitation occurred with energies above 100 eV, except for one weak structure between 1501 and 1502 UT. The bottom panel shows electron fluxes with energies above about 35 keV.

The second figure contains the same types of data from a pass of DE-2 during an extremely quiet period. No large-scale pattern of field-aligned currents is observed in the magnetic field data. (Note that the scale is 100 nT, compared to 300 nT in the first figure.) Instead, fine structure existed with every negative gradient on the dusk side (and with every positive gradient on the dusk side) associated with

an electron precipitation structure. The electric field also shows no large-scale convection cells, but merely an irregular pattern. Electron precipitation extended all across the polar cap.

From a statistical study based on data from a large number of DE-2 passes transiting all local times, the following characteristics were found in the electrodynamic patterns of the auroral and polar cap region during periods of extreme quiescence: the large-scale, field-aligned current system breaks up into small-scale structures distributed through the auroral oval, and over the entire polar cap. Convection patterns are always found in the summer hemisphere (although with large amplitude irregularities superimposed), but the probability of their existence



Data from the Dynamics Explorer-2 satellite taken the next day, during a period of extreme magnetic and auroral quiescence.

• ORIGINAL PAGE IS
OF POOR QUALITY



decreases significantly in mid-winter. Structured electron precipitation extends over the entire polar region independent of season.

Finally, it was found that during these periods of extreme magnetic quiescence, the interplanetary magnetic field, as measured by either the Interplanetary Monitoring Platform-8 (IMP-8) or International Sun Earth Explorer-3 (ISEE-3) spacecrafts, had a northward component, and a high probability of a sunward direction in the component in the magnetic equatorial plane. Such a direction of the interplanetary field produces a minimum area on the magnetopause (the boundary between the Earth's magnetic field and the interplanetary magnetic field), where the two fields are oppositely directed. Oppositely directed fields are thought to allow merging of the two fields, and, therefore, energy transfer from the solar wind to the magnetosphere. The lack of energy being injected into the magnetosphere during these quiet periods is, then, the apparent reason for the disappearance of the large-scale electrodynamic patterns seen during active periods. Large amounts of energy are required to drive the large-scale, field-aligned currents that close in the ionosphere and heat the upper atmosphere through Joule heating, and to accelerate the electrons that plunge into the atmosphere.

Contact: Robert A. Hoffman
Code 696

Sponsor: Office of Space Science and
Applications

Dr. Robert A. Hoffman, Project Scientist for the Dynamics Explorer Project, and Assistant Head of Goddard's Electrodynamics Branch, is interested in coupling between the magnetosphere, ionosphere, and the upper atmosphere. Dr. Hoffman, has received several NASA and Goddard honors.

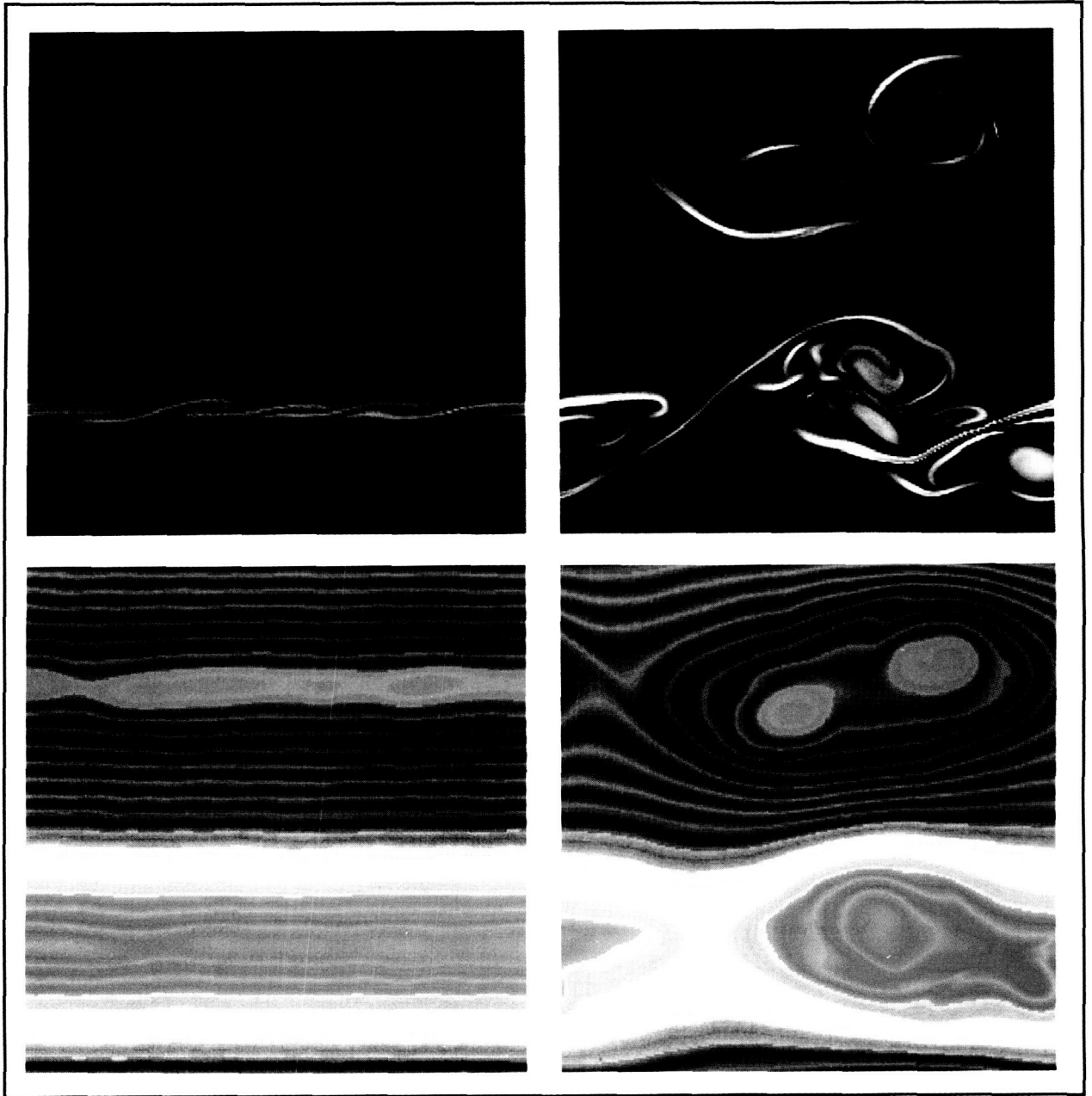
GENERATION OF TURBULENCE IN MAGNETOFLUIDS BY VELOCITY SHEAR

Turbulent magnetic and velocity fields are often observed in interplanetary space as well as in planetary magnetospheres. Twenty years ago, P. Coleman noted that in the solar wind there was a large source of free energy available to generate tur-

bulence, namely, the large velocity difference between fast and slow streams. He conjectured that the Kelvin-Helmholtz instability could be driven by the velocity shear and that the subsequent nonlinear development of the instability could give rise to the observed turbulence. Recent studies in Goddard Space Flight Center's (GSFC) Interplanetary Physics Branch by D. A. Roberts, M. L. Goldstein, W. H. Matthaeus (Bartol Institute), and L. W. Klein tend to support Coleman's hypothesis. Observations of the Earth's magnetotail primarily carried out by E. Hones and colleagues at Los Alamos show evidence of large-scale vortical flows reminiscent of those expected from a Kelvin-Helmholtz instability operating at the magnetopause boundary between the relatively slow-moving magnetospheric plasma and the faster moving magnetosheath plasma.

During the past several years there have been several studies of the Kelvin-Helmholtz instability that have explored both the linear and nonlinear stages of its development. However, to investigate the generation of turbulence, one must not only explore the nonlinear stages of the instability, but one must also be able to compute accurately small-scale structures because power spectra of turbulent fluctuations typically have rather steep spectral slopes as wave number increases (spatial scales decreasing). GSFC researchers and their collaborators have developed computer codes which permit study of the turbulent evolution of the Kelvin-Helmholtz instability in two dimensions by solving either the incompressible or compressible equations of magnetohydrodynamics. To date, the most detailed studies have been carried out using solutions of the incompressible equations. To ensure accuracy, researchers chose as the algorithm a spectral method which employs Fourier transforms to solve the equations in a periodic square domain. The objective at this stage of the research is to understand the fundamental physics of the Kelvin-Helmholtz instability and the evolution of the ensuing turbulence without the complications of more realistic boundary conditions, which would require the use of a rather different algorithm.

Shown in the figure are results from one of the computer simulations. The figure shows the stream lines Ψ , and the vorticity ω (where $\omega = \text{curl } \mathbf{v}$, and \mathbf{v} is the fluid velocity). The left-hand panels show the state of the fluid after only one eddy-turnover time.



The figure illustrates solutions of the two-dimensional incompressible equations of magnetohydrodynamics. The left-hand panels show the state of the magnetofluid after one eddy-turnover time, while the right-hand panels show a late stage of nonlinear evolution (4.5 eddy-turnover times). A false-color logarithmically scaled representation of the vorticity is shown at top (a and b). The bottom panels (c and d) show a false-color representation of streamlines. The nonlinear development results from the strong velocity shear evident in panel a.



On the right, the fluid is shown after 4.5 eddy-turnover times. The vorticity is shown on top, and the stream function on the bottom. There is a strong velocity shear between the fluid in the central half of the periodic domain and the fluid in the top and bottom quarters of the domain. The magnetic field is relatively weak in the center of the box. Consequently, because of the absence of any strong stabilizing effects of a magnetic field, the Kelvin-Helmholtz instability is expected to evolve rapidly in the center of the simulation domain. This evolution is evident in the right-hand panels, which show very complex well-developed vortical structures developing in the region of weak magnetic fields. There is also a strong tendency of the vortices to pair. The distorted shapes of the vortical structures are significant and reflect the accuracy of the code in computing small-scale structures at relatively high magnetic and kinetic Reynolds numbers (1000 in this example).

This work is presently being extended to include effects of compressibility. The simulations were run on GSFC's Cyber 205 using support provided by Code ES at the National Aeronautics and Space Administration Headquarters.

Contact: Melvyn L. Goldstein
Code 692

Sponsor: Office of Space Science and Applications

Dr. Melvyn L. Goldstein, Co-Principal Investigator for the Solar Terrestrial Theory Program and Deputy Project Scientist for the Cluster Mission, has 16 years of experience at Goddard. Dr. Goldstein, who holds a PhD degree from the University of Maryland, has received a Special Achievement Award for his work.

FITTING OF THE FIELD IN A MAGNETIC CLOUD USING LEAST SQUARES

Magnetic clouds observed in the solar wind are large-scale plasma and field objects having locally cylindrical field line symmetry, enhanced magnetic field strength, and lower plasma temperature than the surrounding plasma. Their cross sections at 1 AU can have diameters as large as $\frac{1}{2}$ AU, but are typically $\frac{1}{4}$ AU or smaller. Trial and error solutions to the magnetic field structure of a cloud for various cases have been found successfully. However, this method

is time consuming, and does not necessarily generate an optimum solution. Presented here is a quantitative scheme for fitting a cloud's observed field to a model developed by Burlaga in 1988, which assumes that a cloud is magnetic force-free; the trial-and-error solutions were carried out with the same model.

For a magnetic force-free configuration, the current density in the cloud is proportional to the field everywhere (i.e., $\mathbf{J} = \alpha \mathbf{B}$, giving $\nabla \times \mathbf{B} = \alpha \mathbf{B}$). If α is constant through the cloud, which the Burlaga model assumes, then $\nabla^2 \mathbf{B} = -\alpha^2 \mathbf{B}$. In a cylindrical coordinate system, solutions to this equation are:

$$B_A = B_0 J_0(aR), \quad B_T = B_0 H J_1(aR) \\ \text{and } B_R = 0$$

where B_A is the component of the magnetic field along the axis of the cloud, B_T is the component in the azimuthal direction, B_R is the radial component, J_0 and J_1 are Bessel functions of the zero-th and first order, R is the distance from the cloud's axis, $H = \pm 1$ determines the handedness of the field, and B_0 and a are constants.

The purpose is to obtain (in some sense) optimum fits of field data to the solutions given above, which involves finding the cloud's inclination, scale size (a), strength (B_0), and distance from the observing spacecraft at closest approach using variance and least squares techniques. By simulating the magnetic field of various typical clouds of different inclinations, it was shown that, usually within about 7° (often less), the maximum, intermediate, and minimum variance directions aligned with special cloud axes. By definition, the maximum (minimum) variance direction of the field is that direction along which the field varies the most (least) over the interval of interest. The intermediate direction is perpendicular to both the maximum and minimum variance directions. For the simulated clouds, the intermediate variance direction was nearly aligned with the cloud's axis, and the maximum variance direction was nearly perpendicular to the plane formed by the cloud's axis and the spacecraft trajectory. This finding significantly aids in the fitting procedure described below.

When the actual field within a cloud was compared to the Burlaga model field, it was seen that the field directions matched fairly well for all cases considered,

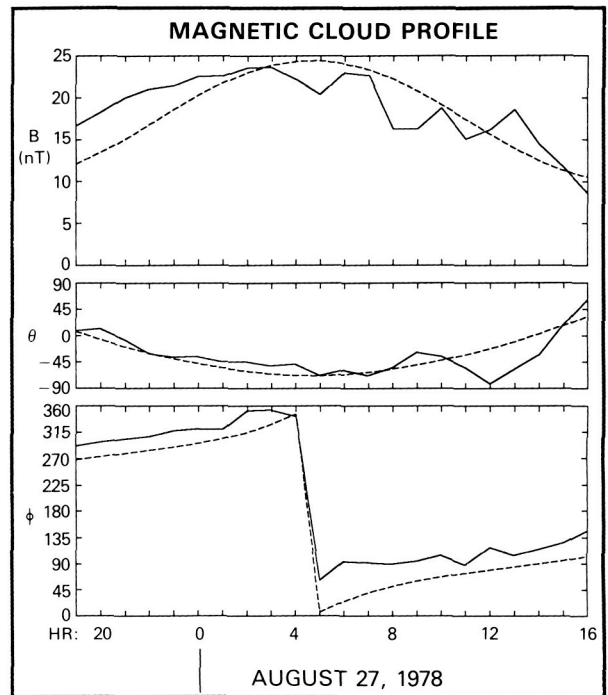
but the field strength (B) was somewhat asymmetric compared to the model, which demands perfect symmetry. The asymmetry is apparently due to the interaction of the cloud with the ambient solar wind plasma. Hence, variance and least squares procedures were developed that employ data composed of field vectors of *unit* length, eliminating the need to find the value for B_0 until all other parameter values are estimated. Presently under consideration is another step that will be carried out just before finding B_0 , i.e., refining the calculation of the inclination of the cloud axis, again using the least squares technique. These steps are summarized as follows:

- 1) The field vectors within the cloud are unit normalized.
- 2) Variance analysis is conducted to find the proper coordinate system in which to work; this gives the approximate inclination of the cloud.
- 3) Least squares are used to find the origin, distance to the cloud's axis at closest approach, and scale size (a).
- 4) Estimate of inclination is refined and step 3 is repeated.
- 5) Least squares procedure is used to find B_0 .

The figure shows a comparison of actual data with the model for a cloud seen in Interplanetary Monitoring Platform-8 (IMP-8) and International Sun-Earth Explorer-3 (ISEE-3) data on August 27, 1978. It should be noted that the peak in B for the data occurs distinctly before the peak in B for the model; otherwise the curves agree very well. This agreement is typical for most of the events studied. However, the high inclination of the cloud's axis ($\theta_0 = -69.7^\circ$) is not typical of the many clouds identified so far. Researchers plan to apply these techniques to a large number of cases to help further their understanding of magnetic clouds in the solar wind.

Contacts: Ronald P. Lepping, Jeffrey Jones, and Leonard F. Burlaga
Codes 695, 694, and 692

Sponsors: Office of Space Science and Applications and Interplanetary Monitoring Platform Project



Magnetic field data (solid curve) and cloud model (dashed curve) in terms of magnitude (B), longitude angle (ϕ), and latitude angle (θ) in solar ecliptic coordinates; $\phi = 0^\circ$ is toward the Sun. The inclination of the cloud's axis was $\theta_0 = -69.7^\circ$, $\phi_0 = 359.8^\circ$.

Dr. Ronald P. Lepping specializes in plasma physics and magnetospheric and interplanetary physics at the Laboratory for Extraterrestrial Physics. He performs magnetometer experiments on IMP-8 (Principal Investigator), Voyagers 1 and 2 (Co-Investigator), and ISTP-GEOTAIL and WIND (Co-Investigator). Dr. Lepping holds a PhD degree in physics from Rensselaer Polytechnic Institute.

Mr. Jeffrey Jones handles analysis and programming in the Laboratory for Extraterrestrial Physics and the Laboratory for Oceans. His interests include mathematical modeling, numerical analysis, and radiative transfer. Mr. Jones has a BS degree in physics.

Dr. Leonard F. Burlaga studies heliospheric plasmas and magnetic fields at Goddard's Laboratory for Extraterrestrial Physics. He has received several achievement awards during his 20 years at Goddard.



SHOCK MAGNETIZATION IN THE SOLAR SYSTEM

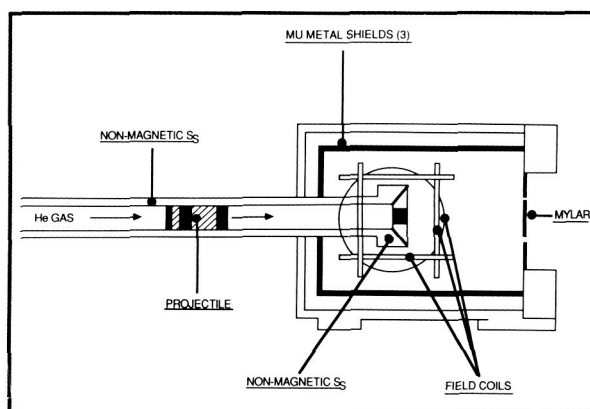
The sources of information about the magnetic fields which were present during the early history of our solar system are the meteorites; the moons, such as the Earth's moon and Phobos; and the asteroids. Any coherent study of magnetization in our solar system, whether focused on different stages in the early history of the solar system or the early existence of a dynamo now extinct, can only be addressed with low-level magnetometer missions attached to spacecraft or in situ magnetometer experiments on the solid bodies and in the laboratory analysis of returned samples and meteorites. A quick perusal of the library of images returned by various spacecraft will readily confirm that impact of the solid solar system bodies, by objects of varying sizes, has been one of the most common events in solar system evolution. Scientists have first-hand information of shock effects in returned lunar samples and in the meteorites. One other important aspect of magnetization in the solar system is that the remanence in lunar rocks, in most meteorites, and likely in most asteroids and moons, is carried by iron metal or iron-nickel alloys. Scientists have an inadequate understanding of the way in which these materials, not found on Earth except in clearly anomalous circumstances, acquire remanence and have these records modified by thermal transients and shock effects.

Results of studies dealing with the effects of shock impact on magnetic properties of ferromagnetic materials are usually discussed under a general heading called shock demagnetization. Shock demagnetization observations fall into three categories: 1) second-order pressure-induced phase transitions, 2) first-order polymorphic-phase transitions, and 3) stress-induced magnetic anisotropy. None of these studies, valuable as they are, address remanence acquisition during shock events or modification of preexisting remanence by shock events, and therefore are of little value to the critical need to understand shock magnetization in the solar system context.

To approach the shock magnetization problem, a light gas gun was built at Goddard Space Flight Center. The gun uses pressurized helium gas to send copper-tipped aluminum projectiles down a 30-foot barrel to the impact site. The samples at the impact site are mounted in a nonmagnetic stainless steel cap

at the end of a nonmagnetic stainless steel barrel extension which resides in a 3-stage mu-metal shield. A 3-axis Helmholtz coil system to control the magnetic field at the sample site is now under construction. This arrangement (as shown in the first figure) will provide the circumstance for careful field control during shock impact experiments.

Preliminary experiments were completed with a unique alloy of copper (Cu) and 1.5 percent iron (Fe). The Cu(Fe) alloy proved to be ideal because: 1) the precipitate particles were shown to be spherical and, even in the larger particles, cubical, meaning that particle-shape variations were controlled; 2) the size of the precipitate particles and the mean interparticle spacing could be controlled independently by varying anneal conditions and iron concentration, meaning that all magnetic size categories (i.e., superparamagnetic, single-domain, and multidomain) could be evaluated and magnetic interactions controlled; 3) the shock-induced first-order transitions could be evaluated, the initial fcc \rightarrow bcc, and subsequently by impacting a remachined disk, the bcc \rightarrow hcp \rightarrow bcc; 4) the shock-induced substructure could be annealed and magnetic changes evaluated; and 5)



The Goddard Space Flight Center light gas gun was built for the purpose of evaluating the effects of shock impact on sample magnetization. The cross section (not to scale) of the sample chamber identifies the nonmagnetic stainless steel barrel extension and cap and the surrounding three-stage mu-metal shield. The field coils, to be built, are indicated; and once constructed they will ensure accurate control of the magnetic field environment at the sample site indicated by the black cube at the end of the barrel.

all of the experiments could be easily done in controlled external fields, and the disk containing the full residual record could be easily recovered intact for characterization. Each of the specimens has an orientation system scribed on the surface, and this is recoverable as part of the record.

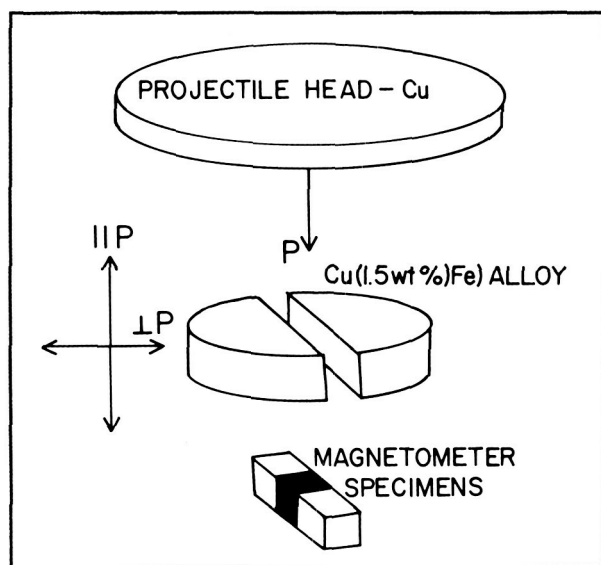
Disks of 0.500 inch diameter and either 0.125 inch or 0.250 inch thickness were cut (and machined) from rods prepared by melting high purity Cu and Fe in a vacuum furnace. The disks were then solution-annealed at 1025 °C and quenched to ambient temperature, after which the disks were reheated to the anneal temperature. Changing the anneal temperature and time of anneal produces any size distribution desired. Shown in the second figure is a schematic illustrating the driver plate, the Cu(Fe) disk, and the strip cut from the impacted disk for the magnetic measurements. The parallel (||) and perpendicular (⊥) directions are identified. The sample holders for the shock experiment were designed with circular symmetry. The thickness of the spall plate was four times the thickness of the driver, as was the width of the momentum trap. No precise

measurements were made to verify impact planarity. Negligible shock heating was noted. Copper was used throughout to ensure no magnetic contamination. Copper has a steep dynamic compressibility curve and therefore reasonable pressure can be achieved for modest impact velocities. Maximum pressure used was ~5.0 GPa assuming a Cu-Cu impact.

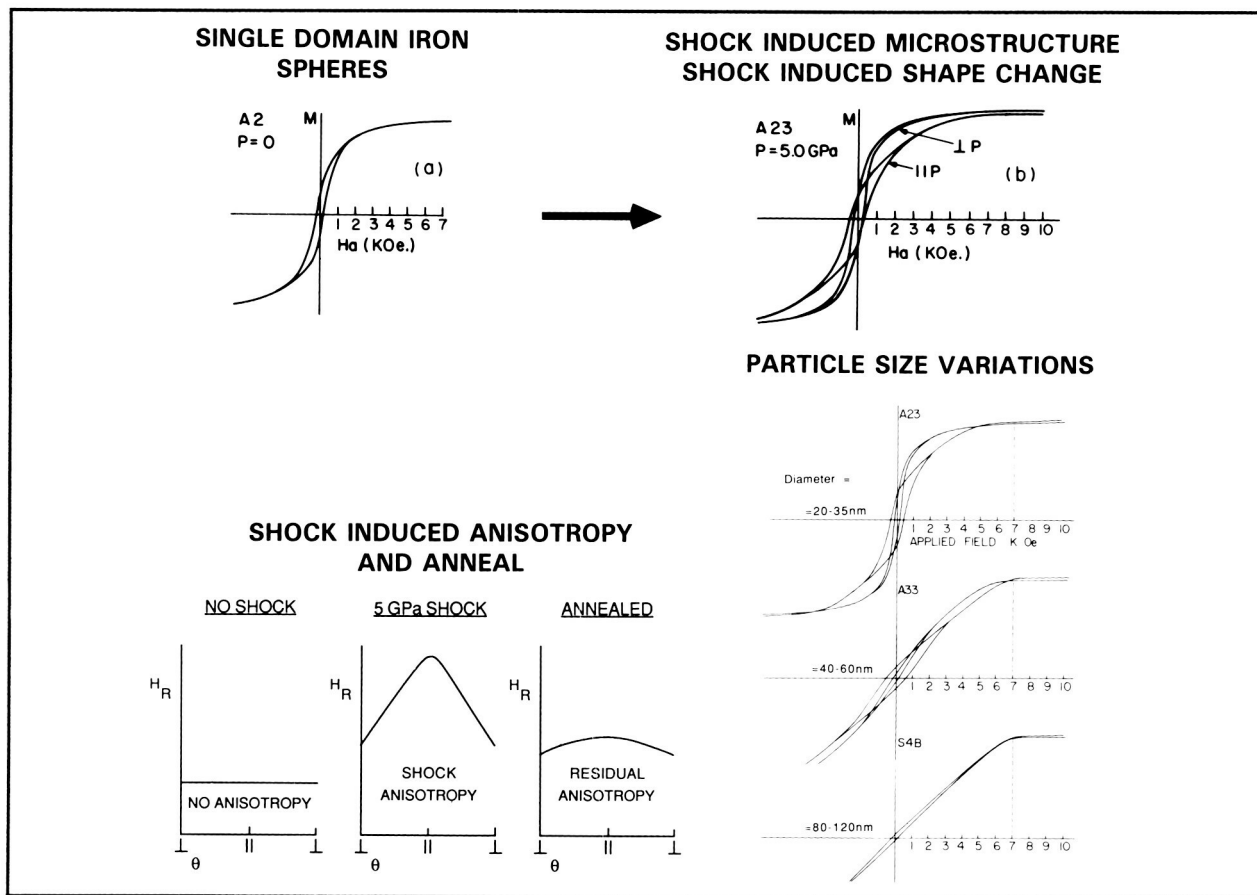
The Cu(Fe) alloys are truly unique. In the pre-shocked samples they consist of mostly untransformed face-centered cubic iron spheres and just enough auto-transformed body-centered cubic spheres located at grain boundaries and the disk surface to allow characterization of the size-dependent properties and the preshocked state. The shock impact transforms a fraction of the fcc spheres to bcc spheres, which can be magnetically characterized. The amount transformed at a given impact level depends on the initial size distribution of the spheres, and for a given sphere size the amount transformed is shock-level dependent. The magnetic hysteresis loops can be used most effectively to characterize the preshock state and the postshock state; to determine the contrasts between different size distributions; to evaluate the shock-induced magnetic anisotropy; and to evaluate the changes taking place when the shock-induced magnetic effects are annealed. (See third figure.)

The research planned and in progress will provide a calibration of the size-dependent magnetic properties of iron spheres. These calibrated samples will then be impacted at different levels to determine:

- The efficiency of remanence acquisition during shock impact in controlled external fields
- The contrasts in remanence acquisition between first-order nonmagnetic-to-magnetic transition and Curie point cooling (thermoremanence)
- Shock magnetization as a shock level-dependent property
- If a shock impact can produce a remanent magnetization in a demagnetized sample when the impact takes place in zero external field; and what effect a shock impact might have on a pre-existing remanence-directed parallel and perpendicular to the shock direction in zero field



The shock impact scenario is a copper (Cu) projectile head on a Cu (0.5 to 1.5 percent iron) alloy disk as indicated. The alloy contains spheres of iron developed during a precipitation anneal. The parallel (||) and perpendicular (⊥) directions are indicated and the cutout identifies the magnetometer specimens used for magnetic analysis.



Preliminary results illustrating the use of magnetic hysteresis loops to evaluate the difference between no shock (A2, $P=0$) and shock (A23 $P=5.0$ GPa) states. The parallel (\parallel) and perpendicular (\perp) magnetic hysteresis loops are indicated. By measuring hysteresis loops as a function of angle (i.e., by rotation through 180° from $\perp P$ to $\parallel P$ to $\perp P$), it was determined that with no shock there is no anisotropy in the remanent coercive force (H_R). After the shock, a definite anisotropy in H_R is noted and we define the shock direction. After annealing, a residual anisotropy remains which seems to be shape related. The anneal removed the microstructural anisotropy. Different size distributions can be characterized via the magnetic hysteresis loops as indicated for A23 ($D=20-35$ nm), A33 ($D=40-60$ nm), and S4B ($D=80-120$ nm).

The studies, once completed, will provide a magnetic calibration of iron and an understanding of shock magnetization which do not presently exist. Scientists will then have a basis for understanding shock magnetization and for evaluating remanent magnetization in solar system solid bodies.

Contact: Peter Wasilewski
Code 691

Sponsor: Solar System Exploration Division
(NASA HQ)

Dr. Peter Wasilewski specializes in magnetic properties of solar system solids. Dr. Wasilewski participated in the 1987/88 Antarctic Meteorite Search Team, and he was a member of the 25th Japanese Antarctic Research Expedition. Dr. Wasilewski received a DSc degree from the University of Tokyo.

SYNTHESIS OF AMORPHOUS SILICATE MANTLES ON ICY GRAIN CORES IN THE INTERSTELLAR MEDIUM

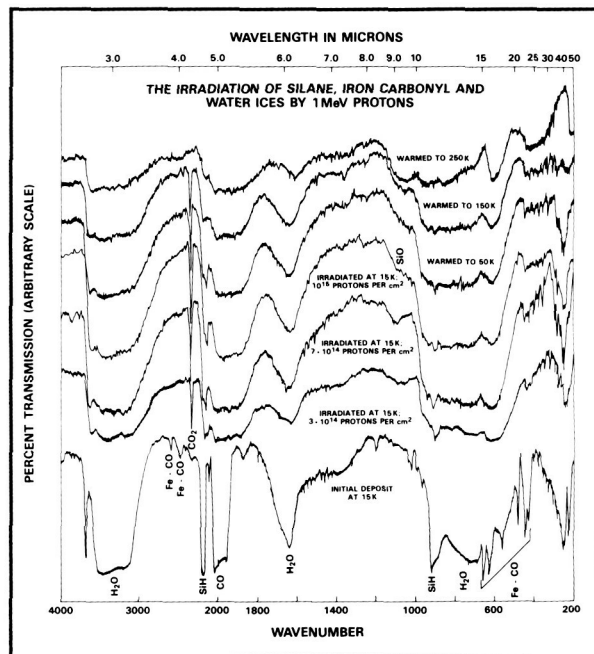
It has long been assumed that most interstellar grains are formed in circumstellar shells, and are mixed into the interstellar medium by circumstellar winds. Processing of refractory grains in the interstellar medium has usually been assumed to be minimal, and the complete destruction of these grains was regarded as a very rare event. Recent calculations of the efficiency of grain destruction in supernova shocks and estimates of the rate at which such shocks are produced in the galaxy drastically reduce estimates of refractory grain life expectancy in the interstellar medium. It is possible that 10 times as many grains are destroyed by such shocks each year than can be supplied by circumstellar outflows. This would imply that a large number of grains must be formed in the interstellar medium by some previously unknown process. Recent experiments were designed to investigate a mechanism by which refractory grains might form in the interstellar medium.

Shocks destroy grains by two processes: large grains are shattered in grain-grain collisions to produce smaller fragments, and small grains or grain fragments are atomized by collisions with energetic ions. After the shock passes and the gas cools down, newly formed molecules, for example water and carbon monoxide, will begin to condense on the surviving grain fragments along with both hydrogen and metal atoms like silicon, iron, and magnesium. This mixture may react completely, forming molecules like silane, iron carbonyl, and magnesium hydride, or may partially react to produce a number of unstable metallic radicals in an ice matrix. Even if stable organo-metallic compounds form initially, irradiation of these grain mantles by both ultraviolet photons and cosmic rays will still produce a number of reactive chemical radicals. Initially, experiments were intended to determine the properties of the product formed by the slow warmup of an ice matrix that contained metallic radicals.

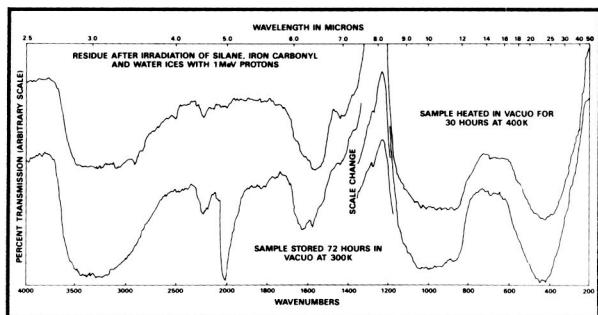
A gas mixture containing silane, iron carbonyl, and water in varying proportions was deposited onto a polished aluminum substrate at 15°K. This deposit was irradiated by 1 MeV protons (in three doses), and then warmed slowly to room temperature. An infrared spectrum of the ice deposit was obtained prior

to irradiation, after each radiation dose, after the sample was warmed to 50°K, and thereafter in 50° K-steps as it was warmed to 300°K, to monitor the chemical changes that occurred during each stage of the experiment. The first figure displays several of these spectra, along with the identification of the chemical species responsible for the larger absorption features. The second figure shows the infrared spectrum of the residue left on the polished aluminum substrate after all of the water had evaporated, and after the residue had been heated in vacuum at 400°K for 30 hours to drive off trapped residual gases.

Broad 10 and 20 μm absorption features due to the amorphous silicate residue are evident in the second figure, as are other features near 3, 6.2 and 6.8 microns that are due to water or hydroxyl groups bound to the silicate matrix. Especially intriguing are features due to CO (near 4.9 μm), and to SiH bonds (near 4.6 μm), both of which were more tightly bound to the silicate than had been expected. Features at 4.9 and 4.6 μm have been observed in the protostellar



Infrared spectra of $\text{Fe}(\text{CO})_5$ - SiH_4 - H_2O (1:1:3 molecular ratio) ice as a function of processing. The bottom curve is the spectrum of the initial deposit, and the higher curves are spectra of the same sample at increased levels of processing. The spectra have been displaced vertically by an arbitrary amount.



Infrared spectra of the residue formed during the same experiment that yielded the spectra shown in the first figure. Spectra were recorded after the residue was stored under vacuum at 300°K for 72 hours (bottom curve), and after vacuum annealing at 400°K for 30 hours (top curve). Spectra have been displaced vertically by an arbitrary amount.

source, W33A; although the feature at 4.9 μm had previously been attributed to CO bound into an ice matrix, these experiments were the first to demonstrate that the 4.6 μm feature may be due to SiH bound into a silicate network. These experiments have also demonstrated convincingly that refractory silicate grains can be produced by surface processes at low temperature in the interstellar medium. Formation of silicate grains at low temperature could result in oxygen-isotopic fractionation between the solid and gas phases, trapping of large quantities of volatiles (including noble gas) in relatively refractory reservoirs, and the catalytic production of large organic molecules. Experiments to test these effects will continue over the next several years.

Contacts: Joseph A. Nuth and Marla H. Moore
Code 691

Sponsor: Solar System Exploration Division

Dr. Joseph A. Nuth, an astrochemist/geochemist with the Laboratory for Extraterrestrial Physics, performs laboratory studies of the formation and metamorphism of refractory silicates in circumstellar shells, the interstellar medium, and the primitive solar nebula. Dr. Nuth received a PhD degree in geochemistry from the University of Maryland.

Dr. Marla H. Moore is a research associate with the University of Maryland's Department of Chemistry, funded through NASA grants. Currently in the

Astrophysics Branch, she is studying the infrared spectra of low-temperature icy mixtures similar to those on comets, interstellar icy mantles, and satellites in the outer solar system.

LOW TEMPERATURE VAPOR PRESSURE MEASUREMENTS OF PLANETARY MOLECULES

The Voyager 1 and 2 flybys, as well as ground-based observations, revealed that the atmospheres of several planetary systems contain complex H-, C-, and N-bearing compounds. In these low temperature environments, some of the species may condense. For example, acetylene (C_2H_4) and diacetylene (C_4H_2), which are photochemically produced from CH_4 , are likely to condense out on Jupiter, Neptune, and possibly Saturn. Cyanoacetylene (HC_3N) and dicyanoacetylene (C_4N_2) have been identified in the solid phase in the upper atmosphere of Titan, where temperatures in the 140–160°K range are encountered. In order to obtain internally consistent models of the concentration profiles of planetary atmospheres, knowledge of the temperature dependence of vapor pressures of the identified species is essential.

Laboratory data on vapor pressures of organics at low temperatures are extremely scarce. Typically, vapor pressure measurements at ambient temperatures are extrapolated using the Clausius-Clapeyron equation to obtain values at low temperatures. In the absence of any knowledge of its temperature dependence, the enthalpy of vaporization or sublimation is generally assumed to be temperature-independent. However, this can lead to significant errors if the temperature level over which the pressure is extrapolated is large. Possible structural phase transitions in the temperature range of interest can add to these errors. It is therefore desirable to obtain laboratory measurements of the vapor pressures of condensed hydrocarbons in the appropriate temperature ranges.

There are several techniques currently available for vapor pressure measurements; however, the vapor pressures of interest are well below the limit of commercial pressure-measuring devices. To address this problem, a new technique—the thin-film infrared (TFIR) method—which is appropriate for these ranges of temperature and pressure has been developed. The method is based on the concept that

at high vacuum, molecules leaving a thin film of material that is held at a constant temperature will not be reabsorbed. The time rate of change of an infrared feature will then be a measure of the loss rate, and therefore the pressure, of the material at that temperature. The rate of loss of the sample is given by Knudsen's equation:

$$R = \frac{p}{(2 \pi m k T)^{1/2}},$$

where p is the vapor pressure of the species at a temperature T , k is the Boltzmann constant, and m is the molecular mass of the species in question. Thus, measurement of the rate of loss of the sample kept at a constant temperature can provide information on the vapor pressure.

In practice, a thin film—typically $\sim 1 \mu\text{m}$ —is deposited on an optical substrate that is attached to the cold finger of a cryocooler. The film is slowly heated to the desired temperature, and its initial spectrum is recorded with a Fourier transform infrared spectrometer. The spectrum is continuously monitored and again recorded at some later time, when approximately 50 percent of the sample has been lost. The change in thickness for that time interval is determined from previously acquired extinction coefficients, and the rate of loss of the sample is ascertained.

The technique has been calibrated with CO_2 , for which there was some meager low temperature data; agreement with the older data is excellent. The method was then applied to measurements of vapor pressures of C_4H_2 , an important molecule in Jupiter's and Titan's atmospheres, thereby providing the first laboratory data for this molecule in that pressure range. Coupled with existing commercially available equipment, this technique permits coverage of an extensive pressure range, and is already providing valuable data for modelers. It is planned to expand this activity to cover other hydrocarbons and nitriles.

This program represents a collaborative effort of Goddard Space Flight Center scientists with Dr. Raj K. Khanna of the University of Maryland and Ms. Christine M. Hudson, who is participating in the National Aeronautics and Space Administration's

Graduate Student Researchers Program. In addition, Dr. Paul N. Romani of Code 693.2 has provided valuable advice about application of the results to models of planetary atmospheres.

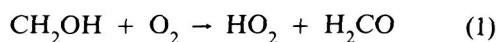
Contact: John E. Allen, Jr.
Code 691

Sponsor: Office of Space Science and Applications

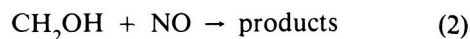
Dr. John E. Allen, Jr., is involved in research of interstellar grains, cometary and planetary atmospheres, and the upper atmosphere with the Astrochemistry Branch of the Laboratory for Extraterrestrial Physics. His professional interests include the application of optical techniques to chemical physics and the application of chemical physics to aeronomy and astrophysics. Dr. Allen received a PhD degree in applied physics from the University of Florida.

CHEMISTRY OF THE HYDROXYMETHYL RADICAL IN THE ATMOSPHERE: ITS REACTION WITH NO AND NO_2

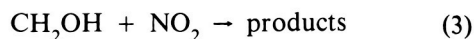
The most likely fate of the hydroxymethyl radical (CH_2OH) in the atmosphere is reaction with molecular oxygen, i.e.,



However, in order to adequately determine the role of this radical in atmospheric chemistry, the rate constants for the reactions of this radical with other atmospheric species must be known. For this reason, researchers have completed measurements of the rate constants for the following reactions:



and



The experimental technique was discharge flow-mass spectrometry. Reaction 2 was studied over the temperature range 230–373 °K, and at pressures of 0.5–1.5 torr. Reaction 3 was studied at 298 °K and pressures of 1 torr.

The results of the measurement of k_2 are presented in the table.



Temperature Dependence of the Rate Constant for the Reaction $\text{CH}_2\text{OH} + \text{NO}$	
T/K	$k_2/10^{-12} \text{ cm}^3 \text{ s}^{-1}$ (a)
230	1.29 ± 0.20
260	1.47 ± 0.16
298	2.19 ± 0.38
373	2.21 ± 0.82
(a) The quoted uncertainties are $\pm 2\sigma$.	

An Arrhenius plot of the data in the table indicates that the reaction obeys the Arrhenius expression only in the interval 230–298 °K. For this interval, an activation energy of (1.2 ± 0.8) kcal/mole is derived.

The result of the measurements of the rate constant for reaction 3 at 298 °K and 1 torr pressure is: $k_3 = (8.3 \pm 4.1) \times 10^{-12} \text{ cm}^3 \text{ s}^{-1}$ where the uncertainty is $\pm 2\sigma$. Qualitative evidence was also obtained that the products of reaction 2 are $\text{HNO} + \text{H}_2\text{CO}$. The evidence suggests that the products of reaction 3 are HNO_2 and H_2CO . However, further study is needed to confirm products of both reactions.

By way of comparison with the rate constant for reaction 1 at 298 °K, k_2 is 4–5 times smaller than k_1 , while k_3 is comparable to k_1 .

This work was performed in collaboration with Dr. Fred Nesbitt, research associate at The Catholic University of America.

Contacts: Walter A. Payne, Jr. and Louis J. Stief
Code 691

Sponsor: Office of Space Science and
Applications

Dr. Walter A. Payne, Jr., an astrophysicist in the Astrochemistry Branch, is a Co-Investigator in the NASA Upper Atmosphere Program and in the NASA Planetary Atmospheres Program. His professional interests include chemical kinetics, photochemistry of small molecules, and laser-induced fluorescence. Dr. Payne, who earned a PhD degree in physical chemistry from Howard University, has been at Goddard for 19 years.

Dr. Louis J. Stief, Head of the Astrochemistry Branch of the Laboratory for Extraterrestrial Physics, is involved with determining the rates and mechanisms of reactions occurring in the upper atmosphere of Earth. His scientific specialties are kinetics and photochemistry of atmospheric and astrophysical systems. Dr. Stief holds a PhD degree from The Catholic University of America, and he has 19 years of experience at Goddard.

KINETICS AND THERMOCHEMISTRY OF THE $i\text{-C}_4\text{H}_{10} + \text{Br} = t\text{-C}_4\text{H}_9 + \text{HBr}$ SYSTEM: RELEVANCE FOR MODELING HYDROCARBON CHEMISTRY OF PLANETARY ATMOSPHERES

Organic hydrocarbon compounds play important roles in the photochemistry of the atmospheres of Earth, Jupiter, Saturn, and Titan. Quantitative knowledge of the kinetic and thermochemical properties of these organic species is fundamental to understanding the chemical reaction mechanisms, pathways, and processes that these species can undergo in the respective atmospheric systems. The most accurate source of data about thermochemical heat of formation, entropy, and chemical bond energies of polyatomic hydrocarbon stable molecules, as well as of reactive intermediates, is laboratory kinetic studies of reaction equilibria that involve reactive chemical intermediates.

A detailed kinetic study designed to accurately establish the energies of C-H bonds, values that hitherto had significant uncertainties associated with them, was performed as a collaborative research effort between the National Aeronautics and Space Administration's (NASA) Goddard Space Flight Center (GSFC) and the Illinois Institute of Technology's (IIT's) Professor David Gutman and students. The hydrocarbon reaction system selected for study was that of the equilibrium reaction $\text{Br} + i\text{-C}_4\text{H}_{10}$ (isobutane) $= \text{HBr} + t\text{-C}_4\text{H}_9$ (tertiary butyl free radical) a reaction involving a polyatomic free radical which can provide new and useful thermochemical information relevant to the fields of combustion chemistry and atmospheric chemistry. The collaborative in-depth study involved separate groups of experiments in which both the forward and reverse reactions were isolated for direct study, and kinetic rate constants were determined as a function

of temperature and pressure over a wide range of experimental conditions. The heat of formation, entropy, and C-H bond energy were then obtained directly from these kinetic measurements. The research at NASA/GSFC employed the technique of flash photolysis-resonance fluorescence, while that at IIT utilized photoionization mass spectrometry.

Results of this study (J. Russell et al, 1988) have: 1) provided the most accurate and first direct determination of the thermochemical heat of formation and entropy of the tertiary butyl free radical; 2) established a more accurate value of the tertiary C-H bond energy; and 3) decreased the uncertainty in predicting related kinetic parameters, such as those for reverse-reaction rate constants and reaction equilibrium constants.

Data derived from this collaborative research have implications for planetary atmospheric studies. Improved understanding of atmospheric observations is made possible and more valid predictive atmospheric models can be made, because such kinetic and thermochemical data enable the following activities: elucidation of plausible reaction pathways and identification of likely reaction intermediates; elucidation of formation processes of polyacetylene and hydrocarbon aerosol clouds; and differentiation between competing explanations of chemical behavior within planetary atmospheric systems.

Contact: David F. Nava
Code 691

Sponsor: Office of Space Science and
Applications

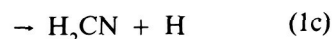
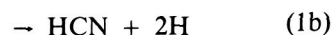
Dr. David F. Nava is an astrophysicist with the Laboratory for Extraterrestrial Physics. He is Co-Investigator for the Upper Atmosphere Research Program and for the Planetary Atmospheres Program, and he was Principal Investigator for NASA's Returned Lunar Sample Program. He also served on the editorial board of Chemical Geology. Dr. Nava, who received a PhD degree in chemistry from Arizona State University, has worked at Goddard for 20 years and has received two NASA Special Achievement Awards and a NASA Exceptional Performance Award.

HYDROGEN CYANIDE FORMATION IN THE ATMOSPHERE OF TITAN; REACTION RATE AND PRODUCT DATA FOR THE N + CH₃ REACTION

Molecular nitrogen is the major component of Titan's atmosphere; it is dissociated by solar radiation and electron impact to yield ground-state and electronically excited atomic nitrogen. The principal fate of ground-state N(⁴S) is probably reaction with methyl (CH₃) and methylene (CH₂) radicals, leading to the formation of hydrogen cyanide (HCN). Models of the photochemistry of the atmosphere of Titan have been forced to use an estimated value of the rate constant for N + CH₃ that was based mainly on meager and indirect data obtained in 1955 from a very complex system. In addition, while HCN has been qualitatively identified as an eventual product of the reaction N + CH₃, there is no direct data on the mechanism of the reaction.

The absolute rate constant for the reaction N + CH₃ has been determined in a discharge flow system coupled with collision-free sampling mass spectrometry at low electron energies. Time-resolved decays of CH₃ in the presence of excess N were measured over a range of experimental conditions. The results are $k(298^\circ\text{K}) = 8.6 \times 10^{-11} \text{ cm}^3 \text{ s}^{-1}$ and $k(200^\circ\text{K}) = 6.9 \times 10^{-11} \text{ cm}^3 \text{ s}^{-1}$. This is a very rapid reaction, with about one collision in two leading to reaction. These are the first direct measurements of this rate constant, and show the reaction rate to be several times faster than that used in the model of the atmosphere of Titan. Thus, the reaction N + CH₃ can readily account for the Voyager spacecraft's observation of HCN on Titan, provided it can be quantitatively established that HCN is indeed a major primary or secondary product of the reaction.

There are three energetically accessible reaction channels:





Although channel 1a is favored energetically, it is forbidden by both spin and orbital symmetry correlation rules. Channel 1b is nearly thermoneutral. Using the same discharge flow-mass spectrometry apparatus employed for the rate constant determinations, quantitative measurements have been made of the products H, H₂, HCN, and H₂CN, or their isotopic variants. It was determined that approximately 90 percent of the reaction occurs via channel 1c forming the H₂CN radical; the remaining 10 percent occurs via channel 1a. Also, unit efficiency was observed for conversion of CH₃ to HCN. Thus, in this system, the major pathway to HCN involves two steps:



On Titan, [H] > [N], so that HCN formations occur primarily via



Experiments are in progress to attempt measurement of the rate constants for reactions 2 and 3. These kinetic and mechanistic results now permit a much-improved model calculation of the HCN distribution in the atmosphere of Titan.

This work was performed in collaboration with Fred Nesbitt, George Marston, David Nava, and Walter Payne.

Contact: Louis J. Stief
Code 691

Sponsor: Office of Space Science and Applications

OBSERVATIONS OF NIGHTTIME STRATOSPHERIC N₂O₅ WITH A BALLOON-BORNE FOURIER SPECTROMETER

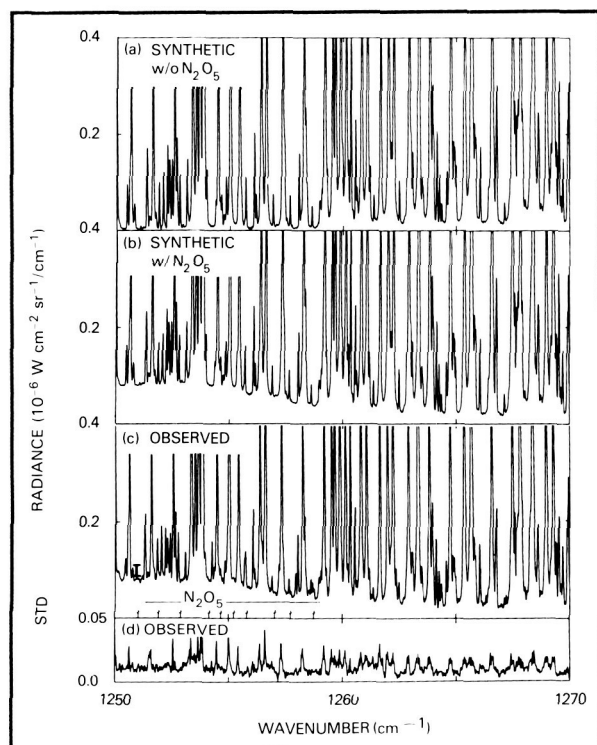
The NO_x catalytic cycle, centered on the rapid interchange of NO and NO₂ free radicals, is the dominant process in the ozone chemistry of the present-day stratosphere at midlatitudes. The destruction of O₃ by NO and NO₂ is governed by competing reactions converting the NO and NO₂ to temporary reservoir species (N₂O₅ and HNO₃). N₂O₅ is pro-

duced almost entirely at night, with about 30–50 percent of the total NO_x being converted to N₂O₅. This N₂O₅ is slowly photolyzed during the daytime to NO₂, producing the diurnal variation in NO₂. Even though knowledge of the stratospheric concentration of N₂O₅ is important to ozone chemistry, very few measurements of this species exist.

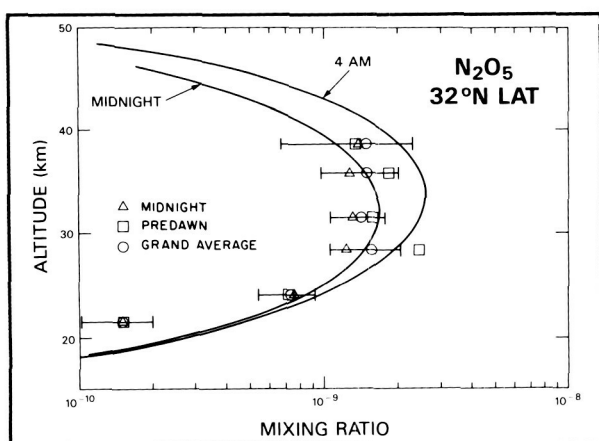
The first infrared spectra of nighttime stratospheric N₂O₅ emissions have been obtained with a high-spectral-resolution (0.044 cm⁻¹), balloon-borne Fourier spectrometer, cooled to 100°K, in September 1986, from Palestine, Texas. These measurements have yielded the first N₂O₅ altitude distributions obtained for the period from midnight to sunrise.

The first figure, parts (a) and (b), illustrates the effect of N₂O₅ on the emission spectrum for a tangent height of 24 km. The synthetic spectrum was generated using the mixing ratio of N₂O₅, inferred from the observed spectra. The broad continuum emission feature appearing between 1250–1260 cm⁻¹ is due to the ν₁₂ band of N₂O₅. Since the spectrum of N₂O₅ is not resolved at 0.04 cm⁻¹ resolution, only the continuum envelope is available for the identification of N₂O₅. Strong emission lines of N₂O and CH₄ are seen superimposed on the N₂O₅ continuum. The observed nighttime average spectrum for the tangent height of 24 km is shown in part (c) for an apodized resolution of 0.04 cm⁻¹, with the corresponding standard deviation spectrum (STD) exhibited in part (d).

The inferred mixing ratios for the midnight to predawn time intervals, along with the corresponding 1-D photochemical predictions are shown in the second figure. The model predictions indicate that the percent variation of N₂O₅ from midnight to dawn is smallest at low altitudes (20 km), and increases steadily with height up to the balloon float altitude (~40 km). The retrieved mixing ratios show good internal consistency, increasing from midnight to predawn for the upper stratosphere (H_T > 25 km), with no observed changes in the lower stratosphere. These observed diurnal changes are in general accordance with the photochemical predictions. The magnitude of the observed changes in N₂O₅ with local time is roughly in agreement with the theoretical change. This conclusion is only tentative, because of the magnitude of the error bars. Even with the error bars, the observed mixing ratios



Grand average nighttime spectrum for $H_T = 24$ km. Panels (a) and (b) illustrate the effects of N_2O_5 emission on the synthetic spectrum. Panels (c) and (d) are the observed spectrum and the corresponding standard deviation, respectively.



Comparison of retrieved N_2O_5 concentration profiles with 1-D photochemical predictions for midnight and predawn. The profile for the grand average is included with 1σ error bars.

are less than the predicted values, with the exception of the observations at 28 km.

The main conclusions derived from the data are: 1) the vertical profile of N_2O_5 has been determined for the 20–40 km altitude range over the midnight to predawn timeframe; 2) the observed profiles are generally lower than 1-D photochemical predictions; and 3) the inferred profiles for upper altitudes (> 25 km) generally indicate N_2O_5 increasing towards predawn; however, the error bars are presently too large to demonstrate this quantitatively.

Contacts: Virgil G. Kunde, John C. Brasunas, and Jay R. Herman
Codes 693 and 616

Sponsor: Office of Space Science and Applications

Mr. Virgil G. Kunde, who specializes in planetary atmospheres and infrared spectroscopy, is Head of the Planetary Astrophysics Section. Mr. Kunde holds an MS degree in astronomy from the University of Maryland, and he has been with Goddard for 26 years.

Dr. John C. Brasunas is Principal Investigator for development of a high-temperature superconductor infrared bolometer, as well as Co-Investigator for both the balloon-borne spectroscopy of the stratosphere and the infrared spectrometer for the CASSINI mission to Saturn. Dr. Brasunas, who holds a PhD degree from Harvard, has received two awards during his four years at Goddard.

Dr. Jay R. Herman, working at the Atmospheric Chemistry and Dynamics Branch, is responsible for atmospheric modeling, algorithm and data interpretation, and radiative transfer in inhomogeneous scattering atmospheres. Dr. Herman, recipient of the 1988 Performance Award, has 21 years of Goddard experience.

THE EFFECT OF MAGNESIUM IN THE LEACHING WATER ON THE RATE OF CORROSION OF NUCLEAR WASTE GLASS

The most dangerous waste products of nuclear power plants are the high-level nuclear wastes. At the present time, it is planned to immobilize high-level



nuclear wastes by mixing them with typical glass-forming oxides, in a ratio of about 1 to 3. This will produce a melted borosilicate glass that can be poured into 10-foot stainless steel canisters and stacked in a shelter open to the outside air. After 10 years or so, the short-lived elements will decay. The canisters can then be buried in a geological repository deep beneath the surface.

If, despite all precautions, ground water should reach the canisters, engineers calculate that the stainless steel could be relied upon for a few centuries. After that, immobilization of the wastes would depend on the resistance of the glass to corrosion. Much effort has been expended by many agencies to make the glass as resistant to corrosion as possible.

Geophysicists at Goddard Space Flight Center (GSFC), in collaboration with Professor B. P. Glass, at the University of Delaware, have been studying microtektites as natural analogs of nuclear waste glasses. Microtektites are small, spherical particles of natural glass that rained on the Earth 0.7, 1.0, 15, and 35 million years ago. Some microtektites are low in silica like nuclear waste glasses, and yet have survived as specks only a fraction of a millimeter in size for periods up to a million years—much longer than the 25,000 years that the nuclear waste glasses are required to survive. Accordingly the geophysicists, with the Office of Commercial Programs, Technology Utilization Branch and Professor Glass, undertook the task of finding a quantitative determination of the corrosion rate of tektite glass in nature.

At the same time, the geophysicists arranged with Aaron Barkatt of Catholic University for laboratory measurements of tektite glass corrosion rates. These measurements showed that tektite glass does not have any special properties that protect it from corrosion. When exposed to very pure deionized water, it corrodes in the laboratory about as fast as any similar glass. To test low-silica microtektites, it was necessary to synthesize them, because the entire world supply could be lost by a sneeze. When the microtektites were leached, it was again found that they corroded like similar glasses.

The geophysicists were faced with a puzzle: on the one hand, laboratory studies of tektites indicated that tektite glass corrodes at the rate of a few tenths of

a millimeter over a million years or so; on the other hand, the study of microtektites showed corrosion rates of a few thousandths of a millimeter in similar timeframes.

Geophysicists then noted that tektites are almost never found on the sea bottom; conversely, microtektites are almost never found on land. It was decided to measure corrosion rates in sea water. Catholic University's Aaron Barkatt discovered that sea water corrodes tektite glass at a rate more than an order of magnitude slower than its corrosion rate by pure (deionized) water.

Professor Barkatt immediately began looking through the elements that make up sea water to see which one confers the protection. It was found that magnesium, which is present in the amount of about 1 gram per liter of water, provides the necessary protection. Barkatt's group investigated two glasses simulating the borosilicate mentioned above; they found that magnesium in the leach water protects these glasses in much the same way as with tektite glass. The use of these results remains under discussion.

Contact: John A. O'Keefe
Code 681

Sponsor: Office of Commercial Programs

Dr. John A. O'Keefe, who works in Goddard's Laboratory for Astronomy and Solar Physics, is responsible for the scientific study of tektite glass in its relation to the Moon's structure and history. He received his PhD degree from the University of Chicago as well as an honorary degree from Alfred University for studies of tektite glass.

VARIATION IN THE SOLAR CONSTANT (1979-1988)

The first definitive measurements of changes in the solar constant were made in December 1978 by channel 10c on the Nimbus-7 Earth Radiation Budget (ERB) experiment. In 1988, this highly stable and sensitive detector continues to monitor small changes in the solar irradiance after 9½ years.

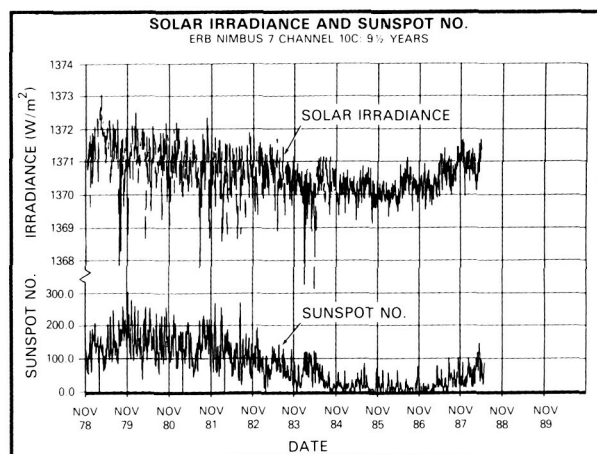
Prior to the fall of 1978, there were no long-term solar irradiance measurements with a precision of

better than 1 percent. Most of these earlier measurements were taken inside the Earth's atmosphere, and uncertainties in applying atmospheric corrections limited the precision obtainable. However, the solar energy output appeared invariant to at least the 1 percent level, so it was commonly termed the "solar constant."

The Nimbus-7 ERB Science Team eagerly grasped the opportunity to include a sensitive, electrically self-calibrating solar sensor on an orbiting platform above the Earth's atmosphere. The detector chosen was a Hickey-Freden (H-F) cavity pyrliometer. The sensor is calibrated by periodically heating the cavity with a measured quantity of electrically generated energy. John Hickey of the Eppley Laboratory, Newport, Rhode Island, is the solar sensor engineer, and also the senior solar scientist on the ERB Science Team.

The Nimbus-7 was launched on October 24, 1978, into a circular, 955-km altitude, Sun-synchronous orbit. After the initial degassing, the ERB experiment started taking scientific measurements on November 16, 1978. The solar sensor views the Sun for about 3 minutes during satellite sunrise, once each orbit. Channel 10c records a reading once each second, and the central 42 seconds, when the Sun is lined up with the axis of the cavity, are extracted. The Nimbus-7 orbits the Earth 13.85 times per day; the ERB experiment operated on a 3-day-on/1-day-off duty cycle until mid-September 1983. In later years, there have been long periods of full-time operation. Thus, channel 10c makes between 150,000 and 215,000 usable measurements per year, depending on the mode of operation. This sensor has an absolute accuracy of ± 0.5 percent, but its long-term stability (precession) is approximately 0.02 percent (0.35 W/m^2). In fact, the experiment scientists consider the measured sensor stability to be limited by the 11 bits per measurement mandated by the spacecraft data system, and not by the sensor itself.

Nine and one-half years of daily averaged total solar irradiance measurements are shown (top curve) in the first figure. The measurements have been normalized to the mean Earth-Sun distance. The last solar activity maximum occurred in 1979/80, but considerable solar activity continued until 1984, when the Sun became relatively quiet. However, in the fall of 1987 solar activity once more began to increase



Daily mean solar irradiance from November 16, 1978 to April 30, 1988. The lower plot is the sunspot number for the same period.

towards the next expected maximum, in 1990/91. The sunspot number graph at the bottom of the first figure shows these changes. During the excited Sun period, short-term variations of up to 0.3 percent to 0.4 percent ($4\text{--}5 \text{ W/m}^2$) were observed in the solar irradiance. Examination showed that large dips in the irradiance occurred when large sunspot groups faced the Earth. This demonstrated an asymmetry in the solar irradiance associated with the dark sunspots. If this was the only phenomenon occurring, the solar constant should be smaller at sunspot maximum than at sunspot minimum. However, several solar scientists pointed out that increases in the solar irradiance were closely correlated to the visible area of bright facular regions.

As time went by, a slow downward drift appeared in the solar constant measurements. The ERB Science Team carefully reviewed the channel 10c calibration record, and concluded that the decrease was real and not instrument-related. However, the decrease amounted to only about -0.015 percent per year; hence, some doubts remained.

Strong evidence that solar constant changes were real and not instrument-related appeared when the signal leveled off in 1984, and then started to increase, as did the sunspot number, in the fall of 1987. Supporting evidence came from similar trends shown in the solar constant measurements reported from the ACRIM-1 solar sensor on the Solar Maximum Mission (SMM) satellite by Richard Willson of the Jet



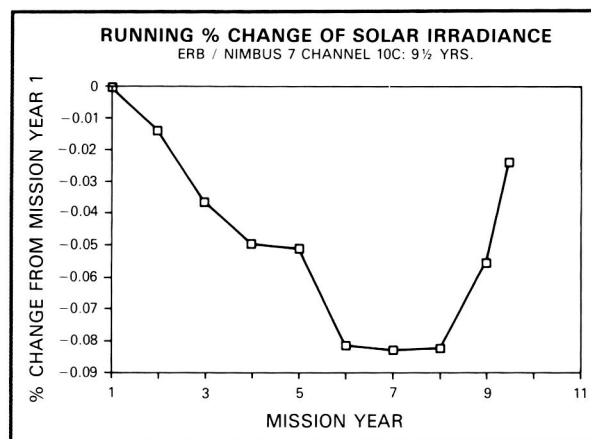
Propulsion Laboratory. The second figure shows the percentage difference of the annual mean solar irradiance from the mean of the first mission year (November 1978–October 1979). As can be seen, the recent irradiance increase from solar activity minimum appears to be more rapid than was the decline from the last activity maximum.

Many solar scientists are presently using the ERB channel 10c data set. Current plans call for the ERB solar measurements to continue at least through 1990. ERB solar data are currently available at Goddard Space Flight Center's National Space Science Data Center.

Contact: H. Lee Kyle
Code 636

Sponsor: Office of Space Science and Applications

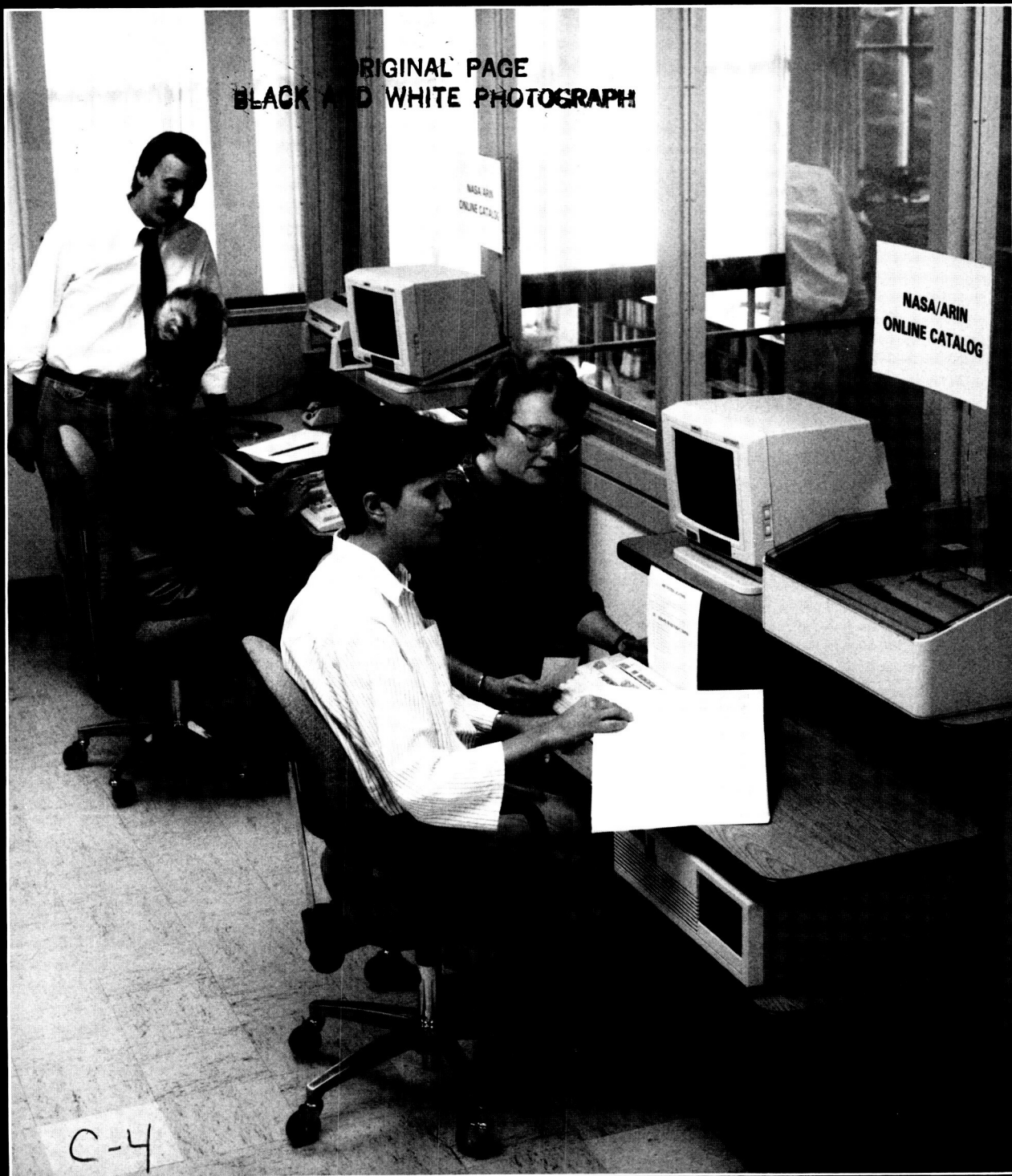
Dr. H. Lee Kyle is Manager of Nimbus-7 Clouds and Earth Radiation Budget data sets preparation. Dr. Kyle, who received a PhD in atomic physics from the



Percentage difference of annual solar irradiance from the mean of the first mission year (November 1978–October 1979).

University of North Carolina, has been a part of Goddard for 29 years. He has received a Certificate of Outstanding Performance and a Group Achievement Award for his work.

Institutional Technology





The Facilities Engineering Division is presently using a Computervision CADD-4X minicomputer-based Computer-Aided Design and Drafting system, in conjunction with personal computers, to maintain and modify as-built drawing files of floor plans for each building at Goddard Space Flight Center.

INSTITUTIONAL TECHNOLOGY

The Management Operations Directorate (MOD) represents Institutional Technology for Goddard Space Flight Center. The year 1988 was a good one for MOD, which maintained a high level of quality support to the Center in carrying out the vital space, science, and communications missions. The Center is assigned 17 major space programs—more than ever before—and MOD's workloads across the board have been affected. In the day-to-day operations, which form the core of Center employees' working lives, MOD met this growing workload efficiently and with excellence. MOD did this, in an era of budget limitations and an increasingly complex environment, by working smarter (technology-wise).

ENHANCED UTILIZATION OF PERSONAL COMPUTERS FOR COMPETITIVE PROPOSAL COST ANALYSES

A Request for Proposal (RFP) always contains the requirement for the offeror to submit cost proposal data in sufficient detail for the Government to fully understand the offeror's cost structure and to permit a thorough analysis of the cost data. The amount of data submitted, and the degree of analysis required, varies with the type of procurement. For example, support-service procurements have a simple

At the beginning of 1988 MOD took a closer look at how the Center does business and how to do it better. It was reaffirmed that MOD's basic purpose is to provide high quality, responsive, and innovative support to the Center, making the system work. As a Directorate, MOD renewed the determination to improve and be innovative in the way it provided this support. From this intense planning effort, which took place within a broad Center effort to review its mission in today's environment, MOD developed several broad long-term goals and numerous specific short-term actions to accomplish these goals. Highlights of some of the specific innovations are set forth here.

data structure because their main direct cost is labor and there are minimal subcontracting efforts. Hardware procurements are usually complex because of work breakdown structures, various direct charges, and extensive subcontracting. All competitive cost analyses include probable cost and prenegotiation evaluation exercises. In addition, all offerors' cost data are compared to the Government's in-house estimate.

Prior to 1984, all of the proposer's information was submitted in hard copy only, with most of the

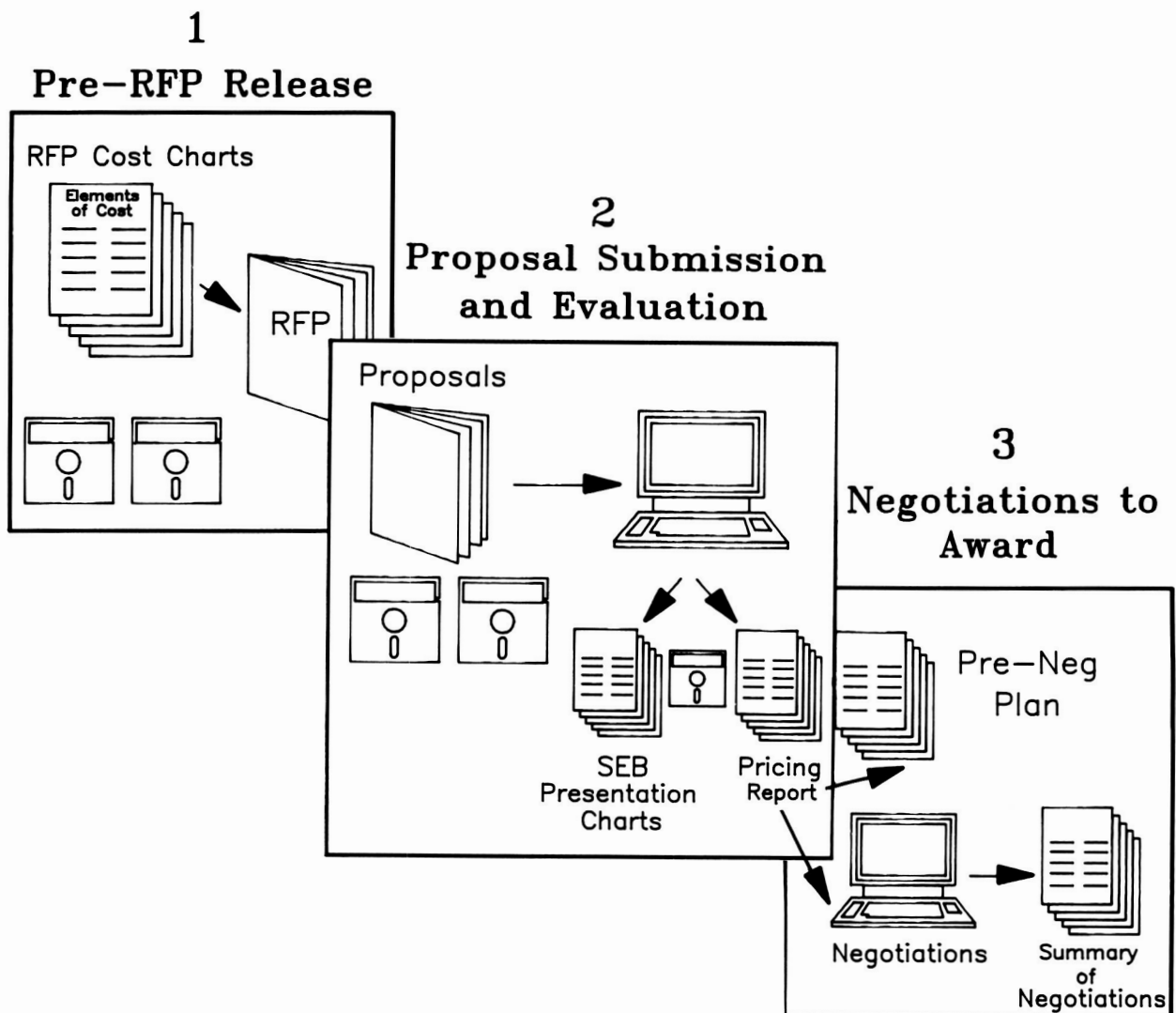
◀ *Electronic innovations are one of the services supplied to the Center by the Management Operations Division.*

Government's analysis being performed with the use of calculators. Where automation was used, it required all of the data to be entered into the computer. This approach made the analysis more difficult, lengthy, and prone to error, particularly for procurements which involved a great deal of cost data and multiple offerors.

The Procurement Pricing Branch began utilizing spreadsheet software in 1984 for cost analysis of large-dollar negotiated procurements as discussed in the 1986 issue of the *Research and Technology Report*, Computer Interface for Cost Proposals.

More specifically, offerors were requested to submit cost data on a 5.25-inch floppy diskette in accordance with a predetermined format. The type of computer and version of Lotus 1-2-3 software intended to be used for evaluation was specified. If offerors chose to submit diskettes, they were required to ensure compatibility with the Branch's hardware and software.

Since that time, a number of enhancements have been made to the process. For example, the ability to generate cost analysis presentation charts suitable for presentation to a Source Evaluation Board (SEB) and the Source Selection Official were developed using



Automated cost proposal submission and evaluation on spreadsheet formats—Data to graphics and to word processing software for final reports.



Lotus Symphony software during the latter part of 1987. Ninety percent of the charts are created by a single keystroke which initiates programming routines called macros. Copies of the software have been provided to the Branch's procurement pricing counterparts at other National Aeronautics and Space Administration (NASA) installations and to NASA Headquarters.

The diagram summarizes the current and planned future approach. The capability to implement the first two phases presently exists and is routinely utilized by the Procurement Pricing Branch. The third phase is in the development stage.

In Phase 1, the cost/price analyst tailors the sample cost proposal preparation instructions and charts to a specific procurement. The tailored end product is provided in hard copy and diskette to the Contracting Officer for incorporation in the RFP. After RFP issuance, in Phase 2, companies intending to submit a proposal request a copy of the diskettes consisting of the tailored cost templates. Offerors input data into predefined fields. Proposals are then submitted on diskette and in hard copy. These information-laden diskettes, and one hard copy of the cost proposal, are distributed to the cognizant cost analyst. All offerors' data are loaded on a personal computer, then studied, and manipulated. Ultimately, SEB-quality presentation charts for all offerors, and a pricing report for the successful offeror, are generated, principally utilizing macro commands.

Portability of these data diskettes to the Contracting Officer for use in preparing the Government pre-negotiation plan and summary of negotiations (Phase 3) are in the early pilot stage. In the interim, the Procurement Pricing Branch has been successful in using lap-top computers at negotiations.

Contacts: Charles Radspinner and Peter Quaid
Code 262

Sponsor: Management Operations Directorate

Mr. Charles Radspinner, who has been at Goddard for 12 years, performs price/cost analyses on major procurements in the Procurement Pricing Branch. He holds a BS degree in accounting from the University of Maryland. Awards that he has earned include the Cost Savings Award for Automation of Standard

SEB Cost Charts, the Group Achievement Award for Procurement Pricing Automation, the Award for Outstanding Performance, and the Code 260 Peer Award. Mr. Radspinner is especially interested in computer automation and has automated cost charts submitted on diskettes.

Mr. Peter Quaid, who has an MA degree in teaching, works at the Procurement Pricing Branch. He analyzes contractors' proposals for fair and reasonable prices and recommends Government cost objectives to the negotiator. Mr. Quaid has 13 years of experience at Goddard.

FACILITIES MATRIX

The Goddard Space Flight Center (GSFC) at Greenbelt is a campuslike complex of 31 major buildings. These buildings house two million square feet of offices, laboratories, and electronic/computer installations. The majority of these buildings were constructed in the early 1960s. Maintenance and repairs are performed as needed due to normal use and aging of the facilities. However, the building systems and components are nearing the end of their life span.

Recent capital improvement efforts have been directed toward rehabilitation of mechanical and electrical systems, roof replacement, alterations/modifications, etc. Budget constraints have resulted in deferral of other building systems rehabilitation. There is a need for the development of a comprehensive repair and rehabilitation plan, so that budget requirements can be better formulated and defended.

An assessment of all GSFC buildings is being conducted to identify major repair and rehabilitation tasks over the next 25 years. Examples are reroofing, replacement of air conditioning systems, and resurfacing of roads and parking lots. The frequency and scope are predicted from manufacturer's recommendations, engineering judgments, local factors, and from the results of building inspections.

An example of such a prediction is the need to replace a builtup roof after 20 years of use. A five-year plan prepared during the sixteenth year would identify this

need during the fifth year of the plan. Subsequent inspections and analyses could verify the condition of the roof and help determine the year in which the roof should be replaced.

A three-dimensional facilities matrix data base has been established to maintain past and predicted maintenance, rehabilitation, and replacement requirements. The three axes are the building systems, year action should be planned, and the cost. This matrix is a microcomputer-based dBase III+ application. Reports can be generated by year, by categories, by buildings, and by fund source; and can also provide status. Summary cost and trend analysis can also be provided. The matrix will permit the development of accurate budget requirements over the next 25 years and detailed planning of spending priorities as funding is received.

Future plans include incorporating the Wallops Flight Facility data base.

Contact: Pradeep Sinha
Code 290

Sponsor: Management Operations Directorate

Mr. Pradeep Sinha, Assistant Chief of the Plant Operations and Maintenance Division, is responsible for directing management and engineering evaluations of the physical plant and for developing maintenance and operating programs. He is also a registered professional engineer with an MS in industrial engineering. Mr. Sinha has earned the Astronaut's Special Achievement Award during his eight years at Goddard.

NASA PROPERTY DISPOSAL MANAGEMENT SYSTEM

At the 18th Annual Supply and Equipment Management Conference, held in October 1985, Goddard Space Flight Center (GSFC) was asked to take the lead in developing a standardized, automated property disposal management system. The details of the plan, cost estimate, and project schedule were presented at the Supply and Equipment Management Officers' meeting held at the Marshall Space Flight

Center on April 22-25, 1986, and approved for implementation as an Agencywide system. GSFC has a fully automated property disposal management system that interfaces with the National Aeronautics and Space Administration (NASA) Equipment Management System (NEMS) and the General Services Administration (GSA). Therefore, this system was chosen as the baseline for development of the standardized system.

The objective of the standardized disposal system, named the NASA Property Disposal Management System (NPDMS), is to provide NASA with an Agencywide automated disposal management system to support operational requirements for the reutilization and disposal of excess personal property no longer required by the Center or contractor. The NPDMS will track NASA-owned property through the disposal process via an on-line system.

The NPDMS will be capable of determining the appropriate time to generate the necessary disposal documents based on dollar value and condition code; to generate transactions; and to effect direct updates to other related systems (i.e., NEMS), most of which are currently processed manually.

The NPDMS will eliminate the existing reference and cross-reference files that are used to control the current processes, and replace them with an ad hoc inquiry capability in an on-line environment. The reduction of paperwork will also be accomplished by the computer-generated transactions, excess pickup documents, magnetic tapes, and reports to GSA and to the Defense Reutilization and Marketing Office.

The NPDMS will provide a variety of reports for monitoring the excess process. Information on status, quantity, dollar value, dispositions, and property category (e.g., precious metal, hazardous materials, artifacts, and exchange/sale) will be available to management for use in the analysis and control of the excess process. The data base will provide easier access to screen for excess equipment.

The Critical Design Document was prepared in August 1987 and reviewed by Headquarters personnel and other centers on August 25-27, 1987, at GSFC. The alpha testing for this system was then scheduled to be conducted at GSFC in December 1988. Lewis Research Center has volunteered to conduct the beta test, scheduled for April 1989.



The GSFC NPDMS Development Team is responsible for implementing this system Agencywide and will maintain the system throughout its life cycle. Implementation is planned to begin in July 1989.

Contacts: Connie S. Higgs and Maureen L. Barber
Code 235

Sponsor: Logistics Management Division

Ms. Connie S. Higgs is the Center Development Project Manager of the NASA Property Disposal Management System (NPDMS). She is involved in the design, development, and implementation of a NASA-wide PDMS. Ms. Higgs has been with Goddard for almost 19 years.

Ms. Maureen L. Barber is responsible for the development and implementation of the NASA Property Disposal Management System to ensure it receives sufficient resources. She works with the Automated Data Processing support contractor, the Center representatives of the Interinstallation Project User Committee, and Headquarters management. Ms. Barber has 20 years of experience at Goddard.

COMPUTER TRANSLATORS IN THE FACILITIES ENGINEERING DIVISION

The Facilities Engineering Division (FED) is presently using a Computervision CADD-4X minicomputer-based Computer-Aided Design and Drafting (CADD) system to maintain as-built drawing files of floor plans of each building at Goddard Space Flight Center (GSFC). These drawings are required by FED design engineers as bases for construction drawings to accommodate changing GSFC facilities needs. The FED also possesses two personal computers (PCs) running Computervision's Personal Architect CADD software, and is in the process of acquiring additional PCs. These PCs will be used on a daily basis by FED engineers to modify floor plan drawings as required for construction. The as-built drawing files are loaded down to the PC, modified, and loaded back up for storage until required again for modification. Due, however, to the fact that externally contracted architectural/engineering (A/E) firms are submitting

drawings designed on PC CADD systems, an issue of compatibility has arisen. The FED must maintain compatibility between its CADD systems and vendors' CADD systems to avoid manual reentry of data. Several methods of translation have been investigated.

One method of data transfer investigated uses the Initial Graphics Exchange Specification (IGES). IGES uses the concept of a neutral file to and from which other systems data base files can be converted using pre and postprocessors. Tests converting small files proved to be successful; however, practical applications yield considerably larger files. During the conversion of large data bases, approximately 30 percent of the data was lost.

The second method of translation was tested as a result of an A/E firm's submittal of 252 contract drawings designed on an AutoCAD PC CADD system. Like the IGES, the AutoCAD Data Exchange Format (DXF) also establishes a common data format for the exchange of information between different vendors' PCs. Since the Personal Architect software also supports the DXF, the AutoCAD file was converted to the DXF, then to the Personal Architect's drawing file. From here, it was translated up to the minicomputer (CADD-4X) through a hard cable and Computervision's direct translator software package. Although the translation was more successful than that of the IGES, a drawing comparison nonetheless indicated a 15 percent loss of data.

To solve the immediate problem of the AutoCAD/CADD-4X compatibility, it was discovered that Computer-Aided Design Services, Inc. (CADSI) had developed a Graphics Data Translator (GDX) software package. The GDX provides the needed link to translate AutoCAD files directly to CADD-4X and vice versa. To conduct a test, CADSI converted the AutoCAD files (on floppy disk) to CADD-4X (on magnetic tape) using the GDX software. After loading the tapes onto the FED's Computervision system and comparing the generated drawings to the original AutoCAD drawings, only a few minor details had been lost. Further investigation led to the decision to have CADSI carry out the entire translation. This precluded the cost of an AutoCAD system, the software, and the associated manpower.

In conclusion, direct translators, for the time being, will be relied upon to provide the means of communication among FED's CADDs-4X system, its PCs, and other CADD systems. Direct translators are less expensive and less time consuming to use when compared to manual data-reentry procedures required to accommodate the CADDs-4X format. Once in the CADDs-4X format, these files can be easily manipulated by FED design engineers to reflect actual "field" conditions as altered during construction. They are also readily accessible to be modified by FED engineers for future renovations and expansions of the existing facilities. The CADD system allows the FED to perform its activities more efficiently to help maintain an essential environment at GSFC, and, in turn, assists the GSFC community toward its goals. The FED will continue to monitor the progress of neutral file translators. In the event that near 100 percent success is achieved, the FED will likely adopt this method as its standard for CADD data base translation.

Contact: Deanna Bentz Courtillet
Code 271

Sponsor: Internal

Ms. Deanna Bentz Courtillet has a BS degree in civil engineering.

Index

<i>Author</i>	<i>Page</i>	<i>Author</i>	<i>Page</i>
Alcorn, Dr. George	11	Fischer, James R.	83
Alemán, Roberto M.	123	Flatow, Fred	8
Allen, Dr. John E., Jr.	277	Flom, Dr. Yury	122
		Florez, José M.	44
Baker, Dr. Daniel N.	248	Forrest, Kathrine A.	68, 69, 70
Barber, Maureen L.	290	Foster, James L.	148
Benner, Dr. Steve M.	45	Frey, Dr. Herbert V.	135
Bertsch, Dr. David L.	235	Frisch, Harold P.	97
Bindschadler, Dr. Robert A.	148	Fung, Dr. Inez	152
Bliven, Dr. Larry F.	207		
Bohn, Charles G.	100	Garvin, Dr. James B.	140
Bonavito, Dr. N. L.	132	Gasser, Max G.	25, 28, 29, 30
Bosworth, John M.	135	Geller, Dr. Marvin A.	164
Brace, Larry H.	251	Gezari, Dr. Daniel Y.	227
Brasunas, Dr. John C.	281	Glaccum, William	219
Breon, Dr. Susan R.	32, 34	Goldberg, Dr. Richard A.	263
Brown, Kenneth S.	145	Goldstein, Dr. Melvyn L.	269
Burlaga, Dr. Leonard F.	271	Gonzales, Luis	6
Burt, I. Joseph	127	Gordon, Scott A.	124
Busalacchi, Dr. Antonio J.	194	Goucher, Gregory W.	103, 114
		Graham, James	219
Camillo, Dr. Peter	149	Grebowsky, Dr. Joseph M.	188
Campbell, William J.	112	Green, Dr. James L.	66
Carnahan, Timothy M.	99		
Castles, Dr. Stephen H.	32, 34	Hall, Dr. Dorothy K.	148
Chan, Dr. Kwing L.	255	Harding, Dr. Alice K.	237
Chang, Dr. Alfred T. C.	148	Harris, Dr. Dale W.	1
Chang, Jy-Tai	169	Harris, Dr. Isadore	255
Chao, Dr. Benjamin Fong	138	Haug, Dr. Edward J.	97
Chou, Dr. Ming-Dah	176	Herman, Dr. Jay R.	281
Choudhury, Dr. Bhaskar	152	Herr, Denver	58
Chu, Dr. Huai-Pu	122	Hibbard, William D.	10
Comiso, Dr. Josefino C.	200	Higgs, Connie S.	290
Connerney, Dr. J. E. P.	257	Hilliard, Lawrence M.	73
Cosner, Charles	82	Hoegy, Dr. Walter R.	231
Costenbader, Jay	89	Hoffman, Dr. Robert A.	266
Courtillet, Deanna Bentz	291	Hoge, Dr. Frank E.	205
Curtis, Dr. Steven A.	259, 263	Hudson, Dr. Robert D.	179
		Huegel, Frederick G.	156
Desch, Dr. Michael D.	258	Hughes, Peter M.	56
Doll, C. E.	62		
Dorband, Dr. John E.	83, 85	Irons, James R.	156
Dwek, Dr. Eli	218, 219		
		Jackman, Dr. Charles H.	189
Esaias, Dr. Wayne E.	198	Jackson, Robert B.	72
Ewin, Audrey J.	39	Jagielski, James M.	96
		Jahoda, Dr. Keith	241
Fedor, Dr. Joseph V.	24	Jeletic, James F.	52, 76
Feldman, Dr. Gene Carl	212	Jhabvala, Dr. Murzy	39

Index (continued)

<i>Author</i>	<i>Page</i>	<i>Author</i>	<i>Page</i>
Johnson, Bertrand L., Jr.	198	Paczkowski, Frank N.	34
Jones, Andrew L.	99	Parker, Bradford H.	122
Jones, Jeffrey	271	Parsons, Chester L.	185, 203
		Payne, Dr. Walter A., Jr.	278
Kaiser, Michael L.	258	Pease, Philip	82
Kaye, Dr. Jack A.	181	Peteet, Dr. Dorothy M.	163
Keating, Thomas	9	Petuchowski, Dr. Sam	234
Keith, Ben	64	Pfaff, Dr. Robert F., Jr.	253
Kerber, Arlene	158		
King, Dr. Michael D.	173	Quaid, Peter	287
Koblinsky, Dr. Chester	210		
Kondo, Dr. Yoji	222	Radspinner, Charles	287
Kunde, Virgil G.	281	Reames, Dr. Donald V.	246
Kyle, Dr. H. Lee	283	Reed, Kenneth	39
		Reph, Mary G.	104
LaBel, Kenneth A.	119	Richards, Catherine Long	71
Lee, Dr. S. Yen	22	Rind, Dr. David	162
Lepping, Dr. Ronald P.	271	Rodriguez, G. Ernest	23
Lerner, Dr. Bao-Ting	130	Rogers, Lonnie J.	75
Levine, Dr. Elissa	158	Rood, Dr. Richard B.	181
Loewenstein, Robert	219	Rossi, Laurence C.	204
Lu, Dr. Yun-chi	82	Rossow, Dr. William B.	170
		Ruley, LaMont	76
Mack, Marilyn	82	Schatten, Dr. Kenneth	232
Mather, Dr. John C.	4	Schmidlin, Francis J.	186
Mattson, Roger	3	Schopf, Dr. Paul S.	192
Mayr, Dr. Hans G.	255	Serlemitsos, Dr. Aristides T.	32, 34
McCabe, Michael	48	Shirah, Greg	78
McClain, Dr. Charles R.	197	Short, Nicholas M., Jr.	112
Mecherikunnel, Dr. Ann T.	229	Silverberg, Dr. Robert	219, 234
Meeson, Dr. Blanche W.	106	Simpson, Dr. Joanne	164
Miller, Warner H.	117	Sinha, Pradeep	289
Montgomery, Dr. Harry	154	Slavin, Dr. James A.	262
Moore, Dr. Marla H.	276	Smith, I. Steve, Jr.	49
Moseley, Dr. Harvey	219, 234	Spaniol, Dr. Craig	43
Mott, Brent	39, 41	Spiegel, Douglas R.	93
		Spinhirne, Dr. James	177
		Stack, Jeannette B.	21
Nava, Dr. David F.	279	Stief, Dr. Louis J.	278, 280
Niedner, Dr. Malcom B., Jr.	260	Stochaj, Steve	240
Noll, Carey E.	109	Streitmatter, Dr. Robert	240
Nuth, Dr. Joseph A.	276	Strong, Dr. James P.	80
		Suarez, Dr. Max J.	192
O'Brien, Maureen	129	Susskind, Dr. Joel	190
O'Keefe, Dr. John A.	282	Sutton, Dr. John F.	43
Oakes, Arnold G.	102	Swank, Dr. Jean H.	244
Olsen, Lola M.	104	Swanson, Theodore D.	47
Ormes, Dr. Jonathan F.	238	Szczur, Martha R.	89
Özel, Dr. Mehmet E.	238		

<i>Author</i>	<i>Page</i>
Taylor, Dr. Patrick T.	142
Thieman, Dr. James R.	108
Thomas, Hans	130
Thomas, Valerie L.	65
Tilton, Dr. James C.	94
Tong, G. Michael	88
Torres, Dr. Arnold L.	184
Travis, Dr. Larry	253
Treinish, Lloyd A.	103, 114
Trombka, Dr. Jacob I.	221
Truskowski, Walt	86
Tueller, Dr. Jack	214
Turkiewicz, Jan M.	168
Valett, Jon D.	92, 93
Valett, Susan Ray	92
Van Sant, J. Timothy	121
Viens, Michael J.	120
Volz, Dr. Stephen M.	34
Vranish, John M.	35, 37
Walsh, Dr. Edward J.	203, 209
Warner, Brent A.	32, 33, 34
Wasilewski, Dr. Peter	273
Webb, Dr. L. Dale	50
Weidow, David A.	78, 93
Wetzel, Dr. Peter J.	169
Wolff, Dr. Charles L.	231
Woodhouse, Christopher E.	117
Zillig, David J.	54, 59

Managing Editor:

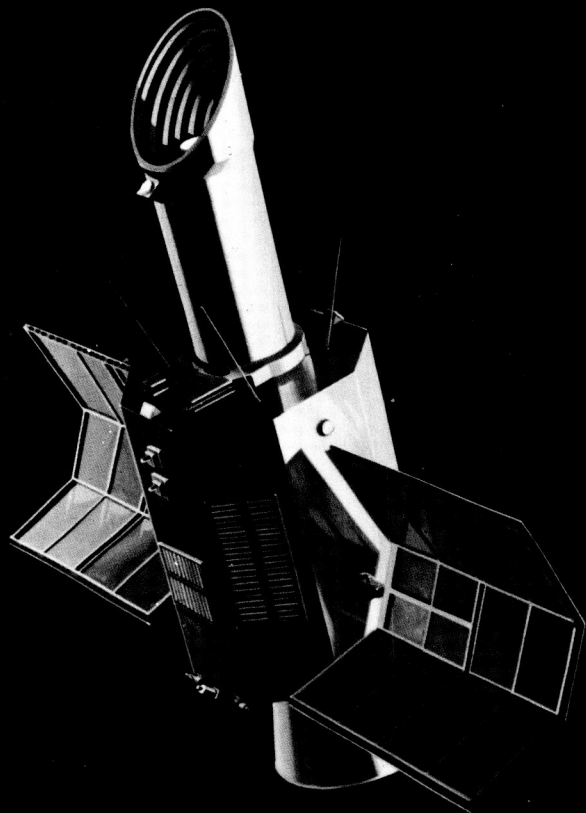
Gerald Soffen

Editors:

Gene Guerny
Karen Moe
Steven Paddack
Walter Sullivan

prepared by Engineering and Economics Research, Inc.

The International Ultraviolet Explorer (IUE), known as "the most productive telescope in the solar system," has been in geosynchronous orbit since 1978. Its longevity is due to the foresight of Goddard Space Flight Center scientists and engineers. A joint program of the United States, Great Britain, and the European Space Agency, the IUE is operated 24 hours a day, providing astronomers with opportunities to obtain astronomical spectra in the ultraviolet range.



NASA

National Aeronautics and
Space Administration

Goddard Space Flight Center
Greenbelt, Maryland 20771